frontiers | Research Topics

Advanced technologies in flow dynamics and combustion in propulsion and power, volume II

Edited by
Lei Luo, Xiao Liu, Bengt Aake Sunden and Songtao Wang

Published in
Frontiers in Energy Research

ISSN 1664-8714
ISBN 978-2-83251-040-7
DOI 10.3389/978-2-83251-040-7

About Frontiers

Frontiers is more than just an open access publisher of scholarly articles: it is a pioneering approach to the world of academia, radically improving the way scholarly research is managed. The grand vision of Frontiers is a world where all people have an equal opportunity to seek, share and generate knowledge. Frontiers provides immediate and permanent online open access to all its publications, but this alone is not enough to realize our grand goals.

Frontiers journal series

The Frontiers journal series is a multi-tier and interdisciplinary set of open-access, online journals, promising a paradigm shift from the current review, selection and dissemination processes in academic publishing. All Frontiers journals are driven by researchers for researchers; therefore, they constitute a service to the scholarly community. At the same time, the *Frontiers journal series* operates on a revolutionary invention, the tiered publishing system, initially addressing specific communities of scholars, and gradually climbing up to broader public understanding, thus serving the interests of the lay society, too.

Dedication to quality

Each Frontiers article is a landmark of the highest quality, thanks to genuinely collaborative interactions between authors and review editors, who include some of the world's best academicians. Research must be certified by peers before entering a stream of knowledge that may eventually reach the public - and shape society; therefore, Frontiers only applies the most rigorous and unbiased reviews. Frontiers revolutionizes research publishing by freely delivering the most outstanding research, evaluated with no bias from both the academic and social point of view. By applying the most advanced information technologies, Frontiers is catapulting scholarly publishing into a new generation.

What are Frontiers Research Topics?

Frontiers Research Topics are very popular trademarks of the *Frontiers journals series*: they are collections of at least ten articles, all centered on a particular subject. With their unique mix of varied contributions from Original Research to Review Articles, Frontiers Research Topics unify the most influential researchers, the latest key findings and historical advances in a hot research area.

Find out more on how to host your own Frontiers Research Topic or contribute to one as an author by contacting the Frontiers editorial office: frontiersin.org/about/contact

Advanced technologies in flow dynamics and combustion in propulsion and power, volume II

Topic editors

Lei Luo — Harbin Institute of Technology, China
Xiao Liu — Harbin Engineering University, China
Bengt Aake Sunden — Lund University, Sweden
Songtao Wang — Harbin Institute of Technology, China

Citation

Luo, L., Liu, X., Sunden, B. A., Wang, S., eds. (2023). *Advanced technologies in flow dynamics and combustion in propulsion and power, volume II*.
Lausanne: Frontiers Media SA. doi: 10.3389/978-2-83251-040-7

Table of contents

frontiers | Frontiers in Energy Research

ORIGINAL RESEARCH
published: 04 April 2022
doi: 10.3389/fenrg.2022.879534

Experimental Study on the Working Characteristics of a Pre-combustion AC Plasma Jet Igniter

Weida Cheng[1], Jinlu Yu[1,2,3], Luyun Jiang[4], Qinyu Miao[1], Lei Zhang[1] and Bingbing Zhao[1]*

[1]Aviation Engineering School, Air Force Engineering University, Xi'an, China, [2]School of Power and Energy, Northwestern Polytechnical University, Xi'an, China, [3]AECC Sichuan Gas Turbine Establishment, Mianyang, China, [4]State Key Laboratory of Laser Propulsion and Application, Department of Aerospace Science and Technology, Aerospace Engineering University, Beijing, China

A new pre-combustion AC plasma jet igniter has been designed. The pre-combustion plasma jet igniter can widen the ignition envelope for the aeroengine and reduce the power consumption of the igniter. To fully exploit the ignition efficiency of the plasma jet, experimental studies concerning the operational parameters and the discharge and arc motion characteristics have been performed. The results showed that three discharge modes were formed in the new igniter, namely, the Intermittent Breakdown Mode (IBM), the Stable Breakdown Mode (SBM) and the Stable-Intermittent Breakdown mode (S-IBM), the three different discharge modes corresponding to different arc shapes and movement processes. Moreover, the addition of kerosene readily changed the discharge state from the SBM to the IBM. The discharge state and discharge power of the igniter were affected by the working parameters. The discharge power increased with increase of the output voltage of the regulator, and an increase in the air supply affected the discharge power when the output voltage of the regulator was varied. After the addition of kerosene, the discharge power of the igniter was reduced to a certain extent, the maximum reduction being up to 47.7%.

Keywords: pre-combustion igniter, plasma, discharge characteristics, arc characteristics, discharge power

OPEN ACCESS

Edited by:
Xiao Liu,
Harbin Engineering University, China

Reviewed by:
Yingwen Yan,
Nanjing University of Aeronautics and Astronautics, China
Hui Wang,
Harbin Institute of Technology, China

***Correspondence:**
Jinlu Yu
yujinlu1@163.com

Specialty section:
This article was submitted to Advanced Clean Fuel Technologies, a section of the journal Frontiers in Energy Research

Received: *19 February 2022*
Accepted: *21 March 2022*
Published: *04 April 2022*

Citation:
Cheng W, Yu J, Jiang L, Miao Q, Zhang L and Zhao B (2022) Experimental Study on the Working Characteristics of a Pre-combustion AC Plasma Jet Igniter. Front. Energy Res. 10:879534. doi: 10.3389/fenrg.2022.879534

1 INTRODUCTION

Owing to their excellent characteristics, plasma sources have been widely studied and applied in the fields of aviation (Starikovskiy and Aleksandrov, 2013), and industrial processing (Korzec and Nettesheim, 2020) as first proposed by Langmuir in 1923. The plasma jet is particular is studied in the field of aeroengine ignition (Kang et al., 2018), because of its high energy and richness in active particles (Ju and Sun, 2015; Yu et al., 2018), which can widen the ignition boundary and shorten the ignition delay time (Matveev et al., 2005; Wang et al., 2019).

Scientists worldwide have undertaken comprehensive studies on plasma ignition technology and obtained in-depth information on topics such as the ignition mechanism and model testing of igniters (Starikovskaia, 2006; Leonov et al., 2010; Ombrello et al., 2010). Wagner et al. (1989) defined the concept of the plasma jet energy density, and performed much research on the plasma assisted ignition mechanism and flame characteristics. It was pointed out that the plasma could significantly accelerate the chain reaction of fuel and change the chemical reaction pathway of conventional combustion ignition. The studies of Kosarev et al. (2016) revealed that the influence of a non-equilibrium plasma on the ignition of a C_2 hydrocarbon fuel is sustained

mainly by the electronic collision products O and H atoms, and by hydrocarbon radicals in the discharge and afterglow; the main mechanism of these active substances is the electronic collision dissociation of fuel and oxygen. Yin et al. (2013) measured the temperature and OH concentration by a no-spark discharge (NSD) in a rectangular quartz reactor. The results show that H_2 collides with electrons or excited state N_2, which lead to the aggregation of H atoms and a reduction in the ignition temperature by about 200 K. Kim et al. (Kim et al., 2011) discussed the influence of the fuel inlet at Mach = 2.0 on the ignition of the plasma torch. The results showed that the high-temperature plasma may be used as an ignition source and as a flame stabilizer to ignite a fresh fuel mixture; also, it was found that the combustion inlet had little affection on the combustion performance. Billingsley et al.(Billingsley et al., 2005) performed an experiment which was based on traditional plasma ignition technology, and injected kerosene obliquely into a plasma jet; thereupon, kerosene was atomized and then ignited by the plasma jet. The results showed that this structure was conducive to atomization of and ignition of the kerosene. Matveev et al. (Matveev et al., 2010) described the concept of a plasma nozzle and presented a variety of configurations of plasma igniter and fuel nozzle, which provided a new approach for reducing electrode ablation and energy consumption of the igniter.

Kwonse and Dooseuk conducted a comparative study in relation to the thermodynamic combustion reaction processes of arc and jet plasmas (Kwonse and Dooseuk, 2018). It was found that the jet plasma had great advantages over the arc plasma in terms of the reaction time for combustion, the plasma volume, the energy and transient temperature change, especially in the case of lean combustion. The advantages of the plasma jet were confirmed, thus providing some support for undertaking experiments on plasma jet ignition technology in the combustor model.

On the basis of current theories, plasma jet ignition has been applied to various combustor models. In the conventional turbofan engine combustor model, compared with the conventional spark ignition technology, the plasma jet ignition technology can greatly broaden the ignition boundary and shorten the ignition delay time. Meanwhile, the ignition delay time is positively correlated with the inlet temperature of the combustor (Wang et al., 2019). In the model of the ramjet combustor with a V-shaped flame holder, the ignition delay time is significantly shortened for a wide range of residual gas coefficients compared with the spark ignition technology, and the ignition delay time is positively correlated with the arc current of the igniter (Zhao et al., 2020). From oil rich to oil lean, the ignition delay time first decreases and then increases with increase of the residual gas coefficient. In extreme cases (relatively oil lean or oil rich), the ignition delay time increases greatly (Zhang et al., 2018). In this research, the feasibility and superiority of plasma jet ignition were verified by an experimental study of the combustor model.

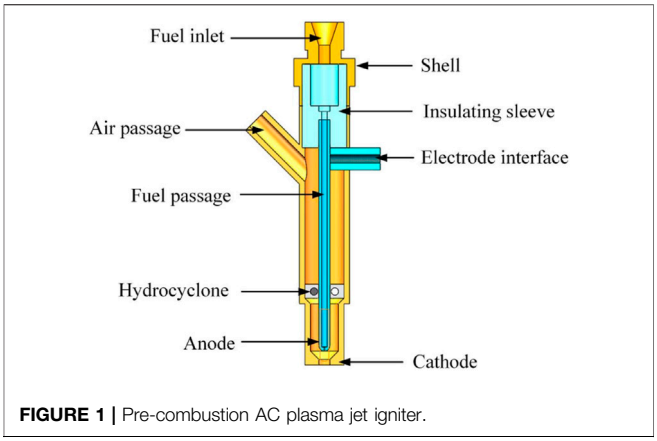

FIGURE 1 | Pre-combustion AC plasma jet igniter.

At present, the plasma jet igniter used in aero-engine ignition is basically powered by DC power supply. DC power supply can increase jet energy by increasing the arc current, but it will cause rapid erosion of the electrode and reduce electrode life (Takita et al., 2007). At the same time, larger and heavier airborne power supply is needed to provide additional arc current. It is not conducive to the promotion and application of plasma jet igniter at the current stage. In order to reduce the igniter power without affecting the injection energy, on the basis of the traditional plasma jet igniter with air as working medium, AC power supply is used to drive gliding arc discharge. Gliding arc plasma has the advantages of balanced plasma and unbalanced plasma (Fridman et al., 1999), which can be used as a moving ignition source (Gao et al., 1999), and at the same time, it has less electrode ablation (Naville et al., 1905). Kerosene is used as a pre-combustion fuel to form a new type of pre-combustion AC plasma jet igniter. Compared with the igniter which uses methane as the pre-combustion fuel (Huang et al., 2018), kerosene is the own fuel of the existing aircraft, which is easy to use. In order to fully understand the pre-combustion AC plasma jet igniter, this passage will focus on the working characteristics of the igniter, which lays the foundation for the subsequent combustor model ignition experiment.

2 EXPERIMENTAL

2.1 Pre-combustion AC Plasma Jet Igniter

The self-designed pre-combustion AC plasma jet igniter consists of three units, that is an air supply unit, a fuel supply unit, and a conductive system. The structure is illustrated in **Figure 1**. In the air supply unit, air flows into the igniter through the air channel at the side of the shell, which is then impacted by the hydro-cyclone. Next, the air generates a cyclone, which is ejected from the converging section of the igniter outlet. In the fuel supply unit, kerosene is delivered to the igniter via the fuel inlet on the shell, by the insulating sleeve which flows into the fuel channel in the anode, then ejected from the hole because of the pressure differential. Finally, kerosene is atomized forming a spray of fine droplets. In the conductive system, the electrode interface touches the anode by the electrode sleeve and connects to the high voltage

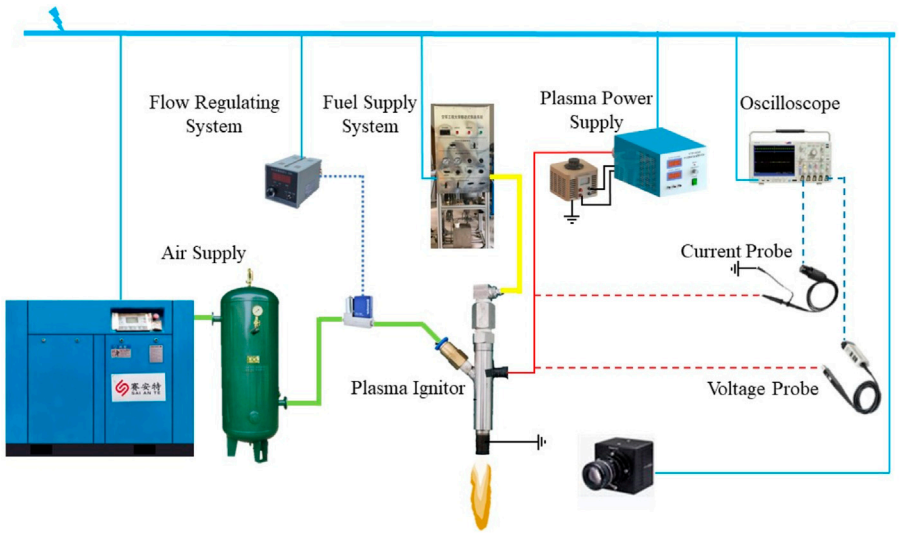

FIGURE 2 | Experimental system for studying the discharge characteristics of the pre-combustion plasma jet igniter.

output of the power source. The bottom of the shell which serves as the cathode is connected to ground. The minimum diameter of the igniter cathode is 14 mm, and the maximum diameter is 18 mm. The size of the igniter cathode ensure that the igniter can be used for subsequent ignition experiments in various combustion chambers. The diameter of the igniter outlet is 4 mm, the diameter of the anode is 4 mm, and the minimum discharge gap between the electrodes is 3 mm. After the igniter has been energized, the high voltage will form a powerful electric field which is intensified between the anode and cathode and when the electric field intensity increases to a certain level, the air and the kerosene-air mixture will break down and form the arc. When the fuel inlet opens, with the three systems acting in unison, fuel and air are mixed at the igniter outlet to form an oil-gas mixture, which is ignited by the electric arc, where upon a pre-combustion plasma jet is formed under the action of swirling flow, hence the combustible mixture in the combustion chamber is ignited.

2.2 Experimental System of Discharge Characteristics

The experimental system for studying the discharge characteristics of the plasma igniter is shown in **Figure 2**. Air is supplied by an air compressor, and the pressure is regulated by the gas cylinder valve. The air is dried by an air dryer, then the air flows through the flow regulating valve which is controlled by the D08-1F mass flow control meter, finally flowing into the air channel of the igniter. The power of the igniter is supplied by the CTP-2000KP power unit. The maximum power output is 1 kW, which is lower than the power of the DC plasma source. The output power of the source can be changed by changing the voltage of the matched voltage regulator. The fuel supply system is self-designed and portable and can control automatically the fuel flow. The precision of the fuel supply unit can reach 0.001 L/min; control of fuel delivery is via an on-off solenoid valve. The oscilloscope used was a Tektronix 4104B unit. The voltage signal was monitored by a Tektronix P6015A high voltage probe and the current signal was detected by a Tektronix TCP0030 AC/DC dual purpose current probe.

3 RESULT AND DISCUSSION

3.1 Discharge Characteristics of the Pre-combustion AC Plasma Jet Igniter

The discharge characteristics of the igniter refer in the main to the variation in the characteristics of the voltage and electric current responses of the igniter with time and as a function of other variables, these characteristics reflecting the evolutionary changes in the working power, discharge stability, voltage, and electric current of the igniter.

3.1.1 Influence of Working Parameters on the Discharge State

In the absence of kerosene, the voltage and current waveforms of the igniter discharge are measured under different regulation voltages (U_a = 40, 80, 120, 160, 200, 240 V) and different igniter air supply rates (W_a = 10, 20, 30, 40, 50, 60 L/min). It was found that there were three different discharge states for the igniter under the different voltage and igniter air supply regimes. They are Stable Breakdown Mode, Intermittent Breakdown Mode and Stable-Intermittent Breakdown Mode.

(1) Stable Breakdown Mode

For the voltage regulator U_a = 240 V, the air supply W_a = 10 L/min, and the discharge power of 276.0 W, the discharge characteristics of igniter are presented in **Figure 3**, in which **Figure 3A** is a macroscopic image of the voltage and current

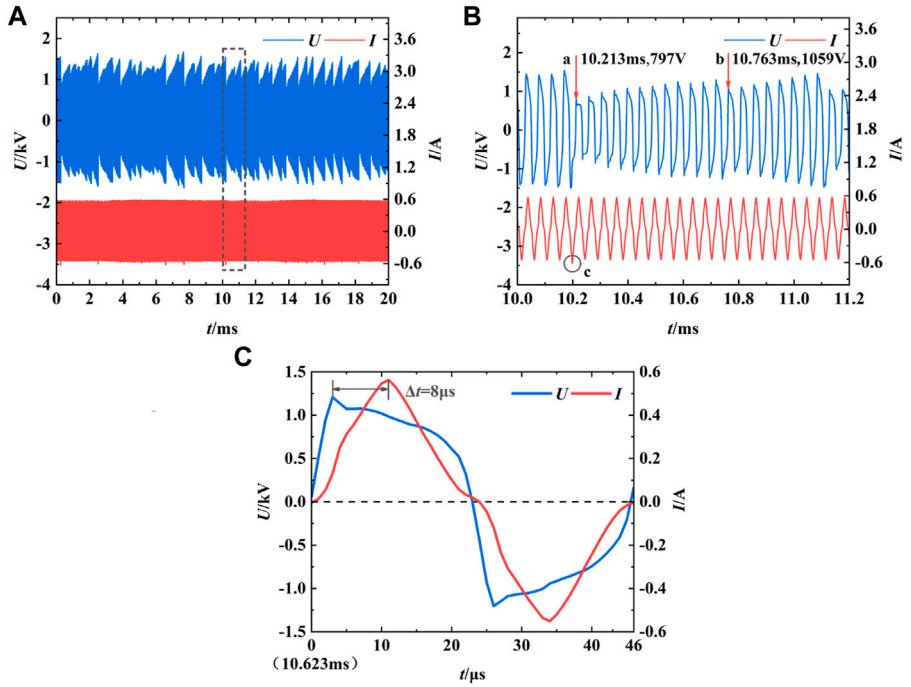

FIGURE 3 | Discharge characteristics for the igniter at U_a = 240 V and W_a = 10 L/min. **(A)** Macro waveform of igniter discharge voltage and current. **(B)** Local waveform of igniter discharge voltage and current. **(C)** Voltage and current waveforms for a single discharge cycle.

waveforms; **Figure 3B** is an enlarged image of the gray box in **Figures 3A,C** is a voltage and current waveform in a single cycle.

From the macroscopic viewpoint of the discharge voltage and current waveforms of the igniter, the voltage waveform is regular and zigzag, and revealing, on the whole, periodicity in the change trend. The voltage is between −2 and 2 kV, and the current waveform does not fluctuate abruptly. The current range is between −0.6 and 0.6 A, and there is no particularly prominent peak. The main reason for this is that the dielectric property between the two electrodes changes after the igniter breaks down, and only a low voltage is needed to maintain the existence of the discharge channel when the arc persists. Even when the arc is extinguished, given the lifetime of charged particles is very short (ps order) (Itikawa, 2007), compared to the lifetime of excited and meta-stable particles is (μs and even ms order) (Korolev et al., 2011; Zhao et al., 2014), the gap between the electrodes is full of excited and meta-stable particles, and the conductivity of electrode gap is enhanced. In the case of the time duration for a short-lived arc, due to the existence of a similar "memory effect", only a relatively low voltage is needed to break down the discharge again to generate the arc, so the peak voltage is small.

In **Figure 3B**, it can be seen that the voltage peak obeys a law of whereby the voltage increases gradually from a small value and then there is a reversal in the voltage response which then decreases rapidly. The positions indicated by arrows at **a** and **b** represent the initial voltage peak in a particular change period, and the region between **a** and **b** is the gliding period of the arc, which has a period of 0.55 ms. The starting voltage peak at **a** is 797 V, the previous peak at a was 1541 V, a value which is 744 V less; the starting voltage peak at **b** is 1059 V, and the previous peak at **b** was 1296 V, a value which is less by 237 V. It can be concluded that for different periods of change, although the rules governing the changes in the peak voltage responses are consistent, the starting peak voltages still have some differences, and the ending peak voltages for the previous period are different from the starting peak voltages for the next period. In going from **a** to **b**, the peak voltage rises slowly, while the peak current basically remains unchanged. At this stage, the increase in the peak voltage is due to the elongation of the arc caused by the breakdown between the two electrodes of the igniter under the action of airflow. To maintain the arc, the voltage between the two electrodes of the igniter should increase with the elongation of the arc within the range of the maximum output power that can be supplied by the power supply, in order to maintain the electric field strength of the arc and further enable the arc to continue to develop. At the same time, the arc plays a role similar to that of the resistance of the arc. The current passes through the arc, and the current only depends on the voltage between the two electrodes of the igniter and the resistance value of the arc. Under the joint action of the two, the final peak value of the current is basically unchanged. The last voltage peak at **a** corresponds to a large peak current, as shown by the circle at **c**. The reason for the peak current appearing at this point is that the arc has fully developed. After the voltage increases a certain extent, a new arc is generated by breakdown at the shortest electrode gap, and two arcs exist at the same time, so a prominent peak in the current response is observed (Du, 2015).

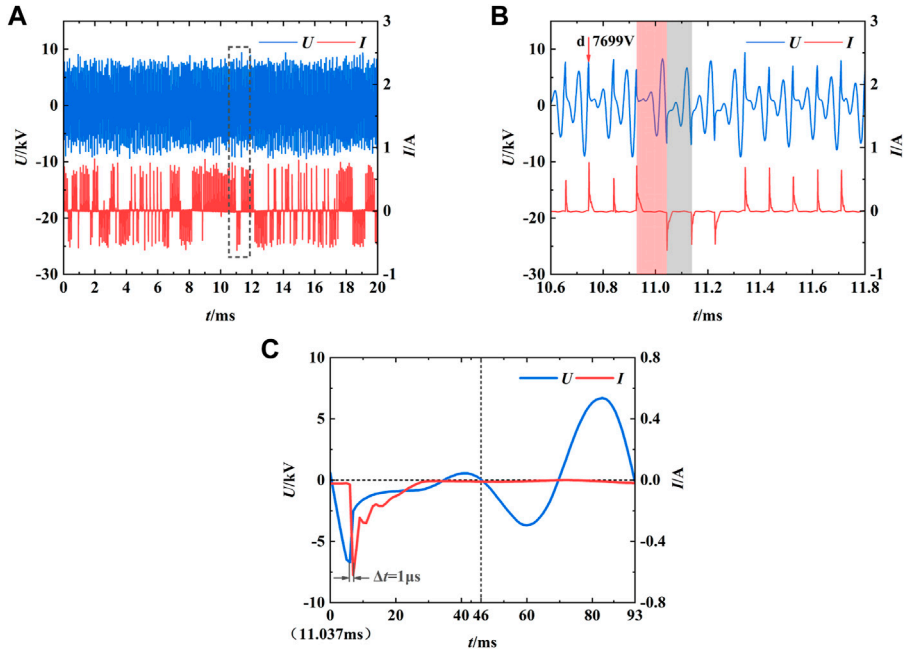

FIGURE 4 | Discharge characteristics of igniter when U_a = 40 V and W_a = 60 L/min. **(A)** Macro waveform of igniter discharge voltage and current. **(B)** Local waveform of igniter discharge voltage and current. **(C)** Voltage and current waveforms in a single discharge cycle.

Taking 10.623 ms in **Figure 3B** as the initial point and taking one of the voltage and current cycles for analysis, as shown in **Figure 3C**, it can be concluded that the duration of one cycle is about 46 μs for the power frequency f_1 = 22 kHz adopted in the experiment. It can be seen that the discharge cycle after the igniter breakdown is consistent with the power cycle. At the initial stage of a cycle, with the rise of voltage, the current increases sharply. In this breakdown event, the electron avalanche process increases, and the number density of electrons in the arc and the surrounding plasma increases rapidly. Because of the Joule effect, the arc is also heated. When the voltage reaches its peak, the electrons accelerate significantly. When the voltage decreases, the current still increases and then reaches its maximum value. The change between the voltage and current is asynchronous. Under such conditions, the retardation time of the current Δt = 8 μs. This time accounts for 17.4% of the discharge cycle. Korolev (Korolev et al., 2011) attributed the "hysteresis effect" of the rise in the current after the voltage drop to a reduction in the gap resistance, which is related to the formation of cathode spots on the arc (Zhao et al., 2013). In **Figure 3C**, the voltage and current waveforms reveal periodicity, but there are still some differences with the sinusoidal patterns, which may be related to the change of conductivity and plasma impedance during the discharge (Zhang et al., 2016). It can be deduced from **Figure 3B** that the initial voltage peak of each cycle of change does not start from 0, because there is only a drop in the peak voltage, and the current always follows the voltage change with a lag time, without the current being zero for a period of time. Therefore, the arc can be viewed as always existing in the whole discharge process, and the arc is not completely extinguished at the junction of the two change cycles; there is breakdown and a new arc is generated. In contrast, the generation of a new arc and the extinction of the original arc occur almost at the same time, and then the new arc is elongated under the action of airflow, and this cycle is constantly repeating, hence the term Stable Breakdown Mode (SBM) is used as a descriptor.

(2) Intermittent Breakdown Mode

When U_a = 40 V, W_a = 60 L/min, and the discharge power is 52.4 W, the discharge characteristics of igniter are shown in **Figure 4**. In **Figure 4A**, compared with **Figure 3A**, there is a great difference between the two modes. For the same time scale, the current in **Figure 4A** no longer changes continuously in the sinusoidal waveform, but shows intermittent peaks, which are both positive and negative. The voltage waveform also does not show the regular serrated edge in **Figure 4A**. On the whole, when U_a = 40 V and W_a = 60 L/min, the voltage is concentrated between −10 and 10 kV, which is much higher than that when U_a = 240 V and W_a = 10 L/min, and the current is concentrated between −0.8 and 0.8 A, which is the same as that when U_a = 240V and W_a = 10 L/min. There are two reasons for initially comparing the differences in the voltage ranges. One is that the voltage outputs of the voltage regulator are different. According to the output characteristics of the power supply, when the power frequency is fixed, the output power for different voltage regulator values will be different, hence the respective peak voltages will be different. The second reason is that the igniter is not always in a breakdown state in accord with the current waveform. When U_a = 40 V and W_a = 60 L/min, the airflow speed would be faster,

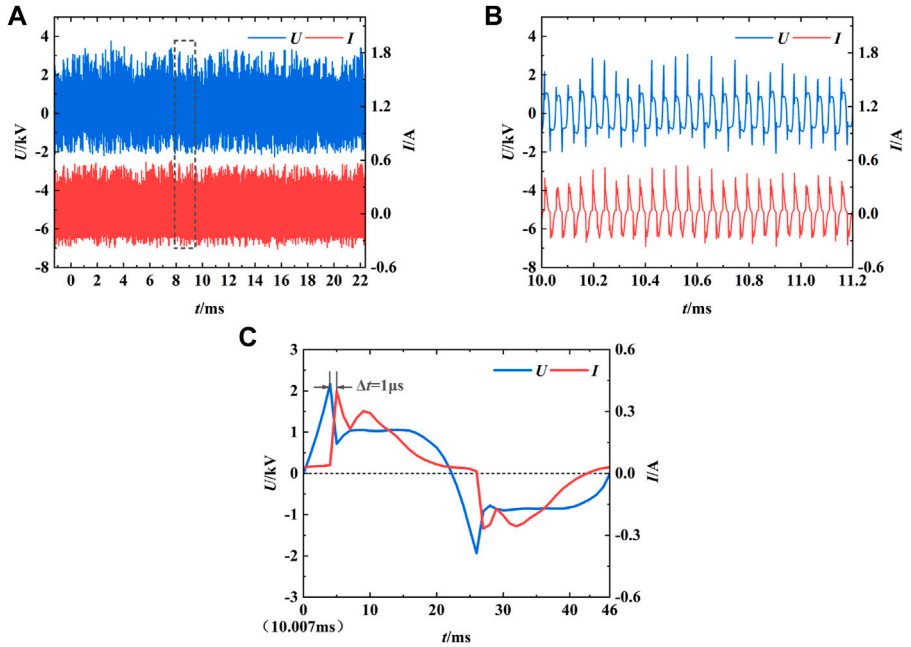

FIGURE 5 | Discharge characteristics of igniter when U_a = 120 V and W_a = 30 L/min. **(A)** Macro waveform of igniter discharge voltage and current. **(B)** Local waveform of igniter discharge voltage and current. **(C)** Voltage and current waveforms in a single discharge cycle.

and the "memory effect" after igniter breakdown would be weaker. The environment when the igniter breaks down again would be basically the same as that when igniter breaks down for the first time, thus the breakdown voltage would basically be equal.

To observe the local voltage and current waveforms clearly and to ascertain the rules which govern the changes in the discharge, it is necessary to examine the forward breakdown, and reverse breakdown discharge waveforms shown in the gray box in **Figure 4A** and amplify them to get **Figure 4B**. The position indicated by the arrow at **d** is one of the breakdown voltage peaks, and the breakdown voltage value is 7699 V, which is much higher than the values 797 V at **a** and 1059 V at **b** in **Figure 3B**. In the voltage waveform in **Figure 4B**, the increase in the peak voltage still exists in the two breakdown processes, but it is not as obvious as in **Figure 3B**; this is related to the insufficient development of voltage over the short time between the two breakdowns. In **Figure 4B**, it can be observed clearly that the current breaks down in both the forward and reverse processes. The light red color block covers the discharge period between forward breakdown and reverse breakdown, and the gray color block covers the discharge period between two adjacent reverse breakdowns. From the width of the two color blocks, it can be seen clearly seen that the discharge period for breakdown in the opposite direction is larger than that for breakdown in the same direction. The difference between the two types of discharge cycles comes from voltage commutation. On the one hand, the gray color block covers two power supply cycles. On the other hand, the red color block covers two and a half power supply

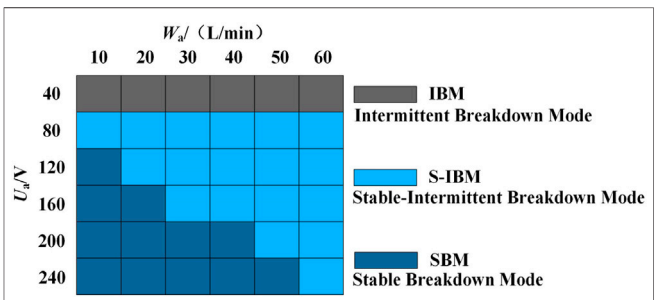

FIGURE 6 | Distribution diagram for the discharge mode under different working conditions.

cycles, so there is a difference in the discharge cycles. It can be seen from **Figure 4A** that the occurrence of the two types of discharge cycles is random, accounting for 50% each, and the discharge laws of the two types are basically consistent. **Figure 4C** shows a discharge period in the same direction as the breakdown. It can be seen that the discharge period is 93 μs, which is about equal to two power supply periods. The current also lags behind the change of voltage, but the lag time Δt = 1 μs is smaller than Δt = 8 μs in **Figure 3C**, which shows that different working parameters such as the voltage regulator voltage and the air supply of the igniter affect the lag time.

Combining (A), (B) and (C) in **Figure 4**, it can be seen that the igniter discharge mode at this time is different from the igniter discharge mode when U_a = 240 V and W_a = 10 L/min, and the current only periodically appears at the breakdown peak,

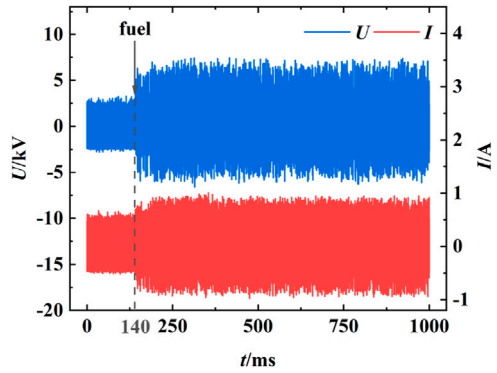

FIGURE 7 | Changes in the igniter voltage and current before and after introduction of kerosene for W_a = 30 L/min and U_a = 120 V.

indicating that the arc does not exist continuously, but periodically appears intermittently along with the igniter breakdown, hence the terminology Intermittent Breakdown Mode (IBM).

(3) Stable-Intermittent Breakdown Mode (S-IBM)

When U_a = 120 V, W_a = 30 L/min, and the discharge power is 105.1 W, the discharge characteristics are as shown in **Figure 5**. Compared with the SBM and the IBM, the peak voltage in **Figure 5A** is between that of the SBM and the IBM, and the peak current is similar for all three modes. From **Figure 5B**, the peak voltage is cluttered and there is no regularity in the change in the voltage response. The breakdown peak is prominent. In comparison with the SBM, the regularity of the current waveform is poor, and the breakdown peak is prominent. In comparison with the IBM, the current response for the positive and negative breakdown cycles alternates in the Stable-Intermittent Breakdown Mode (S-IBM). From **Figure 5C**, for a single discharge cycle, the current not only has sinusoidal waveform typical of that for the SBM and a well-defined breakdown peak as in the IBM, but also the breakdown peak is significantly larger than the sinusoidal waveform. The current delay time Δt = 1 μs is the same as that for the IBM. Given that the working conditions for this mode of operation share some of the characteristics of both the IBM and the SBM, this working condition is termed the S-IBM. In this discharge mode, when the arc continues to glide, breakdown continues to occur, resulting in an additional peak current.

In the absence of kerosene, the discharge patterns under the different working conditions as shown in **Figure 6**. When U_a = 40 V, the discharge mode of the igniter is IBM. When 10 L/min ≤ W_a ≤ 50 L/min, the discharge mode transitions from the IBM through the S-IBM to the SBM with the increase of the igniter air supply; also, the transition zone becomes wider with increase in the air supply of the igniter.

When the output voltage of the voltage regulator is low, the output power of the power supply is low, and this is not enough to provide the energy needed for the continuous

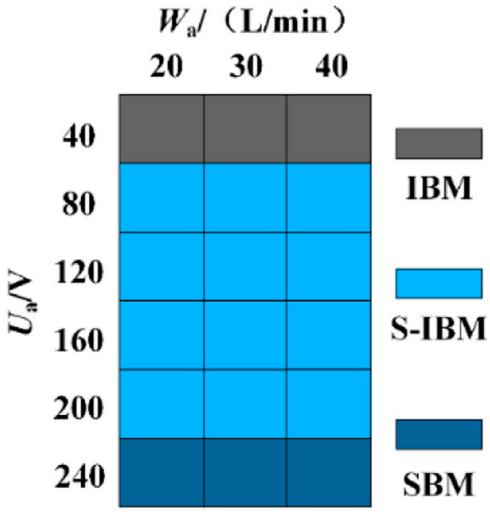

FIGURE 8 | Distribution diagrams for the discharge modes under different working conditions after introduction of kerosene.

gliding of the arc, so the IBM occurs. Under the same air supply, with increase in the voltage regulator, the output power of the power supply also increases. After breakdown, the voltage margin needed to provide elongation of the arc also becomes larger, and this condition can support the gliding of the arc for a longer distance, and in this process, gliding is accompanied by intermittent breakdown. Under the condition of a low air supply, with increase in the voltage regulator, the discharge mode can readily be changed from the S-IBM to the SBM. The reason for this is that when the air supply is relatively low, the cooling effect of the air flow on the arc is weak and it is easier to produce a local thermodynamic equilibrium (LTE) state in the plasma. The conductivity of the arc increases, the impedance decreases and the peak value of the current increases. Before the arc reaches the maximum length, the output power of the power supply can guarantee a

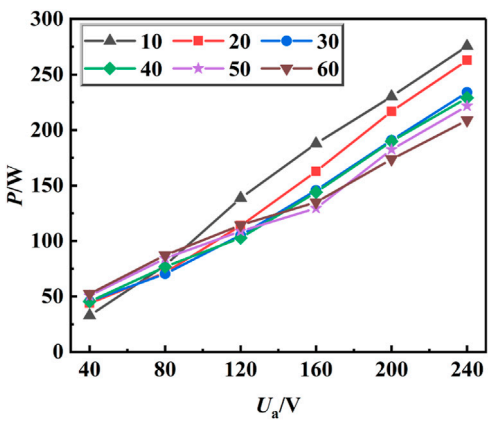

FIGURE 9 | Power diagram for the igniter under various working conditions in the absence of kerosene.

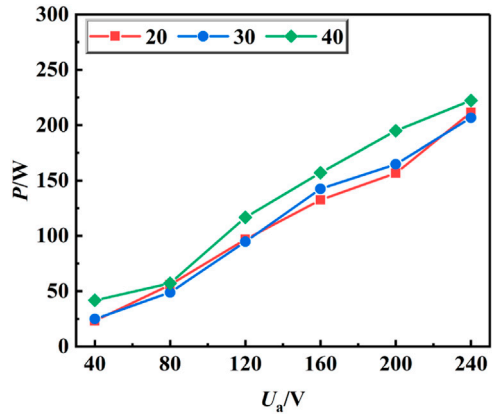

FIGURE 10 | Ignition power diagram for introduction of kerosene.

large and stable peak value for the current. With an increase in the air supply, the cooling effect of the air flow on the arc is enhanced, the outlet velocity of the igniter is accelerated, and the peak value of the sinusoidal waveform for the current is reduced. The locally balanced plasma only exists in the early stages of arc development. With the continuous increase in arc length, the arc reverts into an unbalanced plasma arc, which is more prone to intermittent breakdown, so the igniter is more likely to change from the SBM to the S-IBM; also, the smaller the output is for the voltage regulator, the smaller will be the air supply for the igniter during the transition, and this shows that the discharge mode of the igniter is determined under the joint action of the two parameters.

When W_a = 30 L/min and U_a = 120 V, the voltage and current changes before and after the introduction of kerosene are presented in **Figure 7**. It can be observed that the voltage and current amplitudes are greatly improved after the introduction of kerosene, an increase of almost 200% of that in the absence of kerosene. This result indicates that the fuel has a great influence on the discharge waveform of the igniter. It was also noted that the discharge state changed for various working conditions after the introduction of kerosene is introduced, the respective distribution diagrams for the discharge modes being shown in **Figure 8**.

Compared with the corresponding working conditions in **Figure 6**, it can be found that when U_a = 40 V or U_a = 240 V, the discharge state of the igniter remains the same as the original mode. When 40 V < U_a < 240 V, a large part of the original SBM is changed into the S-IBM. After the introduction of kerosene, the fuel passes through the discharge channel and interacts with the arc generated by of the igniter breakdown. On the one hand, kerosene is partially cracked, and this process consumes energy from the arc. On the other hand, kerosene at normal temperature takes away part of the heat generated by the arc, hence the arc is cooled somewhat, and this is equivalent to increasing the air flow. Therefore, when the power supply output is at a medium level, the discharge state of arc changes from LTE to an unbalanced state, which is reflected in the change of the discharge mode from the SBM to the S-IBM. The change of the discharge mode has a great influence on the ability of the igniter to undergo ignition, and the change of discharge mode affects the thermal effect of the plasma jet, which further affects the ignition performance of the igniter.

3.1.2 Influence of Working Parameters on the Discharge Power

The discharge power P of the igniter under different operating conditions in the absence of kerosene is shown in **Figure 9**. The overall discharge power of the igniter is in the range of 25–275 W. When the air supply is kept constant, the discharge power of the igniter increases with the output voltage of the regulator, and the response is basically linear; however, the growth rate differs for various low rates of the air; the larger the air supply, the smaller the rate of growth. The trend in the rate of growth illustrates that the output voltage of the regulator directly affects the discharge power of the igniter; to improve the discharge power output of the igniter, increase in output the voltage of the regulator would be a more direct and useful method.

When the voltage of the regulator is kept constant, the relationship between the discharge power of the igniter and the air supply of the igniter is not linear but is related to the specific regulator voltage. When $U_a \leq$ 80 V, for the same regulator voltage, the discharge power of the igniter increases as the air supply of the igniter increases, but the absolute difference between the discharge power corresponding to the various air supply rates is small. That is because when the flow rate of the air supply rate increases, the flow rate of the mixture of charged and uncharged particles accelerates, the difficulty of media breakdown increases, the ability to stabilize the arc decreases and the ability to stabilize the power supply rises, and these factors in turn bring about an increase in the power of the igniter. When the voltage of the regulator is relatively low, the maximum power output from the power supply is low, so the absolute difference between the various igniter gas supplies is small, but the relative difference is still large; for example at U_a = 40 V, W_a = 10 L/min the igniter discharge power p = 32 W; when W_a = 60 L/min, the igniter discharge power p = 52 W, a

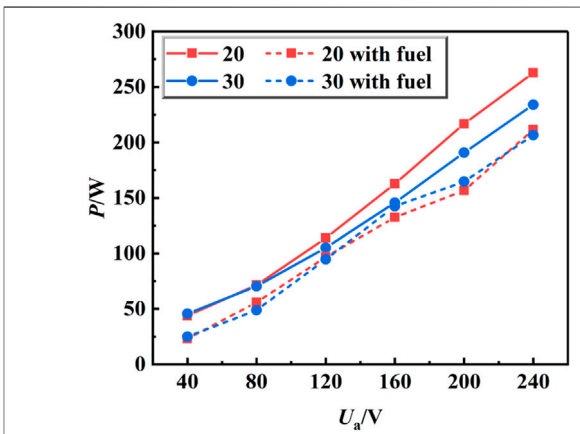

FIGURE 11 | Comparison of igniter power with and without the introduction of kerosene.

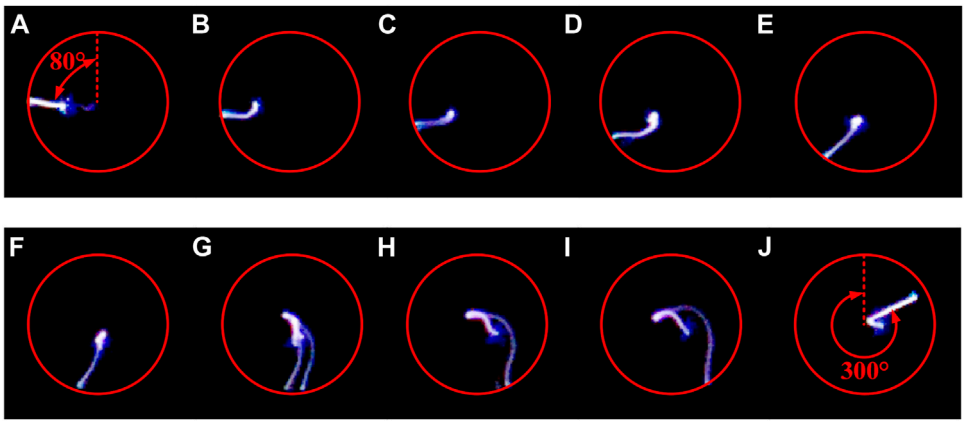

FIGURE 12 | Frontal arc movement process in one cycle when W_a = 10 L/min and U_a = 40 V. **(A)** t = 0 ms, **(B)** t = 0.05 ms, **(C)** t = 0.10 ms, **(D)** t = 0.15 ms, **(E)** t = 0.20 ms, **(F)** t = 0.25 ms, **(G)** t = 0.30 ms, **(H)** t = 0.35 ms, **(I)** t = 0.40 ms, **(J)** t = 0.45 ms.

value which has increased by 62.5%. At $U_a \geq 200$ V, the igniter discharge power decreases with increase in the air supply at the same regulator voltage, and the absolute difference is also increased compared to the situation for the lower regulator voltages; this is related to the increase in the maximum power that can be output from the power supply. For example at U_a = 240 V, the discharge power of the igniter p = 208 W at W_a = 60 L/min, and at p = 275 W at W_a = 10 L/min. This is because as the voltage of the regulator increases, the discharge mode of the igniter also changes, that is, from IBM to S-IBM and then to SBM, as can be seen from **Figure 6**. The igniter is basically in the SBM when the arc plasma is in LTE and the temperature is relatively high The larger the air supply to the igniter, the stronger the cooling effect, the more unstable the arc in the LTE state becomes, thus the lower the degree of ionization of the arc, the increase in the impedance of the arc, the reduction of the current through the arc, hence resulting in the discharge power of the igniter being reduced.

When kerosene is introduced, the discharge power response diagrams for several working conditions are presented in **Figure 10**. When the air supply for the igniter is kept constant, the trend for the discharge power remains constant the increase in the regulator voltage. The response curve for the discharge power of the igniter as a function of the voltage change of the regulator was analyzed for W_a = 20 L/min and W_a = 30 L/min, with and without the introduction of kerosene, as shown in **Figure 11**. It can be seen clearly from the graph, that after introduction of kerosene to the igniter, the discharge power of the igniter is reduced. When W_a = 20 L/min and U_a = 40 V, the discharge power is reduced from a value of 44 W in the absence of kerosene to 23 W after kerosene is introduced, the decline reaching 47.7%. At U_a = 240 V, the discharge power decreased from 262 W in the absence of kerosene to 211 W after kerosene was introduced, the decline being 19.5% this time; this result indicated that with increase of the voltage regulator,

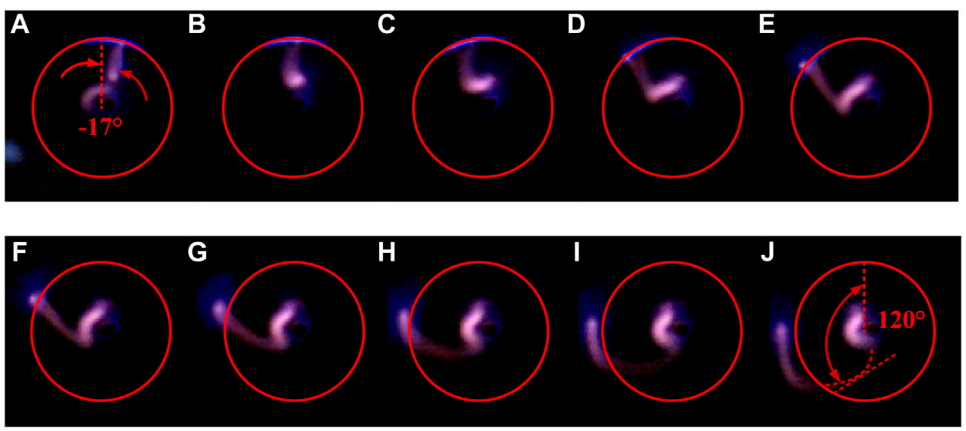

FIGURE 13 | Arc gliding process at W_a = 10 L/min and U_a = 240 V. **(A)** t = 0 ms, **(B)** t = 0.05 ms, **(C)** t = 0.10 ms, **(D)** t = 0.15 ms, **(E)** t = 0.20 ms, **(F)** t = 0.25 ms, **(G)** t = 0.30 ms, **(H)** t = 0.35 ms, **(I)** t = 0.40 ms, **(J)** t = 0.45 ms.

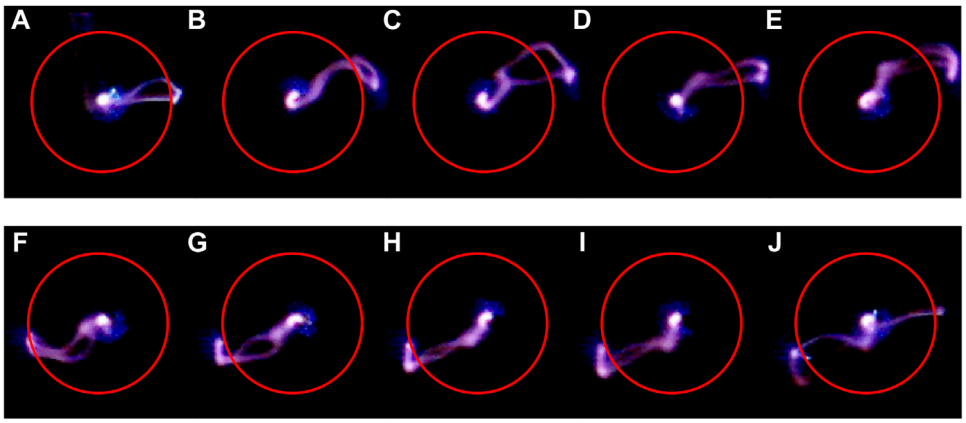

FIGURE 14 | Arc gliding process at W_a = 30 L/min and U_a = 120 V. **(A)** t = 0 ms, **(B)** t = 0.05 ms, **(C)** t = 0.10 ms, **(D)** t = 0.15 ms, **(E)** t = 0.20 ms, **(F)** t = 0.25 ms, **(G)** t = 0.30 ms, **(H)** t = 0.35 ms, **(I)** t = 0.40 ms, **(J)** t = 0.45 ms.

although the absolute value for the decrease of the discharge power increased after kerosene was introduced, the range also decreased. In general, the introduction of kerosene is beneficial to achieving a reduction in discharge power requirements for the igniter.

3.2 Arc Motion Characteristics of Pre-combustion AC Plasma Jet Igniter

To better understand the fundamental differences in the three discharge states, the characteristics of front of the arc for the three discharge states were studied and analyzed. In the experiment, the video frame settings of a high-speed camera were as follows: the filming frame rate was 20,000 fps, and the exposure time was 0.05 ms. The movement process for the front of the arc in one cycle when W_a = 10 L/min and U_a = 40 V is shown in **Figure 12**. The discharge state corresponding to this working condition is IBM, and the red circle in the figure represents the edge of the igniter outlet hole. On the whole, the arc is a brilliant white, and the arc shape is clear. Given that the focal length of the high-speed camera does not change during filming, it can be inferred that under this working condition, the arc basically slides near the same plane, and the displacement in the axial direction of the igniter is small. The arc glides in the red circle, which indicates that the arc does not cross the igniter outlet hole to the metal end face at one end of the igniter outer shell, and this further indicates that the arc moves in the same plane. When t = 0 ms, the arc is generated at the shortest gap between the two electrodes. At this time, the arc is a quasi-balanced plasma column (Du, 2015), which slides counterclockwise between the two electrodes under the swirling flow in the exit area of the igniter. The arc length is continuously lengthening, and the shape of the arc gradually becomes distorted under the action of the airflow. The longer the length of the arc, the greater the energy needed to maintain the arc and the higher the power provided by the power supply. When the output power of the power supply reaches the maximum value, the thermodynamic balance cannot be maintained, the arc changes to an unbalanced state and continues to grow until it disappears, and then a new arc is generated at the shortest electrode gap and continues a repeat of the previous process. It can be readily calculated that one gliding period for the arc is 0.45 ms, and the average gliding angular velocity of the arc in one period ω_1 = 488.89°/ms.

The gliding process for the front of the arc at W_a = 10 L/min and U_a = 240 V is shown in **Figure 13**. The discharge state corresponding to this working condition is SBM. In this discharge state, the arc is generally purplish red with high curvature, and it basically does not slide on the same plane, resulting in a fuzzy arc. In the SBM discharge stage, the arc is basically in a local equilibrium state, with a high degree of ionization for the arc, large arc energy, more energy radiating outward and of short wavelength, so the arc observed is purple in color. In the process of gliding, it can be observed clearly that the arc crosses the red circle, indicating that the arc is at one end of the igniter shell and on the metal end face of the igniter outlet, and the length of the arc is relatively long. To facilitate the analysis of the gliding angular velocity of the arc as in **Figure 13J**, the tangent line of the front end of the arc is used for measurement of the angle, in which the red arc dashed line represents the arc position and the red straight dashed line represents the tangent line at the front end of the arc, thus a value for the gliding angular velocity of the arc ω_2 = 304.44/ms may be obtained. When $\omega_2 < \omega_1$, on the one hand, because the arc exceeds the exit end face of the igniter, the airflow speed decreases, resulting in a decrease in the gliding speed of the arc. On the other hand, because the arc is very tortuous and twisted, the difficulty of gliding increases, which makes the gliding angular velocity for the arc for the SBM less than that for the IBM.

The front of the arc at different times when W_a = 30 L/min and U_a = 120 V is shown in **Figure 14**. The discharge state corresponding to this working condition is S-IBM. On the whole, the color of the arc in this state is between those for the IBM and the SBM, and the degree of distortion of the arc

shape also lies between those for the two discharge states, thus the arc is said to be in a transitional state. It can be seen that in the same filming image, basically two arcs appear, which is due to the fast air flow speed and the fast arc gliding speed, which exceeds the shutter speed, resulting in the phenomenon of multiple arcs. In addition, the dual nature of the image is also related to the accompanying breakdown under the S-IBM, and additional breakdown of the discharge occurs at adjacent times, which is shown in **Figure 14J**. Compared with the IBM and the SBM, there is no obvious period for the arc under this working condition, which is related to the mixing of breakdown modes when the igniter discharges, hence resulting in a disordered discharge.

4 CONCLUSION

This paper introduces a pre-combustion plasma jet igniter driven by AC power supply, and mainly studies the discharge characteristics and arc motion characteristics of the igniter. The igniter exhibited three discharge states which formed under different working conditions, that is, the IBM, the SBM and the S-IBM. Three different discharge states represent different energy and motion characteristics of arc, which provides a basis for the future study of igniter self-ignition characteristics and pre-combustion jet characteristics. By studying the influence of different arc states on self-ignition and pre-combustion flame formation, we can find out the most favorable discharge state for ignition, and control the discharge state to maximize ignition efficiency.

The experiment also found that after the introduction of kerosene, the discharge power of the igniter decreased to a certain extent, with a maximum decrease of 47.7%, which provided a new idea for reducing the energy consumption of the plasma igniter and changed the previous method of increasing the discharge energy to improve the ignition energy. High energy consumption is a difficult problem that restricts the practical direction of the plasma igniter in the aero-engine, so this discovery provides a new direction for realizing the application of the plasma igniter with low energy consumption and high ignition energy in the aero-engine.

DATA AVAILABILITY STATEMENT

The original contributions presented in the study are included in the article/Supplementary Material, further inquiries can be directed to the corresponding author.

AUTHOR CONTRIBUTIONS

WC: Experimental Design, Data Analysis, Writing; JY: Providing overall Ideas, Data Analysis; LJ: Experimental Data Processing, Data Analysis; QM: Experimental Data Processing; LZ: Build Experimental Systems; BZ: Guide the Experimental Operation.

FUNDING

Project supported by the National Natural Science Foundation of China (Grant Nos. 51776223, 91741112).

REFERENCES

Billingsley, M., Sanders, D., O'Brien, W., and Schetz, J. (2005). *Improved Plasma Torches for Appication in Supersonic Combustion*. Ital: AIAA Capua, 3423.

Du, C. M. (2015). *Non-thermal Arc Plasma Technology and Application*. Beijing: Chemical Industry Press.

Fridman, A., Nester, S., Kennedy, L. A., Saveliev, A., and Mutaf-Yardimci, O. (1999). Gliding Arc Gas Discharge. *Prog. Energ. Combustion Sci.* 25 (2), 211–231. doi:10.1016/s0360-1285(98)00021-5

Gao, J., Kong, C., Zhu, J., Ehn, A., Hurtig, T., Tang, Y., et al. (2019). Visualization of Instantaneous Structure and Dynamics of Large-Scale Turbulent Flames Stabilized by a Gliding Arc Discharge. *Proc. Combustion Inst.* 37 (4), 5629–5636. doi:10.1016/j.proci.2018.06.030

Huang, D. H., Yu, J. L., Wang, S. B., Li, Q. Y., and He, L. M. (2018). Experimental Investigation on Characteristics of Pre-combustion Plasma Jet Ignition. *Gaodianya Jishu* 44 (09), 3068. doi:10.13336/j.1003-6520.hve.20180828039

Itikawa, Y. (2007). *Molecular Processes in Plasmas*. Berlin Heidelberg: Springer-Verlag.

Ju, Y., and Sun, W. (2015). Plasma Assisted Combustion: Dynamics and Chemistry. *Prog. Energ. Combustion Sci.* 48, 21–83. doi:10.1016/j.pecs.2014.12.002

Kang, J., Qian, M., Li, G., Liu, S., Ren, C., Zhang, J., et al. (2018). The Effect of Methane Gas Flow Rate on the Streamer Propagation in an Atmospheric-Pressure Methane-Air Plasma Jet. *Phys. Plasmas* 25 (9), 093508. doi:10.1063/1.5046946

Kim, C.-H., Jeung, I.-S., Choi, B., Kouchi, T., Takita, K., and Masuya, G. (2011). Effect of Fuel Injection Location on a Plasma Jet Assisted Combustion with a Backward-Facing Step. *Proc. Combustion Inst.* 33 (2), 2375–2382. doi:10.1016/j.proci.2010.07.057

Korolev, Y. D., Frants, O. B., Geyman, V. G., Landl, N. V., and Kasyanov, V. S. (2011). Low-Current "Gliding Arc" in an Air Flow. *IEEE Trans. Plasma Sci.* 39 (12), 3319–3325. doi:10.1109/tps.2011.2151885

Korzec, D., and Nettesheim, S. (2020). Application of a Pulsed Atmospheric Arc Plasma Jet for Low-density Polyethylene Coating. *Plasma Process. Polym.* 17 (1), 1900098. doi:10.1002/ppap.201900098

Kosarev, I. N., Kindysheva, S. V., Momot, R. M., Plastinin, E. A., Aleksandrov, N. L., and Starikovskiy, A. Y. (2016). Comparative Study of Nonequilibrium Plasma Generation and Plasma-Assisted Ignition for C2-Hydrocarbons. *Combustion and Flame* 165 (5), 259–271. doi:10.1016/j.combustflame.2015.12.011

Kwonse, K., and Dooseuk, C. (2018). Research on the Reaction Progress of Thermodynamic Combustion Based on Arc and Jet Plasma Energies Using Experimental and Analytical Methods. *J. Mech. Sci. Technol.* 32 (4), 1869.

Leonov, S. B., Kochetov, I. V., Napartovich, A. P., Sabel'Nikov, V. A., and Yarantsev, D. A. (2010). Plasma-induced Ethylene Ignition and Flameholding in Confined Supersonic Air Flow at Low Temperatures. *IEEE Trans. Plasma Sci.* 39 (2), 781.

Matveev, I., Matveeva, S., Gutsol, A., and Fridman, A. (2005). *Non-equilibrium Plasma Igniters and Pilots for Aerospace Application*. Nevada: AIAA Reno, 1191.

Matveev, I. B., Matveeva, S. A., Kirchuk, E. Y., Serbin, S. I., and Bazarov, V. G. (2010). Plasma Fuel Nozzle as a Prospective Way to Plasma-Assisted Combustion. *IEEE Trans. Plasma Sci.* 38 (12), 3313–3318. doi:10.1109/tps.2010.2063716

Naville, A., Guye, C. E., and Guye, P. (1905). *Gas Reactions at the Temperature of the Electric Arc*. French Patent FR361827.

Ombrello, T., Won, S. H., Ju, Y., and Williams, S. (2010). Flame Propagation Enhancement by Plasma Excitation of Oxygen. Part II: Effects of O2(a1Δg). *Combustion and Flame* 157 (10), 1916–1928. doi:10.1016/j.combustflame.2010.02.004

Starikovskaia, S. M. (2006). Plasma Assisted Ignition and Combustion. *Phys. D Appl. Phys.* 39, 61. doi:10.1088/0022-3727/39/16/r01

Starikovskiy, A., and Aleksandrov, N. (2013). Plasma-assisted Ignition and Combustion. *Prog. Energ. Combustion Sci.* 39 (1), 61–110. doi:10.1016/j.pecs.2012.05.003

Takita, K., Nakane, H., and Masuya, G. (2007). Optimization of Double Plasma Jet Torches in a Scramjet Combustor. *Proc. Combustion Inst.* 31 (2), 2513–2520. doi:10.1016/j.proci.2006.07.054

Wagner, T. C., O'Brien, W. F., Northam, G. B., and Eggers, J. M. (1989). Plasma Torch Igniter for Scramjets. *J. Propulsion Power* 5 (5), 548–554. doi:10.2514/3.23188

Wang, S.-B., Yu, J.-L., Ye, J.-F., Li, G.-H., Chen, Z., Jiang, L.-Y., et al. (2019). Ignition Characteristics of Pre-combustion Plasma Jet Igniter*. *Chin. Phys. B* 28 (11), 114702. doi:10.1088/1674-1056/ab470e

Yin, Z., Adamovich, I. V., and Lempert, W. R. (2013). OH Radical and Temperature Measurements during Ignition of H2-Air Mixtures Excited by a Repetitively Pulsed Nanosecond Discharge. *Proc. Combustion Inst.* 34 (2), 3249–3258. doi:10.1016/j.proci.2012.07.015

Yu, J., He, L., Hu, Z., Zhang, Q., Xiao, Y., Jiang, Y., et al. (2018). Experimental Investigation on Ignition Limits of Plasma-Assisted Ignition in the Propane-Air Mixture. *Proc. Inst. Mech. Eng. G: J. Aerospace Eng.* 232 (9), 1685–1691. doi:10.1177/0954410017699000

Zhang, H.-L., He, L.-M., Chen, G.-C., Qi, W.-T., and Yu, J.-L. (2018). Experimental Study on Ignition Characteristics of Kerosene-Air Mixtures in V-Shaped Burner with DC Plasma Jet Igniter. *Aerospace Sci. Tech.* 74, 56–62. doi:10.1016/j.ast.2017.12.023

Zhang, S.-Y., Li, X.-S., Liu, J.-B., Liu, J.-L., Li, H.-P., and Zhu, A.-M. (2016). Dimensionless Factors for an Alternating-Current Non-thermal Arc Plasma. *Phys. Plasmas* 23 (12), 120707. doi:10.1063/1.4973223

Zhao, B.-b., Chen, G.-C., He, L.-M., Jin, T., and Jing, B. (2020). Experimental Investigation of Plasma Jet Ignition Characteristics in Kerosene-Air Mixtures. *J. Aerosp. Eng.* 33 (2), 04019113. doi:10.1061/(asce)as.1943-5525.0001108

Zhao, T.-L., Liu, J.-L., Li, X.-S., Liu, J.-B., Song, Y.-H., Xu, Y., et al. (2014). Temporal Evolution Characteristics of an Annular-Mode Gliding Arc Discharge in a Vortex Flow. *Phys. Plasmas* 21 (5), 053507. doi:10.1063/1.4876754

Zhao, T.-L., Xu, Y., Song, Y.-H., Li, X.-S., Liu, J.-L., Liu, J.-B., et al. (2013). Determination of Vibrational and Rotational Temperatures in a Gliding Arc Discharge by Using Overlapped Molecular Emission Spectra. *J. Phys. D: Appl. Phys.* 46 (34), 345201. doi:10.1088/0022-3727/46/34/345201

Conflict of Interest: The authors declare that the research was conducted in the absence of any commercial or financial relationships that could be construed as a potential conflict of interest.

Publisher's Note: All claims expressed in this article are solely those of the authors and do not necessarily represent those of their affiliated organizations, or those of the publisher, the editors and the reviewers. Any product that may be evaluated in this article, or claim that may be made by its manufacturer, is not guaranteed or endorsed by the publisher.

frontiers | Frontiers in Energy Research

ORIGINAL RESEARCH
published: 10 May 2022
doi: 10.3389/fenrg.2022.865431

Experimental Study on the Spray and Self-Excitation Oscillation Characteristics of Gas-Centered Coaxial Injectors

Lu-Hao Liu[1], *Yi-Fan Han*[2], *Shao-Qing Zhang*[1] *and Qing-Fei Fu*[1,3]*

[1]School of Astronautics, Beihang University, Beijing, China, [2]Department of Energy and Power Engineering, Center for Combustion Energy, Tsinghua University, Beijing, China, [3]Aircraft and Propulsion Laboratory, Ningbo Institute of Technology, Beihang University, Ningbo, China

The present article studies the spray and self-oscillation characteristics of liquid sheets generated by a series of gas-centered coaxial injectors. An experimental system has been built to investigate the impacts of gaseous core size and recess length on the breakup and self-oscillation features. The results reveal that the gaseous flow shows an apparent impact on the liquid sheet breakup length with a small gaseous core size. The atomization morphology shows the different patterns under varied pressure drops, and the spray angle is increased with larger recess ratios. Besides, there is a low oscillation frequency at which the self-oscillation phenomenon is activated. The smaller gaseous core sizes and shorter recess lengths could promote self-oscillation. The required liquid flow rate for the self-oscillation phenomena could be raised by increasing the gaseous flow rate, while the self-oscillation frequency hardly varies with it.

Keywords: coaxial injector, self-oscillation, recess length, spray angle, SMD (Sauter mean diameter)

OPEN ACCESS

Edited by:
Xiao Liu,
Harbin Engineering University, China

Reviewed by:
Zongjie Hu,
Tongji University, China
Qing-Lian Li,
National University of Defense Technology, China

****Correspondence:***
Qing-Fei Fu
fuqingfei@buaa.edu.cn

Specialty section:
This article was submitted to Advanced Clean Fuel Technologies, a section of the journal Frontiers in Energy Research

Received: *29 January 2022*
Accepted: *11 April 2022*
Published: *10 May 2022*

Citation:
Liu L-H, Han Y-F, Zhang S-Q and Fu Q-F (2022) Experimental Study on the Spray and Self-Excitation Oscillation Characteristics of Gas-Centered Coaxial Injectors. Front. Energy Res. 10:865431. doi: 10.3389/fenrg.2022.865431

1 INTRODUCTION

Coaxial swirl injectors are widely used in various propulsion systems, such as liquid rocket engines, internal combustion engines, and gas turbine engines (Xue et al., 2004; Li et al., 2011; Liu et al., 2013; Liu et al., 2020; Liu et al., 2021). For instance, gas–liquid coaxial swirl injectors are commonly used in the combustion chamber of liquid rocket engines for better atomization and propellant mixing performance. The general working processes of the coaxial swirl injectors could be described as follows. The swirling effect could be induced by the liquid flowing through tangential holes. It would lead to the formation of a hollow conical liquid sheet. Then, it would expose to the high velocity airflow through the annular channel (Ding et al., 2017; Liu et al., 2018; Bai et al., 2021; Chen et al., 2021). Finally, the liquid sheet would breakup into a series of tiny droplets due to the aerodynamic force that could improve the engine performance. It is noted that the airflow velocity is much larger than the liquid velocity under the typical working conditions in the thrust engine. Therefore, this article examines the breakup processes in which the airflow velocity is much larger than that of the liquid sheet.

There exists plenty of research concentrating on the spray characteristics, such as the spray angle, breakup length, and droplet size distribution of coaxial injectors by experimental observations. For instance, Gautam and Gupta (2009) found that the introduction of a parallel gaseous flow would reduce the spray angle and its impact was more pronounced with larger gaseous velocity. Liu et al. (2006) found that the liquid channel diameter would have an apparent impact on the Sauter mean diameter (SMD) distribution, especially for the relatively large gaseous flow rate conditions. Besides, they have used the Phase Doppler Particle Analyzer to measure the droplet size distribution generated by these coaxial

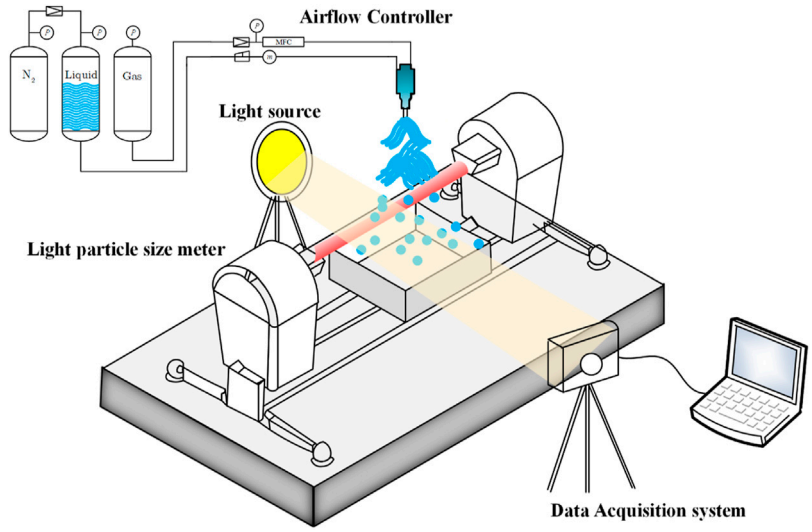

FIGURE 1 | The schematic of the present experimental atomization system.

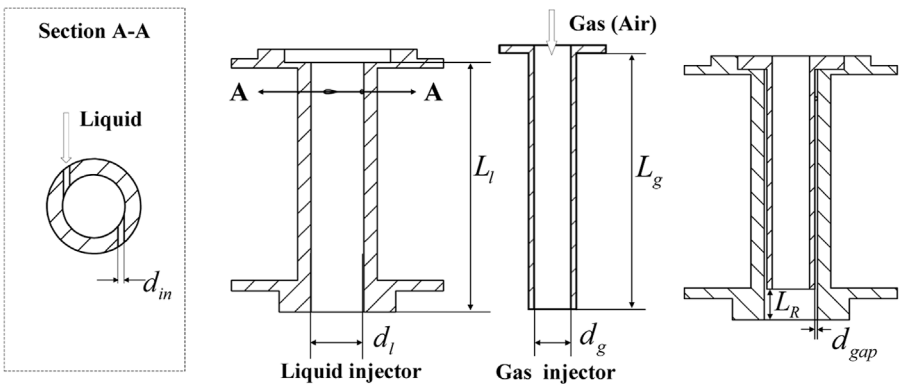

FIGURE 2 | Schematic of coaxial injectors.

TABLE 1 | The geometric parameters of the present gaseous injectors.

No. (gas injector)	L_g (mm)	L_R (mm)	d_g (mm)
G1-1	47	0	7
G1-2	47	0	6
G1-3	47	0	5
G1-4	47	0	4
G1-5	47	0	3
G2-1	40	7	7
G2-2	41	6	6
G2-3	42	5	5
G2-4	43	4	4
G2-5	44	3	3
G3-1	33	14	7
G3-2	35	12	6
G3-3	37	10	5
G3-4	39	8	4
G3-5	41	6	3

TABLE 2 | The geometric parameters of the present liquid injectors.

No. (liquid injector)	n	L_l (mm)	d_{in} (mm)
L1	2	47	1.0

injectors. It was found that the spray performance improved with larger gaseous pressure drops and tangential channel diameters. Jeon et al. (2011) investigated the atomization morphology of the gas-centered coaxial injectors. It was revealed that the spray angle and droplet size would be reduced by increasing the recess ratio. Kulkarni et al. (2010) found that the interactions between the gaseous flow and liquid sheet could induce the unstable surface waves, which could be the main source to rupture the liquid sheet. Besides, Anand et al. (2017) have studied the recess ratio impacts on the atomization characteristics of the coaxial injector. It was illustrated that the

TABLE 3 | Working conditions of the liquid and gas injectors to study the gas core size impacts.

Exp. no.	d_g	V_g (L/min)	Δp_l (MPa)	m_l (g/s)	GLR	Observation method
W-1	7	0, 20, 40, . . ., 280, 300	0.8	45.1	0–2.3839	High-speed camera
W-2	6	0, 20, 40, . . ., 280, 300			0–4.4165	
W-3	5	0, 20, 40, . . ., 280, 300			0–9.1581	
W-4	7	250			1.6555	Particle size analyzer
W-5	6	184			1.6555	
W-6	5	127			1.6555	

TABLE 4 | Working conditions of the liquid injectors to study recess ratio impacts.

Exp. no.	RR	ΔP_l (MPa)	m_l (g/s)
W-7	0	0–1.0	0–48
W-8	1		
W-9	2		

TABLE 5 | Working conditions for the different self-oscillation characteristics of the coaxial injectors.

Exp. no.	Injector no.	d_g (mm)	$\dot{V}_g$ (L/min)
Z-1, Z-4, Z-7	G1-1, G2-1, G3-1, L1	7	250
Z-2, Z-5, Z-8	G1-2, G2-2. G3-2, L1	6	184
Z-3, Z-6, Z-9	G1-3, G2-3, G3-3, L1	5	127
Z10	G1-4, G2-4, G3-4, L1	4	82
Z11	G1-5, G2-5, G3-5, L1	3	46

TABLE 6 | The working conditions of Z-1, Z-2, and Z-3 injectors.

Exp. no.	Injector n.o	RR	d_g (mm)	$\dot{V}_g$ (L/min)
Z-1	G1-1, L1	0	7	20, 40, . . ., 300
Z-2	G1-2, L1	0	6	20 ,40, . . ., 300
Z-3	G1-3, L1	0	5	20, 40, . . ., 300

variation of the recess ratio had a minor impact on the SMD value, while the spray cone angle was reduced by it.

Subsequently, it is a widely existing phenomenon that a pressure oscillation would always happen during the injector tests, which may damage the engine and reduce its performance. Therefore, the oscillation characteristics of the injector should be studied in detail. Bazarov (1996, 1998) and Bazarov and Yang (1998) have established a linear theory to describe the self-oscillation phenomena of the injector. It showed that these phenomena were determined by the liquid flow rate, gaseous flow rate, and recess length. Previous research have found that the recess ratio has a significant impact on the stability of the combustion chamber. A longer recess ratio led to a larger gas core size, which would induce self-oscillation phenomena during the atomization processes. Yang et al. (2008) revealed that there existed three flow patterns inside the coaxial injector with different recess lengths. Im et al. (2005) studied spray and acoustic signals during self-oscillation phenomena. The experimental results showed that the self-oscillation frequency could be influenced by a pressure drop and injector geometric parameters. The self-oscillation frequency could be amplified quickly with larger liquid pressure drops. They also found that larger gas–liquid momentum ratios could suppress the self-oscillation phenomena apparently (Im and Yoon, 2008). Kang et al. (2016) also investigated self-oscillation impacts on atomization features, such as spray morphology and spray angle. They found that the spray was tree shaped when the self-oscillation phenomena happened. The reasons for the distinguished difference in the spray morphology were that the self-shock oscillation phenomena influenced the breakup processes of liquid film, which induced periodic oscillation. Self-pulsation is good for the spray and could uniformize mass flux along the radius direction and increase the spray angle in the field. Besides, Eberhart et al. (2012) studied the stable boundaries of the self-oscillation phenomena of gas–liquid coaxial injectors and found that the Kelvin–Helmholtz instability could be the reason for the induction of the self-excited oscillatory waves. The abovementioned results mainly showed the impacts of flow and injector geometric parameters on the breakup and droplet size distribution features of coaxial injectors. They could provide some useful information on the physical mechanism behind these phenomena.

However, the study of gas–liquid coaxial swirl injector self-excitation oscillation phenomena mainly focused on the liquid-centered coaxial swirl injector, the experimental research about the self-oscillation phenomena of the gas-centered coaxial injectors, which are widely used in the thrust system and are relatively rare. Therefore, the present article investigates the spray and self-oscillation characteristics of a liquid sheet generated by different gas-centered coaxial injectors. The effects of the gas core size and injector geometric parameters on the abovementioned features have been investigated in detail. The whole article is organized as follows. An experimental system is built and the injector structures are introduced in **Section 2**. Then, the experimental observation results are discussed and the impacts of the recess ratio on the breakup features are highlighted in **Section 3**. Finally, the obtained main conclusions are summarized in **Section 4**.

2 EXPERIMENTAL SETUP

2.1 Experimental System

The experimental observation system built in this study is shown in **Figure 1**. Water has been used as the working fluid. The surface

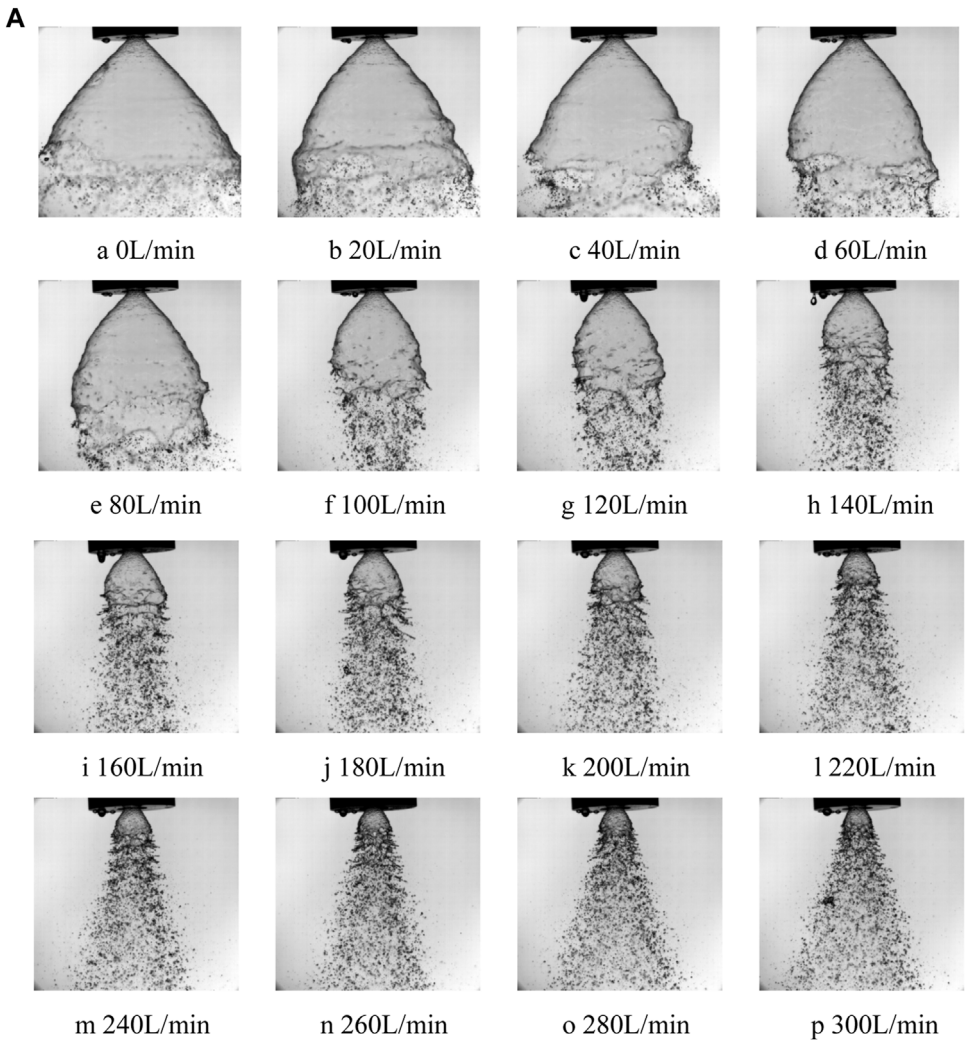

FIGURE 3 | (A) Impacts of the gaseous flow rate on the atomization morphology, W-1 injector. **(B)** Impacts of the gaseous flow rate on the atomization morphology, W-2 injector. **(C)** Impacts of the gaseous flow rate on the atomization morphology, W-3 injector.

tension and density of this fluid are $78mN/m$ and $1000kg/m^3$, respectively. The experimental environment was maintained at atmospheric pressure. The present experimental system contains a piping system, a fluid supply system, coaxial injectors of different sizes, and a measuring and data acquisition system. Each part is introduced as follows. The high pressure nitrogen gas is depressurized first, and it then pushes the working fluids into the pipes. The fluid is ejected from the injectors after going through different types of valves. It is noted that the Coriolis flow meter measures the water flow rate, which has a measurement from 0 to 50 kg/h with a ±0.2% precision. Besides, a high-speed video camera (SpeedCam MicroVis from HSVISION, Inc.) was used to observe the breakup pictures of the liquid sheets. The frame rate was 1,000 frames per second (fps) and the shutter time was $10\mu s$. The average droplet size and its distribution were measured by a particle size analyzer (Malvern Spraytec, with a range of 0.1–900 μm, 10 kHz). The distances between the measurement point and injector exit was about 200 mm.

The coaxial injector schematic models are shown in **Figure 2**. These coaxial injectors contain a liquid and gaseous injector. d_l and d_g are the liquid and gaseous diameters, respectively, and d_{gap} is the flowing width of the liquid channel. L_l, L_g, and L_R are the liquid, gas, and recess length of the injectors, respectively. n and d_{in} are the number of tangential holes and their diameter, respectively. The geometric parameters of the different gaseous and liquid injectors (G1-1 to G3-5 and L1) are shown in **Tables 1**, **2**.

It is shown that the gas–liquid momentum ratio is an important parameter for evaluating the coaxial injector atomization performance, which is defined as

$$GLR = \frac{\rho_g U_g^2}{\rho_l U_l^2} \tag{1}$$

Besides, the recessed length is another important structural parameter of the gas–liquid coaxial injectors, which would influence the atomization and self-excitation oscillation

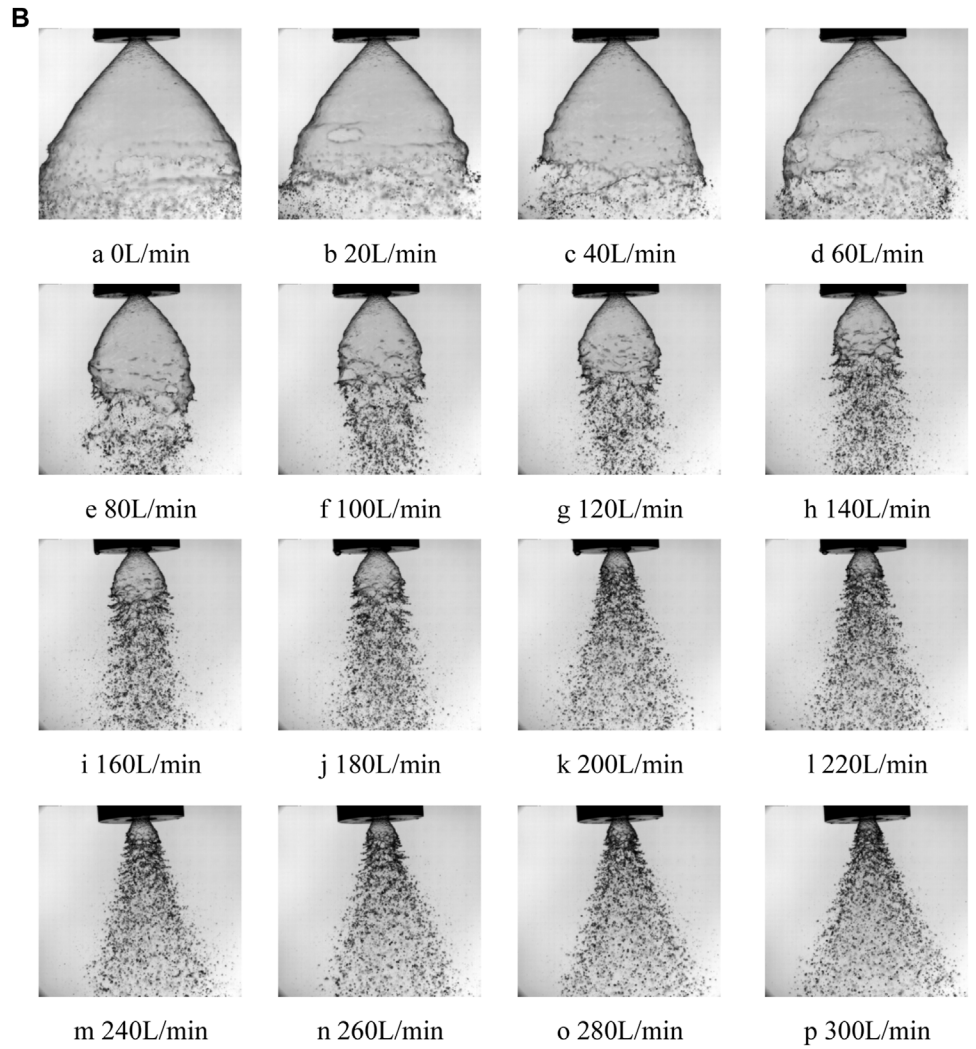

FIGURE 3 | (Continued).

phenomena. It is defined as the ratio of the recessed length to the injector diameter, i.e.,

$$RR = \frac{L_R}{d_g} \tag{2}$$

where d_g is the air core size of the injector.

2.2 Working Condition

Different experiments have been proposed based on the gas–liquid coaxial injector cold-flow experimental platform, using water and compressed air as the working matter. In particular, the G1-1 to G3-3 gas injectors have been combined with the L1 liquid injector. The recess ratios could also be changed to investigate the impacts of these parameters on the atomization and self-oscillation performance. The detailed working conditions are shown in **Table 3**.

It is observed that the liquid flow rates and pressure drops are fixed (45.1 g/s and 0.8 MPa) to study the impacts of different gaseous flow rates on the spray characteristics of the coaxial injectors. The gaseous flow rate varies from 0 to 300 L/min, and the corresponding gas–liquid momentum ratio varies from 0 to 9.158, correspondingly. In particular, W-1, W-2, and W-3 experiments are recorded by the high-speed camera to capture the spray morphology, breakup length, and spray angle, respectively. W-4, W-5, and W-6 experiments use the particle size analyzer to obtain the impacts of air core size on the average droplet size in the spray field.

It is indicated that various experiments have been taken to study the impacts of recess ratios on the atomization performance as well. The working conditions are shown in **Table 4**. The present gaseous flow rate for all injectors in **Table 4**'s conditions are all set as zero to eliminate the impacts of gaseous contraction impact that a liquid injector (L1) has been used. The recess ratios are from 0 to 2 and the corresponded liquid pressure drop could be varied from 0 to 1 MPa, which refers to the liquid flow rate from 0 to 48 g/s.

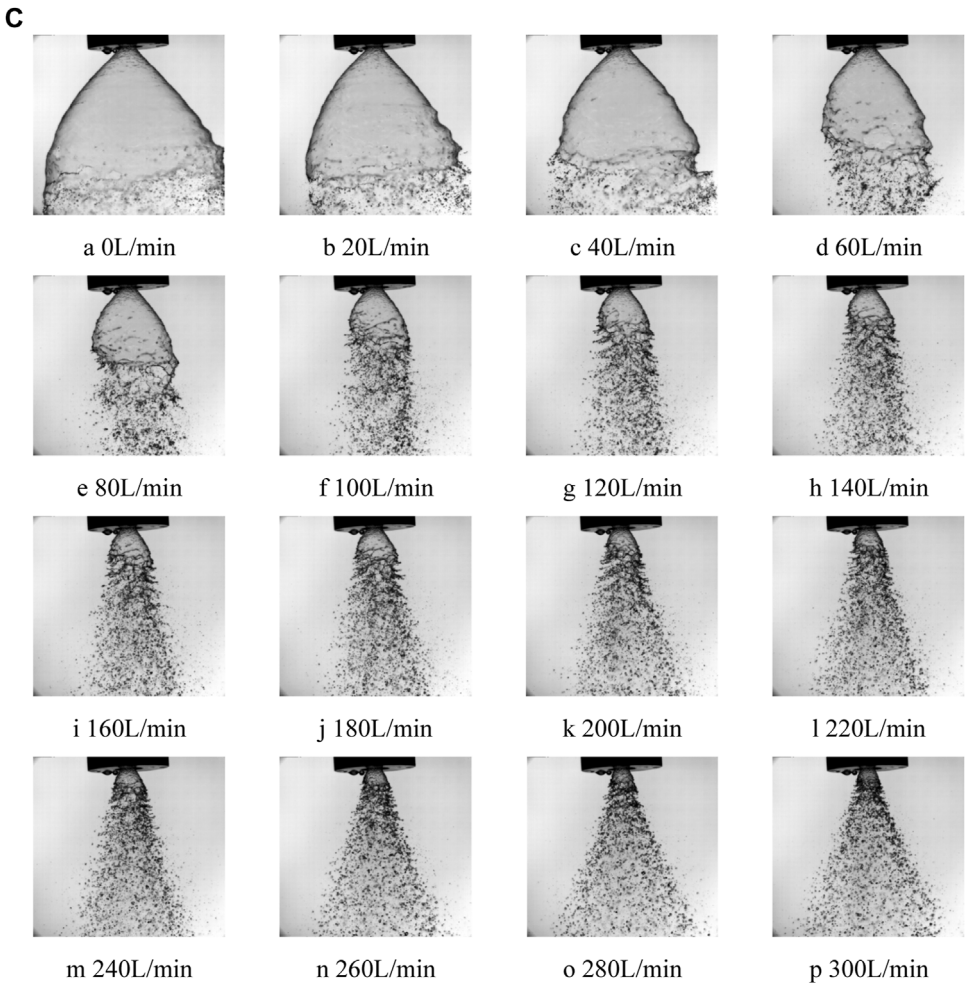

FIGURE 3 | (Continued).

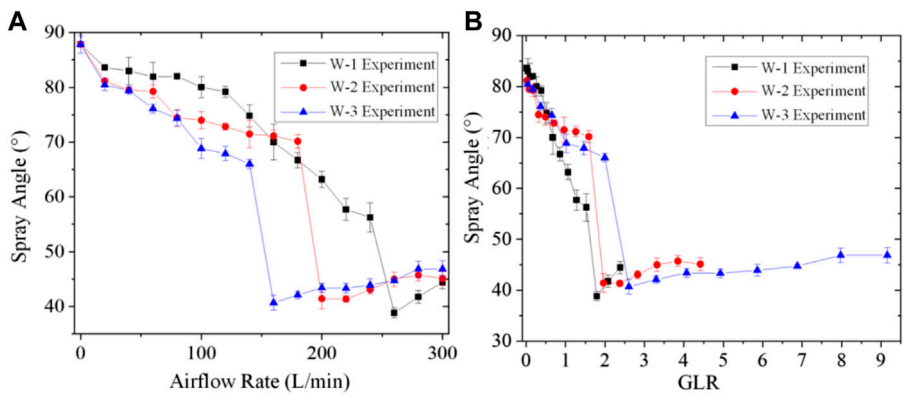

FIGURE 4 | Impacts of the **(A)** gaseous flow rate and **(B)** gas-to-liquid momentum ratio on the spray cone angle for different coaxial injectors.

Besides, in order to study the self-oscillation characteristics of the present coaxial injectors, the following experimental conditions are given, which are shown in **Table 5**.

It is revealed from **Table 5** that the oscillation characteristics would be measured under different gas flow rates and channel diameters. Subsequently, the injectors with no recess length are

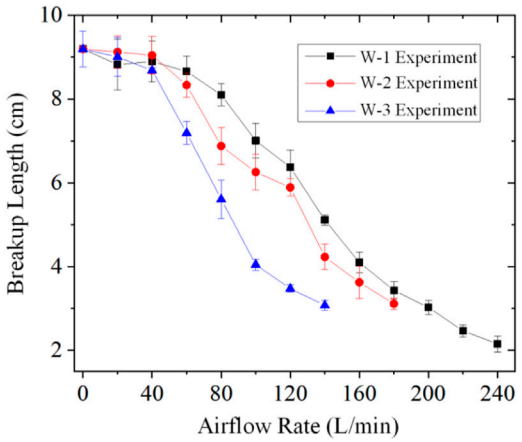

FIGURE 5 | Impacts of the gaseous flow rate on the breakup length for different coaxial injectors.

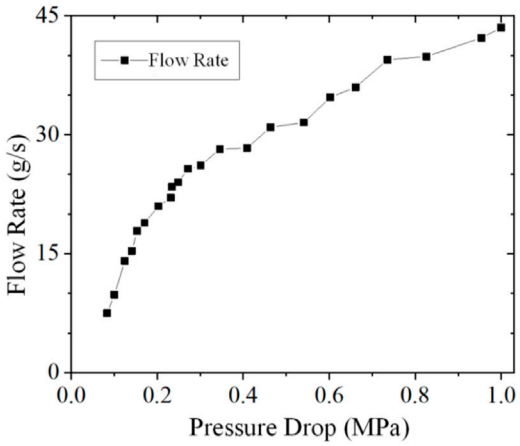

FIGURE 7 | The flow characteristics of the three coaxial injectors.

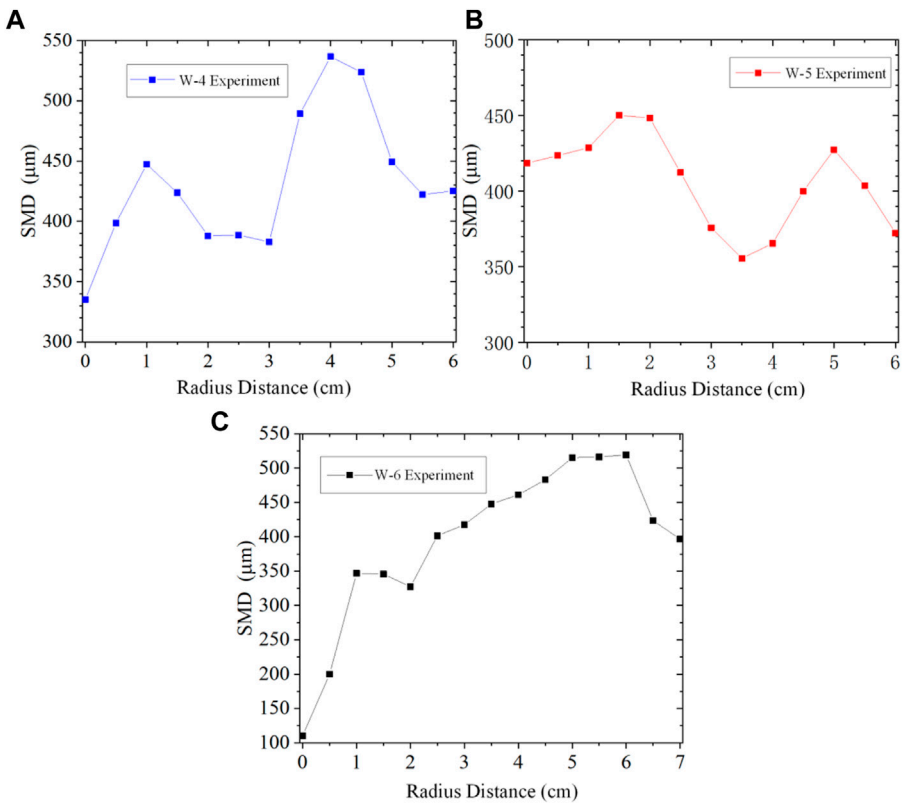

FIGURE 6 | The SMD distribution along the radius distance for the different coaxial injectors: **(A)** W-4 experiment, **(B)** W-5 experiment, and **(C)** W-6 experiment.

further studied to investigate the impacts of the propellant flow rate on the self-excited oscillatory properties. The oscillation characteristics of each injector are measured and analyzed as well. In particular, the experiments are performed using Z-1, Z-2, and Z-3 injector combinations with specific parameters as shown in **Table 6**. It should be noted that the gaseous flow rate could be changed step by step to adjust the liquid flow rate during the self-excitation oscillations under each gas flow rate.

The atomization processes in the Z-1, Z-2, and Z-3 experiments could be captured by the high speed camera to analyze their spray features like the spray angle and breakup

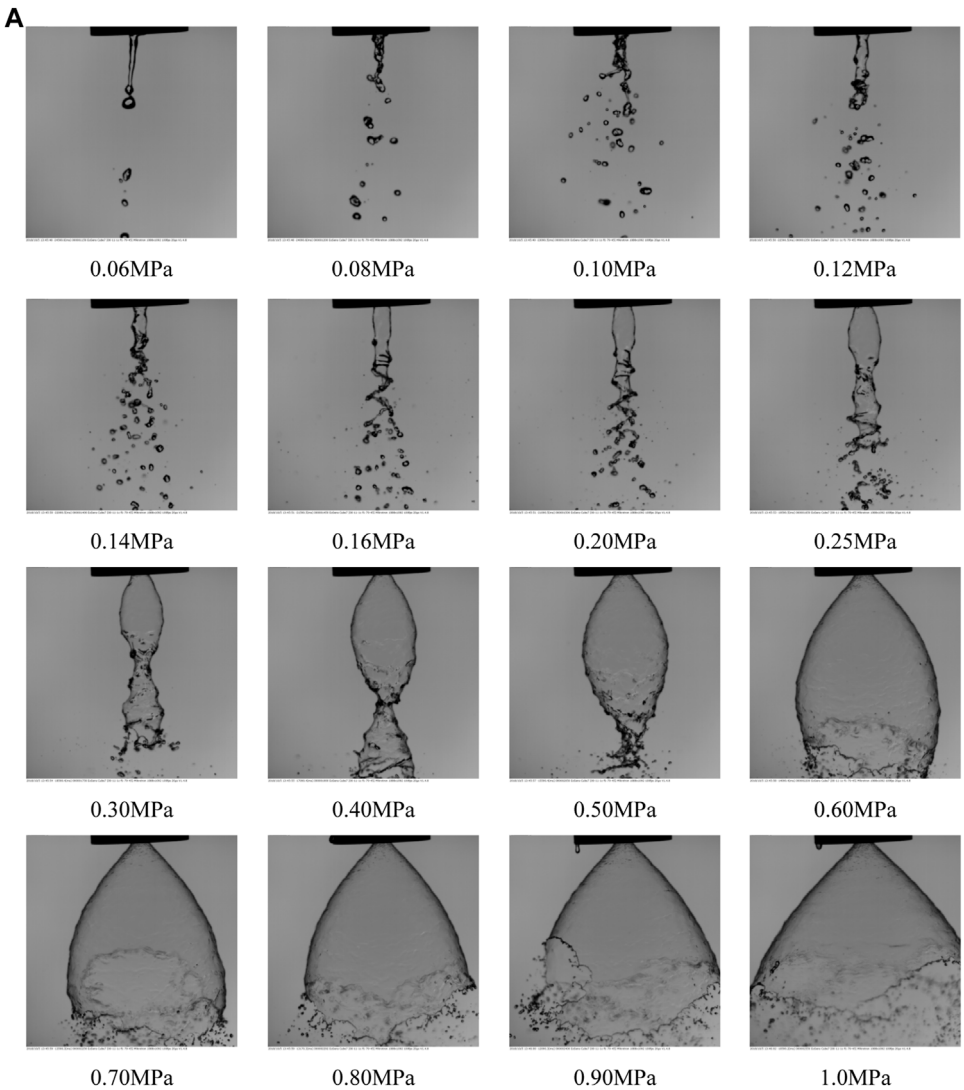

FIGURE 8 | Atomization morphology generated by the **(A)** W-7 experiment, **(B)** W-8 experiment, and **(C)** W-9 experiment.

length. The dominant frequency of the self-oscillation phenomena could be determined by the proper orthogonal decomposition (POD) decomposition method.

3 RESULTS AND DISCUSSION

In this section, the atomization features of the coaxial injectors like the average droplet size, breakup length, and spray angle and the effects of gaseous core size and recess length on them would be studied comprehensively. Besides, as for the self-oscillation characteristics, it includes the dominant frequency and gaseous core size. The impacts of the liquid flow rate and injector geometric parameters on the abovementioned features have been measured and analyzed in detail.

3.1 Atomization Features of Gas-Centered Coaxial Injectors

3.1.1 Impacts of the Gaseous Core Size

The spray morphology under the different gaseous core sizes are shown in **Figure 3**.

From **Figure 3**, it is evident that the spray morphology is quite similar for the different coaxial injectors under certain liquid flow rates. The liquid sheet shows a hollow cone shape when the gaseous flow rate is relatively low. The breakup length reduces with larger aerodynamic force. The liquid sheet then breaks up into small droplets due to the developing unstable surface waves generated by the gas–liquid shear flow.

The spray features of the different injectors have been studied quantitatively. The impacts of the gaseous flow rate on the spray cone angle are shown in **Figure 4A**. It is shown that the spray cone angle decreases first and then increases with larger gaseous

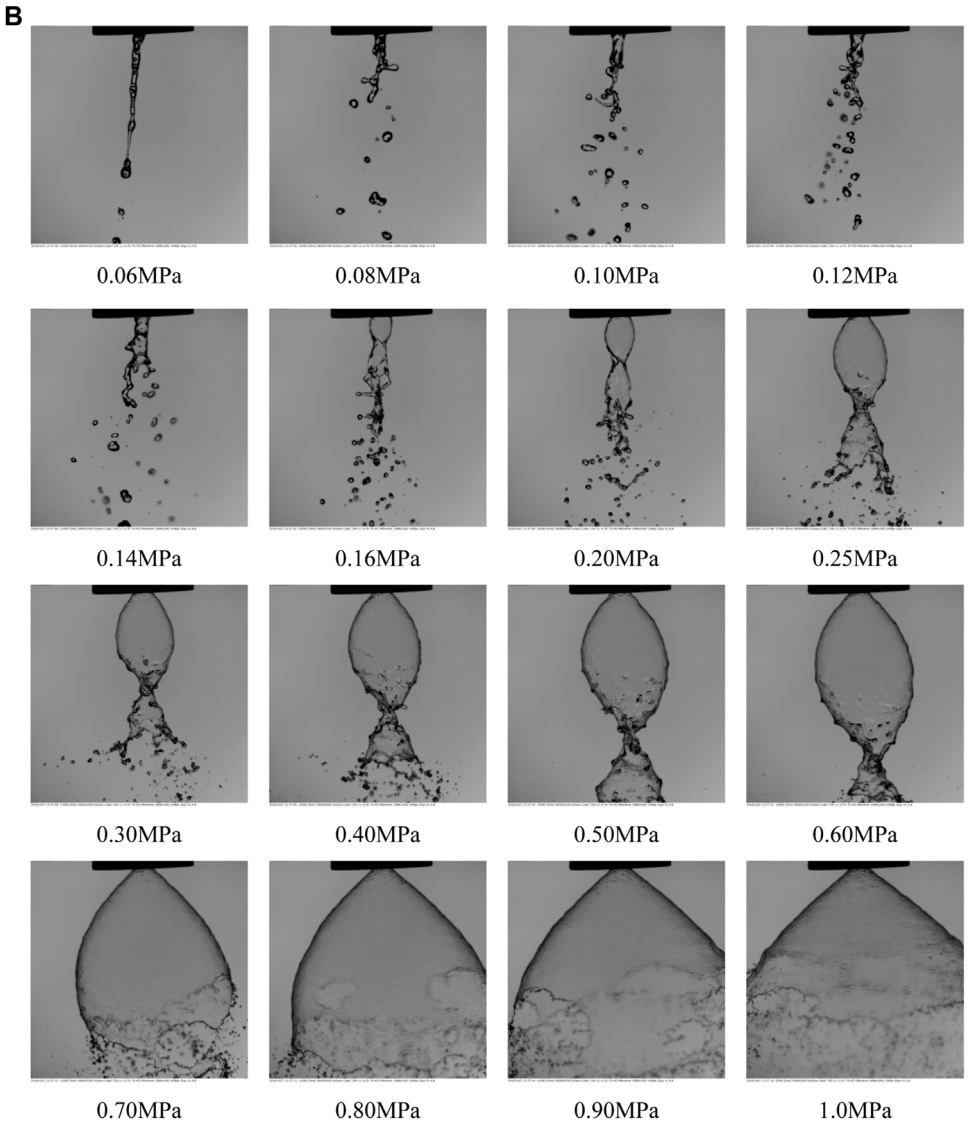

FIGURE 8 | (Continued).

flow rates when the liquid sheet is fully atomized. This is due to the fact that the gas flow rate from the internal gas injector is relatively fast, so the related pressure is less than the atmospheric pressure when the spray is not completely atomized. The pressure difference between the liquid sheet lets it contract inward. It is promoted with the larger gaseous flow that the spray cone angle gradually decreases. The strong air–liquid interaction completely atomizes the liquid sheet at the injector exit when the gaseous flow rate is sufficiently large, and the spray cone angle increases as well. It is revealed from the previous atomization morphology that the critical gaseous flow rate for the full atomization state is smaller with smaller gaseous core size. It could be because the gaseous flow rate is larger with smaller air core size, which leads to larger gas–liquid momentum. This ratio determines the spray pattern during the atomization processes.

The impacts of the gas–liquid momentum ratio on the spray cone angle is shown in **Figure 4B**. It is found that the spray cone angle decreases first and then increases with a larger momentum ratio. The spray pattern changes when this ratio is about 2 and the spray is completely atomized.

The impacts of the gaseous flow rate on the breakup length have been measured as shown in **Figure 5**. It is illustrated that the breakup length is reduced by a larger gaseous flow rate. Since the external liquid injector structure is the same for these three experiments, the breakup length is decreased faster with smaller gas core sizes. This means that the injector with a smaller gaseous core size will have a more apparent impact on the liquid sheet breakup length, which is consistent with the measured results of the spray angle.

Subsequently, the average droplet sizes generated by the different coaxial injectors in the spray field is measured as

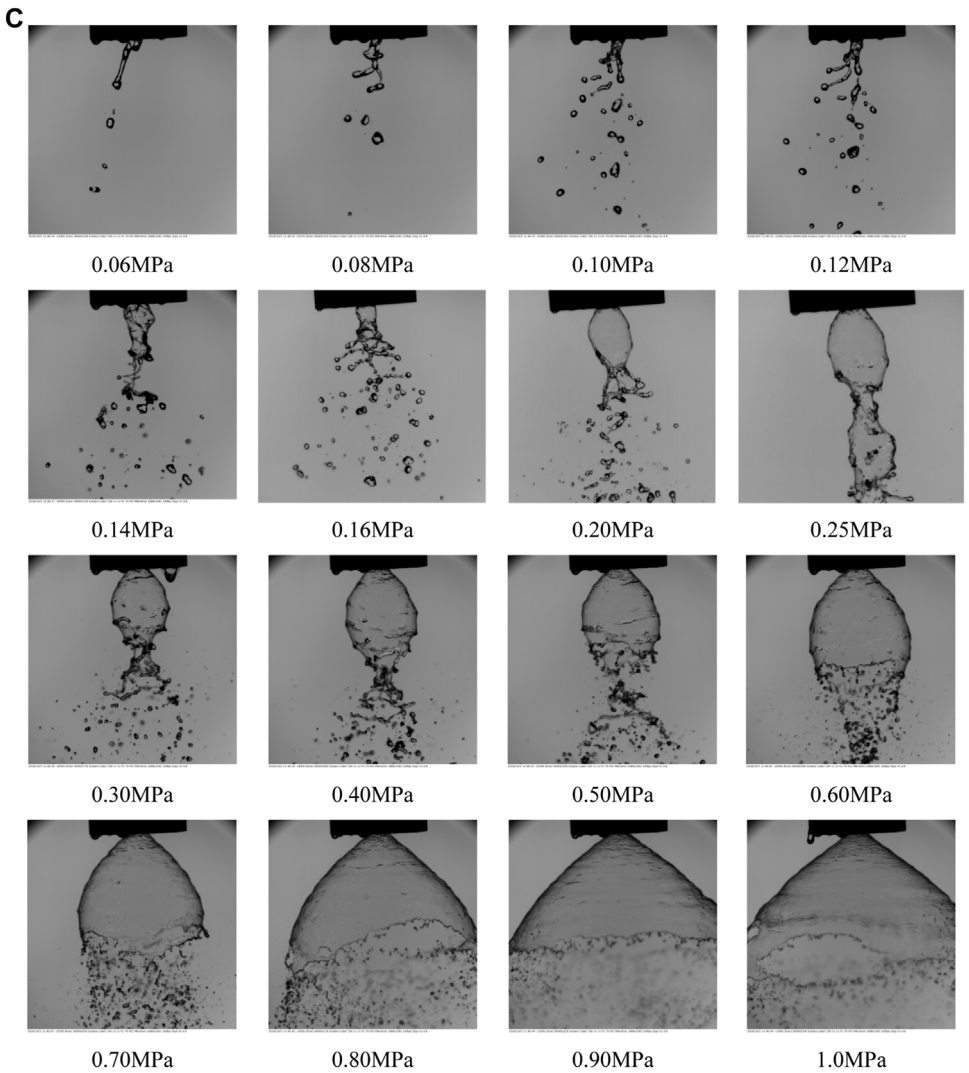

FIGURE 8 | (Continued).

well. The radius distribution of the SMD for the different coaxial injectors are shown in **Figure 6**. The experimental measurement point is at 18 cm below the injector exit.

As shown in **Figure 6**, the SMD values obtained by these three injectors vary along the radial distribution curves, and all of them show a bimodal shape. In particular, these three curves start falling when the SMD reaches the first high point when the radial distance is about 1–2 cm, then it would be raised again to the second high point at about 5 cm. Finally, the SMD is reduced by the larger radius distances. Besides, it can be seen that the bimodal tendency is suppressed by the smaller gaseous core size. It means that under a certain gaseous flow rate, the gaseous flow shows a more apparent impact on the breakup of the liquid film when the gaseous core size is smaller.

3.1.2 Impacts of the Recess Length

It is noted that the recess length also has a pronounced impact on the atomization characteristics. The geometric coefficients of the

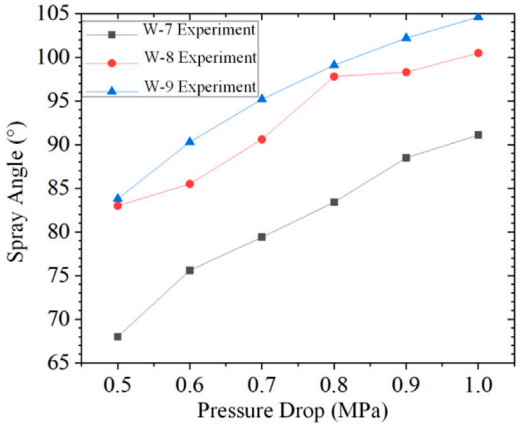

FIGURE 9 | Impacts of recess length on the spray angle under different pressure drops.

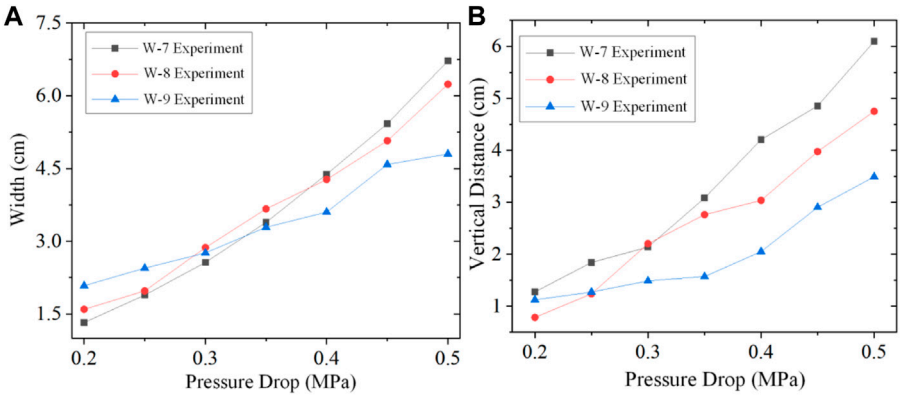

FIGURE 10 | Impacts of recess length on the **(A)** maximum width of the liquid sheet and **(B)** vertical distance with the injector exit under the different pressure drops.

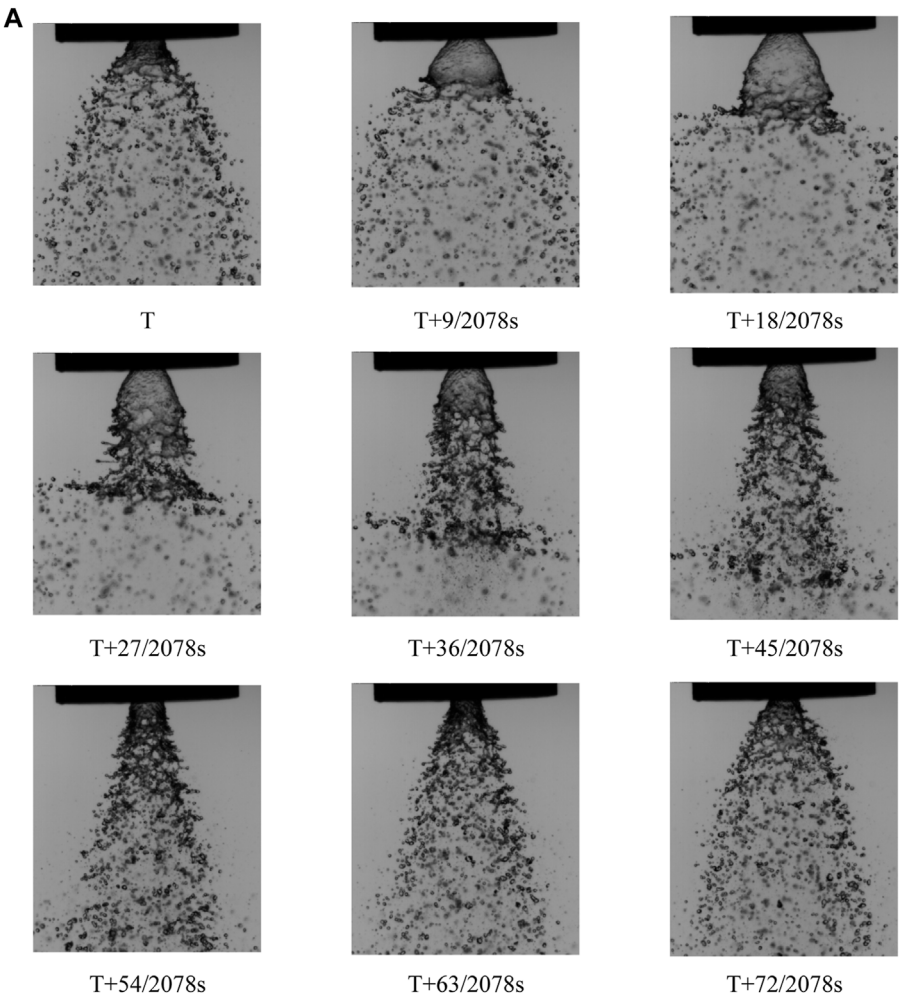

FIGURE 11 | Periodic pictures of the self-oscillation injector when **(A)** the gaseous core size is 7 mm, the gaseous flow rate is 250 L/min, time intervals are about 9/2078 s, and the shutter time is 20 μs; **(B)** the gaseous core size is 6 mm, the gaseous flow rate is 184 L/min, time intervals are about 1/400 s, and the shutter time is 20 μs; and **(C)** the gaseous core size is 5 mm, the gaseous flow rate is 127 L/min, time intervals are about 1/400 s, and the shutter time is 20 μs.

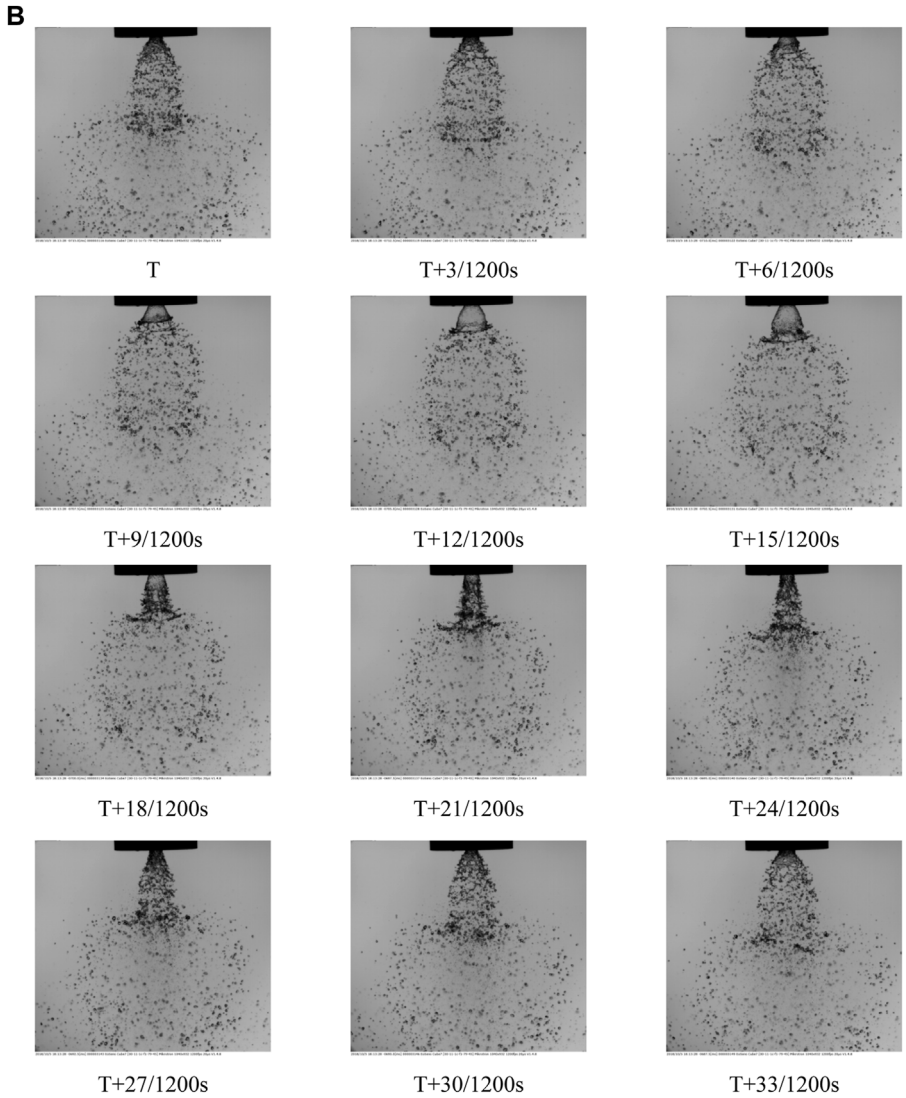

FIGURE 11 | (Continued).

injector in experiments W-7, W-8, and W-9 are the same, and the flow rates of these three experiments are shown in **Figure 7**.

The atomization processes of the W-7 experiment under the different pressure drops are shown in **Figure 8A**. It is found that the injected liquid cannot expand in total to form a liquid film when the pressure drop is lower than 0.1 MPa. It would form both small droplet and twisted ligaments. The rotating liquid column shape is hollow, twisted, and pencil shaped when the injector pressure drop further increases to 0.2 MPa. The liquid film is then divided into two parts. The upper half of the liquid film is expressed as onion shaped, while the liquid film is contracted due to the surface tension; it is then expanded again to a conical liquid film morphology. The lower part of the spray then disappears and the liquid film begins to break when the injector pressure drop reaches about 0.5 MPa. The spray is tulip shaped before a stable conical liquid film, when the pressure drop is further increased (Surya Prakash et al., 2014).

The subsequent atomization processes of the W-8 injector under the different pressure drops are shown in **Figure 8B**. It is shown that the spray in the W-8 experiment has a stronger angular momentum than the spray in the W-7 experiment due to the introduced recess length and shows a higher liquid film rotation and a larger spray cone angle under the same pressure drop.

The atomization performance of the W-9 experiment is shown in **Figure 8C**. The liquid film also shows a droplet-dripping, twisted-ribbon, twisted-pencil, onion-shaped, and stable-conical liquid film as the pressure drop is further increased. It reveals that the critical injector pressure drop is different for each experimental condition. The atomization features are also different for these injectors. Overall, the spray morphology in W-9 experiment is more extended and the angular momentum and spray cone angle are larger than in the W-7 and W-8 experiments.

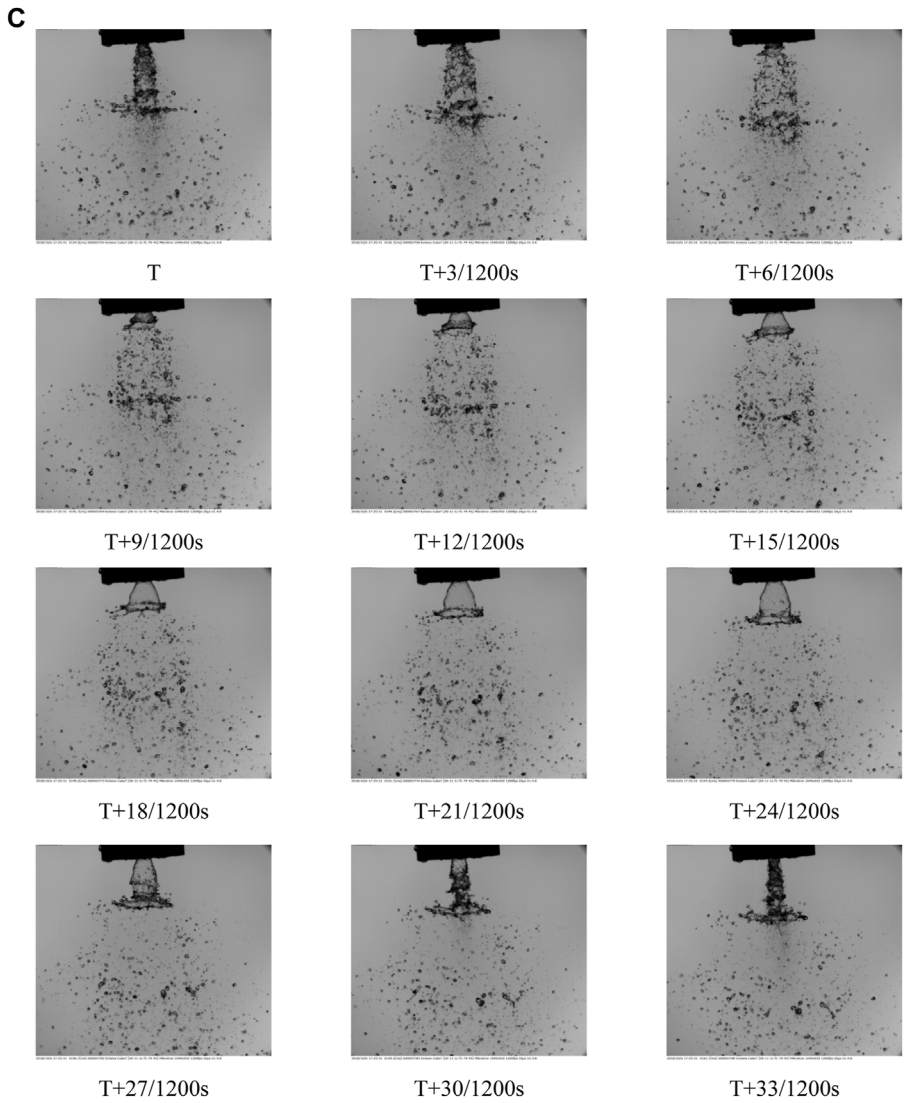

FIGURE 11 | (Continued).

The impacts of the recess length on the spray angle are measured and analyzed in **Figure 9**. It is shown that the spray angle is increased with a larger pressure drop, while the main difference is that the larger the recess length for the corresponding spray angle the larger it is for the same injector pressure drop. Therefore, different spray patterns reveal that the injector recess length has an impact on the spray characteristics of these coaxial injectors.

The maximum width of the liquid sheet in the spray field is measured and shown in **Figure 10**. It is revealed that the maximum width and vertical distance is increased with a larger pressure drop. Besides, the initial maximum width increases with a longer recess length when the pressure drop is relatively low, which means that the swirl intensity is increased by the larger recess length. The balance point of the liquid sheet contraction moves downward due to the surface tension effect. The distance between the injector exit and the maximum width of the liquid sheet is shorter when the recess length is further increased.

3.2 Self-Oscillation Features of Gas-Centered Coaxial Injectors

The self-oscillation phenomena occur for coaxial injectors under certain geometric parameters and working conditions. In the following section, the spray photographs recorded by the high speed camera and the impacts of the gaseous core size on the self-oscillation features are studied comprehensively.

3.2.1 Impacts of the Gaseous Core Size

It is noted that the self-oscillation phenomena are observed in the present experiments. The detailed processes are described as follows. First, the liquid sheet shows a conical shape when it leaves the injector exit. The stable maximum length is defined as the critical length. The liquid film breaks up into small droplets by the strong gas–liquid interaction, which happens near the central axis of the injector. The obtained spray is further

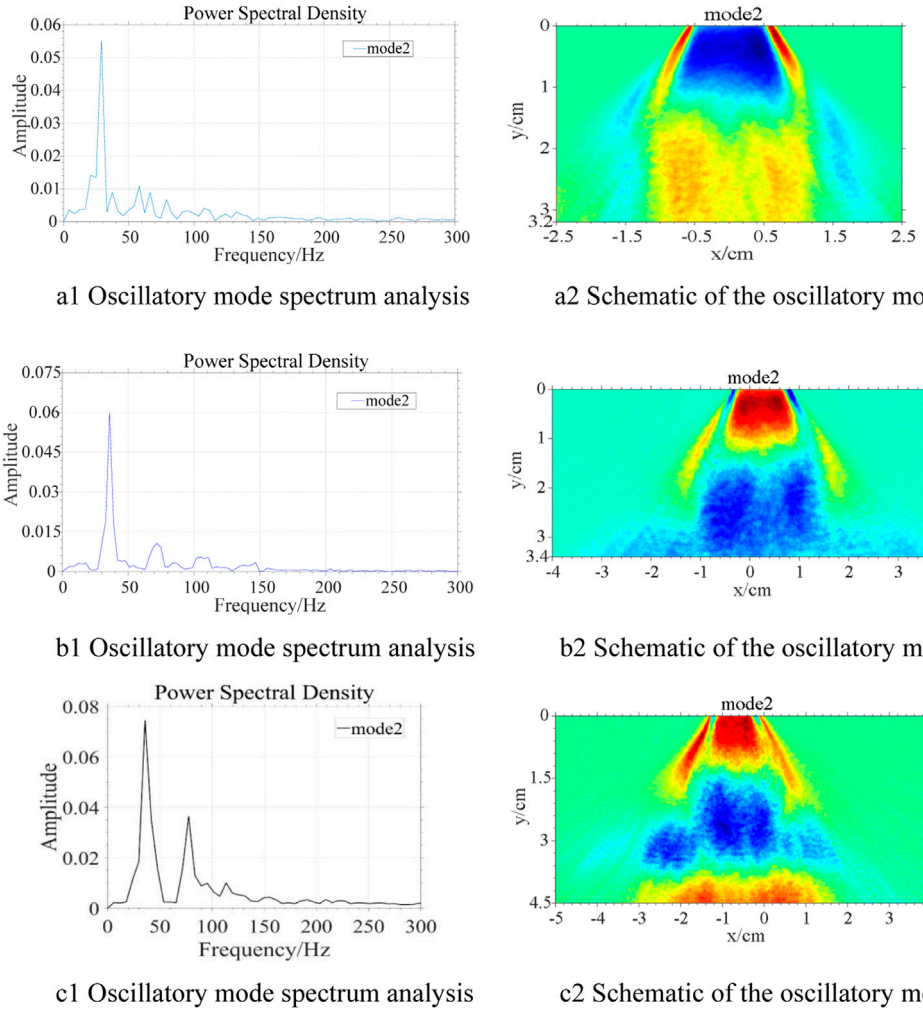

FIGURE 12 | The self-oscillation characteristics (oscillatory mode spectrum and oscillatory mode) of different injectors when the air core size is **(A)** 7 mm, **(B)** 6 mm, and **(C)** 5 mm.

expanded when the space range reaches the maximum length. The complete liquid film is thereby injected from the exit and shows a conical shape again. The abovementioned phenomena are more apparent for small liquid flow rates. The detailed processes of the different injectors are shown in **Figure 11**.

The impacts of the gaseous core size on the self-oscillation features like the critical breakup length and the oscillation frequency are analyzed. The POD is an effective way to extract information of each mode from the experimental data. It decomposes the system into several simple orthogonal modes. The modes containing a large energy are the main features of the original system, and the main features are extracted to obtain the relevant information. It should be noted that the spray density in the field is directly related to the gray value of the spray images. In particular, the gray value is increased with a larger spray density. Therefore, the oscillatory mode and its spectrum could be determined by using the POD method. According to the mode spectrum, the energy spectrum distribution (PSD) of each mode is obtained after the Fourier transform and the frequency characteristics are found from it. The obtained results are shown in **Figure 12**.

As shown in **Figures 12A,B**, there exist a series of low-frequency oscillations that are different from the commonly observed high-frequency oscillations in jet engines. In particular, the self-oscillation frequency is about 29 Hz when the gaseous core size is about 7 mm, and the frequency increases to 36 Hz when the gaseous core size reduces to about 6 mm. The self-oscillation intensity is amplified as its frequency is nearly the same as to when the gaseous core size further shrinks to 5 mm. Besides, as shown in **Figure 12C**, the spray shows more distinguished different modes, which generates various unstable surface waves along the liquid sheet surface. Therefore, the different parts of the liquid sheet lets the liquid sheet be evidently stratified when compared with the other air core size conditions.

The impacts of self-oscillation on the breakup features have been measured as well. The self-oscillation frequency is relatively low

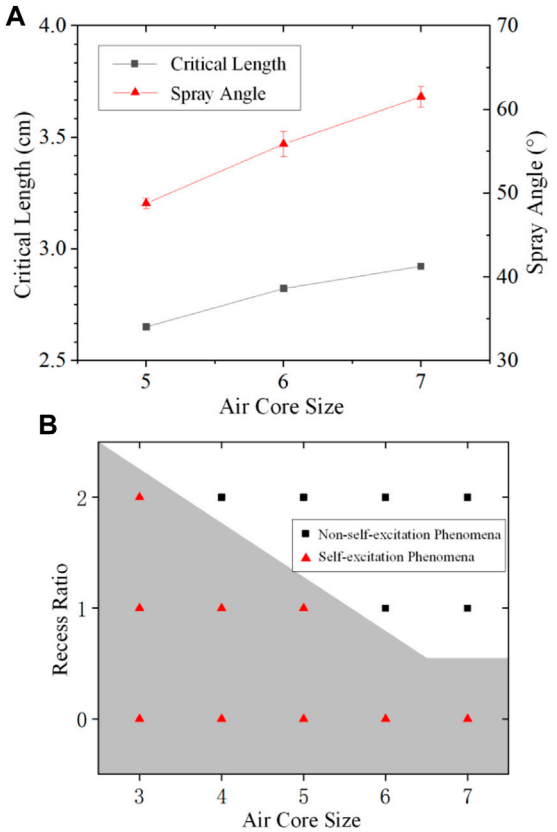

FIGURE 13 | (A) The breakup features of spray under various air core sizes. **(B)** Parameter boundaries of self-excited oscillatory phenomena.

during the self-oscillation phenomena. It leads to the liquid sheet extending in a conical shape when leaving the injector exit. The maximum length at which the liquid sheet stably unfolds in the conical shape is defined as the critical breakup length. As shown in **Figure 13A**, the critical breakup length and spray angle increase with larger gaseous core sizes. It is revealed that the gas–liquid interaction promotes the self-oscillation intensity.

Besides, previous experiments have shown that the injector geometric parameters influence the self-oscillation phenomena as well. The criteria determining whether the self-oscillation phenomena would happen are shown in **Figure 13B**. The larger gaseous core sizes suppress the self-oscillation phenomena, while the recess length shows an opposite impact on the activation of the self-oscillation phenomena as the other parameters are kept the same.

3.2.2 Impacts of the Airflow Rate

In the following subsection, the impacts of the airflow rate and air core size on the self-oscillation phenomena are studied under different working conditions. The experimental results reveal that these phenomena are suppressed by changing the flow rate. The variations of the liquid pressure drop and flow rate for the different gaseous flow rates are measured as shown in **Figure 14** when the self-oscillation phenomena are activated.

The critical liquid flow rate increases with larger gaseous flow rates. There exist two spray patterns, i.e., a steady state spray and conical liquid film when the gas–liquid momentum ratio is relatively large. Therefore, the activation of the self-oscillation phenomena should satisfy a certain momentum ratio. Besides, the injector shows the self-oscillation phenomena when the gaseous core sizes and flow rates are relatively small. The required gaseous flow rate is larger with a larger gaseous core size for the possible self-oscillation phenomenon. Furthermore, the self-oscillation intensity is larger with a greater liquid flow rate and pressure drop.

The impacts of the gaseous core size on the parametric range for activating self-oscillation phenomena under the different gas–liquid momentum ratios are shown in **Figure 15A**.

The smaller gaseous core sizes widen the momentum ratio range to activate the self-oscillation phenomena. The impacts of the gaseous core sizes on the self-oscillation frequencies under the different gaseous flow rates is obtained by analyzing the spray photographs with the eigenorthogonal decomposition method.

As shown in **Figure 15B**, the self-oscillation frequency nearly does not change with the larger gaseous flow rates. In particular, it

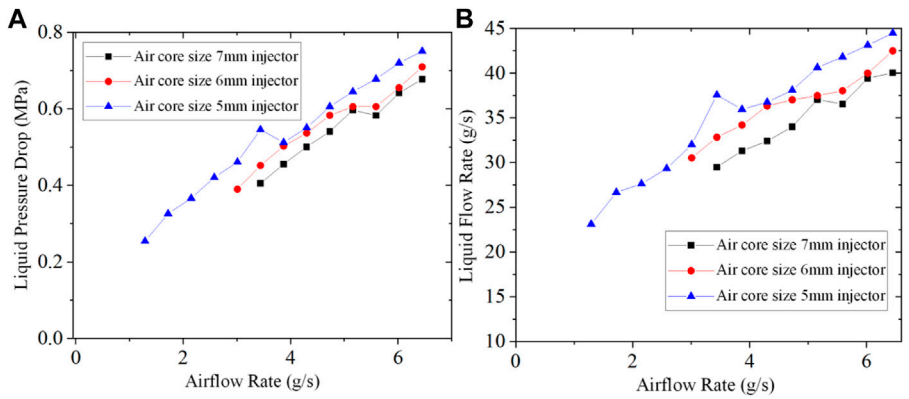

FIGURE 14 | Impacts of the gaseous core size on the **(A)** liquid pressure drop and **(B)** liquid flow rate under the different gaseous flow rates.

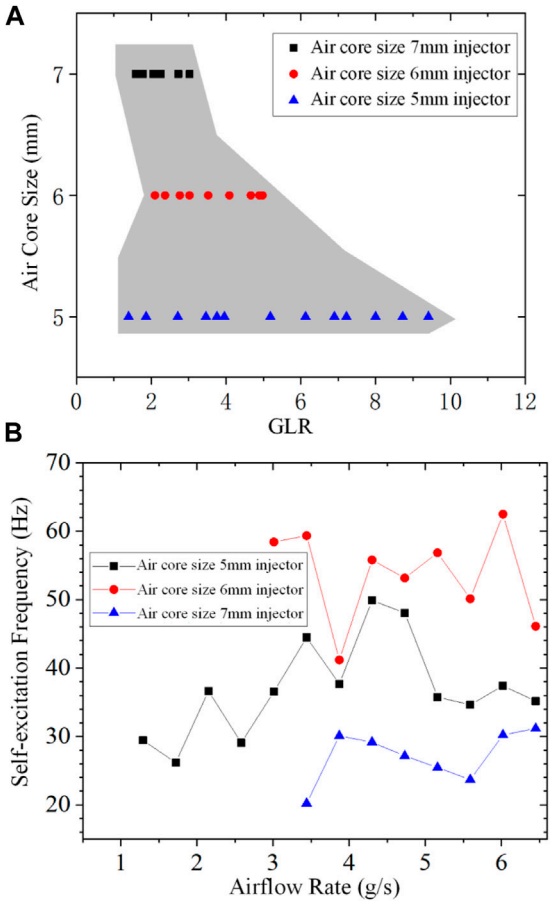

FIGURE 15 | Impacts of the gaseous core size on **(A)** the activation of self-oscillation phenomena under the different gas–liquid momentum ratios under the different gaseous flow rates and **(B)** the self-oscillation frequency under the different gaseous flow rates.

shows a maximum oscillation frequency when the gaseous core size is 6 mm, and the oscillation frequency is further reduced when the gaseous core sizes are about 5 and 7 mm. The physical mechanism behind the present tendency could be investigated in further research.

4 CONCLUSION

The present article investigates the spray and self-oscillation characteristics of a liquid sheet generated by a series of gas-centered coaxial injectors. An experimental observation system has been established to study the impacts of the gaseous core size and recess lengths on the breakup features like the breakup length, spray angle, and the corresponding self-oscillation characteristics. The main conclusions are as follows.

As for the spray characteristics of the liquid sheets generated by coaxial injectors, the gaseous flow shows a more apparent impact on the liquid sheet breakup when the gaseous core size is relatively small. This shows various SMD radius distributions with the different gaseous core sizes. Besides, the atomization morphology shows different patterns for the different injector pressure drops. There exists the drop-dripping, twisted-sheet, twisted-pencil, onion-shaped, and stable conical liquid sheet when the pressure drop is further increased and the spray angle becomes larger in addition to increases in the recess length.

As for the self-oscillation features of these coaxial injectors, the injector geometric parameters and the airflow rate impacts have been investigated. It is illustrated that there exists a relatively low-frequency oscillation for the coaxial injectors when the self-oscillation phenomena are activated. The parametric ranges between the gas–liquid momentum ratio and gaseous core size for the stable self-oscillation was obtained as well. The smaller gaseous core size and shorter recess length promoted the self-oscillation phenomena. The required liquid flow rate for activating the self-oscillation was raised by increasing the gaseous flow rate, while the self-oscillation frequency hardly varied with it.

The spray and self-oscillation characteristics of liquid sheets from the various gas-centered coaxial injectors have been obtained based on the abovementioned conclusions, which provide some useful information in making clear the detailed physical processes and improvements to the atomization quality in many industrial aspects.

DATA AVAILABILITY STATEMENT

The raw data supporting the conclusion of this article will be made available by the authors, without undue reservation.

AUTHOR CONTRIBUTIONS

LL: writing, experiment, and analyzing; YH: writing and data processing; SZ: experiment; QF: supervision and funding.

FUNDING

This research is supported by the National Natural Science Foundation of China (Grant Nos. 11872091, 11922201, and U1837211).

REFERENCES

Anand, R., Ajayalal, P., Kumar, V., Salih, A., and Nandakumar, K. (2017). Spray and Atomization Characteristics of Gas-Centered Swirl Coaxial Injectors. *Int. J. Spray Combustion Dyn.* 9 (2), 127–140. doi:10.1177/1756827716660225

Bai, X., Cao, P., Li, Q., and Cheng, P. (2021). The Break Phenomenon of Self-Pulsation for Liquid-Centered Swirl Coaxial Injectors. *Int. J. Multiphase Flow* 142, 103708. doi:10.1016/j.ijmultiphaseflow.2021.103708

Bazarov, V. (1996). "Influence of Propellant Injector Stationary and Dynamic Parameters on High Frequency Combustion Stability," in Proceeding of the 32nd AIAA/ASME/SAE/ASEE Joint Propulsion Conference and Exhibit, Lake

Buena Vista,FL,U.S.A, July 1996 (American Institute of Aeronautics and Astronautics), 3119. doi:10.2514/6.1996-3119

Bazarov, V. (1998). "Non-linear Interactions in Liquid-Propellant Rocket Engine Injectors," in Proceeding of the 34th AIAA/ASME/SAE/ASEE Joint Propulsion Conference and Exhibit, Cleveland,OH,U.S.A., July 1998 (American Institute of Aeronautics and Astronautics), 4039. doi:10.2514/6.1998-4039

Bazarov, V. G., and Yang, V. (1998). Liquid-Propellant Rocket Engine Injector Dynamics. *J. Propulsion Power* 14 (5), 797–806. doi:10.2514/2.5343

Chen, C., He, X., Liu, C., Yang, Y., and Tang, Z. (2021). Experimental Study on the Flow Field Distribution Characteristics of a Gas-Liquid Swirl Coaxial Injector under Ambient Pressure. *Aerospace Sci. Tech.* 114, 106757. doi:10.1016/j.ast.2021.106757

Ding, J.-W., Li, G.-X., and Yu, Y.-S. (2017). The Instability and Droplet Size Distribution of Liquid-Liquid Coaxial Swirling spray: An Experimental Investigation. *Exp. Therm. Fluid Sci.* 82, 166–173. doi:10.1016/j.expthermflusci.2016.11.014

Eberhart, C., Lineberry, D., and Frederick, R. (2012). "Propellant Throttling Effects on Self-Pulsation of Liquid Rocket Swirl-Coaxial Injection," in Proceeding of the 48th AIAA/ASME/SAE/ASEE Joint Propulsion Conference & Exhibit, Atlanta, Georgia, July 2012 (American Institute of Aeronautics and Astronautics), 4204. doi:10.2514/6.2012-4204

Gautam, V., and Gupta, A. K. (2009). Cryogenic Flow and Atomization from a Coaxial Injector. *J. Propulsion Power* 25 (1), 33–39. doi:10.2514/1.28921

Im, J. H., Kim, D., Yoon, Y., Roh, T., and Koo, J. (2005). "Self-pulsation Characteristics of a Swirl Coaxial Injector with Various Injection and Geometric Conditions," in Proceeding of the 41st AIAA/ASME/SAE/ASEE Joint Propulsion Conference & Exhibit, Tucson, Arizona, July 2005 (American Institute of Aeronautics and Astronautics), 3749. doi:10.2514/6.2005-3749

Im, J. H., and Yoon, Y. (2008). "The Effects of the Ambient Pressure on Self-Pulsation Characteristics of a Gas/liquid Swirl Coaxial Injector," in Proceeding of the 44th AIAA/ASME/SAE/ASEE Joint Propulsion Conference & Exhibit, Hartford,CT, July 2008 (American Institute of Aeronautics and Astronautics), 4850. doi:10.2514/6.2008-4850

Jeon, J., Hong, M., Han, Y. M., and Lee, S. Y. (2011). Experimental Study on spray Characteristics of Gas-Centered Swirl Coaxial Injectors. *J. Fluids Eng.* 133 (12), 121303. doi:10.1115/1.4005344

Kang, Z., Li, Q., Cheng, P., Zhang, X., and Wang, Z.-g. (2016). Effects of Self-Pulsation on the spray Characteristics of Gas-Liquid Swirl Coaxial Injector. *Acta Astronautica* 127, 249–259. doi:10.1016/j.actaastro.2016.05.038

Kulkarni, V., Sivakumar, D., Oommen, C., and Tharakan, T. J. (2010). Liquid Sheet Breakup in Gas-Centered Swirl Coaxial Atomizers. *J. Fluids Eng.* 132 (1), 011303. doi:10.1115/1.4000737

Li, T., Nishida, K., and Hiroyasu, H. (2011). Droplet Size Distribution and Evaporation Characteristics of Fuel spray by a Swirl Type Atomizer. *Fuel* 90 (7), 2367–2376. doi:10.1016/j.fuel.2011.03.011

Liu, H.-F., Li, W.-F., Gong, X., Cao, X.-K., Xu, J.-L., Chen, X.-L., et al. (2006). Effect of Liquid Jet Diameter on Performance of Coaxial Two-Fluid Airblast Atomizers. *Chem. Eng. Process. Process Intensification* 45 (4), 240–245. doi:10.1016/j.cep.2005.08.003

Liu, J., Zhang, X.-Q., Li, Q.-L., and Wang, Z.-G. (2013). Effect of Geometric Parameters on the spray Cone Angle in the Pressure Swirl Injector. *Proc. Inst. Mech. Eng. G: J. Aerospace Eng.* 227 (2), 342–353. doi:10.1177/0954410011432233

Liu, L., Yang, L., Fu, Q., and Cui, X. (2018). Improved Modeling of Free Power-Law Liquid Sheets by Weighted-Residual Approximations. *Int. J. Multiphase Flow* 107, 146–155. doi:10.1016/j.ijmultiphaseflow.2018.05.022

Liu, L. H., Yang, L. J., and Fu, Q. F. (2020). Droplet Size Spatial Distribution Model of Liquid Jets Injected into Subsonic Crossflow. *Int. J. Aerospace Eng.* 12 (1), 931729. doi:10.1155/2020/9317295

Liu, L., Fu, Q., and Yang, L. (2021). Linear Stability Analysis of Liquid Jet Exposed to Subsonic Crossflow with Heat and Mass Transfer. *Phys. Fluids* 33 (3), 034111. doi:10.1063/5.0040538

Surya Prakash, R., Gadgil, H., and Raghunandan, B. N. (2014). Breakup Processes of Pressure Swirl spray in Gaseous Cross-Flow. *Int. J. Multiphase Flow* 66 (7), 79–91. doi:10.1016/j.ijmultiphaseflow.2014.07.002

Xue, J., Jog, M. A., Jeng, S. M., Steinthorsson, E., and Benjamin, M. A. (2004). Effect of Geometric Parameters on Simplex Atomizer Performance. *AIAA J.* 42 (12), 2408–2415. doi:10.2514/1.2983

Yang, L.-j., Ge, M.-h., Zhang, M.-z., Fu, Q.-f., and Cai, G.-b. (2008). Spray Characteristics of Recessed Gas-Liquid Coaxial Swirl Injector. *J. Propulsion Power* 24 (6), 1332–1339. doi:10.2514/1.23977

Conflict of Interest: The authors declare that the research was conducted in the absence of any commercial or financial relationships that could be construed as a potential conflict of interest.

frontiers | Frontiers in Energy Research

ORIGINAL RESEARCH
published: 16 May 2022
doi: 10.3389/fenrg.2022.910304

Experimental and Numerical Studies of Ignition Delay Time and Laminar Flame Speed of JP-10at Elevated Temperature Conditions

Junsen Yang[1], Yi Wu[1], Zhenpeng Zhang[2,3], Yanlei Shang[2,3] and Lun Pan[4]*

[1]School of Aerospace Engineering, Beijing Institute of Technology, Beijing, China, [2]School of Materials Science and Engineering, Southwest Jiaotong University, Chengdu, China, [3]The Pec Institute of Multiscale Science, Chengdu, China, [4]School of Chemical Engineering and Technology, Tianjin University, Tianjin, China

In this work, the laminar flame speeds of JP-10/air mixtures and ignition delay time of JP-10/O_2/Ar mixtures have been studied over a wide range of experimental conditions using a premixed Bunsen flame and a shock tube. Laminar flame speed measurements of the JP-10/air mixture were measured at T = 360–453 K, φ = 0.7–1.3 and p = 1 atm. The ignition delay times of JP-10 with fuel mole fraction of 0.2% JP-10/2.8% O_2/97% Ar were measured with a heated shock tube behind the reflected shock wave at 1183–1478 K and pressure of 3.4 atm. Numerical calculation and sensitivity analysis of the laminar flame speed and ignition delay time of JP-10 were performed by using published detailed and skeletal kinetic mechanisms. The comparison of experimental and numerical results showed that all models tend to overestimate the laminar flame speed under the studied conditions, especially under lower temperature conditions (360–423 K). A temperature dependency empirical correlation of laminar flame speed was then proposed by power law theory. The sensitivity analysis identified three important reactions [$H+O_2$ = $O+OH$, C_5H_5+H (+M) = C_5H_6(+M), $C_3H_3+C_2H_2$ = C_5H_5] that determined the laminar flame speed and ignition delay time.

Keywords: JP-10 fuel, laminar flame speed, ignition delay time, kinetic mechanism analysis, bunsen flame

OPEN ACCESS

Edited by:
Xiao Liu,
Harbin Engineering University, China

Reviewed by:
Yiheng Tong,
China Space Foundation, China
Bo Jiang,
Nanjing University of Science and Technology, China
Yingchun Wu,
Zhejiang University, China

****Correspondence:***
Yi Wu
yi.wu@bit.edu.cn

Specialty section:
This article was submitted to Advanced Clean Fuel Technologies, a section of the journal Frontiers in Energy Research

Received: *01 April 2022*
Accepted: *19 April 2022*
Published: *16 May 2022*

Citation:
Yang J, Wu Y, Zhang Z, Shang Y and Pan L (2022) Experimental and Numerical Studies of Ignition Delay Time and Laminar Flame Speed of JP-10 at Elevated Temperature Conditions. Front. Energy Res. 10:910304. doi: 10.3389/fenrg.2022.910304

1 INTRODUCTION

JP-10 is a high volumetric energy density liquid fuel that is commonly used in ramjet, scarmjet, turbine engine and pulse detonation engines (Smith and Good, 1979; Szekely and Faeth, 1983; Antaki and Williams, 1987; Brophy and Netzer, 1999; Chung et al., 1999; Parsinejad et al., 2006; Akbar, 2012; Courty et al., 2012). Its advantages of a low freezing point, high volumetric energy density and high specific pulse make it a promising fuel candidate for applications in both civilian and military propulsion systems (Brotton et al., 2020; Wang et al., 2021). The combustion of JP-10 in a practical propulsion system is a very complex multidimensional turbulent mixing and combustion reaction process that is strongly influenced by chemical reaction kinetics (Liao et al., 2005; Gu et al., 2011; Seiser et al., 2011; Rocha, 2021; Shang et al., 2021; Wang et al., 2021; Zhang et al., 2021). Due to the different working conditions of the aircraft (such as taking off, cruising, landing, etc.), the combustion of JP-10 covers a wide range of pressure, temperature and equivalence ratio conditions (Feng et al., 2020). Therefore, it is of essential significance to accurately understand and develop chemical kinetics models valided in a wide range of conditions for the development of

TABLE 1 | Laminar flame speed studies of JP-10 in literature.

Author	Flame Configuration	T	P	Equivalence ratio range
Parsinejad et al. (2006)	Spherical flames	450–700 K	1–55 atm	0.7–1.0
Tao et al. (2018)	Counterflow flame	403 K	1 atm	0.8–1.4
	Spherical flame	600–730 K	7.5–14 atm	0.9, 1.05
Zhong et al. (2022)	Spherical flame	420 K	1 atm, 3 atm	0.7–1.3

TABLE 2 | Ignition delay time studies of JP-10 in literature.

Author	T	P	Mixture	Equivalence ratio range
Davidson et al. (2000, 2017)	950–1700 K	1–12 atm	JP-10/O_2/Ar	0.5–2.0
Colket and Spadaccini (2001)	1100–1500 K	3–8 atm	JP-10/O_2/Ar	0.5–1.5
Mikolaitis et al. (2003)	1300–2400 K	9–24 atm	JP-10/Air	1.0
Wang et al. (2007)	1000–2100 K	1.5–5.5 atm	JP-10/O_2/Ar	0.25–2.0
Xiu et al. (2018, 2020) Feng et al. (2018); Feng et al. (2020)	1400–2500 K	0.5–1 atm	JP-10/O_2/He	1

propulsion systems with high performance and high reliability (Feng et al., 2020). To develop and validate highly accurate kinetic models, it is necessary to generate experimentally obtained target parameters of the JP-10 suite for developing chemical kinetic models, such as the pyrolysis process, ignition delay time, laminar flame speed, extinction limit and soot production (Davidson et al., 2001; Nageswara Rao and Kunzru, 2006; Nakra et al., 2006; Vandewiele et al., 2014; Gao et al., 2015; Li et al., 2015; Tao et al., 2018; Johnson et al., 2020). Among these fundamental parameters, laminar flame speed and ignition delay time are the two most commonly used parameters in the evaluation of chemical kinetic models and engineering correlation (Parsinejad et al., 2006; Wang et al., 2007; Courty et al., 2012; An et al., 2015; Desantes et al., 2015).

A perfect chemical reaction kinetic model should meet the requirements of accurately predicting laminar flame speed and ignition delay time at the same time under wide range working conditions. Different from petroleum-derived fuels such as Jet A-1 and RP-3, which consist of hundreds or thousands of molecular species, JP-10 is a synthetic single-component liquid fuel (exo-tetrahydrodicyclopentadiene/exo-TCD with formula $C_{10}H_{16}$), making it a favorable target for kinetic modelling (Vandewiele et al., 2014; Zettervall, 2020). However, a summary of literature listed in **Table 1** and **Table 2** reveals that experimental measurements of laminar flame speed and ignition delay time of JP-10 have not been as extensively investigated as others, such as C_7-C_{12} hydrocarbon fuels. According to the literature, experimental measurements of the ignition delay time of JP-10 have been performed by limited studies in the last two decades (Davidson et al., 2000; Colket and Spadaccini, 2001; Mikolaitis et al., 2003; Wang et al., 2007; Gao et al., 2015).

For instance, Davidson et al. (Davidson et al., 2000) carried out a pioneering experimental measurement of the ignition delay of JP-10/O_2/Ar mixtures behind reflected shock waves with a temperature range of 1200–1700 K. Colket et al. (Colket and Spadaccini, 2001) and Mikolaitis et al. (Mikolaitis et al., 2003) also measured the ignition time of JP-10/air mixtures at almost the same period with higher temperature and pressure conditions. More recently, Gao et al. (Gao et al., 2015) revisited the ignition delay time measurements of JP-10 by using a shock tube system and proposed a new detailed kinetic model. Compared with the ignition delay time, the experimentally obtained laminar flame speed of JP-10 in the literature is even more limited. Parsinejad et al. (Parsinejad et al., 2006) measured the laminar flame speed of a JP-10/air mixture by using a constant volume chamber under various conditions. Courty et al. (Courty et al., 2012) also measured the laminar flame speed of JP-10/air mixtures at an equivalent ratio of 0.7–1.4 and a preheating temperature of 353–453 K. More recently, Zhong et al. (Zhong et al., 2022) measured the laminar flame speed of a JP-10/air mixture at a temperature of 420 K, equivalence ratio of 0.7–1.3 and pressure of 0.1–0.3 MPa. It can be seen that in addition to the limited experimental data for both ignition delay and laminar flame speed, considerable data discrepancies exist among these experiments, making it difficult to refine the developed kinetic mechanism. Therefore, new and accurate measurements are still needed for the ignition delay and linear flame speed of JP-10 in a large range of working conditions.

Apart from the fundamental experimental investigations of JP-10, such as lamianr flame speed and ignition delay time measurements, various kinetic modelling investigations of JP-10 were also conducted (Li et al., 2001; Courty et al., 2012; Gao et al., 2015; Tao et al., 2018; Zettervall, 2020; Zhong et al., 2022). According to the different application situations, the kinetic mechanism of JP-10 can be divided into two types, i.e., combustion and pyrolysis kinetic mechanism. For instance, Li et al. (Li et al., 2001) developed the first combustion kinetic mechanism of JP-10 consisting of 170 reactions and 36 species. Magoon et al. (Magoon et al., 2012) developed a detailed kinetic mechanism consisting of 320 reactions and 7740 reactions. Gao et al. (Gao et al., 2015) obtained a detailed mechanism containing 15518 reactions and 691 species by adding the oxidation reactions into the model of pyrolysis of JP-10 developed by Vandewiele et al. (Vandewiele et al., 2015). However, a detailed kinetic model cannot be efficiently used in high-dimensional CFD numerical

TABLE 3 | Combustion mechanism studies of JP-10 in literature.

Mechanism	Species numbers	Reaction numbers	Author	Experiment for validation
UCSD	36	174	Li et al. (2001)	
Magoon	320	774	Magoon et al. (2012)	
Gao	691	15518	Gao et al. (2015)	species files
Hychem detailed	120	841	Tao et al. (2018)	IDT and LFS and species files
Hychem skeletal	40	232	Tao et al. (2018)	
Z77	30	77	Zetterval (2020)	
Zhong	189	1287	Zhong et al. (2022)	LFS

simulations. More recently, skeletal kinetic models of JP-10 have been developed. For instance, Zettervall et al. (Zettervall, 2020) developed a combustion kinetic model of 30 species and 77 irreversible reactions. Zhong et al. (Zhong et al., 2022) recently proposed a new simplified JP-10 kinetic mechanism consisting of 189 species and 1287 reactions. All of these previous works have made considerable contributions to the development of accurate and useful kinetic mechanisms. Meanwhile, the discrepancy among different kinetic models remains large, and the accuracy in predicting the laminar speed and ignition delay time of laminar flame still needs further study. Reported combustion mechanisms of JP-10 are listed in **Table 3**.

It can be seen from the literature summary that the research on the combustion mechanism of JP-10 is not sufficient at present. From the development process of the mechanism, it is mainly to simplify and integrate the early mechanism and modify it in combination with the experimental data. The new mechanism developed has not been fully verified, especially in the measurement of laminar flame speed, only three published literatures reported their measurement data. The objective of the present work is to fill the measurement gap of laminar flame speed below 450 K, widen the measurement range of equivalence ratio and provide new data of ignition delay time of JP-10. To this end, the following work was carried out. First, the laminar flame speed measurements of JP-10 were performed under a wide range of temperatures and equivalence ratios of T = 360–453 K and φ = 0.7–1.3 under atmospheric pressure conditions. Second, the ignition delay time of JP-10/O_2/Ar mixture with equivalence ratio of 1.0, pressure of 3.4 atm and temperature range of 1183–1478 K was measured by a shock tube system. The experimental results of both laminar flame speeds and ignition delay times are compared with literature data. Third, numerical calculation of the laminar flame speed and ignition delay time was performed using mechanisms of JP-10 found in the literature. Finally, the chemical kinetic characteristics and structure of one-dimensional flames simulated by using different kinetic models of JP-10 are analysed and disccused in detail.

2 EXPERIMENTAL DETAILS

The samples of JP-10 fuel used in this work are provided by the research team from School of Chemical Engineering and Technology, Tianjin University (Jia, 2021; Liu et al., 2022; Qin et al., 2018; Gong et al., 2017). Since the main ingredient of JP-10 fuel, exo-tetrahydrodicyclopentadiene ($C_{10}H_{16}$), is over 96% weight fraction, it could be considered as a kind of single component fuel in research to simplify theoretical modeling. In the present work, laminar flame speed and ignition delay time measurements were performed over a wide range of conditions.

2.1 Laminar Flame Speed

Laminar flame speeds of JP-10 were measured by using a Bunsen flame burner at T = 360–453 K, φ = 0.7–1.3 and atmospheric pressure conditions. All the measurement of laminar speed in the present work is carried out with the Reynolds number of burner outlet gas flow = 1200. **Figure 1** illustrates the experimental laminar flame speed measurement system. The system consists of a Bunsen flame burner, temperature control system, gas feeding lines and optical system.

The burner consists of two contoured nozzles: the first nozzle has an outlet diameter of d_1 = 7 mm to produce the main flame (JP-10/N_2/O_2 mixture), and the second nozzle surrounds the central nozzle with an inner diameter of d_2 = 7.5 mm to obtain a pilot flame (CH_4/air mixture), which anchors the laminar premixed flame and broadens the equivalence ratio range for determination. Previous studies (Wu et al., 2016; Wu et al., 2017) have shown that the influence of pilot flame on the measurement results is negligible. To minimize the effect of the pilot flame on any possible disturbances on the main flame, the methane/air mixture flowrate for the pilot flame is kept as low as reasonably achievable. The burner is filled with ceramic beads to ensure full mixing of fuel and air and to maintain the laminar flow at the nozzle exit. Liquid fuel is stored in a stainless-steel tank and pressurized into a vaporization system (controlled evaporator and mixer/CEM-Bronkhorst) with temperature heating control. The flow rate of liquid fuel and all the gas flow are regulated by a Bronkhorst mass flow controller. Since the carrier gas in the vaporization system adds additional N_2 to the final mixture, the initial supply of N_2/O_2 should be specially adjusted to reproduce the synthetic species composition of air and modify the equivalence ratio of the fuel/air mixture. To avoid condensation of the vaporized liquid fuel and preheating the fuel/air mixture to set values, the feeding lines were wrapped with a flexible heating band, and two circulation heaters were added to the feeding lines. The flow rate and equivalence ratio are regulated and monitored by LabView code. The gas flow temperature of the nozzle outlet which is one of the experimental variables is monitored by another type K thermocouple before and after the image capturing. According to the experience in our experiment, the error range of temperature is limited in 3 K.

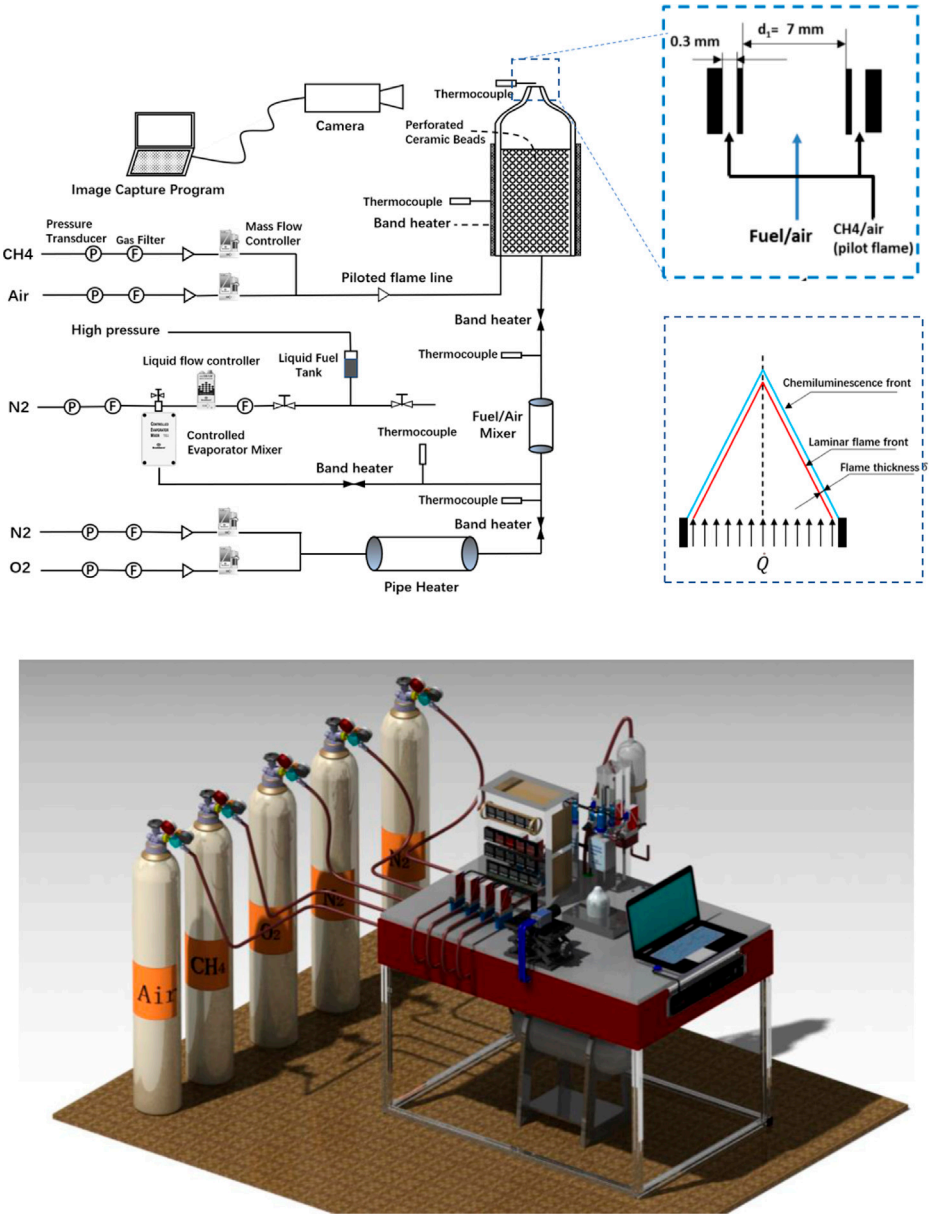

FIGURE 1 | Schematic of the experimental setup of laminar flame speed measurements.

The optical diagnostic is based on a CMOS dual-USB3 camera (Alkeria Celera C2K-M) with a 2048*1088 array. This camera is equipped with a f/16, f = 12 mm, achromatic lens. The area captured by the camera is approximately 100*100 mm^2 so that the pixel resolution of the optical system is 100 μm per pixel. The image acquisition frequency of the camera is kept at 10 Hz. The exposure time of the camera is set in 2000–3000 μs to record the flame image.

The flame area method is used here to determine the laminar flame speed S_L. Given the assumption that the laminar flame speed is the same at the entire flame front surface, the laminar flame speed can be deduced by the law of conservation of mass as follows:

$$\rho_u S_L A = \rho_u \dot{Q} \rightarrow S_L = \dot{Q}/A \tag{1}$$

where $\dot{Q}$ is the volumetric flow rate of the unburned gases at the burner outlet, ρ_u is the density of the unburned gases and A is the flame area at the appropriately chosen location.

ρ_u and $\dot{Q}$ can be calculated accurately since the mass flow rate of fuel and oxidizer gases are regulated by the liquid or gas flow controllers. The flame surface A is obtained by image processing. The recorded flame images are processed by a MATLAB program that is designed to capture the flame front profile based on the inverse Abel transformation. The flame surface area is derived by **Eq. 2**, and **Eq. 1** is used to deduce the laminar flame speed.

$$A = 2\pi \int_a^b f(x)\sqrt{1 + [f'(x)]^2}\,dx \tag{2}$$

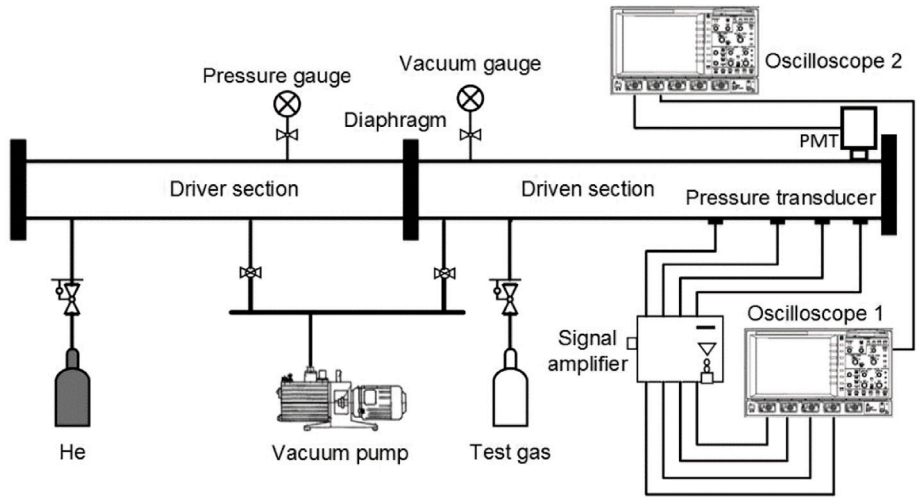

FIGURE 2 | schematic of the shock tube experiments (PMT: photomultiplier).

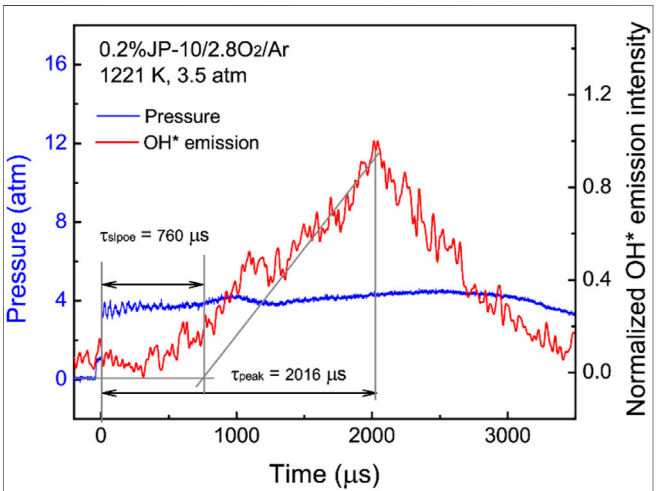

FIGURE 3 | Typical pressure and OH* emission time series during the ignition process of JP-10/O_2/Ar and the definition of ignition delay time.

where a and b are the boundary limits of integration. $f(x)$ is the flame contour profile obtained by image processing. More details on the experimental system and measurement methodology of the laminar flame speed can be found in our previous publications (Wu et al., 2016; Wu et al., 2017).

To reduce the measurement errors in the experiments and data processing, for each operating condition of all the measurements, at least 30 instantaneous images are recorded, and the averaged image is used to calculate the final flame speed. The uncertainty of the determination mainly comes from two resources: the uncertainty of the mass flow rate control (U_{Qm}) and the uncertainty of the calculation of the flame area (U_A). According to the parameters provided by Bronkhorst flow controllers, U_{Qm} is estimated to be ~2%, which roots in 0.5% of reading and 0.1% of full scale. U_A mainly comes from the pixel resolution of images recorded by the camera, which is estimated to be ~3%. The total uncertainty is equal to ~5% deduced from the equation $U = \sqrt{U_{\mathrm{Qm}}^2 + U_A^2}$.

2.2 Ignition Delay Time Measurements

The ignition delay times of JP-10 diluted in Ar are measured in a heated shock tube at Southwest Jiao Tong University, and more details of this apparatus are available in published papers (Shi et al., 2016; Shang et al., 2019). Briefly, as illustrated in **Figure 2**, this shock tube with a 50 mm inner is divided into the driver section (3.26 m) and driven section (4.52 m) by the diaphragms. The tested JP-10/O_2/Ar mixtures were preprepared in a 15 L stainless steel tank using the manometric method. To ensure the gas phase of JP-10, the driven section, mixing tank, and manifolds are heated by wrapped heating taps at 70°C. Since the main component of JP-10 is high-carbon molecule $C_{10}H_{16}$, the saturated vapor pressure at room temperature is less than 400 Pa which means the adsorption in the shock tube would be the main problem to the measurement. The purpose of dilution with Ar is to reduce the adsorption amount of JP-10 in the driven section of the shock tube as much as possible to ensure that the measured equivalence ratio is accurate. During the mixture preparation, the partial pressure of JP-10 is kept less than 0.5 kPa, which is much lower than its saturated vapor pressure at 70°C (2.48 kPa) (Cooper et al., 2002). The prepared mixtures should be allowed to diffuse completely for at least 4 h to achieve homogeneity. Before each experiment, the entire shock tube is evacuated to near vacuum by a vacuum pump.

TABLE 4 | combustion kinetic mechanism used in the present work.

	Species number	Reaction number
UCSD Li et al. (2001)	36	206
Hychem detailed Tao et al. (2018)	120	841
Hychem skeletal Tao et al. (2018)	40	232

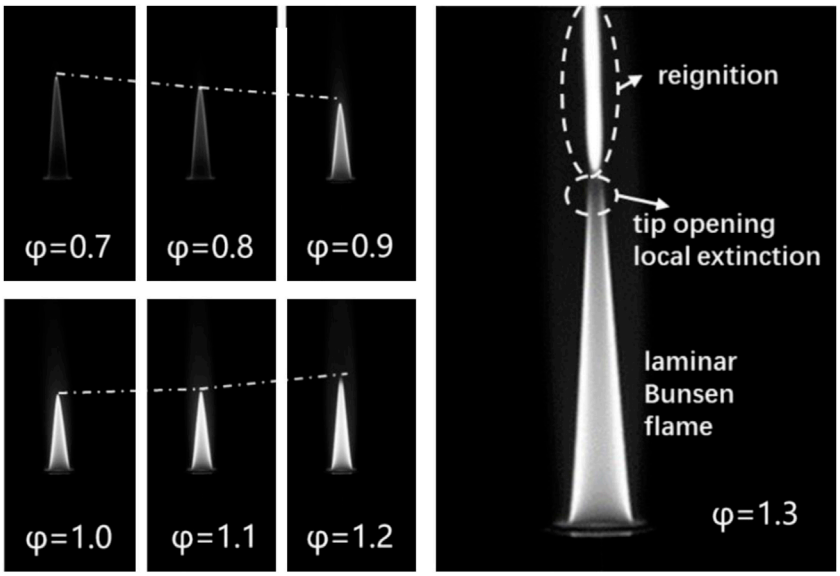

FIGURE 4 | Flame images of the JP-10/air mixture at T = 453 K and φ = 0.7–1.3.

Helium gas is used as the driver gas, and the different temperatures (T) and pressures (*p*) after the reflected shock wave are controlled by adjusting the injection pressures of the driver and driven section. The gas leakage of the system is less than 1 Pa min^{-1}.

Four pressure sensors are fixed along the driven section close to the endwall to determine the shock wave speed, and the OH* emission (307 nm) during fuel ignition is captured by a photomultiplier at the sidewall. **Figure 3** shows the typical pressure and OH* emission time series during the ignition process of JP-10 at 1221 K and 3.5 atm. Consistent with the previous literature (Mikolaitis et al., 2003), the OH* emission has a low intensity with a broad shape. The ignition delay time is defined as the time interval between the onset of the reflected shock wave and the intersection of the baseline with the maximum gradient (τ_{slope}) or the corresponding peak (τ_{peak}) of the OH* emission profile. The uncertainty of the measured ignition delay times is less than 20%.

2.3 Chemical Kinetic Modelling

Calculations are carried out to verify the experimental laminar flame speed and ignition delay time of the JP-10/air mixture. The one-dimensional premixed laminar flame is simulated by premixed laminar flame-speed calculation model, while the ignition delay time is simulated in closed homogeneous batch reactor. For laminar flame speed simulation, the mixture average transport scheme is used, the GRAD and CURV parameters are set to 0.1, and the grid number is large enough to ensure the convergence of the final solution. For ignition delay time simulation, the constant volume approach is used. In the present work, three combustion kinetic mechanisms of JP-10/air are used, i.e., the UCSD (Li et al., 2001), Hychem skeletal and detailed mechanisms developed in Tao's work (Tao et al., 2018). As illustrated in **Table 4**, the UCSD mechanism consists of 36 species and 206 reactions, the Hychem detailed mechanism uses 120 species and 841 reactions, and the Hychem skeletal mechanism reduced from the detailed one includes 40 species and 232 reactions.

TABLE 5 | Summary of the Lewis number of unburned mixtures in the present work calculated with Hychem detailed mechanism.

Temperature	Lewis number	
	φ = 0.7	φ = 1.3
360 K	2.943	0.957
423 K	2.938	0.955
453 K	2.935	0.954

3 RESULTS AND ANALYSIS

3.1 Laminar Flame Speed

3.1.1 Flame Characteristics of JP-10/Air

The laminar flame speeds of JP-10 were measured under a temperature of 360–453 K and an equivalence ratio of 0.7–1.3. **Figure 4** shows the typical Bunsen flame under a preheating temperature of 453 K and atmospheric pressure conditions with constant outlet velocity. With the piloted flame, the main flame of the JP-10/air mixtures can be stabilized over a wide equivalence ratio from φ = 0.7 to φ = 1.3. In the range of equivalence ratios of 0.7–1.0, the intensity of the flame image increases with increasing equivalence ratio, and the height of the flame decreases with increasing equivalence ratio. In the range of equivalence ratios of 1.1–1.2, the opposite trend was observed. As the fuel/air mixture flow was kept constant, according to **Eq. 1**, the trend of the height variation of the flame is opposite to the laminar flame speed variation, which is indeed observed in the present work.

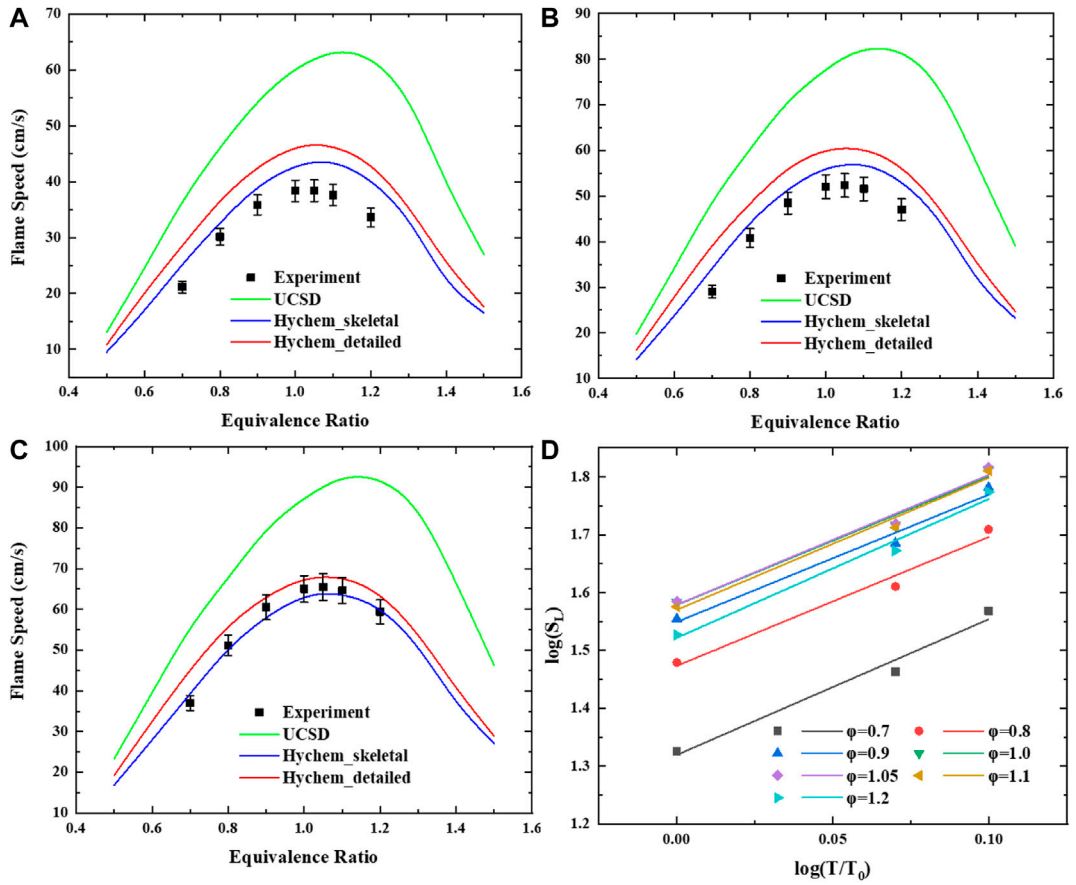

FIGURE 5 | Laminar flame speed of JP-10/air mixtures versus equivalence ratio range of 0.7–1.2 at elevated temperature: **(A)** T = 360 K. **(B)** T = 423 K. **(C)** T = 453 K. **(D)** Log-log plot of the laminar flame speed of JP-10/air under atmospheric temperature and different preheating temperatures.

TABLE 6 | parameters of $S_{L0,i}$ and α_i of correlation equations.

Reference S_{L0} parameters		Slope of Log (S_L)-log (T/T_0)		Temperature exponent $\alpha(\varphi)$ parameters	
$S_{L0,\varphi=1}$	38.79	$\alpha_{\varphi=0.7}$	2.347	α_0	2.220
$S_{L0,1}$	24.60	$\alpha_{\varphi=0.8}$	2.230	α_1	0.475
$S_{L0,2}$	−187.03	$\alpha_{\varphi=0.9}$	2.204	α_2	2.496
$S_{L0,3}$	−393.71	$\alpha_{\varphi=1.0}$	2.224	α_3	−1.597
$S_{L0,4}$	−377.90	$\alpha_{\varphi=1.05}$	2.248		
		$\alpha_{\varphi=1.1}$	2.284		
		$\alpha_{\varphi=1.2}$	2.404		

The flame tip opening phenomenon was observed when the equivalence ratio values were higher than 1.3. Under these conditions, the flame was locally quenched at the flame tip and then reignited above the tip opening region, resulting in another laminar flame with a high soot concentration. **Figure 4** shows the phenomenon of flame tip opening and reignition of the flame. It is found that for all the experimental conditions carried out in this work, no matter what temperature and outlet velocity vary, the flame tip opening phenomenon and reignition always occur once the equivalence ratio is higher than 1.3.

Some researchers have studied the flame tip opening phenomenon and attributed it to the curvature effect on nonequi-diffusive preheated mixtures of fuel/air leading to a change in the burning intensity at the flame tip (Ishizuka, 1982; Law et al., 1982; Mizomoto et al., 1985; Mizomoto and Yoshida, 1987; Sakai et al., 1996; Bouvet et al., 2011). The Lewis number, which is defined as the ratio of the mixture thermal diffusivity to the mass diffusivity of the deficient reactant, is generally considered an important parameter relevant to the flame tip opening phenomenon (Mizomoto and Yoshida, 1987). When the Lewis number of the unburned mixtures is

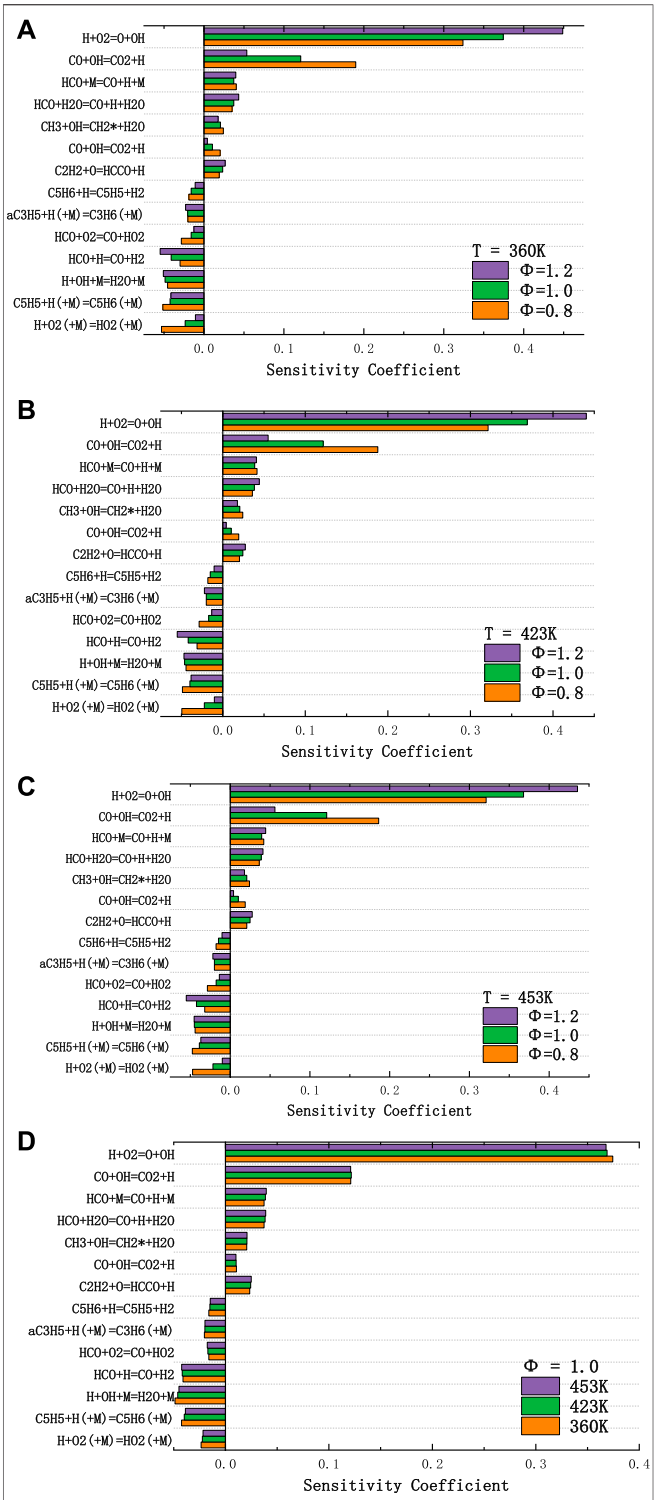

FIGURE 6 | Normalized sensitivity coefficients in predicting laminar flame speed of JP-10/air flame for T= **(A)** 360 K, **(B)** 423 K, **(C)** 453 K, and **(D)** ϕ = 1.0, caculated with Hychem detailed mechanism.

less than 1, the flame burning intensity decreases at the tip, causing local quenching of the flame. The reignited flame above the main flame could possibly be due to the fuel unburned at the tip of the flame being reignited by radiation effects. Previous investigations have found that the flame tip opening phenomenon may appear on the very lean fuel side and the very rich fuel side (Mizomoto et al., 1985; Mizomoto and Yoshida, 1987). The Lewis number of the unburned mixtures in the present work with equivalence ratio and temperature variations were calculated referring to the method of literature (Mizomoto and Yoshida, 1987). As illustrated in **Table 5**, it is observed that the Lewis number decreases with increasing temperature and decreases with increasing equivalence ratio. All the flame tip opening phenomenon observed in this work occur with a Lewis number less than 1.

3.1.2 Effect of Temperature

To investigate the sensitivity to the preheating temperature of the JP-10/air mixture, comparisons of measured and simulated laminar flame speeds for atmospheric pressure and for various preheating temperatures T = 360 K, 423 K, 453 K and φ = 0.7–1.2 are presented in **Figure 5**.

This shows that the laminar flame speed increases with increasing preheating temperature. The results calculated by using UCSD are generally higher than those calculated by the other two mechanisms and the measurements. The detailed mechanism of Hychem predicts a higher laminar flame speed than the skeletal mechanism. For low-temperature cases (T = 360 K, 423 K), the simulation using Hychem-skeletal and Hychem-detailed mechanisms overestimates the laminar flame speed compared with measurements. For higher preheating temperatures, the simulation produces a fairly close approximation of the measurements. In terms of discrepancy, the measurement results of this study are in good agreement with Hychem detailed mechanism and skeletal mechanism, and there is a large discrepancy compared with the predicted value of UCSD mechanism. Compared with the predicted value of UCSD mechanism, the absolute discrepancy is 10–20 cm/s and the relative discrepancy is 20–30%. In some data points with high equivalence ratio, the relative error is more than 30%. Other literatures also reported the great inconsistency with UCSD mechanism which may result from the overestimation of the sensitivity of cyclopentene oxidation reaction to flame speed (Zhong et al., 2022). Compared with Hychem skeletal mechanism, the absolute discrepancy is within 5 cm/s and the relative discrepancy is within 15%. The discrepancy between the experimental data and the predicted value of the mechanism at 360 K is relatively large. The measurement results reach a good consistency with predicted results at 453 K, the absolute discrepancy is within 2 cm/s and the relative discrepancy is within 5%. Compared with Hychem detailed mechanism, the absolute discrepancy is within 8 cm/s and the relative discrepancy is within 15%. The points with large discrepancy are mainly concentrated in the measurement conditions with equivalence ratio of 0.7 and 1.2. The predicted value of detailed mechanism is in good agreement with the measured value at 453 K. The absolute discrepancy of most of the points is within 3 cm/s and the relative discrepancy is within 5%.

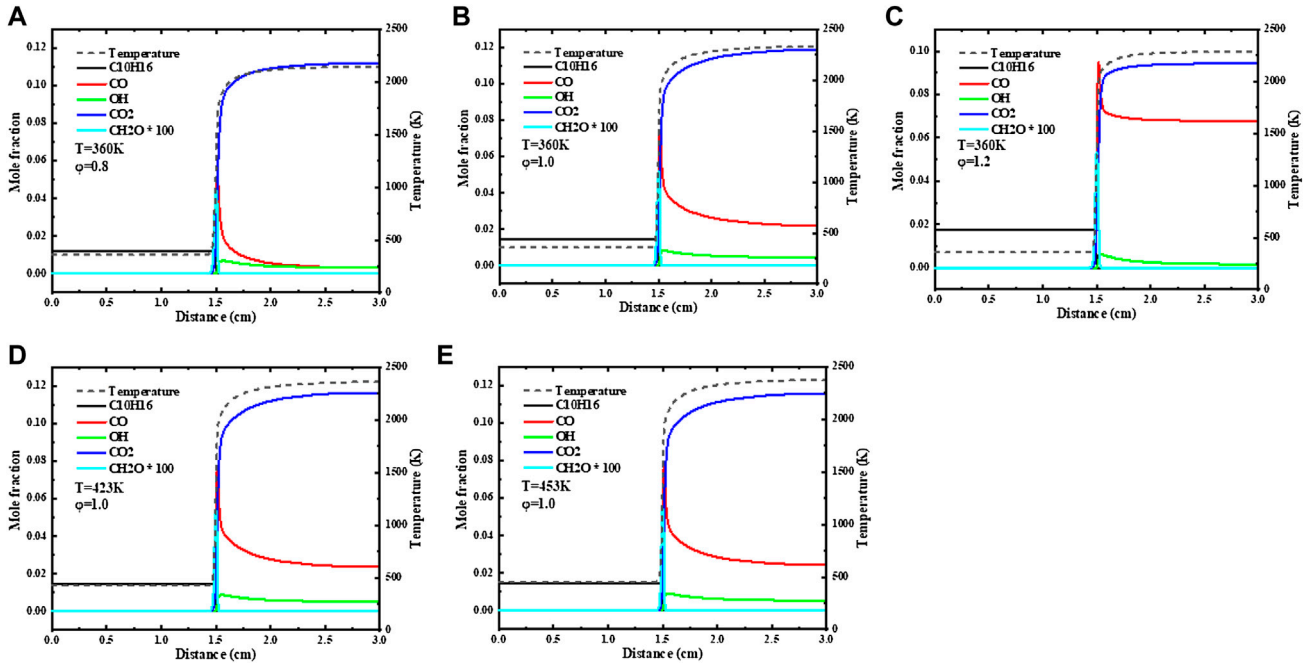

FIGURE 7 | Major species mole fraction and adiabatic flame temperature of JP-10/air flame of T = 360 K, **(A)** φ = 0.8, **(B)** 1.0, **(C)** 1.2; and φ = 1.0, T=**(D)** 423 K, **(E)** 453 K calculated with Hychem detailed mechanism.

According to the power law correlation theory of temperature dependency (Metghalchi and Keck, 1982; Varea et al., 2013) $S_L = S_{L0}(\frac{T}{T_0})^{\alpha}$, the laminar flame speed under higher temperatures can be expressed by a laminar flame speed at the reference conditions of temperature and pressure (S_{L0}) and multiplied by correction factors displaying the temperature dependencies. As shown in **Figure 5**. (d), the laminar flame speed is plotted as a function of the preheating temperature using log-log scales, while straight lines for all of the equivalence ratios tested are observed which illustrates the temperature dependence on the laminar flame speed. The power exponent $\alpha(\varphi)$ is determined from the slope of the straight lines in **Figure 5**. (d). By fitting the slope of the Log(S_L)-Log (T/T_0) lines with the third-order polynomial expression **Eq. 5**, the equivalence ratio dependence coefficients are calculated and listed in **Table 6**.

With the experimental results obtained in the present work, an empirical temperature dependency correlation was proposed by using the power law equation **Eqs. 3–5**, where S_{L0} is the flame speed at T = 360 K, p = 0.1 MPa.

$$S_L = S_{L0}\left(\frac{T}{T_0}\right)^{\alpha} \tag{3}$$

$$S_{L0}(\varphi) = S_{L0,\varphi=1} + S_{L0,1}(\varphi-1) + S_{L0,2}(\varphi-1)^2 + S_{L0,3}(\varphi-1)^3 + S_{L0,4}(\varphi-1)^4 \tag{4}$$

$$\alpha(\varphi) = \alpha_0 + \alpha_1(\varphi-1) + \alpha_2(\varphi-1)^2 + \alpha_3(\varphi-1)^3 \tag{5}$$

3.1.3 Kinetic Analyses

Sensitivity analysis is conducted to identify the important reactions related to JP-10/air laminar flame speed, and fourteen reactions with the largest magnitude of sensitivity coefficient are presented in **Figure 6**. The Hychem detailed mechanism is chosen in the premixed flame simulation for ϕ = 0.8, 1.0, and 1.2 at 1 atm and T = 360 K, 423 K, and 453 K. The normalized sensitivity coefficient (S_i) of the laminar flame speed is calculated using the following formula:

$$S_i = \frac{A_i}{S_L}\frac{\partial S_L}{\partial A_i} \tag{6}$$

where A_i is the pre-exponential factor of the ith reaction. The positive sensitivity indicates that the reactions increase the flame speed, and the negative sensitivity indicates that the reactions slow down the flame speed.

The sensitivity coefficient of most reactions decreases with increasing reaction temperature. Fourteen reactions with the largest magnitude of sensitivity coefficient show that the chain branching reaction H+O_2 = O+OH and chain propagation reaction CO+OH = CO_2+H dominate the chemistry of flame propagation under all conditions studied in the present work. On the other hand, the chain termination reactions H+OH+M = H_2O+M, H+O_2 (+M) = HO_2(+M) and C_5H_5+H (+M) = C_5H_6(+M) play an important role in the slowing the flame speed. The H+O_2 = O+OH reaction is the most sensitive reaction to the flame propagation speed. The formation of the reaction product OH largely affects another reaction with a large sensitivity coefficient, CO+OH = CO_2+H, which in turn affects the rate at which fuel oxidizes to the final product CO_2. At the same time, the competitive reaction of H+O_2 = O+OH, H+O_2 (+M) = HO_2(+M) slows the production of OH, and the

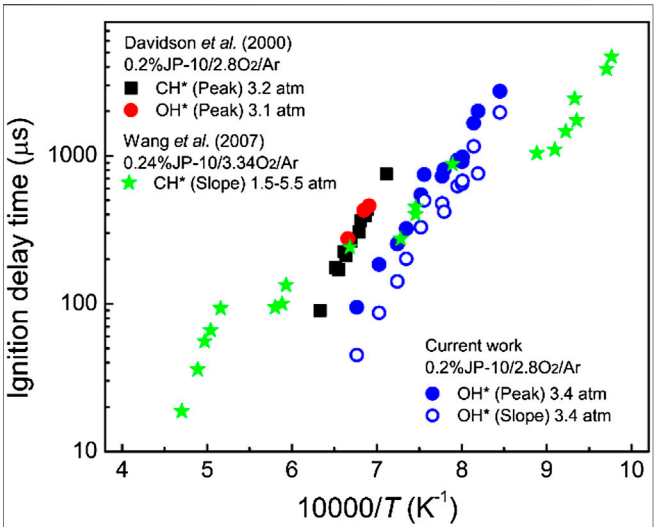

FIGURE 8 | Comparison between our measured ignition delay times and the reported values from the literature (Davidson et al., 2000; Wang et al., 2007).

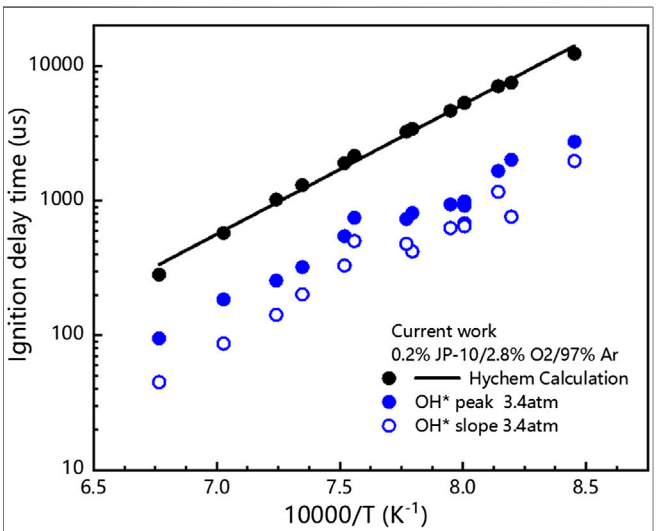

FIGURE 9 | Comparison between our measured ignition delay times and the calculated values with Hychem detailed mechanism.

competitive reaction of CO+OH = CO_2+H, H+OH+M = H_2O + M hinders the oxidation of CO, so these two reactions with large negative sensitivity coefficients reduce the flame propagation speed. In addition, the reactions C_5H_6+H=C_5H_5+H_2, C_5H_5+H (+M) = C_5H_6(+M) and C_5H_6+H=C_5H_5+H_2 related to the pyrolysis products of JP-10 promote and retard the flame propagation speed, respectively.

Figure 7 gives the simulation results of the 1-D flame structure. The adiabatic flame temperature and the mole fraction of some major species related to flame propagation chemistry show the flame structure of JP-10 at initial temperatures of 360 K, 423 K, and 453 K and a pressure of 1 atm. Under the lean fuel condition of equivalence ratio φ = 0.8, the mole fraction of CO is significantly lower than that under stoichiometric ratio conditions and under rich-fuel conditions, and the mole fraction difference at chemical equilibrium between CO_2 and CO reaches a level close to 0.1, which indicates that CO has been fully oxidized and to a certain extent also illustrates the full combustion of JP-10 fuel.

As the equivalence ratio increases, the mole fraction difference at chemical equilibrium between CO_2 and CO continues to shrink. Under the condition of equivalence ratio φ = 1.2, the peak concentration of CO is even higher than the peak concentration of CO_2, which indicates that CO has not been fully oxidized. The change of CH_2O mole fraction with temperature is not significant, but the change trend with equivalence ratio is the same as that of flame speed, which first increases and then decreases. From the previous laminar flame speed sensitivity analysis, it can be seen that H+O_2 = O+OH and CO+OH = CO_2+H are the two most sensitive reactions regarding the laminar flame speed. Therefore, under rich fuel conditions, the relative shortage of O_2 and the relative excess of CO may lead to a decrease in reactivity, which may be one of the reasons for the decrease in laminar flame speed. The flame combustion temperature increases with increasing equivalence ratio, but in the process of increasing the equivalence ratio from 1 to 1.2, the change in the adiabatic flame temperature is not obvious, which also reflects the temperature dependence of the laminar flame speed. Within the range of equivalence ratios φ = 0.7–1.2, the increase in laminar flame speed is more obvious than that in the range of 1–1.2.

3.2 Ignition Delay Time

3.2.1 Comparison of Experimental Results

The measured ignition delay times of JP-10/O_2/Ar mixtures are shown in **Figure 8**, and the available values from the literature (Davidson et al., 2000; Wang et al., 2007) are also adopted for comparison. The ignition delay time of JP-10 decreases markedly with increasing temperature, and the τ peak decreases from 2016 μs at 1221 K to 185 μs at 1422 K. Our measurements have a similar temperature dependence but give lower values in comparison to those of Davidson et al. (Davidson et al., 2000). At temperatures of 1249–1381 K, our measured ignition delay times agree well with the results of Wang et al. (Wang et al., 2007). In the investigated temperature range, however, the reported ignition delay times of JP-10 do not match well with each other. Due to the varying industrial standards, production processes, and preservation conditions, the constituents of JP-10 are usually slightly different. To confirm the reliability of the ignition delay times, some points are repeatedly measured at least two times, and the results indicate that our measurements are credible.

3.2.2 Sensitivity Analysis of Ignition Delay Time

In this work, the detailed mechanism of the hychem is selected to simulate the ignition process of JP-10. The reaction model is a closed homogeneous batch reactor. In the simulation calculation, the time corresponding to the intersection of the tangent at the

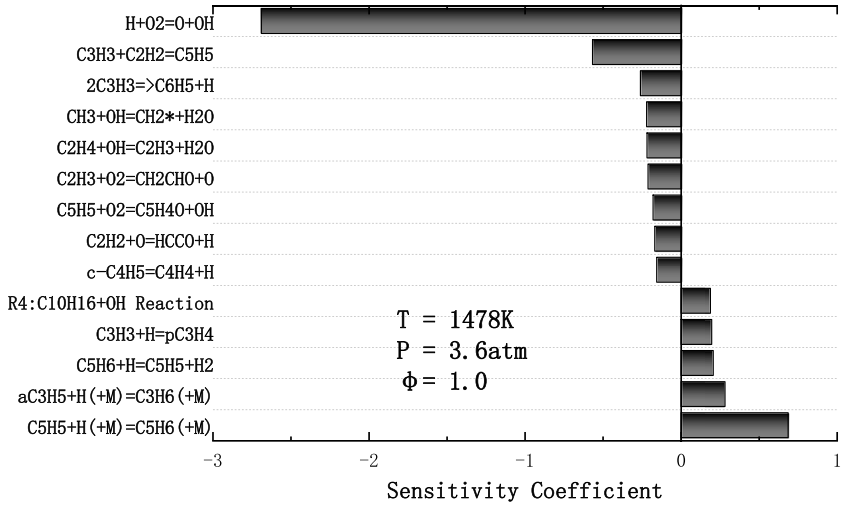

FIGURE 10 | Normalized sensitivity coefficients in predicting ignition delay time of JP-10/O_2/Ar mixture for T = 1478 K, p = 3.6 atm, φ = 1.0 calculated with Hychem detailed mechanism.

maximum slope of the temperature curve and baseline is defined as the ignition time.

Figure 9 shows the measurement results of the ignition delay time of JP-10 and the numerical calculation results using the detailed mechanism of Hychem. **Figure 9** shows that the ignition delay time decreases with increasing premixed gas temperature, and the premixed gas needs a longer time to absorb heat at lower temperatures to reach the ignition conditions. As mentioned above, the experimental data obtained in this paper show an overall smaller trend compared with the experimental data under similar working conditions in the literature, and it is also lower compared with the numerical calculation results, which may be related to the differences in the definitions of ignition delay time and experimental samples.

To further explore the key reactions leading to the ignition process, sensitivity analysis was carried out on the basis of the Hychem mechanism. The sensitivity coefficient is defined as

$$S = \frac{\tau(2.0k_i) - \tau(0.5k_i)}{1.5\tau(k_i)} \tag{7}$$

where τ is the ignition delay time and k_i is the pre-exponential factor of the ith reaction. In this paper, the positive sensitivity coefficient indicates that it can inhibit the ignition process, and the negative sensitivity coefficient indicates that it can promote the ignition process. **Figure 10** shows the key sensitive reactions of JP-10/O_2/Ar mixture ignition at T = 1478 K, p = 3.6 atm and φ = 1.0.

As shown in **Figure 10**, the chain branching reaction $H+O_2 = O+OH$ dominates the ignition chemical process of JP-10. One of the fourteen most important reactions is related to JP-10 fuel. R4 involves the cracking of fuel into C_2, C_3, and C_5 low-carbon molecules, while other key reactions are related to these low-carbon molecules. The reaction of C_3H_3 and C_2H_2 to produce C_5H_5 has a significant impact on the ignition process, and the second largest negative sensitivity coefficient is given. Small radical reactions such as OH have a significant impact on the ignition delay time and participate in most of the fourteen key radical reactions. In addition, the bonding reaction of C_3H_5 and C_5H_5 absorbing H radicals can inhibit the ignition process.

4 CONCLUSION

As a high-density hydrocarbon fuel, JP-10 has an excellent application prospect in the field of aircraft propulsion system, but there are few studies on its combustion kinetics and experimental measurement to verify these mechanisms. In this paper, the basic combustion characteristics of JP-10 (laminar flame speed, ignition delay time) are measured, and kinetic studies are conducted to verify the reported mechanism. The main conclusions are as follows:

1) Experimental study on laminar flame speed of JP-10/air mixture were conducted in Bunsen burner at different equivalence ratios (0.7–1.2), temperatures (360–453 K), atmosphere pressure. Correlation of laminar flame speed is given according to the power law correlation theory of temperature dependency. The comparison between experimental data and mechanism prediction shows that the UCSD mechanism has an overestimation trend in predicting laminar flame speed and the prediction of Hychem mechanisms (detailed and skeletal) is in good agreement with experimental data.
2) Experimental study on ignition delay time of 0.2%JP-10/2.8% O_2/97%Ar mixture were conducted in shock tube at different temperatures (1183K–1478K), 3.4 atm. The comparison shows that the Hychem detailed mechanism overestimates the ignition delay time at our experimental conditions.

3) Kinetic studies show that there are three reactions ($H+O_2$ = O+OH, C_5H_5+H (+M) = C_5H_6(+M), $C_3H_3+C_2H_2$ = C_5H_5) determine the laminar flame speed and ignition delay time at tested temperature and equivalence ratio range.

DATA AVAILABILITY STATEMENT

The original contributions presented in the study are included in the article/**Supplementary Material**, further inquiries can be directed to the corresponding author.

AUTHOR CONTRIBUTIONS

JY (First author): experiment, data processing, writing original draft, conceptualization, methodology; YW (corresponding author): funding acquisition, data curation, writing original draft, supervision; ZZ: experiment, writing original draft, review and; editing; YS: data processing, writing original draft; LP: providing JP-10 fuel, review and; editing.

FUNDING

This research is supported by National Natural Science Foundation of China No.51906016.

SUPPLEMENTARY MATERIAL

The Supplementary Material for this article can be found online at: https://www.frontiersin.org/articles/10.3389/fenrg.2022.910304/full#supplementary-material

Supplementary Table S1 | Measured ignition delay times of JP-10/O2/Ar.

Supplementary Table S2 | Measured laminar flame speed (cm/s) of JP-10/air.

REFERENCES

Akbar, R. (2012). "Detonation Properties of Unsensitized and Sensitized JP-10 and Jet-A Fuels in Air for Pulse Detonation Engines," in 36th AIAA/ASME/SAE/ASEE Joint Propulsion Conference and Exhibit., Las Vegas, NV, July 24–28, 2000.

An, Y.-z., Pei, Y.-q., Qin, J., Zhao, H., and Li, X. (2015). Kinetic Modeling of Polycyclic Aromatic Hydrocarbons Formation Process for Gasoline Surrogate Fuels. *Energy Convers. Manag.* 100, 249–261. doi:10.1016/j.enconman.2015.05.013

Antaki, P., and Williams, F. A. (1987). Observations on the Combustion of Boron Slurry Droplets in Air. *Combust. Flame* 67 (1), 1–8. doi:10.1016/0010-2180(87)90009-5

Bouvet, N., Chauveau, C., Gökalp, I., Lee, S.-Y., and Santoro, R. J. (2011). Characterization of Syngas Laminar Flames Using the Bunsen Burner Configuration. *Int. J. Hydrogen Energy* 36 (1), 992–1005. doi:10.1016/j.ijhydene.2010.08.147

Brotton, S. J., Malek, M. J., Anderson, S. L., and Kaiser, R. I. (2020). Effects of Acetonitrile-Assisted Ball-Milled Aluminum Nanoparticles on the Ignition of Acoustically Levitated Exo-Tetrahydrodicyclopentadiene (JP-10) Droplets. *Chem. Phys. Lett.* 754, 137679. doi:10.1016/j.cplett.2020.137679

Brophy, C., and Netzer, D., (1999). "Effects of Ignition Characteristics and Geometry on the Performance of a JP-10/O2 Fueled Pulse Detonation Engine," in 35th Joint Propulsion Conference and Exhibit, Los Angeles, CA, June 20–24, 1999, 2635. doi:10.2514/6.1999-2635

Chung, H. S., Chen, C. S. H., Kremer, R. A., Boulton, J. R., and Burdette, G. W. (1999). Recent Developments in High-Energy Density Liquid Hydrocarbon Fuels. *Energy fuels.* 13 (3), 641–649. doi:10.1021/ef980195k

Colket, M. B., and Spadaccini, L. J. (2001). Scramjet Fuels Autoignition Study. *J. Propuls. Power* 17 (2), 315–323. doi:10.2514/2.5744

Cooper, M. A., Shepherd, J. E., Sobota, T. H., and Moore, K. C. (2002). *Thermal and Catalytic Cracking of JP-10 for Pulse Detonation Engine Applications*. Pasadena, CA: California Institute of Technology.

Courty, L., Chetehouna, K., Halter, F., Foucher, F., Garo, J. P., and Mounaïm-Rousselle, C. (2012). Experimental Determination of Emission and Laminar Burning Speeds of α-pinene. *Combust. Flame* 159 (4), 1385–1392. doi:10.1016/j.combustflame.2011.11.003

Davidson, D. F., Horning, D. C., Herbon, J. T., and Hanson, R. K. (2000). Shock Tube Measurements of JP-10 Ignition. *Proc. Combust. Inst.* 28 (2), 1687–1692. doi:10.1016/s0082-0784(00)80568-8

Davidson, D., Horning, D., Oehlschlaeger, M., and Hanson, R., (2001). "The Decomposition Products of JP-10," in 37th Joint Propulsion Conference and Exhibit, Salt Lake City, UT, July 8–11, 2001, 3707. doi:10.2514/6.2001-3707

Desantes, J. M., López, J. J., Molina, S., and López-Pintor, D. (2015). Design of Synthetic EGR and Simulation Study of the Effect of Simplified Formulations on the Ignition Delay of Isooctane and N-Heptane. *Energy Convers. Manag.* 96, 521–531. doi:10.1016/j.enconman.2015.03.003

Davidson, D. F., Shao, J., Parise, T., and Hanson, R. K. (2017). "Shock Tube Measurements of Jet and Rocket Fuel Ignition Delay Times," in presented at the 55th AIAA Aerospace Sciences Meeting, Grapevine, TX, January 9–13, 2017.

Feng, X.-t.-f. E., Pan, L., Zhang, X., and Zou, J.-J. (2020). Influence of Quadricyclane Additive on Ignition and Combustion Properties of High-Density JP-10 Fuel. *Fuel* 276, 118047. doi:10.1016/j.fuel.2020.118047

Feng, X.-t.-f. E., Zhi, X., Zhang, X., Wang, L., Xu, S., and Zou, J.-J. (2018). Ignition and Combustion Performances of High-Energy-Density Jet Fuels Catalyzed by Pt and Pd Nanoparticles. *Energy & Fuels* 32 (2), 2163. doi:10.1021/acs.energyfuels.7b03342

Gao, C. W., Vandeputte, A. G., Yee, N. W., Green, W. H., Bonomi, R. E., Magoon, G. R., et al. (2015). JP-10 Combustion Studied with Shock Tube Experiments and Modeled with Automatic Reaction Mechanism Generation. *Combust. Flame* 162 (8), 3115–3129. doi:10.1016/j.combustflame.2015.02.010

Gong, S., Zhang, X., Bi, Q., Liu, Z., and Liu, G. (2017). Experimental Measurement of JP-10 Viscosity at 242.7-753.3 K Under Pressures up to 6.00 MPa. *J. Chem. Eng. Data* 62 (11), 3671–3678. doi:10.1021/acs.jced.7b00396

Gu, X., Li, Q., Huang, Z., and Zhang, N. (2011). Measurement of Laminar Flame Speeds and Flame Stability Analysis of Tert-Butanol-Air Mixtures at Elevated Pressures. *Energy Convers. Manag.* 52 (10), 3137–3146. doi:10.1016/j.enconman.2011.05.002

Ishizuka, S. (1982). An Experimental Study on the Opening of Laminar Diffusion Flame Tips. *Symposium Int. Combust.* 19 (1), 319–326. doi:10.1016/s0082-0784(82)80203-8

Jia, T. (2021). Mechanistic Insights into the Thermal Oxidative Deposition of C10 Hydrocarbon Fuels. *Fuel* 285, 119136. doi:10.1016/j.fuel.2020.119136

Johnson, S. E., Davidson, D. F., and Hanson, R. K. (2020). Shock Tube/laser Absorption Measurements of the Pyrolysis of JP-10 Fuel. *Combust. Flame* 216, 161–173. doi:10.1016/j.combustflame.2019.11.026

Law, C. K., Ishizuka, S., and Cho, P. (1982). On the Opening of Premixed Bunsen Flame Tips. *Combust. Sci. Technol.* 28 (3-4), 89–96. doi:10.1080/00102208208952545

Li, H., Liu, G., Jiang, R., Wang, L., and Zhang, X. (2015). Experimental and Kinetic Modeling Study of Exo-TCD Pyrolysis under Low Pressure. *Combust. Flame* 162 (5), 2177–2190. doi:10.1016/j.combustflame.2015.01.015

Li, S. C., Varatharajan, B., and Williams, F. A. (2001). Chemistry of JP-10 Ignition. *AIAA J.* 39 (12), 2351–2356. doi:10.2514/2.1241

Liao, S. Y., Jiang, D. M., Cheng, Q., Gao, J., Huang, Z. H., and Hu, Y. (2005). Correlations for Laminar Burning Velocities of Liquefied Petroleum Gas-Air Mixtures. *Energy Convers. Manag.* 46 (20), 3175–3184. doi:10.1016/j.enconman.2005.03.020

Liu, Y., Shi, C., Pan, L., Zhang, X., and Zou, J.-J. (2022). Synthesis and Performance of Cyclopropanated Pinanes with High Density and High Specific Impulse. *Fuel* 307, 1219062022.

Magoon, G. R., Aguilera-Iparraguirre, J., Green, W. H., Lutz, J. J., Piecuch, P., Wong, H.-W., et al. (2012). Detailed Chemical Kinetic Modeling of JP-10 (Exo-tetrahydrodicyclopentadiene) High-Temperature Oxidation: Exploring the Role of Biradical Species in Initial Decomposition Steps. *Int. J. Chem. Kinet.* 44 (3), 179–193. doi:10.1002/kin.20702

Metghalchi, M., and Keck, J. C. (1982). Burning Velocities of Mixtures of Air with Methanol, Isooctane, and Indolene at High Pressure and Temperature. *Combust. Flame* 48, 191–210. doi:10.1016/0010-2180(82)90127-4

Mikolaitis, D. W., Segal, C., and Chandy, A. (2003). Ignition Delay for Jet Propellant 10/Air and Jet Propellant 10/High-Energy Density Fuel/Air Mixtures. *J. Propuls. Power* 19 (4), 601–606. doi:10.2514/2.6147

Mizomoto, M., Asaka, Y., Ikai, S., and Law, C. K. (1985). Effects of Preferential Diffusion on the Burning Intensity of Curved Flames. *Symposium Int. Combust.* 20 (1), 1933–1939. doi:10.1016/s0082-0784(85)80692-5

Mizomoto, M., and Yoshida, H. (1987). Effects of Lewis Number on the Burning Intensity of Bunsen Flames. *Combust. Flame* 70 (1), 47–60. doi:10.1016/0010-2180(87)90158-1

Nageswara Rao, P., and Kunzru, D. (2006). Thermal Cracking of JP-10: Kinetics and Product Distribution. *J. Anal. Appl. Pyrolysis* 76 (1), 154–160. doi:10.1016/j.jaap.2005.10.003

Nakra, S., Green, R. J., and Anderson, S. L. (2006). Thermal Decomposition of JP-10 Studied by Micro-flowtube Pyrolysis-Mass Spectrometry. *Combust. Flame* 144 (4), 662–674. doi:10.1016/j.combustflame.2005.08.035

Parsinejad, F., Arcari, C., and Metghalchi, H. (2006). Flame Structure and Burning Speed of Jp-10 Air Mixtures. *Combust. Sci. Technol.* 178 (5), 975–1000. doi:10.1080/00102200500270080

Qin, Z., Gong, S., Zhang, X., Bi, Q., Liu, Z., and Liu, G. (2018). Experimental Measurement of JP-10 Density at 267 to 873 K under Pressures up to 6.00 MPa. *J. Chem. Eng. Data* 64 (1), 218–225. doi:10.1021/acs.jced.8b00729

Rocha, R. C. (2021). Structure and Laminar Flame Speed of an Ammonia/Methane/Air Premixed Flame under Varying Pressure and Equivalence Ratio. *Energy fuels.* 35 (9), 7179–7192.

Sakai, Y., Konishi, K., and Ishihara, A. (1996). Tip Opening and Burning Intensity of Bunsen Flames Diluted with Nitrogen. *JSME Int. J. Ser. B, Fluids Therm. Eng.* 39 (1), 164–170. doi:10.1299/jsmeb.39.164

Seiser, R., Niemann, U., and Seshadri, K. (2011). Experimental Study of Combustion of N-Decane and JP-10 in Non-premixed Flows. *Proc. Combust. Inst.* 33 (1), 1045–1052. doi:10.1016/j.proci.2010.06.078

Shang, Y., Shi, J., Ning, H., Zhang, R., Wang, H., and Luo, S. (2019). Ignition Delay Time Measurements and Kinetic Modeling ofCH_4 Initiated by CH_3NO_2. *Fuel* 243, 288–297. doi:10.1016/j.fuel.2019.01.112

Shang, Y., Wang, Z., Ma, L., Shi, J., Ning, H., Ren, W., et al. (2021). Shock Tube Measurement of NO Time-Histories in Nitromethane Pyrolysis Using a Quantum Cascade Laser at 5.26 Mm. *Proc. Combust. Inst.* 38 (1), 1745–1752. doi:10.1016/j.proci.2020.07.026

Shi, J. C., Ye, W., Bie, B. X., Long, X. J., Zhang, R. T., Wu, X. J., et al. (2016). Ignition Delay Time Measurements on $CH_4/CH_3Cl/O_2$/Ar Mixtures for Kinetic Analysis. *Energy fuels.* 30 (10), 8711–8719. doi:10.1021/acs.energyfuels.6b01466

Smith, N. K., and Good, W. D. (1979). Enthalpies of Combustion of Ramjet Fuels. *AIAA J.* 17 (8), 905–907. doi:10.2514/3.61244

Szekely, G. A., and Faeth, G. M. (1983). Effects of Envelope Flames on Drop Gasification Rates in Turbulent Diffusion Flames. *Combust. Flame* 49 (1), 255–259. doi:10.1016/0010-2180(83)90168-2

Tao, Y., Xu, R., Wang, K., Shao, J., Johnson, S. E., Movaghar, A., et al. (2018). A Physics-Based Approach to Modeling Real-Fuel Combustion Chemistry - III. Reaction Kinetic Model of JP10. *Combust. Flame* 198, 466–476. doi:10.1016/j.combustflame.2018.08.022

Vandewiele, N. M., Magoon, G. R., Van Geem, K. M., Reyniers, M.-F., Green, W. H., and Marin, G. B. (2014). Experimental and Modeling Study on the Thermal Decomposition of Jet Propellant-10. *Energy fuels.* 28 (8), 4976–4985. doi:10.1021/ef500936m

Vandewiele, N. M., Magoon, G. R., Van Geem, K. M., Reyniers, M.-F., Green, W. H., and Marin, G. B. (2015). Kinetic Modeling of Jet Propellant-10 Pyrolysis. *Energy fuels.* 29 (1), 413–427. doi:10.1021/ef502274r

Varea, E., Modica, V., Renou, B., and Boukhalfa, A. M. (2013). Pressure Effects on Laminar Burning Velocities and Markstein Lengths for Isooctane-Ethanol-Air Mixtures. *Proc. Combust. Inst.* 34 (1), 735–744. doi:10.1016/j.proci.2012.06.072

Wang, H., Zhang, B., Gong, S., Wang, L., Zhang, X., and Liu, G. (2021). Experimental and Modeling Studies of Exo-Tetrahydrobicyclopentadiene and Tetrahydrotricyclopentadiene Pyrolysis at 1 and 30 Atm. *Combust. Flame* 232, 111536. doi:10.1016/j.combustflame.2021.111536

Wang, S., Gou, H.-j., Fan, B.-c., He, Y.-z., Zhang, S.-t., and Cui, J.-p. (2007). Shock Tube Study of JP-10 Ignition Delay Time. *Chin. J. Chem. Phys.* 20 (1), 48–52. doi:10.1360/cjcp2007.20(1).48.5

Wu, Y., Modica, V., Rossow, B., and Grisch, F. (2016). Effects of Pressure and Preheating Temperature on the Laminar Flame Speed of Methane/air and Acetone/air Mixtures. *Fuel* 185, 577–588. doi:10.1016/j.fuel.2016.07.110

Wu, Y., Rossow, B., Modica, V., Yu, X., Wu, L., and Grisch, F. (2017). Laminar Flame Speed of Lignocellulosic Biomass-Derived Oxygenates and Blends of Gasoline/oxygenates. *Fuel* 202, 572–582. doi:10.1016/j.fuel.2017.04.085

Zettervall, N. (2020). Reduced Chemical Kinetic Reaction Mechanism for JP-10-Air Combustion. *Energy fuels.* 34 (12), 16624–16635. doi:10.1021/acs.energyfuels.0c02971

Zhang, X., Wang, J., Chen, Y., and Li, C. (2021). Effect of CH_4, Pressure, and Initial Temperature on the Laminar Flame Speed of an NH_3-Air Mixture. *ACS Omega* 6 (18), 11857. doi:10.1021/acsomega.1c00080

Zhong, B.-J., Zeng, Z.-M., and Zhang, H.-Z. (2022). An Experimental and Kinetic Modeling Study of JP-10 Combustion. *Fuel* 312, 122900. doi:10.1016/j.fuel.2021.122900

Conflict of Interest: The authors declare that the research was conducted in the absence of any commercial or financial relationships that could be construed as a potential conflict of interest.

Publisher's Note: All claims expressed in this article are solely those of the authors and do not necessarily represent those of their affiliated organizations, or those of the publisher, the editors and the reviewers. Any product that may be evaluated in this article, or claim that may be made by its manufacturer, is not guaranteed or endorsed by the publisher.

frontiers | Frontiers in Energy Research

ORIGINAL RESEARCH
published: 15 June 2022
doi: 10.3389/fenrg.2022.928358

Aerodynamic Performance of the Single-Stage Transonic Turbine With Different Reaction Degrees

Qiankun Jia[1], *Senpei Xu*[1], *Peipei Sun*[2] *and Wei Du*[1]*

[1]School of Energy Science and Engineering, Harbin Institute of Technology, Harbin, China, [2]Aero Engine Academy of China, Beijing, China

A numerical method was used to investigate the reaction degree effects on the aerodynamic performance and flow structure of the single-stage transonic turbine. The SST-γ-θ turbulence model was employed to predict a transition for the boundary layer near the blade surface. This work utilized a public PW-E^3 blade profile from NASA. Five different reaction degrees were adopted, corresponding to Ω = 0.15, 0.27, 0.33, 0.44 and 0.59. In addition, different off-design conditions were considered with three reaction degrees. The efficiency, blade surface pressure and high Mach number distributions were significantly associated with the reaction degrees. Results indicated that the highest efficiency point was observed at Ω = 0.33. The trailing edge shocks and the reflected waves were visible in the cascade channels. The Shock wave was easily detected in the stator channel at lower reaction degrees while it was displayed in a rotor with a higher reaction degree. When the reaction degree was increased, the high Mach number region was expanded in the rotor channels while it was reduced in stators. Besides, the highest efficiency points were also observed around π = 1.5 for all operating conditions. Furthermore, the critical pressure ratio was discovered and the maximum mass flow rate gradually decreases as the reaction degree increases.

Keywords: transonic turbine, reaction degrees, shock waves, off-design conditions, aerodynamic performance

OPEN ACCESS

Edited by:
Xiao Liu,
Harbin Engineering University, China

Reviewed by:
Jian Liu,
Central South University, China
Shaopeng Lu,
Shanghai Jiao Tong University, China
Hongxin Zhang,
Nanjing University of Aeronautics and Astronautics, China

***Correspondence:**
Wei Du
hitdw9211@outlook.com

Specialty section:
This article was submitted to Advanced Clean Fuel Technologies, a section of the journal Frontiers in Energy Research

Received: *25 April 2022*
Accepted: *12 May 2022*
Published: *15 June 2022*

Citation:
Jia Q, Xu S, Sun P and Du W (2022) Aerodynamic Performance of the Single-Stage Transonic Turbine With Different Reaction Degrees. Front. Energy Res. 10:928358. doi: 10.3389/fenrg.2022.928358

1 INTRODUCTION

More power and higher efficiency are considered to be the permanent goals for high-performance gas turbine design (Sandberg and Michelassi, 2022). The high turbine inlet temperature and highly loaded means high efficiency and power for the gas turbine (Wei et al., 2022; Luo et al., 2022). By increasing the stage load of a turbine, the number of turbine stages is reduced and the turbine expansion ratio is increased, which can improve the work capacity of the turbine effectively and a higher thrust-to-weight ratio is obtained. However, the turbine exit Mach number is raised inevitably due to the increase of the turbine expansion ratio. Therefore, the turbine components are operated on high load and transonic speed conditions.

The shock waves are generated in the transonic turbine cascade channels with high exit Mach number and high expansion ratio. In particular, due to the high exit Mach number conditions, shock waves are found at the trailing edge, which can cause a shock loss and also interference with the wake (Yao and Carson, 2006). Trailing edge shock waves are thought to be one of the most important reasons for the losses in transonic turbine cascades, and controlling the shock loss in transonic turbines can improve the aerodynamic performance of the turbine effectively. Thus, it is quite necessary to study transonic turbines with high exit Mach number and high expansion ratio,

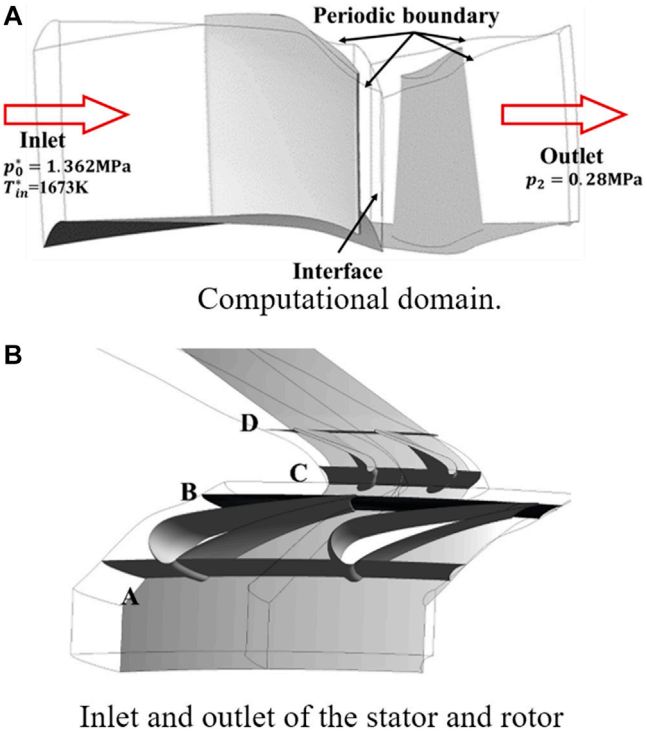

FIGURE 1 | Geometry. **(A)** Computational domain. **(B)** Inlet and outlet of the stator and rotor.

especially single-stage transonic turbines. Recently, many researchers have investigated the flow characteristics and loss mechanisms in transonic turbine cascades (Zhang et al., 2014; Rehman et al., 2019). A high-fidelity large eddy simulation was used to study some of the complex flow phenomena occurring in bladed components by Hou et al. (2010), Lu and Dawes (2015). The moving shock, shock-boundary layer interaction, and shock-wake interaction were accurately described and analyzed for the transonic turbine cascades. Börner and Niehuis (2021) investigated the dynamics of the interaction between the shock waves and the laminar separation flow in a transonic turbine by using high-speed schlieren and surface hot-film sensor. Their results indicated that the low frequencies characteristic of the shock wave motions and the pulsations of the separated bubbles were found by statistical analysis of the schlieren images, and an unsteady shock wave on the suction surface was observed at the upstream of the trailing edge. Zhao et al. (2016) discussed a variety of blade losses for transonic turbines. They concluded that the negative curvature design of the blade suction surface profile was beneficial to reduce the trailing edge losses. Duan et al. (2018) used the RANS (Reynolds-Averaged Navier-Stokes) method to evaluate the loss characteristics of two representative transonic turbine blades. The results showed that the boundary layer losses and trailing edge losses determined the loss level in the subsonic flow region. However, the losses generated by the shock waves seemed to play a decisive role in the supersonic flow region. Furthermore, the losses increased gradually with the rising of the exit Mach number. Teia (2020) proposed a new supersonic loss model for transonic turbines by analyzing data from schlieren images and experimental measurements. Their main results showed that pitch to chord ratio has a powerful influence on the shock system. Therefore, the manner by which shock loss and shock-induced mixing loss were distributed to constitute the overall supersonic losses. Clark et al. (2018) discussed relied on the physics of shock reflections itself to achieve a bowed airfoil and circumferentially asymmetric vane spacing. It also predicted that two methods of forcing reduction could reduce the unsteady pressures on the blade as intended. Liu et al. (2022) studied the transition process of turbulent wakes. They found that the viscous effect got weakened for the supersonic flow with a high Reynolds number, generating the large scale vortex streets.

Pau and Paniagua (2010) found that there were serious aerodynamic losses due to the injection of coolant at the trailing edge in transonic turbines, and reduced the turbine's performance. Denton (1993) predicted that trailing edge shock losses were probably the largest single loss in transonic turbine Cascades. Gao et al. (2019) showed that there was an optimal flow to ensure that the injection at the trailing edge could increase the static pressure at the tail of the suction side. Therefore, the blade load and trailing edge loss were reduced effectively. Sieverding (1983) used experimental and numerical simulations. It was found that coolant injection through the trailing edge had a positive impact on the base pressure at the trailing edge. The maximum base pressure rise was up to 15% of the downstream dynamic pressure at the transonic exit Mach number. Therefore, the coolant injection at the trailing edge could increase the base pressure and eventually reduce the aerodynamic losses. Moreover, Raffel and Kost (1998) utilized the PIV (Particle Image Velocimetry) technology to quantitatively measure the transient flow field. The results indicated that the shock waves caused the separation of the boundary layer on the suction surface in the supersonic flow field, which not only increased the viscous losses but also increased the secondary flow losses. In particular, it had a negative influence on the cooling performance of the suction surface. Carnevale et al. (2014) investigated the coupling between film cooling and shock system in a transonic flow field. It confirmed that the maximum uncertainty level was observed downstream of the region where the shock waves interacted with the boundary layer. Especially, the shock generated complex flow structures. A number of researchers have discussed and evaluated the blade tip leakage losses in transonic turbines (Zhang et al., 2011; Atkins et al., 2012), and analyzed the aerodynamic thermal characteristics (De Maesschalck et al., 2014; Arisi et al., 2015). In particular, the Very Large Eddy Simulation approach was conducted to predict the Over-Tip Leakage (OTL) flow of the transonic turbine cascades by Wang et al. (2021). It was found that the flow structure of separated vortices and shock waves became more complex in the clearance cavity with the increase of the blade tip clearance. In particular, a change of the reaction degree affected the leakage flow in turbine blades due to the variation in the blade loading (Yoon, 2013). For the optimal design of transonic turbine blade shapes, Joly et al. (2010) introduced a Multi-Objective Optimization which was applied to the redesign of a transonic blade. The objective of the steady-flow optimization was to

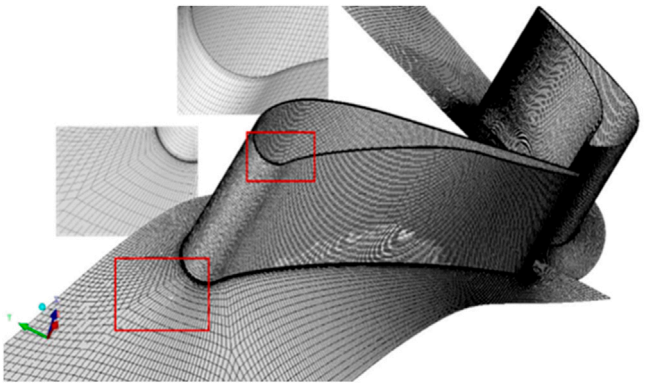

FIGURE 2 | Mesh distribution.

TABLE 1 | Overall performance parameters of Case A1–Case A5.

Case	Ω	π	q_m [kg/s]	η
A1	0.15	4.52	29.54	79.78%
A2	0.27	4.46	29.54	86.13%
A3	0.33	4.38	29.52	86.87%
A4	0.44	4.23	29.33	86.48%
A5	0.59	4.40	28.08	83.81%

attenuate the propagation of shock waves downstream of the vane while reducing the losses. Subsequently, a multi-objective optimization method was applied to the three-dimensional design of transonic turbine blade rows by Puente et al. (2015). The decrease of the rotor dynamic pressure was verified by unsteady numerical simulations of multi-stage blades. In addition, Ji et al. (2017) selected three transonic turbine cascades and used the adjoint method to optimize the design of turbine cascades with different back pressures to find the geometric parameters with the best aerodynamic performance. Meanwhile, the adjoint method was also used to analyze the evident shock features in the turbine cascade. Sonoda et al. (2004) introduced a numerical optimization concept for aerodynamic design based on evolutionary algorithms. A stronger trailing edge excitation was split into several weaker trailing edge excitations by optimal design. Thus, the flow losses in the turbine cascade were probably reduced. To attenuate the downstream static pressure transition caused by trailing edge shocks, artificial intelligence combined with an adaptive mesh CFD solver was used to design and optimize the transonic turbine blade shapes (Shelton et al., 1993). The results showed that the shock intensity on the suction surface near the trailing edge was reduced and the outlet flow field was more uniform.

From the previous studies, it was found that a large number of research results focused on discussing the potential losses due to trailing edge shock waves in transonic turbines. Most of the above studies have been devoted to investigating the blade tip leakage and coolant injection in the trailing edge of transonic turbines. Moreover, many researchers have adopted advanced blade optimization design methods to decrease the possible losses by trailing edge shocks. Actually, the reaction degrees are essential in the aerodynamic design of turbomachinery (Noor et al., 2012). However, only a small number of publications focused on investigating the influence of the reaction degree parameters on the aerodynamic performance in transonic turbines. In this paper, the is selected as a research variable. It is significant to

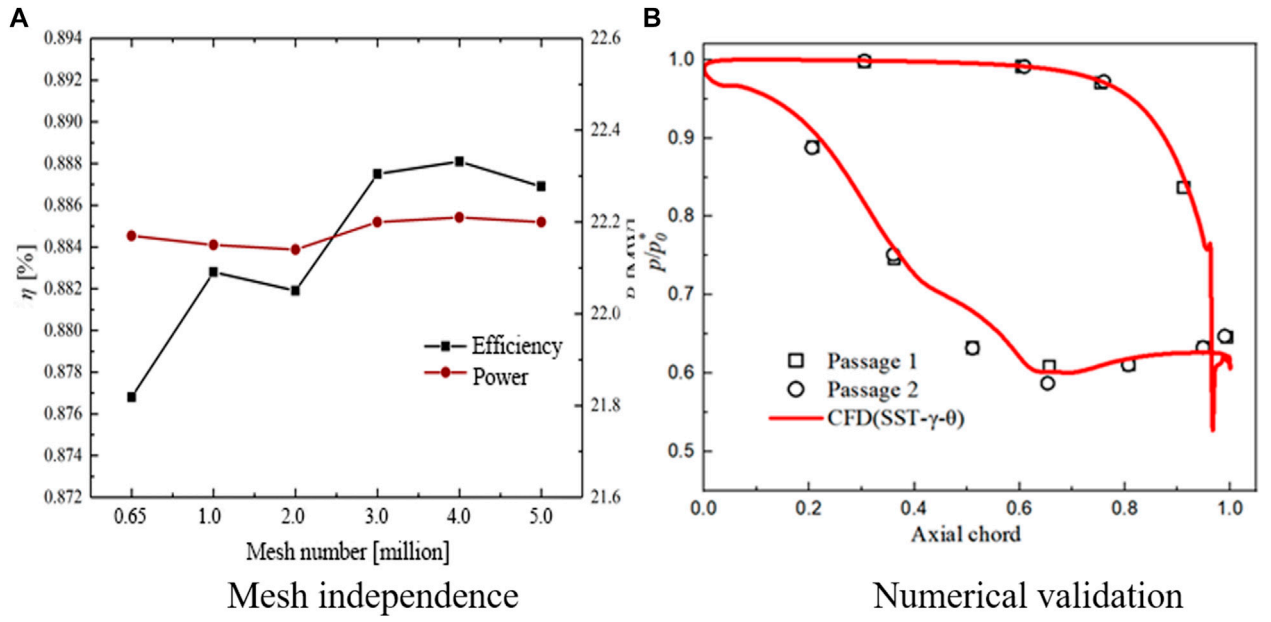

FIGURE 3 | Mesh independence verification. **(A)** Mesh independence; **(B)** Numerical validation

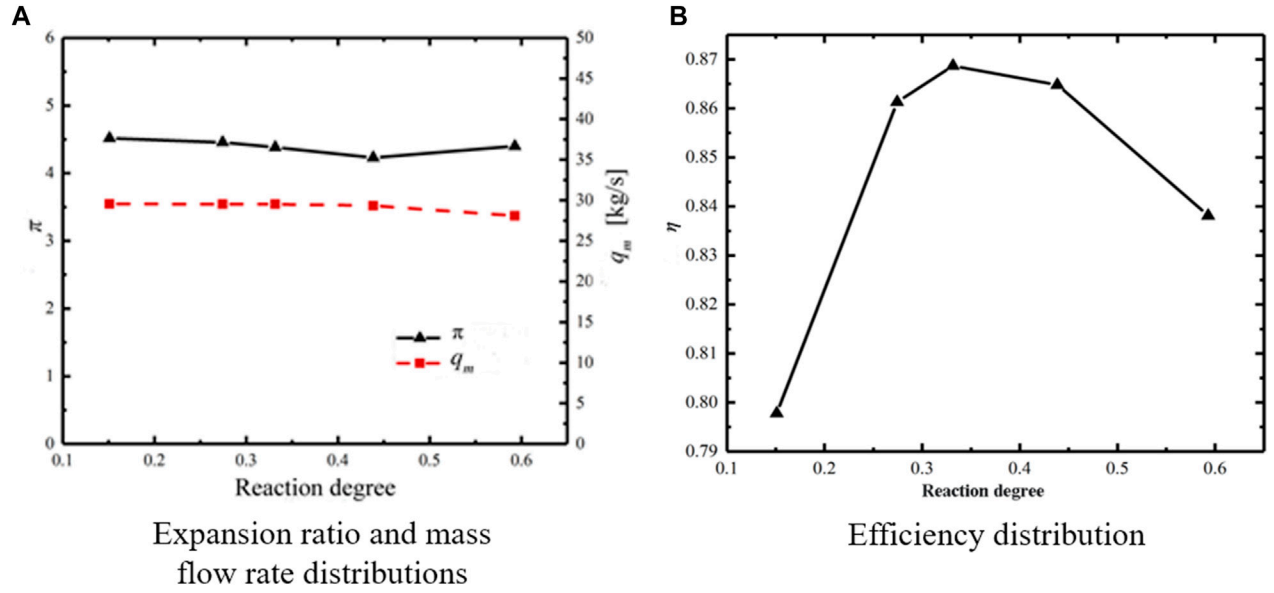

FIGURE 4 | Numerical results for different reaction degrees. **(A)** Expansion ratio and mass flow rate distributions. **(B)** Efficiency distribution.

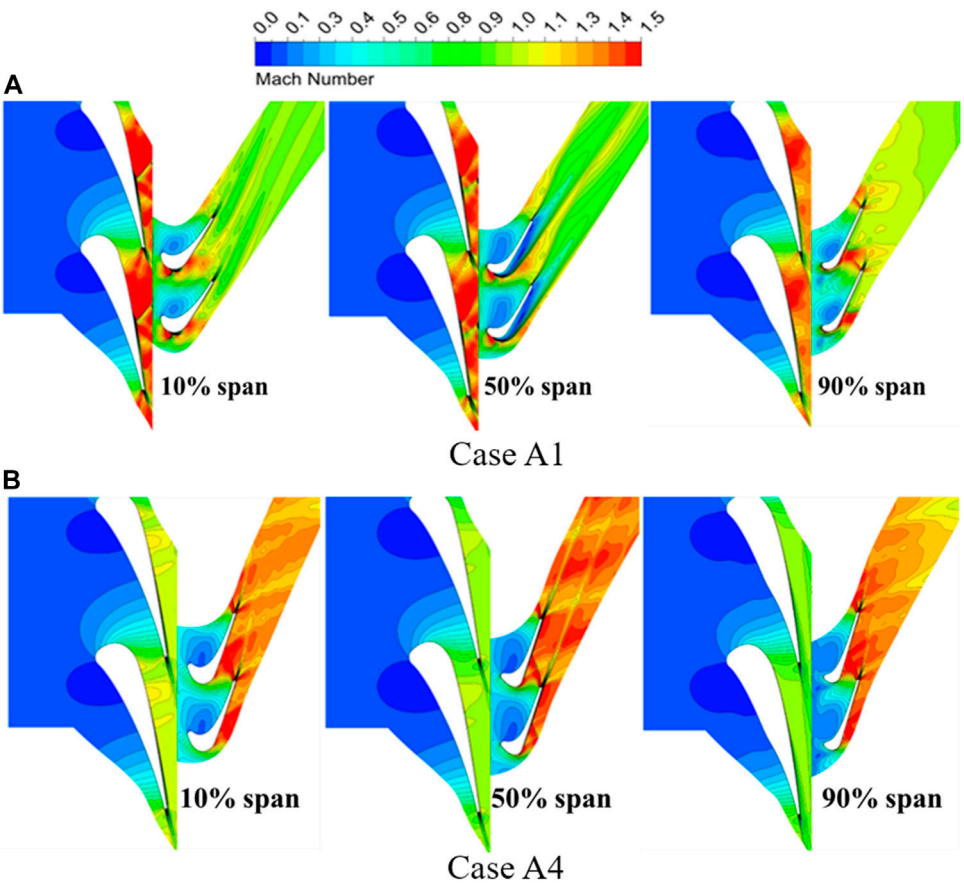

FIGURE 5 | Mach number distribution for different blade height sections between Case A1 and A4. **(A)** Case A1. **(B)** Case A4.

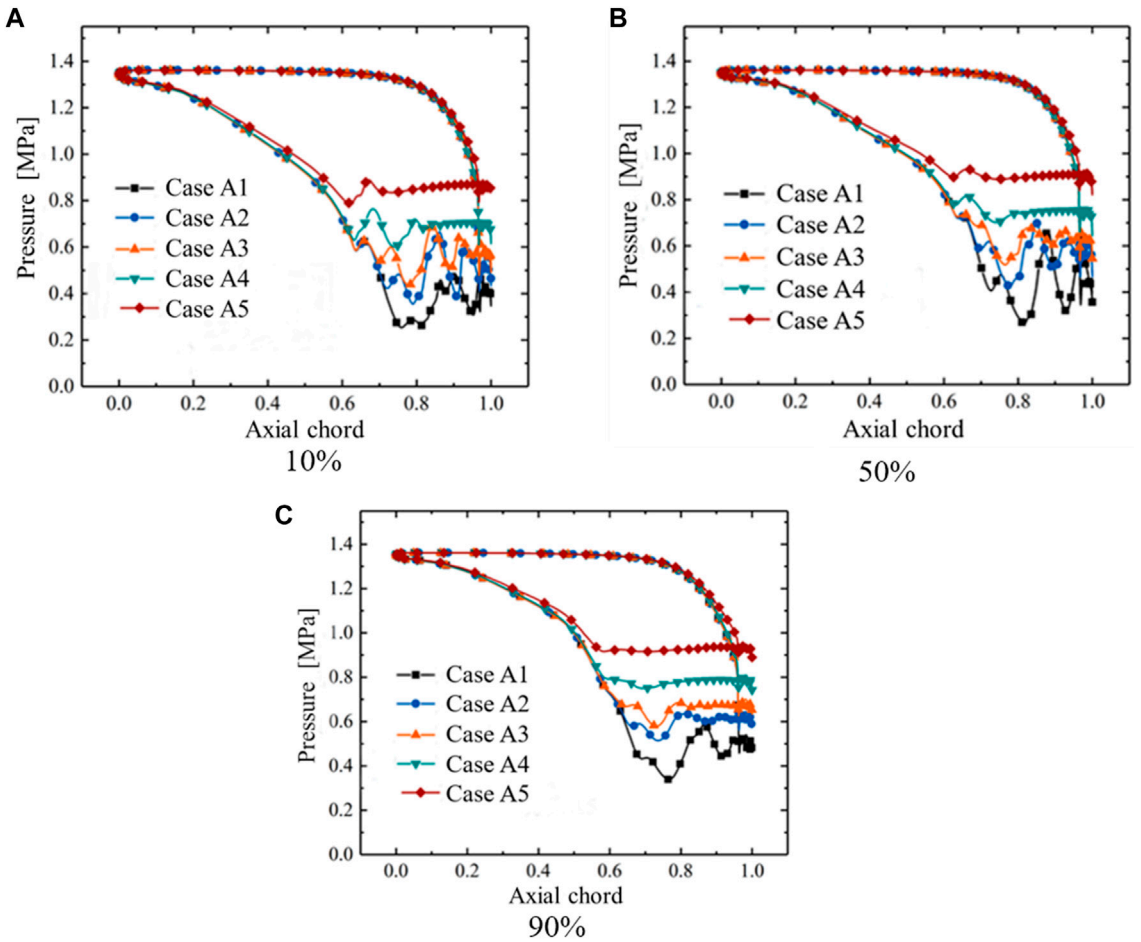

FIGURE 6 | Blade surface pressure distribution of stator from Case A1 to Case A5. **(A)** 10%. **(B)** 50%. **(C)** 90%.

explore whether different reaction degrees can impact the flow field characteristics of transonic turbine cascades. Details of the waves structure in the cascades and the flow on the blade surface are considered. In addition, the performance of transonic turbines operating off-design conditions is investigated numerically.

2 NUMERICAL METHODOLOGY

2.1 Computational Domain and Blade Modeling

Figure 1A presents the Computational domain. The public PW-E^3 blade profile is utilized (Thulin et al., 1982). The parameters at the stator and rotor mid-span are provided. The stator numbers are 24 and the rotor numbers are 54. The inlet foil angles are and in the stator and rotor, respectively. The tip gap is 0.0185 in which is equivalent to 0.8% of the rotor height. In this study, an in-house Blade-Editor code independently completed by Harbin Institute of Technology is further developed for the blade design of the single-stage transonic turbine. The Blade-Editor code based on the 11-parameter method models the blade by three profiles, which is stacked to form a 3D blade shape. To investigate the effect of inversion on the aerodynamic performance of transonic turbines, five different reaction degrees are introduced, Ω = 0.15, 0.27, 0.33, 0.44 and 0.59. The reaction degree parameters are adapted by adjusting the blade shape of the rotor, while the stator is not changed. **Figure 1B** shows a schematic view of the inlet and outlet of the rotor and stator blades. Section A and Section B represent the inlet and outlet of the stator, respectively. Similarly, Section C and Section D is the inlet and outlet of the rotor.

2.2 Solver and Boundary Conditions

The RANS equations are solved by the commercial CFD software ANSYS CFX, which is selected to calculate the three-dimensional steady flow and heat transfer (Ananthakrishnan and Govardhan, 2018). The SIMPLE algorithm is used to handle the pressure-velocity coupling. To reduce the numerical dissipation, a second-order upwind scheme is used to discretize the computational domain. The SST-γ-θ turbulence model is chosen to analyze the flow behavior in single-stage turbine cascade channels (Kiran and Anish, 2017). During the computational procedure, the residuals

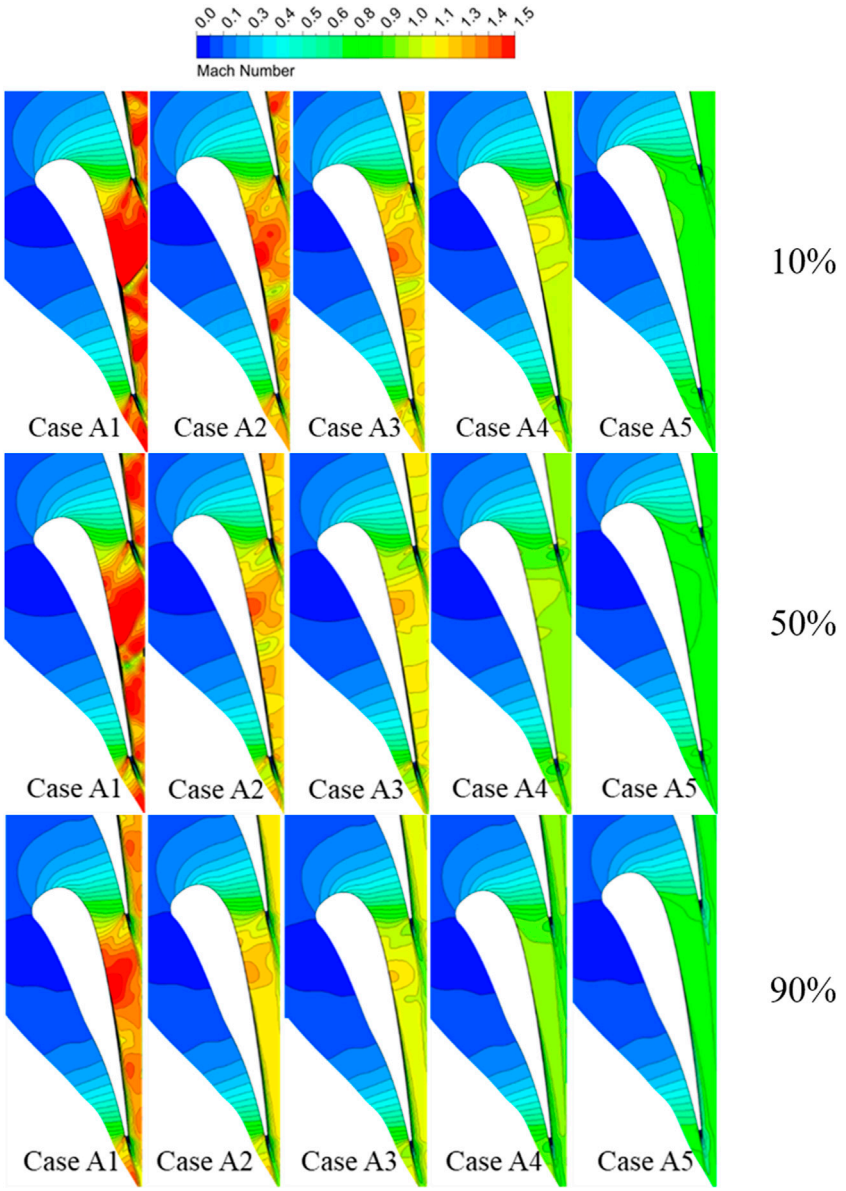

FIGURE 7 | Mach number distribution of stators from Case A1 to Case A5.

for the continuity equation and momentum equations are ensured to be less than 10^{-5}. In this paper, the RANS model is adopted to solve the governing equations:

$$\frac{\partial \rho}{\partial t} + \frac{\partial}{\partial x_j}\left(\rho \bar{u}_j\right) = 0 \tag{1}$$

$$\frac{\partial}{\partial t}\left(\rho \bar{u}_i\right) + \frac{\partial}{\partial x_j}\left(\rho \bar{u}_i \bar{u}_j\right) = \frac{\partial p}{\partial x_i} + \frac{\partial}{\partial x_j}\left[\mu\left(\frac{\partial \bar{u}_j}{\partial x_i} + \frac{\partial \bar{u}_i}{\partial x_j}\right) - \rho\overline{u_l' u_j'}\right] - \frac{2}{3}\frac{\partial}{\partial x_j}\left(\mu \frac{\partial \bar{u}_j}{\partial x_i}\right) \tag{2}$$

$$\frac{\partial}{\partial t}\left(\rho c_p \bar{T}\right) + \frac{\partial}{\partial x_j}\left(\rho c_p \bar{u}_j \bar{T}\right) = \frac{\partial}{\partial x_j}\left[\frac{\mu}{Pr}\frac{\partial}{\partial x_j}\left(c_p \bar{T}\right) - \rho c_p \overline{x_l' T'}\right] + S_E \tag{3}$$

For the numerical simulation of the turbine devices, the rotor speed should not be ignored. In this present study, the rotor speed is set to 13,232 r/min. Real gas is employed as the working fluid which is closer to the real transonic turbine working environment. In particular, the total temperature and total pressure conditions are determined at the entrance to the computational domain, corresponding to T_{in}^{*} = 1673K and p_0^{*} = 1.362MPa. A constant static pressure (p_2 = 0.28MPa) is applied as the outlet condition.

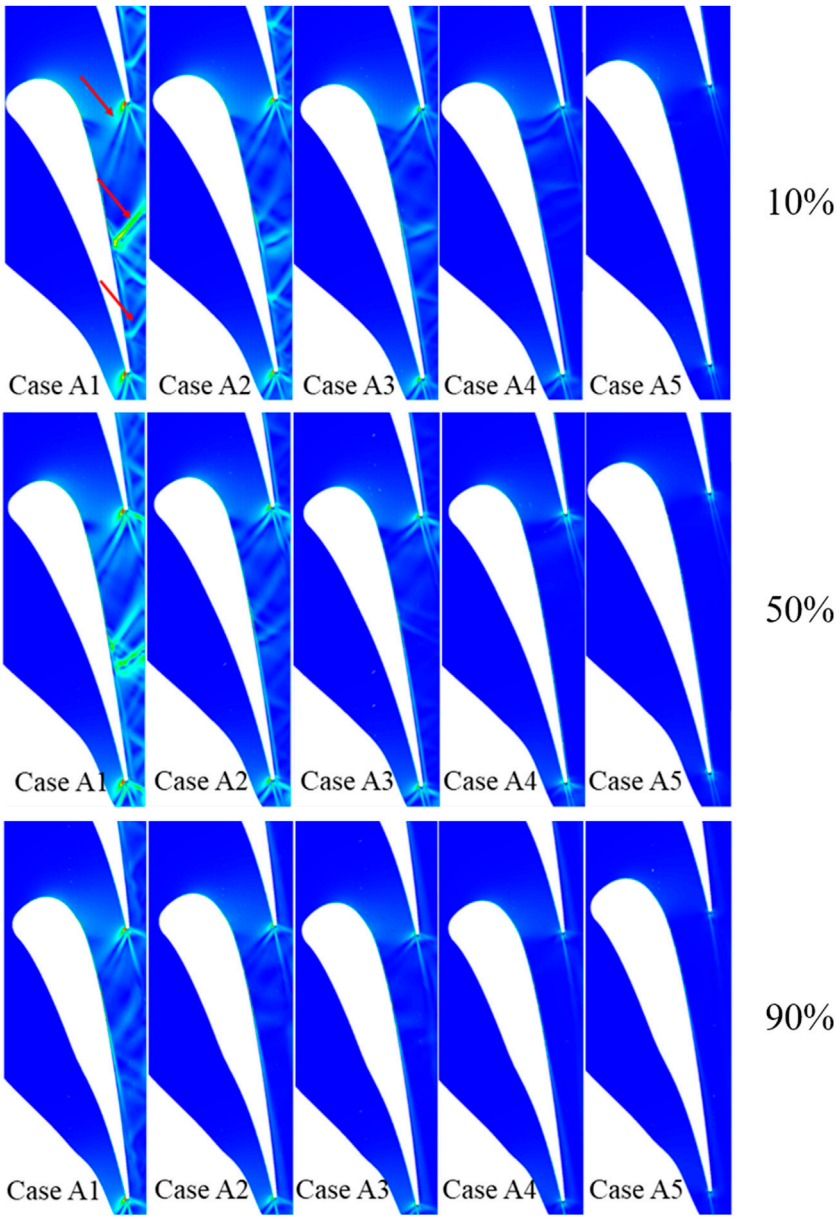

FIGURE 8 | Density gradient distribution of stators from Case A1 to Case A5.

A periodic boundary condition is adopted at the two sides of the domain and the no-slip wall condition is set for all walls, as shown in **Figure 1A**. In addition high-resolution turbulence numerics and a high-resolution advection scheme are utilized in this study to reduce the computational errors.

2.3 Parameter Definition

The reaction degree Ω is defined as (Gardner, 1979; Dixon and Hall, 2013):

$$\Omega = \frac{p_{s,out} - p_{r,out}}{p_{s,in} - p_{r,out}} \tag{4}$$

Where $p_{\mathrm{s,in}}$ and $p_{\mathrm{s,out}}$ are the mean static pressure for the inlet and outlet of stators, respectively. $p_{\mathrm{r,out}}$ is the mean static pressure for the outlet of rotors. Besides, $p_{\mathrm{s,out}}$ is also used as the mean static pressure for the inlet of rotors.

The power P is defined as:

$$P = M \cdot \omega \tag{5}$$

Where M is the torque of the rotor blades, ω is the angular velocity of the rotor blades.

The efficiency of the stage η is defined as:

$$\eta = \frac{P}{q_m \cdot c_p \cdot T_{in}^* \cdot \left[1 - \left(p_2^*/p_0^*\right)^{\frac{k-1}{k}}\right]} \tag{6}$$

Where c_p is heat capacity of the gas, κ is the isentropic exponent.

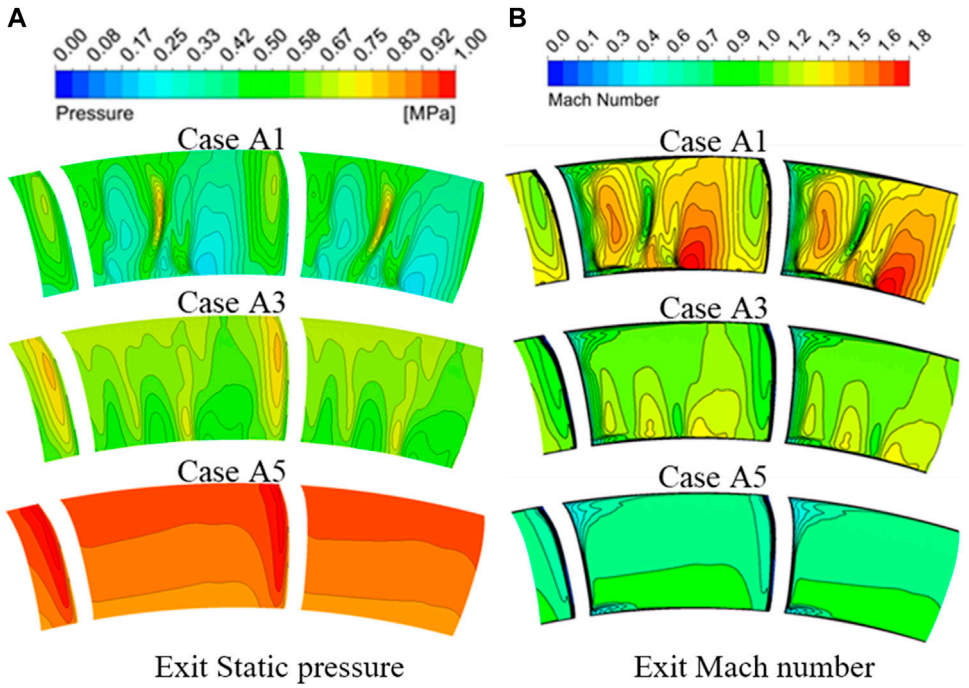

FIGURE 9 | Exit Static pressure and Mach number distribution of stators. **(A)** Exit Static pressure. **(B)** Exit Mach number.

2.4 Mesh Information and Numerical Validation

An in-house grid generation code is used to create the structured mesh. The quality of the structured mesh is above 0.3, showing the stability and accuracy of the in-house grid code. **Figure 2** illustrates the overall view of the structured mesh and details of the mesh near the top and hub of the blade. To ensure that the Y Plus value is less than 1, the first layer grid height near the blade wall is set to 0.005 mm, which meets the calculation requirements of the SST-γ-θ turbulence model. The O-Grid and H-Grid are applied to capture the flow structure for the blade passage, and this modeling method makes the mesh more uniform. A mesh independence verification is introduced in this work. **Figure 3** shows the η and P distributions with different mesh numbers. It is found that the monitored values are kept almost constant as the grid number is more than 3.0 million. Therefore, 3.0 million grid elements are chosen in this study.

The blade surface pressure experimental data of PW-E^3 stator blade mid-span cascade was used to validate the numerical method in this study. To approximate the experimental conditions, ideal air is adopted. **Figure 3B** shows the comparison of the experimental results and numerical results. The result with SST-γ-θ turbulence model delivers perfect accuracy for pressure distribution by comparison with the experimental data.

3 RESULTS AND DISCUSSION

3.1 Overall Performance

Table 1 presents the overall performance parameters from Case A1 to Case A5, including reaction degrees, expansion ratio, efficiency, mass flow rate. To obtain the approximate expansion ratio π = 4.4, the method of adjusting the outlet back pressure was utilized. Meanwhile, the stator blade shape was slightly adjusted to stabilize the mass flow rate around 29.53 kg/s (relative error less than 5%). **Figure 4A** presents the distributions of expansion ratio and mass flow rate at different reaction degrees, and the black solid line and the red dashed line indicate the expansion ratio and mass flow rate, respectively. For Case A4, the maximum expansion ratio error is 3.84% at Ω = 0.44. The biggest mass flow rate error is 4.81% for Case A5. It seems that the expansion ratio and mass flow rate are not deviated from the design condition, corresponding to π = 4.4 and q_m = 29.53kgs. **Figure 4B** provides the distribution of efficiency. The result shows that the efficiency of the stage shows a considerable increase with the reaction degrees grows from 0.15 to 0.33. Then it experiences a decreasing trend as the reaction degree is above 0.33. Thus, the highest η is found at Ω = 0.33 for Case A3. For Case A5, the efficiency of stage is diminished by 3.52% compared to Case A3. From the above results, it can be found that the efficiency of the stage is directly associated with the reaction degrees.

Cases A1 and A4 are adapted to analyze the overall flow structure in a transonic turbine. **Figure 5** shows the contours of Mach number distribution along with the blade height at 10%, 50%, 90% span sections for Case A1 and Case A4. It suggests that the primary expansion and acceleration regions of the fluid are observed in the stator cascade channels for Case A1. The red zones in the graph indicate that supersonic flow may have occurred. However, it is difficult to recognize the acceleration region in the rotor channels compared to the stator. In addition, a

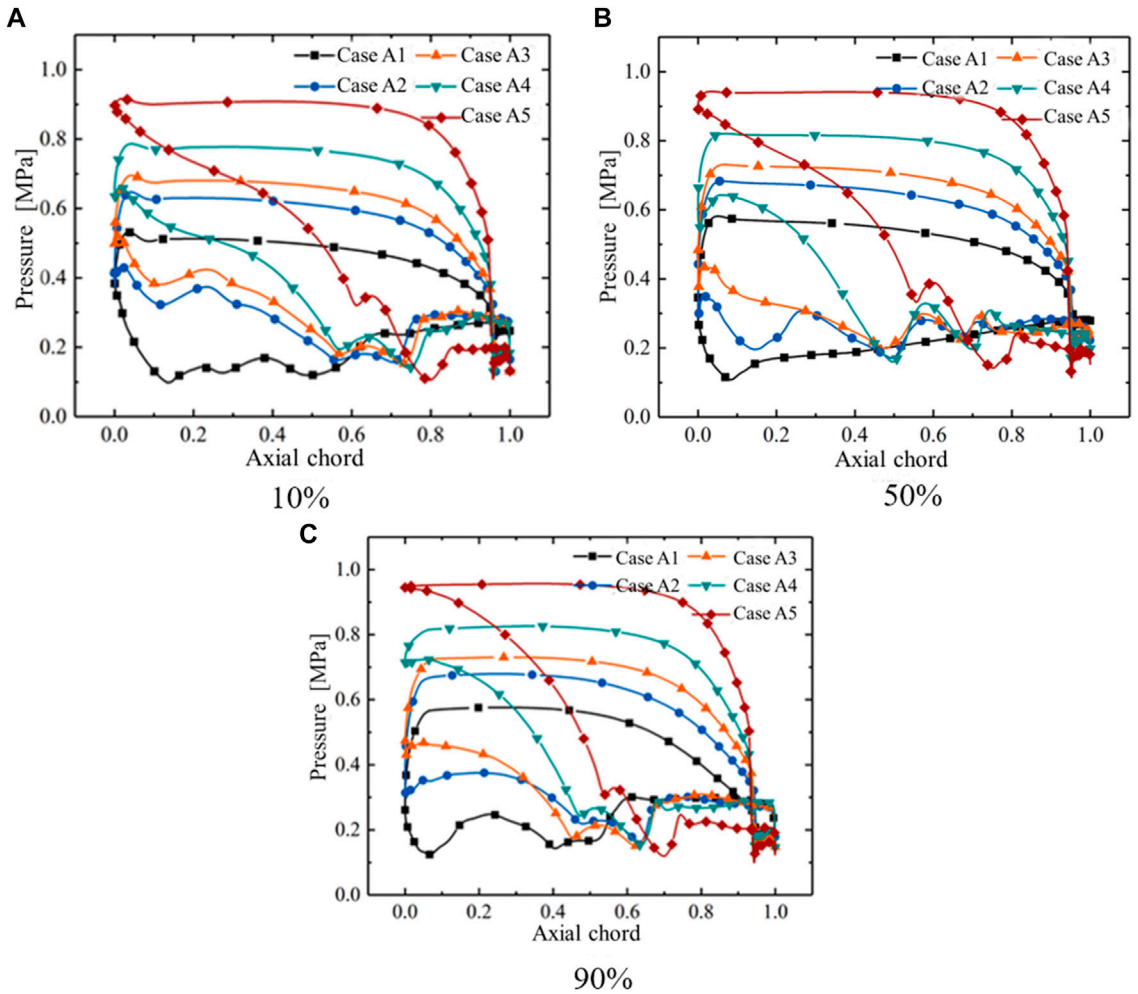

FIGURE 10 | Blade surface pressure distribution of rotor from Case A1 to Case A5. **(A)** 10%. **(B)** 50%. **(C)** 90%.

distinct line is noticed in the stator cascade channels, which is an indication of the appearance of the shock structures. Then the Mach number zones are suddenly decreased through the shocks and continue to expand and accelerate, and this transition is noted near the trailing edge of the stator. Therefore, shocks may be the key factor for the complex wave system in the stators. It should be noticed that the local high Mach number areas are displayed near the leading edge of the rotor, as shown in **Figure 5A**. This phenomenon becomes more obvious at 10% span near the endwall.

For Case A4, the flow characteristic is quite different compared to Case A1. According to **Figure 5B**, the local supersonic regions and shock waves are not observed in the stator cascade channels. It suggests that a high reaction degree blade shape design is likely to provide a more uniform flow in stator channels. Thus, the relatively stabilized flow state can still be achieved for the fluid in the rotors. Besides, for case A4, the expansion and acceleration of the flow are monitored in the rotor channels, but not in the stator. The flow field in the outlet of rotors is characterized by complex wave systems. The Mach number near the trailing edge is significantly reduced after passing through the inner trailing shock. In addition, the outer trailing shocks near the trailing edge also interfere with the wake. Both of the shocks are considered as the decisive factors affecting the efficiency of the turbine stage. Moreover, the flow characteristics of the rotor inlet are also more uniform, and the high Mach number areas near the leading edge of the rotors are gradually decreased. Therefore, the flow field is sensitive to the blade height for Case A1 which represents a low reaction degree design. In general, the wave system structure becomes more complex due to the influence of end wall losses in low reaction degree designs.

3.2 Flow Analysis for Stators

Figure 6 presents the blade surface pressure distribution of the stator cascade channels from Case A1 to Case A5. The results indicate that the stators are after-loaded blade shapes. In addition, the pressure distributions on the suction surface side for all cases with different reaction degrees present significant discrepancies, which are mainly concentrated in

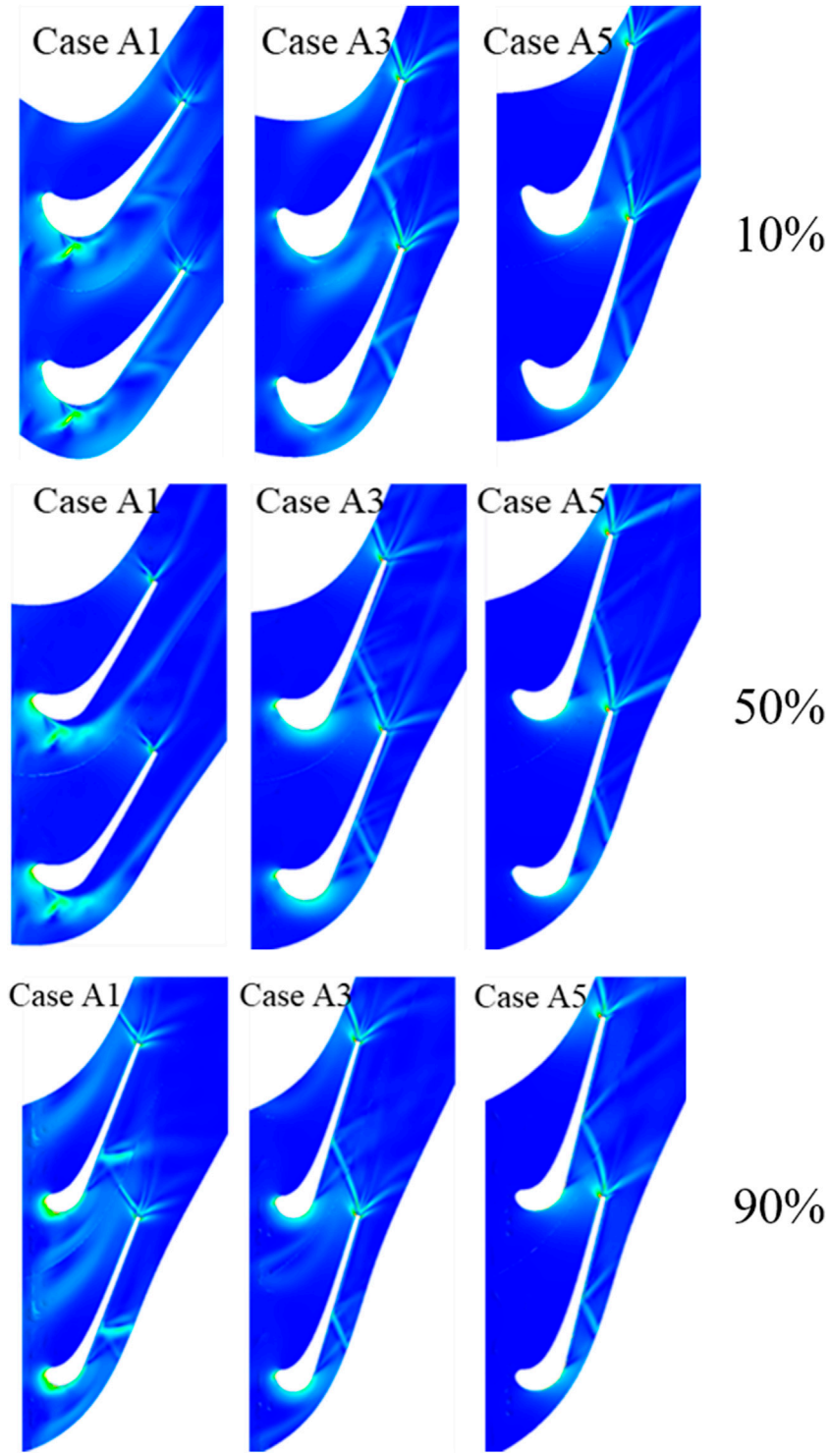

FIGURE 11 | Density gradient distribution of rotors for different cases.

the tail of the suction surface in the axial chord range of above 0.6. **Figure 6C** demonstrates the lower pressure fluctuations at 90% span. It means that the flow field near the blade top is potentially more uniform. However, the flow structures in the middle section and the section near the end wall of the stators are assumed to become more complex through the lines with

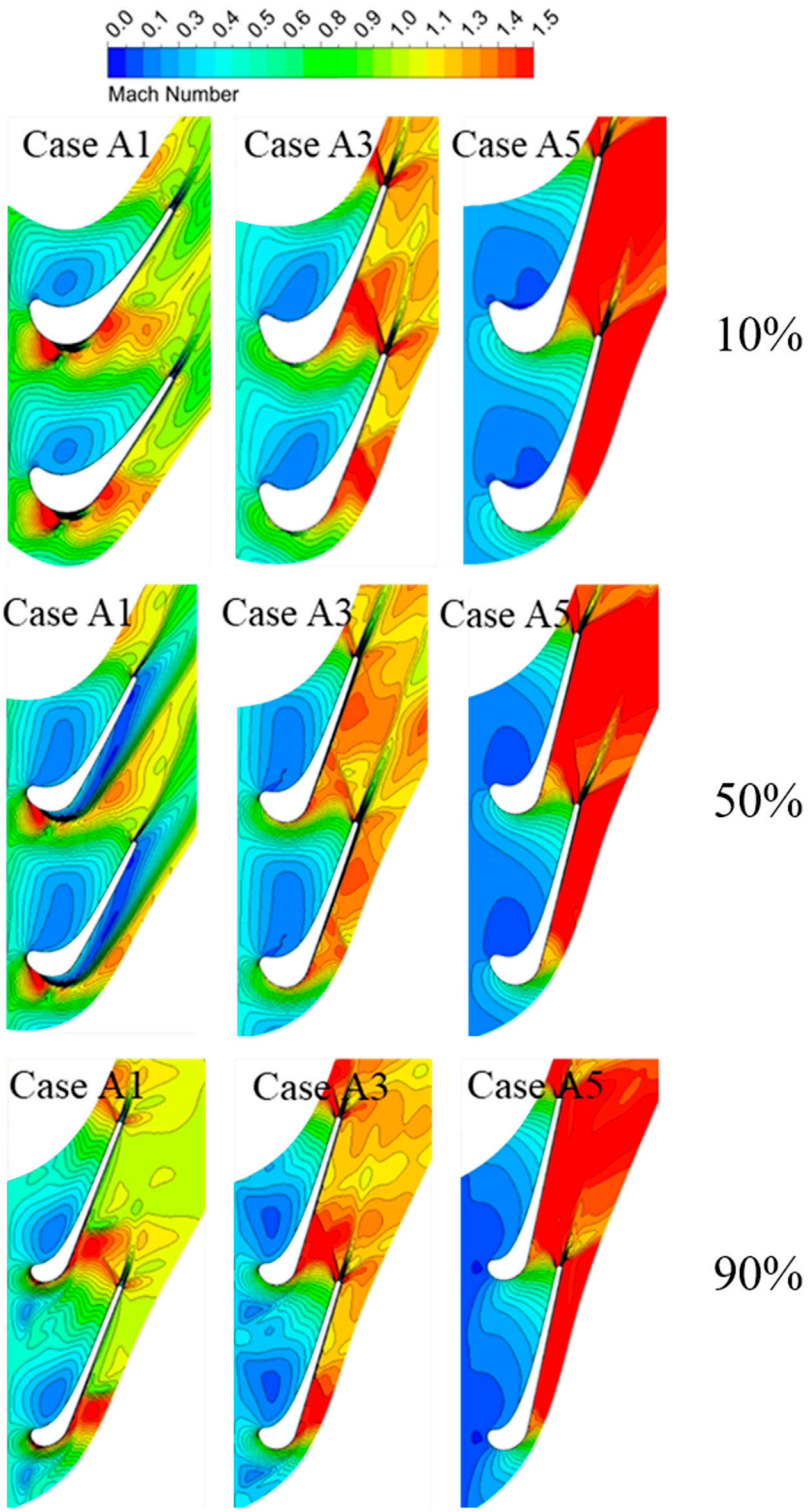

FIGURE 12 | Mach number distribution of rotors for different cases.

irregular and violent fluctuations, as shown in **Figures 6A,B**. In particular, the initial position where pressure fluctuations emerge is progressively backward as the reaction degree decreases by comparing five different cases. Probably because of the low reaction degree designs, the visible pressure fluctuations are found in the tail of the suction surface for

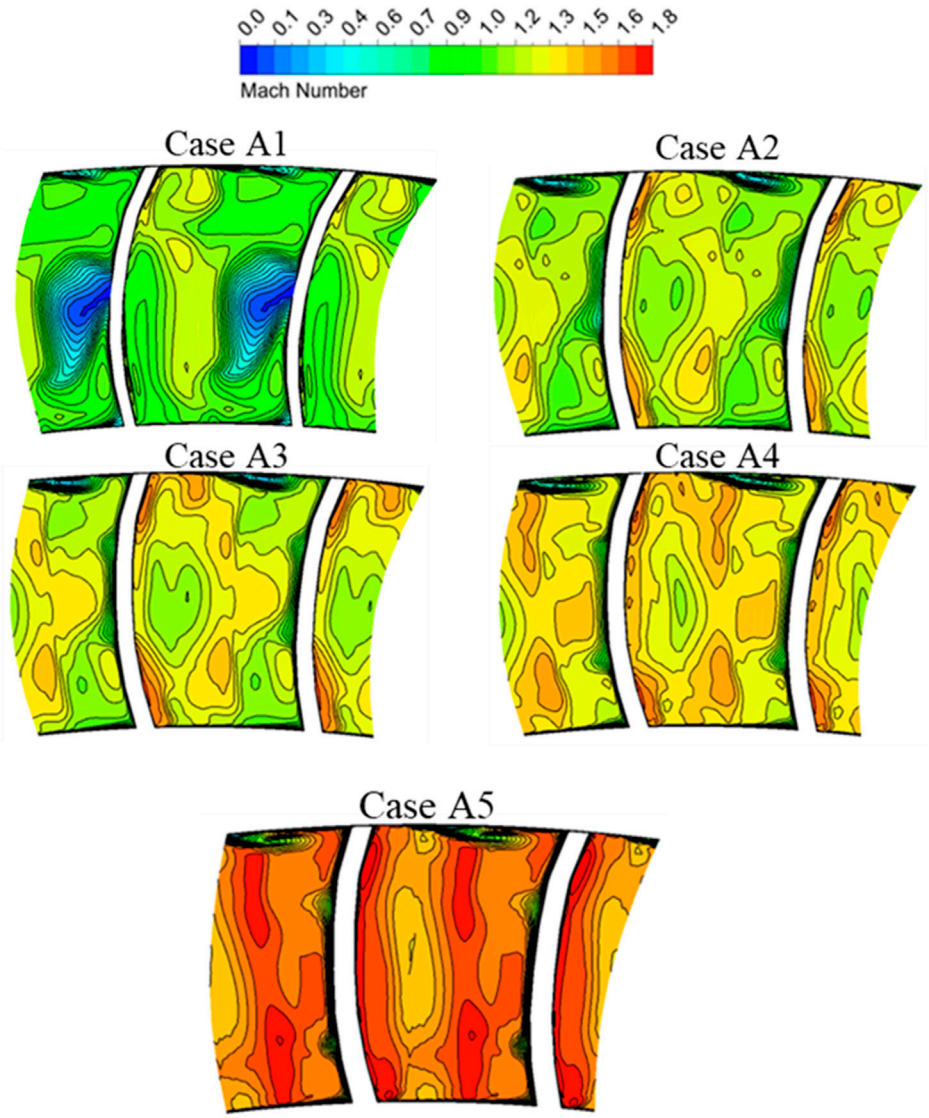

FIGURE 13 | Exit Mach number distribution of rotors.

Case A1, Case A2, Case A3. Associated with **Figure 8**, the trailing edge shocks are presumed as one of the primary reasons for the strong pressure fluctuations at the suction surface.

To investigate the distinctive details of the wave system and flow structure in the stator channels, the Mach number distribution of stators is analyzed from Case A1 to Case A5, as shown in **Figure 7**. In addition, the red zones at the end of channels decreased progressively with increasing the blade height, which means a definite diminution of the high Mach number regions. The results of Case A3 indicate the turbulent Mach number distribution in the stator channels and the possible emergence of complex vortex surfaces. Furthermore, this phenomenon is more easily observed for lower reaction degree cases. The strip dividers are mixed in the red accelerated areas especially Case A1 and Case A2, which are assumed to have generated shock waves. Because of the smaller curvature of the front end of the suction, the flow achieves the sonic velocity at first. Then, it continues to expand and accelerate, and the speed is dropped abruptly after crossing the trailing edge shocks. For all cases, the red areas implying supersonic velocities diminish gradually as the reaction degree increases. In particular, the red supersonic areas are invisible and the intermittent expansion and acceleration regions do not exist for Case A4 and Case A5. Meanwhile, the regions with Mach number above 1 are not observed in the stator channels for Case A5, and the shocks structures in Case A5 are not organized in the density gradient distribution in **Figure 8**. It suggests that the flow field is possible in a subsonic state, and the shock waves are not generated. In addition, it implies that the ability of

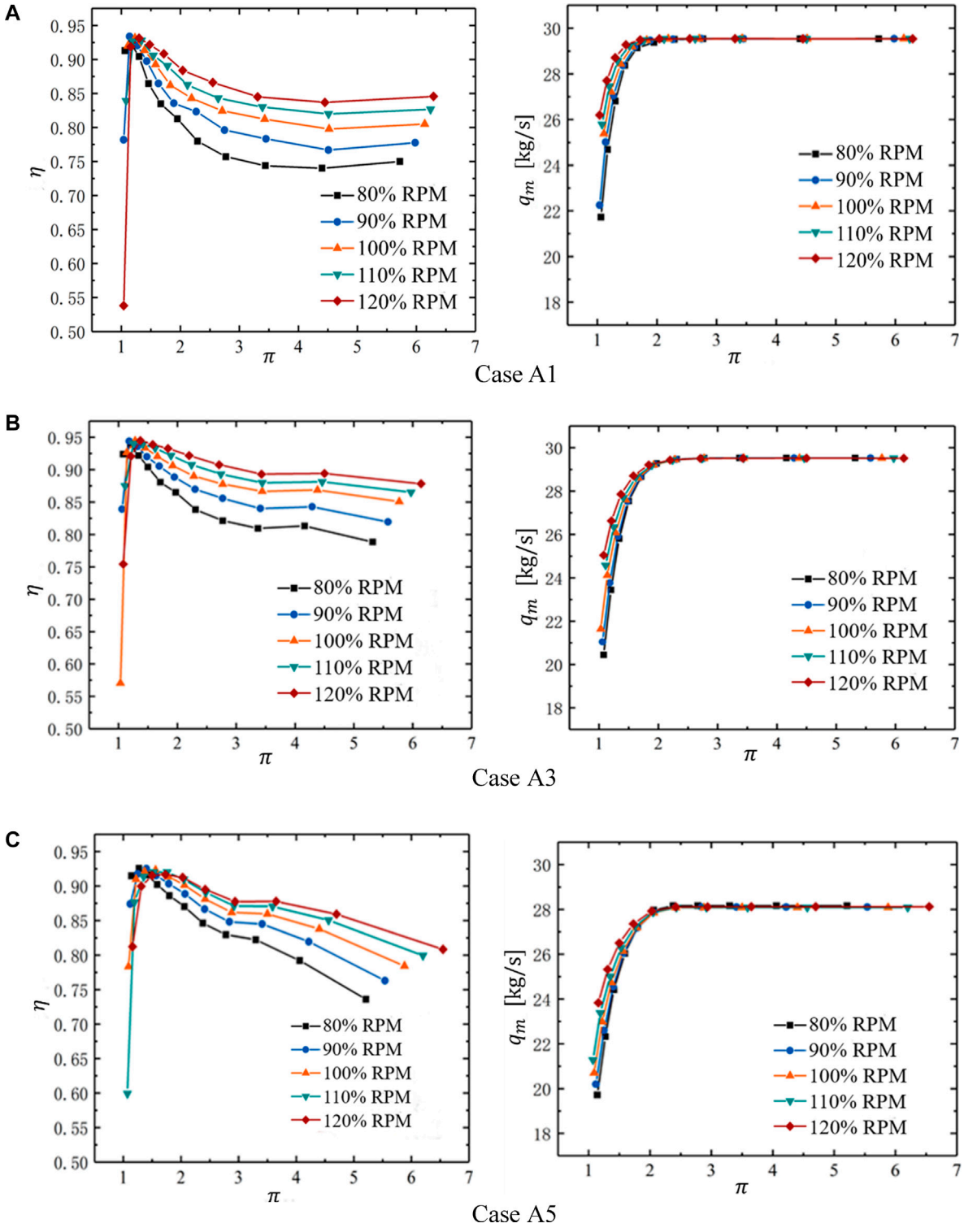

FIGURE 14 | Efficiency and Mass flow rate characteristic line of different reaction degrees. **(A)** Case A1. **(B)** Case A3. **(C)** Case A5.

expansion and acceleration in the stators are gradually diminished as the reaction degree grows. Besides, the mean maximum Mach numbers at the outlet of the stators are calculated from Case A1 to Case A5, corresponding to 1.88, 1.47, 1.32, 1.12 and 0.87. Therefore, the acceleration capacity of the flow is weakened after passing the shock

waves, so the maximum Mach number at the stator exit is also significantly reduced with the increase of reactive degrees.

Figure 8 shows the density gradient distribution of stators from Case A1 to Case A5. The highlighted structures in the flow channel are the locations of significant density gradient changes. The density gradient is changed probably due to the compression of the flow after passing through the shocks. It is shown that the density gradient is increased rapidly. Then the density gradient is decreased after crossing the trailing edge shock waves. In addition, the stronger shock waves occur at the position indicated by the arrow in **Figure 8**, and the pressures start to rise at the same locations on the suction surface in **Figure 6**. For five cases, the angle between the inner trailing shocks and the chord direction is gradually increased. The landing point in the relative blade is closer to the leading edge. In particular, the shocks structures are more sensitive to blade height and reaction degrees. The radial stripes on the trailing edge are more pronounced in the lower reaction degree schemes, e.g., Case A1, Case A2. However, the trailing edge shocks are almost invisible. Thus, it indicates that the shock structures may be stronger in a lower reaction degree case than a higher case.

Figure 9 presents the Exit Static pressure and Mach number distribution of stators. In general, the distribution of static pressure and Mach number shows a quite opposite trend as the reaction degree increases. **Figure 9A** illustrates that the static pressure distributions also show essentially the same trend with increasing reaction degrees. On the other hand, Mach number distributions in **Figure 9B** demonstrate a different color change as compared to static pressure. The exit Mach number of the stators is increased with the decrease of the reaction degrees. Thus, the cases with a lower Mach number probably have a higher static pressure in the outlet of the stator. A quite interesting phenomenon is that several vortex structures are observed in the static pressure and Mach number distributions in Case A1 and Case A3. It indicates that the aerodynamic parameters of the stators are more sensitive to a lower reaction degree. A lower reaction degree design may enlarge the scale of the vortex. The static pressure and Mach number at the outlet are influenced due to the combined effect of the continuous vortex characteristics and the shocks at the trailing edge. Subsequently, the flow characteristics impact the flow field of the following rotor. The predicted Mach number distribution of the rotor runner may be consistent with the above assumptions, as shown in **Figure 12**. The relatively regular laminar distributions of the static pressure and Mach number are revealed for Case A5. However, slender vortex structures are observed in the area close to the suction surface and the pressure surface. For Case A1, the existence of a localized slender vortex is noticed in the high static pressure region and the corresponding low Mach number region. It implies that the trailing edge shocks are present in the above areas.

3.3 Flow Analysis for Rotors

To explain the impact of reaction degrees on the flow field of the rotor cascade channels, the blade surface pressure distributions are analyzed from Case A1 to Case A5. **Figure 10** illustrates that The load at the front of the rotor blade is gradually reduced and the load at the tail is increased as the reaction degree grows. Therefore, the rotor is a front-loaded blade shape for Case A1 and the after-loaded blade shapes are assumed for Case A4 and Case A5. A higher reaction degree design demands the greater strength requirements of the blade tail. In particular, the blade surface pressure of the rotor is more sensitive to the reaction degree compared to the stator in **Figure 6**. The change is found on both the Pressure surface side and the Suction surface side. The blade surface pressure on the pressure surface side is increased progressively with the increase of the reaction degrees. Similarly, the pressures on suction surfaces of the rotor display the same tendency as the pressure surfaces at less than 0.8 axial chord. For all cases, it suggests that the blade surface pressure of the suction surface is raised rapidly. Furthermore, the location of the pressure lifting is essentially consistent with the location of the trailing edge shocks reflected in the suction surface, as shown in **Figure 11**. Therefore, the trailing edge shocks are presumed to be the key factor for the predicted pressure rise at the suction surface.

Figure 11 illustrates the density gradient distribution in the rotor cascade channels. For Case A1, the significant increase of density gradient distribution occurs at the leading edge of the rotor, which is more visible near the end wall. The structures even weaken the effect of trailing edge shocks. Besides, the trailing edge surge structure is significantly visible for Case A5, which is different from the distribution of shocks in **Figure 8**. In addition, the inner trailing shocks at the trailing edge are reflected after touching the neighboring blades. The shocks are more inclined with the increase of reaction degrees, and the angle with the blade is smaller. Thus, the reflective position of the suction surface is closer to the trailing edge.

Figure 12 shows the Mach number distribution of rotors for different cases. The red high Mach number regions gradually grow with the increase of the reaction degrees, which is opposite to the Mach number distribution in the stator channels. It indicates that the expansion and acceleration of the fluid are enhanced in the rotor channels. In addition, the existence of the red supersonic regions at the leading edge of the rotor suction surface for Case A1. It speculates that the stator may have a higher exit Mach number with a lower reaction degree, which can be confirmed in **Figures 7**, **9B**. Then, the sonic speed was achieved at the rotor inlet. Besides, the abrupt reductions of the high Mach number distribution are observed at the trailing edge for different cases. It is presumed that the supersonic flow has encountered the trailing edge shocks in this area, and this phenomenon is more visible in **Figure 11**.

Figure 13 presents the exit Mach number distribution of rotors for different cases. The exit Mach number of the rotor is significantly increased with increasing reaction degrees. For Case A1, there is a distinct cloud of low-energy fluid near the suction surface of the middle channel. It seems that the expansion and acceleration in the rotor channels are weakened due to the lower reaction degrees. The action of the lateral secondary flow is

emphasized by coiling up the low-energy fluid of the boundary layer, which accumulates at the suction surface. In addition, with the increase of the reaction degrees, it can be found that the sequence is high Mach number-low Mach number-high Mach number-low Mach number from the pressure surface to the suction surface, approximately. It is assumed that losses are generated after passing through the shock waves. The flow decelerates and the pressure rises, resulting in the appearance of a low Mach number region on the left side. The flow continues to expand and accelerate. However, there is another loss after encountering the reflected wave of the shocks. The second low Mach number region is not obvious due to the intensity of the reflected waves being less than the shocks.

3.4 Off-Design Conditions Analysis

To study the operating performance of transonic turbines with high expansion ratios at off-design conditions, **Figure 14** illustrates the efficiency and flow distribution for different pressure ratios and speed range from Case A1 to Case A5. It shows that the speed, pressure ratio, and reaction degree have a significant influence on the performance of the transonic turbine. For all cases, a similar trend is observed in the efficiency characteristic lines. As the pressure ratio increases, η is increased rapidly at pressure ratios between 1 and 1.5. As the pressure ratio continues to be increased, η is decreased and then reduced slightly. Therefore, the positions of highest η are found around $\pi = 1.5$. It is assumed to be the design operating point of the turbine. This is because the fluid velocity continues to rise with the increase of π. The supersonic phenomena may emerge. It implies the production of shocks and the appearance of shock losses. For different speeds, the turbine efficiency is improved as the speed increases after the design operating point. At low-speed conditions, η is more sensitive to the change of pressure ratio. Besides, the decreasing trend of η is more obvious for the higher reaction degree cases as π is above 3. But the change of η is invisible for Case A1. This is because the high reaction degree of the blade shape has a larger flow deflection angle, and the shock loss is increased after the pressure ratio is raised. For different reaction degree cases, the trend of the flow characteristic line is essentially similar. The q_m of the turbine is rapidly increased with the increase of π. Furthermore, the highest q_{m} is distributed with a drop pressure ratio between 2 and 3. The q_{m} is grown with the increase of speed before $\pi = 2.5$. Subsequently, π continues to increase and the q_{m} is almost constant. It is speculated that blockage occurs in the flow channels due to reaching the critical pressure ratio. In general, the critical pressure ratio that achieves the largest flow is increased with the increase of reaction degrees.

4 CONCLUSION

Five cases of reaction degrees were used to analyze the aerodynamic performance and cascade flow structure of a single-stage transonic turbine. In addition, off-design conditions were calculated for different cases. The main conclusions were summarized as follows:

1) The efficiency of transonic turbines was more sensitive to the reaction degrees. The turbine efficiency distribution was showed a trend of increasing and then decreasing with the increase of the reaction degrees at the designed operating conditions. Thus, the maximum efficiency was obtained at $\Omega = 0.33$.
2) The expansion and acceleration of the fluid were observed in the rotor cascade channels at relatively higher reaction degrees. However, this phenomenon was found at a lower reaction degree in the stators. In addition, the shock waves were monitored at the supersonic regions. The shock waves were assumed to be the key factor in the generation of complex flow structures.
3) The stators were all after-loaded blade shapes. But the rotors were turned from front-loaded to after-loaded due to the increase of reaction degrees. In particular, the inner trailing shocks crossed the cascade channel and formed reflected shocks in the adjacent blades. The angles between the inner trailing shocks and the chord length direction in stators were increased, and the reflection point of the shocks was progressively closer to the leading edge as the reaction degrees increased. However, the angles of the rotors were reduced and the reflection point was gradually moved closer to the trailing edge.
4) For off-design conditions analysis, the efficiency distribution had presented a trend of increasing and then decreasing with the rise of the pressure ratio. In particular, the highest efficiency distribution was marked around $\pi = 1.5$. The blockage occurred at the critical pressure ratio. The critical pressure ratio became larger with increasing reaction degrees, and the max flow rate was reduced.

DATA AVAILABILITY STATEMENT

The original contributions presented in the study are included in the article/Supplementary Material, further inquiries can be directed to the corresponding author.

AUTHOR CONTRIBUTIONS

QJ is responsible for the main calculation, analysis, and Writing. SX is responsible for Calculation, PS is responsible for analysis, WD is responsible for Ideal and the overall guidance.

ACKNOWLEDGMENTS

The authors acknowledge the financial support provided by Natural Science Fund for Excellent Young Scholars of Heilongjiang Province (No. YQ2021E023), Natural Science Foundation of China (Nos. 52106041 and 52076053), China Postdoctoral Science Foundation funded project (2021M690823), National Science and Technology Major Project (Nos. 2017-III-0009-0035 and 2019-II-0010-0030).

REFERENCES

Ananthakrishnan, K., and Govardhan, M. (2018). Influence of Fillet Shapes on Secondary Flow Field in a Transonic Axial Flow Turbine Stage. *Aerosp. Sci. Technol.* 82-83, 425–437. doi:10.1016/j.ast.2018.08.040

Arisi, A., Xue, S., Ng, W. F., Moon, H. K., and Zhang, L. (2015). Numerical Investigation of Aerothermal Characteristics of the Blade Tip and Near-Tip Regions of a Transonic Turbine Blade. *J. Turbomach.* 137 (9), 091002. doi:10.1115/1.4029713

Atkins, N. R., Thorpe, S. J., and Ainsworth, R. W. (2012). Unsteady Effects on Transonic Turbine Blade-Tip Heat Transfer. *J. Turbomach.* 134 (6), 061002. doi:10.1115/1.4004845

Börner, M., and Niehuis, R. (2021). Dynamics of Shock Waves Interacting with Laminar Separated Transonic Turbine Flow Investigated by High-Speed Schlieren and Surface Hot-Film Sensors. *J. Turbomach.* 143 (5), 051010. doi:10.1115/1.4050330

Carnevale, M., D'Ammaro, A., Montomoli, F., and Salvadori, S. (2014). "Film Cooling and Shock Interaction: An Uncertainty Quantification Analysis with Transonic Flows," in ASME Turbo Expo 2014: Turbine Technical Conference and Exposition, Düsseldorf, Germany, June 16–20, 2014 (American Society of Mechanical Engineers ASME). V05BT13A001. doi:10.1115/gt2014-25024

Clark, J. P., Anthony, R. J., Ooten, M. K., Finnegan, J. M., Dean Johnson, P., and Ni, R.-H. (2018). Effects of Downstream Vane Bowing and Asymmetry on Unsteadiness in a Transonic Turbine. *J. Turbomach.* 140 (10), 101006. doi:10.1115/1.4040998

De Maesschalck, C., Lavagnoli, S., and Paniagua, G. (2014). Blade Tip Carving Effects on the Aerothermal Performance of a Transonic Turbine. *J. Turbomach.* 137 (2), 021005. doi:10.1115/1.4028326

Denton, J. D. (1993). "Loss Mechanisms in Turbomachines," in ASME 1993 International Gas Turbine and Aeroengine Congress and Exposition, Cincinnati, Ohio, USA, May 24–27, 1993 (American Society of Mechanical Engineers ASME). V002T14A001. doi:10.1115/93-GT-435

Dixon, S. L., and Hall, C. (2013). *Fluid Mechanics and Thermodynamics of Turbomachinery*. Oxford: Pergamon Press.

Duan, P., Tan, C. S., Scribner, A., and Malandra, A. (2018). Loss Generation in Transonic Turbine Blading. *J. Turbomach.* 140 (4), 041006. doi:10.1115/1.4038689

Du, W., Luo, L., Jiao, Y., Wang, S., Li, X., and Sunden, B. (2021). Heat transfer in the Trailing Region of Gas Turbines - A State-of-the-Art Review. *Applied Thermal Eng.* 199, 117614. doi:10.1016/j.applthermaleng.2021.117614

Gao, J., Wei, M., Fu, W., Zheng, Q., and Yue, G. (2019). Experimental and Numerical Investigations of Trailing Edge Injection in a Transonic Turbine Cascade. *Aerosp. Sci. Technol.* 92, 258–268. doi:10.1016/j.ast.2019.05.069

Gardner, W. (1979). *Energy Efficient Engine: High Pressure Turbine Uncooled Rig Technology Report*. USA: NASA-Lewis Research Center.

Hou, W. T., Qiao, W. Y., and Luo, H. L. (2010). Shock-Wave/Boundary-Layer Interaction in a Transonic Turbine Cascade. *Proc. Inst. Mech. Eng. Part G J. Aerosp. Eng.* 225 (1), 77–85. doi:10.1243/09544100JAERO745

Ji, L., Yu, J., Li, W., and Yi, W. (2017). Study on Aerodynamic Optimal Super/transonic Turbine Cascade and its Geometry Characteristics. *Proc. Inst. Mech. Eng. Part G J. Aerosp. Eng.* 231 (3), 435–443. doi:10.1177/0954410016638875

Joly, M., Verstraete, T., and Paniagua, G. (2010). "Attenuation of Vane Distortion in a Transonic Turbine Using Optimization Strategies: Part I-Methodology," in ASME Turbo Expo 2010: Power for Land, Sea, and Air, Glasgow, UK, June 14–18, 2010 (American Society of Mechanical Engineers ASME), 653–662. doi:10.1115/GT2010-22370

Kiran, K. N., and Anish, S. (2017). An Investigation on the Effect of Pitchwise Endwall Design in a Turbine Cascade at Different Incidence Angles. *Aerosp. Sci. Technol.* 71, 382–391. doi:10.1016/j.ast.2017.09.032

Kopper, F., Milano, R., Davis, R., Dring, R., and Stoeffler, R. (1981). *Energy Efficient Engine High-Pressure Turbine Supersonic Cascade Technology Report*. USA: Lewis Research Center.

Liu, C., Zhang, J., Jia, D., and Li, P. (2022). Experimental and Numerical Investigation of The Transition Progress of Strut-Induced Wakes in the Supersonic Flows. *Aero. Sci. Technolo.* 120, 107256. doi:10.1016/j.ast.2021.107256

Lu, Y., and Dawes, W. N. (2015). "High Order Large Eddy Simulations for a Transonic Turbine Blade Using Hybrid Unstructured Meshes," in ASME Turbo Expo 2015: Turbine Technical Conference and Exposition, Montreal, Quebec, Canada, June 15–19, 2015 (American Society of Mechanical Engineers ASME). V02CT44A005. doi:10.1115/GT2015-42283

Luo, L., Yan, H., Du, W., Su, W., Wang, S., and Huang, D. (2022). Numerical Study of A Novel Curved Pin Fin For Heat Transfer Enhancement Within Aeroengine Turbine Blade. *Aerospace Sci. Technol.* 123, 107436. doi:10.1016/j.ast.2022.107436

Noor, H., Genrup, M., and Fransson, T. (2012). "Selection of One-Dimensional Design Parameter 'Reaction Degree' for 1st Stage of a Cooled Gas Turbine," in ASME Turbo Expo 2012: Turbine Technical Conference and Exposition, Copenhagen, Denmark, June 11–15, 2012 (American Society of Mechanical Engineers ASME), 2345–2354. doi:10.1115/GT2012-69758

Pau, M., and Paniagua, G. (2010). Investigation of the Flow Field on a Transonic Turbine Nozzle Guide Vane with Rim Seal Cavity Flow Ejection. *J. Fluids Eng.* 132 (11), 111101. doi:10.1115/1.4002887

Puente, R., Paniagua, G., and Verstraete, T. (2015). Design Trade-Off Study between Efficiency and Rotor Forcing Attenuation in a Transonic Turbine Stage. *Appl. Math. Model.* 39 (2), 838–850. doi:10.1016/j.apm.2014.07.003

Raffel, M., and Kost, F. (1998). Investigation of Aerodynamic Effects of Coolant Ejection at the Trailing Edge of a Turbine Blade Model by PIV and Pressure Measurements. *Exp. Fluids* 24 (5), 447–461. doi:10.1007/s003480050194

Rehman, A., Liu, B., and Asghar, M. A. (2019). Secondary Flow and Endwall Optimization of a Transonic Turbine. *Energies* 12 (21), 4103. doi:10.3390/en12214103

Sandberg, R. D., and Michelassi, V. (2022). Fluid Dynamics of Axial Turbomachinery: Blade- and Stage-Level Simulations and Models. *Annu. Rev. Fluid Mech.* 54 (1), 255–285. doi:10.1146/annurev-fluid-031221-105530

Shelton, M. L., Gregory, B. A., Lamson, S. H., Moses, H. L., Doughty, R. L., and Kiss, T. (1993). "Optimization of a Transonic Turbine Airfoil Using Artificial Intelligence, CFD and Cascade Testing," in ASME 1993 International Gas Turbine and Aeroengine Congress and Exposition, Cincinnati, Ohio, USA, May 24–27, 1993 (American Society of Mechanical Engineers ASME). V03AT15A012. doi:10.1115/93-GT-161

Sieverding, C. H. (1983). The Influence of Trailing Edge Ejection on the Base Pressure in Transonic Turbine Cascades. *J. Eng. Power* 105 (2), 215–222. doi:10.1115/1.3227405

Sonoda, T., Arima, T., Olhofer, M., Sendhoff, B., Kost, F., and Giess, P.-A. (2004). A Study of Advanced High-Loaded Transonic Turbine Airfoils. *J. Turbomach.* 128 (4), 650–657. doi:10.1115/1.2221325

Teia, L. (2020). New Supersonic Loss Model for the Preliminary Design of Transonic Turbine Blades and the Influence of Pitch. *J. Turbomach.* 142 (4), 041008. doi:10.1115/1.4045983

Thulin, R. D., Howe, D. C., and Singer, I. D. (1982). *Energy Efficient Engine High-Pressure Turbine Detailed Design Report*. Cleveland OH, USA: Lewis Research Center.

Wang, T., Xuan, Y., and Han, X. (2021). The Effects of Tip Gap Variation on Transonic Turbine Blade Tip Leakage Flow Based on VLES Approach. *Aerosp. Sci. Technol.* 111, 106542. doi:10.1016/j.ast.2021.106542

Wei, D., Lei, L., Yinghou, J., Songtao, W., Xingchen, L., and Cong, C. (2022). The Interaction Between The Latticework Duct And Film Cooling On The Thermal Performance With Different Film Cooling Hole Locations. *Inter. J. Thermal Sci.* 179, 107627. doi:10.1016/j.ijthermalsci.2022.107627

Yao, J., and Carson, S. (2006). "HPT/LPT Interaction and Flow Management in the Inter-turbine Space of a Modern Axial Flow Turbine," in ASME Turbo Expo 2006: Power for Land, Sea, and Air, Barcelona, Spain, May 8–11, 2006 (American Society of Mechanical Engineers ASME), 1783–1795. doi:10.1115/GT2006-90636

Yoon, S. (2013). The Effect of the Degree of Reaction on the Leakage Loss in Steam Turbines. *J. Eng. Gas Turbines Power* 135 (2). doi:10.1115/1.4007772

Zhang, Q., He, L., and Rawlinson, A. (2014). Effects of Inlet Turbulence and End-Wall Boundary Layer on Aerothermal Performance of a Transonic Turbine Blade Tip. *J. Eng. Gas Turbines Power* 136 (5), 052603. doi:10.1115/1.4026002

Zhang, Q., O'Dowd, D. O., He, L., Wheeler, A. P. S., Ligrani, P. M., and Cheong, B. C. Y. (2011). Overtip Shock Wave Structure and its Impact on Turbine Blade Tip Heat Transfer. *J. Turbomach.* 133 (4), 041001. doi:10.1115/1.4002949

Zhao, W., Luo, W., Zhao, Q., and Xu, J. (2016). "Investigation on the Reduction of Trailing Edge Shock Losses for a Highly Loaded Transonic Turbine," in ASME Turbo Expo 2016: Turbomachinery Technical Conference and Exposition,

Seoul, South Korea, June 13–17, 2016 (American Society of Mechanical Engineers ASME). V02BT38A005. doi:10.1115/GT2016-56131

Conflict of Interest: The authors declare that the research was conducted in the absence of any commercial or financial relationships that could be construed as a potential conflict of interest.

Publisher's Note: All claims expressed in this article are solely those of the authors and do not necessarily represent those of their affiliated organizations, or those of the publisher, the editors and the reviewers. Any product that may be evaluated in this article, or claim that may be made by its manufacturer, is not guaranteed or endorsed by the publisher.

NOMENCLATURE

Abbreviations

c_p Heat capacity [kJ/(kg·K)]

$\mathbf{M}$ Torque [N·m]

p Pressure[MPa]

p_0^* Inlet total pressure of Computational domain [MPa]

p_2 Outlet static pressure of Computational domain [MPa]

p_2^* Outlet total pressure of Computational domain [Mpa]

$p_{r,out}$ Outlet total pressure of rotor [MPa]

$p_{s,in}$ Inlet total pressure of stator [MPa]

$p_{s,out}$ Outlet total pressure of stator [MPa]

P Power [MW]

q_m Mass flow rate [kg/s]

T_{in}^* Inlet total temperature of Computational domain [K]

Greek symbols

Ω Reaction degree

π Pressure ratio

η Efficiency [%]

ω Angular velocity [s^{-1}]

κ Isentropic exponent

Abbreviations

CFD Computational fluid dynamics

SST Shear Stress Transport model

frontiers | Frontiers in Energy Research

ORIGINAL RESEARCH
published: 23 June 2022
doi: 10.3389/fenrg.2022.913770

Research on the Influence of Surface Roughness on the Flow Field in the Cascade

Yanhua Wang[1], *Jun Dai*[1], *Shaowei Zhou*[2], *Meng Wang*[1]* *and Zhongyi Wang*[1]

[1]College of Power and Energy Engineering, Harbin Engineering University, Harbin, China, [2]China Ship Research and Design Center, Wuhan, China

Fouling, corrosion, and icing are common causes of increased compressor blade roughness due to special operating conditions and natural environment. Roughness increase would influence on flow field, especially in supersonic compressor cascades where incident waves can interact with reflected shock waves. Studies have shown that the boundary layer condition of the blade varies with wall roughness, which affects both the incident shock wave and the reflected shock wave. In order to study the effect of the distribution of roughness, the flow field under different roughness settings is simulated. The results show that flow loss is reduced with increasing roughness at the incidence point of an incident wave and the trailing edge of the suction side.

Keywords: supersonic cascade, shock wave, roughness, total pressure loss, performance

OPEN ACCESS

Edited by:
Lei Luo,
Harbin Institute of Technology, China

Reviewed by:
Xiangjun Li,
Dalian Maritime University, China
Lucheng Ji,
Tsinghua University, China

***Correspondence:**
Meng Wang
wangmeng_a@hrbeu.edu.cn

Specialty section:
This article was submitted to Advanced Clean Fuel Technologies, a section of the journal Frontiers in Energy Research

Received: *06 April 2022*
Accepted: *09 May 2022*
Published: *23 June 2022*

Citation:
Wang Y, Dai J, Zhou S, Wang M and Wang Z (2022) Research on the Influence of Surface Roughness on the Flow Field in the Cascade. Front. Energy Res. 10:913770. doi: 10.3389/fenrg.2022.913770

INTRODUCTION

With the development of high-speed compressors, the phenomenon of the supersonic flow field inside the cascade is very common. In the cascade, the shock wave interacts with the supersonic flow field. When the shock wave interacts with the laminar boundary layer, even a very weak shock wave can cause the laminar boundary layer to separate, leading to a decrease in performance. The interaction between shock waves and the laminar boundary layer is unsteady in some cases, which leads to blade vibration and shock wave oscillation in cascade flow. The shock wave oscillation causes pressure fluctuations and blade load changes.

Fouling, erosion, corrosion, and fatigue oxidation on the blade surface are inevitable phenomena in the working process of the compressor. These cause changes in the surface roughness of the compressor blade (Aldi et al., 2014). However, surface roughness affects the resistance and flow condition of the blade surface (Boyle et al., 2001; Boyle and Stripf, 2008; Seung et al., 2010; Back et al., 2012), making the interaction between the shock wave and boundary layer more complex, which affects the separation of the boundary layer (Graham and Kost, 1979; Hou et al., 2011), the distribution of Mach number, and the wake inevitably (Irimpan and Menezes, 2018). Then, the resistance and loss of the blade surface change, which changes blade performance. Surface roughness also can control the boundary layer flow. Compared with other boundary layer flow control methods such as suction and jet flow, surface roughness can change blade surface separation and the transition process without increasing structural complexity, thus affecting compressor profile loss and integral stage performance. Therefore, it is very important to study the effect of surface roughness on the flow field in the compressor cascade. Schilichting used Nikuradse data to correlate different roughness types and put forward the concept of equivalent gravel roughness in practice (Li et al., 2016). Syverud et al. show that the increase in roughness has the most obvious effect on the discharge coefficient (Melino et al., 2011).

TABLE 1 | Main parameters of the compressor cascade.

Design parameter	Value
Blade chord length	85 mm
Leading edge radius/chord	0.00128
Solidity	1.5294
Maximum blade thickness/chord	0.0255
Stagger angle	146.93°
Designed inflow Mach number	1.75
Inlet angle of fluid	147.5°

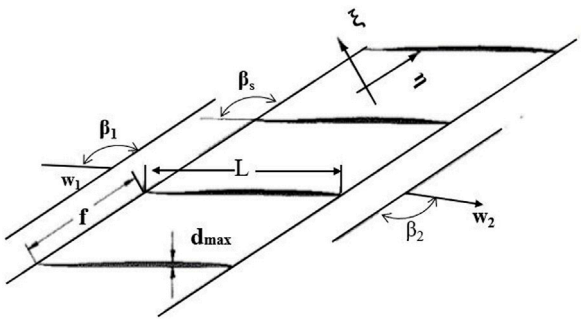

FIGURE 1 | Cascade geometric parameters.

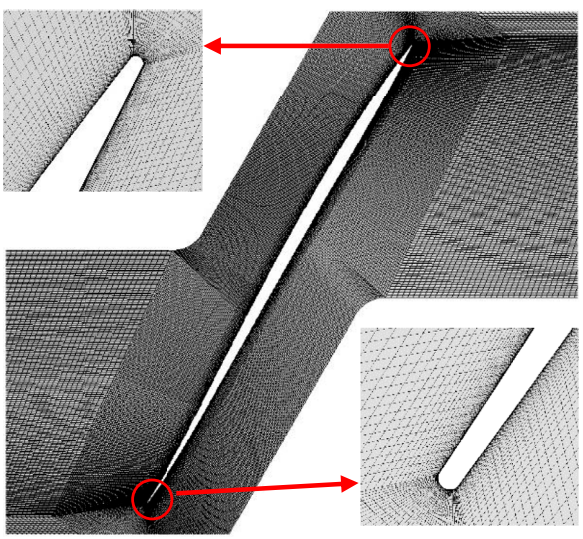

FIGURE 2 | Grid of the cascade.

Yunfei Zhao et al. have studied the influence of different shapes of models and different roughness on the downstream flow field. The results show that roughness causes the formation of flow streaks and shear layers in the wake, thereby increasing the non-uniformity of the downstream flow field stability (Syverud and Bakken, 2006; Rainer et al., 2009). The results of the study by Fouflias and Kurz, et al. (Tweedt et al., 1988; Yao and Carson, 2006; Zhao et al., 2016) show that the increase in suction surface roughness has a more

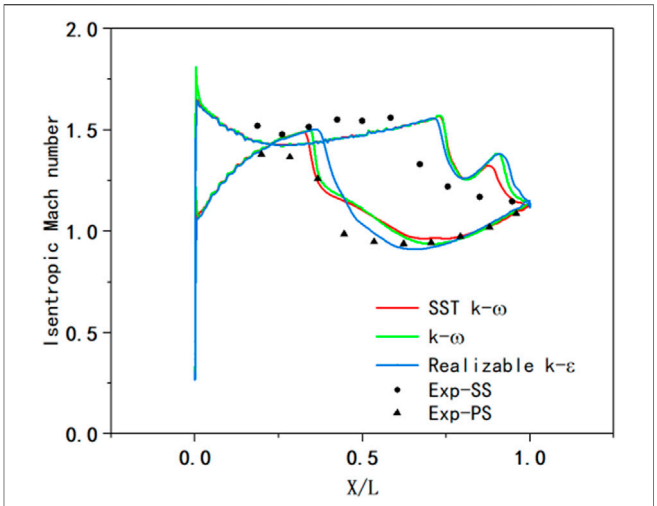

FIGURE 3 | Effect of different turbulence models on isentropic Mach number on the blade surface.

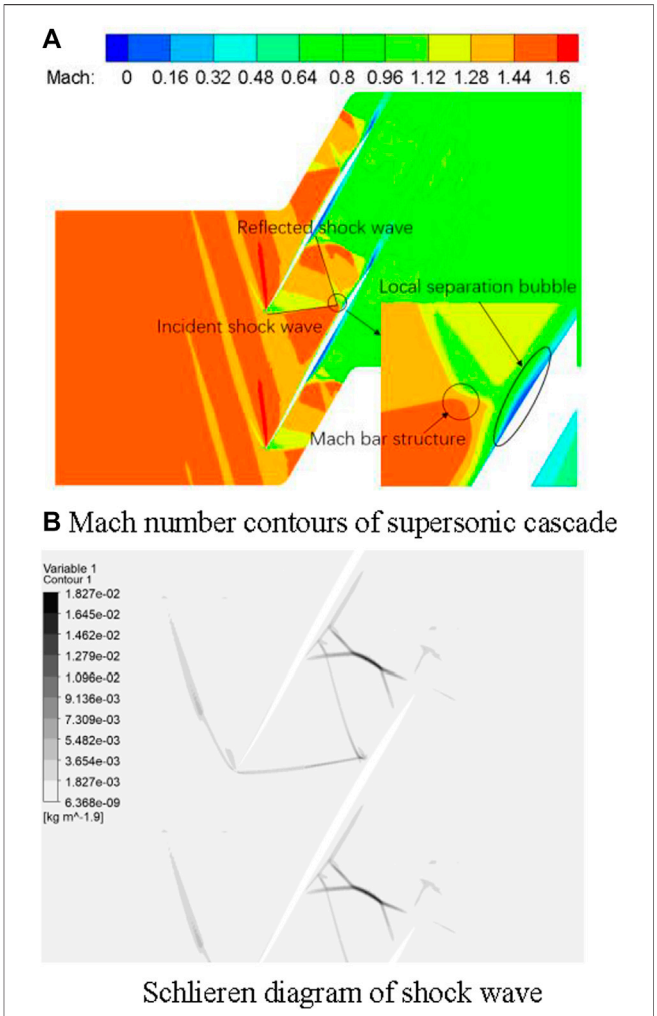

FIGURE 4 | Flow field contours of the cascade. **(A)** Mach number contours of the supersonic cascade. **(B)** Schlieren diagram of the shock wave.

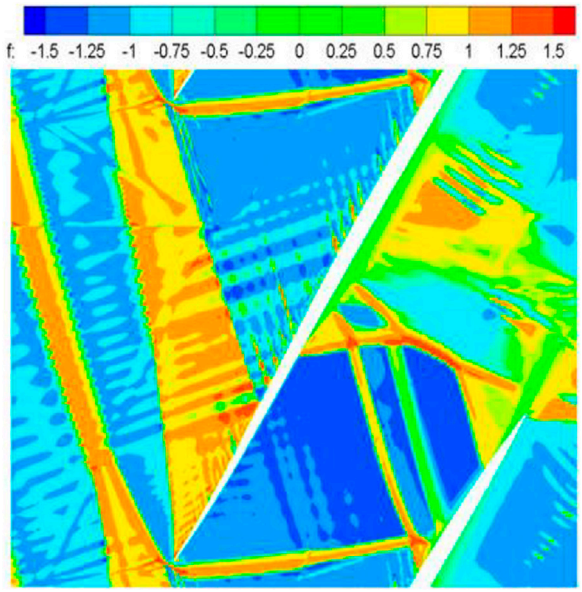

FIGURE 5 | Shock function contours of the cascade.

obvious effect on cascade performance. Aldi studied the performance curve changes of NASA stage 37 under six kinds of roughness with non-uniform linear distribution of the blade span direction, and the results show that the increase in blade tip roughness caused more serious performance degradation (Yi et al., 2016). The results of Zhao's study (Zhou et al. (2016) show that the strength of the expansion wave at the suction surface near the throat increases and the intersection point of the shock waves and the reflected shock wave at the suction side of the trailing edge moves downstream, thus reducing the interference loss of shock waves.

Through the analysis of surface roughness, this study discusses the relationship between surface roughness and compressor cascade loss and provides a theoretical basis for a subsequent compressor design.

MODEL AND RESEARCH OBJECT

Model

In this study, the supersonic cascade ARL-SL19 is taken as the research object. According to reference (Tweedt et al. 1988), the blade profile coordinates with chord length as dimensionless and relevant main parameters are obtained. The specific parameters are shown in **Table 1** and **Figure 1**(Tweedt et al. 1988).

Grid of Model

To make sure $y^+ < 1$ near the wall, the distance between the first layer of the wall grid and the wall is 0.001 mm. The grid is densified near the trailing edge and the leading edge of the cascade. The cascade grid is shown in **Figure 2**.

NUMERICAL CALCULATION METHOD AND VERIFICATION

Grid and Turbulence Independence

The simulation method used in this article is a steady method. The viscosity setting is given by Sutherland's law, and the wall boundary condition is based on no-slip wall. The inlet Mach number is 1.586, the outlet static pressure ratio (P_2/P_1) is 2.3, the inlet static pressure is 101,325 Pa, and the inlet airflow angle is 57.5°. The model with grid numbers 7.1×10^4, 8.5×10^4, 9.8×10^4, 1.2×10^5, and 1.3×10^5 is calculated. Compared with the experimental results, when the grid number reaches 1.2×10^5, further increasing the grid number will not affect the

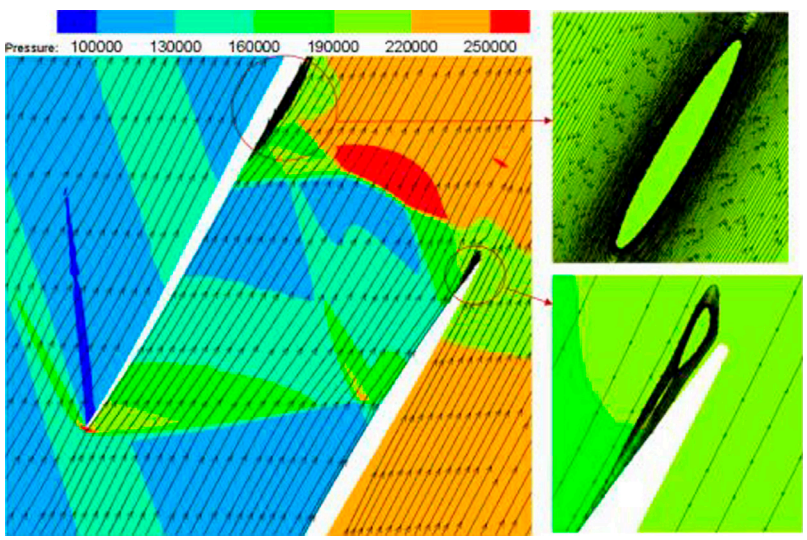

FIGURE 6 | Pressure contours of the cascade.

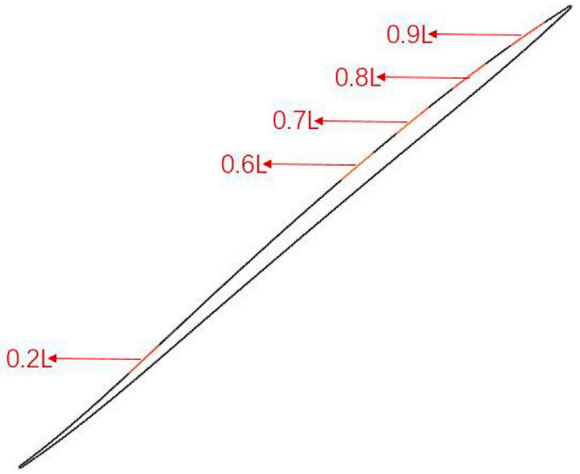

FIGURE 7 | Distribution of surface roughness of the cascade.

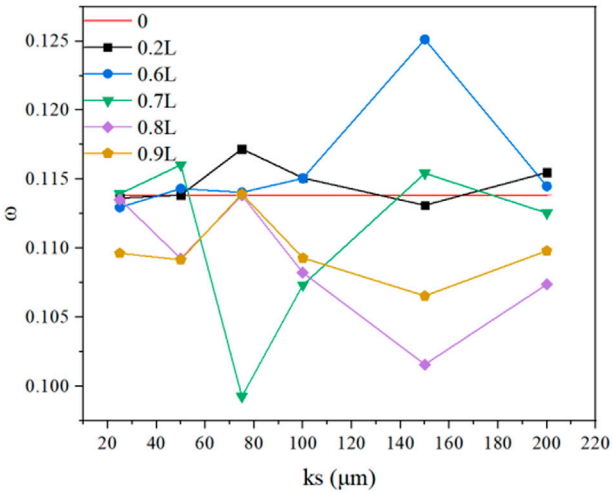

FIGURE 8 | Variation of total pressure loss.

calculation results, which is basically consistent with the experimental results. Therefore, this grid is used in the subsequent calculation. Then, according to the **Figure 3** isentropic Mach number distribution (SS is the suction surface, and PS is the pressure surface), the effect of the *SST K-ω*, *K-ω* and *realizable K-ω* turbulence models on the simulation result is also studied in this article. According to the comparison of simulation and experimental results, the *SST K-ω* turbulence model is more consistent with the experimental data. So, the *SST K-ω* turbulence model is used in the subsequent calculation.

Setting of Surface Roughness

In order to introduce surface roughness, the equivalent gravel roughness k_s of a rough wall is studied in this article. The relationship between k_s and contour arithmetic mean deviation (R_a) is expressed as **(1)**:

$$k_s = 6.2R_a. \tag{1}$$

CALCULATION AND ANALYSIS

Calculation Results of Smooth Surface

In the case of the smooth wall, the cascade is simulated and the flow field is analyzed. The distribution of the flow field in the cascade is shown in **Figure 4**. It can be seen that at the position of about 0.7 times the chord length (0.7L) of the suction surface, the shock wave is incident on the suction surface and the reflected wave is generated and interacts with the boundary layer. The Mach rod structure and local bubble separation can be seen from the Mach number contours. The interaction between shock waves and the boundary layer will lead to boundary layer separation, generation of separation bubble, and increase in flow loss. The interaction between the shock wave and the boundary layer, the size of the separation bubble and the size of the separation area at the end of the blade are related to the flow state of boundary layers and the strength of shock waves.

The shock function can better represent the interaction between the shock structure and wave system in the cascade. Its expression is as follows:

$$f_{shock} = \frac{V \cdot \nabla p}{a|\nabla p|}. \tag{2}$$

In **Equation 2**, $\boldsymbol{V}$ is the velocity vector, ∇p is the pressure gradient, and a is the local sound velocity. The value of shock function is a scalar, and its size can directly reflect the compression or expansion degree of flow. When the flow is compressed, the value of shock function is positive; when the airflow expands, the value of shock function is negative; if the value of shock function is greater than 1, it indicates that there is a shock wave or a strong compression wave in the flow field.

Figure 5 shows the distribution of shock wave function. In **Figure 4**, Mach number distribution and the Schlieren diagram of the cascade are in good agreement with shock function distribution. It can be seen that the working fluid produces a shock wave at the inlet of the cascade. The shock waves act on 0.7L of the suction surface and then generate a reflected shock wave and a λ-type normal shock wave at the trailing edge of the suction surface. **Figure 6** shows streamline distribution in the cascade. Compared with **Figure 5**, it can be seen that the action of the incident shock wave induces boundary layer separation at the suction surface 0.7L; the interaction between the shock wave and boundary layer at the trailing edge of the suction surface and pressure surface under the action of a λ - type normal shock wave induces backflow of the working fluid, resulting in airflow blockage in the cascade. This weakens the interaction of shock waves.

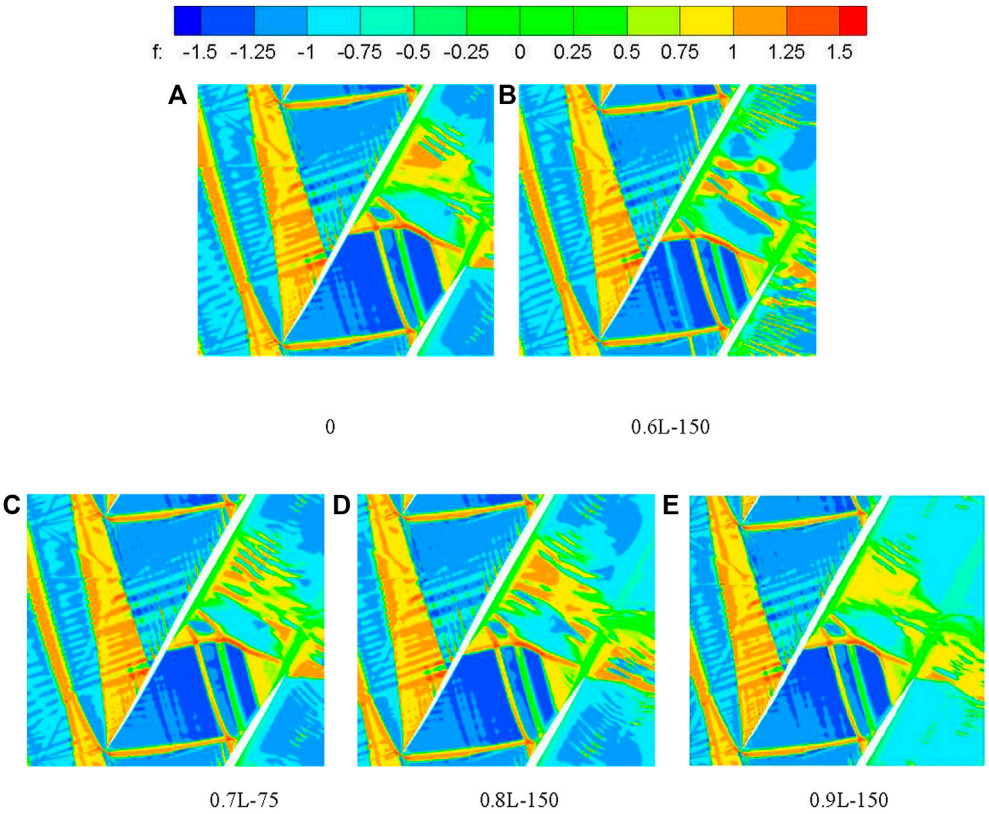

FIGURE 9 | Shock function contours of the supersonic cascade and Partially enlarged.

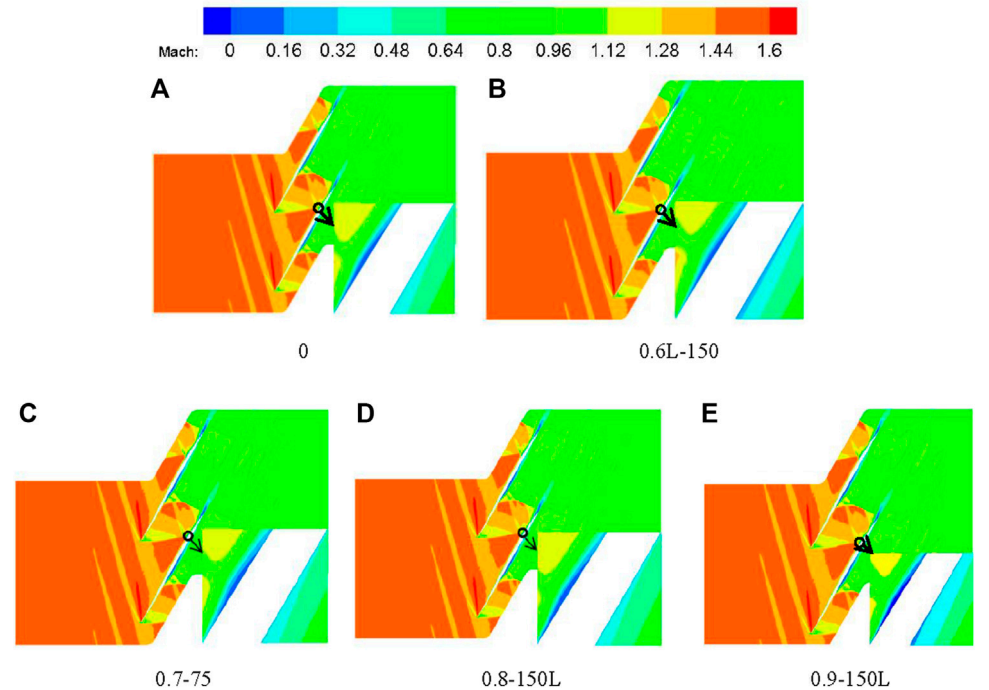

FIGURE 10 | Mach number contours of the supersonic cascade and Partially enlarged.

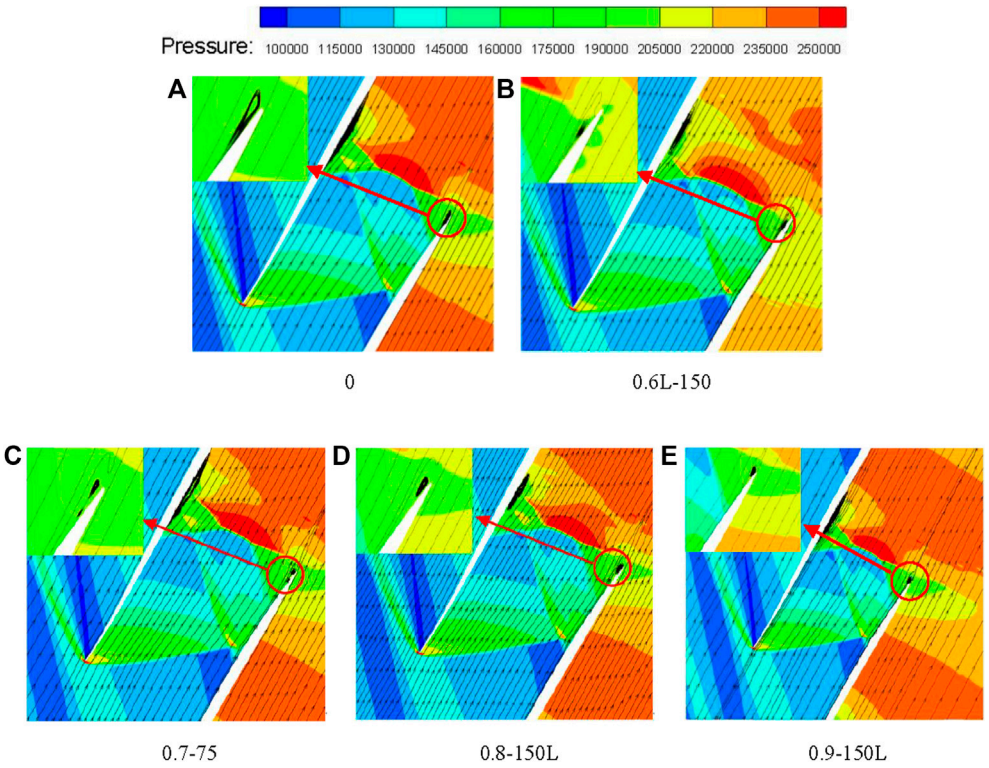

FIGURE 11 | Pressure contours of the supersonic cascade and Partially enlarged.

Position of Roughness Distribution

In **Figures 4**, **5**, it can be seen that the incident shock wave and the reflected shock wave act on the suction surface at 0.7L. In order to explore the influence of different surface roughness distribution positions on the cascade channel, rough surfaces were set at the leading edge, shock wave reflection position, and trailing edge of the cascade. The surface roughness is arranged at 0.2, 0.6, 0.7, 0.8, and 0.9L of the suction surface, as shown in **Figure 7**. The k_s values at each position were set as 25, 50, 75, 100, 150, and 200 μm. For the convenience of description, they are uniformly expressed, such as 0.2L–25, which means that the roughness at 0.2 chord length is 25 μm. The total pressure loss is used to represent the energy loss. Its expression is as follows:

$$\omega = \frac{p_1^* - p_2^*}{p_1^* - p_1}. \tag{3}$$

In **Equation 3**, p_1^* is the total pressure at the inlet, p_1 is the static pressure at the inlet, and p_2^* is the total pressure at outlet.

The total pressure loss of the cascade under different working conditions is shown in **Figure 8**. The results show that the total pressure loss in cascades increases when uses of artificial roughness are at 0.2 L. The total pressure loss is caused by the friction between the gas and blade surface. As for 0.6L, the total pressure loss becomes high with increased surface roughness. When k_s is 150 μm, the total pressure has most to lose. The total pressure loss in cascades decreases when uses of artificial roughness are at 0.7, 0.8, and 0.9 L. Adding roughness to the rear of a reflected shock wave can effectively restrain the formation of the separation bubble and reduce total pressure loss. Compared with the smooth cascade, the maximum changes in total pressure loss are 9.91 and -12.8% when the roughness distribution is 0.6 and 0.7L, respectively.

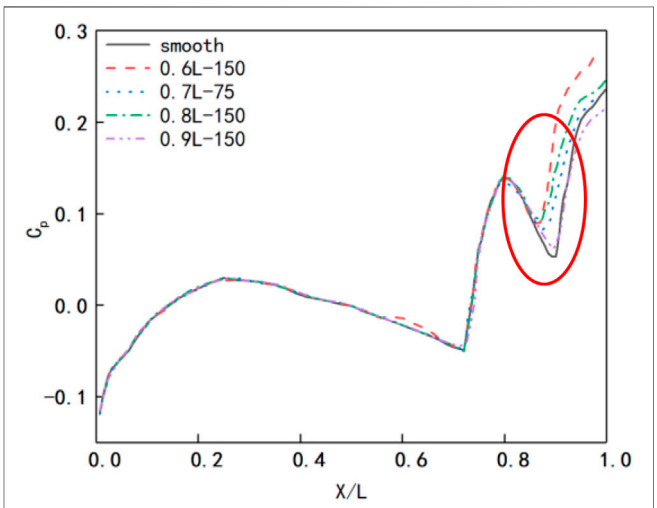

FIGURE 12 | Variation of static pressure loss with roughness height.

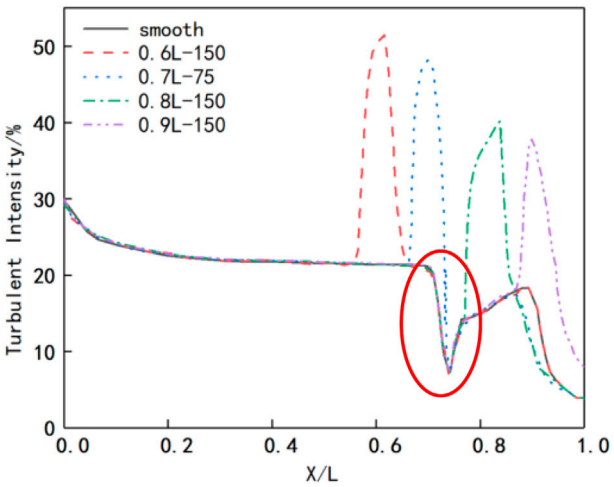

FIGURE 13 | Variation of turbulent intensity on the suction side with roughness height.

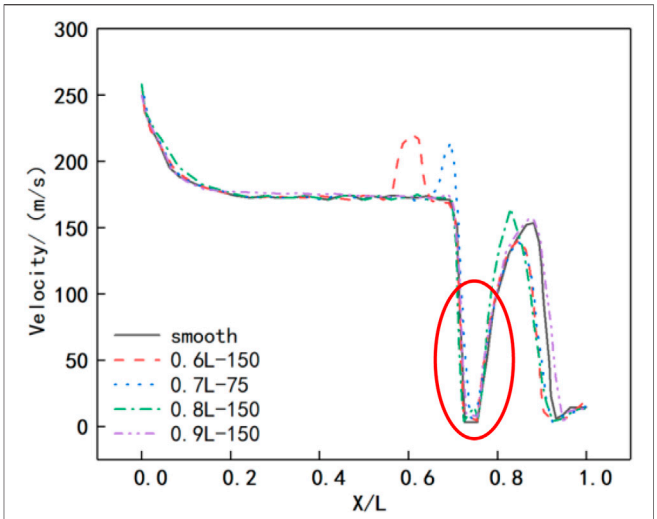

FIGURE 15 | Variation of velocity on the suction side with roughness height.

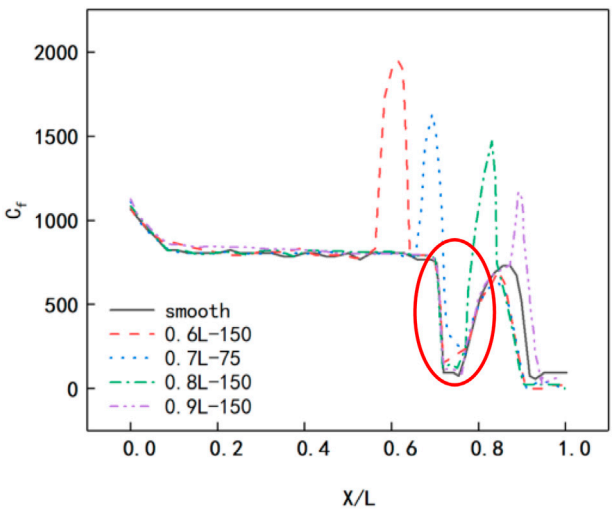

FIGURE 14 | Variation of the skin friction coefficient on the suction side with roughness height.

The Influence of Surface Roughness on the Flow Field

Combined with **Figure 8**, the flow fields of the smooth surface, 0.6L–150, 0.7L–75, 0.8L–150, and 0.9L–150 are compared and analyzed. The influence of the surface roughness of the cascade on the flow field is discussed.

Figure 9 shows the distribution of shock wave function in the cascade. The interaction points of the shock wave and boundary layer are distributed at 0.7L under five conditions. Compared with the smooth surface, the intensities of an incident shock wave and reflected shock wave under 0.6L–150 working condition are increased and the intensity of the λ-type normal shock wave near the pressure surface at the trailing edge of the cascade is enhanced. At the same time, the strength of the shock wave behind the trailing edge is enhanced, and the strength of the shock train is enhanced. Under the working conditions of 0.7L–50, 0.8L–150, and 0.9L–150, the intensities of the incident shock wave and reflected shock wave is weakened. The intensity of the λ-type normal shock wave, which is near the suction surface at the trailing edge of the cascade, is obviously weakened. At the same time, the strength of the shock wave and shock train behind the trailing edge is weakened, which is most obvious under the working condition of 0.9L–150.

Figures 10, **11** show the Mach number and pressure distribution in the cascade. Compared with **Figures 10**, **11**, the shock-induced bubble separation appears at the interaction position between the suction surface shock wave and the boundary layer and at the interaction between the reflected shock wave and the boundary layer on the pressure surface. At the trailing edge of the suction surface and the incident point of the reflected shock wave on the pressure surface, the backflow is induced and the flow in the cascade is blocked. Compared with the smooth surface, the separation bubble size increases and the working fluid reflux area increases under the working condition of 0.6L–150; the separation bubble size decreases, and the working fluid reflux area decreases under 0.7L–75, 0.8L–150, and 0.9L–150 working conditions. The fluid reflux area on the suction side under the 0.9L–150 working condition is the smallest, but compared with 0.7L–75 and 0.8L–150 working conditions, it has a larger fluid reflux area on the pressure side.

Figure 12 shows the pressure coefficient distribution curve on the suction surface of the cascade. The pressure coefficient is defined as follows:

$$C_p = \frac{p_i - p_1}{p_1^* - p_1}. \tag{4}$$

In **Equation 4**, P_i is the static pressure value of the suction surface of the cascade.

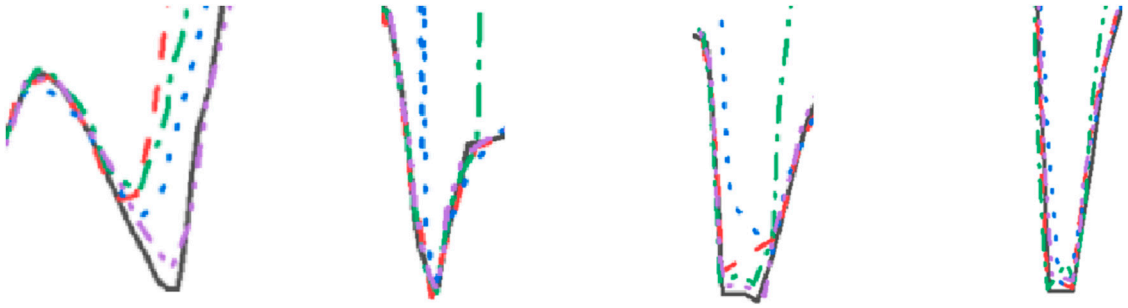

FIGURE 16 | Partial enlargement of the curve.

The overall variation trend of the suction surface pressure coefficient is the same under different working conditions. However, with the increase of roughness, the pressure coefficient from the leading edge of suction to 0.7L is higher than that from 0.7L to the trailing edge, which is higher than that of the smooth surface. Compared with the smooth surface, the pressure coefficient at the trailing edge increases under 0.6L–150 working condition and decreases under 0.7L–75 and 0.8L–150 working conditions; 0.9–150 working condition is basically the same as 0.6–150 working condition. The results show that there is a reverse pressure gradient at 0.6L on the suction surface under 0.6L–150 working condition,, and the reverse pressure gradient at the trailing edge increases at the same time. The flow state of the working fluid becomes worse, and the backflow area at the trailing edge increases, which increases the total pressure loss. The pressure gradient at the trailing edge decreases under 0.7L–75, 0.8L–150, and 0.9–150 working conditions, which makes the total pressure loss smaller, and the total pressure loss reaches the minimum under 0.7L–75 working condition.

Figure 13 shows the turbulence intensity distribution on the suction surface. It can be seen that setting roughness on the suction surface can effectively improve the turbulence intensity at the location where roughness is set. In 0.6L–150, 0.8L–150, and 0.9L–150 working conditions and the starting and disappearing positions of the separation bubble are the same as those of the smooth condition. But, under 0.7L–75 working condition, the starting position of the separation bubble moved 1.7% of chord length downstream, which can also be clearly seen in **Figures 14**, **15**. **Figure 14** shows that the skin friction coefficient at the position where roughness setting is greater at the smooth surface under 0.6L–150, 0.7L–75, and 0.8L–150 working conditions because roughness setting on the suction surface can exert stronger disturbance to the separation shear layer. **Figure 14** also shows that the skin friction coefficient at 0.7L of 0.7L–75 working condition is the largest.

Figure 15 is the velocity distribution curve. There is little difference in the velocity at the separation bubble position in the five working conditions, but it can also be seen that the velocity at the separation bubble position under 0.7L–75 working condition is slightly higher than that in the other five working conditions. The aforementioned phenomenon indicates that the roughness setting under 0.7L–75 working condition can delay the separation in laminar flow and exert stronger disturbance on the separation shear layer, which inhibits the development of separation bubbles.

The **Figure 16** is **Figure 12** to **Figure 12** Partial enlargement of the curve

CONCLUSION

In this study, the supersonic cascade ARL-SL19 is taken as the research object. In order to explore the influence of surface roughness on the flow field inside the cascade, different roughness is set at the incident point of a shock wave of the suction surface, in front of and behind the incident point, and at the leading edge and trailing edge of the suction surface. The numerical simulation result of different roughness conditions are compared with the results of the original model. The conclusions are as follows:

1) When the suction surface is smooth, an incident shock wave is generated at the leading edge of the cascade. At the 0.7L of the suction surface, Mach rod structures and separation bubbles are formed because of the interaction between the boundary layer and the incident shock wave. The combined actions of the reflected shock wave and λ-type normal shock wave at the trailing edge of the suction surface disturbs the internal flow field of the cascade, resulting in backflow between 0.5 L of the pressure surface and the trailing edge of the suction surface, which increases total pressure loss of the cascade.
2) There is no significant effect on the performance of the cascade with artificial roughness at 0.2 L. The total pressure loss changes in 1% when the roughness is set at 0.2 L. The position of shock waves is far away from the leading edge, and the working fluid at the leading edge of the cascade suction side is diffused flow. Increasing the roughness at the leading edge does not change the shock state.
3) Increasing the roughness before the shock incidence point will increase the total pressure loss. Under the condition

of 0.6L–150, the strength of the shock wave at the suction surface and the trailing edge is enhanced. The 0.6L of the suction surface and reverse pressure gradient at the trailing edge increases, which is not conducive to the flow of working fluid. At the same time, the wake loss increases. The total pressure loss of the cascade is increased by 9.91%.

4) The total pressure loss can be reduced by increasing the roughness at the shock incident point and the trailing edge of the suction surface. After the roughness is set, the shock intensity and the reverse pressure gradient are weakened, and the backflow condition is improved; at the same time, the separation bubble induced at the shock incident point is reduced. Under the 0.7L–75 condition, the total pressure loss of the cascade is reduced by 12.8%.
5) The roughness setting at 0.7L–75 working condition can delay the separation in laminar flow and exert stronger disturbance on the separation shear layer, which inhibits the development of separation bubbles.

DATA AVAILABILITY STATEMENT

The original contributions presented in the study are included in the article/Supplementary Material; further inquiries can be directed to the corresponding author.

AUTHOR CONTRIBUTIONS

YW is responsible for numerical simulation calculation. JD is responsible for data collation. SZ is responsible for data collection and summary. MW is responsible for data analysis. ZW is responsible for overall thinking.

FUNDING

This work was supported by the National Science and Technology Major Project (J2019- Ⅲ-0017).

REFERENCES

Aldi, N., Morini, M., Pinelli, M., Spina, P. R., Suman, A., and Venturini, M. (2014). Performance Evaluation of Nonuniformly Fouled Axial Compressor Stages by Means of Computational Fluid Dynamics Analyses. *J. Turbomach.* 136 (2), 021016. doi:10.1115/1.4025227

Back, S. C., Hobson, G. V., Song, S. J., and Millsaps, K. T. (2012). Effects of Reynolds Number and Surface Roughness Magnitude and Location on Compressor Cascade Performance. *J. Turbomach.* 134 (5), 051013–051016. doi:10.1115/1.4003821

Boyle, R. J., Spuckler, C. M., Lucci, B. L., and Camperchioli, W. P. (2001). Infrared Low-Temperature Turbine Vane Rough Surface Heat Transfer Measurements. *J. Turbomachinery-transactions Asme* 123 (1), 168–177. doi:10.1115/1.1333693

Boyle, R. J., and Stripf, M. (2008). Simplified Approach to Predicting Rough Surface Transition. *J. Turbomach.* 131 (4), 1345–1357. doi:10.1115/gt2008-51543

Graham, C. G., and Kost, F. H. (1979). *Shock Boundary Layer Interaction on High Turning Transonic Turbine Cascades*. San Diego, CA, United states: American Society of Mechanical Engineers (ASME). Paper presented at the ASME 1979 International Gas Turbine Conference and Exhibit and Solar Energy Conference, GT 1979, March 12, 1979 - March 15, 1979.

Hou, W. T., Qiao, W. Y., and Luo, H. L. (2011). Shock-wave/boundary-layer Interaction in a Transonic Turbine Cascade. *Proc. Institution Mech. Eng. Part G J. Aerosp. Eng.* 225 (1), 77–85. doi:10.1243/09544100jaero745

Irimpan, K. J., and Menezes, V. (2018). Effect of Surface Roughness on the Heating Rates of Large-Angled Hypersonic Blunt Cones. *Acta Astronaut.* 144, 331–338. doi:10.1016/j.actaastro.2018.01.011

Li, Y., Zhang, K., Zheng, B., and Yang, F. (2016). Effect of Local Velocity on Diffusion-Induced Stress in Large-Deformation Electrodes of Lithium-Ion Batteries. *J. Power Sources* 319 (4), 168–177. doi:10.1016/j.jpowsour.2016.04.056

Melino, F., Morini, M., Peretto, A., Michele, P., and Pier, R. S. (2011). Compressor Fouling Modeling: Relationship between Computational Roughness and Gas Turbine Operation Time. *J. Eng. Gas Turbines Power* 134 (5), 1011–1019. doi:10.1115/gt2011-46089

Rainer, K., Klaus, B., and Meron, W. (2009). Degradation Effects on Industrial Gas Turbines. *J. Eng. Gas Turbines Power* 131 (6), 062401. doi:10.1115/1.3097135

Seung, C. B., June, H. S., and Seung, J. S. (2010). Impact of Surface Roughness on Compressor Cascade Performance. *J. Fluids Eng.* 132 (6), 064502. doi:10.1115/1.4001788

Syverud, E., and Bakken, L. E. (2006). *The Impact of Surface Roughness on Axial Compressor Performance Deterioration*. Barcelona, Spain: ASME Turbo Expo 2006. Paper presented at the 2006 ASME 51st Turbo Expo, May 6, 2006 - May 11, 2006.

Tweedt, D. L., Schreiber, H. A., and Starken, H. (1988). Experimental Investigation of the Performance of a Supersonic Compressor Cascade. *J. Turbomachinery-transactions Asme* 110 (4), 456–466. doi:10.1115/1.3262219

Yao, J., and Carson, S. (2006). *HPT/LPT Interaction and Flow Management in the Inter-turbine Space of a Modern Axial Flow Turbine*. Barcelona, Spain: ASME Turbo Expo 2006. Paper presented at the 2006 ASME 51st Turbo Expo, May 6, 2006 - May 11, 2006.

Yi, S., Liu, W., Xu, D., Gang, D., and Yi, S. (2016). A Combined Experimental and Numerical Investigation of Roughness Induced Supersonic Boundary Layer Transition. *Acta Astronaut.* 118, 199–209. doi:10.1016/j.actaastro.2015.10.008

Zhao, Y., Lou, W., Zhao, D., and Xu, J. (2016). *Investigation on the Reduction of Trailing Edge Shock Losses for a Highly Loaded Transonic Turbine*. Seoul, Korea, Republic of. Paper presented at the ASME Turbo Expo 2016: Turbomachinery Technical Conference and Exposition, GT 2016, June 13, 2016 - June 17, 2016.

Zhou, Y., Zhao, Y., Xu, D., Chai, Z., and Liu, W. (2016). Numerical Investigation of Hypersonic Flat-Plate Boundary Layer Transition Mechanism Induced by Different Roughness Shapes. *Acta Astronaut.* 127, 209–218. doi:10.1016/j.actaastro.2016.05.027

Conflict of Interest: The authors declare that the research was conducted in the absence of any commercial or financial relationships that could be construed as a potential conflict of interest.

Publisher's Note: All claims expressed in this article are solely those of the authors and do not necessarily represent those of their affiliated organizations, or those of the publisher, the editors, and the reviewers. Any product that may be evaluated in this article, or claim that may be made by its manufacturer, is not guaranteed or endorsed by the publisher.

frontiers | Frontiers in Energy Research

ORIGINAL RESEARCH
published: 14 July 2022
doi: 10.3389/fenrg.2022.951177

Experimental Investigation on Two-Phase Rotating Detonation Fueled by Kerosene in a Hollow Directed Combustor

Sainan Xue[1], *Zhuojun Ying*[2], *Hu Ma*[1]* *and Changsheng Zhou*[1]

[1]School of Mechanical Engineering, Nanjing University of Science and Technology, Nanjing, China, [2]Gas Turbine Establishment, Chengdu, China

The operating characteristic of two-phase rotating detonation fueled by kerosene in a hollow combustor with the isolation section is experimentally studied. When the air mass flow rate is 1.5 kg/s, the equivalence ratio is 0.98, and the total temperature of the mixture is 650 K, the stable rotating detonation wave (RDW) is obtained, which verifies the feasibility of the designed two-phase rotating detonation combustor (RDC). It is found that there is a high-frequency oblique shock induced by the upstream rotating detonation wave in the isolation section. A series of experimental tests have been carried out by changing the total temperature of incoming air , which is an important factor affecting the initiation. When the equivalent ratio of reactants is between 0.950–1.152, a stable single-wave detonation is formed. With the increase of equivalent ratio, the time of detonation wave establishment decreases, the intensity and frequency of detonation wave increases, and the temperature of engine tail flame rises. The equivalent chamber pressure Δp_{φ} was defined, and the curve of the performance of the RDC with the equivalent ratio was obtained. The velocity of the RDW increases with the increase of equivalent ratio, and the chamber pressure has an optimal value, a higher or lower equivalent ratio will lead to the decrease of equivalent chamber pressure and the combustion chamber performance.

Keywords: rotating detonation wave, hollow combustor, kerosene, two-phase, equivalent ratio

OPEN ACCESS

Edited by:
Lei Luo,
Harbin Institute of Technology, China

Reviewed by:
Shengbing Zhou,
Chongqing University, China
Yue Huang,
Xiamen University, China
Honghui Teng,
Beijing Institute of Technology, China

***Correspondence:**
Hu Ma
mahuokok@163.com

Specialty section:
This article was submitted to Advanced Clean Fuel Technologies, a section of the journal Frontiers in Energy Research

Received: *23 May 2022*
Accepted: *13 June 2022*
Published: *14 July 2022*

Citation:
Xue S, Ying Z, Ma H and Zhou C (2022) Experimental Investigation on Two-Phase Rotating Detonation Fueled by Kerosene in a Hollow Directed Combustor. Front. Energy Res. 10:951177. doi: 10.3389/fenrg.2022.951177

INTRODUCTION

The rotating detonation engine is a new propeller with multitudinous inherent advantages of being simple, self-pressurizing, and environment friendly and having compact configuration. Compared to conventional combustion chambers, it can increase power up to 10% while saving 25% in fuel consumption. Among the rotating detonation combustion chamber schemes, the one that differs from the current mainly used annular chamber is the hollow combustion chamber, which has no inner column in the chamber. With the elimination of the inner column, the hollow chamber can effectively avoids the problem of heat dissipation from the inner wall and takes no consideration of the corresponding cooling measures. The increasing number of studies in recent years (Teng et al.,

Abbreviations: C-J, Chapman-Jouguet; CRD, continuous rotating detonation; CRDW, continuous rotating detonation wave; DAQ, data acquisition device; DDT, deflagration-to-detonation transition; FFT, fast Fourier transform; RDW, rotating detonation wave; RDC, rotating detonationcombustor; STFT, short-time Fourier transform.

2020; Wang et al., 2021a; Huang et al., 2021; Yan et al., 2021) foretells that rotating detonation engines will have enormous application prospects in the future.

Researchers from Peking University conducted a number of numerical studies (Tang et al., 2013; Yao et al., 2017; Liu et al., 2020), using a rotating detonation combustion chamber without the inner wall, to explore the injection model via an array of holes and found the fuel-based impulse in 1900s, which is approximate to that in the annular combustion chamber under the same condition. Huang et al. (2019) showed the effects of the pintle injector on the H_2/air continuous rotating detonation wave (CRDW) in a hollow chamber, and analyzed the relationship between continuous rotating detonation (CRD) and tangential instability. Zhang et al. (2016) and Zhang et al. (2021) observed that rotating detonation is an implication to the high-frequency tangential instability. And instead of the annular combustion chamber, it is easier to establish an H_2/air rotating detonation in the hollow combustion chamber. Lin et al. (2015) and Lin et al. (2020) experimentally validated that utilizing the pre-detonator and increasing mass flow rate play an important role in the stability of detonation propagation. The result indicated that injecting enough CH_4/O_2 mixture is the essential condition for sustaining a stable CRDW. Kawasaki et al. (2019a) and Kawasaki et al. (2019b) investigated the thrust and impulse of RDE using a propellant of C_2H_2-O_2 for experiments, varying in the inner cylinder radius from 31 to 0 mm. The results confirmed the engine performance with no-inner-cylinder configuration approximate to the others. Anand et al. (2016) carried out the experimental research with an H_2-air hollow RDC, and calculated that the concomitant detonation wave speeds are upward of 90% of the ideal Chapman–Jouguet (C-J) speed at rich conditions of operation. Liu et al. (2021) focused on the characteristics of the methane-air CRDW in a small chamber. The propagation velocity accounts for 99% of the theoretical C-J velocity in the chosen test.

The researchers demonstrated through the above experiments that rotating detonation can not only be established in the hollow combustion chamber, but also outperform the conventional RDE. In solving the problem about a hollow RDC without the narrow ring slot, it cannot be simply assumed to be a two-dimensional problem. It requires a highly complex three-dimensional resolution. Moreover, due to the same injection pattern with the annular chamber, a large reflux region with high pressure loss is observed at the head of a hollow RDC.

Currently, gaseous fuels were generally used in the studies of the hollow RDC. Wang et al. (2018), Peng et al. (2018), and Peng et al. (2019) obtained the single- and double-rotating detonation wave in the experiments based on hydrocarbon fuels such as methane and ethylene. Analyzing the rotating detonation propagation modes, the range of stable operating conditions is significantly smaller due to the worse detonation of methane. Nevertheless, the combined advantages of liquid fuels are higher in practice. Zheng et al. (2020) studied the instability RDW propagation characteristics of liquid kerosene in an RDC with an air-heater, and conjectured the main reason for the fluctuations of detonation wave velocity and pressure peaks along with time. Three different types of instability were observed in the experiments: temporal and spatial instability, mode transition, and re-initiation. Subsequently, Wang et al. (2021b) numerically investigated the effects of total pressures and equivalence ratios on the operation characteristics of RDE. Increasing the width of RDC was submitted by Wang et al. (2021c), which is a more reliable choice to successfully initiate the stable rotating detonation waves.

In this article, the operating characteristic of the two-phase rotating detonation fueled by kerosene in a hollow combustor is experimentally studied. Through analyzing the test results, the flow field of the isolation section and combustion chamber is distinctly obtained.

EXPERIMENTAL SYSTEM AND METHODOLOGY

Experimental System

In order to investigate the kerosene-air hollow RDC operating under a high total enthalpy flow, a direct-connected RDE is designed for the experiments. As shown in **Figure 1**, the system consists of seven main components, including compressed air supply system, air-heater, fuel supply system, ignition system, RDE with a solation section, control system, and acquisition system.

1 Compressed air supply system

The air is stored in the large capacity high-pressure tank through the compressor, and flows through the pipeline into the chamber before entering the air-heater through gas filter, reduction valve, vortex flow meter, electromagnetic valve, and ball valve in sequence. According to this line, the air mass flow rate is ensured to be stabilized at 1.5–2.5 kg/s for experimental requirements.

2 Air-heater

To create the condition of high-temperature and high-pressure incoming flow, the cold air in the main circuit needs to be heated. Controlling the total temperature of the incoming flow is achieved by regulating the mass flow of hydrogen. To replenish the amount of oxygen consumed by the hydrogen fuel combustion through the oxygenating equipment, the oxygen content of the hot air is 23%.

3 Fuel delivery system

The RDE is fueled by liquid aviation kerosene (RP-3), which is stored in a high-pressure tank. Kerosene is squeezed into an injection device by nitrogen, which flows through some valves in an extrusion process. To prevent blocking the electromagnetic valve and injector by kerosene impurities, gauze filter and filter element are installed at the front of the unit. This is necessary to provide the stability and reliability of fuel delivery for RDE.

4 Ignition system

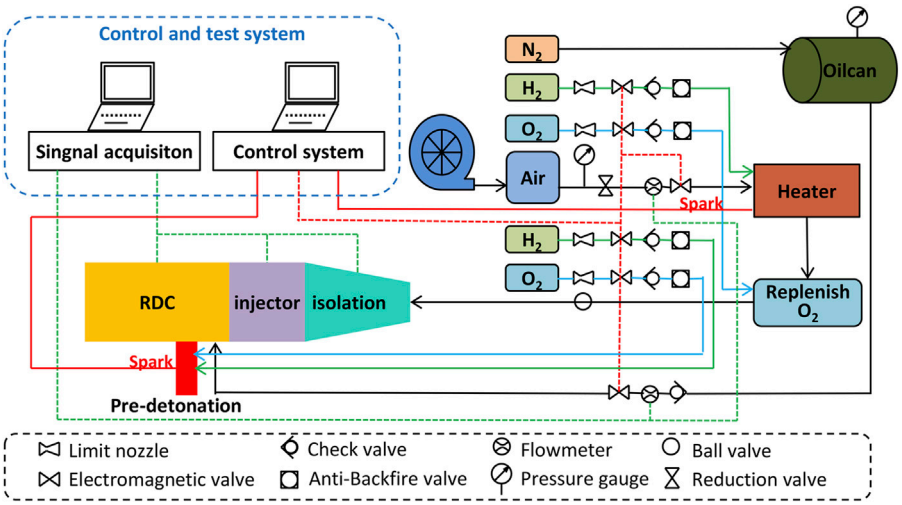

FIGURE 1 | Experimental system diagram.

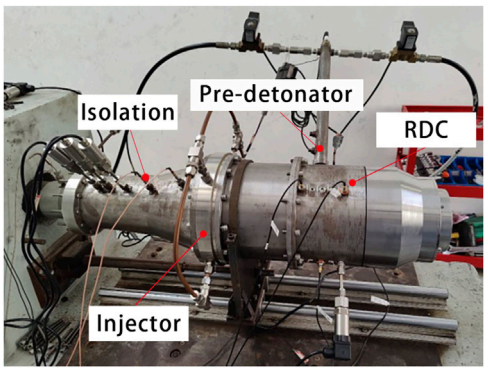

FIGURE 2 | Photograph of the RDC test system.

A high-energy pre-detonator is applied to ignite the RDE, and its diameter is 20 mm. Two Laval-nozzles are respectively set in the delivery system. Hydrogen and oxygen are used as reactions in a pre-detonator, injected orthogonality in a non-premixed manner, which mix at the head of the pre-detonator. The detonable mixture is ignited by an automotive spark plug, and its ignition energy is 50 mJ, which is developed to establish a rotating detonation wave through the deflagration-to-detonation transition (DDT) process.

5 Experimental RDE

RDE includes an isolation section and a rotating detonation combustion chamber, as shown in **Figure 2**. Perforating the outer wall of isolation and the chamber, the pressure taps are used to monitor the high-frequency and steady-state pressure signals in operation.

6 Control system

Control system is composed of a computer, a sequence control module (8 channels), six electromagnetic valves, two sparks, and control lines as shown in the red line in **Figure 1**. To achieve the fuel supply and ignition timing accurately, the system needs the effective control of valves and sparks.

7 Acquisition system

Based on the NI-SRC3 synchronization technology and a 16-bit ADC resolution, an NI high-frequency data acquisition device (DAQ) is used to capture instantaneous multichannel pressure signals. The device is sampled at an acquisition frequency of 2 MS/s. The inlet of the RDC thermocouple and static pressure transducer are set to measure the total temperature and static pressure. The pressure of isolation and chamber are acquired by PCB sensors (PCB113B24), which are installed flush with the inner walls. The frequency of PCB sensors is 500 kHz, and the response time is less than 1 μs and the measurement precision is 1%FS. In addition, the steady pressure of reactant plenums and isolation have been considered. The data of air and fuel mass flow, pressure, and temperature, are collected by vortex flowmeters, are shown on the real-time detective monitor.

Furthermore, in this article a short-term test was carried out, the operation time of RDE is 1–2 s. After a single cycle, the room-temperature air flows into the RDE for 3 s to protect the sensor from damage caused by the sustaining impact of the sensor due to high-temperature and high-pressure detonation products and heat conduction from the high-temperature inner wall.

Experimental Methodology

To develop a more profound investigation, isolation, injector, and walls of chamber are designed to be removable and replaceable based on the modular design. In this experiment, a hollow rotating detonation combustor with an isolation and a unique internal injection is selected as an object of the study. The outer diameter and length of the detonation combustor are 200 and

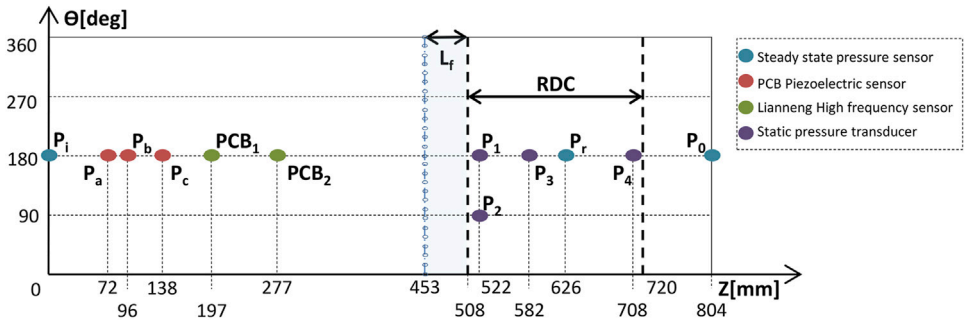

FIGURE 3 | Locations of the sensors.

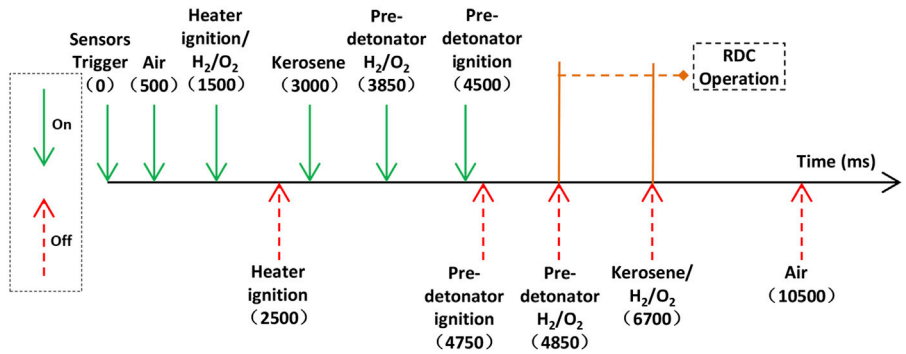

FIGURE 4 | Time sequence of the experimental test.

212 mm, and a convergent nozzle is taken. It is 804 mm from the inlet of the isolation to the outlet of the nozzle.

The location of the sensors at the isolation is shown in **Figure 3**, which are installed on the outside wall of the isolation to measure the pressure trend of the leading shock wave and analyze the internal structure of the flow field. Three PCB sensors are, respectively, installed at the locations of a, b, and c in the isolation to infer the ending location of the normal shock wave. As the air flow is slow at the inlet of the air, a steady state pressure sensor is used to acquire the total pressure of the inlet (P_i). Similarly, sensors are installed at 94 mm from the inlet of RDC and the throat of the nozzle to measure the steady state pressure of RDC (P_r) and the total pressure of the outlet (P_o). The position of the piezoresistive sensors PCB_1 and PCB_2 are, respectively, corresponding to d and e as shown in **Figure 3**, and these two PCB provide the data of pressure to analyze the induced shock wave from the chamber to isolation. The holes of injection are marked by blue circles, which are located at distance Lf, as shown in **Figure 3**. Two high-frequency sensors are placed in the same section, with an axial interval of 14 mm to the inlet of RDC, but the circumferential interval between P_1 and P_2 is clockwise 90° to judge the rotating direction of RDW. Sensor P_3 and P_4 are located axially at 60 and 186 mm from the location of P_1.

In this series of experiments, all operations are performed sequentially, as shown in **Figure 4**. Firstly, sensors are triggered so that the data acquisition system starts running and recording the high-frequency pressure oscillation in the RDC. Then, the room-temperature air is injected for one second, and the flow field is beginning to stabilize. Hydrogen and oxygen are injected into the air-heater, simultaneously the spark of heater ignites. The time set of ignition duration is 1 s for dependability. After kerosene is ejected from injection holes, which is broken into liquid film, and then turn into droplets by the shear of high-speed air flow. The droplet of Kerosene is rapidly evaporated under the action of high-temperature air, and is mixed with the air. The fresh reaction mixture is filled into the combustion chamber. Following the pre-detonator begins to fill hydrogen and oxygen and ignites by a spark plug. In the chamber, the air-kerosene mixture is lit through the DDT process establishing the rotating detonation wave . All supplies are closed successively in the end.

RESULTS AND DISCUSSION

RDC Operation Process Analysis

1 Feasibility of internal injection mode

The experimental test is carried out with a hollow RDC, in which the area of inlet throat is 8725 mm^2. The air mass flow rate is 1.5 kg/s, and the equivalence ratio is 0.98. When the total temperature of the incoming flow is stable at 650 K, **Figure 5A** shows the signal curves of pressure. Before the heater ignites, the air is injected at the earliest,

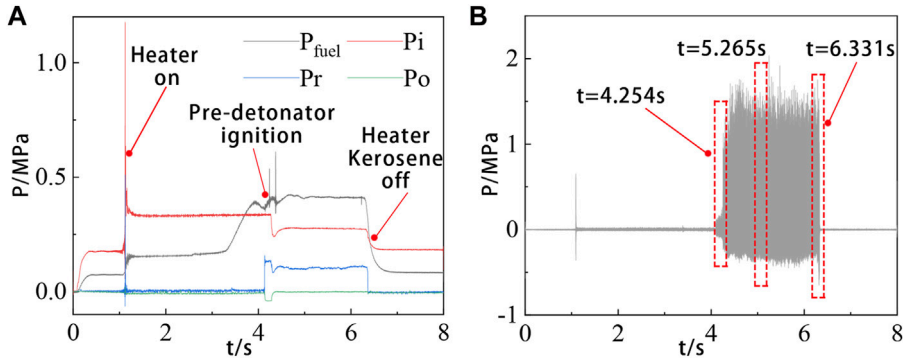

FIGURE 5 | Results of operating at T_0 = 650K, $\dot{m}_{air}$ = 1.5kg/s, and φ = 0.98.

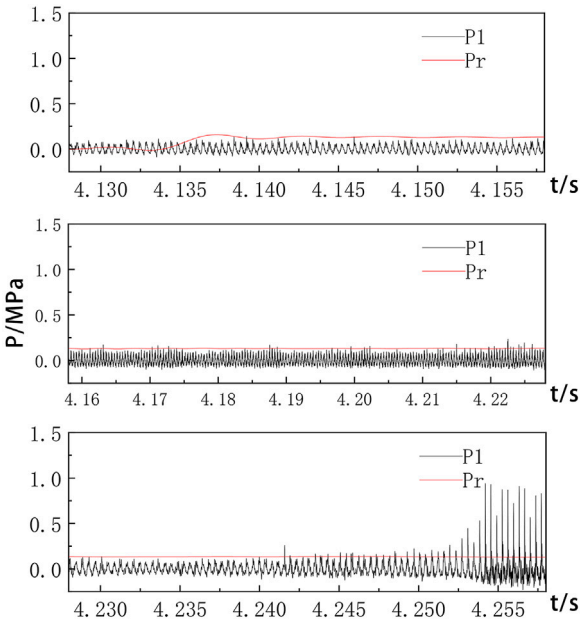

FIGURE 6 | Local segmentation of the pressure signals in the initiation.

and conduced that the inlet pressure increases gradually. After ignition, the inlet pressure peaks abruptly, and then declines fleetly to 0.33 MPaT the value of the pressure is stable until the pre-detonator sparks. When the RDE starts to operate, the propagation of the detonation wave is affected by the isolation section, and the downtrend of the inlet pressure could be directly related to this. The heater and kerosene supply system are shut off, while the air supply system keeps working, so the pressure recovers to the level before the heater ignites.

Figure 5B shows a visualized curve of the original pressure signal of P_1 in the combustion chamber after a high-pass filtering. The complete combustion process demonstrated how the stable rotating detonation wave is formed. When t = 4.100 s, pre-detonator ignites, and the oscillation of combustion process is shown in **Figure 6**. After ignition, the chamber pressure increases and remains at 0.12 MPa. Kerosene is sprayed from the injection hole, which does not evaporate completely in time. Kerosene and air are heterogeneously mixed to reduce the combustion efficiency. Therefore, kerosene and air are difficult to initiate, the detonation wave cannot be immediately established after ignition, the initial combustion mode in RDC is a deflagration combustion. Finishing the DDT process at t = 4.254 s, the rotating detonation wave begins to stably propagate.

To get a visualized view, the signal data are magnified nearby t = 5.265 s, as shown in **Figure 7A**. The propagation period of the detonation wave is 367 μs. **Figure 7B** shows the results obtained by the fast Fourier transform (FFT) of the high-frequency dynamic pressure signal measured by P_1. The dominant frequency of RDC is 2721 Hz, and the corresponding average velocity is 1710 m/s.

As shown in **Figure 8**, when the fuel electromagnetic valve is closed at 6.331 s. The fuel injection pressure and mass flow gradually decline, but the air injection pressure and mass flow remain invariable, accordingly the equivalence ratio of the combustor gradually decreases, and the RDE enters the quenching stage. The propagation frequency of the rotating detonation wave presents a downward trend with time, and finally flameouts completely at 6.353 s.

The above analysis elucidates that the internal injection method adopted in this article is feasible, and the self-sustained rotating detonation wave can be obtained.

2 Flow characteristic of isolation

The dynamic pressure signals in the isolation captured by PCB_1 and PCB_2 sensors in the test are shown in **Figure 9A**. The pressure peaks of detonation wave at the position of PCB_2 closer to the chamber are significantly higher, and the pressure signal of PCB_1 fluctuates slightly. By magnifying the signal data in the red dotted box, the complex shock waves in the isolated section are observed. The curve of PCB_2 shows obvious characteristics of multi-wave peaks, and the pressure changes in the range of ± 1 MPa. **Figure 9B** indicates a single period of three-wave peaks, namely T_1 = 362 μs, T_2 = 364 μs, and T_3 = 368 μs, which are approximate to the average period of the combustion chamber.

Figures 9C–F respectively show the fast Fourier transform (FFT) and the short-time Fourier transform (STFT) results of the PCB_1 and PCB_2 pressure signals. A recognizable line appears at

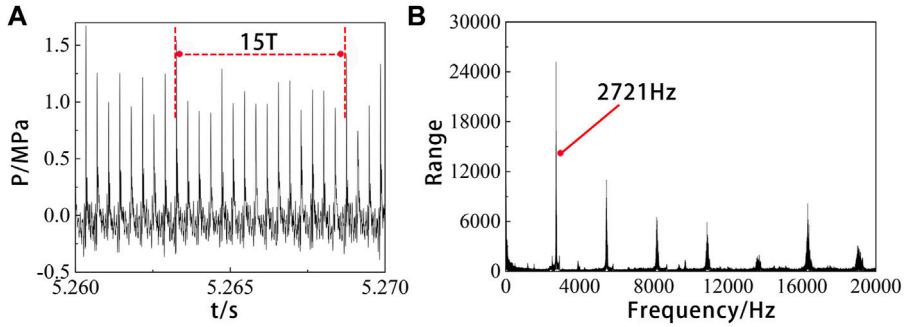

FIGURE 7 | Pressure signals of P1 by operating at T_0 = 650K, $\dot{m}_{air}$ = 1.5kg/s, andφ = 0.98. **(A)** Local high-frequency pressure signals; **(B)** The STFT frequency distribution.

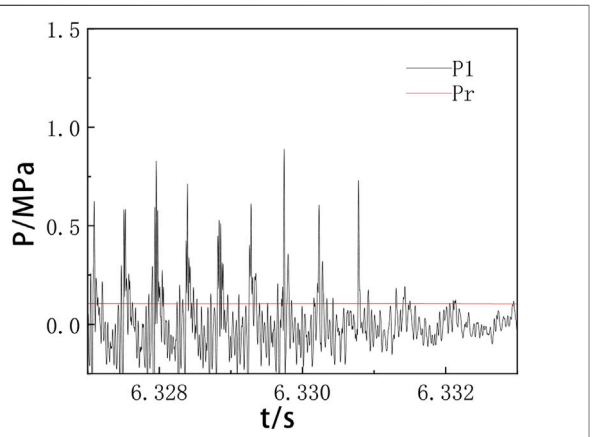

FIGURE 8 | Local segmentation of the pressure signals in the quenching stage.

f = 2721 Hz, which indicates that a stable convergence value is obtained for operating frequency. The corresponding average velocity is 1708.8 m/s, which is consistent with the dominant frequency of the combustion chamber.

It is inferred from the above phenomenon that there is high-frequency rotating oblique shock waves induced by the detonation wave upstream in the isolation. The propagation of shock waves is sophisticated, two of them are inferred to be the forward spiral shock waves generated in the RDC. Influenced by the internal injection structure, the shock waves are divided into two waves with different velocities, which move upstream in the isolation section. The remaining shock waves are deduced as reflected waves when passing through the throat of isolation.

Influence on Rotating Detonation Combustion Characteristic

1 The factor of air total temperature

The parameters based on the previous experiments are unaltered except the total temperature of incoming air. The total temperature of the experimental control group are 562 K and 480 K.

When the total temperature is 562 K, the signal transformation of P_1 by FFT and STFT is conducted, as shown in **Figure 10**. The dominant frequency of a single wave is 2778 Hz, slightly higher than 2710 Hz at 650 K, which is consistent with the theoretical law that the propagation velocity of detonation wave decreases with the increase of initial temperature.

The detonation time of the combustion chamber t_1 = 4.22 s, correspondingly the frequency is 2563 Hz. After successful initiation, the frequency of detonation wave gradually rises until reaching a stable value of 2778 Hz at 4.41 s (t_2). The process takes 0.19 s. After the heater and fuel valve are turned off, the frequency rapidly drops to 2319 Hz at t_3. The actual operating time of RDC is 1.26 s (t_3-t_1) until the engine completely extinguishes. The engine operates in a single-wave mode all the time. In these experiments, the dominant frequency increased slightly, but not significantly.

The combustion chamber works in a stable single-wave mode throughout the whole process. Although the total temperature of the air inlet decreases by nearly 100 K compared with 650 K, its dominant frequency increases slightly, and the change of the total temperature has no obvious effects on the wave velocity of the detonation wave. It is illustrated that the effect of total temperature on the velocity of detonation wave is not obvious.

When the total temperature of incoming flow descends to 480 K, initiation fails and rotating detonation wave is not established, as shown in **Figure 11**. By processing the data collected by P_1, the dominant frequency of the combustor is only 249 Hz, and there is no obvious frequency red line in the STFT conversion. Hence, the combustor is in a low-frequency unstable oscillation combustion mode.

The conclusion is that the variation of total temperature will affect whether the rotating detonation wave is formed. The lower limit of the air total temperature at inlet for the successful initiation in this article is between 480 and 562 K. Kerosene evaporation slows down when the inlet temperature is too low. Because of the two-phase combustion, the combustion is in an unstable low-frequency oscillation combustion state. Rotating detonation wave is not obtained.

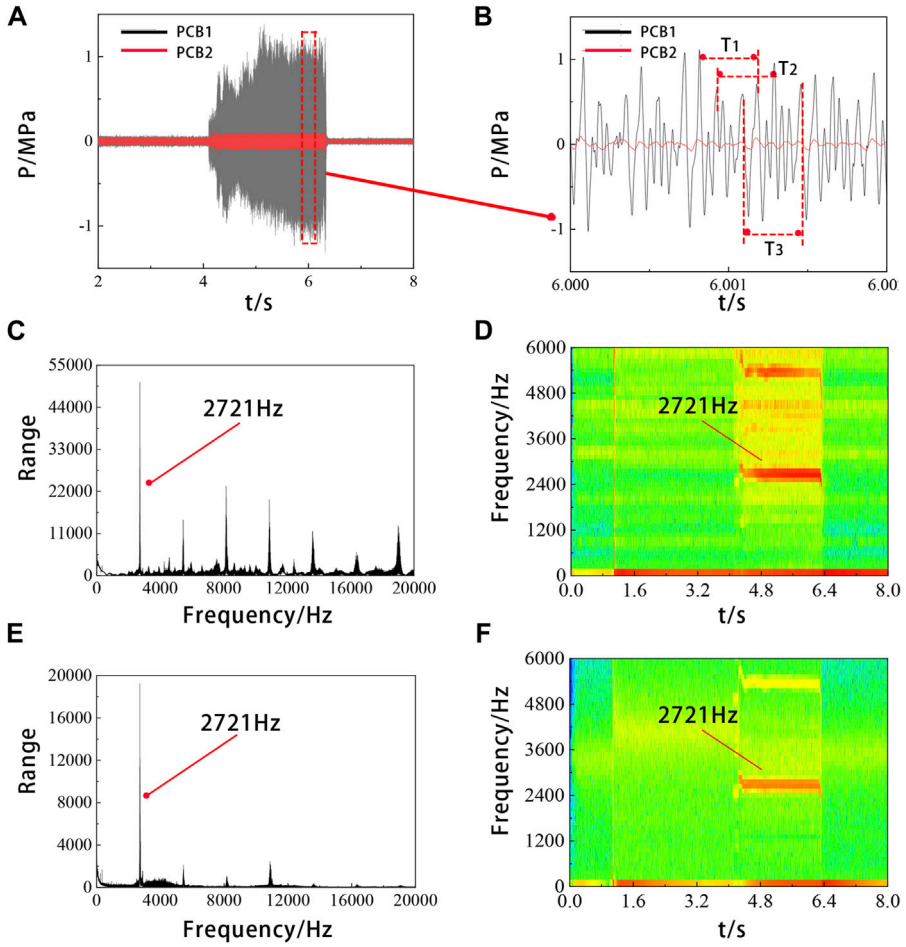

FIGURE 9 | Results of operating at T_0 = 650K, $\dot{m}_{air}$ = 1.5kg/s, and φ = 0.98. **(A)** High-frequency pressure signals in the isolation; **(B)** Local high-frequency pressure signals; **(C)** The FFT frequency distribution by PCB_1; **(D)** The STFT frequency distribution by PCB_1; **(E)** The FFT frequency distribution by PCB_2; **(F)** The STFT frequency distribution by PCB_2.

2 The factor of equivalence ratio

The supply of kerosene is controlled by adjusting the injection pressure, and the mass flow rate of kerosene is calibrated as $\dot{m}_f = 183.96\Delta p^{0.497}$. The air mass flow rate and total temperature are invariant, and the reactant equivalent ratios are set to 0.914, 0.950, 0.987, 1.086, and 1.152.

When the equivalent ratio φ, respectively, are 0.914 and 0.950, a continuous rotating detonation wave is not formed. When φ = 0.950, there is a deflagration flame at the initial stage, but the flame is quenched quickly. It is concluded that the mixing efficiency is reduced. The differential pressure influences on the kerosene mass flow, which is caused by the internal injection configuration, and the effective depth penetration have shrunk when the mixture is combusted. The pressure curves in **Figure 12** describe that the peak of the pressure signal measured by P_1 is relatively low, in the chamber the stable rotating detonation is not found. In the high-speed image on the right, a narrow blue tail flame at the outlet of the nozzle can be seen. When the equivalent ratio is increased to 0.987, 1.086, and 1.152, respectively, the stable detonation waves are formed in the rotating detonation chamber, and it is presented a single-wave mode.

The curves of the steady state pressure of RDC (P_r) and the total pressure of the outlet (P_o) under three working conditions are shown in **Figures 13A–C**. After ignition, the stable pressure in the combustion chamber amplifies due to the combustion products of high temperature and high pressure. When the rotating detonation wave is formed, the fuel injection holes are partially blocked due to the partial high pressure of RDW, and the steady state pressure in the RDC decreases to a certain extent until it flameout.

When the equivalent ratio is 0.987, the establishment process of detonation wave is the longest. When the equivalent ratio is 1.152, the stable pressure amplitude is the largest in the state of detonation. It illustrates that the equivalent ratio is an important factor affecting the establishment and intensity of detonation wave in the kerosene two-phase rotating detonation combustor without the inner column. When the equivalent ratio decreases, the time taken to establish the detonation wave increases, whereas

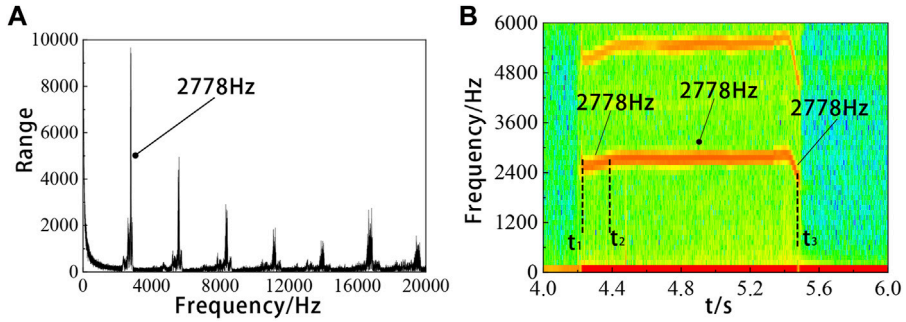

FIGURE 10 | Results of operating at T_0 = 562K, $\dot{m}_{air}$ = 1.5kg/s, and φ = 0.98. **(A)** The FFT frequency distribution by PCB_1; **(B)** The STFT frequency distribution by PCB_1.

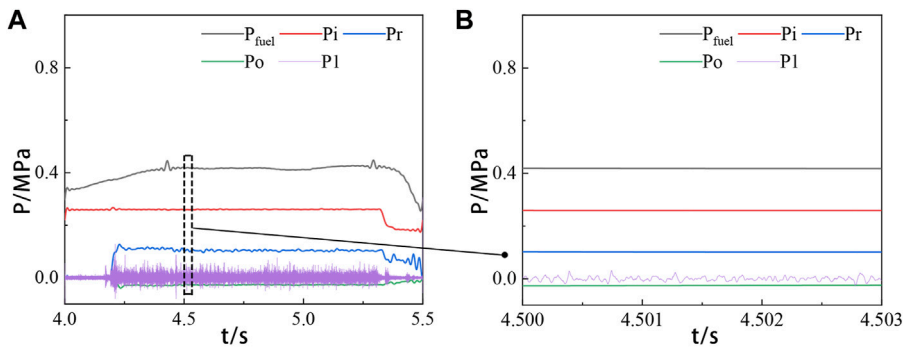

FIGURE 11 | Results of operating at T_0 = 480K, $\dot{m}_{air}$ = 1.5kg/s, φ = 0.98. **(A)** Static pressure signals and high-frequency pressure signals by P_1; **(B)** Local signals.

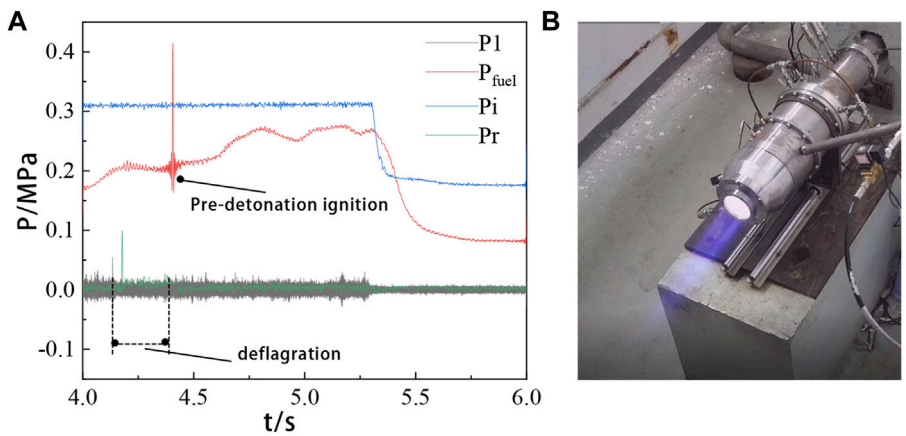

FIGURE 12 | Results of operating at T_0 = 650K, $\dot{m}_{air}$ = 1.5kg/s, φ = 0.95. **(A)** Static pressure signals and high-frequency pressure signals by P_1; **(B)** The Photograph of RDE.

when the equivalent ratio increases, the intensity of detonation wave decreases.

Figures 13D–F show the signal data taken from the stable working stage under three working conditions, respectively. The intervals between two detonation waves are 381 μs, 351, and 348 μs. The corresponding instantaneous velocities of rotating detonation waves are 1,648.3 m/s, 1791.4 m/s, and 1803.1 m/s.

As shown in **Figure 14**, **Figure 15**, and **Figure 16**, after the FFT transformation of the signal P_1, the propagation frequency are 2658, 2847, and 2895 Hz, respectively, which are close to the

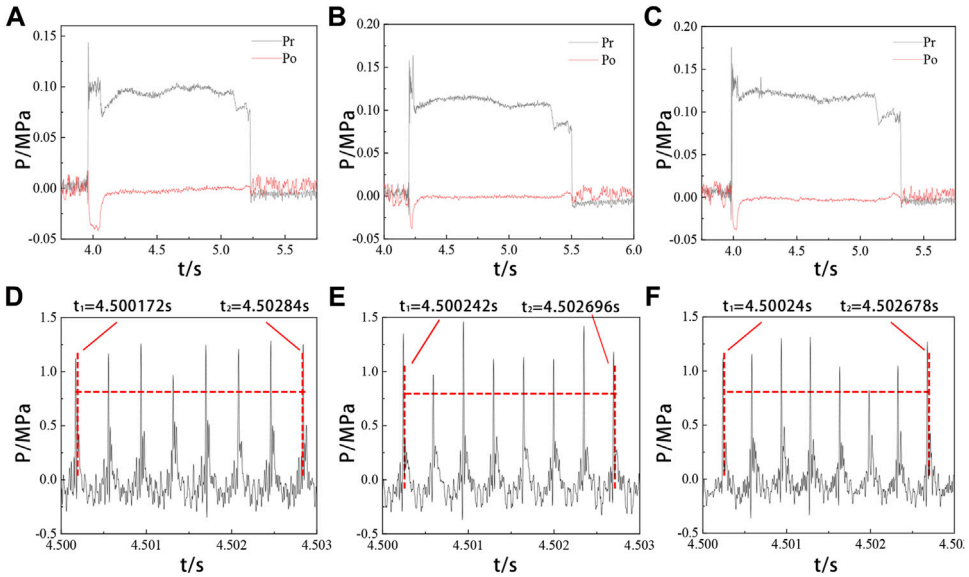

FIGURE 13 | Results of operating at φ = 0.987 , φ = 1.086 , φ = 1.152. **(A)**—**(C)** Static pressure signals; **(D)**—**(F)** Local pressure signals.

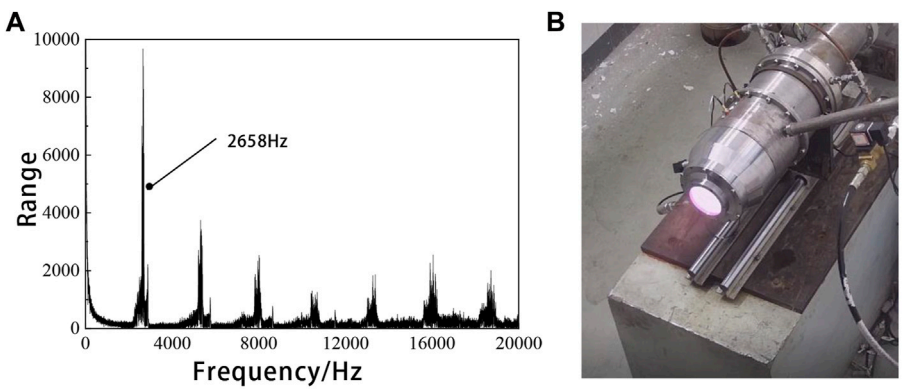

FIGURE 14 | Results of operating at T_0 = 650K, $\dot{m}_{air}$ = 1.5kg/s, φ = 0.987. **(A)** The FFT frequency distribution by P_1; **(B)** The Photograph of RDE.

instantaneous stabilized pressure frequency of the combustion chamber. When the equivalent ratio increases, the instantaneous velocity and average velocity of the combustion chamber rises correspondingly.

The color of the flame is generally related to the temperature of the flame and the material of the fuel. In this article, only kerosene-air combustion is discussed, so the color of the flame represents the change in temperature. When the equivalent ratio is between 0.987 and 1.152, the RDC is a stable single-wave detonation, and the detonation wave frequency increases with the increase of the equivalent ratio. When the equivalent ratio is 1.086, there is a bright white tail flame at the outlet of the nozzle. And when the equivalent ratio is higher, the color of flame turns orange red. It is common sense that the higher the temperature and the darker the color. Therefore, with the increase of the equivalent ratio, the temperature of the engine exhaust gas is higher.

To evaluate the change of combustor performance with the equivalent ratio, the velocity of RDW is calculated based on the propagation frequency obtained by the aFFT, and the results are shown in **Figure 17**. Generally, a higher combustor pressure corresponds to a better engine propulsive performance, and the condition of the outlet pressure of the nozzle is constant. In experiments when the equivalent ratio is between 0.987–1.152, we found a rule that the pressure at the throat is close to the atmospheric pressure, and at the outlet of the nozzle, the detonation wave is a complete expansion. Hence, the equivalent chamber pressure (Δp_φ) is defined as the chamber pressure difference per kilogram of kerosene that can be produced by combustion. Also, it can be obtained by

$$\Delta p_\varphi = \frac{(p_r - p_0)}{\dot{m}_f}, \tag{1}$$

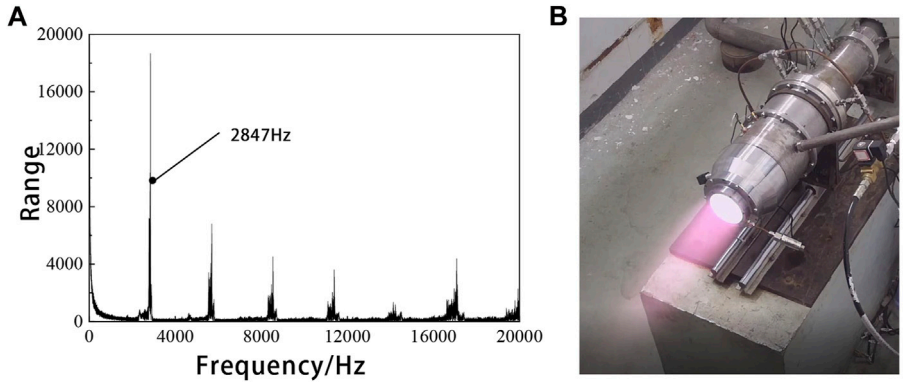

FIGURE 15 | Results of operating at T_0 = 650K, $\dot{m}_{air}$ = 1.5kg/s, φ = 1.086. **(A)** The FFT frequency distribution by P_1; **(B)** The Photograph of RDE.

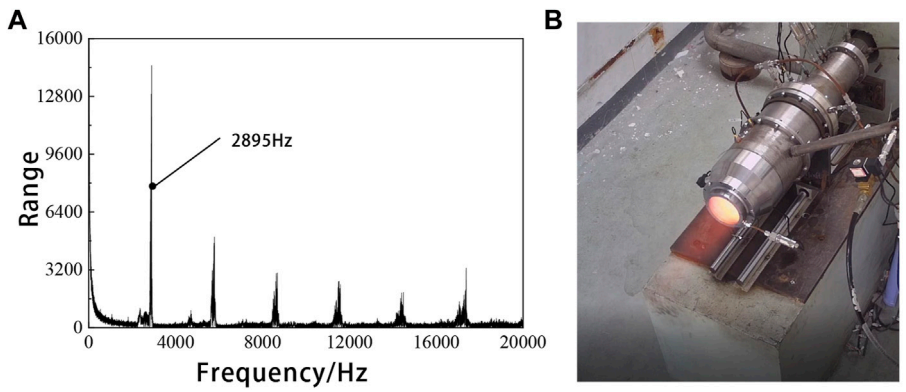

FIGURE 16 | Results of operating at T_0 = 650K, $\dot{m}_{air}$ = 1.5kg/s, φ = 1.152. **(A)** The FFT frequency distribution by P_1; **(B)** The Photograph of RDE.

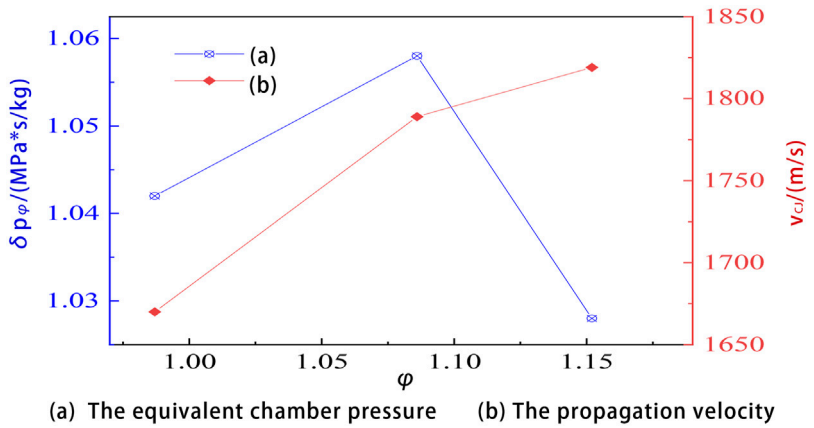

FIGURE 17 | Performance of the RDC with the equivalent ratio. **(A)** The equivalent chamber pressure; **(B)** The propagation velocity.

where P_r is the stable state pressure of the RDC when operating, P_o is the outlet pressure, and $\dot{m}_f$ corresponds to the consumption of fuel. The equivalent chamber pressure is Δp_φ and its unit of measurement is MPa·s/kg.

Equivalent chamber pressure reflects the propulsion performance of the engine to a certain extent. In this articler, the relation curve of the performance of the RDC with the change of equivalent ratio was obtained as shown in **Figure 17**. When the

equivalent ratio is near 1, the detonation wave velocity increases with the increase of the equivalent ratio. When the equivalent ratio exceeds 1.086, the propagation velocity increases slowly, and the maximum propagation velocity reaches 1819 m/s, exceeding 90% of the C-J velocity. The equivalent chamber pressure increases first and then decreases with the increase of the equivalent ratio, and comes to the lowest when φ = 1.152. The equivalent ratio has a great influence on the performance of the RDC. An optimal equivalent chamber pressure exists when the equivalent ratio is between 0.987 and 1.152. A higher or lower equivalent ratio will lead to lower equivalent chamber pressure, which will affect the combustion efficiency and reduce the combustion chamber performance.

CONCLUSION

In this article, a hollow RDC with the isolation section is investigated by varying the air total temperature of the incoming and the equivalent ratio. The room-temperature air and kerosene are selected as the oxidizer and fuel, respectively. The main conclusions are drawn as follows:

1 When the air mass flow rate is 1.5 kg/s, the equivalent ratio is 0.98 and the total temperature of the mixture is 650 K, the RDW undergone the DDT process is established by the pre-detonator, and the average velocity of RDW is 1710 m/s. The result of the test demonstrates that the scheme of two-phase hollow RDC is feasible.

2 It is found that there is a high-frequency oblique shock induced by the upstream rotating detonation wave in the isolation section.

3 The total temperature of incoming air is an important factor affecting the initiation. When the total temperature of air is 562 K in the experimental test, the rotating detonation combustion operates in a stable single-wave mode throughout the whole process. The dominant propagation frequency is slightly faster than that at 650 K. In a series of tests, which have been carried out, the lower limit of the air total temperature for the successful initiation is between 480 and 562 K.

4 The effects of the equivalent ratio on the performance of the RDC is significant. The supply of kerosene is controlled by adjusting the injection pressure. After recalibrating the mass flow rate of kerosene, the experimental tests are conducted. When the equivalent ratio of reactants is 0.914 or 0.950, the rotating detonation waves are not established smoothly. When φ = 0.950, there is a deflagration flame in the initial stage, but the flame is quenched quickly. When the equivalent ratio is increased to 0.987, 1.086, and 1.152, respectively, a stable single detonation waves are formed in the RDC. When the equivalent ratio increases, the time taken to establish the detonation wave decreases, the intensity and the frequency of detonation wave increases, and the temperature of engine exhaust gas is higher.

5 The equivalent chamber pressure Δp_{φ} was defined, and the curve of the performance of the RDC with the equivalent ratio was obtained. The velocity of the RDW increases with the increase of equivalent ratio, and the equivalent chamber pressure has an optimal value, a higher or lower equivalent ratio will lead to the decrease of equivalent chamber pressure and the combustion chamber performance.

DATA AVAILABILITY STATEMENT

The raw data supporting the conclusion of this article will be made available by the authors, without undue reservation.

AUTHOR CONTRIBUTIONS

SX: experimental design, data analysis, and writing; ZY: building experimental systems and experimental data processing; HM: providing overall ideas and data analysis; and CZ: guiding the experimental operation.

FUNDING

This work was supported by the National Natural Science Foundation of China (12072163, 5210060296, and 11802134) and the National Defense Science and Technology Key Laboratory Foundation (HTKJ2020KL011004-1).

ACKNOWLEDGMENTS

Throughout the writing of this dissertation, the authors have received a great deal of support and assistance. They would particularly like to thank their teammates and professor for their wonderful collaboration and wise counseling. In addition, they would like to thank their parents and Yuge Zhang for their patient support and sympathetic ear.

REFERENCES

Anand, V., St. George, A. C., Gutmark, E. J., and Gutmark, E. (2016). "Hollow Rotating Detonation Combustor," in 54th AIAA Aerospace Sciences Meeting, 4-8 January 2016 (San Diego, California, USA: AIAA). doi:10.2514/6.2016-0124

Huang, S., Li, Y., Zhou, J., Liu, S., and Peng, H. (2019). Effects of the Pintle Injector on H2/air Continuous Rotating Detonation Wave in a Hollow Chamber. *Int. J. Hydrogen Energy* 44, 14044–14054. doi:10.1016/j.ijhydene.2019.04.011

Huang, Y., Xia, H., Chen, X., Luan, Z., and You, Y. (2021). Shock Dynamics and Expansion Characteristics of an Aerospike Nozzle and its Interaction with the Rotating Detonation Combustor. *Aerosp. Sci. Technol.* 117, 106969. doi:10.1016/j.ast.2021.106969

Kawasaki, A., Inakawa, T., Kasahara, J., Goto, K., Matsuoka, K., Matsuo, A., et al. (2019). Critical Condition of Inner Cylinder Radius for Sustaining Rotating

Detonation Waves in Rotating Detonation Engine Thruster. *Proc. Combust. Inst.* 37, 3461–3469. doi:10.1016/j.proci.2018.07.070

Kawasaki, A., Yokoo, R., Goto, K., Kim, J.-H., Matsuoka, K., Kasahara, J., et al. (2019). "An Experimental Study of In-Space Rotating Detonation Rocket Engine with Cylindrical Configuration," in AIAA Propulsion and Energy 2019 Forum, 19-22 August 2019 (Indianapolis, IN: AIAA), 19–22. doi:10.2514/6.2019-4298

Lin, W., Tong, Y., Lin, Z., Nie, W., and Su, L. (2020). Propagation Mode Analysis on H2-Air Rotating Detonation Waves in a Hollow Combustor. *AIAA J.* 58, 5052–5062. doi:10.2514/1.J058254

Lin, W., Zhou, J., Liu, S., and Lin, Z. (2015). An Experimental Study on CH4/O2 Continuously Rotating Detonation Wave in a Hollow Combustion Chamber. *Exp. Therm. Fluid Sci.* 62, 122–130. doi:10.1016/j.expthermflusci.2014.11.017

Liu, S.-J., Huang, S.-Y., Peng, H.-Y., and Yuan, X.-Q. (2021). Characteristics of Methane-Air Continuous Rotating Detonation Wave in Hollow Chambers with Different Diameters. *Acta Astronaut.* 183, 1–10. doi:10.1016/j.actaastro.2021.02.035

Liu, X.-Y., Chen, Y.-L., Xia, Z.-J., and Wang, J.-P. (2020). Numerical Study of the Reverse-Rotating Waves in Rotating Detonation Engine with a Hollow Combustor. *Acta Astronaut.* 170, 421–430. doi:10.1016/j.actaastro.2020.02.008

Peng, H. Y., Liu, W. D., Liu, S. J., Zhang, H. L., and Zhou, W. Y. (2019). Realization of Methane-Air Continuous Rotating Detonation Wave. *Acta Astronaut.* 164, 1–8. doi:10.1016/j.actaastro.2019.07.001

Peng, H., Liu, W., Liu, S., and Zhang, H. (2018). Experimental Investigations on Ethylene-Air Continuous Rotating Detonation Wave in the Hollow Chamber with Laval Nozzle. *Acta Astronaut.* 151, 137–145. doi:10.1016/j.actaastro.2018.06.025

Tang, X., Wang, J., and Shao, Y. (2013). 3-D Simulation of Rotating Detonation Wave in Combustion Chambers without Inner Wall. *J. Aerosp. Power* 28, 792–799. doi:10.13224/j.cnki.jasp.2013.04.013

Teng, H., Zhou, L., Yang, P., and Jiang, Z. (2020). Numerical Investigation of Wavelet Features in Rotating Detonations with a Two-step Induction-Reaction Model. *Int. J. Hydrogen Energy* 45 (7), 4991–5001. doi:10.1016/j.ijhydene.2019.12.063

Wang, B., Xie, Q., Wen, H., Teng, H. H., Zhang, Y. N., Zhou, L., et al. (2021). Research Progress of Detonation Engines. *Joutnal Propuls. Technol.* 42 (4), 721–737. doi:10.13675/j.cnki.tjjs.210109

Wang, F., Weng, C. S., Wu, Y. W., Bai, Q. D., Zheng, Q., and Xu, H. (2021). Effects of Total Pressures and Equivalence Ratios on Kerosene/air Rotating Detonation Engines Using a Paralleling CE/SE Method. *Def. Technol.* 17 (6), 1805–1816. doi:10.3969/j.issn.2214-9147.2021.06.00110.1016/j.dt.2020.09.015

Wang, Y., Le, J., Wang, C., and Zheng, Y. (2018). A Non-premixed Rotating Detonation Engine Using Ethylene and Air. *Appl. Therm. Eng.* 137, 749–757. doi:10.1016/j.applthermaleng.2018.04.015

Wang, Z., Yan, Y., Wang, K., Zhu, Y., Hao, Z. M., Fan, W., et al. (2021). Effects of Combustor Width on Propagation Modes of Rotating Detonation Waves Utilizing Liquid Kerosene. *J. Propuls. Technol.* 42 (4), 842–850. doi:10.13675/j.cnki.tjjs.200256

Yan, C., Teng, H., and Ng, H. D. (2021). Effects of Slot Injection on Detonation Wavelet Characteristics in a Rotating Detonation Engine. *Acta Astronaut.* 182, 274–285. doi:10.1016/j.actaastro.2021.02.010

Yao, S., Han, X., Liu, Y., and Wang, J. (2017). Numerical Study of Rotating Detonation Engine with an Array of Injection Holes. *Shock Waves* 27 (3), 467–476. doi:10.1007/s00193-016-0692-6

Zhang, H., Liu, W., and Liu, S. (2016). Effects of Inner Cylinder Length on H2/air Rotating Detonation. *Int. J. Hydrogen Energy* 41, 13281–13293. doi:10.1016/j.ijhydene.2016.06.083

Zhang, H., Liu, W., and Liu, S. (2021). Research on H2/Air Rotating Detonation in the Hollow Chamber with Double Injection. *Int. J. Hydrogen Energy* 46, 23067–23074. doi:10.1016/j.ijhydene.2021.04.102

Zheng, Q., Meng, H. L., Weng, C. S., Wu, Y. W., Feng, W. K., and Wu, M. L. (2020). Experimental Research on the Instability Propagation Characteristics of Liquid Kerosene Rotating Detonation Wave. *Def. Technol.* 16 (6), 1106–1115. doi:10.3969/j.issn.2214-9147.2020.06.00310.1016/j.dt.2020.06.028

Conflict of Interest: The authors declare that the research was conducted in the absence of any commercial or financial relationships that could be construed as a potential conflict of interest.

Publisher's Note: All claims expressed in this article are solely those of the authors and do not necessarily represent those of their affiliated organizations, or those of the publisher, the editors, and the reviewers. Any product that may be evaluated in this article, or claim that may be made by its manufacturer, is not guaranteed or endorsed by the publisher.

frontiers | Frontiers in Energy Research

ORIGINAL RESEARCH
published: 05 August 2022
doi: 10.3389/fenrg.2022.948134

Numerical Investigation on Aerodynamic Performances of the Single-Stage Transonic Turbine With Various Coolant Ejection Positions and Coolant Mass Flow Rates

Jinming Zhang, Xun Zhou, Wei Du and Senpei Xu*

School of Energy Science and Engineering, Harbin Institute of Technology, Harbin, China

The effects of film cooling holes on the suction surface and the coolant mass flow were studied in this research, which focused on load distribution and flow characteristics such as shock migration. A high and low degree of reaction scheme (degree of reaction = 0.3, 0.53) is selected to numerically investigate the aerodynamic performance with consideration of air film cooling. The results show that the above factors have different influences on the intensity and the trailing edge shock direction. The reflected shock weakens and then recovers when the coolant ejection position approaches and departs from the reflection point. Altering the coolant ejection position or coolant mass flow rate mainly affects the load at the front and middle of the blade and has some effects on the pressure rise at the trailing edge as well. There is an optimal position (x/C_{ax} = 0.6) and optimal coolant volume (10% mainstream mass flow rate) for flattening the pressure rise and weakening shocks, thereby reducing losses.

Keywords: transonic turbine, coolant mass flow rate, coolant ejection position, trailing edge shock, aerodynamic performance

OPEN ACCESS

Edited by:
Xiao Liu,
Harbin Engineering University, China

Reviewed by:
Jun Li,
Xi'an Jiaotong University, China
Jingjun Zhong,
Shanghai Maritime University, China
Baitao An,
Institute of Engineering Thermophysics, (CAS), China

****Correspondence:***
Xun Zhou
zhouxun@hit.edu.cn

Specialty section:
This article was submitted to Advanced Clean Fuel Technologies, a section of the journal Frontiers in Energy Research

Received: *19 May 2022*
Accepted: *14 June 2022*
Published: *05 August 2022*

Citation:
Zhang J, Zhou X, Du W and Xu S (2022) Numerical Investigation on Aerodynamic Performances of the Single-Stage Transonic Turbine With Various Coolant Ejection Positions and Coolant Mass Flow Rates. Front. Energy Res. 10:948134. doi: 10.3389/fenrg.2022.948134

1 INTRODUCTION

The pursuit of efficiency, light weight, and large thrust results in an ultra-high-load operating condition for aero-engine turbine blades. With the continual increase of load in modern turbines, a higher turbine exit Mach number is acquired owing to a larger turbine pressure ratio. However, the transonic speed condition usually brings up complex shock structures within the transonic turbine blade passage, especially at the trailing edge. The trailing edge shock has two branches. The inner trailing shock impinges on the suction surface of the adjacent blade, and it will have an impact on the flow field and increase losses. The other one, called the outer trailing shock, strikes into the exit of the passage, which will have a great effect on the flow behaviors downstream of the blade cascade and interact with the trailing trace. The trailing edge shock loss accounts for a major part of the loss (Yang, 2014). Therefore, controlling shock loss in transonic turbines can effectively improve the aerodynamic performance.

There are numerous simulations and experiments to clarify various loss mechanisms. Langston et al. (1977) achieved the endwall flow visualization using ink and then investigated crossflows in a turbine cascade passage (Langston 1980). Denton (1993) predicted that trailing edge shock losses were major losses in transonic turbine cascades. Michelassi et al. (1997) predicted that the transition

started in this area where the shock impinged on the suction side, and experiments also confirmed that. Bian et al. (2020) found that a separation bubble might lead to reflection, due to the rising incident angle of the oblique shock wave. In particular, it was obtained using a hybrid RANS/LES strategy. Employing experiments in a compression tube and simulations of computational fluid dynamics (CFD), Yasa et al. (2007) demonstrated the decrease of circumferential velocity as a contributor to the rising positive incidence angles. In addition, the increase affected losses associated with the trailing edge. Corriveau and Sjolander (2004) measured and compared the midspan aerodynamic performance with three different airfoils at design incidence. These results indicated the aft-loaded airfoil blade produced the least losses among all airfoil blades around the design Mach number. Nevertheless, when it reached the over-design Mach number, the performance of the aft-loaded airfoil blade would worsen more quickly. For all operating conditions, the front-loaded airfoil blade had the worst performance. Zhou et al. (2020) revealed that shock wave near the trailing edge was largely determined by the scope of the base region. Thus, it was useful to increase the trailing wedge angle to decrease shock losses.

The optimization of the blade profile design is one mainstream method to reduce shock losses in the transonic turbine at present. Ji et al. (2004) pointed out that trailing edge thickness and blade surface velocity distribution near the trailing edge were the substantial factors of overall performance; the reasonable blade design could eliminate or weaken the reflected shock on the suction surface. Sonoda et al. (2006) applied the evolutionary algorithm to optimize the pressure-side profile near the trailing edge; after adjusting, it could induce such a double shock system or multi-shock system to reduce the trailing edge shock losses. Zhao et al. (2016) adopted a negative curvature on the uncooled suction side. This blade delayed the intersection point of the reflected pressure-side (PS) trailing edge shock with the SS trailing edge shock, resulting in lower shock losses. Shelton et al. (1993) combined AI with an inviscid and adaptive grid CFD solver to achieve the optimization of a transonic turbine airfoil. The optimal design successfully dropped the intensity of shock waves near the trailing edge on the suction surface, resulting in a more uniform outlet flow field. Chen et al. (2018) adjusted the curvature of transonic turbine blades and increased the relative length of the diffuser section after the throat region, which constructed a local acceleration region and a series of compression shocks, thereby not only increasing the turbine blade load but also attenuating the strength of the shock within the blade cascade.

It is well known that the performance of a gas turbine can be significantly improved by raising the turbine inlet temperature, which also leads to the severer operating condition for the single-stage transonic turbine. To cope with the components' extremely high thermal load, it is essential to introduce effective cooling means into the gas turbine. The two mainstream cooling methods in turbines are film cooling and jet cooling. It also has been concluded that coolant from the air film cooling holes or cooling slots on the suction surface can supply a certain amount of energy for the flow within the boundary layer, which is helpful to decrease the adverse pressure gradient in the area where shock waves exist. In addition, trailing edge coolant ejection is enabled to reduce shock losses by increasing the base pressures (Deckers and Denton, 1997).

Day et al. (2000) measured diverse coolant geometries including cylindrical and fan-shaped holes in an annular cascade; the latter had larger increases in aerodynamic losses relative to the uncooled blade. Rehder (2012) found that the central trailing edge ejection configuration obtained the lowest loss level, revealing its superiority over the PS cut-back and slot and PS film cooling configurations. The louver cooling scheme has the best performance, as shown by Zhang and Hassan (2012), who compared different-shaped hole cooling schemes at different blowing ratios, while it should prevent the film cooling hole from this region, where the mainstream flow field became supersonic under the extremely high blowing ratio. Wang and Zhao (2013) numerically and experimentally investigated the performance of the transonic turbine cascade with different trailing edge ejections. The ejection model's prediction results were validated using experimental data in this study, and the influences on the vortex by symmetry slot ejection and PS cut-back ejection are shown. The adiabatic film cooling effectiveness and heat transfer coefficient were experimentally investigated by Chappell et al. (2008), who compared different-shaped holes and configurations in the suction side grill region. The round radial hole arrangement obtained the best performance, considering the largest coverage of blowing ratios and streamwise locations. Kodzwa and Eaton (2010) measured the two rows of compound-angle round holes on the pressure surface of a transonic rotor blade, and they found that high levels of turbulence motivated the cooling film reattachment on the surface. Andrey et al. (2018) selected the unguided turning angle as a variant to optimize blades, which increased base pressure by raising the unguided turning angle. Based on the aerodynamic flow field measurements, El-Gabry et al. (2015) found that the upstream hub coolant had difficulty reaching the PS because of the second flow. Burdet and Abhari (2006) added the feature-based film cooling jet module as a separate module in the computational mesh using the implicit immersed boundary method and evaluated the prediction of the adiabatic cooling effectiveness on the blade surface. Furthermore, the optimization of the film cooling hole arrangement had been realized using the CFD code. Saha et al. (2013) surveyed a transonic film-cooled NGV with all the cooling air ejections placed on the front part of it before the throat. They found that the aerodynamic losses varied with the cold airflow regardless of the position of the air film holes; moreover, the suction side cooling was more sensitive than the PS cooling to aerodynamic losses caused by the variation of blow ratio. Alameldin et al. (2014) proposed a simplified method of directly introducing the coolant into the vane surface as a boundary condition, and the computational results were in great agreement with the experimental results of Saha et al. (2013). To analyze the film cooling and shock wave interaction, an uncertainty quantification methodology was presented by Carnevale et al. (2014), regarding the variability of geometrical parameters as uniform probability distributions. The downstream of the shock impingement region was where the

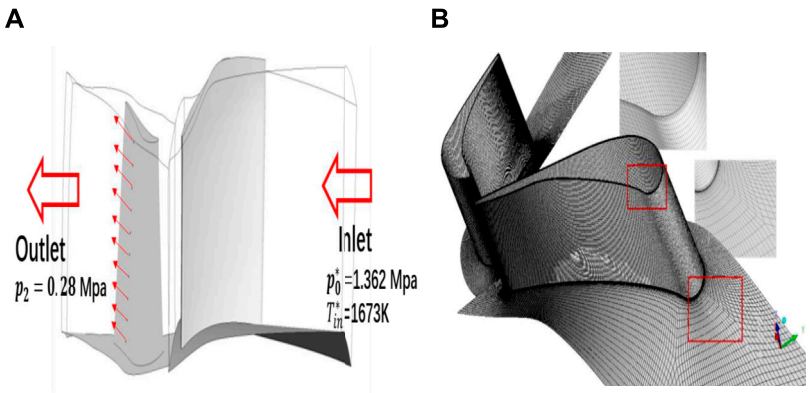

FIGURE 1 | Computational model. **(A)** Geometry. **(B)** Grid system.

maximum level of uncertainty was determined. By conducting a series of experiments and computational calculations on a high-pressure turbine blade cascade with trailing edge injection, Gao et al. (2019) explored the aerodynamic loss behaviors of the blade at different exit Mach numbers and mass flow ratios. They summarized that the overall flow angle could be increased with trailing edge ejection at all exit Mach numbers.

It should be noted that most of the above computational and experimental results were obtained regardless of the influence of different degrees of reaction (DORs). However, the DOR has great importance in weighing the degree of gas expansion inside the turbine rotor, which determines the intricate flow field and causes further significant changes in turbine performance. The coolant ejection after mixing with the mainstream interferes with the shock at the trailing edge. The present study numerically investigates the effects of film cooling hole positions and coolant mass flow rates on the aerodynamic characteristics of a transonic turbine with different DORs at high exit Mach number, aiming to summarize the aerodynamic characteristics of such single-stage transonic turbine and provide detailed flow behavior patterns with the movement of cooling hole rows.

2 COMPUTATIONAL SETUP AND VALIDATION

2.1 Computational Model

The public PW-E^3 blade profile is adopted in the present work (Thulin et al., 1982). An internal Blade-Editor code independently completed by the Harbin Institute of Technology has been further developed for the blade design of the single-stage cooled transonic turbine. The Blade-Editor code based on the 11-parameter method models the blade using three profiles, which are stacked to form a 3D blade shape. The mass flow rate of a single-stage blade cascade is approximately 29.53 kg/s. To weigh the effect of different DORs, high- and low-DOR designs were employed, with DOR = 0.3, 0.53. The DOR was defined as DOR = $\frac{p_{s,out}-p_{r,out}}{p_{s,in}-p_{r,out}}$ (Gardner, 1979; Dixon and Hall, 2013).

A row of uniformly arranged 10 air film holes is set along the spanwise direction on the rotor blades suction surface. Each hole in the same row has identical geometrical parameters. In this work, the round holes with diameters of 0.5 mm are adopted. In addition, the coolant from each hole ejects at 45° downstream of the channel. **Figure 1** shows the computational model.

2.2 Boundary Condition and Computational Fluid Dynamics Validation

The CFD problems in this study were solved using CFX. All the walls are set to no-slip condition. The rotational speed is given as 13,232 r/min. The boundary condition includes the inlet total temperature of 1,673 K and the inlet total pressure of 1.362 MPa, and the drop pressure ratio is approximately 4.4. Considering the actual situation, the cooling structure will be set for both rotor and static blades. There are usually multiple rows of air film cooling holes. To simplify the model, the coolant total mass flow rate is set to 5% of the mainstream flow rate; thus, the $q_{m,c}$ is given as 3 g/s, and the coolant total inlet temperature is employed as 804 K.

The shear stress transport (SST)-γ-θ transition model has higher accuracy in the simulation of the flow structure in the gas turbine and is widely applied to study turbine blade surfaces and film cooling effectiveness (Li et al., 2017; Occhioni et al., 2017). Therefore, the turbulence model is selected as the SST-γ-θ model. The computational mesh generation is realized using the self-developed automatic grid generation codes mentioned in the last section. Moreover, the structured grids are generated using the O-4H topology for the rotor and static blades. The generated mesh is shown in **Figure 1B**. The mesh quality has been checked using the ICEM CFD, and the results show that the mesh quality is greater than 0.3, which meets the requirements of this research for mesh quality. The y+ values near the wall are all less than 1, which meets the requirements of the turbulence model.

To get an excellent trade-off between the prediction accuracy and computer resources, a mesh independence verification is conducted regarding the exit maximum number as the parameter. It also can be seen from **Figure 2** that the maximum Mach number increases with the increase of grid number. When the

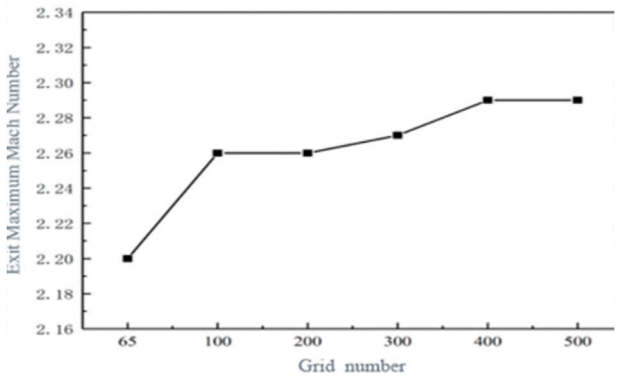

FIGURE 2 | Exit maximum Mach number of different gird numbers.

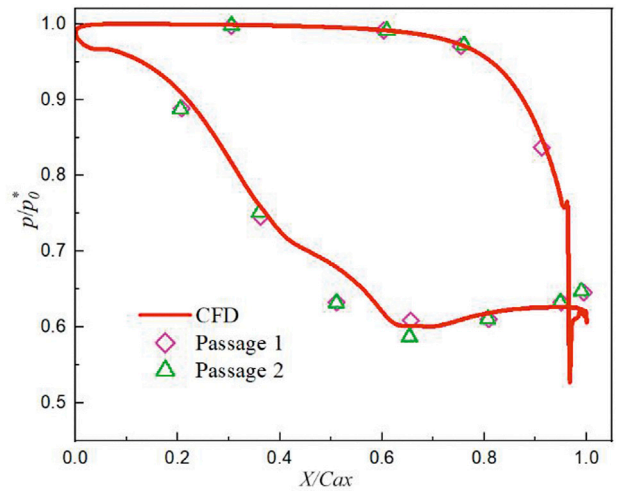

FIGURE 3 | Comparison of numerical result with experimental data.

grid number reaches more than 4 million, the exit maximum Mach number is almost constant. The number of grid elements in the range of 3–4 million is a more stable choice for the calculation results. Therefore, 3.77 million grid elements are selected in this study.

The numerical simulation was compared with Kopper's experimental data about the midspan pressure distribution of the PW-E^3 stator (Kopper et al., 1981). From **Figure 3**, it can be seen that the numerical result using the SST-γ-θ turbulence model is consistent with the experimental data.

3 RESULTS AND DISCUSSION

3.1 Effect of Film Cooling Hole Position on Aerodynamic Performance

3.1.1 Research Program Design

This section aims to investigate the relationships between the trailing edge shock or its reflected shock and the coolant ejection on the suction side. As a result, the film cooling holes are distributed on the SS. The specific study schemes are listed in **Table 1**. As for low-DOR blade airfoils (DOR = 0.3), the air film cooling holes are located at x/C_{ax} = 0.4, 0.5, 0.6, and 0.7, which are called Cases BL1, BL2, BL3, and BL4, respectively. Besides, Case BL0 without air film holes is set as the baseline. In the high-DOR group (DOR = 0.53), the air film cooling holes are located at x/C_{ax} = 0.4, 0.6, 0.7, and 0.8, which are called Cases BH1, BH2, BH3, and BH4, respectively. Case BH0, which has no film hole, is set as the baseline.

TABLE 1 | Research schemes for the effect of film cooling hole position.

Case	DOR	Film cooling holes position	Case	DOR	Film cooling holes position
BL0	0.30	No	BH0	0.53	No
BL1		0.4	BH1		0.4
BL2		0.5	BH2		0.6
BL3		0.6	BH3		0.7
BL4		0.7	BH4		0.8

TABLE 2 | Research schemes for the effect of various coolant mass flow rates.

Case	DOR	Percentage of $q_{m,c}$ in mainstream (%)	Case	DOR	Percentage of $q_{m,c}$ in mainstream (%)
BLM1	0.30	2.5	BHM1	0.53	2.5
BLM2		5	BHM2		5
BLM3		7.5	BHM3		7.5
BLM4		10	BHM4		10

3.1.2 The Effect of Film Cooling Hole Position

Figure 4 shows the surface pressure distribution along the spanwise direction for the two DOR blade designs. The addition of coolant affects blade load distribution and shock intensity. At the blade root, there is some pressure rise due to the coolant from the film cooling holes for DOR = 0.53, as shown in **Figure 4A**, and the load has been reduced slightly. However, the load increases first and then decreases in the low-DOR blade. **Figure 4B** presents different pressure distributions for two DOR blade designs, the high-DOR blade's load also reduces modestly at the midspan of the blade, but the addition of coolant does not affect the pressure distribution for the low-DOR blade. In **Figure 4C**, the high-DOR blade's load increases at the leading edge (LE) and trailing edge (TE) at the blade tip. As for the low-DOR blade, the overall load has increased.

For DOR = 0.53, after introducing the coolant, one large pressure rise still exists at approximately 0.9 of the flow direction range, indicating that the shock at this location has not disappeared. Based on the comparison of different cases for DOR = 0.53, the amplitude and slope of pressure rise decrease as the location of the air film hole moves forward to the TE. In particular at the blade tip, the sharp pressure rise

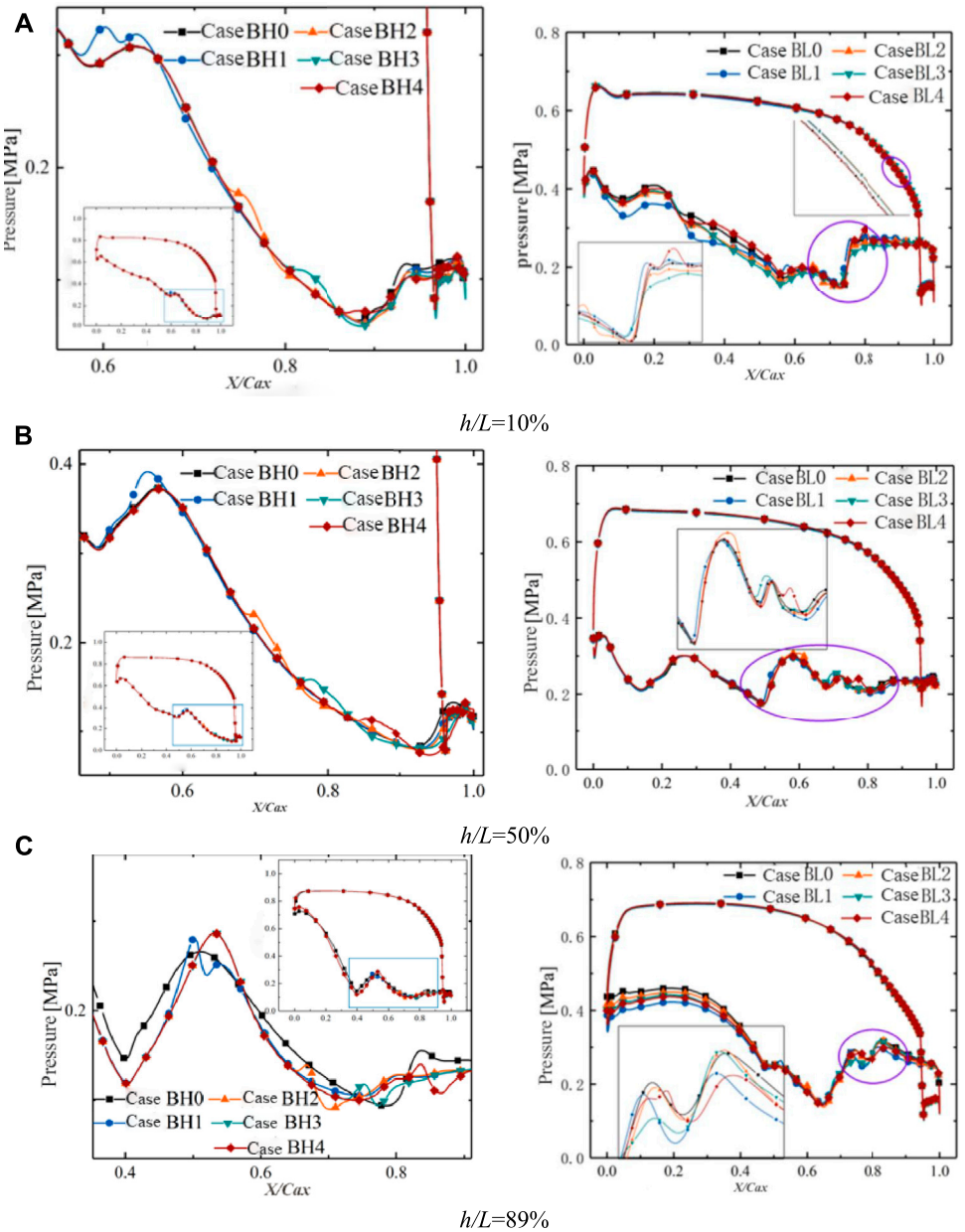

FIGURE 4 | The pressure distribution in different height sections for two degrees of reaction (DORs). **(A)** *h/L* = 10%, **(B)** *h/L* = 50%, and **(C)** *h/L* = 89%.

gradually transforms into a flat one and happens in advance. As a result, it can be assumed that the shock is weakening until it disappears.

For DOR = 0.3, the right figures in **Figure 4** show that the shock exists at the nondimensional flow position range above 0.5. From **Figure 4A**, since the coolant ejects before the pressure rise in Case BL3, there is a pressure drop at the blade root before the pressure rise, and the pressure is relatively smaller after a mild rise. It is considered here to be a weaker shock. The same conclusion at the first large pressure rise can be concluded from **Figure 4C**. It is noted that there is a consequent slighter pressure rise and an adverse pressure gradient. These fluctuations in Cases BL1 and BL2 are the same as those in BL0. In addition, Case BL3 has less pressure after the first big pressure rise, but the pressure raises to this in BL0 after the second pressure rise, which represents an enhanced shock. For Case BL4, the pressure rise is smoother and smaller because of the forward position of the coolant ejection.

Figure 5 shows the density distribution in the 10% and 89% blade span sections. Comparing Case BL2 with Case BL4 in the *h/L* = 10% section, we found that as the coolant ejection

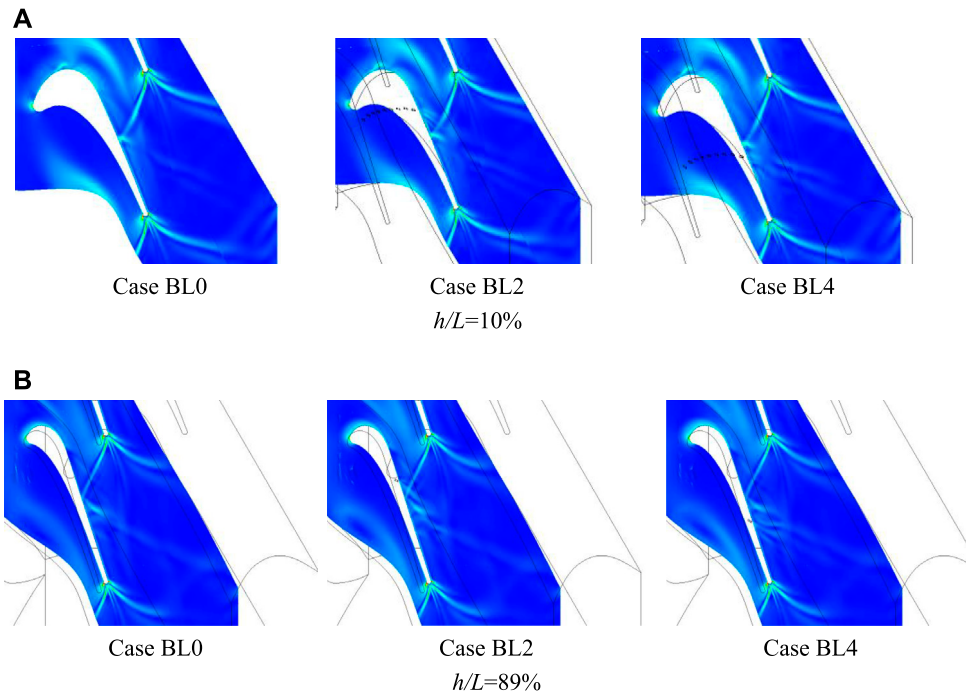

FIGURE 5 | Density gradient distribution in the different sections of low-degree-of-reaction (DOR) blade airfoil. **(A)** h/L = 10% and **(B)** h/L = 89%.

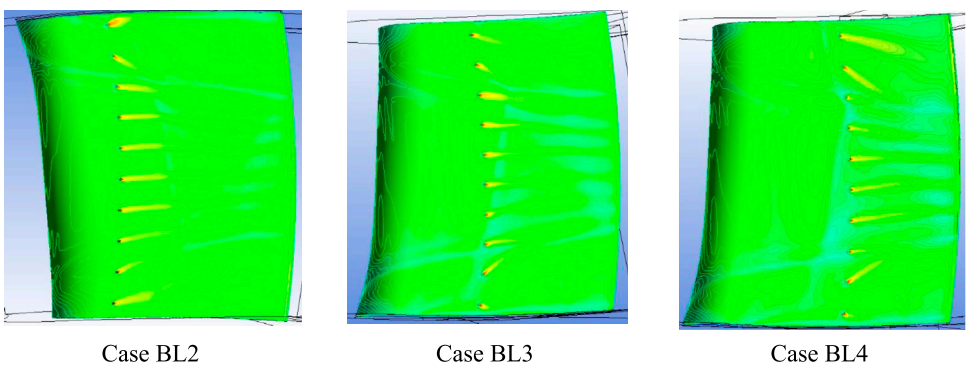

FIGURE 6 | Adiabatic film cooling effectiveness η contours of low-degree-of-reaction (DOR) blade airfoil.

position approaches the reflection point of the shock, which is located on the suction surface of the adjacent blade, the reflected shock is mitigated accordingly. In **Figure 5A**, when the position of the film cooling holes reaches downstream of the shock reflection point, the reflected shock reappears, and the coolant jet causes a significant disturbance to the flow inside of the passage. The same pattern is observed in the 89% blade span section. It can be concluded that if the row of the cooling hole is next to the reflection point, the shock intensity will suffer undermining.

Figure 6 shows the spanwise single-row cooling effectiveness distribution. The adiabatic film cooling effectiveness was defined (Zeng et al., 2018). As the cooling hole row location reaches the shock reflection point, the direction of coolant ejection into the channel varies. Because the distance between the row and the shock reflection point reaches a minimum, the shock intensity suffers weakening. Case BL2 has the best cooling effectiveness among the cases.

There are intricate secondary flow structures after coolant ejection near the blade tip. Because of the low coolant momentum, the coolant might be deflected to the midspan region by the secondary flow shown in **Figure 6**. As the cooling hole row deviates from the reflection point, the coolant momentum decreases further after more oblique shocks. In particular near the blade tip, the coolant ejects more toward the midspan region and obtains poor cooling effectiveness.

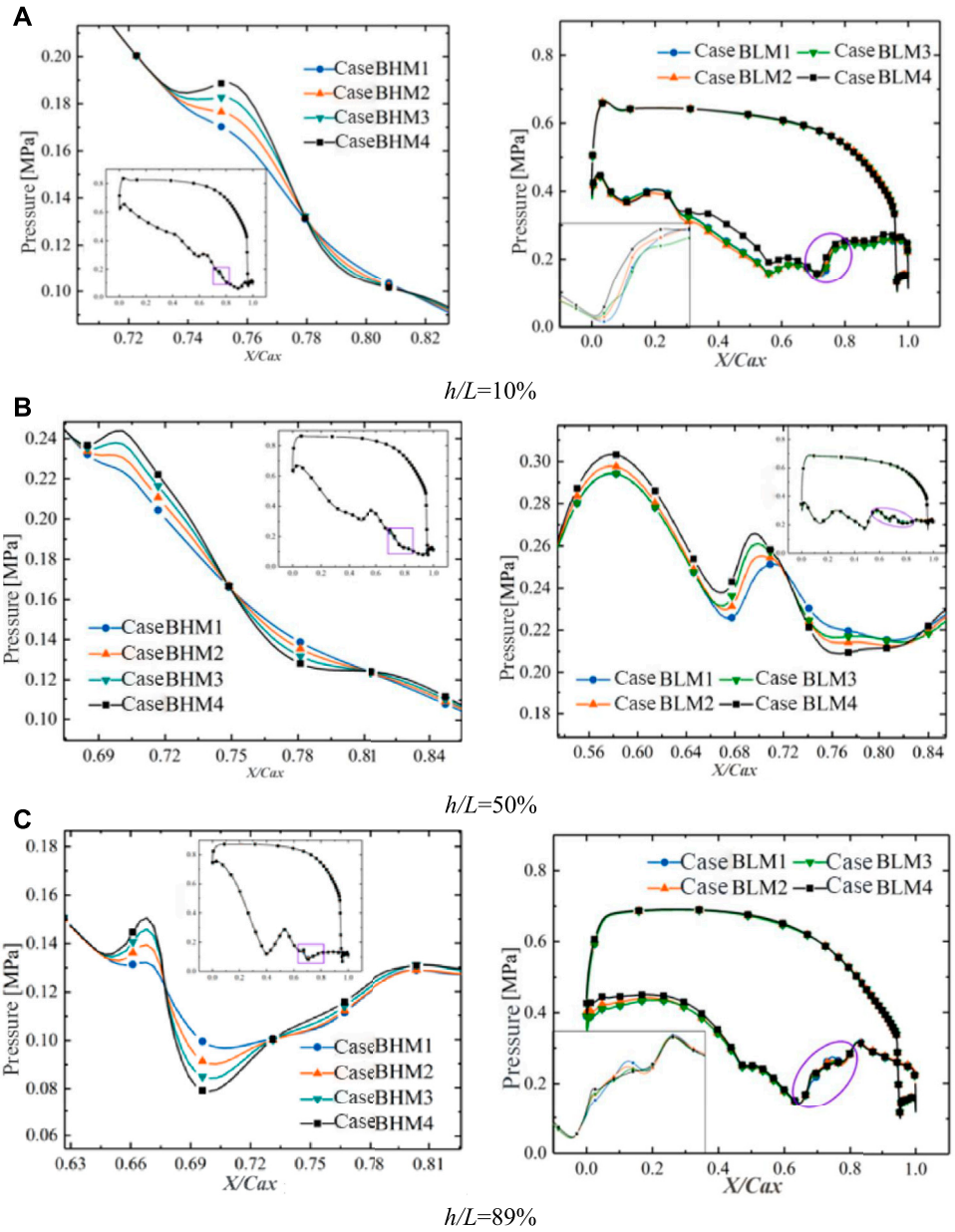

FIGURE 7 | The pressure distribution in different height sections for two degrees of reaction (DORs). **(A)** *h*/*L* = 10%, **(B)** *h*/*L* = 50%, and **(C)** *h*/*L* = 89%.

3.2 Effect of Coolant Mass Flow Rate on Aerodynamic Performance

3.2.1 Research Program Design

Compared to other cases, the pressure rise is featured as the smoothest in Case BH2 and the severest in Case BL2, which suggests the intense interference induced by coolant. The row of film cooling holes is located at $x/C_{ax} = 0.6$, to investigate the effect of various $q_{m,c}$ on aerodynamic performance in this section. The specific research program designs are listed in **Table 2**. Considering the influence of different DORs, two high- and low-DOR blade airfoils are the same as in the last section. The $q_{m,c}$ = 3 g/s is selected as the baseline. In addition, Cases BLM1, BLM2, BLM3, and BLM4 are established for a lower-DOR blade airfoil, with $q_{m,c}$ = 1.5, 3.0, 4.5, and 6.0 g/s, respectively. Cases BHM1, BHM2, BHM3, and BHM4 are established for a higher-DOR blade airfoil. They have coolant mass flow rate configurations identical to those of the lower-DOR blade airfoil cases.

3.2.2 Effect of Coolant Mass Flow Rate

Figure 7 shows the pressure distribution in the *h*/*L* = 10%, 50%, and 89% sections for two different DORs. The different coolant mass flow rates impact the load distribution and pressure fluctuations to varying degrees. The variation of $q_{m,c}$ exerts

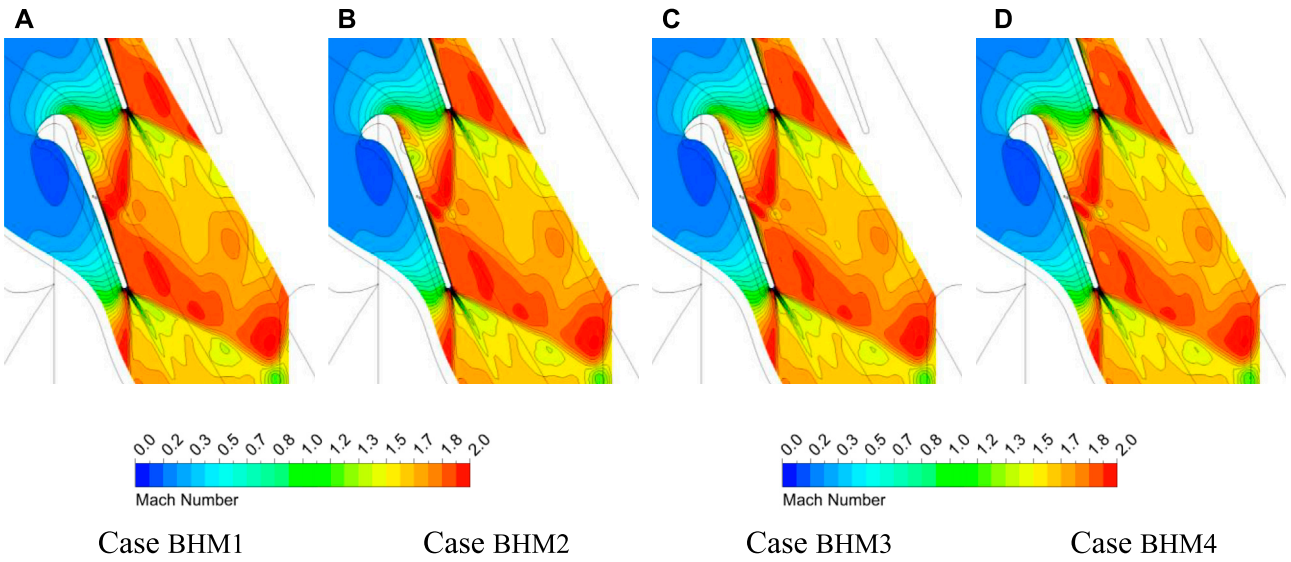

FIGURE 8 | Mach number contours in the *h/L* = 89% section of high-degree-of-reaction (DOR) blade airfoil. **(A)** Case BHM1, **(B)** Case BHM2, **(C)** Case BHM3, and **(D)** Case BHM4.

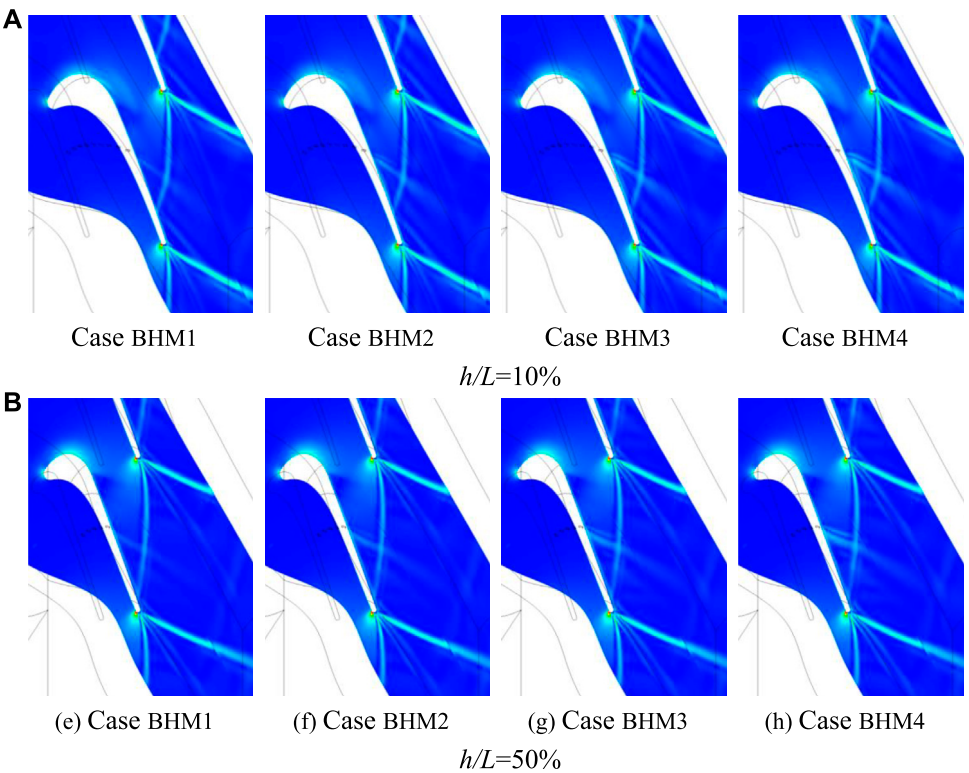

FIGURE 9 | Density gradient distribution in the different height sections of high-degree-of-reaction (DOR) blade airfoil. **(A)** *h/L* = 10% and **(B)** *h/L* = 50%.

little impact on the load for the high-DOR blade airfoil. Despite there being no evident difference in the load at the midspan of the blade for DOR = 0.3, the suction surface pressure increases with the lifting coolant mass flow rates at the blade root and tip. When $q_{m,c}$ is up to 6 g/s (coolant is 1% of the mainstream mass flow rate), the pressure reaches a maximum at the LE so that the load reduces to a minimum at the blade root and tip.

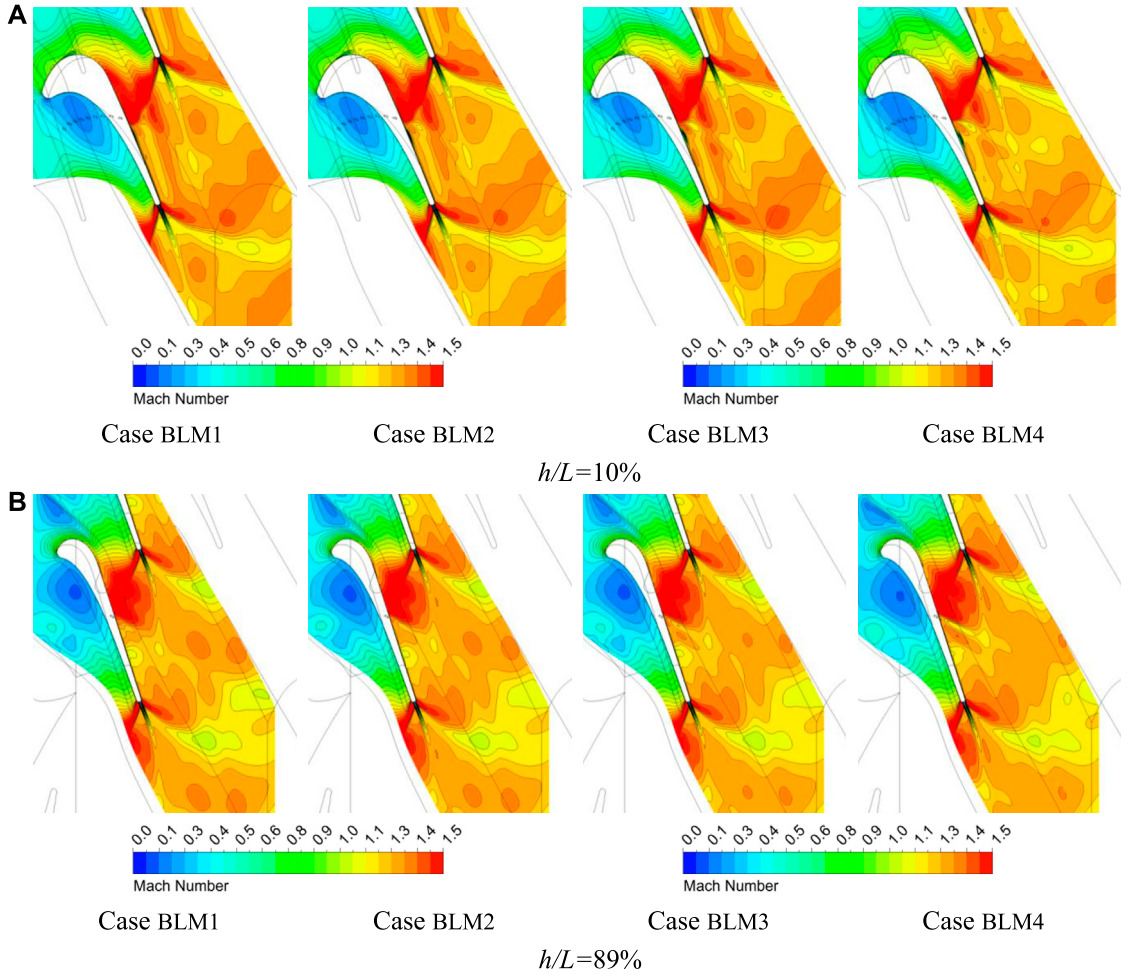

FIGURE 10 | Mach number contours in different height sections of low-degree-of-reaction (DOR) blade airfoil. **(A)** *h/L* = 10% and **(B)** *h/L* = 89%.

For DOR = 0.53, as the coolant mass flow rate persistently rises, the pressure rise range gradually increases, and the adverse pressure gradient also scales up. There is a trend of pressure rebound at the TE, as shown in **Figure 7**. The rebound amplitude increases with lifting coolant mass flow rates. The increase is easier to observe at the blade tip (as shown in **Figure 7C**). As the coolant mass flow rate increases, the influence of coolant ejection expands, and the low Mach number region narrows. The wall boundary layer has been thickened by coolant ejection, and the low Mach number region expands at the coolant ejection position downstream, especially near the blade tip (as shown in **Figure 8**). The high Mach number region at the upstream of the inner trailing shock is crossed by a strip of low Mach number band formed by the coolant. The mainstream continues to accelerate after mixing with the coolant, which leads to a local high Mach number region appearing near the film cooling holes downstream. Then, the airflow decelerates again because of the thickening boundary layer. The above flow behaviors are consistent with the pressure fluctuations existing at the downstream suction surface in **Figure 7C**.

Figure 9 shows the density distribution in the *h/L* = 10% and 50% sections. It is inferred that increasing $q_{m,c}$ contributes to the thickening wall boundary layer, which conforms to the analysis mentioned above. The increasing $q_{m,c}$ also leads to the enhancement of disturbance in the flow channel and the strength of shock intensity. This disturbance encounters the inner trailing shock in the flow channel, and the intersection moves toward the middle of the flow channel, which causes the landing point of the inner trailing shock on the adjacent blade to shift toward the TE.

Besides the load of the front and middle of the blade, **Figure 9** demonstrates that increasing $q_{m,c}$ affects the pressure fluctuations at the TE for DOR = 0.3. At the blade root, the pressure rise enlarges in advance at the TE, as shown in **Figure 9A**. It is considered a strengthened shock. Among all cases, Case BLM3 has the weakest shock, which means it has the lowest shock losses. There is a similar tendency for pressure to rise at the midspan in **Figure 9B**.

Figure 10 depicts the Mach number distributions in different spanwise sections. It is found that the low Mach number region in the trailing trace scales up along with $q_{m,c}$ rise. The coolant creates a

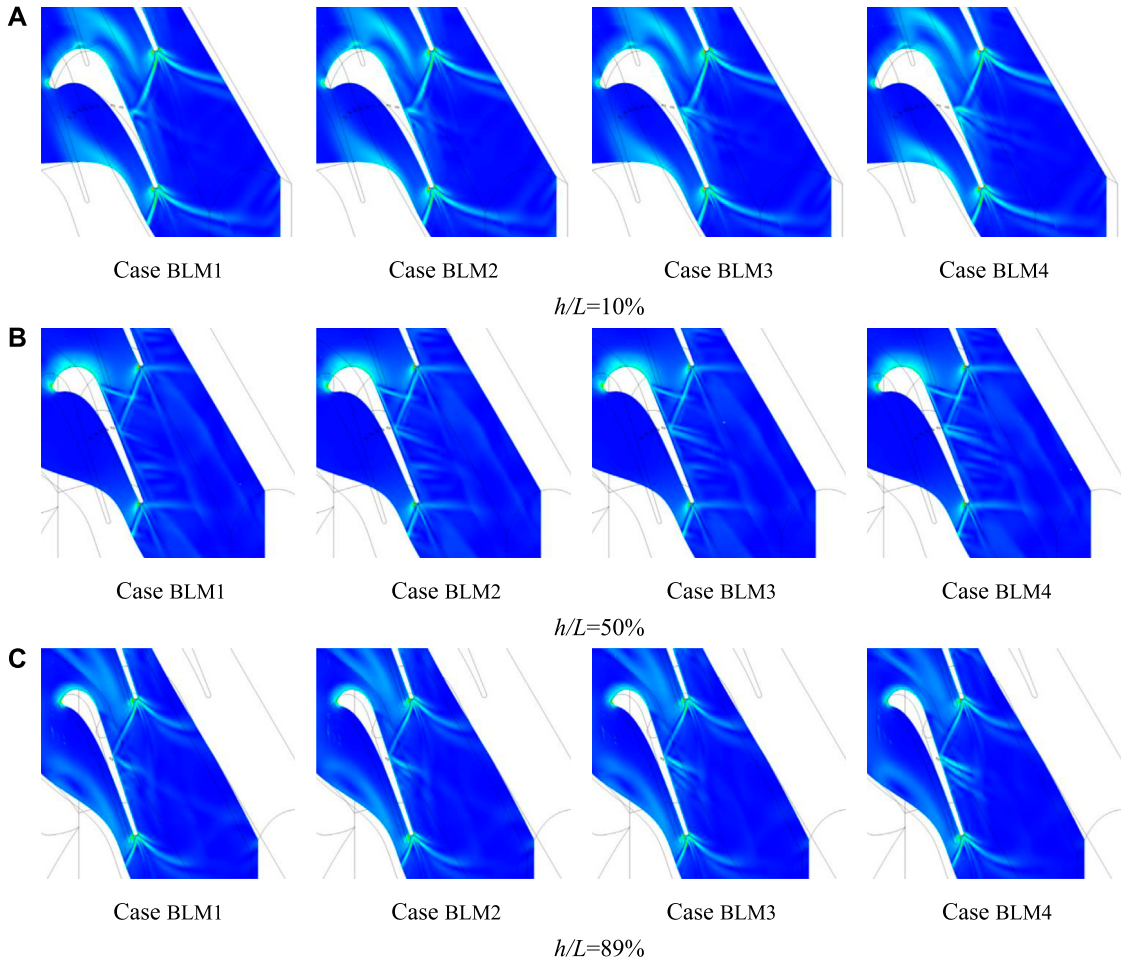

FIGURE 11 | Density gradient distribution in the different height sections of low-degree-of-reaction (DOR) blade airfoil. **(A)** *h/L* = 10%, **(B)** *h/L* = 50%, and **(C)** *h/L* = 89%.

disturbance after ejecting into the flow channel, which forms a narrow low Mach number region like in the high-DOR blade airfoil. Since the location of film cooling holes is close to the landing point of the inner trailing shock, this disturbance does not pass through the inner trailing shock but interferes with the reflected shock. At the blade root and tip, the high Mach number region narrows as $q_{m,c}$ increases downstream the inner trailing shock shown in **Figure 10**. It also suggests that a stronger shock exists in these regions.

The density distributions in different spanwise sections for DOR = 0.3 are given in **Figure 11**. As $q_{m,c}$ rises, the landing point of the inner trailing shock moves to the LE at the blade root, and the angle between the outer trailing shock and the chord direction gradually becomes smaller. However, this landing point is closer to the TE at the midspan. In addition, the disturbance of coolant deflects toward the LE and obtains enhancement at the same time. It agrees with the advance of pressure rise, as shown in **Figure 7B**. In **Figure 11C**, the landing point also moves toward the TE at the blade tip. The angle between the outer trailing shock and the chord direction here increases with the increase of coolant mass flow rate.

4 CONCLUSION

In this study, the effect of coolant on the aerodynamic performance of the transonic turbine blade cascade is investigated numerically. To understand the aerodynamic flow behaviors within the rotor due to various coolant ejection positions and coolant mass flow rates, two designed high-DOR (=0.53) and low-DOR (=0.3) blade airfoils are compared and analyzed. The main findings are summarized as follows:

1) In the process of film cooling hole position migrating to the TE, the reflected shock is weakened and then recovered when the cooling holes approach and depart from the reflection point of shock. The pressure rise weakens at the TE for the high-DOR blade airfoil. For the low-DOR blade airfoil, it was weak at first and then became stronger. When the row of film cooling holes locates at x/C_{ax} = 0.6, the pressure rise reaches a minimum.
2) The increase of coolant mass flow rates thickens the downstream boundary layer, which is more impactful for the low-DOR blade airfoil. When the coolant mass flow

rate is 1% of the mainstream flow, the load reduces to a minimum. As the coolant mass flow rate increases, the inner trailing shock gets enhanced, and the shock incidence point shifts back to the LE at the blade root, but this incidence point is closer to the TE at the midspan and tip of the blade. The outer trailing shock inclines to cover the wall at the blade root and deviates from the wall at the blade tip.

DATA AVAILABILITY STATEMENT

The original contributions presented in the study are included in the article/Supplementary Material, and further inquiries can be directed to the corresponding author.

AUTHOR CONTRIBUTIONS

XZ is responsible for the overall guidance, JZ is responsible for the main calculation and analysis, WD is responsible for the technical guidance, SX is responsible for writing the original draft.

ACKNOWLEDGMENTS

The authors acknowledge the financial support provided by the National Science and Technology Major Project (No. 2017-II-0007-0021 and No. 2019-II-0010-0030) and the Natural Science Foundation of China (No.52106041 and No.52076053).

REFERENCES

Alameldin, A., El-Gabry, L. A., Fridh, J., and Saha, R. (2014). "CFD Analysis of Suction and Pressure Side Film Cooling Influence on Vane Aero Performance in a Transonic Annular Cascade," in Proceedings of the ASME Turbo Expo 2014: Turbine Technical Conference and Exposition. Volume 2C: Turbomachinery (Düsseldorf, Germany: ASME). doi:10.1115/GT2014-26617

Andrey, G., Vladimir, G., and Nikolai, L. (2018). Experimental and Numerical Study of Transonic Cooled Turbine Blades[J]. *Int. J. Turbomach. Propuls. Power* 3 (2), 16. doi:10.3390/ijtpp3020016

Bian, X., Wang, Q., Su, X., and Yuan, X. (2020). Interaction Mechanisms of Shock Waves with the Boundary Layer and Wakes in a Highly-Loaded NGV Using Hybrid RANS/LES. *Chin. J. Aeronautics* 33 (1), 149–160. doi:10.1016/j.cja.2019.07.008

Burdet, A., and Abhari, R. S. (2006). Three-Dimensional Flow Prediction and Improvement of Holes Arrangement of a Film-Cooled Turbine Blade Using a Feature-Based Jet Model. *J. Turbomach.* 129 (2), 258–268. doi:10.1115/1.2437778

Carnevale, M., D'Ammaro, A., Montomoli, F., and Salvadori, S. (2014). "Film Cooling and Shock Interaction: An Uncertainty Quantification Analysis with Transonic Flows," in Proceedings of the ASME Turbo Expo 2014: Turbine Technical Conference and Exposition. Volume 5B: Heat Transfer (Düsseldorf, Germany: ASME). doi:10.1115/GT2014-25024

Chappell, J., Ligrani, P., Sreekanth, S., and Lucas, T. (2008). "Suction-Side Gill-Region Film Cooling: Effects of Hole Shape and Orientation on Adiabatic Effectiveness and Heat Transfer Coefficient," in Proceedings of the ASME Turbo Expo 2008: Power for Land, Sea, and Air. Volume 4: Heat Transfer, Parts A and B (Berlin, Germany: ASME), 745–758. doi:10.1115/GT2008-50798

Chen, Y., Wang, L., and Ma, G. J. (2018). Profile Design of High Load Transonic Turbine. *Gas. Turbine Exp. Res.* 31, 18–37. (in Chinese).

Corriveau, D., and Sjolander, S. A. (2004). Influence of Loading Distribution on the Performance of Transonic High Pressure Turbine Blades. *J. Turbomach.* 126 (2), 288–296. doi:10.1115/1.1645534

Day, C. R. B., Oldfield, M. L. G., and Lock, G. D. (2000). Aerodynamic Performance of an Annular Cascade of Film Cooled Nozzle Guide Vanes under Engine Representative Conditions. *Exp. Fluids* 29, 117–129. doi:10.1007/s003489900062

Deckers, M., and Denton, J. D. (1997). "The Aerodynamics of Trailing-Edge-Cooled Transonic Turbine Blades: Part 1 — Experimental Approach," in Proceedings of the ASME 1997 International Gas Turbine and Aeroengine Congress and Exhibition. Volume 1: Aircraft Engine; Marine; Turbomachinery; Microturbines and Small Turbomachinery (Orlando, Florida, USA: ASME). doi:10.1115/97-GT-518

Denton, J. D. (1993). *The 1993 IGTI Scholar Lecture:* Loss Mechanisms in Turbomachines. *J. Turbomach.* 115 (4), 621–656. doi:10.1115/1.2929299

Dixon, S. L., and Hall, C. (2013). *Fluid Mechanics and Thermodynamics of Turbomachinery*. Oxford: Pergamon Press.

El-Gabry, L. A., Saha, R., Fridh, J., and Fransson, T. (2015). Measurements of Hub Flow Interaction on Film Cooled Nozzle Guide Vane in Transonic Annular Cascade. *J. Turbomach.* 137 (8), 081004. doi:10.1115/1.4029242

Gao, J., Wei, M., Fu, W., Zheng, Q., and Yue, G. (2019). Experimental and Numerical Investigations of Trailing Edge Injection in a Transonic Turbine Cascade. *Aerosp. Sci. Technol.* 92, 258–268. doi:10.1016/j.ast.2019.05.069

Gardner, W. (1979). *Energy Efficient Engine: High Pressure Turbine Uncooled Rig Technology Report*. USA: NASA-Lewis Research Center.

Ji, L., Huang, H., Chen, J., Yu, H. L., and Xu, J. Z. (2004). Design and Test of a Supersonic Cascade Used for the Vaneless Counter-rotating Turbine [J]. *J. Eng. Thermophys.* 25 (1), 45–48. (in Chinese).

Kodzwa, P. M., and Eaton, J. K. (2010). Film Effectiveness Measurements on the Pressure Surface of a Transonic Airfoil[J]. *J. Propuls. Power* 26, 837. doi:10.2514/1.46668

Kopper, F., Milano, R., Davis, R., Dring, R., and Stoeffler, R. (1981). *Energy Efficient Engine High-Pressure Turbine Supersonic Cascade Technology Report*. USA: Lewis Research Center.

Langston, L. S. (1980). Crossflows in a Turbine Cascade Passage. *J. Eng. Power*. 102 (4), 866–874. doi:10.1115/1.3230352

Langston, L. S., Nice, M. L., and Hooper, R. M. (1977). Three-Dimensional Flow within a Turbine Cascade Passage. *J. Eng. Power* 99 (1), 21–28. doi:10.1115/1.3446247

Li, X., Ren, J., and Jiang, H. (2017). "On the Reliability of RANS Turbulence Models for Endwall Cooling Prediction," in Proceedings of the ASME Turbo Expo 2017: Turbomachinery Technical Conference and Exposition. 5A: Heat Transfer (Charlotte, North Carolina, USA: ASME). doi:10.1115/GT2017-65207

Michelassi, V., Rodi, W., and Gieß, P.-A. (1997). "Experimental and Numerical Investigation of Boundary-Layer and Wake Development in a Transonic Turbine Cascade," in Proceedings of the ASME 1997 International Gas Turbine and Aeroengine Congress and Exhibition. Volume 1: Aircraft Engine; Marine; Turbomachinery; Microturbines and Small Turbomachinery (Orlando, Florida, USA: ASME). doi:10.1115/97-GT-483

Occhioni, G., Shahpar, S., and Li, H. (2017). "Multi-Fidelity Modelling of a Fully-Featured HP Turbine Stage," in Proceedings of the ASME Turbo Expo 2017: Turbomachinery Technical Conference and Exposition. Volume 2A: Turbomachinery (Charlotte, North Carolina, USA: ASME). doi:10.1115/GT2017-64478

Rehder, H.-J. (2012). Investigation of Trailing Edge Cooling Concepts in a High Pressure Turbine Cascade-Aerodynamic Experiments and Loss Analysis. *J. Turbomach.* 134 (5), 051029. doi:10.1115/1.4004748

Saha, R., Fridh, J., Fransson, T., Mamaev, B. I., and Annerfeldt, M. (2013). "Suction and Pressure Side Film Cooling Influence on Vane Aero Performance in a Transonic Annular Cascade," in Proceedings of the ASME Turbo Expo 2013: Turbine Technical Conference and Exposition. Volume 6A: Turbomachinery (San Antonio, Texas, USA: ASME). doi:10.1115/GT2013-94319

Shelton, M. L., Gregory, B. A., Lamson, S. H., Moses, H. L., Doughty, R. L., and Kiss, T. (1993). "Optimization of a Transonic Turbine Airfoil Using Artificial Intelligence, CFD and Cascade Testing," in Proceedings of the ASME 1993 International Gas Turbine and Aeroengine Congress and Exposition. Volume 3A: General (Cincinnati, Ohio, USA: ASME). doi:10.1115/93-GT-161

Sonoda, T., Arima, T., Olhofer, M., Sendhoff, B., Kost, F., and Giess, P.-A. (2006). A Study of Advanced High-Loaded Transonic Turbine Airfoils. *J. Turbomach.* 128 (4), 650–657. doi:10.1115/1.2221325

Thulin, R. D., Howe, D. C., and Singer, I. D. (1982). *Energy Efficient Engine High-Pressure Turbine Detailed Design Report*. Cleveland OH, USA: Lewis Research Center.

Wang, Y., and Zhao, L. (2013). Investigation on the Effect of Trailing Edge Ejection on a Turbine Cascade. *Appl. Math. Model.* 37 (9), 6254–6265. doi:10.1016/j.apm.2013.01.023

Yang, L. (2014). Numerical Study on Flow Structure and Loss of Large Expansion Ratio Transonic Turbine. *J. Propuls. Technol.* 35 (5), 632–640.

Yasa, T., Paniagua, G., and Bussolin, A. (2007). Performance Analysis of a Transonic High-Pressure Turbine. *Proc. Institution Mech. Eng. Part A J. Power Energy* 221 (6), 769–778. doi:10.1243/09576509JPE467

Zeng, L., Chen, P., Li, X., Ren, J., and Jiang, H. (2018). Influence of Simplifications of Blade in Gas Turbine on Film Cooling Performance. *Appl. Therm. Eng.* 128, 877–886. doi:10.1016/j.applthermaleng.2017.09.008

Zhang, C. X.-Z., and Hassan, I. (2009). Computational Study of the Effects of Shock Waves on Film Cooling Effectiveness. *J. Eng. Gas. Turbines Power.* 131 (3), 031901. doi:10.1115/1.3026568

Zhao, W., Luo, W., Zhao, Q., and Xu, J. (2016). "Investigation on the Reduction of Trailing Edge Shock Losses for a Highly Loaded Transonic Turbine," in Proceedings of the ASME Turbo Expo 2016: Turbomachinery Technical Conference and Exposition. Volume 2B: Turbomachinery (Seoul, South Korea: ASME). doi:10.1115/GT2016-56131

Zhou, Z. H., Liu, H. X., Zhou, K., and Li, C. (2020). Shock System Model of Highly Loaded Turbine Cascade[J]. *J. Aerosp. Eng.* 33 (1), 04019107. doi:10.1061/(asce)as.1943-5525.0001095

Conflict of Interest: The authors declare that the research was conducted in the absence of any commercial or financial relationships that could be construed as a potential conflict of interest.

Publisher's Note: All claims expressed in this article are solely those of the authors and do not necessarily represent those of their affiliated organizations, or those of the publisher, the editors, and the reviewers. Any product that may be evaluated in this article, or claim that may be made by its manufacturer, is not guaranteed or endorsed by the publisher.

NOMENCLATURE

c_p Heat capacity [kJ/(kg · K)]

C_{ax} Axial chord length [mm]

h Section height [mm]

L Blade height [mm]

$\mathbf{M}$ Torque [N · m]

p_0^* Inlet total pressure of Computational domain [MPa]

p_2 Outlet static pressure of Computational domain [MPa]

p_2^* Outlet total pressure of Computational domain [MPa]

$p_{r,out}$ Outlet total pressure of rotor [MPa]

$p_{s,in}$ Inlet total pressure of stator [MPa]

$p_{s,out}$ Outlet total pressure of stator [MPa]

q_m Mass flow rate [kg/s]

$q_{m,c}$ Coolant mass flow rate [g/s]

T_{in}^* Inlet total temperature of Computational domain [K]

Greek Symbols

π Pressure ratio

η Efficiency [%]Adiabatic film cooling effectiveness

$\boldsymbol{\eta}$ Efficiency [%]Adiabatic film cooling effectiveness

ω Angular velocity [s^{-1}]

κ Isentropic exponent

Abbreviations

DOR Degree of reaction

PS Pressure-side

SS Suction side

LE Leading edge

TE Trailing edge

CFD Computational fluid dynamics

SST Shear Stress Transport model

frontiers | Frontiers in Energy Research

TYPE Original Research
PUBLISHED 11 August 2022
DOI 10.3389/fenrg.2022.950559

OPEN ACCESS

EDITED BY
Lei Luo,
Harbin Institute of Technology, China

REVIEWED BY
Xiaochen Mao,
Northwestern Polytechnical University, China
Li Jia,
Chang'an University, China

*CORRESPONDENCE
Yan-Hua Wang,
wangyanhua@hrbeu.edu.cn

SPECIALTY SECTION
This article was submitted to Advanced Clean Fuel Technologies, a section of the journal Frontiers in Energy Research

RECEIVED 23 May 2022
ACCEPTED 12 July 2022
PUBLISHED 11 August 2022

CITATION
Wang L-S, Wang Z-Y, Wang Y-H, Wang M and Sun H-O (2022), Numerical simulation of low reynolds number 2-d rough blade compressor cascade. *Front. Energy Res.* 10:950559. doi: 10.3389/fenrg.2022.950559

Numerical simulation of low reynolds number 2-d rough blade compressor cascade

Li-Song Wang, Zhong-Yi Wang, Yan-Hua Wang*, Meng Wang and Hai-Ou Sun

Harbin Engineering University, Harbin, China

In this paper, a double-circular-arc cascade was used as the research object to study the effect of roughness on the compressor cascade under the conditions of different incoming attack angles. The Reynolds number of the cascade is 1.5×10^5 . The profile of the suction surface is changed to simulate the change in surface roughness. A uniformly distributed 238 control points were selected on the suction surface profile of the smooth blade. The 238 points are increased randomly along with the normal phase of the wall, and a smooth curve connects these points to obtain a rough suction surface profile. In this study, numerical simulation methods were used to calculate the cascade flow field under 5 kinds of attack angles and 6 kinds of suction surface roughness (including smooth surface). In this paper, $k-\omega$ SST and large eddy simulation were used for numerical simulation calculation with the model respectively. The calculation results show that the effect of roughness on the flow field of the cascade is different under different angles of attack. When $70 < k_s^+ < 130$ the rough suction surface can increase the lift coefficient of the compressor blade.

KEYWORDS

roughness, boundary layer, compressor cascade, suction, large eddy simulation

1 Introduction

Due to the different geographical locations and the social environment, the air will be mixed with solid or liquid particles such as dust, pollen, aerosols, etc (Bons 2010). The air in coastal areas will also contain salt spray particles (Mishra 2015). It is necessary to continuously consume a large amount of air to ensure the stable operation of the gas turbine. Inevitably, small-sized pollutant particles in the air will also enter the gas turbine. These solid or liquid particles will mix with the oil mist and adhere to the surface of the gas turbine components (Chen and Griffith, 2022b). When the gas turbine is running the compressor is the first part that comes into contact with the air, so the deposition of pollutant particles on the wall is also the most obvious. The deposition of solid or liquid particles in the air on the surface of the compressor components will eventually cause the wall to become rough. Especially when the surface of the compressor blade becomes rough, it will cause the performance degradation of the compressor and gas turbine. Alessio Suman (Suman et al., 2017) et al. analyzed the distribution of particles on compressor blades through computational fluid dynamics (CFD).

The analysis has shown that particular fluid-dynamic phenomena and airfoil shape influence the pattern deposition. In the past, many scholars have conducted related studies on the influence of roughness on compressor performance (Chen et al., 2021; Chen and Griffith, 2022a). Mark P. Simens and Ayse G. Gungor used a flat plate with a strong inverse pressure gradient as the research object to study the effect of roughness on laminar separation bubbles. These numerical experiments indicate that laminar separation and turbulent transition are mainly affected by the type, height, and location of the roughness element (Simens and Gungor 2013). Jongwook Joo et al. (Joo et al., 2017). Regularly arranged rectangular blocks on the surface of the blade to simulate the rough surface, and used large eddy simulation to calculate the effect of roughness on the flow field of the NACA65 compressor cascade. Nicola Aldi et al. used NASA Stage 37 and NASA Stage 35 as research objects, simulated by imposing different spanwise distributions of surface roughness to analyze its effect on compressor performance (Nicola et al., 2013; Sun et al., 2018). Ravi J Chotalia and Dilipkumar Bhanudasji Alone (Chotalia and Alone 2017) studied the performance degradation of the single-stage transonic axial flow compressor due to the uniform roughness created by the aerosols. Yonghong Tang et al. found that doubling or halving the roughness value of all components of a centrifugal compressor in the hydraulically rough flow regime will result in a change in the peak efficiency of the compressor by about 1.72% (Tang et al., 2019). A test program on the GE J85-13 jet engine quantified the increased surface roughness and the distribution of salt deposits in an axial compressor (Syverud and Bakken 2006). Dongjae Kong (Kong, Jeong, and Song 2017) conducted experimental measurements on the smooth and rough compressor cascade passage flow field.

In recent years, compressor design technology has become more and more advanced, and compressor performance parameters have gradually improved. However, it can be noticed that the compressor blades are now more twisted than before. During the operation of the compressor, the gas flow around the blades is more complicated. It becomes complicated to analyze the influence of rough wall surface on the flow field around the compressor blade. Cascade passages are often used to analyze the two-dimensional flow process of compressor blades. The blades are straight along the span, so the transmission movement of the surrounding airflow along the blade height direction disappears. Therefore, this study used double-curved cascades as the research object and uses a combination of steady-state numerical simulation and Large-eddy simulation (LES) to study the effect of blade surface roughness on the performance of compressor cascades.

2 Model development

2.1 Geometric model

2.1.1 Smooth cascade blade

A cascade was used to simulate the effect of roughness on the compressor. The blade profile is a compressor blade designed at the NASA Lewis Research Center. The blade section of the cascade is a double-circular-arc blade with 65 degrees of camber, a 20.5° stagger angle, a solidity of 2.14, and a 228.6 mm chord length. Both the radius of the leading and trailing edge is 0.9144 mm (Zierke and Deutsch 1990). The profile of the blade is shown in 1.1.11Figure 1. After the profile of the rough blade is generated, analyze the height change value of the control point on the suction surface to obtain the specific value of the roughness on the suction surface.

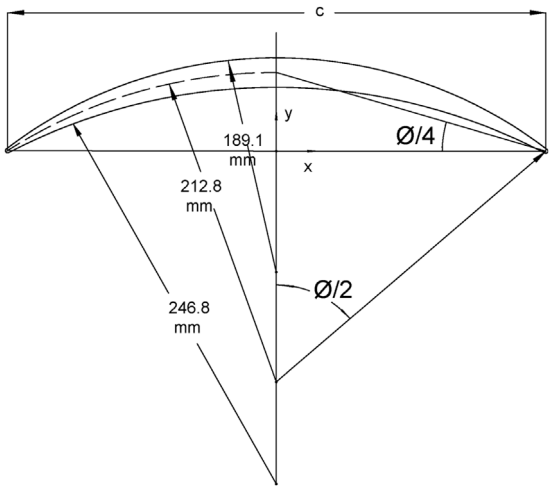

FIGURE 1
Blade profile.

TABLE 1 Blade geometry.

c	**228.6 mm**	**Σ**	**2.14**
S	106.8 mm	AR	1.61
t_{max}	12.5 mm	Γ	20.5°
r_{LE}	914.4 μm	κ_1	53.0°
r_{TE}	914.4 μm	κ_2	-12.0°
		Φ	65.0°

The equation for the pressure surface, suction surface, and camber line of the double-circular-arc blade used in the current study can be written as

$$x_p^2 + \left(y_p + 219.7\right)^2 = 246.8^2 \quad (1)$$

$$x_s^2 + \left(y_s + 149.5\right)^2 = 189.1^2 \quad (2)$$

and

$$x_c^2 + \left(y_c + 179.4\right)^2 = 212.8^2 \quad (3)$$

The chord length of this cascade blade is 228.6 mm, and the radius of the leading edge and trailing edge are both 0.9144 mm.

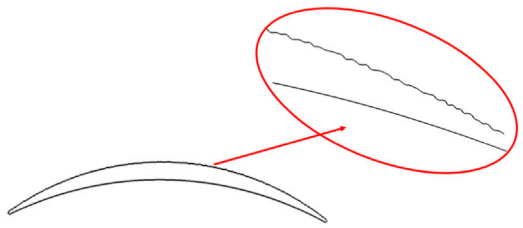

FIGURE 2
Rough blade profile.

The aspect ratio (*AR*) is 1.61. The geometric parameters of the blade profile are shown in Table 1.

3 Rough cascade blade

In past research, researchers often used two methods to study the effect of roughness on the compressor cascade. Mirko Morini et al. (Morini et al., 2011; Nicola et al., 2014; Shi et al., 2017) used the wall equation to simulate the roughness on the compressor blade, while Sun Hai-Ou et al. (Sun et al., 2021) changed the profile of the blade.

Previous research (Syverud and Bakken 2006) data has shown that the roughness on the suction surface of the compressor blade has a greater impact on performance. So only the suction side of the blade profile was been altered in this study. The rough blade profile is shown in Figure 2.

In this research, the method of replacing the blade profile was used to simulate the rough wall surface, to describe the rough wall surface more realistically. 238 control points were selected on the suction surface profile of the smooth blade, and each control point was moved at a random distance in the direction perpendicular to the wall. A spline curve is formed by the newly obtained 238 control points. The shape of this curve is regarded as the profile of the rough blade, as shown in Figure 2.

3.1 Numerical mesh

Irregular contours on rough walls cause inconvenience to mesh generation. The quality and structure of the grid determine the accuracy and convergence of the numerical simulation, especially for large-eddy simulations. As shown in Figure 3, O-Block was used around the blade surface and the number of the mesh is 160 million. The y^+ value is less than 1, 1500 nodes was set at chord direction on the blade. The number of mesh nodes in the boundary layer of the blade surface is more than 40. Δx^+ is one of the parameters for evaluating the quality of the grid, which is defined as follows.

$$\Delta x^+ = \frac{u_\tau \cdot \Delta x}{v} = \frac{y^+}{y} \cdot \Delta x \tag{4}$$

The range Δx^+ of the grid in this study is $1< \Delta x^+ <10$.

4 Numerical simulation

The influence of the angle of attack of the cascade on the flow field around the blade is also considered. k_s^+ is a dimensionless parameter representing roughness, which is defined as follows:

$$k_s^+ = R_e \frac{k_s}{c} \sqrt{\frac{C_f}{2}} \tag{5}$$

$$C_f = \left[2.87 + 1.58 \lg \frac{c}{k_s}\right]^{-2.5} \tag{6}$$

The geometric mean roughness *Ra* satisfies the relationship of $k_s = 6.2R_a$ between k_s. Where C_f is the wall shear stress coefficient, and *c* is the chord length of the blade. The Re in the formula is the Reynolds number using the chord as the characteristic length. Schlichting's (Schlichting and Gersten 1965) research shows that when $k_s^+ <5$, the roughness has almost no effect on the flow loss, and the surface is Hydraulically smooth; when $5< k_s^+ <70$, the airflow loss is determined by Re and k_s^+ together, which is the Transitional rough; when $k_s^+ >70$, the loss of airflow is no longer affected by Re and is only related to k_s^+, which is fully rough. In this study, a total of 6 types of roughness blades (including smooth blades) were numerically simulated, and 5 different incoming attack angles (*i*) were included, as shown in Table 2.

Figure 4 shows the computational domain model of the cascade. The single-passage numerical simulation requires less computer and can increase the calculation speed of numerical simulation. The boundary conditions of the calculation model are as follows:

The Inlet Reynolds number is 1.5×10^5, and the total temperature of Inlet is 288.15 K. The incoming flow contained a freestream turbulence level of 10%, which is the same with the measurement. The cascade blade was set to smooth, adiabatic and non-slip wall condition, static pressure outlet condition was used on the outlet surface. The inlet Reynolds number is based on the blade chord.

In the steady-state calculation, the $k-\omega$ SST turbulence model was selected as the turbulence model, and the $\gamma-\theta$ transition model was used. LES was used to calculate the unsteady state of airflow. The principal idea behind LES is to reduce the computational cost by ignoring the smallest length scales, which are the most computationally expensive to resolve, via low-pass filtering of the Navier–Stokes equations. It is advantageous in solving the gas flow state near the wall.

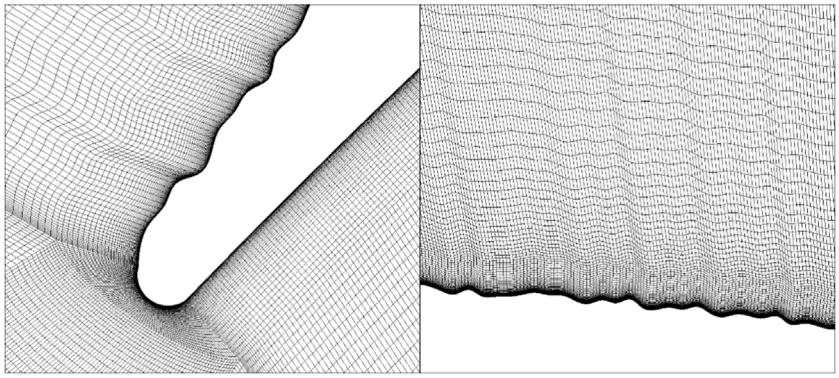

FIGURE 3
Cascade Blade surface Mesh.

TABLE 2 Incoming attack angle (i) and wall roughness (k_s^+).

k_s^+i	0.00	11.80	65.05	105.94	141.21	196.47
0°	S-0	R1-0	R2-0	R3-0	R4-0	R5-0
-5°	S-5	R1-5	R2-5	R3-5	R4-5	R5-5
-8°	S-8	R1-8	R2-8	R3-8	R4-8	R5-8
+5°	S+5	R1+5	R2+5	R3+5	R4+5	R5+5
+8°	S+8	R1+8	R2+8	R3+8	R4+8	R5+8

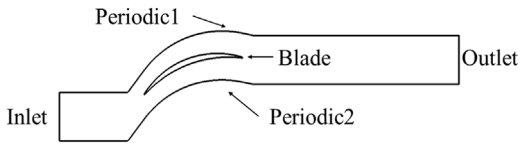

FIGURE 4
Geometrical cascade domain.

5 Simulation result

At different angles of attack, the C_p distribution on the airfoil surface is shown in Figure 5, the C_p is defined as follows:

$$C_p = \frac{P - P_{in}}{P_{in}^* - P_{in}} \tag{7}$$

It can be seen from Figure 5 that under different surface roughness, the distribution C_p varies with the angle of attack almost the same. Compared with the case of 0° angle of attack, at a negative angle of attack, the pressure coefficient of the blade surface decreases. But the trend shows the difference when the angle of attack is positive. When $i = +5°$ the C_p is much higher than the case of $i = 0°$ before 0.7 chord, but lower after 0.7 chord. However, this position became 0.35 chord when $i = +8°$. Notice the general fluctuation of the pressure coefficient curve on the suction side of the rough blade. When reading the wall pressure data, directly select the suction surface profile as the target object. The irregularity of the rough blade profile causes data fluctuations on the curve.

Under the same angle of attack, when the roughness of the suction surface is different, the distribution of the pressure coefficient is shown in Figure 6. The simulation results show that when the i is positive, the C_p hardly changes with the roughness of the suction surface.

When i is less than or equal to 0, the C_p changes with the roughness value. When k_s^+ is greater than 105.94, the pressure coefficient of the rough suction surface is smaller than that of the smooth blade, and the pressure coefficient continues to decrease as the roughness increases. When k_s^+ is less than 105.94, the pressure coefficient of the rough blade surface is greater than that of the smooth blade. With the increase k_s^+, the pressure coefficient of the rough blade gradually approaches the pressure coefficient of the smooth blade.

So for the blades of the cascade, the lift coefficient is the area value enclosed by the pressure coefficient curve in Figure 5 and Figure 6. The abscissa of Figure 7 is the lift coefficient of the blade, and the ordinate is the angle of attack and the equivalent sand roughness on the suction surface of the cascade blade, the lift coefficient is defined as follows:

$$c_L = \frac{L}{\frac{1}{2}\rho v_\infty^2 l} \tag{8}$$

Where L is the lift, ρ is the density, v_∞ is the far-field velocity, and l is the chord length. For the cascade blade $L = L_p - L_s$, and when l is the dimensionless chord length, the range is from 0 to 1. Where the density is considered to be constant.

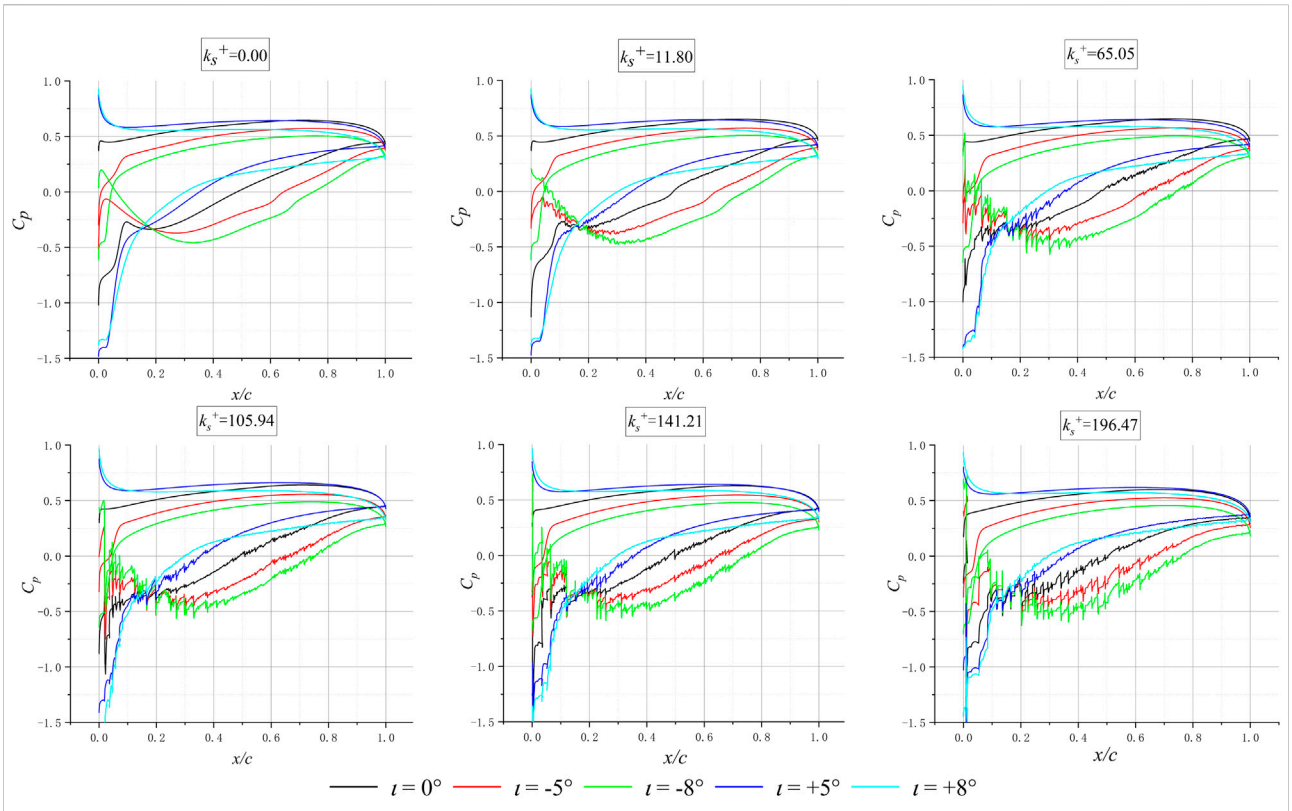

FIGURE 5
Pressure Coefficient under different *i*.

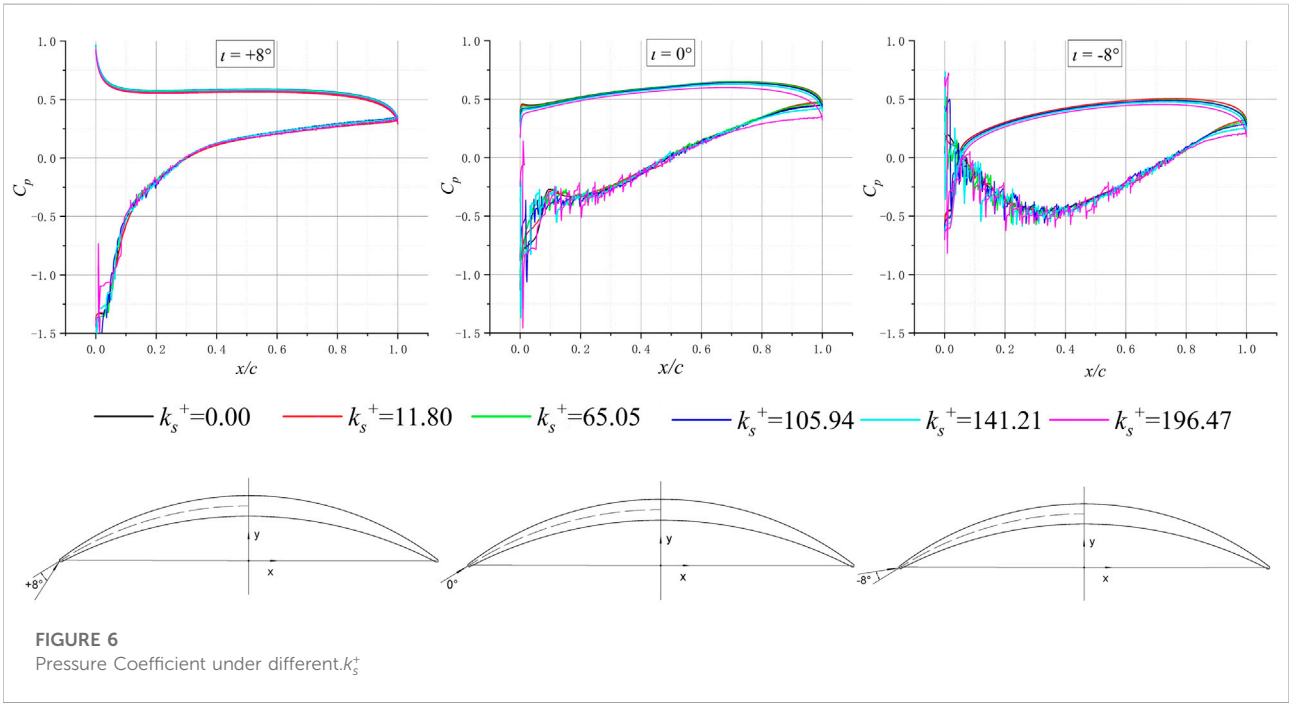

FIGURE 6
Pressure Coefficient under different.k_s^+

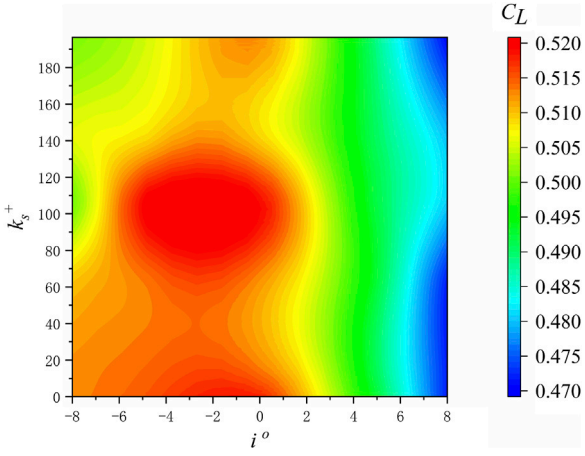

FIGURE 7
Lift coefficient.c_L

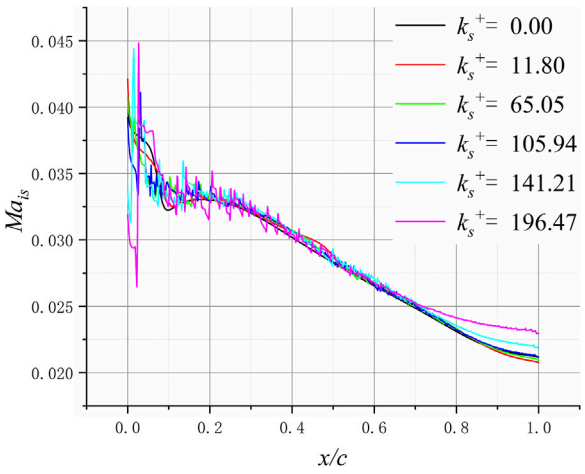

FIGURE 8
Suction surface Isentropic Mach number.

The pressure coefficient is along the y-axis direction, as shown in Figure 1. The effect of the roughness of the suction surface on the lift coefficient of the blade is not completely negative. When $70 < k_s^+ < 130$ the rough suction surface can increase the lift coefficient of the compressor blade. However, this phenomenon only occurs when $i < 0°$. When the angle of attack of the cascade is positive, the roughness on the suction surface of the blade no longer affects the lift coefficient. Figure 7 shows that a suitable negative angle of attack has a positive effect on the lift coefficient of the compressor cascade blade.

The premature separation of the airflow on the low-roughness wall destroys the original gas flow state near the wall and also causes the thickness of the boundary layer near the trailing edge of the blade to be significantly reduced.

As the roughness of the blade surface increases, the separation bubbles disappear. The boundary layer separation gradually thickens, and the position of the airflow separation is advanced. These phenomena can be observed in Figure 9.

The isentropic Mach number on the suction surface of the blade is shown in Figure 8. Starting from 0.7 chord length, the isentropic Mach value begins to change due to the increase in roughness. In addition, when k_s^+ = 11.80 and k_s^+ = 65.05, separation bubbles appear at 0.2 chord length. When the wall surface is smooth, the airflow maintains a laminar state before 0.7 chord length, after which the airflow gradually changes to a turbulent state after passing through the transition zone. However, the wall becomes rough, the laminar flow is disturbed, and becomes turbulent flow at 0.2 chord length. It can be found in Figure 9 that the separation bubble disappears at 0.4 chord length, and the airflow near the wall becomes laminar again. After 0.4 chord length, the airflow into the wall has been maintained in a laminar state until the 0.8 chord length position. Figure 10 shows the velocity distribution near the suction surface of the cascade. The abscissa is the position of the chord length, and the ordinate is the distance from the suction surface.

In previous studies, the inlet velocity of the cascade was often used as the far-field velocity when calculating the airflow displacement thickness on the suction surface. Figure 10 shows the velocity distribution in the cascade passage. It can be easily found from the figure that the velocity of the airflow is different at different chord length positions. So our team used different far-field velocities at different position when calculating the displacement thickness.

Figure 11 shows the performance of the displacement thickness on the suction surface under different roughness. Since the incoming Mach number is very small, the density is assumed to be constant when calculating the displacement thickness. Overall, the displacement thickness increases with roughness. However, when the roughness is small (k_s^+ = 11.80), the displacement thickness of the blade back surface begins to increase at x/c = 0.2, which is greater than the displacement thickness of the smooth blade cascade. But when x/c = 0.4, the displacement thickness starts to decrease, when x/c = 0.46, the displacement thickness value of the rough blade is equal to the case of the smooth wall, and is smaller than that of the smooth wall after that.

In this paper, x_d represents the value of x when it is equal to the displacement thickness of the smooth blade. The position of x_d lags with increasing roughness. When the roughness is 11.80, the critical position is at 0.46 chord, and when the roughness is 65.05, the critical position is at 0.6 chord.

The shape factor (H_{12}) of the suction surface of the blade is shown in the Figure 12, the shape factor of the smooth blade is almost kept around 2, and slightly increased near the leading and trailing edges. When the roughness of the k_s^+ = 11.80, the shape

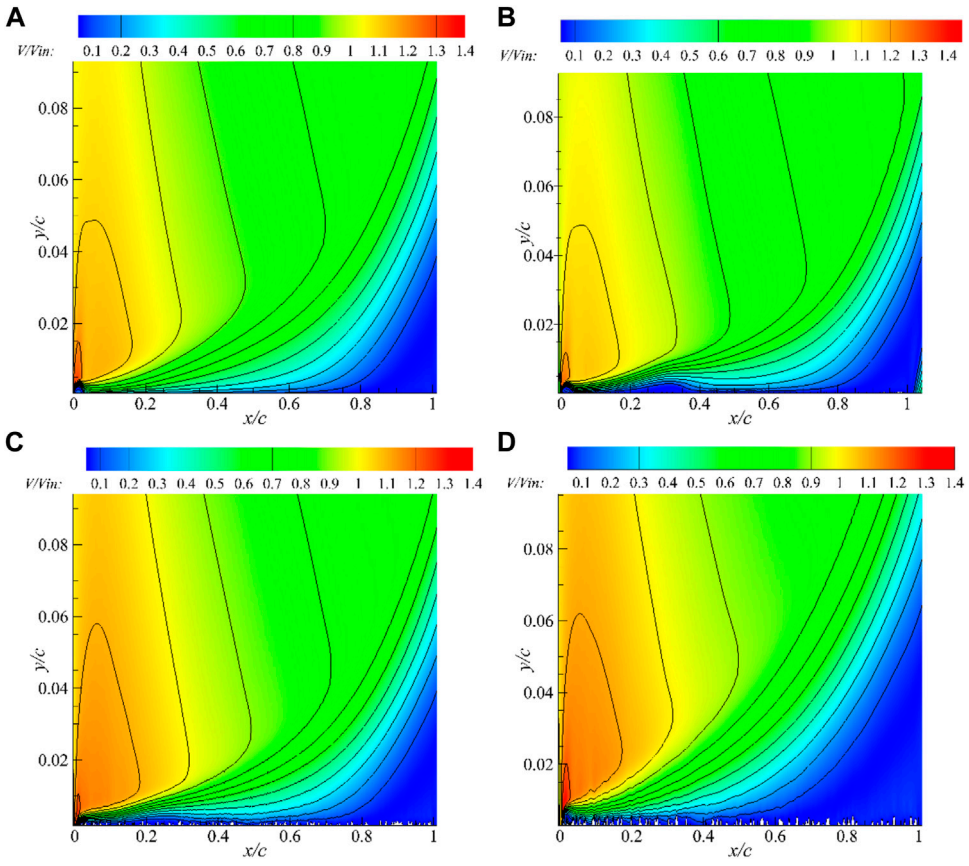

FIGURE 9
V/V_{in} in the cascade passage. "*V*" is the velocity and "*Vin*" represents the velocity of the inlet boundary.

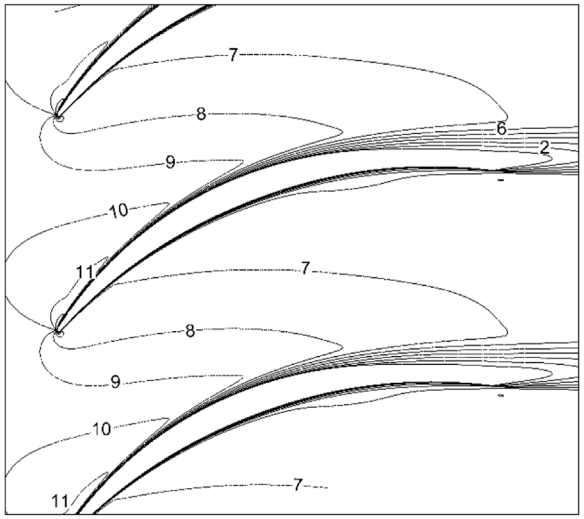

FIGURE 10
Velocity (m/s) in cascade passage.

factor value increases from the leading edge of the blade and suddenly increases after the chord length of 0.11, where the airflow starts to transition. From the shape factor, it can be found that the appearance of roughness induces an early transition of the boundary layer on the back surface of the leaf. But when the roughness is 11.80, the airflow on the back surface of the blade returns to the laminar state again at the chord length of 0.75. After the boundary layer is regenerated, the shape factor of rough leaves is also slightly reduced compared to smooth blade.

Figure 13 shows the outlet airflow angle of the cascade. The outlet angle of the cascade varies with the roughness of the suction surface and is affected by the angle of attack of the incoming flow. When the angle of attack of the incoming flow is negative, the airflow angle of the outlet increases with the increase of roughness. When the angle of attack of the incoming flow is positive, even if the suction surface of the cascade becomes rough, the airflow angle at the outlet will hardly change. Once the angle of attack of the incoming flow is greater than 0, the increase of the reverse pressure gradient when the flow passes through the cascade passage will cause the airflow to

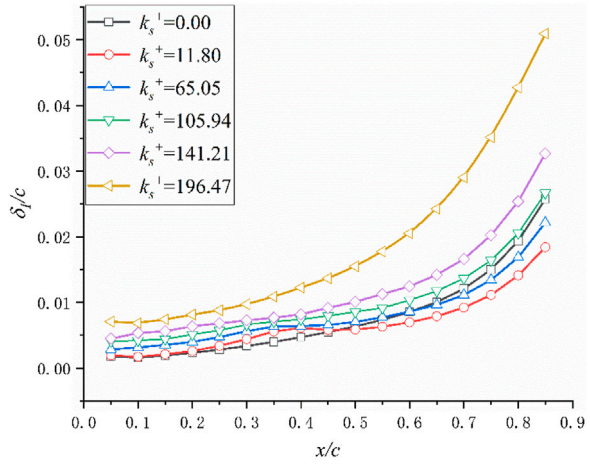

FIGURE 11
Displacement thickness (δ_1) on the suction surface.

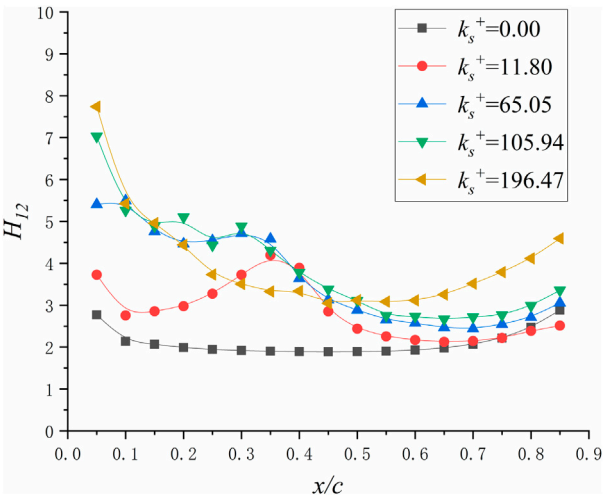

FIGURE 12
H_{12} on the suction surface.

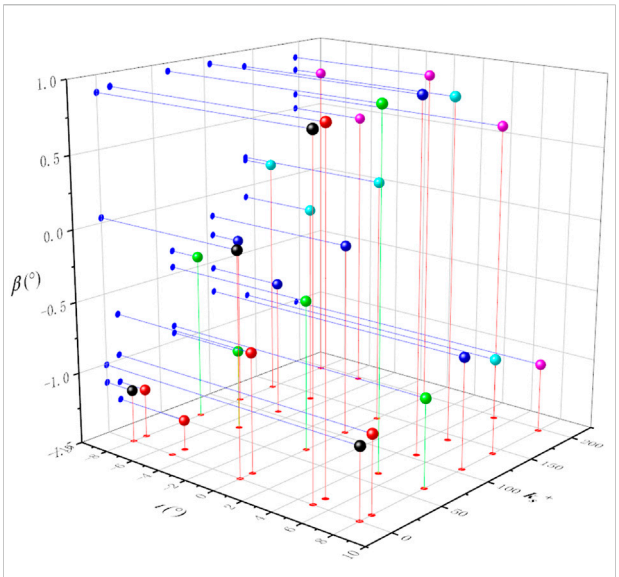

FIGURE 13
Outlet flow angle.

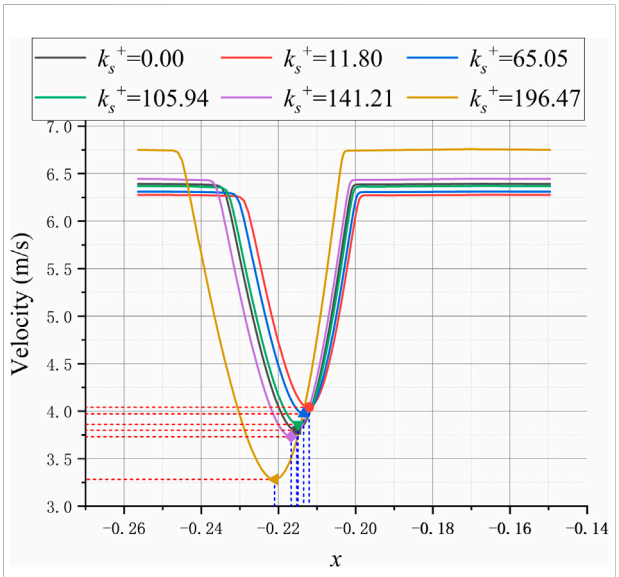

FIGURE 14
Position 1 velocity (m/s).

transition in advance. The rough wall surface on the suction surface will be completely covered by the boundary layer with increased thickness. Rough suction surface no longer has an interference effect on the mainstream area.

The velocity distribution along the x direction was measured at position 1. Position 1 is at 150% chord length from the leading edge of the blade. The effect of roughness on the velocity distribution is linear. As the roughness increases, the minimum velocity decreases linearly, as shown in Figure 14. The position of the minimum velocity is biased towards the suction surface of the blade.

Take the speed extreme point of the smooth blade as the zero point, and the extreme point position is positive toward the pressure surface and negative toward the suction surface. When $k_s^+ \leq 105.94$, the rough suction surface has a positive influence on the speed extreme point, and when $k_s^+ > 105.94$, the rough wall has a negative influence on the speed extreme point position.

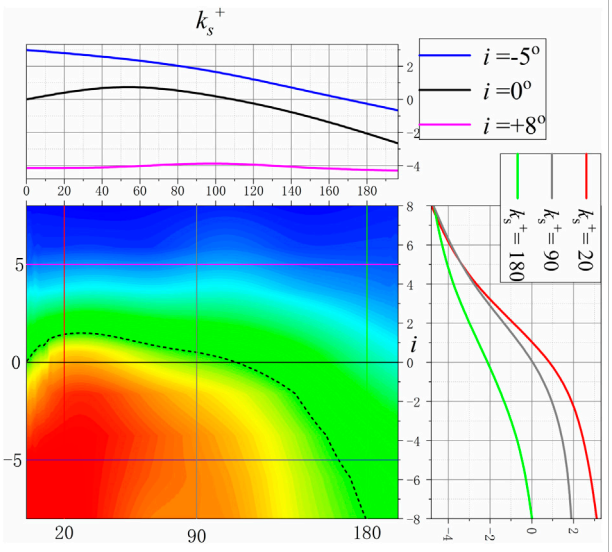

FIGURE 15
Minimum Velocity coordinate.

Figure 15 is the contour of the velocity extreme point position and the velocity minimal value. When i is positive, the roughness does not affect the velocity distribution on the B-to-B plane. Meanwhile, as the roughness increases, the velocity of the blade exit is less sensitive to the angle of attack of the incoming flow. As the roughness of the suction surface increases, the velocity gradient at the exit of the cascade increases. The mixing loss of the secondary flow of the blade wake and the main flow increases due to the increase of the velocity gradient. The increase in roughness will also reduce the sensitivity of the cascade flow field to the angle of attack of the incoming flow.

The calculation result of LES is shown in Figure 16 Figure 17to Figure 18. Vorticity in the cascade passage is shown in the figure. In continuum mechanics, vorticity is a pseudovector field that describes the local spinning motion of a continuum near some point (the tendency of something to rotate), as would be seen by an observer located at that point and traveling along with the flow. It is an important quantity in the dynamical theory of fluids and provides a convenient framework for understanding a variety of complex flow phenomena, such as the formation and motion of vortex rings (Guyon et al., 2002; Higham et al., 2015).

For a smooth cascade passage, the vorticity on the suction surface starts to change at 50% chord length. At the beginning of 0.36 chord length of the suction surface, the high-value area of the vorticity begins to become concentrated and gathers into a cluster. This phenomenon indicates that the airflow changes from laminar flow to turbulent flow from this position. The vortex first moves tightly against the suction surface force towards the trailing edge of the blade, and its size is gradually increasing. At 0.8 chord length, the vortex starts to break away from the suction surface. Unlike the suction surface, the airflow on the pressure surface does not turn into turbulence until it passes the trailing edge, and a larger vortex V2 is formed. The vortex V1 on the suction surface collides with the vortex V2 on the pressure surface downstream of the blade.

The vortex V2 is impacted by the high-speed, small-scale vortex V1 at the trailing edge of the blade. V2 is crushed and divided into a large-scale vortex and multiple small-scale vortices. The large-scale vortices continue to move downstream along the main flow direction, and the small-

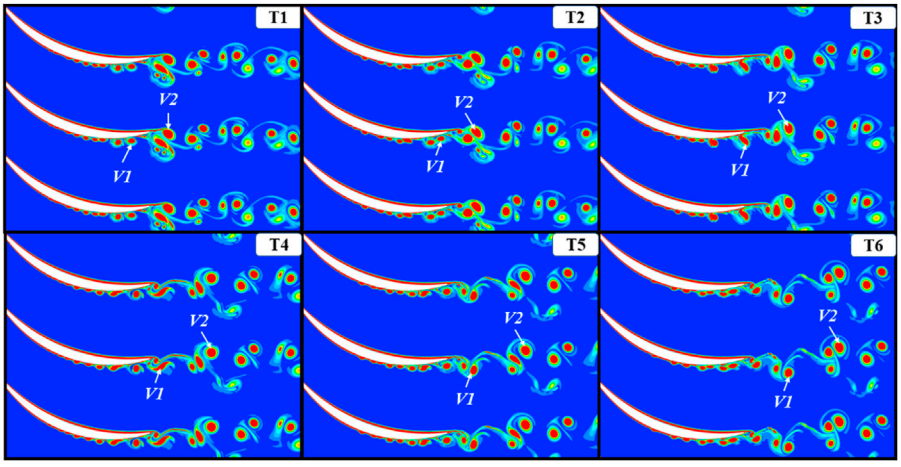

FIGURE 16
Smooth cascade vorticity.

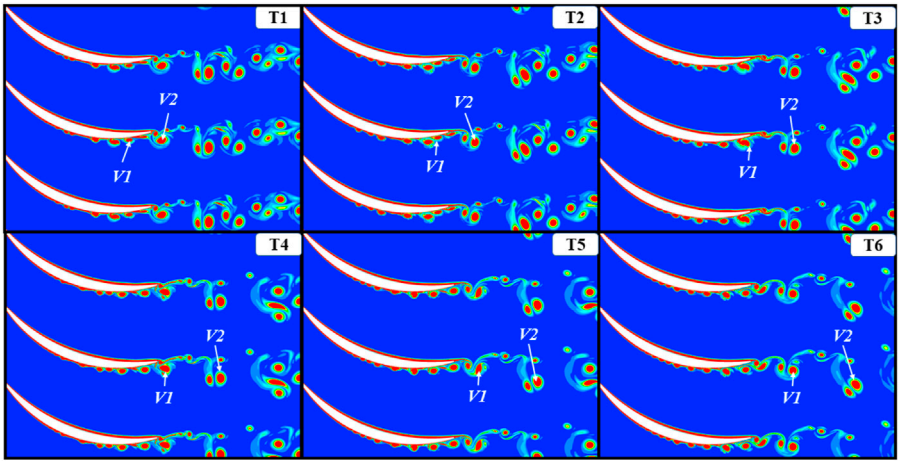

FIGURE 17
Rough cascade vorticity (k_s^+ =11.80)

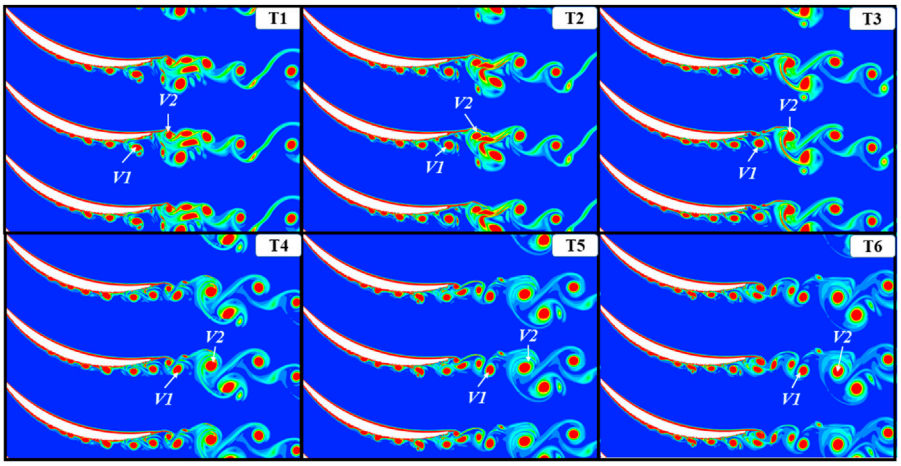

FIGURE 18
Rough cascade vorticity (k_s^+ =196.47)

scale vortices are gradually consumed during the movement and almost disappear at T6. The shape of V1 changes from the previous round shape to a long strip shape at T4, and it returns to a round shape at T5. At t4, V1 is deformed under the influence of the vortex generated by the trailing edge of the pressure surface. However, in a short period, V1 regained its round shape under the influence of the mainstream, and the scale of the vortex was not affected.

When k_s^+ = 11.80, the airflow transitions at 0.36 chord length of the suction surface. The mountain-like profile on the rough suction surface interferes with the airflow near the wall. The airflow that has just been transformed into turbulence is disturbed by the profile, and the size of the vortex is reduced. The vortex disappears after the turbulent flow of 5% chord length, and the airflow becomes laminar again. The pressure gradient along the flow direction causes the airflow to turn turbulence again at 0.6 chord. Different from the smooth surface, the vortex has not been away from the wall before the tail edge of the blade. In the flow direction of the airflow, the scale of the eddy is gradually increased. Furthermore, when k_s^+ = 11.80 compared to the smooth wall surface, the scale of the vortex is reduced.

Figure 16 is the vorticity amount of the passage when k_s^+ = 196.47. Referring to Schichting's research conclusion, the suction surface is fully rough now. When the suction surface is completely rough, the scroll is significantly increased, and the movement of the airflow has become

more complex. The transfer of airflow occurs at 0.33 chord of the suction surface, which is the same as $k_s^+ = 11.80$. However, the phenomenon of the airflow is retrogradely laminar flow disappears when the wall is Fully Rough. Due to the increase in roughness, the disturbance of the wall faces the airflow is more pronounced. The large-scale vortex near the wall is broken by the influence of the mountain-like rough profile. The vortex is broken into the main vortex and multiple small-scale vortices and the small-scale vortex is sandwiched between the wall and the main vortex. The main vortex is squeezed away and gradually moves away from the wall.

6 Conclusion

In this study, we simulated the effect of a 2D-rough surface on a double-circular-arc blade cascade. The profile of the suction surface was replaced to simulate a rough surface. From the above discussion, one may conclude that the sensitivity of the pressure coefficient distribution on the blade surface to the angle of attack does not correlate with the roughness at the suction of the blade. When the incoming flow angle of attack is positive, the velocity distribution of the trailing edge of the cascade along the b-b direction and the airflow angle at the outlet will not change with the roughness. When $70 < k_s^+ < 130$ the rough suction surface can increase the lift coefficient of the compressor blade. However, this phenomenon only occurs when $i < 0°$.

Unfortunately, only the effect of two-dimensional roughness on the airflow in the cascade passage was simulated in this study. The impact of the three-dimensional roughness of the blade surface on the flow of the cascade is more complicated. Meanwhile, the numerical calculation of the three-dimensional rough wall also puts forward a greater demand on the computer, which is currently difficult to supply the requirements. So one important future direction of studying the effect of the rough blade on the compressor cascade is establishing the relationship between the two-dimensional flow and the three-dimensional flow in the rough cascade. And more experiments should be conducted for the compressor cascade.

Data availability statement

The original contributions presented in the study are included in the article/supplementary material, further inquiries can be directed to the corresponding author.

Author contributions

L-SW is mainly responsible for rough blade calculation and data collation in this research Z-YW is responsible for the guidance and assistance of numerical simulation calculations in this research Y-HW is responsible for providing guidance and assistance in the writing of the article in this research MW is responsible for providing advice and guidance on the research content in this research H-OS is responsible for revising and optimizing the article during the research.

Funding

This work was supported by the National Science and Technology Major Project (J2019-III -0017).

Conflict of interest

The authors declare that the research was conducted in the absence of any commercial or financial relationships that could be construed as a potential conflict of interest.

Publisher's note

All claims expressed in this article are solely those of the authors and do not necessarily represent those of their affiliated organizations, or those of the publisher, the editors and the reviewers. Any product that may be evaluated in this article, or claim that may be made by its manufacturer, is not guaranteed or endorsed by the publisher.

References

Bons, J. P. (2010). A review of surface roughness effects in gas turbines. *J. Turbomach.* 132 (2), 021004. doi:10.1115/1.3066315

Chen, Y., Escalera Mendoza, A. S., and Todd Griffith, D. (2021). Experimental and numerical study of high-order complex curvature mode shape and mode coupling on a three-bladed wind turbine assembly. *Mech. Syst. Signal Process.* 160, 107873. doi:10.1016/j.ymssp.2021.107873

Chen, Y., and Griffith, D. T. (2022a). Experimental and numerical investigation of the structural dynamic characteristics for both surfaces of a wind turbine blade. *J. Vib. Control*, 107754632210974. doi:10.1177/10775463221097470

Chen, Y., and Griffith, D. T. (2022b). Finite cross-section method for mode shape recognition of highly coupled beam-type structures. *J. Vib. Acoust.*, 144. doi:10.1115/1.4053977

Chotalia, R. J., and Alone., D. B. (2017). "Numerical investigations on influence of uniform blade surface roughness on the performance characteristics of a transonic axial flow compressor stage," in ASME 2017 Gas Turbine India Conference, Bangalore, India, December 7–8, 2017.

Guyon, E., Hulin, J. P., Petit, L., Mitescu, C., and Jankowski, D. (2002). Physical hydrodynamics. *Appl. Mech. Rev.* 55 (10), B96–B97. doi:10.1115/1.1497485

Higham, N. J., Dennis, M. R., Glendinning, P., Martin, P. A., Santosa, F., and Tanner, J. (2015). *The princeton companion to applied mathematics*, 1–80. doi:10.1515/9781400874477

Joo, J., Medic, G., and Sharma, O. (2017). "Large-eddy simulation of roughened NACA65 compressor cascade," in ASME Turbo Expo 2017: Turbomachinery

Technical Conference and Exposition, Charlotte, North Carolina, USA, June 26–30, 2017.

Kong, D., Jeong, H., and Song, S. J. (2017). Effects of surface roughness on evolutions of loss and deviation in a linear compressor cascade. *J. Mech. Sci. Technol.* 31 (11), 5329–5335. doi:10.1007/s12206-017-1027-y

Mishra, R. K. (2015). Fouling and corrosion in an aero gas turbine compressor. *J. Fail. Analysis Prev.* 15, 837–845.

Morini, M., Pinelli, M., Ruggero Spina, P., and Venturini, M. (2011). Numerical analysis of the effects of nonuniform surface roughness on compressor stage performance. *J. Eng. Gas. Turbine. Power* 133 (7), 745–753. doi:10.1115/1.4002350

Nicola, A., Morini, M., Pinelli, M., Spina, P. R., Suman, A., and Venturini, M. (2014). Numerical analysis of the effects of surface roughness localization on the performance of an axial compressor stage. *Energy Procedia* 45, 1057–1066. doi:10.1016/j.egypro.2014.01.111

Nicola, A., Morini, M., Pinelli, M., Spina, P. R., Suman, A., and Venturini, M. (2013). Performance evaluation of nonuniformly fouled axial compressor stages by means of computational fluid dynamics analyses. *J. Turbomach.* 136, 021016, doi:10.1115/1.4025227

Schlichting, H., and Gersten, K. (1965). *Boundary-layer theory*. doi:10.1007/978-3-662-52919-5

Shi, X., Liu, H., Long, F., Tang, J., Wang, L., Abdul Amir, H. F., et al. (2017). Study on the influence of blade roughnesson axial flow compressor stage performance. *MATEC Web Conf.* 108, 08008. doi:10.1051/matecconf/201710808008

Simens, M. P., and Gungor, A. G. (2013). "The effect of surface roughness on laminar separated boundary layers," in ASME Turbo Expo 2013: Turbine Technical Conference and Exposition.

Suman, A., Morini, M., Rainer, K., Aldi, N., Brun, K., Pinneli, M., et al. (2017). Estimation of the particle deposition on a subsonic axial compressor blade. *J. Eng. Gas Turbines Power* 139. doi:10.1115/1.4034209

Sun, H.-O., Wang, L.-S., Wang, Z.-Y., Wang, M., Wang, Y.-H., Wan, L., et al. (2021). Simulation of the effect of nonuniform fouling thickness on an axial compressor stage performance. *Adv. Mech. Eng.* 13 (7), 168781402110304. doi:10.1177/16878140211030403

Sun, H Ou, Wang, L., Wan, L., and Qu, F. (2018). "Study on the performance variation of compressor under salt fog scale," in ASME Turbo Expo 2018: Turbomachinery Technical Conference and Exposition.

Syverud, E., and Bakken, L. E. (2006). "The impact of surface roughness on axial compressor performance deterioration," in ASME Turbo Expo 2006: Power for Land, Sea, and Air, 491–501.

Tang, Y., Xi, G., Wang, Z., and Tian, Y. (2019). Quantitative study on equivalent roughness conversion coefficient and roughness effect of centrifugal compressor. *J. Fluids Eng.* 142, 021208. doi:10.1115/1.4044843

Zierke, W. C., and Deutsch, S. (1990). Closure to "discussion of 'the measurement of boundary layers on a compressor blade in cascade: Part 4—flow fields for incidence angles of −1.5 and −8.5 degrees'" (1990, ASME J. Turbomach., 112, p. 255). *J. Turbomach.* 110 (2), 255. doi:10.1115/1.2927641

Nomenclature

k_s^+ Dimensionless roughness
Re Reynolds number
Ra Surface Roughness
AR Aspect ratio
C_f Wall shear stress coefficient
k_s Equivalent sand diameter
c Chord
i Incoming attack angle
c_p Pressure coefficient
c_L Lift coefficient
Ma Mach number
V Velocity
δ_1 Displacement thickness
$\boldsymbol{H_{12}}$ Shape factor
β Exit angle

Subscripts and superscripts

p Pressure side
s Suction side
LE Leading-edge
TE Trailing-edge
in Inlet
out Outlet
is Isentropic
* Total

frontiers | Frontiers in Energy Research

TYPE Original Research
PUBLISHED 17 August 2022
DOI 10.3389/fenrg.2022.969525

OPEN ACCESS

EDITED BY
Lei Luo,
Harbin Institute of Technology, China

REVIEWED BY
Banglin Deng,
Shenzhen University, China
Hongliang Luo,
Hiroshima University, Japan
Lei Shi,
Shanghai Jiao Tong University, China
Haifeng Liu,
Tianjin University, China

*CORRESPONDENCE
Long Liu,
liulong@hrbeu.edu.cn

SPECIALTY SECTION
This article was submitted to Advanced Clean Fuel Technologies, a section of the journal Frontiers in Energy Research

RECEIVED 15 June 2022
ACCEPTED 12 July 2022
PUBLISHED 17 August 2022

CITATION
Liu D, Han X, Liu L and Ma X (2022), Investigation of the scavenging process in two-stroke uniflow scavenging marine engines by a real-time multi-stage model.
Front. Energy Res. 10:969525.
doi: 10.3389/fenrg.2022.969525

Investigation of the scavenging process in two-stroke uniflow scavenging marine engines by a real-time multi-stage model

Dai Liu, Xiao Han, Long Liu* and Xiuzhen Ma

College of Power and Energy Engineering, Harbin Engineering University, Harbin, China

The increasing demand of digital twin marine engine requires real-time physical models for prediction. In two-stroke uniflow scavenging marine engines, a real-time physical model for the scavenging process is rarely found since it is difficult to describe the complex in-cylinder air motion. Without an accurate prediction of the fresh air loss and residual burned gas in the cylinder, the precision of combustion and emission simulation cannot be guaranteed as well. In a marine engine digital twin system, the scavenging ratio and fresh air skip are the vital for the further simulation of combustion and emission. To predict them in real-time, a novel zero-dimensional (0D) multi-stage scavenging model is proposed in this article. In the cylinder zone, the complex gas motion is ideally divided to four stages: exhaust gas blowdown, perfect displacement, displacement-mixing, and perfect mixing. The duration of each stage is determined by the engine design and control parameters. Then, the thermodynamic conditions at each stage are simulated to obtain the mass of residual burned gas, fresh air inlet, and outlet. The results of the 0D model agree well with the results of the CFD simulation, and the mean relative errors of temperature, pressure, and total mass do not exceed 3%, 4%, and 2%, respectively, which indicates the potential for the two-stroke marine engine digital twin system. It could also be applied in a control-oriental engine model or engine diagnostics in the future.

KEYWORDS

uniflow scavenging process, zero-dimensional multi-stage model, real-time simulation, two-stroke marine engine, digital twin

1 Introduction

Large bore two-stroke engines are the main power units for vessels. With the critical challenges of emission and energy regulations, an efficient combustion strategy and low/zero carbon fuels have become the main approaches to improve engine efficiency and reduce emissions. Deng et al. (2018) explored the possibility and limitations of lean burn from the aspect of exhaust emissions Liu et al. developed a flexible spray model (Liu et al. 2022) and optimized the stochastic combustion model (Liu et al. 2022) to cope with the emissions issues and optimize the combustion. Zheng et al. (2018) developed a

thermodynamic model to analyze the effects of different turbocharging parameters on engine boost pressure and pumping loss qualitatively. Furthermore, with the significant increase in engine complexity, simulation is increasingly becoming an important tool to support an engine's full life cycle development. Luo et al. (2022) set up a three-dimensional (3D) model of a HPDI natural gas two-stroke marine engine, where the influence of geometry parameters on mixture flow, combustion, and emissions were presented and discussed. Liu et al. (2019) investigated the effects of injection strategies of dual fuels on combustion characteristics and emissions by the CFD simulation. In the course of study, it is found that the scavenging process affects the global engine performance in a two-stroke engine (Tomislav et al., 2022), and it should be properly designed and controlled for different fuels. Recently, based on traditional modeling and simulation, the digital twin technology has become a high-level sublimation of modeling and simulation technology and will further boost the development of engines (Liu et al., 2021), including the scavenging process of marine engines. In the digital twin system, models with different dimensions would be established for a geometrical design (Zhou et al., 2021) or a real-time performance investigation (Bondarenko and Fukuda., 2020). In most of digital twin applications, such as power systems, real-time models play a vital role in engine optimization, control, and diagnostics (Jiang et al., 2022). To develop reliable real-time engine models, researchers investigated different approaches, such as the 0D/QD model (developed by simplified physical, semi-physical, or empirical equations) and the data-driven model (developed by a machine-learning algorithm). The data-driven model (Wang et al., 2020) requires a large amount of data for training and verification, which has been widely applied in vehicle engines. However, the applications of the data-driven model in marine engine research are limited due to the lack of experimental data, especially for the large bore low-speed marine diesel engines. Therefore, the 0D/QD model (time is the only independent variable) is a good choice for the marine engine digital twin system in the current status.

Many researchers developed a quasi-model for combustion in two-stroke marine engines (Ji et al., 2016; Liu et al., 2020). However, there are rare literature studies to describe the uniflow scavenging process in a marine two-stroke engine, due to its complex mixing of fresh air and exhaust gas in the cylinder. The control of fresh air escaping to the exhaust and residual exhaust gas in the cylinder is influenced by many design and control parameters, such as scavenge port geometry and exhaust valve lift. The complex gas motion would further affect the formation of the air/fuel mixture, flame propagation, combustion quality, pollutant formation, exhaust temperature, and so on. Thus, it is important to develop a scavenging model with high accuracy and real-time performance for the forecast of combustion and emission in future digital twin systems.

An ideal scavenging model includes perfect displacement, perfect mixing, and short-circuiting, but the real scavenging process is normally a combination of them in different stages and zones, which can be observed in many CFD (Andersen et al., 2014; Wang et al., 2016) and experimental research studies (Ma et al., 2021). Therefore, a 0D scavenging model could be a combination of these sub-processes, either by a multi-stage (the scavenging process is divided in different stages based on the engine events) or multi-zone (cylinder is divided in different zones during the scavenging process) approach. Each stage or zone can be assumed as a displacement, mixing, or short-circuiting process. Foteinos and Papazoglou (Foteinos et al., 2019) updated the three-zone scavenging model, originally presented in (Kyrtatos and Koumbarelis, 1988) and applicable to two-stroke uniflow scavenged marine diesel engines, proposed a semi-empirical zero-dimensional three-zone model for a two-stroke uniflow-scavenged diesel engine based on the results of CFD simulations: the pure air zone, mixing zone, and pure exhaust gas zone. However, the multi-zone model introduced many calibration parameters for each zone's mass transformation. Since a 0D scavenging model is aiming to simulate the in-cylinder residual exhaust gas and fresh air to the exhaust pipe for further combustion and performance simulation, the detailed in-cylinder mass exchange process is not necessary. And the multi-stage model, which could simulate the thermodynamic conditions before combustion, is sufficient for a real-time model application. To avoid the inaccuracy of thermal homogeneity of the incoming and exiting gases, Bajwa (Bajwa and Patterson, 2019) proposed a single-zone multi-stage model for a cross-scavenged engine, but its design and control parameters are different from those of the uniflow scavenging process.

To develop a real-time model for the design and control of the uniflow-scavenging process in a two-stroke marine engine digital twin system, a zero-dimensional multi-stage scavenging model is proposed in this article. The stages are determined by the scavenging ports and the exhaust valve's opening and closing timings. The mass of fresh air/burned gas, temperature, and pressure in the cylinder are simulated in each stage accurately, and can also be derived from the intake pressure and exhaust valve opening and closing timings on the impact of the scavenging process law. Based on the fresh air and burned gas-mixing process from the CFD simulation, a novel displacement–mixing (simultaneous) sub-stage was proposed to predict the mixing conditions and combined with other stages determined by the scavenging ports and exhaust valve's opening and closing timings. The mass of fresh air/burned gas, temperature, and pressure in the cylinder are simulated in each stage accurately, which are the key influential factors for the spray and combustion in the two-stroke engine digital twin system.

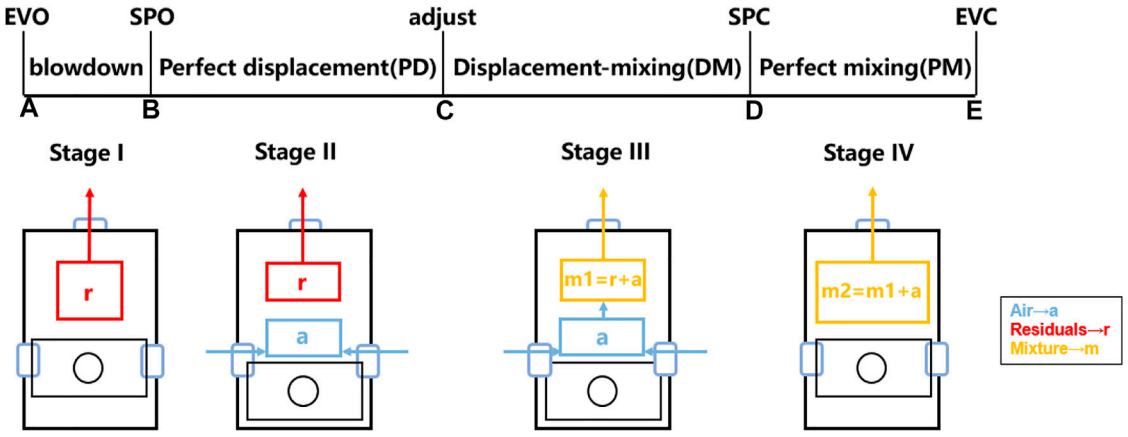

FIGURE 1
Schematic diagram of the zero-dimensional multi-stage model.

TABLE 1 Key parameters of the ZDMS model.

Stage I–IV		Stage I (A→B)	Stage II (B→C)	Stage III (C→D)	Stage IV (D→E)	
Parameter	**Gas component**	**A**	**B**	**C**	**D**	**E**
P	Gas (total gas)	P_A	P_B = Pp	P_C = Pp	P_D = Pp	P_E
T	Air		Ta_B = Ta	Ta_C = Ta	Ta_D = Ta	
	Residuals	Tr_A	Tr_B	Tr_C		
	Gas (total gas)	T_A = Tr_A	T_B = Tr_B	T_C	T_D	T_E
M	Air		ma_B = 0	ma_C	ma_D	ma_E
	Residuals	mr_A	mr_B	mr_C	mr_D	mr_E
	Gas (total gas)	m_A = mr_A	m_B = mr_B	mm_C = m_C	m_D	mm_E = m_E

P_A, P_B, P_C, P_D, P_E, cylinder pressure at times A, B, C, D, and E; Pp, the average pressure of the scavenge ports and the exhaust pipe; Ta, fresh air temperature; Ta_B, Ta_C, Ta_D, fresh air temperature at times B, C, D; Tr_A, Tr_B, Tr_C, residual exhaust gas temperature at times A, B, C; T_A, T_B, T_C, T_D, T_E, cylinder temperature at times A, B, C, D, and E; ma_B, ma_C, ma_D, ma_E, fresh air mass at times B, C, D, and E; mr_A, mr_B, mr_C, mr_D, mr_E, residual exhaust gas mass at times A, B, C, D, and E; m_A, m_B, m_C, m_D, m_E, cylinder total gas mass at time A, B, C, D, and E; mm_C, mm_E, mixture mass at time C, E.

2 Methodology

2.1 Zero-dimensional multi-stage (ZDMS) model

In the novel multi-stage model, the four stages are assumed: blowdown, perfect-displacement (PD), displacement-mixing (DM), and perfect-mixing (PM) in Figure 1. The blowdown stage begins with the exhaust valves opening (EVO) (A) and ends with the scavenging ports opening (SPO) (B), and the cylinder is occupied by residual exhaust gas. The PD stage is from point B to point C and the DM stage is from point C to point D, where the point C is used to adjust the ratio of PD and DM, and the cylinder is occupied by air and residuals or mixture one. The PD stage begins with the scavenging port closing (SPC) (D) and ends with the exhaust valve closing (EVC) (E), and there is only final mixture two in the cylinder at this stage. A summary of the key parameters of the ZDMS model is as shown in Table 1, where the orange indicates known quantities; the green indicates some key unknown quantities.

2.1.1 Stage-I: Blowdown (A-B)

When the exhaust valve is opened, the in-cylinder pressure is normally higher than pressure in the exhaust pipe, which leads to the residuals flowing to the exhaust pipe as a blowdown process. Although the in-cylinder pressure might be lower than the pressure in the exhaust pipe, it is an unexpected situation in the scavenging process which would not be considered in the

model. Therefore, the piston movement and loss of exhaust gas would lead to a sharp decrease in the pressure and temperature of the cylinder, where the pressure decreases from P_A to Pp, as shown in Figure 1. The discharge of exhaust gas during this process is regarded as an isentropic expansion process, the details are as follows.

$$Tr\_B = Tr\_A\left(\frac{P\_B}{P\_A}\right)^{\frac{K-1}{K}} \tag{1}$$

$$mr\_A = \frac{P\_A * V\_A}{R * T\_A} \tag{2}$$

$$mr\_B = \frac{P\_B * V\_B}{R * T\_B} \tag{3}$$

The following are assumed during this stage:

- The isentropic index of all gases is constant.
- The wall of the cylinder is adiabatic.
- The gases in the cylinder are ideal, while gas constant is a constant value.

2.1.2 Stage-II: Perfect-displacement (B-C)

During this stage, the pressure of the residual exhaust gas and fresh air in the cylinder are assumed to be equal with an average manifold pressure, the temperature of the residual exhaust gas still remains from the results of the blowdown stage, and the temperature of the fresh air with $\dot{m}_{in}$ is equal to that of the scavenge ports. For the entire cylinder, its overall temperature is the average temperature obtained by the ratio of residual exhaust gas and fresh air mass to the total mass. The formulas described in this stage are as follows:

$$Tr\_C = Tr\_B \tag{4}$$

$$ma\_C = \dot{m}_{in} * (t\_C - t\_B) \tag{5}$$

$$mr\_C = mr\_B - \frac{Ta\_C}{Tr\_C} * ma\_C \tag{6}$$

$$mm\_C = mr\_C + ma\_C \tag{7}$$

$$Tm\_C = \frac{mr\_C}{mr\_C + ma\_C} * Tr\_C + \frac{ma\_C}{mr\_C + ma\_C} * Ta\_C \tag{8}$$

The following are assumed during this stage:

- The temperature and density of the fresh air in the cylinder are constant.
- The temperature of the exhaust gas is constant.
- The process occurs at a constant cylinder pressure.
- The entering fresh air pushes out the exhaust gas by a perfect displacement mechanism.
- There is no mass or heat that is allowed to cross the interface between the two gases.
- The wall of the cylinder is adiabatic.

2.1.3 Stage-III: Displacement-mixing (C-D)

The pressure of the residual exhaust gas and fresh air in the cylinder are still equal to the average manifold pressure. The temperature of fresh air remains the same as the scavenge port temperature, and the temperature of mixture one during the DM stage is consistent with the overall temperature at the end of the PD stage. The mass of the fresh air at the end of stage-III is the sum of the charged fresh air during this stage and the air in mixture one. The mass of the mixture decreases because of discharging through the exhaust valves, and final mass at this stage can be calculated by the following formulas.

$$Tm\_D = Tm\_C \tag{9}$$

$$Ta\_D = Ta\_C \tag{10}$$

$$ma\_CD = \dot{m}_{in} * (t\_D - t\_C) \tag{11}$$

$$mm\_D = \frac{P\_D * \left(V\_D - \frac{ma\_CD}{\rho\_D}\right)}{R * Tm\_D} \tag{12}$$

$$mm\_a\_D = \frac{ma\_C}{m\_C} * mm\_D \tag{13}$$

$$ma\_D = ma\_CD + mm\_a\_D \tag{14}$$

$$m\_D = ma\_CD + mm\_D \tag{15}$$

$$Tma\_D = \frac{mm\_D}{m\_D} * Tm\_D + \frac{ma\_CD}{m\_D} * Ta\_D \tag{16}$$

where *ma_CD* represents the charging fresh air mass during the DM stage, and *mm_a_D* represents the mass of air in the mixture at time D.

The following are assumed during this stage:

- The temperature and density of the fresh air in the cylinder are constant.
- The temperature of the exhaust gas is constant.
- The process occurs at a constant cylinder pressure.
- The exhaust gas and fresh air from the last stage are mixed ideally and form a homogeneous mixture one.
- The ratio of fresh air and residual exhaust gas in mixture 1 remains the same as the original mixing ratio for this stage.
- The wall of the cylinder is adiabatic.

2.1.4 Stage-IV: Perfect-mixing (D-E)

With the piston movement, the fresh air and mixture one from the last stage mix perfectly and formed homogenous mixture two. With the piston moving upward, the cylinder volume decreases and mixture two is discharged with the exhaust valve opening, so the temperature and pressure may increase or increase depending on the valve lift subsequently.

$$dm\_DE = \dot{m}_{out} * (t\_E - t\_D) \tag{17}$$

$$mm\_E = m\_E = m\_D - dm\_DE \tag{18}$$

TABLE 2 6EX340EF two-stroke engine specifications.

Parameter	Value
Bore	340 mm
Stroke	1,600 mm
Connecting Rod	1,600 mm
Compression Ratio	20.5
75% Load Power	3,672 kW
75% Load Speed	142.5 rpm
75% Load BSFC	179.71 g/kWh
SPO	140°CA
SPC	220°CA
75% Load EVO	111°CA
75% Load EVC	270.6°CA

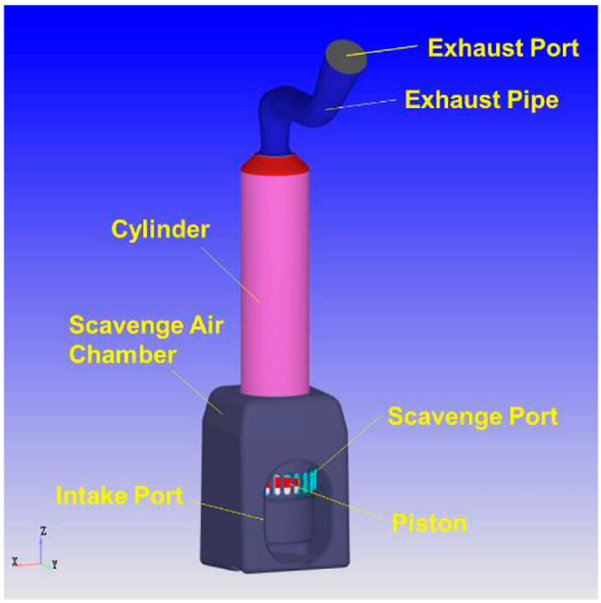

FIGURE 2
Schematic diagram of the 6EX340EF diesel engine model structure.

$$ma\_E = \frac{ma\_D}{m\_D} * m\_E \tag{19}$$

$$mr\_E = \frac{mr\_D}{m\_D} * m\_E \tag{20}$$

$$T\_E = \frac{ma\_E}{m\_E} * Ta + \frac{mr\_E}{m\_E} * Tr\_E \tag{21}$$

$$P\_E = \frac{m\_E * R * T\_E}{V\_E} \tag{22}$$

The following are assumed during this stage:

TABLE 3 Mesh number and calculation time statistics.

Refinement strategy	Mesh number	Calculation time (h)
AMR0 FIX1	8207-27217	1.9
AMR1 FIX1	8207-27217	1.2
AMR3 FIX1	9216-449434	5.2
AMR4 FIX1	9092-1001151	26.9
AMR3 FIX2	31880-538353	9.6
AMR4 FIX2	32066-1000866	42.1
AMR1 FIX3	168701-1340090	76.0
AMR3 FIX3	168701-1340090	67.0
AMR4 FIX3	168698-1340090	86.1

- Mixture one and fresh air from the last stage are mixed ideally and form a homogeneous mixture two.
- The whole cylinder is occupied by mixture 2.
- The wall of the cylinder is adiabatic.

2.2 CFD model development and validation

Two-stroke engine experiments are costly and cannot obtain detailed fluid parameters of the scavenging process. Therefore, the corresponding CFD models validated by several cylinder pressure curves can be used to represent the engine and investigate the fluid characteristics with more operating conditions. Consequently, the real-time zero-dimensional model can be derived and finally applied to two-stroke marine engine digital twin systems. In this article, to confirm the accuracy of the ZDMS model, the corresponding CFD simulation model was carried out by CONVERGE. The simulation was based on a 6EX340EF marine low-speed diesel engine developed by China Shipbuilding Power Engineering Institute Co., Ltd. and the experimental data are also from the manufacturer. During the numerical simulation, the initial temperature and pressure of the scavenge port and exhaust pipe were obtained from experiments, while the cylinder mean temperature was derived from the measured cylinder pressure data. All the gases in the cylinder were marked as waste gas, the gases in the intake region were marked as fresh air, and the specific boundary conditions are described in Supplementary Appendix S1. Table 2 shows the engine specifications. Figure 2 shows the schematic diagram of the engine model structure.

The CFD simulation adopts the RNG k-ε (renormalization group) turbulence model. Mesh quality will directly affect the computational results and computing time, so in this article, the mesh independence analysis was carried out. For the simulation of the scavenging process of the 6EX340EF diesel engine, the simulated base mesh was set as 4 cm, and the velocity and

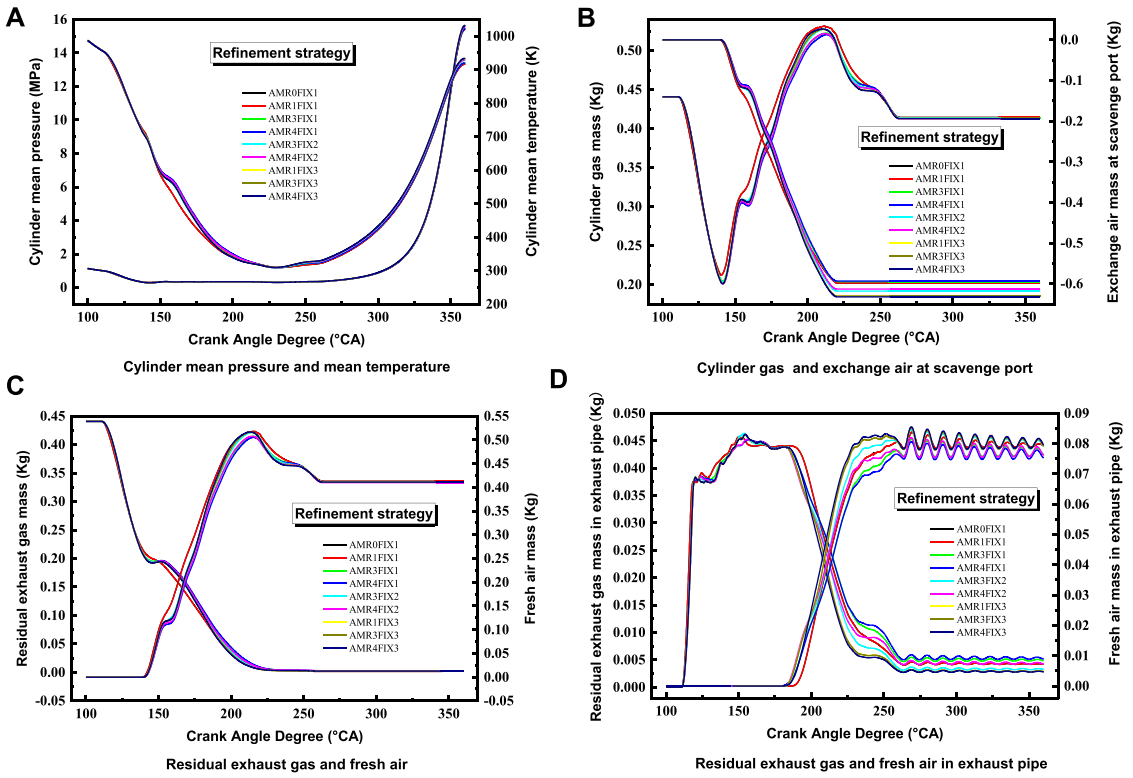

FIGURE 3
Variation of parameters such as **(A)** Cylinder mean pressure and mean temperature, **(B)** Cylinder gas and exchange air at scavenge port, **(C)** Residual exhaust gas and fresh air and **(D)** Residual exhaust gas and fresh air in exhaust pipe under different mesh refinement strategies.

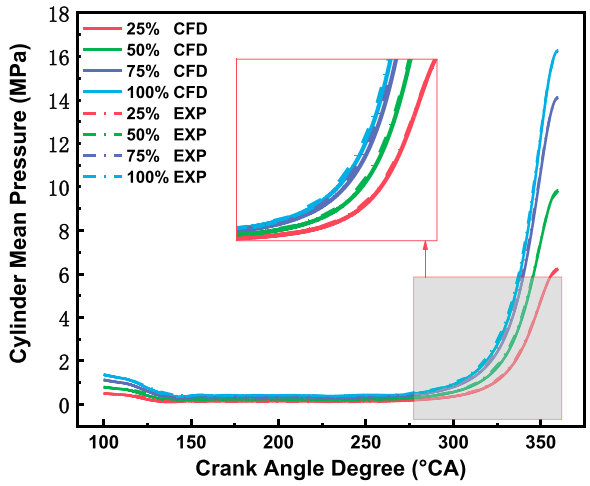

FIGURE 4
Comparison of the simulation and experimental cylinder pressures under different conditions.

temperature-adaptive mesh refinement strategy (AMR) of 3–4 levels was adopted in the cylinder, and the fixed refinement strategy (FIX) of 1–3 levels was adopted in the whole cylinder, scavenge port, and exhaust valve. Based on the simulation results, three refinement strategies are added for a supplementary explanation. Table 3 below shows the number of meshes and computation time in the scavenging process under different refinement strategies. The mesh refinement strategy with a short computation time is selected under the condition of satisfying computation accuracy. Figure 3 shows the parameter variation under different mesh refinement strategies. In summary, it is most reasonable to select the refinement strategy with a 4 cm base mesh, three levels of AMR strategy, and three levels of FIX strategy for this scavenging process simulation.

The numerical simulation research ranges from 100°CA to 360°CA and the cylinder mean pressure in different conditions was compared with the experiment in Figure 4. Table 4 shows the relative deviation of simulation and experimental cylinder pressure at compression top dead center (TDC), and all the relative deviations were less than 0.1%, which illustrates the accuracy and reality of this CFD model.

TABLE 4 Comparison of the simulation and experimental cylinder pressure relative deviations under different conditions.

	25% Load	50% Load	75% Load	100% Load
Simulated initial pressure (MPa)	0.51	0.8	1.13	1.37
Experimental initial pressure (MPa)	0.51	0.8	1.13	1.37
Relative error	0	0	0	0
Simulated end pressure (MPa)	6.23	9.83	14.12	16.27
Experimental end pressure (MPa)	6.23	9.82	14.12	16.28
Relative error	0	0.1%	0	0.06%

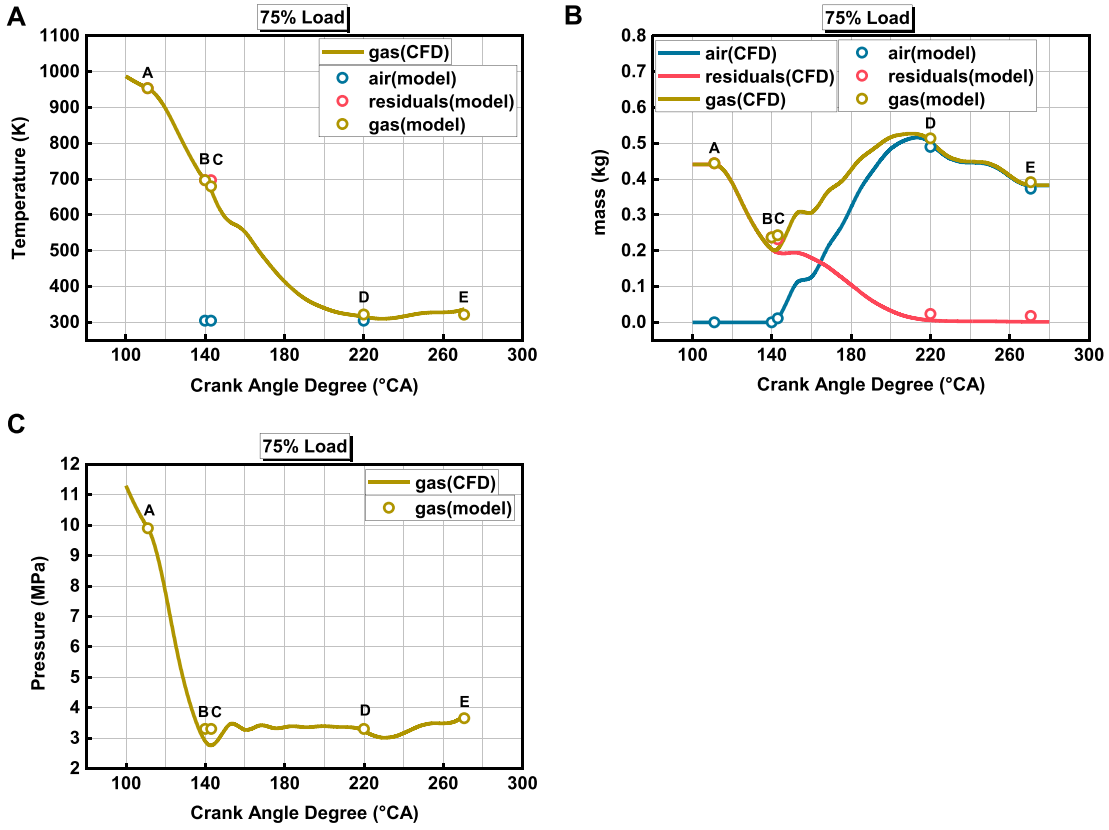

FIGURE 5
Evolution of **(A)** temperature, **(B)** mass and **(C)** pressure of each stage as predicted by the ZDMS model and the CFD model for the 75% load.

TABLE 5 Input parameter settings of the 6EX340EF engine under different loads.

	25% Load	50% Load	75% Load	100% Load
Speed (rpm)	98.9	124.6	142.5	157.0
Intake pressure (MPa)	0.1453	0.2363	0.3423	0.4246
Intake temperature (K)	309.7	301.0	304.1	307.6
Initial cylinder pressure (MPa)	0.446	0.701	0.99	1.201
Exhaust pressure (MPa)	0.1343	0.2173	0.3183	0.4046
Exhaust valve opening and closing (°CA)	111–261.6	111–267.4	111–270.6	111–275.5

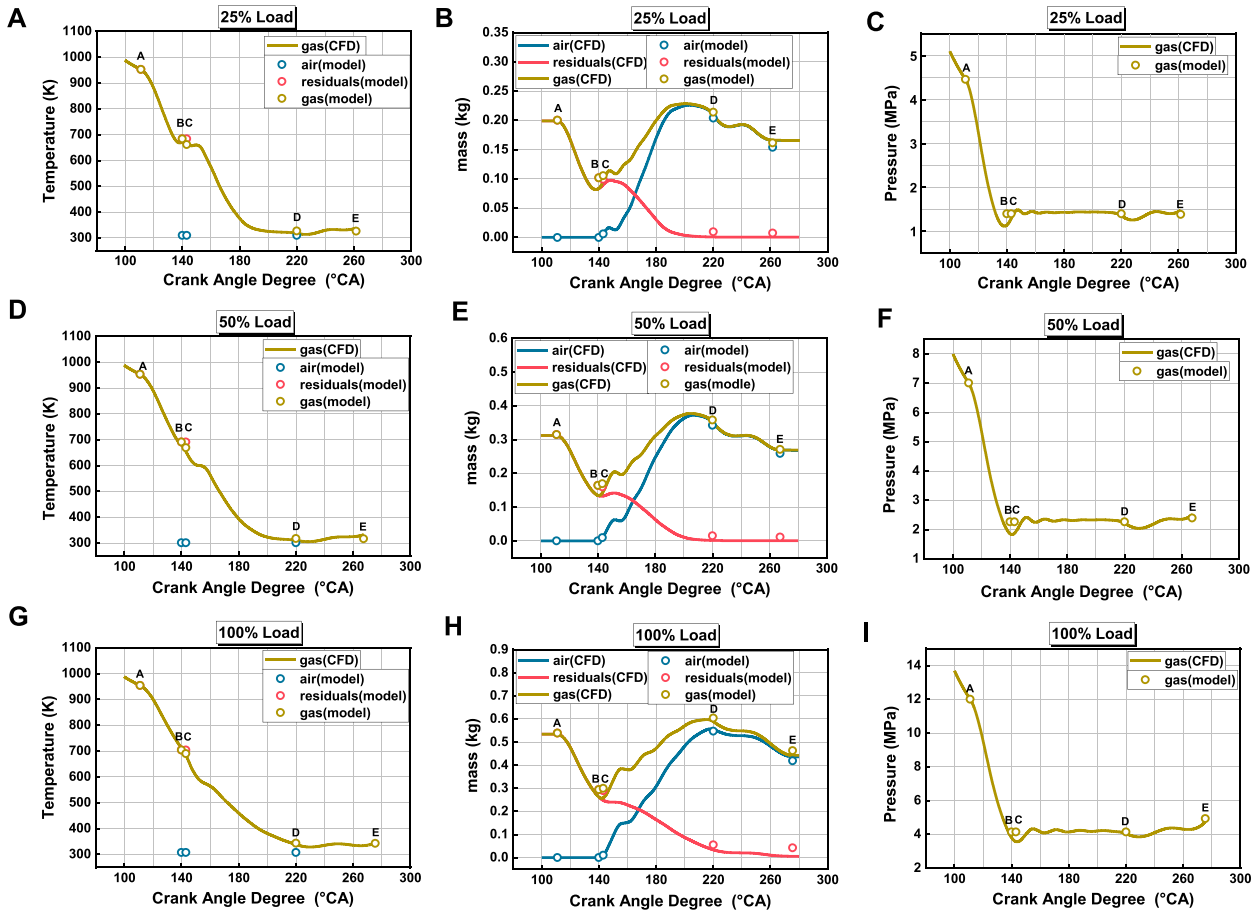

FIGURE 6
Comparison of the results of ZDMS model and CFD model for parameters such as **(A)** temperature, **(B)** mass and **(C)** pressure at 25% load, **(D)** temperature, **(E)** mass and **(F)** pressure at 50% load, and **(G)** temperature, **(H)** mass and **(I)** pressure at 100% load.

3 Results and discussion

3.1 Comparison of the ZDMS model against CFD results

The novel ZDMS model was compared against the results from the CFD simulations. The predicted fresh air mass, residuals mass, total gas mass, temperature, and pressure using the ZDMS were compared to the results predicted by the CFD model. The comparison results under 75% load are presented in Figure 5, where CFD results are presented with a solid line and the results of the ZDMS model are presented with a circle scatter.

As Figure 5 shows, at the beginning of the scavenging process (A), there is only high temperature and pressure residual exhaust gas in the cylinder. During the blowdown stage, the exhaust gas is discharged continuously, and the temperature and pressure in the cylinder gradually decrease, which is also represented well in the ZDMS model (A→B). As the inlet port is opened and the increasing fresh air enters the cylinder after point B, the pressure in the cylinder fluctuates initially and becomes steady soon in the CFD model. This process is also represented in the ZDMS model from point B to C, where point C is used to adjust the ratio of the PD stage and the DM stage and it is found that a good calculation occurs

TABLE 6 RTX-8 engine specifications.

Parameter	Value
Bore	520 mm
Stroke	2,658 mm
Connecting Rod	2,658 mm
Compression Ratio	21.8
SPO	146°CA
SPC	214°CA

TABLE 7 Input parameter settings of the RTX-8 engine under different load conditions.

	25% Load	50% Load	75% Load	100% Load
Speed (rpm)	65.3	82.2	94.0	103.2
Intake pressure (MPa)	0.1576	0.2790	0.3970	0.4960
Intake temperature (K)	300.19	317.66	329.18	326.97
Initial cylinder pressure (MPa)	0.407	0.513	0.963	1.095
Exhaust pressure (MPa)	0.1532	0.2568	0.3823	0.4583
Exhaust valve opening and closing (°CA)	122.5–276.1	122.5–271.4	120.3–255.5	120.7–252.5

when C is close to B. Then, with fresh air entering, the cylinder temperature decreases and the gas mass increases, which is consistent with the ZDMS model (C→D). After that, the exhaust valve is remains open, and with the discharging of mixture two, the cylinder temperature and pressure tends to decrease, but increases quickly caused by the piston moving up,

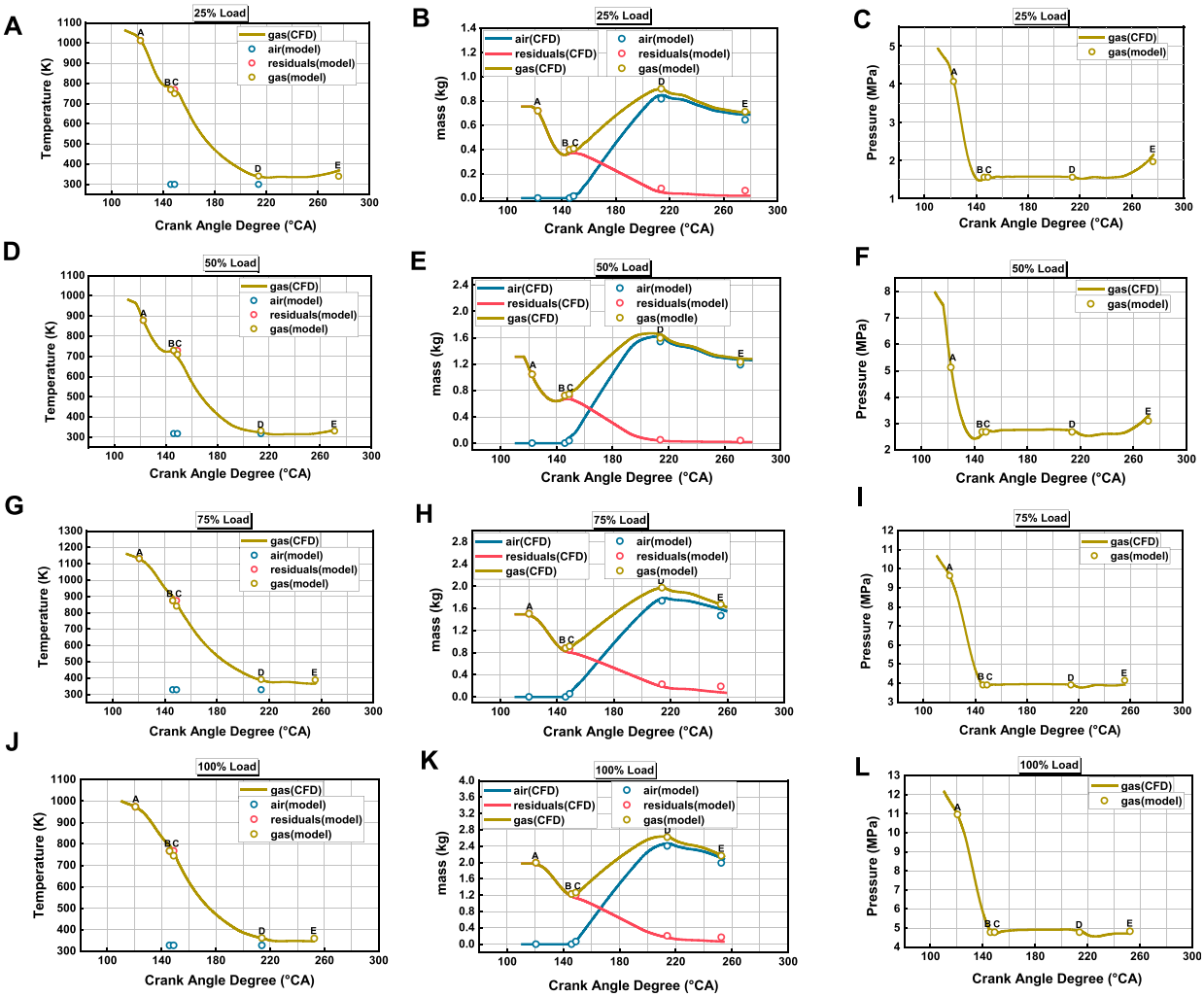

FIGURE 7
Comparison of the results of ZDMS model and CFD model for parameters such as **(A)** temperature, **(B)** mass and **(C)** pressure at 25% load, **(D)** temperature, **(E)** mass and **(F)** pressure at 50% load, **(G)** temperature, **(H)** mass and **(I)** pressure at 75% load, and **(J)** temperature, **(K)** mass and **(L)** pressure at 100% load.

here the ZDMS model is still in good agreement with the CFD results (D→E). It is worth proposing that the CFD simulation described the change process in detail, while the ZDMS model provided accurate stage conditions.

Furthermore, the ZDMS model under different conditions is verified by the CFD model. Table 5 shows the model input parameters for different loads, and Figure 6 shows the comparison results between the CFD model and the ZDMS model at 25%, 50%, and 100% load conditions with good agreement. In addition, another two-stroke engine was additionally selected and the comparative verification of the scavenging process was carried out. Table 6 and Table 7 show the engine specifications and parameters under different loads, respectively. As shown in Figure 7, the model still maintains a high agreement with the CFD results, which indicates the prediction ability in the scavenging process of the two-stroke uniflow scavenge engine.

TABLE 8 Relevant input parameters under 75% load.

Parameters (unit)	Value
Intake pressure (MPa)	0.3183, 0.3203, 0.3223, 0.3263, 0.3293, 0.3333, 0.3373, 0.3423, 0.3483, 0.3543
Exhaust valve opening and closing (°CA)	91–250.6, 96–255.6, 101–260.6, 106–265.6, 111–270.6, 116–275.6, 121–280.6, 126–285.6, 131–290.6, 136–295.6

3.2 Influence of different factors on the scavenging process

To further investigate the scavenging process with the 0D model, charging efficiency (CE) and residual exhaust coefficient (REC), which are common evaluation indicators for the scavenging process, are proposed and calculated by the following formulas.

$$CE = \frac{mass\ of\ delivered\ fresh\ charge\ retained\ in\ the\ cylinder}{reference\ mass} = \frac{m_a}{P_s \cdot V/R \cdot T_s} \tag{23}$$

$$REC = \frac{mass\ of\ residual\ exhaust\ gas\ retained\ in\ the\ cylinder}{mass\ of\ delivered\ fresh\ charge\ retained\ in\ the\ cylinder} = \frac{m_r}{m_a} \tag{24}$$

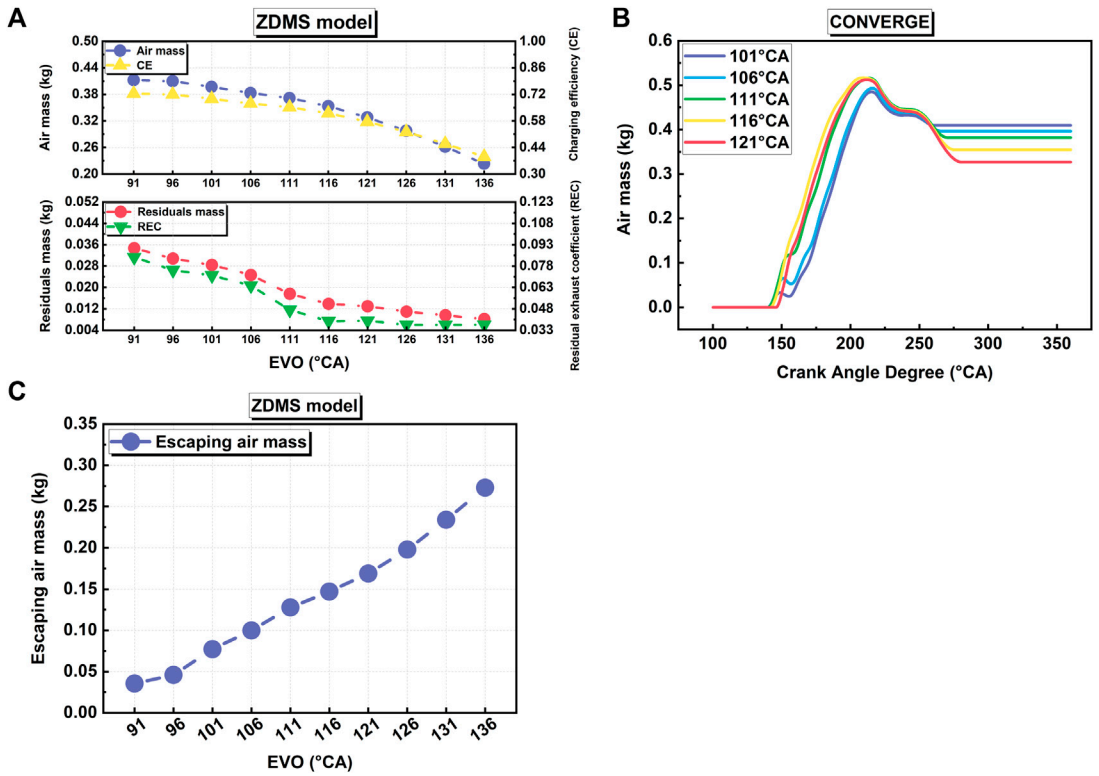

FIGURE 8
(A,B) Air mass, CE, residuals mass, REC, and **(C)** escaping air mass at 75% load with different intake pressures.

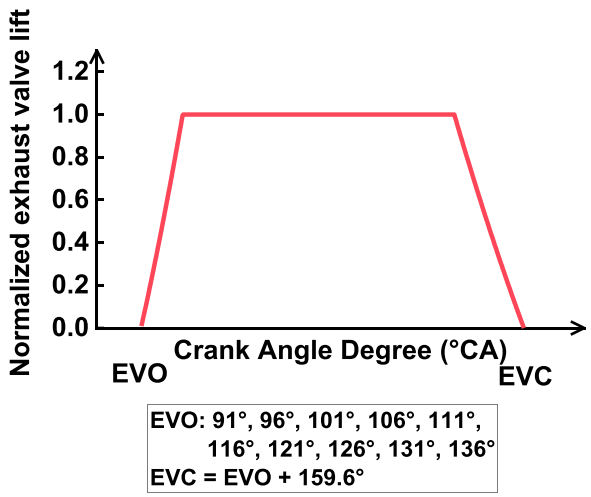

FIGURE 9
Opening profile of exhaust valves.

In this article, the effect of different intake pressures and exhaust valve opening and closing timings on the in-cylinder mass, *CE* and *REC* at the end of the scavenging process were investigated in the 6EX340EF engine at 75% load. Table 8 shows the settings of the relevant input parameters.

As shown in Figures 8A,B, the increase of the intake pressure results in the rise of the fresh air mass and CE with a decrease of residuals mass and REC. The change of them becomes negligible after the intake pressure increases to a certain value (around 0.34 MPa in this stage). A higher intake pressure could increase the mass of the fresh air in and out. As the mass of escaping fresh air increases (as shown in Figure 8C) with the growing intake pressure, the increased fresh air inlet cannot compensate the loss of fresh air. Therefore, the trapped air mass is only determined by the pressure of the inlet air, which is indicated by the CFD model and the 0D model in Figure 8.

For the two-stroke uniflow scavenging engine, its scavenging process can be adjusted by the VVA system (Zhang et al., 2013). In this research, the exhaust valve opening duration is fixed at 159.6°, and the exhaust valve opening timing is gradually delayed from 91°CA to 136°CA. Figure 9 shows the normalized exhaust valve lift (EL) with different opening and closing timings.

As Figure 10A shows, with the delay of the exhaust valve's opening and closing timings, the air mass and CE decrease, due to the less residuals discharging during the blowdown stage which affects the

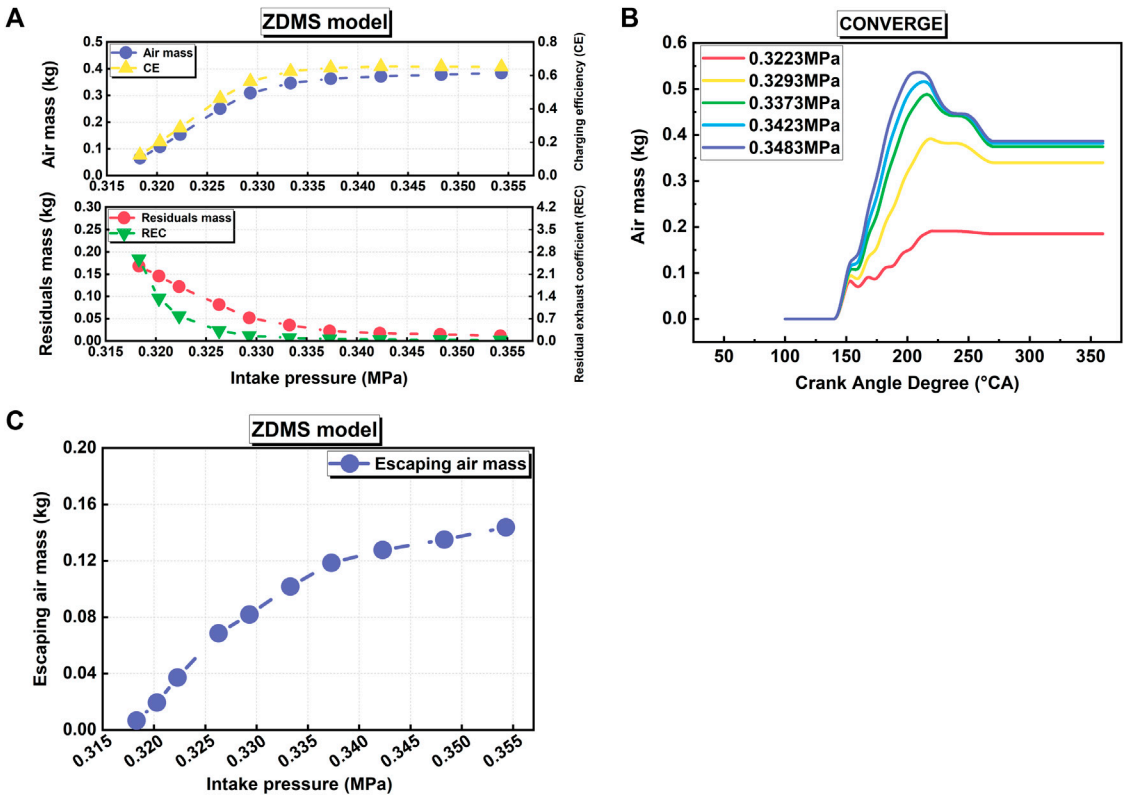

FIGURE 10
(A,B) Air mass, CE, residuals mass, REC, and **(C)** escaping air mass at 75% load with different EVOs.

final air mass trapped in the cylinder. As the PM stage becomes longer, more mixture two flows out of the cylinder, leading to the residual mass and REC decreases. Figure 10B shows that the predicted results of the ZDMS model are in good agreement with the CFD results. With the delay of the exhaust valve opening, the mass of the escaping air increases, which is shown in Figure 10C.

4 Summary and conclusion

In this article, a zero-dimensional multi-stage scavenging model is proposed to simulate the two-stroke engine's uniflow scavenging process. The whole scavenging process is divided into four stages, in which the effects of different scavenging mechanisms are implicitly considered. In the model, the masses, temperature, and pressure of air and residual gas in different stages are predicted by a series of thermodynamic equations. Then, the results of the 0D model are compared with the CFD simulation results in two different engines, and a good agreement is found between the 0D and CFD models, which verifies the accuracy of the proposed model. Finally, the effects of the intake pressure and exhaust valve opening/closing timing on the scavenging process in the cylinder are also investigated, which indicates the same trend and influence in the CFD models. Therefore, the model is an accurate, efficient, and simple alternative to the complex CFD simulations if the details of the scavenging process are not considered. The model provides the initial conditions for subsequent combustion, which can be used as a scavenging process simulation module in the marine engine digital twin system.

The key elements of a digital twin system include the physical entity, the twin model, the twin data, and the dynamic interaction between them. The focus of the problems solved by the digital twin system varies in different stages of the whole life cycle of a marine engine, among which an accurate performance prediction is an important goal in the development of a digital twin system for marine engines during the performance verification part of the design phase and the test phase. The zero-dimensional multi-stage model proposed in this article better simulates the two-stroke engine scavenging process, and can be used as a part of the main mechanism model. By retaining data interfaces, the novel model can establish potential correlations with monitoring data such as environmental data, control data, and sensing data measured and processed from the marine engine entity to realize the dynamic interactions, and then coupling with other mechanism models to obtain a set of twin models closely related to the engine entity. As the core of the performance digital twin system, the twin model mainly focuses on the prediction of engine performance indexes such as power, economy, environment, etc.

Data availability statement

The original contributions presented in the study are included in the article/Supplementary Material; further inquiries can be directed to the corresponding author.

Author contributions

DL: Writing and providing overall ideas; XH: Writing, data processing, and analysis; LL: Guiding the manuscript writing; XM: Supervision and funding.

Funding

This research is funded by Research of Controllable Combustion Technology in Marine Diesel Engine from National Key R&D Program of China, Ministry of Science and Technology (Grant No. 2017YFE0116400) and Marine Low-Speed Engine Project Phase I (Grant No. CDGC01-KT0102-001).

Conflict of interest

The authors declare that the research was conducted in the absence of any commercial or financial relationships that could be construed as a potential conflict of interest.

Publisher's note

Supplementary material

The Supplementary Material for this article can be found online at: https://www.frontiersin.org/articles/10.3389/fenrg.2022.969525/full#supplementary-material

References

Andersen, F. H., Hult, J., Nogenmyr, K. J., and Mayer, S. (2014). CFD analysis of the scavenging process in marine two-stroke diesel engines. Proceeding of the ASME 2014 Internal Combustion Engine Division Fall Technical Conference. October 2014, Columbus, Indiana, USA, ICEF 1, 1–13. doi:10.1115/icef2014-5438

Bajwa, A. U., and Patterson, M. (2019). A New single-zone multi-stage scavenging model for real-time emissions control in two-stroke engines. Proceeding of the ASME 2019 Internal Combustion Engine Division Fall Technical Conference. October 2019, Chicago, IL, USA, 20–23.

Bondarenko, O., and Fukuda, T. (2020). Development of a diesel engine's digital twin for predicting propulsion system dynamics. *Energy* 196, 117126. doi:10.1016/j.energy.2020.117126

Deng, B. L., Li, Q., Chen, Y. Y., Li, M., Liu, A. D., Ran, J. Q., et al. (2018). The effect of air/fuel ratio on the CO and NOx emissions for a twin-spark motorcycle gasoline engine under wide range of operating. *Energy* 169, 1202–1213. doi:10.1016/j.energy.2018.12.113

Foteinos, M., Papazoglou, A., Kyrtatos, N., Stamatelos, A., Zogou, O., Stamatellou, A., et al. (2019). A three-zone scavenging model for large two-stroke uniflow marine engines using results from CFD scavenging simulations. *Energies* 12 (9), 1719. doi:10.3390/en12091719

Ji, C. W., Yang, J. X., Liu, X. L., Zhang, B., Wang, S. F., Gao, B. B., et al. (2016). A quasi-dimensional model for combustion performance prediction of an SI hydrogen-enriched methanol engine. *Int. J. Hydrogen Energy* 41 (39), 17676–17686. doi:10.1016/j.ijhydene.2016.07.146

Jiang, J. J., Li, H., Mao, Z. W., Liu, F. C., Zhang, J. J., Jiang, Z. N., et al. (2022). A digital twin auxiliary approach based on adaptive sparse attention network for diesel engine fault diagnosis. *Sci. Rep.* 12 (1), 675. doi:10.1038/s41598-021-04545-5

Kyrtatos, N. P., and Koumbarelis, I. (1988). A three-zone scavenging model for two-stroke uniflow engines. *J. Eng. Gas. Turbine. Power* 110 (3), 531–537. doi:10.1115/1.3240167

Liu, H. F., Li, J. R., Wang, J. T., Wu, C. H., Liu, B., Dong, J. J., et al. (2019). Effects of injection strategies on low-speed marine engines using the dual fuel of high-pressure direct-injection natural gas and diesel. *Energy Sci. Eng.* 7, 1994–2010. June. doi:10.1002/ese3.406

Liu, L., Peng, Y., Liu, D., Han, C. F., Zhao, N. B., Ma, X. Z., et al. (2020). A review of phenomenological spray penetration modeling for diesel engines with advanced injection strategy. *Int. J. Spray Combust. Dyn.* 12 (145), 175682772093406. doi:10.1177/1756827720934067

Liu, Y. Q., Li, X., Ren, W. C., and Sui, Y. F. (2021). Digital twin boosting leap-forward development of aero engine. *Aerosp. Power* 2021 (02), 24–29. (in Chinese).

Liu, L., Mei, Q. H., and Jia, W. N. (2022). A flexible diesel spray model for advanced injection strategy. *Fuel* 314 (145), 122784. doi:10.1016/j.fuel.2021.122784

Liu, L., Peng, Y., Huang, L., Han, C. F., and Ma, X. Z. (2022). Evaluation of impingement effects on high-power diesel engine mixing process with an optimized stochastic combustion model. *Fuel* 328 (145), 125239. doi:10.1016/j.fuel.2022.125239

Luo, W. F., Liu, H. F., Liu, L., Liu, D., Wang, H., and Yao, M. F. (2022). Effects of scavenging port angle and combustion chamber geometry on combustion and emmission of a high-pressure direct-injection natural gas marine engine. *Int. J. Green Energy* 00 (00), 1–13. doi:10.1080/15435075.2022.2079380

Ma, F. K., Yang, W., Wang, Y. F., Xu, J. F., and Li, Y. F. (2021). Experimental research on scavenging process of opposed-piston two-stroke gasoline engine based on tracer gas method. *Int. J. Engine Res.*, 1–12. doi:10.1177/14680874211036613

Tomislav, S., Vedran, M., Vedran, M. V., and Igor, W. (2022). CFD analysis of a large marine engine scavenging process. *Processes* 10 (1), 141. doi:10.3390/PR10010141

Wang, X. Y., Ma, J., and Zhao, H. (2016). *Evaluations of scavenge port designs for a boosted uniflow scavenged direct injection gasoline (BUSDIG) engine by 3D CFD simulations*. SAE Technical Papers. doi:10.4271/2016-01-1049

Wang, B. W., Zhang, G. B., Wang, H. Z., Xuan, J., and Jiao, K. (2020). Multi-physics-resolved digital twin of proton exchange membrane fuel cells with a data-driven surrogate model. *Energy AI* 1, 100004. doi:10.1016/j.egyai.2020.100004

Zhang, Y., Zhao, H., Ojapah, M., and Cairns, A. (2013). CAI combustion of gasoline and its mixture with ethanol in a 2-stroke poppet valve DI gasoline engine. *Fuel* 109, 661–668. doi:10.1016/j.fuel.2013.03.002

Zheng, Z. Q., Feng, H., Mao, B., Liu, H. F., and Yao, M. F. (2018). A theoretical and experimental study on the effects of parameters of two-stage turbocharging system on performance of a heavy-duty diesel engine. *Appl. Therm. Eng.* 129, 822–832. doi:10.1016/j.applthermaleng.2017.10.044

Zhou, Y., Xing, T., Song, Y., Li, Y. J., Zhu, X. F., Li, G., et al. (2021). Digital-twin-driven geometric optimization of centrifugal impeller with free-form blades for five-axis flank milling. *J. Manuf. Syst.* 58, 22–35. doi:10.1016/j.jmsy.2020.06.019

Nomenclature

Abbreviations

BDC bottom dead center
BD blowdown
BSFC brake specific fuel consumption
CA crank angle
CFD computational fluid dynamics
CE charging efficiency
DM displacement-mixing
EVO exhaust valve opening
EVC exhaust valve closing
EL exhaust valve lift
PD perfect-displacement
PM perfect-mixing
REC residual exhaust coefficient
RNG renormalization group
SE scavenging efficiency
SPO scavenging port opening
SPC scavenging port closing
TDC top-dead center
ZDMS zero-dimensional multi-stage

Symbols

AIA axis inclination angle
K isentropic exponent
Δm mass difference
$\dot{m}_{in}$ intake mass flow
$\dot{m}_{out}$ exhaust mass flow
m massmixture
P pressure
R ideal gas constant
SOA swirl orientation angle
T temperature
V volume

Subscripts

a air
ex exhaust
m massmixture
p pipe
r residual
s scavenged

Greek Symbols

ρ density

frontiers | Frontiers in Energy Research

TYPE Original Research
PUBLISHED 25 August 2022
DOI 10.3389/fenrg.2022.985220

OPEN ACCESS

EDITED BY
Xiao Liu,
Harbin Engineering University, China

REVIEWED BY
Shao-Fei Zheng,
North China Electric Power University, China
Yiheng Tong,
Space Engineering University, China
Feng Zhang,
Hunan University, China
Jin-yuan Qian,
Zhejiang University, China

*CORRESPONDENCE
Wenxiong Xi,
13739076081@163.com

SPECIALTY SECTION
This article was submitted to Advanced Clean Fuel Technologies, a section of the journal Frontiers in Energy Research

RECEIVED 03 July 2022
ACCEPTED 18 July 2022
PUBLISHED 25 August 2022

CITATION
Liu J, Xu M, Ma K, Liu C and Xi W (2022), Heat transfer and flow structures of supercritical n-decane in a regenerative cooling channel loaded with non-uniform heat flux.
Front. Energy Res. 10:985220.
doi: 10.3389/fenrg.2022.985220

Heat transfer and flow structures of supercritical n-decane in a regenerative cooling channel loaded with non-uniform heat flux

Jian Liu[1], Mengyao Xu[1], Kai Ma[2], Chaoyang Liu[3] and Wenxiong Xi[1]*

[1]Research Institute of Aerospace Technology, Central South University, Changsha, China, [2]Xi'an Modern Chemistry Research Institute, Xi'an, China, [3]College of Aerospace Science and Engineering, National University of Defense Technology, Changsha, China

A harsh and complex thermal environment in the combustor threatens safe working of scramjets. In this study, heat transfer and flow structures of supercritical n-decane under 3 MPa in a regenerative cooling channel loaded with non-uniform heat flux distributions are investigated, including uniform, sinusoidal, increased, and decreased heat flux distributions. A verified $k-\omega$ SST turbulence model was employed, and a corresponding mesh independence study was performed. From this work, the fluid temperature at the outlet of the heated channel is only determined by the averaged heat flux, and all the regenerative cooling channels achieve the same temperature although loaded with different heat flux distributions. Compared with the fluid temperature, the wall temperature distribution is more sensitive to the variations of heat flux distribution. The regenerative cooling channels loaded with the sinusoidal heat flux distributions exist in several high-temperature regions, and the channel loaded with linear distributions changes the trend of temperature distribution. A larger temperature gradient is found in the regenerative cooling channel wall with a lower thermal conductivity. This work provides a good insight into the characteristics of the flow and temperature field of regenerative cooling channels loaded with non-uniform heat flux considering the effect of conjugate heat transfer.

KEYWORDS

regenerative cooling, non-uniform, material, temperature distribution, conjugate heat transfer

Introduction

As the core component of a hypersonic vehicle, a scramjet engine faces an extremely severe thermal environment because of large aerodynamic heating and combustion heat generation (Zhu et al., 2018; Zhang et al. 2020). Traditional passive cooling methods are difficult to satisfy high thermal protection requirements and ensure the operation of the

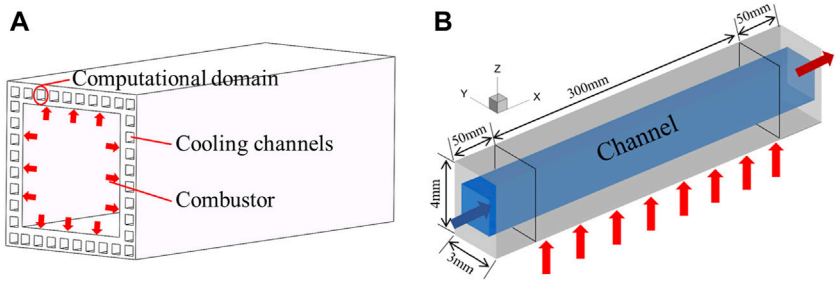

FIGURE 1
Regenerative cooling channels and computational domain. **(A)** Schematic of a typical scramjet combustor. **(B)** Single regenerative cooling channel.

hypersonic vehicles. Many researchers pay attention to active thermal protection to provide higher efficiency thermal protection for propulsion systems, especially for a scramjet engine (Ding et al., 2019; Zuo et al., 2021). Using fuel as the coolant, regenerative cooling is a typical convective cooling method with quantities of cooling channels mounted inside the combustor wall (Jing et al., 2017; Zhao et al., 2018; Jin et al., 2020). The fuel flows through the cooling passages and absorbs excess heat from the combustion chamber inner walls before entering the combustor. First, it takes away large heat generation in the chamber and avoids heat damage to the structures. At the same time, the pre-heated fuel can take part in the combustion process efficiently and adequately. Regenerative cooling fully takes advantage of the physical properties of the fuel which makes it the most prospective way for thermal protection in scramjet engines.

As a typical propulsion fuel, endothermic hydrocarbon not only has a physical heat sink with latent heat of the vaporization process but also provides a chemical heat sink in its endothermic reaction. In recent years, the heat transfer characteristics of endothermic hydrocarbon fuels has become a focus in the aerospace field (Chen et al., 2016; Xu and Meng 2016; Li H, et al., 2019; Wang and Pan 2020; Zhang and Sun 2020; Xu et al., 2021). Chen et al. (2016) numerically investigated the influence of downstream blockage flow patterns and effects of throttle on temperature distributions and heat transfer. The results indicated that resistance in the downstream region would make a difference in the pressure field and formed a transverse pressure gradient. At the same time, the throttle structure with a small diameter played an important role in resisting mass flow rate difference, and when it was set at the inlet of the branch the wall temperature of the channel tended to be uniform. Xu and Meng, (2016) studied the influence of surface heat flux and inlet fluid velocity on fluid dynamics and heat transfer characteristics of RP-3 at 5 MPa in cooling tubes and revealed that hydrocarbon fuels could improve heat transfer by absorbing heat from endothermic chemical reactions. Xu, Lin, and Li (2021) numerically evaluated flow and heat transfer characteristics of hydrocarbon fuel under both mild and terrible-cracked conditions. The flow and heat transfer characteristics in cooling channels with different lengths and heat fluxes were investigated. In addition, the researchers found the fuel flow and heat transfer characteristics of hydrocarbon varied with the fuel mass flow and heat flux, which can enhance both heat transfer and deterioration.

Many researchers focused on heat transfer enhancement technology in regenerative cooling (Ulas and Boysan 2013; Brinda and Sumangala 2016; Feng et al., 2017; Pu et al., 2018; Zuo et al., 2018; Han et al., 2021; Liu et al., 2022; Luo et al., 2022). Han et al. (2021) intended to improve the heat transfer performance of n-decane under supercritical pressure in horizontal tubes by adding ZnO nanofluids and summed up heat transfer corrections in detail. Ulas and Boysan, (2013) analyzed the thermodynamic characteristics in triangle-shaped micro-cooling channels with different aspect ratios. They found that when the aspect ratio was higher, a better performance of the heat sink was provided. Zuo et al. (2018) numerically analyzed the influence of film injection locations, film injection temperature, and film slot velocity on heat transfer and flow structures in a regenerative cooling channel. The basic performance and safe operating conditions are evaluated and analyzed when film cooling and regenerative cooling existed at the same time.

Some numerical calculation investigations have been carried out to simulate the flow and heat transfer process of liquid fuels in cooling channels (Zhang et al., 2016; Li et al., 2018; Li X et al., 2020). Zhang et al. (2016) applied the verified k–ω SST model to explore the cooling performance of the regenerative cooling channels with different aspect ratios, fin thickness, and coolant inlet temperature, and the turbulence model was validated by the experiments. The results indicated that wall temperature remained decreased when the aspect ratio of the channel was increased from 1 to 8 in regenerative cooling channels, but the reduction rate decreased slowly. With

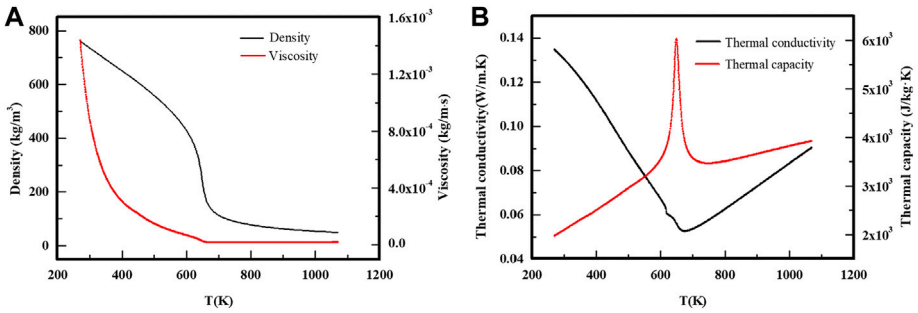

FIGURE 2
Related thermophysical properties of n-decane at 3 MPa obtained from SUPERTRAPP software. **(A)** Density and viscosity. **(B)** Thermal conductivity and thermal capacity.

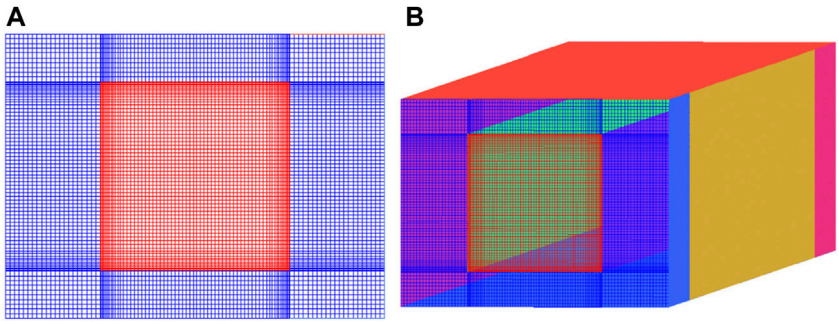

FIGURE 3
Structured meshes and local mesh details. **(A)** Cross section of the grids. **(B)** Full view of the grids.

the given channel aspect ratio and flow region, the decreased fin thickness provided decreased thermal diffusion coefficients. Li et al. (2018) selected a verified k–ω SST model to analyze the influence of truncated ribs on overall heat transfer performance and pressure drop characteristics under Re = 1800–3,700. A heat transfer improvement and an increase of pressure drop are found at the same time. Li Y et al. (2020) employed a verified v^2f turbulence model to study the flow characteristics and heat transfer of twelve ribbed geometrical structures with different rib heights and slit-length-to-rib-lengths. They found that low ribs with a slit provided a decreased Nusselt number and friction factor, while the phenomenon in high ribs was the opposite. It is noted that producing short slits on high ribs is a feasible way to improve thermal performance.

Some experiments are performed to study the principles of flow and heat transfer characteristics (Li Z, et al., 2019; Wörz et al., 2019; Peszynski and Tesař 2020; Yan et al., 2020). Li H et al. (2019) carried out experiments under different engine-like working conditions to investigate the dynamic characteristics of the hydrocarbon fuel at high temperatures. It was found that the settling time of fuel outlet temperature and wall temperature first increased and then decreased with the increased fuel outlet temperature. The settling time increased with the increased heat flux for both outlet fuel temperature and wall temperature. Wörz et al. (2019) first experimentally studied the heat transfer and flow characteristics for gas turbine blades and then compared them with numerical results by adopting two common algebraic models and three implemented explicit algebraic models. The results indicated that the higher-order heat flux model would bring a remarkable improvement in heat transfer. Yan et al. (2020) experimentally investigated the parameter effect on heat transfer of kerosene at supercritical pressure and made comparisons with the currently existing heat transfer corrections.

Because of the complex heat flux during the working process, the non-uniform temperature field existing in the combustor wall affects the durability of the combustor chamber. In this work, a straight rectangular regenerative cooling channel is selected with a square cross section Su et al. (2020). The flow and heat transfer characteristics of hydrocarbon fuel in the regenerative cooling channel of scramjets under high Mach number and hard thermal

TABLE 1 Wall material and heat flux density of all the cases.

Heat flux function	Case name	Material	Distribution correlation (W/m^2)
Uniform distribution	A	Stl	1.5×10^6
Sinusoidal distribution (cases B1~B7)	B1	Stl	$1.5 \times 10^6 + 7.5 \times 10^5 \cdot \sin(2\pi/0.3 \times (x\text{-}0.05))$
	B2	Stl	$1.5 \times 10^6 + 7.5 \times 10^5 \cdot \sin(2\pi/0.1 \times (x\text{-}0.05))$
	B3	Stl	$1.5 \times 10^6 + 7.5 \times 10^5 \cdot \sin(2\pi/0.05 \times (x\text{-}0.05))$
	B4	Stl	$1.5 \times 10^6 + 7.5 \times 10^5 \cdot \sin(2\pi/0.025 \times (x\text{-}0.05))$
	B5	Stl	$1.5 \times 10^6 + 3.75 \times 10^5 \cdot \sin(2\pi/0.05 \times (x\text{-}0.05))$
	B6	Stl	$1.5 \times 10^6 + 11.25 \times 10^5 \cdot \sin(2\pi/0.05 \times (x\text{-}0.05))$
	B7	Stl	$1.5 \times 10^6 + 15 \times 10^5 \cdot \sin(2\pi/0.05 \times (x\text{-}0.05))$
Increased distribution (cases C1~C3)	C1	Stl	$7 \times 10^5 + 4 \times 10^6 \cdot x$
	C2	Stl	$11 \times 10^5 + 2 \times 10^6 \cdot x$
	C3	Stl	$13 \times 10^5 + 1 \times 10^6 \cdot x$
Decreased distribution (cases D1~D3)	D1	Stl	$17 \times 10^5 - 1 \times 10^6 \cdot x$
	D2	Stl	$19 \times 10^5 - 2 \times 10^6 \cdot x$
	D3	Stl	$23 \times 10^5 - 4 \times 10^6 \cdot x$
Material (cases E1~E3)	E1	Al	$1.5 \times 10^6 + 7.5 \times 10^5 \cdot \sin(2\pi/0.05 \times (x\text{-}0.05))$
	E2	Stl	$1.5 \times 10^6 + 7.5 \times 10^5 \cdot \sin(2\pi/0.05 \times (x\text{-}0.05))$
	E3	Ti	$1.5 \times 10^6 + 7.5 \times 10^5 \cdot \sin(2\pi/0.05 \times (x\text{-}0.05))$

environment conditions are studied. Given suitable inlet mass flow and a size-specified rectangular regenerative cooling channel, the flow and heat transfer field of n-decane at 3 MPa with different heat flux distributions are investigated, including uniform heat flux, sinusoidal heat flux, and linear heat flux distributions (Ruan et al., 2017; Li X et al., 2020). In addition, the effects of thermal conductivity of the regenerative cooling channel are investigated by using different materials.

Computational domain and thermophysical properties

Computational domain

In Figure 1A, a typical combustor with multiple regenerative cooling channels compacted in the walls around the combustor is displayed. Considering the symmetry and periodicity of the combustor, a single rectangular cross-section regenerative cooling channel is selected as the computational domain to save the computational efforts, as shown in Figure 1B.

The rectangular computational domain is built with a heated length of 300 mm and a fluid region cross section of 2 mm × 2 mm. Four solid walls with a certain thickness are placed around the fluid passage, and fluid–solid coupling is considered. The heat flux is loaded from the outer wall of the combustor, i.e., the bottom wall. Along the normal direction (z-axis) and spanwise direction (y-axis), the wall thickness is, respectively, 1 and 0.5 mm. In order to ensure a fully-developed regime and exclude the effect of boundary development on heat transfer, two extended channels are arranged upstream and downstream with a length of 50 mm.

Thermophysical properties

Thermophysical properties of supercritical n-decane change greatly when the temperature approaches the critical point. It is crucial to get the exact thermophysical properties in the calculation including density, viscosity, thermal capacity, and thermal conductivity. The corresponding data are obtained by SUPERTRAPP software which was developed by the National Institute of Standards and Technology, United States (Huber, 2007). For the three physical properties of density, viscosity, and thermal conductivity, the User-Defined Function was used in FLUENT to input the related data profiles including the temperature and the corresponding physical property data, and then UDF folders were loaded. For the thermal capacity of the fluid, the piecewise-linear function in the fluid material definition

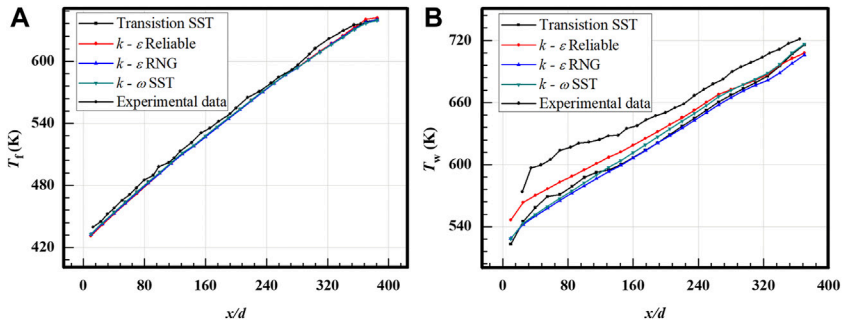

FIGURE 4
Verification of the turbulence model. **(A)** Fluid temperature. **(B)** Wall temperature.

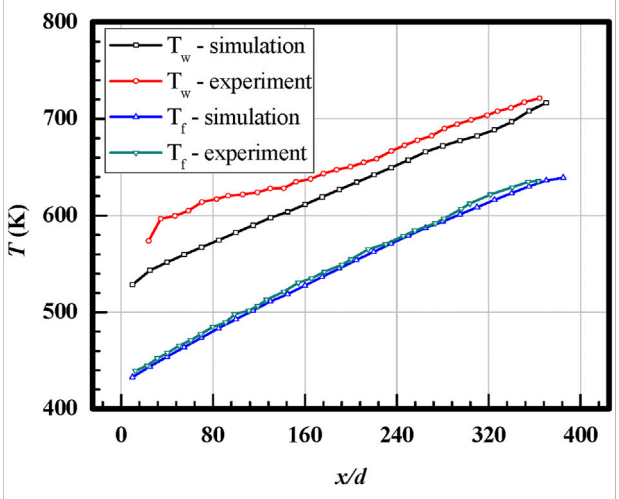

FIGURE 5
Comparison of the fluid and wall temperature, respectively, from the experimental results and predicted by the $k-\omega$ SST model.

panel in FLUENT 19.0 was used to input the points within the computational temperature range. The details of thermophysical properties including density, viscosity, thermal conductivity, and thermal capacity that varied with temperature are shown in Figure 2.

Numerical method and verification

Grid and boundary conditions

In this study, structured grids are adopted to discretize the computational domains by commercial software ANSYS ICEM CFD 19.0. The mesh details of overview and cross sections of streamwise direction are displayed in Figure 3. The k–ω SST model is adopted to solve the turbulence equations. To meet the wall y + requirement of the k–ω SST model, the height of the first layer and the growth rate in the mesh system are set at 0.01 mm and 1.1, respectively. Also, the corresponding wall y+ is less than 1 for all the considered cases.

Three-dimensional turbulent flow and heat transfer are performed in the rectangular regenerative cooling channel, as shown in Figure 1. In the calculation, the mass flow rate of the inlet is 0.0028 kg/s with an initial temperature of 423 K, and the corresponding Reynolds number is 5,385. The outlet is set as pressure-outlet with an operation pressure of 3 MPa. It is noted that only the bottom wall is the heated wall with a length of 300 mm. Other sidewalls, including the upstream and downstream extended channel walls, are both set as adiabatic.

To investigate the effects of non-uniform heat flux, four kinds of heat flux distributions, namely, uniform distribution (Case A), sinusoidal distribution (Case B), increased distribution (Case C), and decreased distribution (Case D), are designed. For the sinusoidal distribution of Case B1–Case B4, the cycle of sinusoidal function is change, and amplitude is changed for Case B5–Case B7. For the increased distribution of Case C1–Case C3, the increased rate is changed but setting the same averaged heat flux. Similar to Case C, the decreased rate of Case D1–Case D3 is changed but the same averaged heat flux is maintained. The details of heat flux distribution along the heated wall are provided in Table 1. The non-uniform heat flux distributions in each case are realized by User-Defined Functions in ANSYS FLUENT 19.0. For all the cases, the averaged heat flux is set at 1.5 MW/m^2 which provides the convenience for comparisons.

In the calculation, the effects of gravity with a value of 9.81 m/s^2 are considered because of the drastic change in thermophysical properties. The interface between fluid and solid domains is coupled, and stainless steel is selected as the wall material in Case A–Case E. The density and thermal capacity of the steel are 7,930 kg/m^3 and 500 J/kgK, respectively. The change of thermal conductivity of solid material is also considered in the calculation, and a linear correlation of thermal conductivity is used. The linear correlation of thermal

TABLE 2 Related data calculated by different mesh regimes.

Mesh name	Mesh number (million)	Averaged temperature of heated walls (K)	Pressure drop (Pa)
Mesh 1	3.07	912.66 (-0.00219%)	1992.0 (+0.05522%)
Mesh 2	4.32	912.70 (+0.00219%)	1990.7 (-0.01004%)
Mesh 3	5.98	912.68	1990.9
Mesh 4	8.01	912.74 (+0.00657%)	1990.3 (-3.01371%)

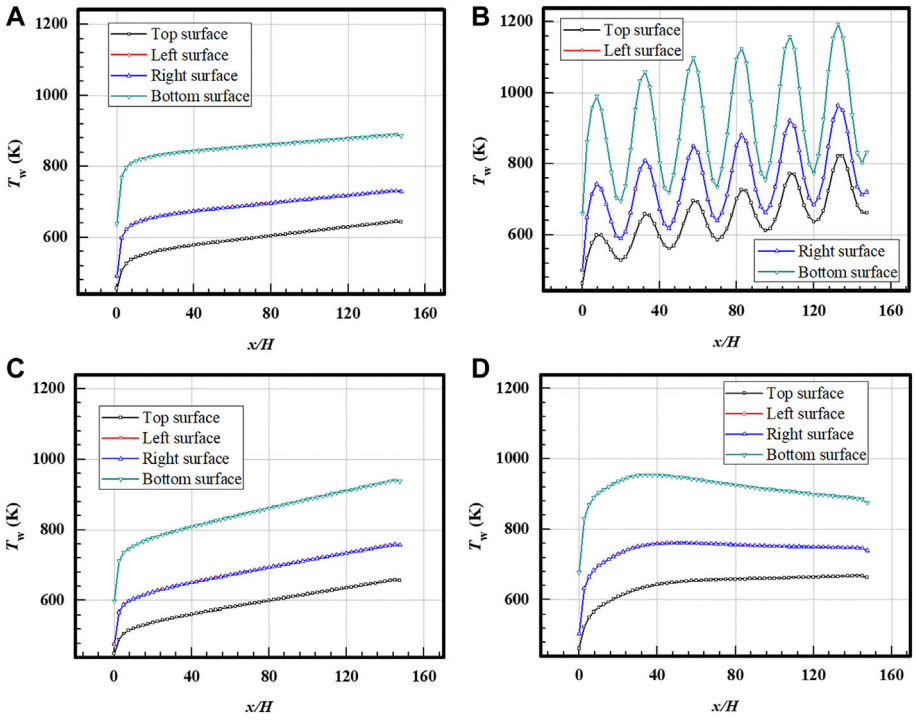

FIGURE 6
Temperature distributions along the streamwise direction on channel walls loaded with different heat flux distributions. **(A)** Case A; **(B)** Case B3; **(C)** Case C2; **(D)** Case D2.

conductivity for the steel is 12.1 W/mK at 290 K and 28.5 W/mK at 1300 K.

Numerical methods and governing equations

The mass, momentum, and energy conversation equations employed are provided in Eqs 1–3, respectively (Yan and Gu 2011; Tang et al. 2020):

$$\frac{\partial \rho}{\partial t} + \frac{\partial}{\partial x_i}\left(\rho u_i\right) = 0, \tag{1}$$

$$\frac{\partial \left(\rho u_i\right)}{\partial t} + \frac{\partial}{\partial x_i}\left(\rho u_i u_j\right) = -\frac{\partial p}{\partial x_i} + \frac{\partial}{\partial x_j}\left[\mu\left(\frac{\partial u_i}{\partial x_j} + \frac{\partial u_j}{\partial x_i}\right) - \frac{2}{3}\delta_{ij}\frac{\partial u_j}{\partial x_i}\right] + \frac{\partial}{\partial x_j}\left(-\rho u'_i u'_j\right) + \rho \vec{g}, \tag{2}$$

$$\frac{\partial}{\partial t}\left(\rho E\right) + \frac{\partial}{\partial x_i}\left(u_i\left(\rho E + p\right)\right) = \frac{\partial}{\partial x_i}\left(\lambda_{eff}\frac{\partial T}{\partial x_i} - \sum_{j'} h_{j'} J_{j'} + u_j\left(\tau_{ij}\right)_{eff}\right). \tag{3}$$

The heat conduction formula is given as follows in Eq. 4 Dai et al. (2013):

$$\frac{\partial}{\partial x_i}\left(\lambda \nabla T\right) = \rho c_P \frac{\partial T}{\partial t}. \tag{4}$$

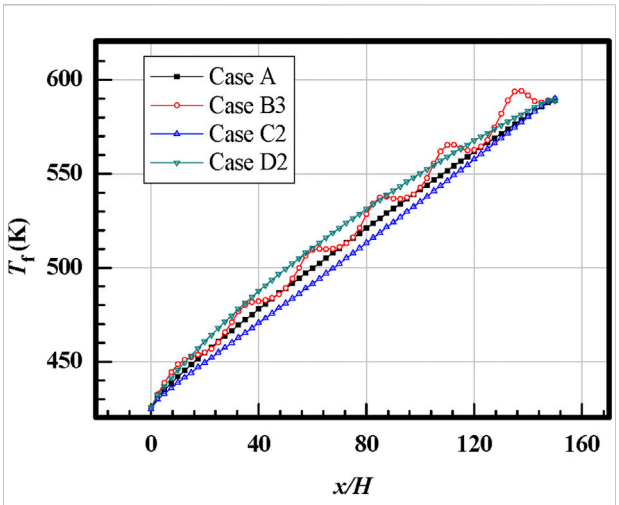

FIGURE 7
Fluid temperature distributions along the streamwise direction for cases loaded with different heat flux distributions.

A verified k–ω SST turbulence model is used in many previous investigations for supercritical fluids and is calculated by Eqs 5–8 Sun et al., (2019):

$$\frac{\partial(\rho k)}{\partial t}+\frac{\partial(\rho u_i k)}{\rho x_i}=P_k-\beta^* k\omega+\frac{\partial}{\partial x_i}\left[(\mu+\sigma_k u_t)\frac{\partial k}{\partial x_i}\right], \quad (5)$$

$$\frac{\partial(\rho\omega)}{\partial t}+\frac{\partial(\rho u_i\omega)}{\partial x_i}=\varphi\rho S^2-\beta\rho\omega^2+\frac{\partial}{\partial x_i}\left[(\mu+\sigma_\omega\mu_t)\frac{\partial\omega}{\partial x_i}\right]+2(1-F_1)\rho\sigma_{\omega 2}\frac{1}{\omega}\frac{\partial k}{\partial x_i}\frac{\partial\omega}{\partial x_i}, \quad (6)$$

$$F_1=\tanh\left[\left[\min\left[\max\left[\frac{\sqrt{k}}{\beta^*\omega y},\frac{500\nu}{y^2\omega}\right],\frac{4\rho\sigma_{\omega 2}k}{CD_{k\omega}y^2}\right]\right]^4\right], \quad (7)$$

$$CD_{k\omega}=\max\left[2\rho\sigma_{\omega 2}\frac{1}{\omega}\frac{\partial k}{\partial x_i}\frac{\partial\omega}{\partial x_i},10^{-10}\right]. \quad (8)$$

The finite volume method is implemented to accomplish the discretization of mass, momentum, and energy conservation equations. A double-precision pressure-based steady solver is adopted to get the flow and heat transfer characteristics of supercritical n-decane. The second-order upwind scheme is applied to the discretization, including pressure, momentum, turbulent kinetic energy, specific dissipation rate, and energy. Also, the SIMPLEC scheme is employed to deal with coupling of pressure and velocity. The convergence of the calculation determines that residuals of the continuity equation, velocity components, k and ω items are below 10^{-5}, and the residual of the energy equation is below 10^{-9}. In addition, the temperature on the heated walls is also monitored to judge the convergence.

Model validation and mesh independence study

For numerical simulation, it is necessary to verify the reliability of the turbulence model and determine the sensitivity of the generated meshes. For this work, turbulence model validation is performed by comparing the predicted result with the result of the previous experiment carried out by Liu et al., (2015). The verification of the turbulence model is performed in a circular tube with an inner diameter of 2 mm. The boundary conditions are set the same as the experiments. Four different turbulence models, namely, k–ε reliable, k–ε RNG, k–ω SST, and transition SST, are employed, and the predicted results are compared with experimental data, respectively. The fluid temperature and wall temperature along the streamwise direction are compared in Figure 4.

As shown in Figure 4, the fluid temperature predicted by different turbulence models overlaps together which is very close to the experimental results. As for wall temperature distributions, the results of the k–ω SST turbulence model also have good agreement with the experimental data, and the error of averaged temperature is less than 5%. From a mechanistic point of view, the k–ω SST model considers the transmission of turbulent tangent stresses, making the SST k–ω model more accurate and reliable to predict a wider range of flows. In addition, the k–ω SST model can predict the flow field well according to the previous research. Therefore, the k–ω SST model is selected.

Figure 5 shows the results of fluid temperature and wall temperature varied along the streamwise direction predicted by the k–ω SST turbulence model. Both the fluid temperature and wall temperature increase along the streamwise direction, and the wall temperature is larger than the fluid temperature to provide the temperature gradient. Like the other turbulence models, the fluid temperature distributions predicted by the k–ω SST model are highly consistent with the experimental data. For wall temperature, the overall relative error is below 5%, and a relatively large error is found upstream of the tube. It is expected that the large error is caused by the upstream extended channel in the simulation work. Some heat is transferred upstream of the tube by the solid wall of the upstream extended channel, and the temperature increase becomes relatively gentle in the simulations. Overall, the k–ω SST turbulence model has shown enough reliability in the simulations.

A mesh independence study is also performed in this work, and Case A is selected to assess the mesh sensitivity. Also, four kinds of mesh regimes are built, respectively, with a grid number of 3.07, 4.32, 5.98, and 8.01 M. Area-weighted averaged temperature on the heated surfaces and the pressure drop between the inlet and outlet predicted by the different mesh regimes are provided to evaluate the mesh sensitivity, as shown

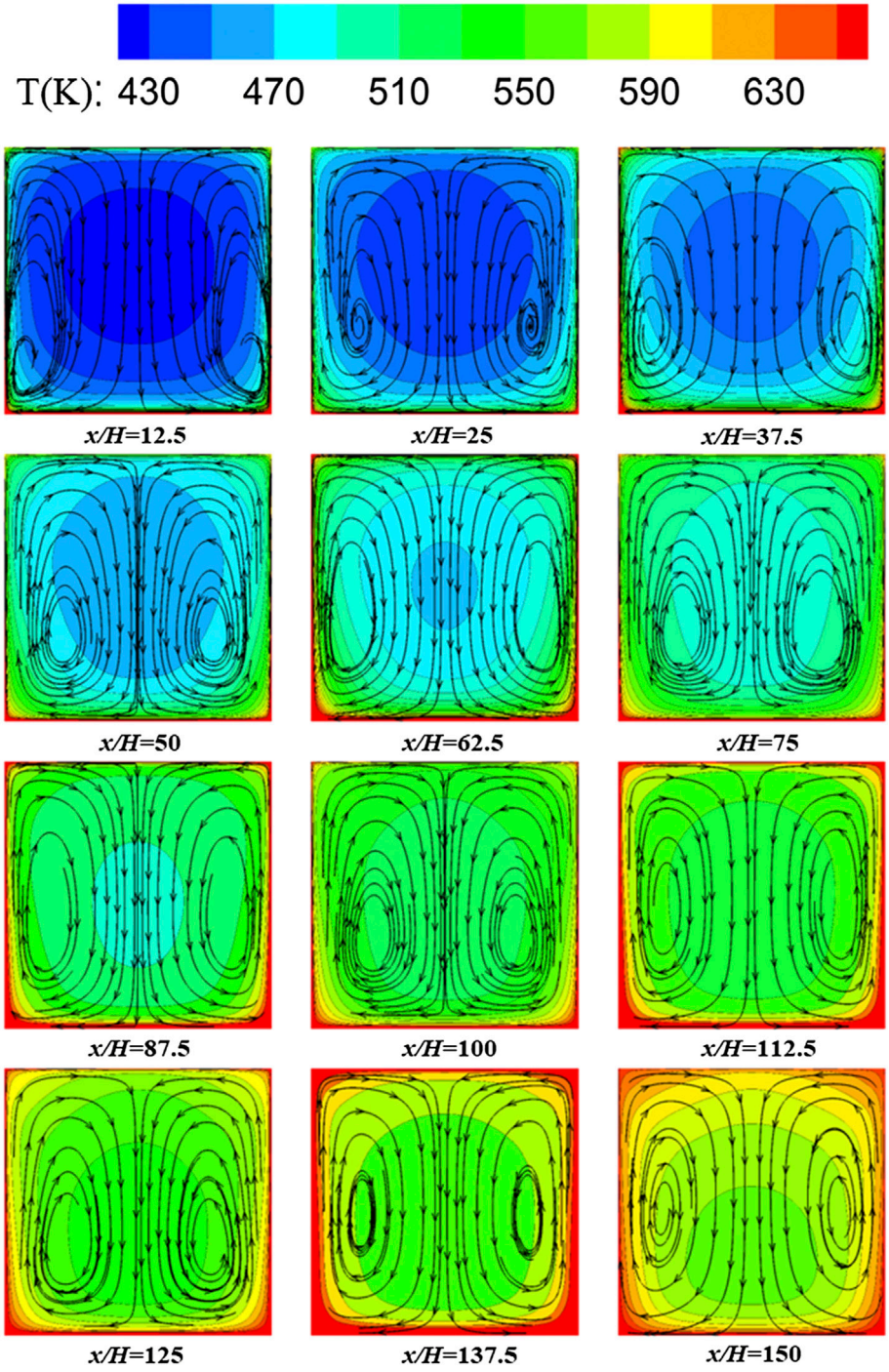

FIGURE 8
Streamlines and temperature contours on y-z sections for the case loaded with sinusoidal heat flux distributions (Case B3).

in Table 2. From the table, the results of all mesh regimes are very close, especially for the mesh regime of 4.32 and 5.98 M. When the grid number increases from 4.32 to 5.98 M, the error of averaged temperature and pressure drop is below 0.01%. Considering calculation accuracy and computational efforts, the mesh regime of 5.98 M is selected.

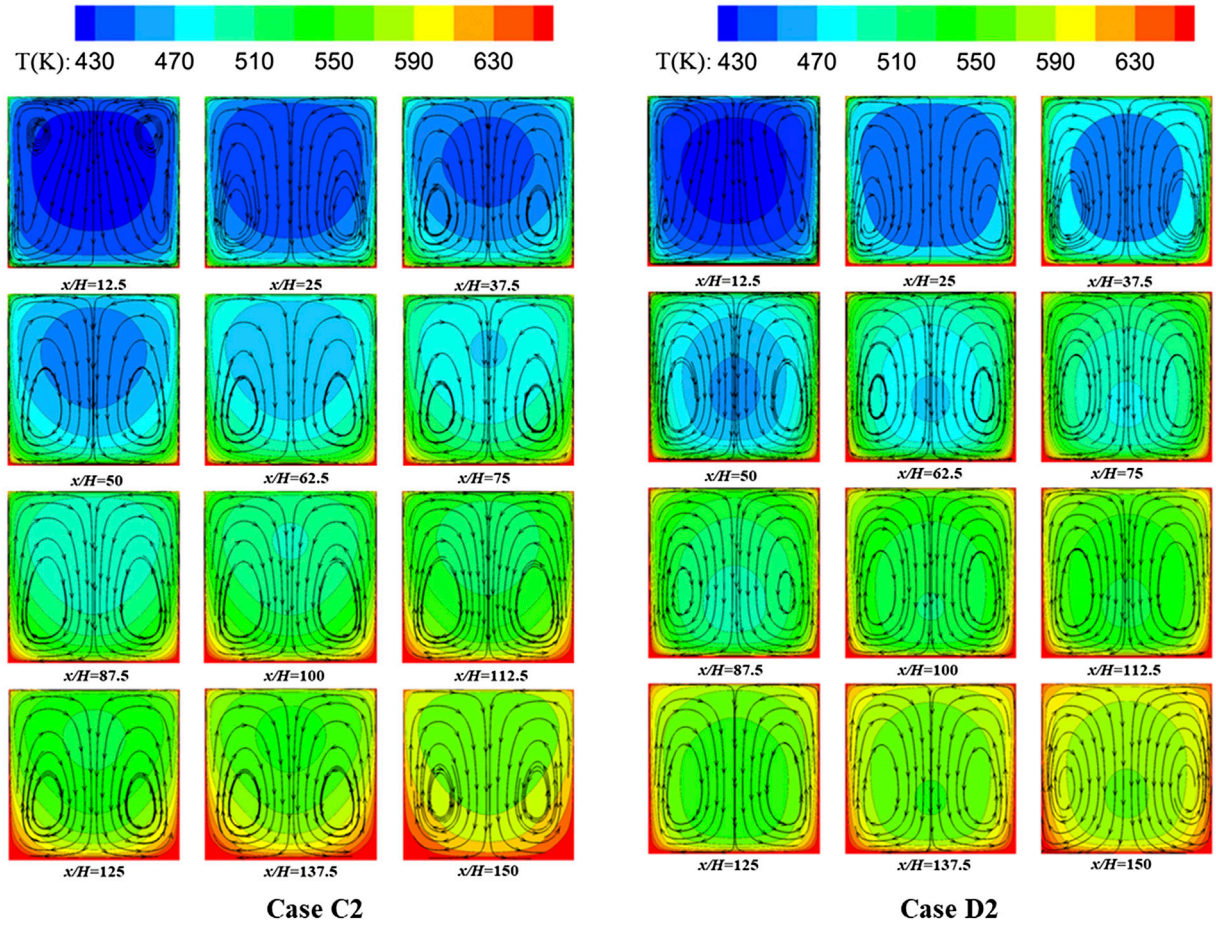

FIGURE 9
Streamlines and temperature contours on *y-z* sections for the cases, respectively, loaded with the increased and decreased heat flux distributions (Case C2 and Case D2).

Results and discussion

Comparisons of temperature distribution

Figure 6 presents wall temperature trends along the streamwise direction loaded with different heat flux distributions. Each wall temperature value is obtained by averaging the temperature in the cross section within the solid domain perpendicular to the streamwise direction. A series of cross sections are built along the streamwise direction, and the distribution of wall temperature is displayed. The bottom surfaces are heated, and the highest temperature is obtained. The heat is transferred in the solid material from the sidewalls to the top wall. Therefore, the temperature in the sidewalls (left and right surfaces) is medium, and the temperature on the top surface is the lowest.

In Figure 6, four kinds of heat flux distributions are selected, respectively, Case A, Case B3, Case C2, and Case D2. As shown in Figure 6A (the case loaded with the uniform heat flux distribution), the wall temperature has a relatively constant increased ratio in most locations except for a sharp rise at the inlet. In Figure 6B (the case loaded with the sinusoidal heat flux distribution), the wall temperature distribution exhibits a trend of sinusoidal increase which is corresponding to the heat flux distribution imposed on the walls. It is noted that the period of the increased temperature distribution is consistent with the sinusoidal heat flux distribution. The heated bottom wall also provides the highest temperature distribution. In Figure 6C (the case loaded with increased heat flux distribution), the temperature increases more quickly than that in Case A downstream of the thermal boundary fully developed region. The quickly increased wall temperature is caused by the increased wall heat flux along the streamwise direction. In Figure 6D (the case loaded with a decreased heat flux distribution), the wall temperature distribution first increases quickly upstream and then exhibits stably or slowly decreases downstream.

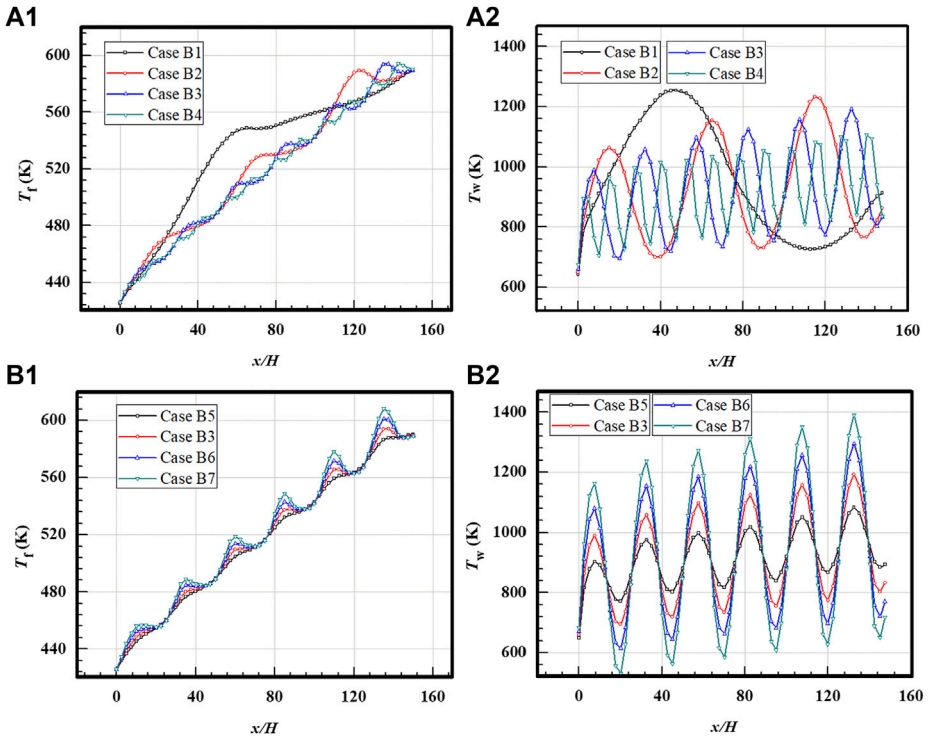

FIGURE 10
Temperature distributions for cases loaded with sinusoidal distributions. **(A1)** Fluid temperature for cases with different cycles. **(A2)** Averaged wall temperature for cases with different cycles. **(B1)** Fluid temperature for cases with different amplitudes. **(B2)** Wall temperature for cases with different amplitudes.

Comparing the four cases with different heat flux distributions in Figure 6, it is found that the wall temperature is greatly affected by the heat flux different distributions. For the uniform case (Case A), the wall temperature increases slowly along the streamwise direction. The distribution trends of the wall temperature have a similarity with the heat flux distribution. When the decreased distribution of heat flux is loaded in Case D, the wall temperature displays a decreased trend after the thermal boundary is fully developed, and the high-temperature region is found upstream. This phenomenon is caused by the large thermal conductivity coefficient in the solid material, and heat diffuses around the solid materials. It is noted that the bottom wall temperature is more affected by the variations of heat flux distributions which are directly loaded with heat flux.

Bulk fluid temperature distributions along the streamwise direction of the aforementioned cases are shown in Figure 7. Each data point in the figure is obtained by area-averaging all the result points of temperature on the *y-z* section, and 61 *y-z* sections are built along the streamwise direction. The distribution of heat flux is totally different for all the cases, and the averaged heat flux is the same. Therefore, the same outlet fluid temperature is obtained by all the cases loaded with different heat flux distributions based on the principle of energy conservation. Similar to the wall temperature, fluid temperature distribution also shows the dependency on heat flux distributions. Compared with the wall temperature, the dependency on heat flux distributions is much weakened because the heat is difficult to be transferred reversed in the streamwise direction. Overall, the wall temperature distribution is more sensitive to the variations of heat flux distributions than the fluid temperature.

Streamlines and temperature contours on *y-z* sections for the case loaded with sinusoidal heat flux distributions (Case B3) are presented in Figure 8. Twelve *y-z* sections are selected with *x/H* ranging from 12.5 to 150. From the figure, low-temperature regions are located at the core part of the mainstream. The high-temperature region is mainly located at the bottom. With flow developing along the channel, the high-temperature region approaches the core part of the mainstream. It is noted that the fluid near the walls is heated fast, and the temperature distribution on *y-z* sections becomes more symmetrical at the end of the heated region. It is concluded that the temperature contours inside the solid walls approach uniform associating with the decreased temperature difference of the heated wall and the

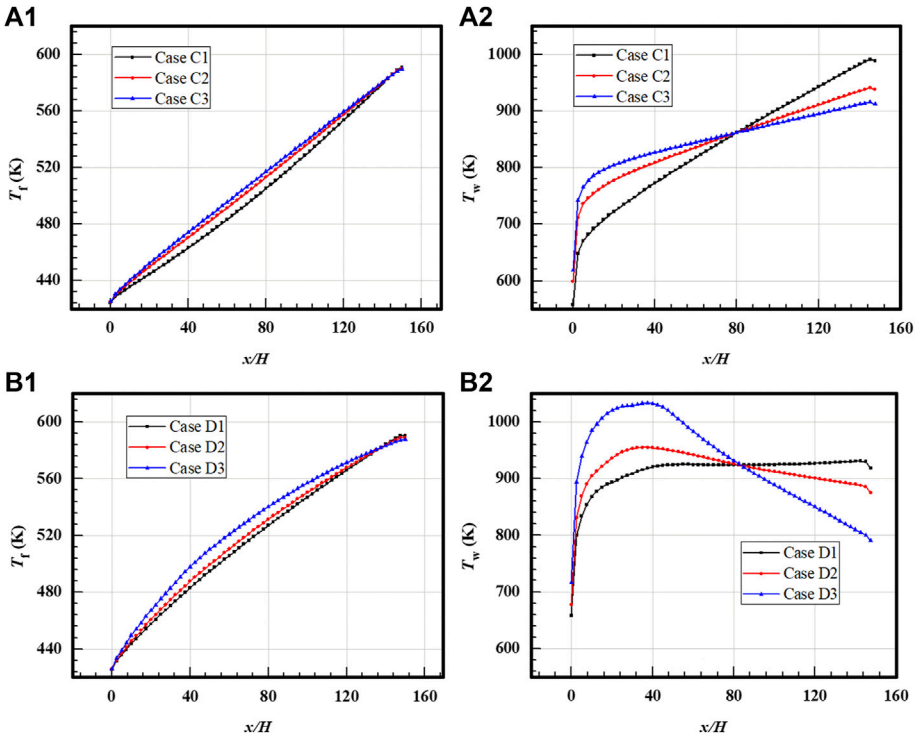

FIGURE 11
Temperature distributions for cases loaded with linear distributions. **(A1)** Fluid temperature for cases with increased distributions. **(A2)** Wall temperature for cases with increased distributions. **(B1)** Fluid temperature for the cases with decreased distributions. **(B2)** Wall temperature for the cases with decreased distributions.

mainstream when the mainstream is heated along the channel. Two counter-rotating vortices are found in the *y-z* sections in Figure 8. The pair of vortices is caused by buoyancy force generated by density variation depending on temperature and gravity effect considered in the computational model. Overall, the mainstream is downward flow in the *y-z* sections because of higher fluid temperature close to the bottom heated wall. The pair of vortices is pushed to the sidewalls, and upward flows are found in the region close to the sidewalls.

Streamlines and temperature contours on *y-z* sections for the cases, respectively, loaded with the increased and decreased heat flux distributions (Case C2 and Case D2) are compared in Figure 9. The same sections in Figure 8 are selected. The temperature characteristics on the *y-z* sections are affected by the heat flux distributions in Case C2 and Case D2. For the case with an increased heat flux distribution, a large temperature difference exists between the bottom wall and the mainstream, even at the end of the heated region. For the case with a decreased heat flux distribution, the fluid near the wall is heated fast because high heat flux is loaded upstream of the channel. After a long heat diffusion process along the channel, the temperature distribution becomes more symmetrical for Case D2.

Effects of related distribution parameters

To reveal the characteristics of regenerative cooling channels loaded with different kinds of heat flux distributions, effects of related distribution parameters are studied in this section, such as the cycle and amplitude of the sinusoidal distributions and the inclination angle of the increased and decreased distributions.

Figure 10 presents temperature distribution along the streamwise direction loaded with sinusoidal heat flux distributions with different cycles and amplitudes. Each data is obtained by averaging all the data points of temperature on the *y-z* sections, including fluid temperature (A1 and B1) and wall temperature (A2 and B2). For all the considered cases, the averaged heat flux is set the same. As shown in Figure 10A1 and Figure 10B1, the outlet temperature is kept the same and close to 590 K based on the energy conservation principle. For the cases with different cycles shown in Figure 10A1, the number of heat transfer peaks has an agreement with the cycles of sinusoidal heat flux distributions. Overall, the fluctuations of temperature distribution along the streamwise direction become weakened with the cycles of sinusoidal distributions becoming small even though the same amplitude is applied. When the same cycle is applied, the

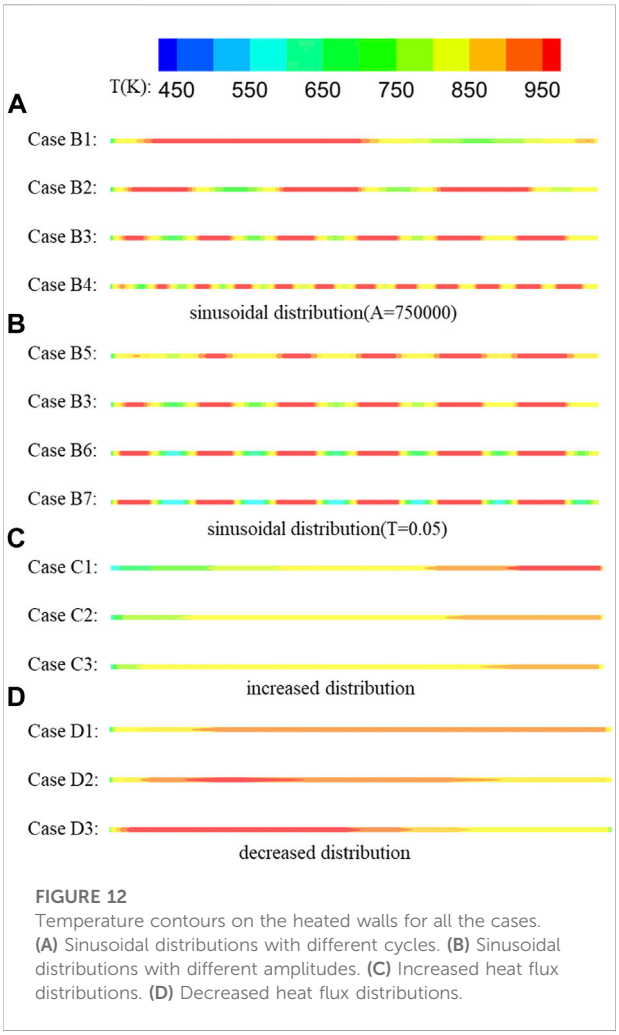

FIGURE 12
Temperature contours on the heated walls for all the cases. **(A)** Sinusoidal distributions with different cycles. **(B)** Sinusoidal distributions with different amplitudes. **(C)** Increased heat flux distributions. **(D)** Decreased heat flux distributions.

fluctuations of temperature distribution are increased with the increased amplitude as shown in Figure 10B1. It is noted that when the fluctuation of heat flux distributions is strong enough, the fluid temperature in some regions exceeds the outlet temperature because of the conjugate heat transfer with the solid walls. Compared with the fluid temperature, the wall temperature distributions display a similar trend with stronger fluctuations as shown in Figure 10A2 and Figure 10B2, which have good agreements with the heat flux distributions. The strongly fluctuated wall temperature interacts with the fluid temperature by coupled heat transfer. Overall, the wall temperature is more sensitive to the change in heat flux.

Temperature distributions for the cases loaded with increased and decreased heat flux distributions at different inclination ratios are provided in Figure 11. Fluid temperature and wall temperature for the cases loaded with increased heat flux distributions are shown in Figure 11A1 and Figure 11A2, and the cases loaded with decreased heat flux distributions are shown Figure 11B1 and Figure 11B2, respectively. Though the same outlet temperature is obtained in all the cases, the variations in the trend of temperature along the streamwise direction are affected by heat flux distributions. For the fluid temperature, the upstream temperature increases slowly and then increases fast along the streamwise direction for the cases with increased heat flux distributions, while the cases loaded with decreased heat flux distributions show a reversed trend. The wall temperature in the outlet region changes greatly for different cases, and it mainly depends on the local heat flux. If the inclination ratio for the cases with increased heat flux distributions is increased, a larger wall temperature is obtained at the outlet of the heated region. When the heat flux distribution is decreased, the upstream wall temperature exceeds the downstream wall temperature at a larger decreased rate. For the cases with a decreased heat flux distribution, the wall temperature becomes relatively stable when a suitable decreased rate is applied.

Temperature contours of the bottom heated walls loaded with different heat flux distributions are displayed in Figure 12. Figure 12A includes the sinusoidal heat flux distributions with the same amplitudes, i.e., Case B1–Case B4. Figures 12B–D, respectively, include Case B5–Case B7, Case C1–Case C3, and Case D1–Case D3. Effects of non-uniform heat flux distributions on wall temperature are more clearly visible in the temperature contours. Several high-temperature regions are found in the cases with the sinusoidal heat flux distributions. With the decreased cycles of the sinusoidal heat flux distributions, the temperature variations become weakened along the streamwise direction, and the overall temperature distribution becomes more uniform, as shown in Case B4. When the decreased heat flux distribution is applied, high-temperature regions move upstream. When a suitable decreased rate is applied, a relatively constant temperature distribution is achieved, as shown in Case D1.

Effects of thermal conductivity

Effects of thermal conductivity are also considered in this work. Fluid temperature and wall temperature loaded with sinusoidal heat flux distributions in the cooling channel with different solid materials are presented in Figure 13. Three kinds of solid materials are used, Al (202.4 W/mK), steel (18.17–26.77 W/mK), and Ti (7.44 W/mK). For the fluid temperature shown in Figure 13A, the same temperature is obtained at the end of the heated wall even with different temperature variations in the heated process. The temperature variations become stronger when a larger thermal conductivity is applied. The phenomenon is also found in the wall temperature distribution shown in Figure 13B. A more fluctuated fluid and wall temperature distribution are found for the cooling channel with low thermal conductivity, i.e., Ti. It is concluded that a larger temperature gradient is found in the solid wall with low thermal conductivity.

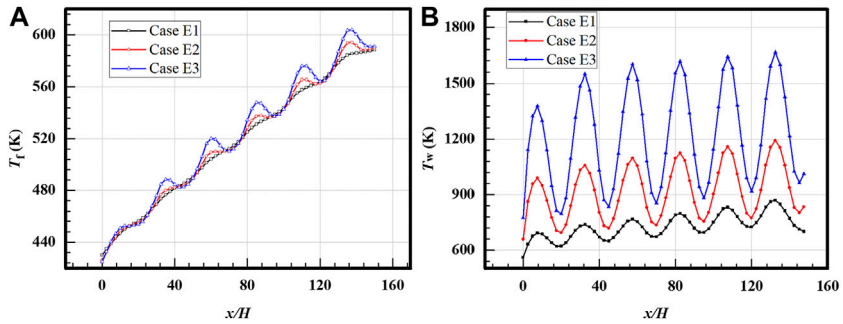

FIGURE 13
Temperature distributions of cases with different thermal conductivities, respectively, Al, steel, and Ti. **(A)** Fluid temperature. **(B)** Wall temperature.

Conclusion

In this work, flow structures and heat transfer of hydrocarbon fuel in the regenerative cooling channels loaded with non-uniform heat flux distributions are investigated. Different kinds of heat flux distributions are applied coupled with solid wall heat conduction, including uniform heat flux distributions, sinusoidal heat flux distributions, increased heat flux distributions, and decreased heat flux distributions. Related parameters of distribution curves are fully analyzed to reveal the flow and heat transfer characteristics loaded with non-uniform heat flux distributions. In addition, effects of gravity and thermal conductivity of solid materials are also considered in this work. Some useful conclusions that emerged from this study are provided as follows:

1) The fluid temperature at the outlet of the heated channel is only determined by the averaged heat flux, and all the regenerative cooling channels achieve the same temperature although loaded with different heat flux distributions. The wall temperature is greatly affected by the heat flux distributions and displays a similar trend with the corresponding loaded heat flux distributions. Compared with the fluid temperature, the wall temperature distribution is much sensitive to the variation of heat flux distribution.
2) The regenerative cooling channels loaded with the sinusoidal heat flux distributions exist in several high-temperature regions according to the peaks of the sinusoidal curve, and the fluctuations of temperature distribution along the streamwise direction become weakened with the cycles of sinusoidal distributions becoming small. The heat flux with linear distributions can change the trend of temperature distribution. For the cooling channel with decreased heat flux distributions, an almost uniform temperature field distribution is achieved at a suitable decreased rate of heat flux, such as Case D1.
3) For the effect of thermal conductivity, a larger temperature gradient is found in the regenerative cooling channel wall with lower thermal conductivity. This work provides a good insight into the characteristics of the flow and temperature field of regenerative cooling channels loaded with non-uniform heat flux considering the conjugate heat transfer effect.

Data availability statement

The original contributions presented in the study are included in the article/Supplementary Material; further inquiries can be directed to the corresponding author.

Author contributions

All authors listed have made a substantial, direct, and intellectual contribution to the work and approved it for publication.

Funding

The research work is financially supported by the start-up funds of Central South University (202045012).

Conflict of interest

The authors declare that the research was conducted in the absence of any commercial or financial relationships that could be construed as a potential conflict of interest.

Publisher's note

References

Brinda, R., Daniel, R. J., and Sumangala, K. (2016). Effect of aspect ratio on the ladder type triangle micro channels employed micro cooling systems. *Int. J. Enterp. Netw. Manag.* 7, 172. doi:10.1504/IJENM.2016.077532

Chen, Y., Wang, Y., Bao, Z., Zhang, Q., and Li, X.-Y. (2016). 'Numerical investigation of flow distribution and heat transfer of hydrocarbon fuel in regenerative cooling panel. *Appl. Therm. Eng.* 98, 628–635. doi:10.1016/j.applthermaleng.2015.12.088

Dai, B., Zheng, B., Liang, Q., and Wang, L. (2013). 'Numerical solution of transient heat conduction problems using improved meshless local Petrov–Galerkin method. *Appl. Math. Comput.* 219, 10044–10052. doi:10.1016/j.amc.2013.04.024

Ding, R., Wang, J., He, Fei, Dong, G., and Tang, L. (2019). 'Numerical investigation on the performances of porous matrix with transpiration and film cooling. *Appl. Therm. Eng.* 146, 422–431. doi:10.1016/j.applthermaleng.2018.09.134

Feng, Y., Cao, J., Li, X., Zhang, S., Jiang, Q., Yu, R., et al. (2017). 'Flow and heat transfer characteristics of supercritical hydrocarbon fuel in mini channels with dimples. *J. Heat. Transf.* 139, 122401. doi:10.1115/1.4037086

Han, Z., Zhou, W., Yu, W., and Jia, Z. (2021). 'Experimental investigation on heat transfer of n-decane-ZnO nanofluids in a horizontal tube under supercritical pressure. *Int. Commun. Heat Mass Transf.* 121, 105108. doi:10.1016/J.ICHEATMASSTRANSFER.2021.105108

Huber, M. (2007). NIST 4. thermophysical properties of hydrocarbon mixtures database: version 3.0, world wide web-internet and web information systems, Online. Available at: https://tsapps.nist.gov/publication/get_pdf.cfm?pub_id=200144 (Accessed August 7, 2022).

Jin, X., Shen, C., Wu, Xianyu., and Yan, Li (2020). 'Numerical study on regenerative cooling characteristics of kerosene scramjets. *Int. J. Aerosp. Eng.* 2020, 1–12. doi:10.1155/2020/8813929

Jing, T., He, G., Li, W., Qin, F., Wei, X., Liu, Y., et al. (2017). 'Flow and thermal analyses of regenerative cooling in non-uniform channels for combustion chamber. *Appl. Therm. Eng.* 119, 89–97. doi:10.1016/j.applthermaleng.2017.03.062

Li H, H., Jiang, Q., Jiang, Y., Zhou, W., Wen, B., Huang, H., et al. (2019). 'Experimental study on the thermodynamic characteristics of the high temperature hydrocarbon fuel in the cooling channel of the hypersonic vehicle. *Acta Astronaut.* 155, 63–79. doi:10.1016/j.actaastro.2018.11.021

Li X, X., Xie, G., Liu, J., and Sunden, B. (2020). 'Parametric study on flow characteristics and heat transfer in rectangular channels with strip slits in ribs on one wall. *Int. J. Heat Mass Transf.* 149, 118396. doi:10.1016/j.ijheatmasstransfer.2019.07.046

Li Y, Y., Xie, G., and Sunden, B. (2020). 'Flow and thermal performance of supercritical n-decane in double-layer channels for regenerative cooling of a scramjet combustor. *Appl. Therm. Eng.* 180, 115695. doi:10.1016/j.applthermaleng.2020.115695

Li, Y., Sun, F., Xie, G., and Jiang, Q. (2018). 'Improved thermal performance of cooling channels with truncated ribs for a scramjet combustor fueled by endothermic hydrocarbon. *Appl. Therm. Eng.* 142, 695–708. doi:10.1016/j.applthermaleng.2018.07.055

Li Z, Z., Wang, H., Jing, K., Wang, L., Yu, L., Zhang, X., et al. (2019). 'Kinetics and modeling of supercritical pyrolysis of endothermic hydrocarbon fuels in regenerative cooling channels. *Chem. Eng. Sci.* 207, 202–214. doi:10.1016/j.ces.2019.06.019

Liu, B., Zhu, Y., Yan, J.-J., Lei, Y., Zhang, B., Jiang, P.-X., et al. (2015). 'Experimental investigation of convection heat transfer of n-decane at supercritical pressures in small vertical tubes. *Int. J. Heat Mass Transf.* 91, 734–746. doi:10.1016/j.ijheatmasstransfer.2015.07.006

Liu, C., Zhang, J., Jia, D., and Li, P. (2022). 'Experimental and numerical investigation of the transition progress of strut-induced wakes in the supersonic flows. *Aerosp. Sci. Technol.* 120, 107256. doi:10.1016/J.AST.2021.107256

Luo, W., Han, H., Jiang, R., Yu, R., and Zhu, Q. (2022). '3D numerical investigation of trans-critical heat transfer enhancement in regeneration cooling channel with crescent rib. *Int. J. Therm. Sci.* 172, 107287. doi:10.1016/J.IJTHERMALSCI.2021.107287

Peszynski, K., and Tesař, V. (2020). 'Algebraic model of turbulent flow in ducts of rectangular cross-section with rounded corners. *Flow Meas. Instrum.* 75, 101790. doi:10.1016/j.flowmeasinst.2020.101790

Pu, H., Li, S., Dong, M., Jiao, S., and Shang, Y. (2018). 'Numerical method for coupled thermal analysis of the regenerative cooling structure. *J. Thermophys. Heat Transf.* 32, 326–336. doi:10.2514/1.t5224

Ruan, B., Huang, S., Meng, H., and Gao, X. (2017). 'Flow dynamics in transient heat transfer of n-decane at supercritical pressure. *Int. J. Heat Mass Transf.* 115, 206–215. doi:10.1016/j.ijheatmasstransfer.2017.08.038

Su, C. H., Gao, F., Zhang, Q., Xiao, H., Zhang, C., and Xia, X. (2020). 'Modeling and analysis of regenerative cooling channels for scramjet engine. *MATEC Web Conf.* 316, 03002. doi:10.1051/matecconf/202031603002

Sun, F., Li, Y., Sunden, B., and Xie, G. (2019). 'The behavior of turbulent heat transfer deterioration in supercritical hydrocarbon fuel flow considering thermal resistance distribution. *Int. J. Therm. Sci.* 141, 19–32. doi:10.1016/j.ijthermalsci.2019.03.027

Tang, L., Cao, Z., and Pan, J. (2020). 'Investigation on the thermal-hydraulic performance in a PCHE with airfoil fins for supercritical LNG near the pseudo-critical temperature under the rolling condition. *Appl. Therm. Eng.* 175, 115404. doi:10.1016/j.applthermaleng.2020.115404

Ulas, A., and Boysan, E. (2013). 'Numerical analysis of regenerative cooling in liquid propellant rocket engines. *Aerosp. Sci. Technol.* 24, 187–197. doi:10.1016/j.ast.2011.11.006

Wang, N., and Pan, Y. (2020). 'Correlation for heat transfer of RP-3 kerosene flowing in miniature tube at supercritical pressures. *Mod. Phys. Lett. B* 34, 2050116. doi:10.1142/S021798492050116X

Wörz, B., Wieler, M., Viola, D., Peter, J., and Rabs, M. (2019). Heat transfer in a square ribbed channel: Evaluation of turbulent heat transfer models. *Int. J. Turbomach. Propuls. Power* 4, 18. doi:10.3390/ijtpp4030018

Xu, K., and Meng, H. (2016). 'Numerical study of fluid flows and heat transfer of aviation kerosene with consideration of fuel pyrolysis and surface coking at supercritical pressures. *Int. J. Heat Mass Transf.* 95, 806–814. doi:10.1016/j.ijheatmasstransfer.2015.12.050

Xu, Q., Lin, G., and Li, H. (2021). 'Evaluation model for fast convective heat transfer characteristics of thermal cracked hydrocarbon fuel regenerative cooling channel in hydrocarbon-fueled scramjet. *Appl. Therm. Eng.* 199, 117616. doi:10.1016/J.APPLTHERMALENG.2021.117616

Yan, B. H., and Gu, H. Y. (2011). 'CFD analysis of flow and heat transfer of turbulent pulsating flow in a tube in rolling motion. *Ann. Nucl. Energy* 38, 1833–1841. doi:10.1016/j.anucene.2011.05.020

Yan, J., Liu, S., Guo, P., and Bi, Q. (2020). 'Experiments on heat transfer of supercritical pressure kerosene in mini tube under ultra-high heat fluxes. *Energies* 13, 1229. doi:10.3390/en13051229

Zhang, M., and Sun, B. (2020). 'Mechanism and influence factor analysis of heat transfer deterioration of transcritical methane. *Int. J. Energy Res.* 44, 9050–9063. doi:10.1002/er.5614

Zhang, S., Li, X., Zuo, J., Jiang, Q., Cheng, K., Yu, F., et al. (2020). Research progress on active thermal protection for hypersonic vehicles. *Prog. Aerosp. Sci.* 119, 100646. doi:10.1016/j.paerosci.2020.100646

Zhang, S., Yu, F., Zhang, D., Jiang, Y., Jiang, Q., Wen, B., et al. (2016). 'Parametric numerical analysis of regenerative cooling in hydrogen fueled scramjet engines. *Int. J. Hydrogen Energy* 41, 10942–10960. doi:10.1016/j.ijhydene.2016.03.176

Zhao, G., Sun, M., Wang, H., and Ouyang, H. (2018). 'Investigation of combustion characteristics in a scramjet combustor using a modified flamelet model. *Acta Astronaut.* 148, 32–40. doi:10.1016/j.actaastro.2018.04.005

Zhu, Y., Peng, W., Xu, R., and Jiang, P. (2018). Review on active thermal protection and its heat transfer for airbreathing hypersonic vehicles. *Chin. J. Aeronautics* 31, 1929–1953. doi:10.1016/j.cja.2018.06.011

Zuo, J., Wei, D., Zhang, S., Jiang, Q., Wen, B., Cui, N., et al. (2021). 'Parametric numerical analysis on the interaction between combustion and hydrocarbon fueled supersonic film cooling. *Aerosp. Sci. Technol.* 111, 106535. doi:10.1016/J.AST.2021.106535

Zuo, J., Zhang, S., Jiang, Q., Wen, B., and Cui, N. (2018). 'Performance evaluation of regenerative cooling/film cooling for hydrocarbon fueled scramjet engine. *Acta Astronaut.* 148, 57–68. doi:10.1016/j.actaastro.2018.04.037

Nomenclature

Latin characters

Cp fluid thermal capacity (J/kg·K)

d turbulent kinetic energy (m^2/s^2)

D outer diameter of the circular pipe (m)

H height of the channel (m)

k turbulent kinetic energy (m^2/s^2)

P pressure (Pa)

T temperature (K)

u velocity (m/s)

x streamwise direction

y spanwise direction

z normal direction

Greek symbols

β thermal expansion coefficient (W/m·K)

λ thermal conductivity (W/m·K)

μ fluid dynamic viscosity (Pa·s)

ρ fluid density (kg/m^3)

ω specific energy dissipation rate (s^{-1})

Subscripts

f fluid

s solid

avg average

frontiers | Frontiers in Energy Research

TYPE Original Research
PUBLISHED 14 September 2022
DOI 10.3389/fenrg.2022.994811

OPEN ACCESS

EDITED BY
Xiao Liu,
Harbin Engineering University, China

REVIEWED BY
Jian Liu,
Central South University, China
Weijiang Xu,
Northwestern Polytechnical University, China
Xingsi Han,
Nanjing University of Aeronautics and Astronautics, China

*CORRESPONDENCE
Wei Du,
hitdw9211@outlook.com

†These authors have contributed equally to this work

SPECIALTY SECTION
This article was submitted to Advanced Clean Fuel Technologies, a section of the journal Frontiers in Energy Research

RECEIVED 15 July 2022
ACCEPTED 23 August 2022
PUBLISHED 14 September 2022

CITATION
Kong Z, Zhang T and Du W (2022), Influence of grooved rib tip structure on tip loss and heat transfer in a gas turbine blade.
Front. Energy Res. 10:994811.
doi: 10.3389/fenrg.2022.994811

Influence of grooved rib tip structure on tip loss and heat transfer in a gas turbine blade

Zhiqi Kong[1†], Tianyi Zhang[1†] and Wei Du[2*†]

[1]Beijing Power Machinery Institution, Beijing, China, [2]School of Energy Science and Engineering, Harbin Institute of Technology, Harbin, China

This study focuses on the effects of three groove tip structures (full rib groove tip, partial rib tip on the suction side, and partial rib tip on the pressure side) on tip leakage flow, aerodynamic characteristics of a cascade, and heat transfer in a gas turbine blade. The groove's width B = 1.6 mm, while the tip clearance is τ = 1.2 mm. Results of the flow parameters, fluid flow, and heat transfer in the recessed channel are discussed. The results show that all ribbed tips obtain more uniform outlet flow angle distribution and higher aerodynamic performance than the plane tips. The total aerodynamic pressure loss of the ribbed tips on the pressure side is the same as that of complete ribbed tips. The evolution mechanisms are different, although both can improve the turbine efficiency. Although the partial rib tip on the pressure side weakens the mixing of the channel vortex and leakage vortex near the trailing edge and has the best control effect on the leakage vortex, the lack of the suction side rib will make it easier for the low-energy fluid to flow into the gap from the front of the suction side, which is not conducive to reducing the leakage flow inside the gap; the full rib tip not only minimizes the tip relative leakage flow and leakage loss but also increases the channel vortex loss. With the complex vortex system in the groove and the rib blocking effect at the leakage outlet, the suction-side rib tip becomes the tip structure with the best leakage flow control effect under the same clearance, but the leakage vortex loss is the highest.

KEYWORDS

turbine blade, squealer tip, tip leakage flow, leakage vortex loss, aerodynamic characteristics

Introduction

The gas turbine has the advantages of compact structure, large thrust weight ratio, rapid start-up regulation, and low carbon emission, and it is widely used in aviation propulsion, gas power generation, ship power, distributed energy supply, and other fields.

As a rotating part, as shown in Figure 1, in order to avoid friction between the rotating blade and the casing, a clearance of 1%–2% blade height is generally retained between them, which is called tip clearance. The tip gap between the high-speed spinning rotor and the stationary casing inevitably results in the leakage of high-temperature gas. The blade tip clearance of the turbine is bound to make the blade tip completely exposed to high-temperature gas, resulting in blade tip oxidation and ablation, increasing the turbine

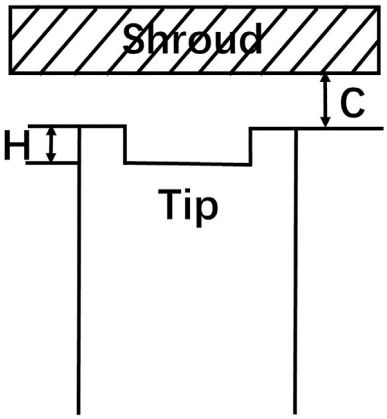

FIGURE 1
Rotor blade groove tip clearance.

energy loss and shortening the service life of the blade. Bunker R S (Bunker, 2001; Bunker, 2006) research shows that the larger the clearance, the greater is the stage efficiency and performance loss. Compared with large engines, the smaller the blade height of small engines, the greater is the proportion of moving blade tip clearance in radial blade height, and the more sensitive are the efficiency and temperature to the change of clearance.

Researchers at home and abroad have carried out a lot of research work on the aerodynamic and heat transfer characteristics of high-pressure turbine blade tips. Predecessors have studied the flow and heat transfer mechanism of the aforementioned different types of tip structures. Heyse et al. (Nyland et al., 1971) compared two kinds of shoulder wall tips: the shoulder wall tip with a single pressure surface rib and the shoulder wall tip with a single suction surface rib. The shoulder wall tip with the rib on the suction surface has an obvious effect of reducing leakage loss than the plane tip. Nho et al. (2012) studied the leakage flow of the double-cogged tip structure and plane tip structure, and the results showed that the losses of the double-cogged tip structure were smaller than those of the plane tip structure. Wang et al. (2015) carried out two-dimensional cascade experiments to study the internal flow field of the shrouded tip. The deflection angle of the leakage flow is very small, while the deflection of the mainstream is large after the outflow. It is verified that there is a mixing loss between the leakage fluid of the shrouded structure and the high-temperature mainstream.

The geometry of the rib will shift the flow vortex system in the groove in the tip area and affect the aerodynamic situation of the cascade. Both active and passive measures, including modifications to gap height or tip geometry type, and tip air cooling (Metzger et al., 1989; Teng et al., 2001; Azad et al., 2002; Ahn et al., 2005; Bunker, 2005; Key and Arts, 2006), have been considered and investigated by researchers to account for the tough aerothermal conditions on the blade tips. Lee and Choi (Lee and Choi, 2010a; Lee and Choi, 2010b) studied the influence of clearance on the aerodynamic losses between flat and squealer tip blades. The results revealed that the cavity squealer tip was beneficial to reduce the leakage flow from the leading edge to the mid-chord region of the blade compared to the plane tip blade. In addition, the tip leakage loss increased with increasing clearance, but the passage vortex loss did not change significantly in a cavity squealer tip blade. Metzger (Wheeler et al., 2011) researched the heat transfer characteristics of blade tip clearance of static grooves under different Reynolds numbers and aspect ratios through an experimental method. The deeper the groove, the smaller is the heat transfer coefficient. Park et al. (2015) analyzed the influence of the number of grooves on the heat transfer and flow of the blade tip structure. The research shows that increasing the number of grooves is beneficial to weakening the total pressure loss coefficient, and adding transverse ribs is beneficial to reducing the heat transfer coefficient of the leading edge. Tallman (2004) studied the rib tip before and after improvement by numerical simulation. The results indicate that pressure edge rounding will increase the leakage flow, while suction edge rounding will undermine the leakage vortex. The improved method of the grooved blade tip proposed by Mischo et al. (2011) can greatly lower the reflux intensity in front of the groove and improve the loss in the gap and the heat transfer characteristics of the blade tip.

In the process of studying the corresponding leakage flow mechanism of the tip structure and vortex evolution, predecessors are also exploring the factors that have a great impact on blade performance. Heyes et al. (1992) experimentally investigated the tip leakage performance of a linear cascade with various tip geometries, including plain tips and pressure-side (PS) and suction-side (SS) squealer tips. The results showed that the squealer tip, especially the suction-side form, helped control the leakage flow and leakage loss. Key and Arts (2006), respectively, studied the leakage flow of the plane tip structure and grooved tip structure at high speed. The results show that slight backflow occurs in the groove. The grooved blade tip has a stronger weakening effect on the tip leakage vortex than the plane blade tip and causes the secondary flow of the channel to deflect to the blade tip, which can further reduce the total pressure loss at the outlet. Lee et al. (2009) measured the internal flow field and total pressure loss of different rib heights at the groove tip under different clearance dimensions and the same tip clearance. In the case of the same gap size, the higher the rib height, the smaller the total loss, the closer the rib height, and the higher the efficiency. Bunker et al. (Azad et al., 2000) studied the change of heat transfer at the rib tip after changing the rib height under the plane cascade. In 2000, Azad et al. (Newton et al., 2006) conducted experiments on the surface heat transfer characteristics of the GE-E3 grooved blade tip. Newton (Kang and Lee, 2016) and Krishnababu et al. (Virdi et al., 2015) compared the heat transfer and flow characteristics of the plane blade tip, partial rib blade tip

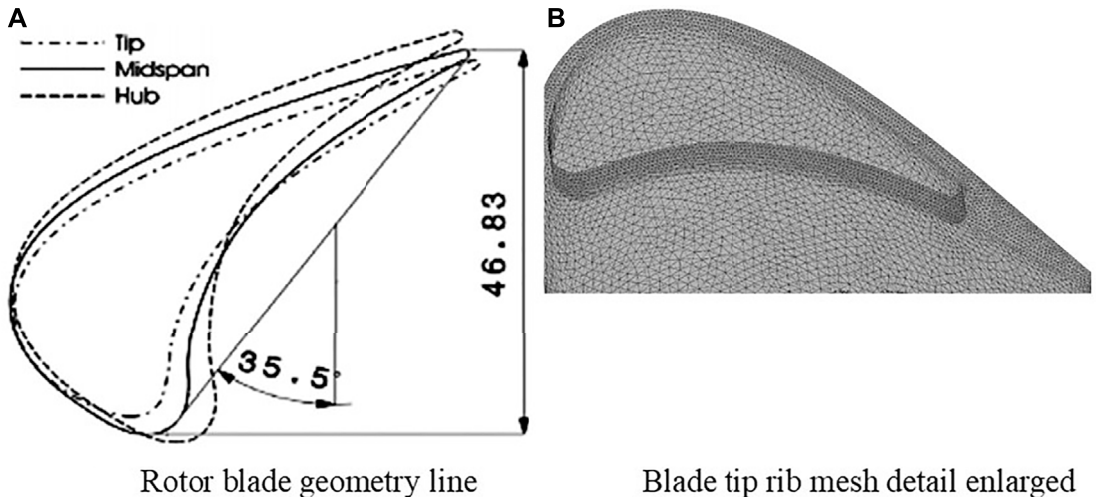

FIGURE 2
Physical model and mesh detail. **(A)** Rotor blade geometry line. **(B)** Blade tip rib mesh detail enlarged.

TABLE 1 Geometric parameters of different sections of the model.

Blade profile parameter	Tip section value	Midsection value	Bottom section value
Number of blades		54	
Inlet geometric angle [°]	40.7	52.4	60.9
Outlet geometric angle [°]	−67.4	−66.6	−65.4
Axial chord length [mm]	43.41	46.83	50.08
Leaf height [mm]	46.54	42.47	38.40
Throat diameter [mm]	16.08	14.42	13.25
Throat area [mm^2]		54780.5	
Inlet angle [°]		45	
Pitch [mm]		46.3	
Groove width [mm]		1.6	

on the single suction side, and full rib blade tip. The leakage flow of the grooved blade tip is lower than that of the plane blade tip, the strength of the leakage vortex is weaker, the heat transfer coefficient is lower, and the rib on the suction side will enhance the leakage flow.

Computational models

The physical model and mesh detail are presented in Figure 2. The blade prototype is LISA 1.5 with high power and a low aspect ratio first stage rotor blade of the turbine. Considering blade distortion, a three-dimensional blade is formed. The LISA 1.5 axial turbine in the turbomachinery Laboratory of the Federal University of Technology in Zurich was obtained by Dr. Behr (Yamamoto et al., 1995) after improving the original Lisa stage 2 turbine. His study records the complete blade geometry and experimental data in detail. The specific geometric parameters at different sections are shown in Table 1. The structural diagram of the three grooved blade tops used in this study is displayed in Figure 3.

Numerical analysis

Boundary conditions

The boundary conditions for simulation calculation are given in Table 2, and the turbulence model selected the SST

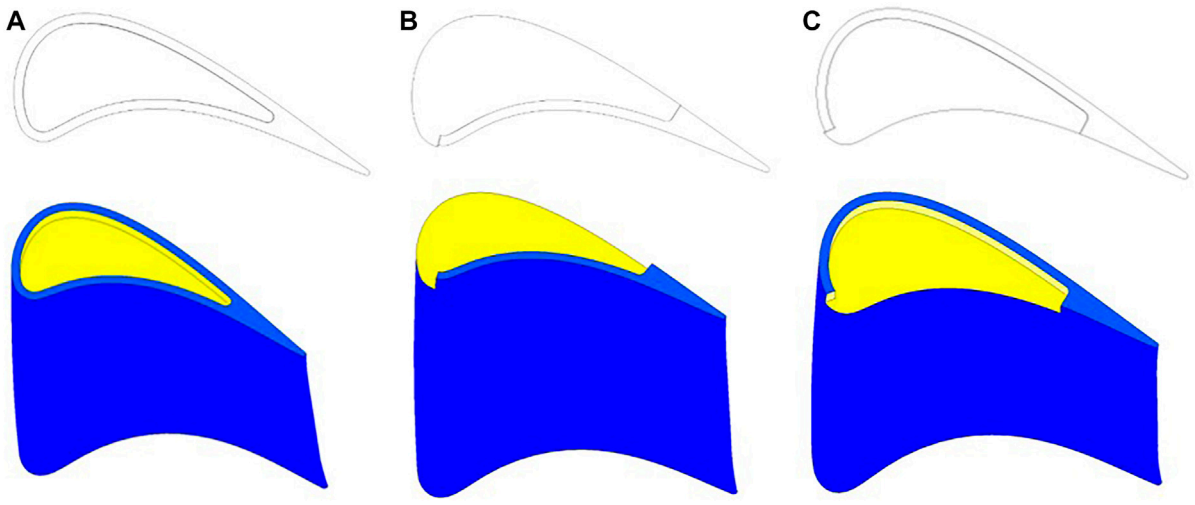

FIGURE 3
Structural diagram of the blade top without the cold air groove. **(A)** Full rib groove tip structure. **(B)** Pressure-side partial rib groove blade tip structure. **(C)** Suction-side partial rib groove blade tip structure.

TABLE 2 LISA 1.5 calculation boundary conditions of the turbine blade.

Boundary	Parameter	Numerical value
Inlet	Total temperature	328.152 K
	Total pressure	138576 Pa
	Turbulence intensity	5%
Outlet	Static pressure	99975.8 Pa
Blade	Surface temperature	Adiabatic
Cold air inlet	Total temperature	/
	Mass flow	0 kg/s

k-ω, which added γ-θ transition. We used ideal gas in the calculation. The length of the inlet segment is 1.5 times the string length, and the length of the outlet segment is 2.5 times the string length. In the Boundary conditions part, we have shown the relevant boundary condition. Except for the inlet and outlet, the surface of the blade, hub, and casing are assigned the properties of insulation, no-slip, and smooth wall, respectively. The "Stage" treatment is adopted for the turn-to-static interface.

Mesh generation

Wall-resolved RANS grids with y+<1.2 were applied to the blade wall and casing surfaces (Wang et al., 2018). The grid thickness on the solid wall of the blade of the first layer is 1.0×10^{-5} m, and the number of boundary layers is 15.

Numerical calculation and validation

In this study, the efforts to verify the accuracy of the CFX simulations are conducted. The RMS residuals of the monitored equations (continuity, momentum, and energy) reach the −4th, −5th, and −7th powers of 10, respectively. The geometry used for aerodynamic numerical verification is LISA 1.5. The straight blades formed by stretching the blade tip profile of the high-pressure turbine form three rows of a fan-shaped cascade, and the clearance height is set to 0.68 mm. The total pressure coefficient distributed along the spines at the outlet section of each blade row is compared with the experiment of Behr in 1995. It is found that the calculation results of the three turbulence models used in the simulation are in line with the experimental trend. However, as shown in Figure 4, the k-ε and k-ω models underpredicted the results, the distribution trend, and range of the k-ω SST model with γ-θ transition are in good agreement.

The model used for heat transfer numerical verification is a linear turbine cascade with film cooling. The straight blade was obtained by stretching the blade tip profile of the first stage rotor blade of the GE-E3 turbine and scaling up. The geometric parameters of the calculation model are shown in table 3. The gap height is fixed to $\tau/H = 1\%$, and the length of inlet and outlet sections are 1.5 times and 2.5 times the chord length, respectively. It includes 13 cooling holes, the diameter D of which is 1.29 mm.

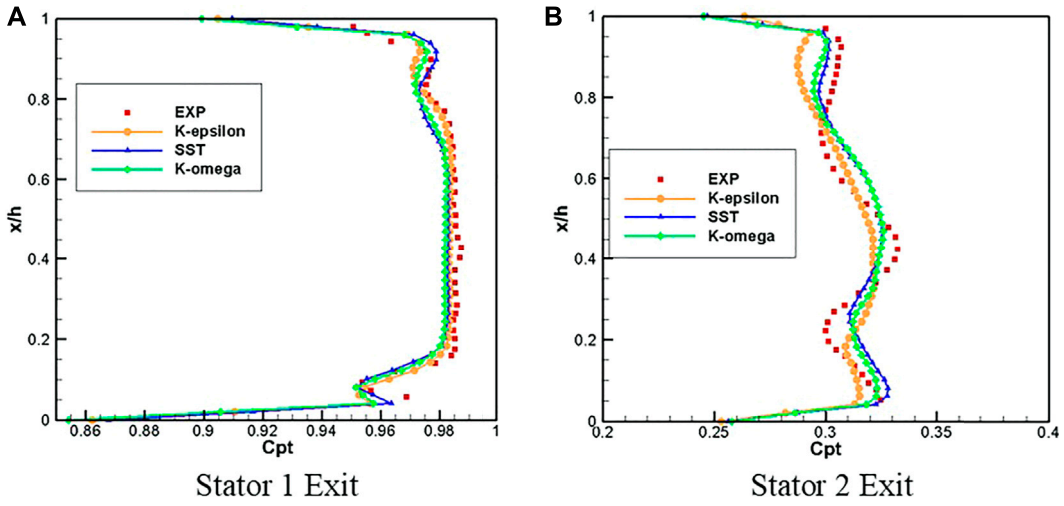

FIGURE 4
Comparison of numerical results with experimental data on the total pressure loss coefficient at the outlet (Behr T.,1995). **(A)** Stator 1 Exit. **(B)** Stator 2 Exit.

TABLE 3 Geometric parameters of the blade tip of the cooling film hole groove.

Blade profile parameter	Numerical value
Leaf height [mm]	122
Axial chord length [mm]	86.1
Pitch [mm]	91.5
Inlet geometric angle [°]	32
Tip clearance [mm]	1.97
Groove depth [mm]	5.08
Rib width [mm]	2.29
Cooling film hole diameter [mm]	1.29

Figure 5 shows the proven tip for verification of heat transfer characteristics, Figure 5B, a schematic diagram of the blade tip hole, and the distance between the middle arc film holes is shown in 5D. Ignoring the influence of compressibility on heat transfer performance, the heat transfer coefficient h and cooling efficiency at the top of the blade tip rib and the bottom of the groove are calculated and are compared with the plane tip test measured by Kwak under subsonic conditions. In Figure 6, all turbulence models overestimate the h value on the tip surface, especially at the top of the groove rib and near the trailing edge, the predicted results of the k-ε model have the biggest gap with the experimental results, and the range of z1 with high leading edge h is the largest; the high position z3 of the SST turbulence model h is close to the middle of the blade, and the range is the smallest, which is closest to the experimental value. Thus, the k-ωSST model is considered decently acceptable.

Solution method

Steady-state incompressible inviscid fluid flow is controlled by the following equation (Liu et al., 2021):

$$\frac{\partial(\rho\bar{u}_i)}{\partial x_i} = 0. \tag{1}$$

Continuity equation
Momentum equation

$$\frac{\partial(\rho\bar{u}_i\bar{u}_j)}{\partial x_j} = -\frac{\partial\bar{P}}{\partial x_i} + \frac{\partial}{\partial x_j}\left((\mu+\mu_t)\left(\frac{\partial\bar{u}_i}{\partial x_j} + \frac{\partial\bar{u}_j}{\partial x_i}\right)\right). \tag{2}$$

The energy equation for fluid is as follows:

$$\frac{\partial\left(\rho\overline{\mu_j}h_{tot}\right)}{\partial x_j} = \frac{\partial}{\partial x_j}\left(\lambda\frac{\partial T}{\partial x_j} + \frac{\mu_t}{Pr_t}\frac{\partial h}{\partial x_i}\right) + \frac{\partial}{\partial x_j}\left((\mu+\mu_t)\overline{\mu_i}\left(\frac{\partial\overline{\mu_i}}{\partial x_j} + \frac{\partial\overline{\mu_j}}{\partial x_i}\right)\right). \tag{3}$$

The numerical simulation for the fluid flow and heat transfer for the tip leakage flow were conducted with the commercial solver ANSYS-CFX (2019 R2). All predicted quantities were at a steady state. The minimum convergence criterion for the continuity equation is 1e–6.

Data reduction

The total pressure loss coefficient is defined as follows:

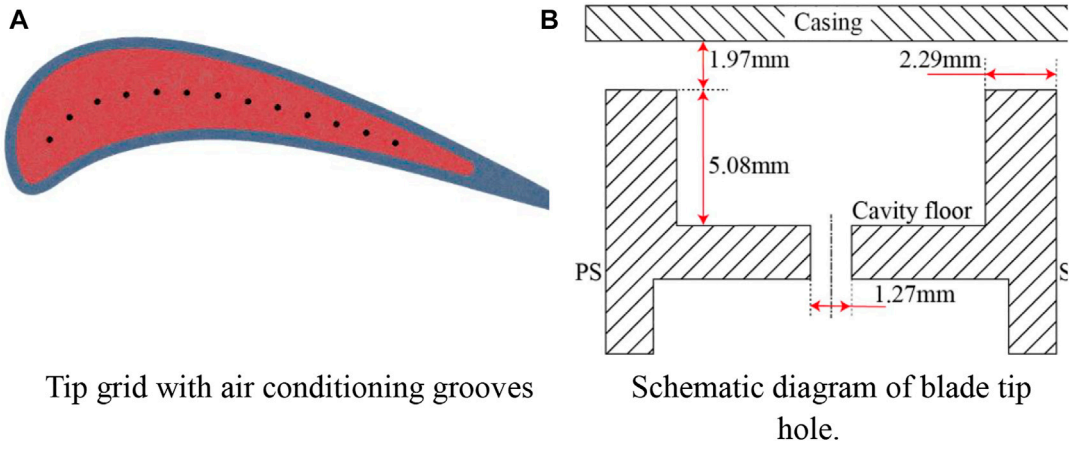

FIGURE 5
Grooved tip for verification of heat transfer characteristics (Nyland T W, Englund D R, Anderson R C,1971). **(A)** Tip grid with air conditioning grooves. **(B)** Schematic diagram of the blade tip hole.

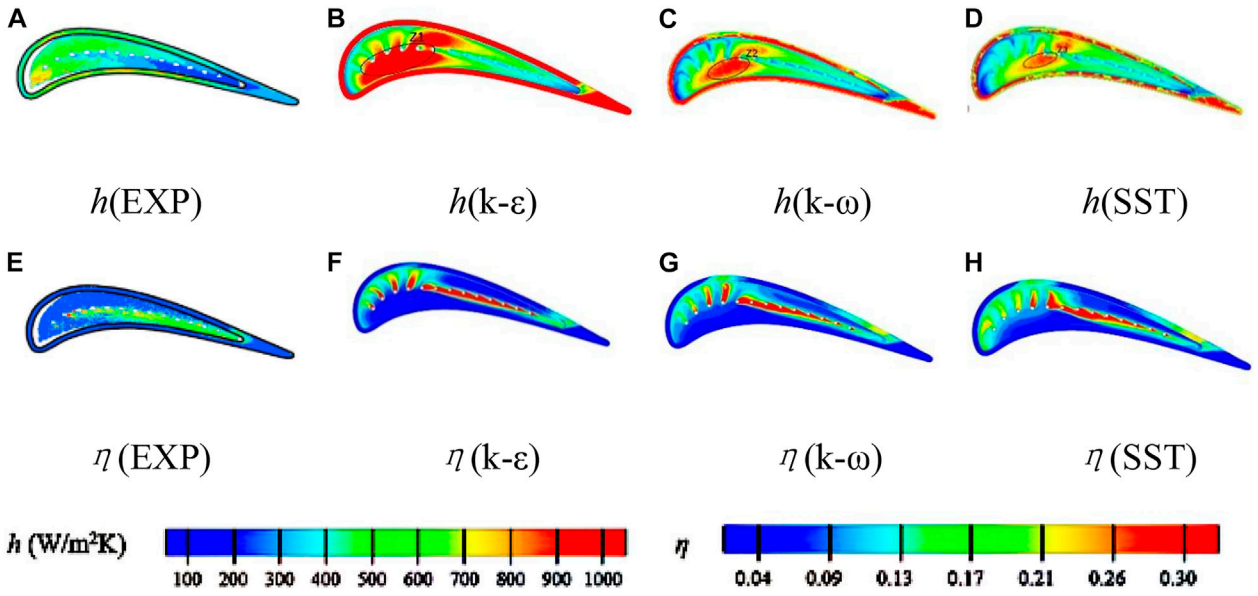

FIGURE 6
Thermodynamic verification: **(A–D)** h and **(E–H)** η comparison of the tip.

$$C_{pt} = \frac{(p_0^* - p^*)}{\left(p_0^* - \overline{p_l}\right)}, \tag{4}$$

where p_0^* is the total inlet pressure, p^* is the local total pressure, and $\overline{p_l}$ is the average outlet static pressure.

The static pressure coefficient is defined as follows:

$$C_p = \frac{p^* - p_1}{p_0^* - p_1}, \tag{5}$$

where p_0^* is the total inlet pressure,p is the local static pressure, and p_1 is the outlet static pressure.

The energy loss coefficient of the cascade with cooling air is defined as follows:

$$\eta_p = \frac{(G_r + G_B)0.5c_1^2}{G_r H_r + \sum_i G_{Bi} H_{Bi}}, \tag{6}$$

where G_r is the gas flow at the cascade inlet, G_B is the total cooling airflow, c_1 is the average gas flow rate at the outlet, $H_r$is the

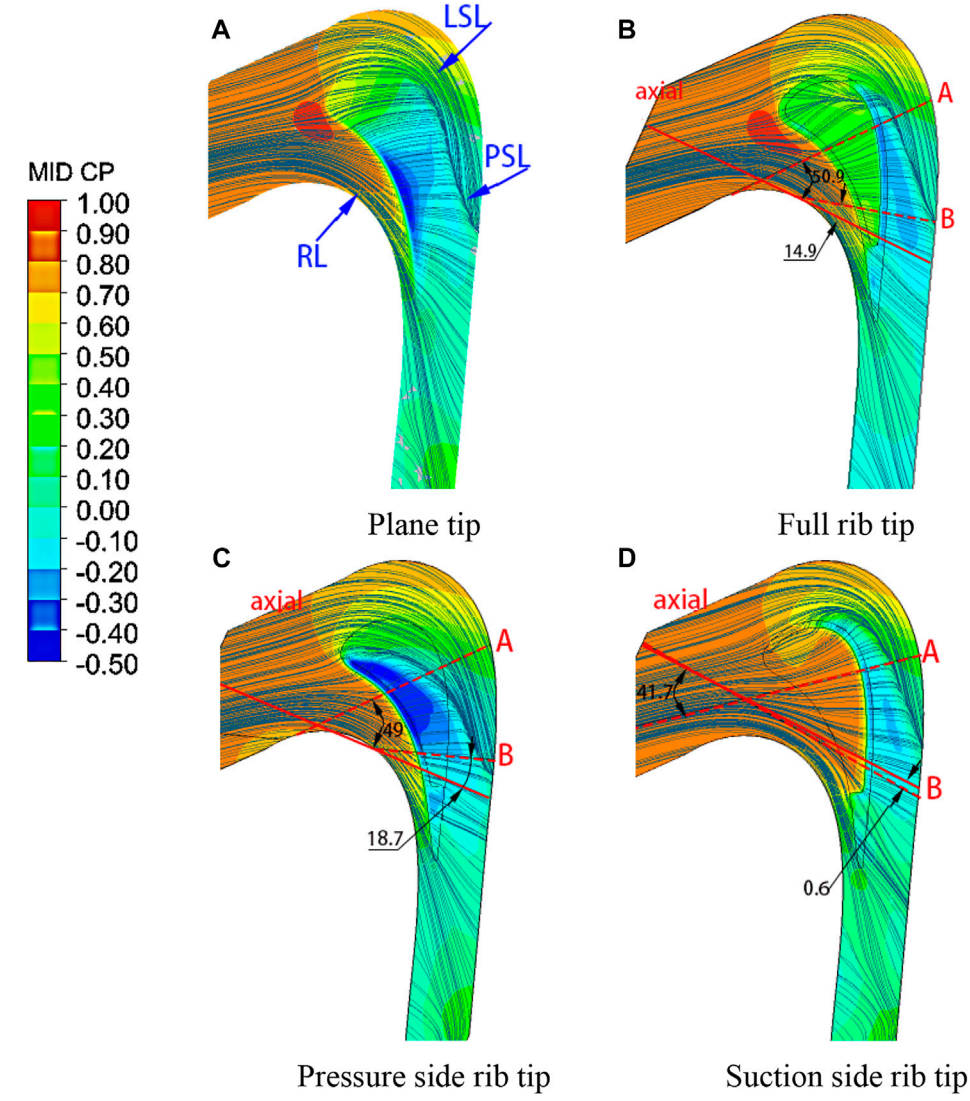

FIGURE 7
Flow line and end wall static pressure distribution in the middle section of blade tip clearance. **(A)** Plane tip. **(B)** Full rib tip. **(C)** Pressure-side rib tip. **(D)** Suction-side rib tip.

available energy of the main airflow, and $H_B$is the cooling gas available energy.

H_r and H_B are calculated according to the parameters in front of the cascade and the average static pressure behind the cascade:

$$H_r = C_{pr}T^*_{r0}\left[1-\left(\frac{p_1}{p^*_{r0}}\right)^{\frac{k_r-1}{k_r}}\right], \tag{7}$$

$$H_{Bi} = C_{pB}T^*_{B0i}\left[1-\left(\frac{p_1}{p^*_{B0i}}\right)^{\frac{k_B-1}{k_B}}\right], \tag{8}$$

where C_{pr} is the total pressure-specific heat capacity of the imported gas, T^*_{r0} is the total gas temperature at the cascade inlet, p_1 is the outlet static pressure, p^*_{r0} is the total inlet gas pressure, k_r is the entropy index of imported gas, C_{pB} is the total pressure-specific heat capacity of cascade cooling air, T^*_{B0} is the total temperature of the cascade cooling air, p^*_{B0i} is the total cold air pressure at the film hole inlet, and k_B is the total cold air pressure at the film hole inlet.

The heat transfer coefficient h is defined (Du et al., 2021a) as follows:

$$h = \frac{q}{T_w - T_0}, \tag{9}$$

where q is the heat flux. T_w and T_0 are considered as the temperature of the isothermal wall and incoming flow, respectively.

The adiabatic film cooling efficiency (Du et al., 2021b) is defined as follows:

$$\eta = \frac{T_{aw} - T_0}{T_c - T_0}, \tag{10}$$

where T_c is the cold air temperature at the inlet. T_w and T_0 are considered as the temperature of the isothermal wall and incoming flow, respectively.

Results and discussion

Aerodynamic performance analysis

Figure 7 shows the flow line and end wall static pressure distribution in the middle section of blade tip clearance. The end wall static pressure program shows that the pressure gradient on the pressure side of the plane tip is larger than that of the ribbed tip, indicating that the speed of leakage flow entering the plane tip clearance is large. Because of the blocking effect of ribs, the ribbed tip forms a low-pressure area on the suction side of greater than 75% axial position. In the ribbed tip structure, the low-pressure area of the pressure-side rib tip is relatively large and distributed at the trailing edge, indicating that the tail pressure gradient and leakage flow turning angle are the largest. The pressure distribution at the full rib tip is relatively uniform. As shown in Figure 7, the flow line in the middle section of the gap shows that the blade tip flow is divided into three flow zones, the leakage flow zone, channel flow zone, and buffer zone, with three flow boundaries: attachment line RL, leakage flow off-line LSL, and channel flow off-line PSL. As shown in Figures 7B, the full rib and in Figures 7C the single pressure-side rib tip, the low-speed fluid in the cascade channel area rushes into the gap and mixes with the leakage flow, resulting in the separation of the leading edge of the blade tip. The LSL is close to the suction side, which shows that the two tips can improve the leakage flow, and the control effect on the pressure rib tip is better. The LSL position of the suction rib tip is the most forward and farthest from the suction side, indicating that the air mixing is the strongest, and the range of leakage vortex is the largest.

Consequently, based on the aforementioned analysis, the following conclusions can be drawn.

(1) Compared with the flat blade tip, the full rib tip and pressure-side rib tip have a better ability to weaken the leakage vortex;
(2) The pressure-side rib tip has the best control effect on the leakage vortex;
(3) The suction-side rib tip is not conducive to the control of the leakage vortex.

As shown in Figure 7, in order to deeply analyze the tip leakage flow, sections "A" and "B" parallel to the direction of the tip leakage flow streamline.

The total pressure loss distribution diagram can reflect the flow state of leakage flow in the blade tip complete clearance space and straight cascade channel. Figure 8 is the total pressure loss distribution cloud diagram of section "A" and section "B".

The rib structure will make the leakage vortex size broader and the leakage vortex core lower. As shown in Figure 8B, part of the leakage flow forms a vortex system in the groove, the mixing intensity between the leakage flow and the main flow decreases, and the size of the leakage vortex decreases. As shown in Figure 8C, when the airflow strikes the end wall, it is hindered by the rib on the pressure side to slow down, and a small separation bubble is formed above the rib. The leakage vortex is attached to the rib surface again, the blade tip intrusion flow makes the leakage flow unable to reach the suction side, and the gap leakage flow flows out directly from the suction side without ribs. As shown in Figure 8D, the lack of ribs on the pressure side makes the airflow enter the groove at a high speed, and the ribs on the suction side reduce the leakage flow speed, resulting in a large leakage vortex loss at the gap outlet.

Figure 8 is the total pressure loss distribution cloud diagram of the section "B". The size and loss of the leakage vortex are higher than those in section "A", indicating that the leakage vortex is gradually developed along the flow direction. The position of the vortex core at the ribbed blade tip rises upward, and the leakage vortex is attached to the suction-side surface.

Consequently, based on the aforementioned analysis, the following conclusions can be drawn.

(4) Under the same tip clearance dimensions, the ribbed blade tip effectively reduces the leakage loss;
(5) The pressure-side rib tip has a better control effect on the gap leakage flow.

Figure 9 shows the total pressure distribution cloud diagram at the outlet of the cascade. Generally, the higher the total pressure at the outlet, the lower the loss is. Under the same clearance, the high-pressure area of the full rib tip and pressure-side rib tip is larger, indicating that their loss is lower than that of the suction-side rib tip.

Flow field analysis

Figure 10 shows the streamlined distribution of section "A" and section "B", which intuitively shows the leakage flow in the cascade and the evolution of the internal vortex system.

As shown in Figures 10A, there is a slight backflow in the groove, resulting in the upward lifting of the fluid at the outlet of the gap. The leakage flow forms a leakage vortex outside the rib on the suction side. Along the flow direction, the intensity of the vortex in the groove from a to B weakens, and most of the leakage flow directly passes through the gap on the suction side. As shown in Figures 10B, the stagnation effect of pressure-side ribs reduces the fluid flow rate entering the blade tip clearance. Part of

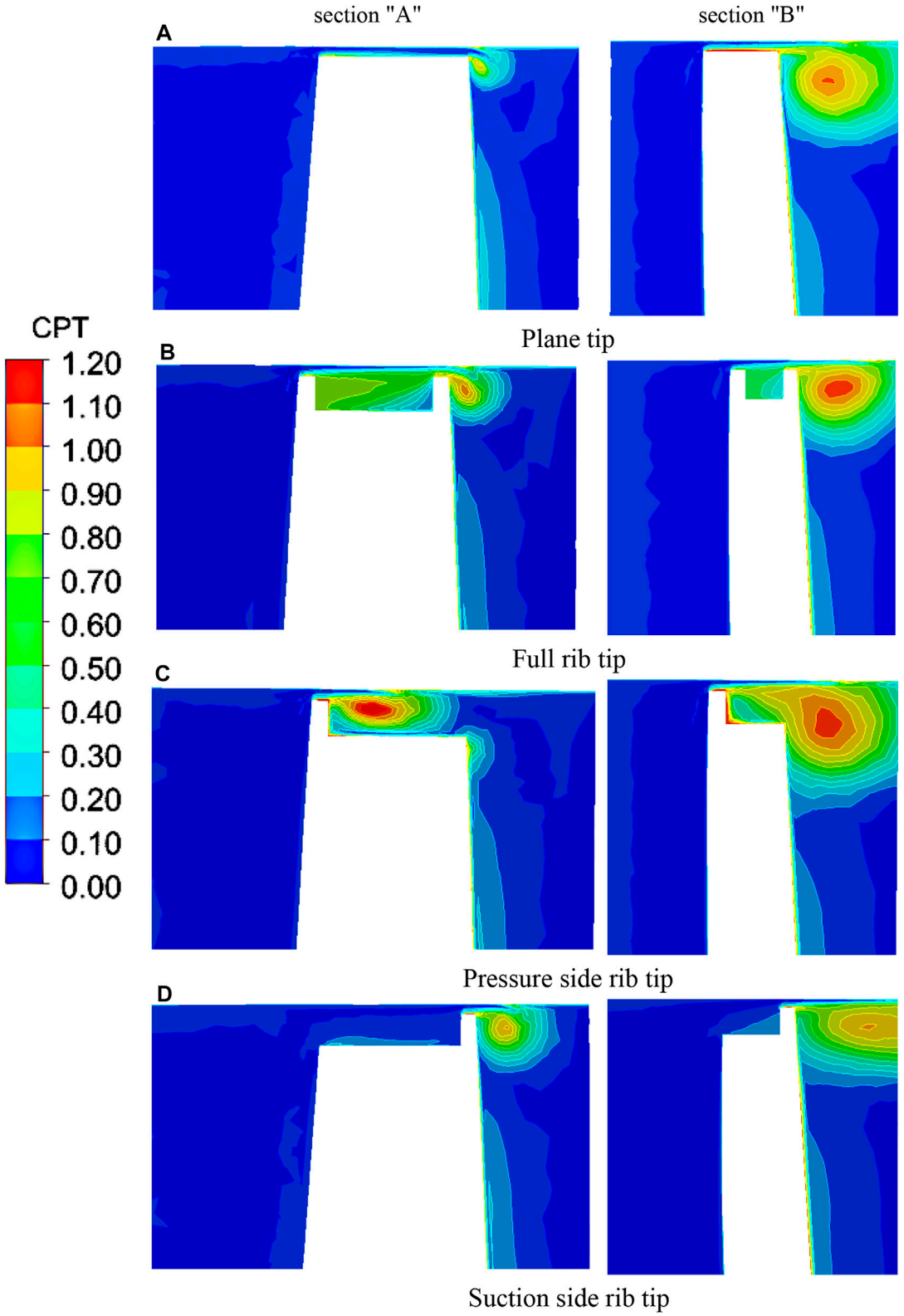

FIGURE 8
Total pressure loss distribution cloud diagram of section "A" and section "B". **(A)** Plane tip. **(B)** Full rib tip., **(C)** Pressure-side rib tip. **(D)** Suction-side rib tip.

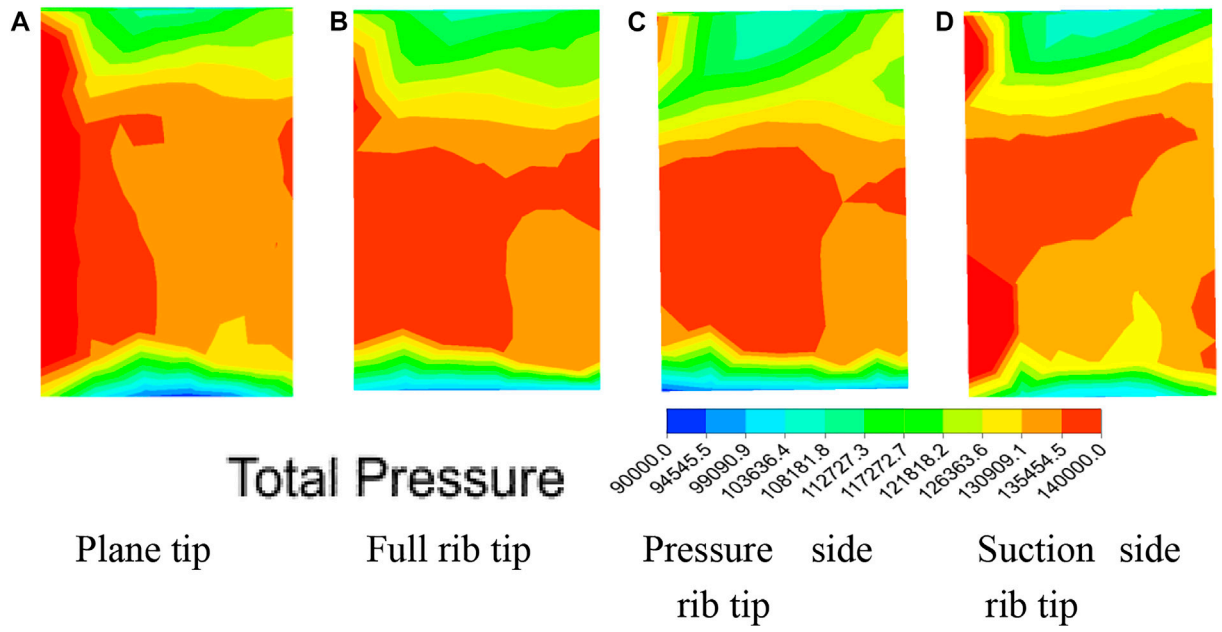

FIGURE 9
Total pressure distribution cloud diagram at the outlet. **(A)** Plane tip. **(B)** Full rib tip. **(C)** Pressure-side rib tip. **(D)** Suction-side rib tip.

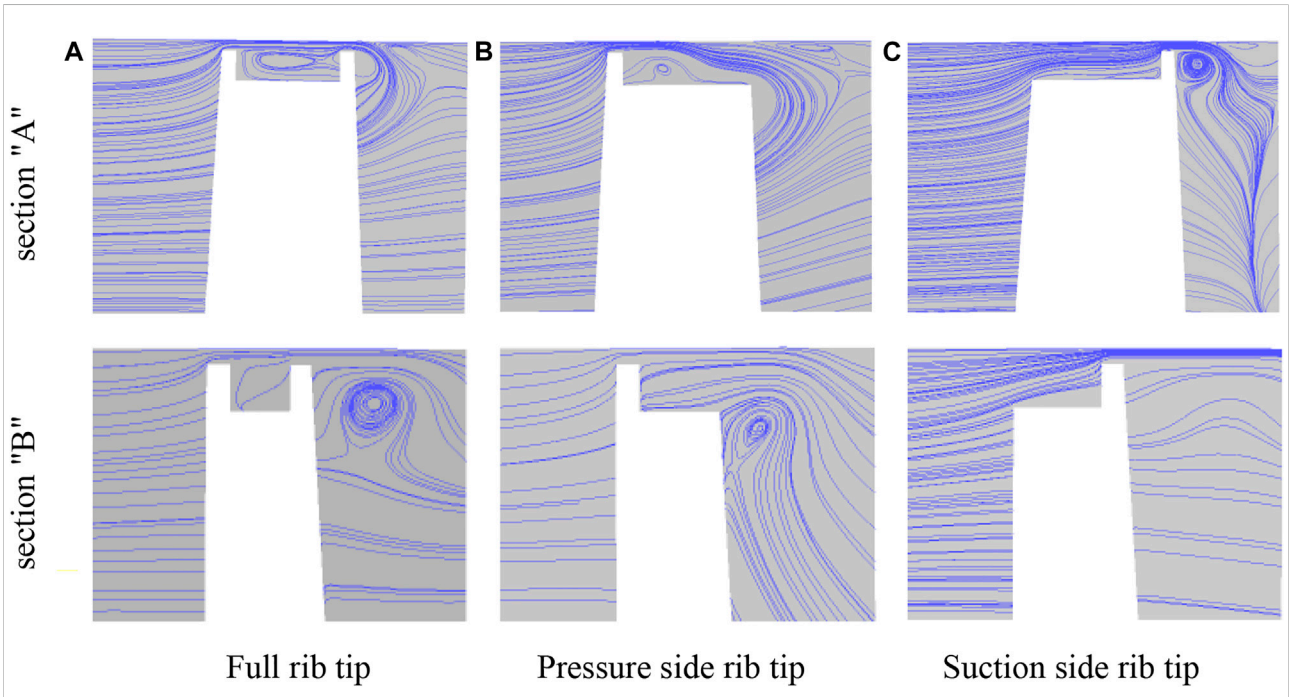

FIGURE 10
Streamline distribution of sections "A" and "B". **(A)** Full rib tip. **(B)** Pressure-side rib tip. **(C)** Suction-side rib tip.

TABLE 4 Outlet aerodynamic parameters of different non-cooled tip structures.

Non cooled tip structure	Total pressure loss at the outlet	Relative leakage flow [kg/s]
Plane tip	0.1583	0.008316
Full rib groove tip	0.145005	0.008010
Pressure-side rib tip	0.144804	0.010190
Suction-side rib tip	0.147401	0.004066

the leakage flow enters the groove cavity in the form of a wall jet to form a relatively developed vortex system. The mixing process of the tip intrusion flow and pressure-side leakage flow at A is intensive, resulting in the leakage flow being unable to reach the suction side. The situation at tail edge B is similar to that of the full rib blade tip, the flow perpendicular to the bottom of the groove appears on the suction side, the strength of the leakage vortex outside the suction side is weakened, and the vortex core position is the lowest. As shown in Figure 10C, the loss of ribs on the pressure side leads to large flow velocity, but the vortex system in the groove is underdeveloped, and a miniature vortex is formed at the junction of the suction-side rib and the bottom of the groove. The strength of the leakage vortex outside the suction side is much stronger than that of the other two blade tips because part of the fluid impacts the suction-side rib, and the vortex core position is closer to the suction-side wall.

Aerodynamic loss evaluation

As aerodynamic losses affect aero-engine performance and efficiency, this section discusses the influence of groove tip structures and leakage flow rates on these losses. The total pressure loss coefficient is defined as follows:

$$C_{pt} = \frac{\left(p_0^* - p^*\right)}{\left(p_0^* - \overline{p_l}\right)}, \tag{11}$$

where p_0^* is the total inlet pressure, p^* is the local total pressure, and $\overline{p_l}$ is the average outlet static pressure.

According to the aforementioned analysis, under the same tip clearance, the non-cooled ribbed tip structure will not only affect the leakage flow but also cause changes in the leakage vortex and channel vortex. Table 4 shows the effects of different tip structures on aerodynamic parameters such as total loss and relative leakage flow of the cascade.

It can be seen from the aforementioned table that under the same clearance conditions, the loss of the structure after adding ribs to the blade tip is smaller than that of the plane blade tip, and the total pressure loss at the outlet of the rib tip on the pressure side is the smallest, about 0.144804. The total aerodynamic pressure loss of the rib tip on the pressure side is basically the same as that of the full rib tip, which is considerably lower than that of the rib on the suction side, and the maximum tip loss is 0.147401.

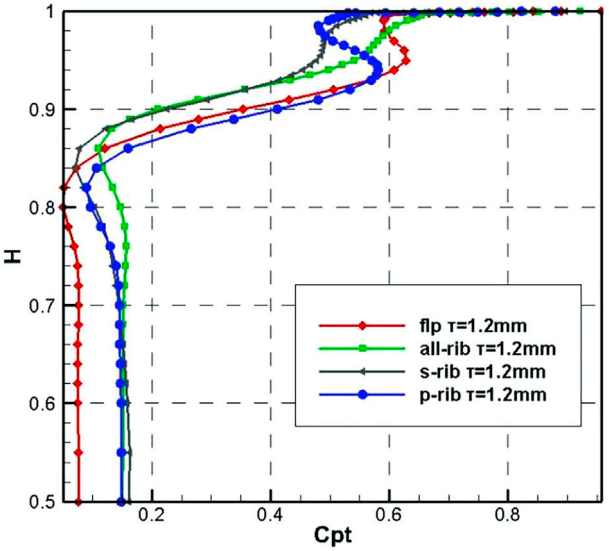

FIGURE 11
Average total pressure loss coefficient of pitch is distributed along the blade height.

In terms of relative leakage flow, adding ribs to the plane blade tip will form an air seal on the gap, but the rib blade tip on the pressure side is not conducive to reducing the leakage flow. The leakage flow in the gap is the highest, about 18.4% more than that of the plane blade tip; although the full rib groove tip has a control effect on the leakage flow, it is not as obvious as the rib tip on the suction side. As described earlier, the rib tip on the suction side becomes the tip structure with the best control effect on the leakage flow under the same clearance by virtue of the complex vortex system in the groove and the rib blocking effect at the leakage outlet, and the relative leakage flow is about 0.004066 kg/s, about 51.1% less leakage than the flat blade tip.

Figure 11 shows the distribution of the total pressure loss coefficient along the blade height after the pitch averaging algorithm at the outlet of the aforementioned four-ribbed blade tip structures. As shown in Figure 10, the high loss area of

0.94–0.98H is dominated by the leakage vortex, and the high loss area of 0.82–0.90H is dominated by the channel vortex; the three kinds of ribbed groove tips reduce the loss around 0.95H blade height and increase the loss near 0.84H blade height, which shows that the addition of ribs at the plane tip can inhibit the tip leakage vortex but promote the development of the channel vortex. Among the three kinds of ribbed tips, the loss value of the whole rib tip is the largest at the blade height of 0.84H, and the loss of the rib groove tip on the pressure side is the smallest near the blade height of 0.95H, which indicates that the rib groove tip on the pressure side has the strongest weakening effect on the tip leakage vortex and also has a certain weakening effect on the channel vortex.

To sum up, under the same clearance condition, the loss of all ribbed groove tips is smaller than that of plane tips, the total pressure loss at the outlet of rib tips on the pressure side is the smallest, but the leakage flow in the clearance is the highest, and the tip loss of ribs on the suction side is the highest, which has the best effect on leakage flow control.

Conclusion

This study compares the plane tip, full rib groove tip, pressure-side rib tip, and suction-side rib tip under the condition of no cold air injection in the same tip clearance, explores the development and evolution process of secondary flow in the tip area, and analyzes the influence of the tip structure on leakage flow and cascade aerodynamic characteristics. The main conclusions are summarized as follows:

(1) Under the same clearance size, all ribbed tips can obtain stronger aerodynamic performance than plane trips. The full rib tip is beneficial to control the relative leakage flow and leakage vortex loss, but the increase in channel vortex loss makes the total pressure loss slightly higher than the pressure-side rib tip.
(2) The pressure-side rib tip has the best control effect on the leakage vortex and the lowest aerodynamic total pressure loss, but it is not conducive to reducing the clearance leakage flow. The suction-side rib tip has the least leakage flow, but the largest leakage vortex loss.
(3) For the internal flow field of the ribbed blade tip, the vortex intensity in the groove decreases along the flow direction, and the vortex intensity of the leakage vortex increases along the flow direction. There is backflow in the groove of the full rib tip, and most of the leakage flow forms a leakage vortex (TLV) directly at the outlet of the suction side.

Data availability statement

The original contributions presented in the study are included in the article/Supplementary Material; further inquiries can be directed to the corresponding author.

Author contributions

ZK, TZ, and WD contributed to the conception and calculation of the study. ZK organized the database. TZ performed the statistical analysis. ZK wrote the first draft of the manuscript. All authors contributed to manuscript revision, read, and approved the submitted version.

Conflict of interest

The authors declare that the research was conducted in the absence of any commercial or financial relationships that could be construed as a potential conflict of interest.

Publisher's note

All claims expressed in this article are solely those of the authors and do not necessarily represent those of their affiliated organizations, or those of the publisher, the editors, and the reviewers. Any product that may be evaluated in this article, or claim that may be made by its manufacturer, is not guaranteed or endorsed by the publisher.

References

Ahn, J. Y., Mhetras, S., and Han, J. C. (2005). Film cooling effectiveness on a gas turbine blade tip using pressure-sensitive paint. *J. Heat. Transf.* 127 (5), 521–530. doi:10.1115/1.1909208

Azad, G. S., Han, J. C., and Boyle, R. J. (2000). Heat transfer and flow on the squealer tip of a gas turbine blade. *J. Turbomach.* 122 (4), 725–732. doi:10.1115/1.1311284

Azad, G. S., Han, J. C., Bunker, R. S., and Lee, C. P. (2002). Effect of squealer geometry arrangement on a gas turbine blade tip heat transfer. *J. Heat. Transf.* 124 (3), 452–459. doi:10.1115/1.1471523

Bunker, R. S. (2001). A review of turbine blade tip heat transfer. *Ann. N. Y. Acad. Sci.* 934 (1), 64–79. doi:10.1111/j.1749-6632.2001.tb05843.x

Bunker, R. S. (2006). Axial turbine blade tips: Function, design, and durability. *J. Propuls. Power* 22 (2), 271–285. doi:10.2514/1.11818

Bunker, R. S. (2005). A review of shaped hole turbine film-cooling technology. *J. Heat. Transf.* 127, 441–453. doi:10.1115/1.1860562

Du, W., Luo, L., Jiao, Y., Wang, S., Li, X., and Sunden, B. (2021). Heat transfer in the trailing region of gas turbines – a state-of-the-art review. *Appl. Therm. Eng.* 199, 117614. doi:10.1016/j.applthermaleng.2021.117614

Du, W., Luo, L., Wang, S., and Sunden, B. (2021). Film cooling in the trailing edge cutback with different land shapes and blowing ratios. *Int. Commun. Heat Mass Transf.* 125 (1), 105311. doi:10.1016/j.icheatmasstransfer.2021.105311

Heyes, F. J. G., Hodson, H. P., and Dailey, G. M. (1992). The effect of blade tip geometry on the tip leakage flow in axial turbine cascades. *J. Turbomach.* 114 (3), 643–651. doi:10.1115/1.2929188

Kang, D. B., and Lee, S. W. (2016). Effects of squealer rim height on heat/mass transfer on the floor of cavity squealer tip in a high turning turbine blade cascade. *Int. J. Heat Mass Transf.* 99, 283–292. doi:10.1016/j.ijheatmasstransfer.2016.03.121

Key, N. L., and Arts, T. (2006). Comparison of turbine tip leakage flow for flat tip and squealer tip geometries at high-speed conditions. *J. Turbomach.* 128 (2), 213–220. doi:10.1115/1.2162183

Lee, S. W., Moon, H. S., and Lee, S. E. (2009). Tip gap height effects on flow structure and heat/mass transfer over plane tip of a high-turning turbine rotor blade. *Int. J. Heat Fluid Flow* 30, 198–210. doi:10.1016/j.ijheatfluidflow.2008.12.009

Lee, S. W., and Choi, M. Y. (2010). Tip gap height effects on the aerodynamic performance of a cavity squealer tip in a turbine cascade in comparison with plane tip results: Part 1-Tip gap flow structure. *Exp. Fluids* 49 (5), 1039–1051. doi:10.1007/s00348-010-0848-6

Lee, S. W., and Choi, M. Y. (2010). Tip gap height effects on the aerodynamic performance of a cavity squealer tip in a turbine cascade in comparison with plane tip results: Part 2-Aerodynamic losses. *Exp. Fluids* 49 (3), 713–723. doi:10.1007/s00348-010-0849-5

Liu, C., Zhang, J., Jia, D., and Li, P. (2021). Experimental and numerical investigation of the transition progress of strut-induced wakes in the supersonic flows. *Aerosp. Sci. Technol.* 120, 107256. doi:10.1016/j.ast.2021.107256

Metzger, D. E., Bunker, R. S., and Chyu, M. K. (1989). Cavity heat transfer on a transverse grooved wall in a narrow flow channel. *J. Heat. Transf.* 111 (1), 73–79. doi:10.1115/1.3250661

Mischo, B., Burdet, A., and Abhari, R. S. (2011). Influence of stator-rotor interaction on the aerothermal performance of recess blade tips. *J. Turbomach.* 133 (1), 011023. doi:10.1115/1.4001134

Newton, P. J., Lock, G. D., Krishnababu, S. K., Hodson, H. P., Dawes, W. N., Hannis, J., et al. (2006). Heat transfer and aerodynamics of turbine blade tips in a linear cascade. *J. Turbomach.* 128 (2), 300–309. doi:10.1115/1.2137745

Nho, Y. C., Park, J. S., Yung, J. L., and Kwak, J. S. (2012). Effects of turbine blade tip shape on total pressure loss and secondary flow of a linear turbine cascade. *Int. J. Heat Fluid Flow* 33 (1), 92–100. doi:10.1016/j.ijheatfluidflow.2011.12.002

Nyland, T. W., Englund, D. R., and Anderson, R. C. (1971). *On the dynamocs of short pressure probes: Some design factors affecting frequency response[R]*. Washington: NASA Lewis Research Center Cleveland. NASA TND-6151

Park, J. S., Lee, S. H., and Lee, W. S. (2015). Heat transfer and secondary flow with a multicavity gas turbine blade tip[J]. *J. Thermophys. Heat Transf.* 30 (1). doi:10.2514/1.T4541

Tallman, J. A. A. (2004). "Computational study of tip desensitization in axial flow turbines part2: Turbine rotor simulations with modified tip shapes [R]," in Proceedings of the ASME Turbo Expo 2004: Power for Land, Sea, and Air, Vienna, Austria. ASME Paper No. GT2004-53919.

Teng, S., Han, J. C., and Azad, G. S. (2001). Detailed heat transfer coefficient distributions on a large-scale gas turbine blade tip. *J. Heat. Transf.* 123 (4), 803–809. doi:10.1115/1.1373655

Virdi, A. S., Zhang, Q., and He, L. (2015). Aerothermal performance of shroudless turbine blade tips with relative casing movement effects [J]. *J. Propuls. Power* 2, 34. doi:10.2514/1.B35331

Wang, J., Sunden, B., Zeng, M., and Wang, Q. (2015). Film cooling effects on the tip flow characteristics of a gas turbine blade. *Propuls. Power Res.* 4 (1), 9–22. doi:10.1016/j.jppr.2015.02.003

Wang, Y., Song, Y., Yu*, J., and Chen, F. (2018). Effect of cooling injection on the leakage flow of a turbine cascade with honeycomb tip. *Appl. Therm. Eng.* 133, 690–703. doi:10.1016/j.applthermaleng.2018.01.090

Wheeler, A. P. S., Atkins, N. R., and He, L. (2011). Turbine blade tip heat transfer in low speed and high speed flows[J]. *J. Turbomach.* 133 (4), 41. doi:10.1115/1.4002424

Yamamoto, A., Kaba, K., and Matsunuma, T. (1995). "Measurement and visualization of threedimensional flows in a linear turbine cascade [R]. ASME Turbo Expo," in Proceedings of the ASME 1995 International Gas Turbine and Aeroengine Congress and Exposition, Houston, TX. ASME Paper No. 95-GT-341.

Glossary

B groove width;

τ tip clearance;

H leaf blade height;

D diameter of cooling holes;

p_0^* total inlet pressure;

p^* local total pressure;

$\overline{p_l}$ average outlet static pressure;

p local static pressure;

p_1 outlet static pressure;

G_r gas flow at the cascade inlet;

G_B total cooling airflow;

c_1 average gas flow rate at the outlet;

H_r available energy of the main airflow;average static pressure in front of the cascade;

H_B cooling gas available energy.;average static pressure behind the cascade;

H_r available energy of the main airflow;average static pressure in front of the cascade;

H_B cooling gas available energy.;average static pressure behind the cascade;

C_{pr} total pressure-specific heat capacity of the imported gas;

T_{r0}^* total gas temperature at the cascade inlet;

p_{r0}^* total inlet gas pressure;

k_r entropy index of the imported gas;

C_{pB} total pressure-specific heat capacity of the cascade cooling air;

T_{B0}^* total temperature of the cascade cooling air;

p_{B0i}^* total cold air pressure at the film hole inlet

k_B total cold air pressure at the film hole inlet.

q heat flux

T_w temperature of the isothermal wall

T_0 temperature of the incoming flow

T_c cold air temperature at the inlet

h heat transfer coefficient

z_1 the area with the high heat transfer coefficient

z_2 the area with the high heat transfer coefficient

z_3 the area with the high heat transfer coefficient

m relative leakage flow

frontiers | Frontiers in Energy Research

TYPE Original Research
PUBLISHED 14 September 2022
DOI 10.3389/fenrg.2022.974508

OPEN ACCESS

EDITED BY
Xiao Liu,
Harbin Engineering University, China

REVIEWED BY
Weihua Cai,
Northeast Electric Power University, China
Ratna Kishore Velamati,
Amrita Vishwa Vidyapeetham University, India
Xiaoqing Qiang,
Shanghai Jiao Tong University, China
Shijun Sun,
Beijing Institute of Technology, China

*CORRESPONDENCE
Xin Du,
xindu@hit.edu.cn

SPECIALTY SECTION
This article was submitted to Advanced Clean Fuel Technologies, a section of the journal Frontiers in Energy Research

RECEIVED 21 June 2022
ACCEPTED 04 August 2022
PUBLISHED 14 September 2022

CITATION
Tao C, Du X, Zhou X, Luo Y, Xu W, Wang S and Wang Z (2022), Effect of compound lean blades on separation structures in high loaded compressor cascades under high subsonic condition.
Front. Energy Res. 10:974508.
doi: 10.3389/fenrg.2022.974508

Effect of compound lean blades on separation structures in high loaded compressor cascades under high subsonic condition

Chuansijia Tao[1], Xin Du[1]*, Xun Zhou[1], Yizhou Luo[1], Wenjuan Xu[2], Songtao Wang[1] and Zhongqi Wang[1]

[1]School of Energy Science and Engineering, Harbin Institute of Technology, Harbin, China, [2]Center for Turbulence Control, Harbin Institute of Technology, Shenzhen, China

Three-dimensional separation is an inherent flow feature in the blade-end corner of compressors passage, which is a primary source of entropy generation and loss. This paper researches the effect of key geometrical parameters (camber angle, solidity, dihedral angle of compound lean blade) and incoming condition (Mach number) on the evolution of corner separation in a low aspect ratio linear cascade. The underlying flow mechanism is explored in detail. The evolution of typical flow characteristics with the variation of inlet Mach number, camber angle and solidity is interpreted. For different blade loading levels, there are different corner separation forms and vortex structures. The influence of dihedral angle on the flow field structure and flow loss is analyzed, thus the effect mechanism of the compound lean blade in different flow environment is explored. Without the trailing edge shedding vortex, positive dihedral angle alleviates the low momentum fluid accumulation and corner separation at the incidence angle about 0°, but exacerbates the deteriorating corner separation at large positive incidence angle. When the trailing edge shedding vortex and the suction surface separating vortex exist together, positive dihedral angle promotes the upstream migration of the trailing edge shedding vortex, which helps to truncate the suction surface separating vortex. This variation of vortex structures is conducive to weaken the development of corner separation and delay corner stall.

KEYWORDS

compressor cascade, high subsonic, high loaded, corner separation, compound lean blades

1 Introduction

As the trend of compressor development is high loading and high efficiency, it's required to increase the pressure ratio per stage and improve flow structure (Tang and Liu, 2020; Tang et al., 2020). With the blade tip speed constraints, enhancing loading per stage is a common method to obtain the pressure ratio per stage (Dickens and Day, 2011). With the low-reaction design, the rotor flow control strategy is simplified (Qiang et al., 2008;

Sun et al., 2018; Sun et al., 2020; Sun et al., 2021), while the inlet Mach number and the static pressure rise of the stator are significantly increased (Sun et al., 2019; Zhang et al., 2019; Sun et al., 2022). Increasing Mach number enhances the compressibility and shear stress of the flow, which results in suction surface entropy generation, wake loss, and possibly boundary layer separation loss increasing rapidly. Moreover, the peak suction surface velocity will reach sonic conditions when inlet Mach number is about 0.7. The supersonic region is terminated by a normal shock in general, which leads to shock loss (Denton, 1993; Shi and Ji, 2021).

With the subsonic inflow, the main method to increase the static pressure rise of the stator is to increase the turning angle. As the blade loading and flow turning is raised, the pressure gradient transverse to the main flow direction enhances (Koller et al., 2000; Kusters et al., 2000; Song et al., 2002; Song et al., 2006; Song et al., 2008). This caused significant cross-passage flow, which transports low momentum fluid into the suction-hub corner region. The low momentum fluid accumulated in the corner region suffers adverse pressure gradient and forms three-dimensional separation, which is an inherent flow feature in the blade-end corner of compressors passage (Zheng et al., 2021; Tang et al., 2020). Large coverage of boundary layer separation and complicated disordered vortex structures significantly impair the stage efficiency (Ju et al., 2020; Li et al., 2020; Zhao et al., 2020; Hu et al., 2021; Vuong and Kim, 2021).

Solidity is one of the most significant geometrical parameters in preliminary design, which have remarkable impact on flow turning capacity, blade loading, and effective operating range (Howell, 1945; Zweifel, 1945; Carter, 1950; Lieblein et al., 1953). With pursuit of empirical solidity inputs in mean-line and through-flow design, performance prediction models containing solidity are necessary for multistage compressor. Bruna et al. (2006) chose inlet flow angle, inlet Mach number, AVDR, Reynolds number, and solidity as model parameters to study profile loss. Sans et al. (2014) updated the correlations for CDA blades. In our previous studies, the influence of maximum thickness position, solidity and camber angle on aerodynamic performance is quantitative assessed, and the optimal maximum thickness position matching solidity and camber angle is provided for high loading stator airfoil (Tao et al., 2021).

Compound lean blade, a kind of 3D stacking, is employed for controlling the corner separation and cutting down the flow losses since 1980s (Wang, 1981). The physical mechanism is that compound lean blade alters spanwise pressure gradient to off-load the endwall region relative to the mid-span section. Weingold et al. (1995) employed controlled diffusion airfoil (CDA) and compound lean stator in a 3-stage compressor. Experimental data verified the effectiveness of the compound lean stator in reducing corner separation and detailed the quantitative efficiency increment in a multistage environment. Gümmer et al. (2001) combined sweep and compound lean and applied this concept to the transonic compressor stators of the BR710 engine and published results. A three-dimensional Navier–Stokes code used for numerical assessment demonstrated that the low momentum fluid near endwall tends to be transported toward mid-span, enhancing the radial mixing process. Nowadays, compound lean blade was associated with other flow control methods, such as boundary layer suction (Song et al., 2006; Ding et al., 2018), vortex generator jet (Li et al., 2016; Li et al., 2017), and non-axisymmetric endwall (Lin et al., 2014). To reveal the universal application conditions of compound lean blade, Xu and Du et al. established performance characteristics prediction models for the compound lean blade and presented the interaction of solidity, aspect ratio and dihedral angle in NACA65 compressor cascade (Xu et al., 2019; Xu et al., 2018). Due to flow complexity, high experimental costs and reducing sharply effective operating range with the increment of Mach number, the systematic investigation on the application conditions of compound lean blade are lacking and worthy of attention in high subsonic flow circumstance.

In this paper, the numerical calculation carried out in abundant low aspect ratio linear cascades has been applied to explore the effect of key geometrical parameters and incoming condition on the evolution of corner separation mechanism. The flow phenomenon in cascades with five camber angles, nine solidities and six dihedral angles is compared under two different incoming flow conditions of medium subsonic (Ma = 0.5) and high subsonic (Ma = 0.8). The underlying pressure fields and vortex structures are revealed subsequently. The typical flow evolution brought by the high subsonic inlet and the high loading blade is observed and explained. For the deteriorated corner separation under high subsonic inlet conditions, the compound lean blade is applied to control the flow field and corner separation. The development law of the flow field with dihedral angle of compound lean blade is discussed in different flow environments. The current research is launched in order to acquire a better understanding of the flow mechanism in high loading cascades, and is of great significance to the guidance of compound lean blade application.

2 Investigation programs and numerical method

2.1 Investigation programs

The investigated cascades are used for the second stage stator of a 3-stage compressor. The airfoil features CDA velocity distribution. The investigation about the selected airfoil has been detailed in reference (Tao et al., 2021). Geometrical parameters are shown in Table 1. The straight blade refers to $\alpha = 0^{\circ}$. Maximum thickness is normalized by chord length. The research ranges cover the usually used values in high subsonic cascade applications. The geometric

TABLE 1 Parameters and flow conditions of research.

Parameters	Value								
Chord b/(m)	0.0242								
Blade height h/(m)	0.0243								
Solidity σ	1.4	1.5	1.6	1.7	1.8	1.9	2.0	2.1	2.2
AVDR	1.25								
Inlet Blade angle β_{1p}/(°)	50°		54°		56°		58°		60°
Outlet Blade angle β_{2p}/(°)	10°								
Camber angle θ/(°)	40°		44°		46°		48°		50°
Maximum thickness c_{max}	4.5%								
Dihedral angle α/(°)	−30° ~30°								

parameters of airfoil geometry are presented in Supplementary Figure S1.

The stacking line of compound lean blade is perpendicular to the chord length direction, consisting of a straight line at mid-span and two Bezier curves in endwall region. The schematic diagram of stacking line is shown in Supplementary Figure S1B, where P_1 and P_2 are the dimensionless control parameters of Bezier curves. The parameters C_1 and C_2 are the compound lean height. According to the results of reference (Ling et al., 2014), the total pressure loss is the lowest when compound lean height is 50% blade height in linear cascade. Therefore, the compound lean height is selected as 50%h in this paper. The parameters α_1 and α_2 are the dihedral angle at hub and shroud respectively. As the stacking line is symmetrical in linear cascade, $P_1 = P_2$, $C_1 = C_2$, $\alpha_1 = \alpha_2$.

2.2 Numerical method and validation

The NUMECA IGG/AutoGrid5 module is applied for structured grids generation (NUMECA International, 2015). The computation domain mesh has a mixed O-and H-block topology, as shown in Supplementary Figure S2. The inlet and outlet of the computational domain are located 100%b ahead of the leading-edge and 100%b behind the trailing-edge, respectively. The measurement plane is located 40%b behind the trailing-edge. The thickness of the first grid layer is 10^{-6} m, and 5 m × 10^{-6} m near the hub and shroud, to insure y^+ <3 at solid boundary and satisfy the solving demands of the selected turbulence model.

The grid independence investigation is carried out including six meshes with 0.6–2.2 million cells. As shown in Supplementary Figure S3, when further refining the mesh with grids number beyond 1.97 million, the results almost have no modification. The spanwise distribution of total pressure loss coefficient and deviation angle of different meshes is drawn in Supplementary Figure S4. When the number of grids is above 1.65 million, the spanwise distribution of total pressure loss coefficient and deviation angle varies with the number of grids not significantly. Therefore, the spanwise node number adopted is 73 in this study, and the total grids number is about 1.97 million.

The code solver ANSYS CFX™ is used to solve the Reynolds-Averaged Navier-Stokes (RANS) equations with the finite volume technique. The equations governing the flow domain are written in a tensor form as follows:

$$\frac{\partial \rho}{\partial t} + \nabla \cdot (\rho U) = 0 \tag{1}$$

$$\frac{\partial (\rho U)}{\partial t} + \nabla \cdot (\rho U \cdot U) = -\nabla p + \nabla \cdot \tau \tag{2}$$

$$\frac{\partial (\rho h)}{\partial t} + \nabla \cdot (\rho U h) = \nabla \cdot (\lambda \nabla T) + \tau \cdot \nabla U \tag{3}$$

where the stress tensor τ, is related to the strain rate by the constitutive equation of the Newtonian fluid as follows:

$$\tau = \mu\left(\nabla U + (\nabla U)^T - \frac{2}{3}\delta \nabla \cdot U\right) \tag{4}$$

A high-resolution scheme was used for the advection scheme and turbulence modeling. The two-equation turbulence models SST coupled with γ-Re_θ transition model was finally chosen for its capability to accurately predict complex flows *Average*

Inlet boundary conditions are prescribed with total pressure (430 kPa), total temperature (440 K) and inflow angle. No-slip and adiabatic conditions are imposed at the solid walls, while translational periodic boundary condition is used in the pitchwise direction. The mass-flow specified at the outlet is modified to achieve Ma = 0.8 at the inlet. Non-reflecting boundary conditions are used at inlet/outlet planes.

The MOGA profile in literature (Song and Ng, 2006; Song et al., 2006) is selected to validate the calculation methods. Inlet total pressure is 121 kPa, while total temperature is 319 K. The inflow angle is 48.4°. No-slip and adiabatic conditions are imposed at the solid walls, while translational periodic boundary condition is used in the pitchwise direction. The Mach number at the inlet is 0.6–0.95, which includes the Mach number of this research. The comparison between

experimental and numerical results at different incoming Mach number is shown in Supplementary Figure S5. It can be seen that the trend of numerical simulation is basically consistent with experiments. The error of losses between numerical simulation and experiments is about 5%–10% and due to the combined effects of CFD under-prediction and AVDR influence.

3 Results discussion

3.1 Effect of mach number on the straight cascades

3.1.1 Performance parameters changing with incidence angle

In order to evaluate the effect of *Ma* on the straight cascades quantitatively, Supplementary Figure S6 shows the performance parameters (total pressure loss coefficient ω and diffusion factor D) at different incidence angles. The mass-averaged total pressure loss coefficient and diffusion factor are determined as follows:

$$D = 1 - \frac{v_2}{v_1} + \frac{\Delta v_u}{2v_1\sigma} \tag{5}$$

$$\omega = \frac{P_1^* - P_2^*}{P_1^* - P_1} \tag{6}$$

where, v_1,v_2, and Δv_u are inlet velocity, outlet velocity and tangential velocity variation. P_1^* and P_1 are total and static pressure at the cascade inlet, while $P_2^*$and $P_2$are total pressure and static pressure at the outlet.

When the camber angle increases, ω and D gradually increase, while the effective operating range gradually narrows. As the Mach number increases from 0.5 to 0.8, ω and D continue to increase, while the effective operating range gradually narrows further. Under high subsonic condition, the effective operating range is less than 1° when camber angle is 50°. By exploring the change of flow with camber angle and Mach number, it is possible to search for methods to maintain a steady working range and to improve the overall performance of high loading cascade.

3.1.2 Distribution of performance parameters

In order to detect in more detail how *Ma* variation affects the distribution of loss, spanwise distribution of total pressure loss coefficient under different *Ma* and θ at $i = 0.5°$are compared in Supplementary Figure S7. It is observed that the rise of camber angle and inlet Mach number increases both the loss near the endwall and the mid-span loss, while the loss near the endwall increases more significantly. This observation means that the coverage of the region affected by the endwall cross-passage flow and the low momentum fluid accumulated in the corner region tends to expand with the increase of *Ma* and θ. On the other hand, the increase of *Ma* and θ enhances the shear stress of the flow, resulting in the entropy generation of the blade.

The variation of axial distribution of surface static pressure coefficient not only reflects the load distribution at different spanwise positions, but also determines the development of boundary layer. The axial distribution of surface static pressure coefficient varies with *Ma* and θ at $i = 0.5°$ are presented in Supplementary Figure S8. It shows that the rise of *Ma* and θ will increase not only the pressure difference between the suction surface and pressure surface, but also the streamwise adverse pressure gradient on the suction surface and pressure surface. The increase of the pressure difference between the suction surface and pressure surface promotes the endwall cross-passage flow, which intensifies the accumulation of low momentum fluid in the corner region. The low momentum fluid in the corner region suffers enhanced streamwise adverse pressure gradient, which results in more complex boundary layer separation. These lead to significant growth of endwall loss.

3.1.3 Evolution of 3D corner separation flow

In order to reveal the separation mechanism leading to the loss variation, comparisons of the three-dimensional corner separation structures are made in more detail. Supplementary Figures S9–S12 depicts the radial pressure gradient and surface limiting streamlines on the suction surface, the transverse pressure gradient and surface limiting streamlines on the endwall, as well as the distribution of total pressure loss coefficient across the trailing edge when camber angle is 40°–48°. Through these figures, the evolution of flow separation with the increase of camber angle, Mach number and incidence angle can be observed.

At $Ma = 0.5$, the corner separation is not serious when camber angle is 40° (as shown in Supplementary Figures S9A,C,E,G,1). With the increase of incidence angle, the trend of the surface limiting streamlines on suction surface converging to the mid-span intensifies. The onset of the separation migrates forward as the incidence angle increases. At the incidence angle of 4°, small reverse flow of the suction-hub corner region begins to appear near the trailing edge (as shown in Supplementary Figure S9G). The coverage of the corner separation and the reverse flow expand with the growth of incidence angle, which results in the rise of loss in suction-hub corner region.

The increase of camber angle leads to the intensification of the convergence trend of suction surface limiting streamlines, as well as the expansion of the coverage of corner separation and reverse flow. At the incidence angle of 0°, small reverse flow of the suction-hub corner region occurs near the trailing edge when camber angle is 44° (as shown in Supplementary Figure S10C). For camber angles of 46° and 48°, the reverse flow exists at all incidence angles (as shown in Supplementary Figures S11, S12). When the incidence angle exceeds 4.5°, the corner separation almost extends to the mid-span (as shown in Supplementary Figure S12I). As a result, the high loss area of the end region

across the trailing edge almost extends to mid-span, while the loss increased sharply.

When the Mach number rises to 0.8, both the transverse pressure gradient of the endwall and the radial pressure gradient of the suction surface increase (as shown in Supplementary Figures S9B,D,F,H,J). The varied pressure gradient field enhances the trend of the suction surface limiting streamlines converging to the mid-span of the blade. The form of corner separation maintains, while the coverage of the corner separation and the reverse flow expand, especially under the condition of large positive incidence angle. Reverse flow of the suction-hub corner region begins to appear earlier than $Ma = 0.5$. Expanded corner separation and reverse flow results in the growth of endwall loss and the narrowing of the effective operating range under high subsonic inlet condition.

Supplementary Figure S13 depicts the radial pressure gradient and surface limiting streamlines on the pressure surface, the transverse pressure gradient and surface limiting streamlines on the endwall, and the distribution of total pressure loss coefficient across the trailing edge when camber angle is 40°–48°. With the growth of camber angle, the radial pressure gradient on the pressure surface rises gradually, which is more significant at the incidence angle of −0.5° than 0°. Enhanced by higher radial pressure gradient, the limiting streamlines of the pressure surface converge towards the mid-span. The pressure surface separation of the mid-span occurs at the camber angle of 48° even (as shown in Supplementary Figures S13G,H). Large separation coverage leads to the sharply rise of the loss at the mid-span of pressure surface, especially at large negative incidence angle (as shown in Supplementary Figure S13G). Therefore, the available working range of negative incidence angle gradually narrows with the increase of camber angle.

Supplementary Figures S14, S15 depict the flow fields of suction surface and pressure surface respectively at $\theta = 50°$. Impacted by higher radial pressure gradient, the corner separation almost extends to the mid-span, especially at $Ma = 0.8$. Moreover, the mid-span separation occurs near the trailing edge, resulting in the growth of mid-span loss. Due to the interaction of corner separation and mid-span trailing edge separation on the suction surface, the flow structure deteriorates and the corner stall is more easily to occur. The minimum loss incidence angle is the critical incidence angle. When the incidence angle continues to increase by 0.1°, it will cause the interaction between corner separation on both sides (expansion on one side and suppression on the other side, as shown in Supplementary Figure S14J). Corner stall will lead to a sharp increase of the total pressure loss and a decrease in the diffuser factor, which can be observed in Supplementary Figure S6.

It can be reflected in Supplementary Figure S15 that large-scale separation occurs at the mid-span of pressure surface at $Ma = 0.8$, which causes the loss of the mid-span on the pressure side to enhance (as shown in Supplementary Figures S15B,D,F,H,J). This phenomenon gradually improves with the increase of the incidence angle. With the suction-hub corner stall and the narrow effective operating range, the large-scale separation at the mid-span of the pressure surface exists from surge to stall.

Research above illustrates that the increase of Mach number and camber angle not only increase the blade loading, but also aggravate the corner separation of suction surface, especially in the cascade with a camber angle of 50° under the condition of high subsonic flow. Under the condition of high subsonic inlet, the effect of flow control on the typical flow phenomena is worth studying in high-loaded cascades.

3.2 Effect of dihedral angle on high-loaded cascade

Because compound lean blade alters spanwise pressure gradient to off-load the endwall region, it is applied to affect the flow in high loading cascades. We provide the evaluation of dihedral angle action in high-loaded cascades under high subsonic inlet conditions systematically.

3.2.1 Performance parameters changing with incidence angle

Supplementary Figure S16 shows the incidence characteristics of both straight blade and compound lean blade with different camber angels and solidities at $Ma = 0.8$. With the increase of solidity, the incidence characteristics of total pressure loss coefficient move upper right, and the characteristics of diffusion factor moves towards the right. When the camber angle is 40°–48°, the effective operating ranges of compound lean blades are narrower than straight blades. It is worth noting that positive dihedral angle widens the effective operating ranges in cascades with a camber angle of 50°.

3.2.2 Effect of solidity on blade loading

Focusing on the straight blade with a camber angle of 44°, it is discussed why the incidence characteristics of total pressure loss coefficient move towards the right with the growth of solidity. The axial distribution of surface static pressure coefficient varies with solidity are depicted in Supplementary Figure S17. It can be observed that the blade loading decreases with the growth of solidity, while the distribution of surface static pressure coefficient at mid-span gradually assumes the characteristics of negative attack angle. The reason is that the throat width and the throat location vary due to the change of the solidity, resulting in the variation of the relative shrinking degree of the passage. Therefore, the fluid near the leading edge twists, and the attack angle acting on the leading edge is different from the incidence angle.

Supplementary Figure S18 depicts the effect of solidity on the flow fields of suction surface at $\theta = 44°$. As the increase of solidity

reduces the blade loading, the transverse pressure gradient on the endwall decreases. The low momentum fluid accumulation in the corner is weakened, while the coverage of corner separation and reverse flow shrinks. This leads to the reduction of end loss. In addition, the reduced blade loading is also effective to control the thickening of the boundary layer, which reduces the loss at the mid-span. By combining the limiting streamlines and the distribution of surface static pressure coefficient, it can be found that the effect of increasing the solidity on the flow is similar to the negative incidence angle. This results in the migration towards the right of the incidence characteristics of total pressure loss coefficient with the increase of solidity.

3.2.3 Flow in cascades with normal camber angle

In order to evaluate the effect of compound lean blades on corner separation, the comparison of incidence characteristics among different dihedral angles with the camber angle of 40°–48° is given in Supplementary Figure S19. The positive dihedral angles reduce the total pressure loss at small incidence angle, but increase the loss under the condition of large positive incidence angle. At θ = 44°, the incidence characteristics of two negative dihedral angles are depicted moreover. The effect of negative dihedral angle on the incidence characteristics is opposite to that of positive dihedral angle.

In the cascade with the camber angle of 40°, the total pressure loss is mainly caused by the corner separation of the suction surface, so the influence of dihedral angle on the flow of the suction surface is explored. Supplementary Figure S20 depicts the effect of dihedral angle on the flow fields of suction surface at three different incidence angles. The increase of dihedral angle will increase the radial pressure gradient, which propels the suction surface limiting streamlines to converge towards the mid-span more dramatically. At the incidence angle of 4°, the limiting streamlines on the suction surface converges to the mid-span significantly, while the corner separation coverage of straight blades expands (as shown in Supplementary Figure S20C). Therefore, the effect of dihedral angle on corner separation is more significant at large positive incidence angles.

To compare the effect of positive and negative dihedral angle on the corner separation, the cascades with the camber angle of 44° is investigated. Influence of the dihedral angle on the spanwise distribution of total pressure loss coefficient across the trailing edge at three different incidence angles are shown in Supplementary Figure S21. At the incidence angle of 0°, positive dihedral angle reduces the end loss. At the incidence angle of 2° and 4°, positive dihedral angle increases the end loss and enlarges the high loss region near the endwall. The effect of negative dihedral angle on end loss is opposite to that of positive dihedral angle. In addition, under the incidence angle of 0°, the positive dihedral angle will also cause the loss of mid-span to increase. As a result, the total pressure loss coefficient at this incidence angle is not significantly reduced by positive dihedral angle, which is reflected in Supplementary Figure S19.

Since compound lean blade mainly alters the pressure gradient near the endwall, Supplementary Figure S22 shows the axial distribution of surface static pressure coefficient at 95% relative height position with different dihedral angles. The axial location of the lowest pressure on the suction surface moves forward when the dihedral angle is 30°, while the adverse pressure gradient of the suction surface reduces near the endwall. Moreover, positive dihedral angle increases the attack angle acting on the leading edge. The effect of negative dihedral angle on the pressure gradient near the endwall is opposite to that of positive dihedral angle.

Supplementary Figure S23 draws the flow fields on suction surface of the blades with a camber angle of 44° at three different incidence angles. The positive dihedral angle increases the radial pressure gradient of the suction surface, which promotes the low momentum fluid in the corner region to the mid-span. This intensifies the trend of the suction surface limiting streamlines converging towards the mid-span (as shown in Supplementary Figures S23J,K,L). Negative dihedral angle has the opposite effect. At the incidence angle of 0°, the reverse flow near the trailing edge is small, and the positive dihedral angle reduces its size (as shown in Supplementary Figures S23G,J). At the incidence angle of 4°, the reverse flow near the trailing edge of the straight blade is large and close to the mid-span (as shown in Supplementary Figure S23I). The positive dihedral angle fails to limit the reverse flow to a small range, resulting in high local loss (as shown in Supplementary Figure S23L). The negative dihedral angle weakens the tendency of the limiting streamlines converging to the mid-span, and limits the reverse flow near the trailing edge to a small spanwise range (as shown in Supplementary Figures S23C,F).

In order to detect the location of vortex core in the corner separation region, the vortex identification Q criterion is used, which is defined as follows:

$$Q = \frac{1}{2}\left(\Omega_{ij}\Omega_{ij} - S_{ij}S_{ij}\right) \tag{7}$$

where, Ω_{ij} is the vorticity tensor; S_{ij} is the shear strain tensor. Q represents the local balance between the shear strain rate and vorticity magnitude (Chakraborty et al., 2005). When Q decreases, vortex structures can be captured completely. However, if Q is too low, too many broken small vortex will be captured. Therefore, the vortex structures in the cascade can be completely and clearly observed only by properly selecting the Q. Supplementary Figure S24 provides the comparison of vortex structures identified by the iso-surface of Q = 5,000 between straight blade and compound lean blade with the dihedral angle of 30° at the incidence angle of 0°. For the straight blade, the pressure leg of horseshoe vortex (HPV) develops and migrates towards the suction surface of adjacent blades. The passage vortex (PV) and the separating vortex on suction surface (SSV) grow and expand, until SSV covers PV. The SSV continues to develop and gradually separates from the solid

wall, forming a lamellar separation vortex, whose boundary on suction surface is the corner separation line. The reverse flow is stuck between the lamellar separation and the suction surface. The SSV and reverse flow are the main sources of loss in the whole cascade.

As compound lean blade increases the radial pressure gradient, more low momentum fluid in the corner region is squeezed towards the mid-span, and HPV merges with the PV of adjacent blades later. The PV and the layered SSV form earlier than that in the straight cascade. The two vortexes merge with each other to form a large suction surface corner separation. The reverse flow between the suction surface and SSV is smaller than that of straight cascade, which effectively reduces the end loss.

Supplementary Figure S25 depicts the vortex structures identified by the iso-surface of Q criterion of straight blade and compound lean blade with the dihedral angle of 30° at the incidence angle of 4°. At the incidence angle of 4°, the evolution of each vortex structure is similar to that at the incidence angle of 0°, but their size is larger than 0°, especially the SSV. For the compound lean blade with a dihedral angle of 30°, the SSV is significant at 10% relative axial chord location. Moreover, complex separation structures exist near the trailing edge. The above two aspects result in the increase of the loss of compound lean blade with a dihedral angle of 30°.

Supplementary Figure S26 illustrates the flow fields on suction surface of the blades with a camber angle of 48°. The effect of dihedral angle on the flow fields of suction surface is similar to Supplementary Figures S20, S23. Near the incidence of 0°, the positive dihedral angle reduces the total pressure loss effectively, because the positive dihedral angle shrinks the reverse flow. However, when the incidence angle is large, the positive dihedral angle increases the actual attack angle acting on the leading edge near the endwall. The reverse flow near the trailing edge extends to the mid-span, which leads to the end loss and the overall loss increase at the same time (as shown in Supplementary Figures S26F,I,L).

3.2.4 Flow in high-loaded cascades

The effect of compound lean blades is the most significant when the camber angle is 50°. Incidence characteristics with different dihedral angles for the camber angle of 50° are given in Supplementary Figure S27. Positive dihedral angle not only reduces the total pressure loss at the minimum loss incidence angle, but also widens the effective operating range to 2°, although that is less than 1° of straight blade.

The spanwise distribution of total pressure loss coefficient across the trailing edge at the incidence angle of 0.5° is shown in Supplementary Figure S28. Positive dihedral angle reduces the end loss and increases the loss of mid-span simultaneously.

Supplementary Figure S29 shows the flow fields on suction surface with $\theta = 50°$ at five different incidence angles. The trailing edge separation line expands towards the leading edge with the increase of dihedral angle, and the loss at the mid-span of suction surface increases correspondingly. The separation line of corner separation is "cut off" by the trailing edge separation line. So the corner separation line cannot continue to expand towards the mid-span, which expands to the mid-span in the straight cascade originally. It is the reason why positive dihedral angle reduces the end loss. This flow phenomenon can also be observed through the 3D streamlines depicted in Supplementary Figure S30.

Supplementary Figure S31 shows the flow fields on pressure surface with $\theta = 50°$. There are large-scale limiting streamlines entrainment and spiral points at the mid-span of the pressure surface, as well as a high loss area at the pressure surface across the trailing edge correspondingly. The large-scale separation and high loss region expand with the rise of positive dihedral angle.

Comparison of vortex structures between straight blade and compound lean blade with the dihedral angle of 30° at the incidence angle of 0.5° is provided in Supplementary Figure S32. Different from the vortex structures in the cascade with a camber angle of 44°, an obvious trailing edge shedding vortex (TESV) near the trailing edge of the suction surface and a large-scale concentrated shedding vortex (CSV) at the mid-span of the pressure surface can be observed. As the TESV restricts the spanwise development of the SSV, the TESV of the positive dihedral angle of 30° expands upstream and limits the SSV in a small area. As the corner separation is limited, corner stall is effectively delayed, which is the reason for widening the effective operating range. Moreover, positive dihedral angle pushes the fluid near the endwall to the mid-span, which enlarges the CSV and causes more loss at the mid-span of pressure surface.

It can be concluded from above analysis that the effect of solidity on corner separation is linear. Different from solidity, the influence of dihedral angle on corner separation depends on the vortex structures. When only the SSV exists but the TESV doesn't, the positive dihedral angle intensifies the convergence of the limiting streamlines to the mid-span on the suction surface. At the incidence angle about 0°, the coverage of the corner separation and reverse flow is small, when the positive dihedral angle squeeze more fluid near the endwall into the mid-span. This helps to alleviate the low momentum fluid accumulation and corner separation, and reduce the endwall loss. At large positive incidence angle, the corner separation extends to the mid-span. At this time, the positive dihedral angle fails to control the corner separation and reverse flow in a small range, which result in increasing endwall loss. When the TESV and the SSV exist together, the positive dihedral angle makes the TESV move upstream. This helps to truncate the SSV in advance, which result in controlling the further development of corner separation and delaying corner stall. Therefore, the endwall loss is effectively reduced and the available positive operating range is widened

4 Conclusion

The effect of key geometrical parameters (camber angle, solidity, dihedral angle) and incoming condition (inlet Mach number) on the evolution mechanism of the 3D corner separation has been investigated in a linear compressor cascade with low aspect ratio. The main conclusions are as follows:

1) Although the increase of Mach number and camber angle increases the blade loading, it also aggravates the low momentum fluid accumulation and suction-hub corner separation. Especially in the cascade with a camber angle of 50° under high subsonic inlet condition, the rapidly deteriorating corner separation reduces the effective operating range to less than 1°.

2) With the growth of solidity, the blade loading decreases and the surface static pressure distribution assumes the characteristics of negative attack angle acting on the leading edge. The accumulation of low momentum fluid is weakened, as well as the coverage of corner separation and reverse flow. Because the effect of increasing the solidity on the flow is similar to the negative incidence angle, the incidence characteristics of total pressure loss coefficient migrate towards the right.

3) Positive dihedral angle reduces the adverse pressure gradient of the suction surface near the endwall, increases the attack angle and the radial pressure gradient of the suction surface. The variation of pressure field promotes the low momentum fluid in the corner region to the mid-span. At the incidence angle about 0° without the TESV, positive dihedral angle alleviates the low momentum fluid accumulation and corner separation, and reduces the endwall loss. When the incidence angle is large and positive, the corner separation extends towards the mid-span. At this time, the positive dihedral angle exacerbates the deteriorating corner separation, which results in increasing endwall loss. The effect of negative dihedral angle on the flow field is opposite to that of positive dihedral angle.

4) When the TESV and the SSV exist together, positive dihedral angle promotes the upstream migration of the TESV, which helps to truncate the SSV. This variation of vortex structures helps to weaken the development of corner separation and delay corner stall. Therefore, positive dihedral angle effectively reduces the endwall loss and widens the effective operating range from less than 1°–2°.

Data availability statement

The original contributions presented in the study are included in the article/Supplementary Material, further inquiries can be directed to the corresponding author.

Author contributions

CT provides innovation, numerical simulation experiment, results discussion and writing for this article. XD provides financial support and guidance about the content of the article. XZ, SW, and ZW provide financial support. WX provides guidance about the content and some technical work. YL has engaged in some technical work.

Funding

This research is supported by the National Natural Science Foundation of China (Grant No. 51906049) and the National Science and Technology Major Project (2017-II-0007-0021).

Conflict of interest

The authors declare that the research was conducted in the absence of any commercial or financial relationships that could be construed as a potential conflict of interest.

Publisher's note

Supplementary material

The Supplementary Material for this article can be found online at: https://www.frontiersin.org/articles/10.3389/fenrg.2022.974508/full#supplementary-material

SUPPLEMENTARY FIGURE S1
(A) Geometric parameters of airfoil geometry **(B)** Stacking line of compound lean blade.

SUPPLEMENTARY FIGURE S2
Configuration of calculation mesh grids **(A)** Grids diagram; **(B)** Mesh grids at the leading edge; **(C)** Mesh grids at the trailing edge.

SUPPLEMENTARY FIGURE S3
Effect of grid points number on the loss and deviation angle **(A)** Total pressure loss coefficient; **(B)** Deviation angle.

SUPPLEMENTARY FIGURE S4
Effect of grid points number on the spanwise distribution of loss and deviation angle **(A)** Total pressure loss coefficient; **(B)** Deviation angle.

SUPPLEMENTARY FIGURE S5
Variation of total pressure loss coefficient at outlet with incoming Mach number and axial isentropic Mach number distribution at the inlet Mach number of 0.77 **(A)** Variation of total pressure loss coefficient at outlet with incoming Mach number; **(B)** Axial distribution of isentropic Mach number at the inlet Mach number of 0.77.

SUPPLEMENTARY FIGURE S6
Influence of Mach number on incidence characteristics of total pressure loss coefficient and diffusion factor with different camber

angels (h/b = 1, σ = 1.8) **(A)** Total pressure loss coefficient; **(B)** Diffusion factor.

SUPPLEMENTARY FIGURE S7
Spanwise distribution of total pressure loss coefficient at the measure plane under different Mach numbers and camber angels (h/b = 1, σ = 1.8, i = 0.5°).

SUPPLEMENTARY FIGURE S8
Axial distribution of surface static pressure coefficient at 70% and 95% relative height position under different Mach numbers and camber angels (h/b = 1, σ = 1.8, i = 0.5°) **(A)** 70% relative height position; **(B)** 95% relative height position.

SUPPLEMENTARY FIGURE S9
Radial pressure gradient and surface limiting streamlines on the suction surface, transverse pressure gradient and surface limiting streamlines on the endwall, and the distribution of total pressure loss coefficient across the trailing edge (h/b = 1, σ = 1.8, θ = 40°) **(A)** i = –1.5°, Ma = 0.5; **(B)** i = -1.5°, Ma = 0.8; **(C)** i = 0°, Ma = 0.5; **(D)** i = 0°, Ma = 0.8; **(E)** i = 2°, Ma = 0.5; **(F)** i = 2°, Ma = 0.8; **(G)** i = 4°, Ma = 0.5; **(H)** i = 4°, Ma = 0.8; **(I)** i = 6°, Ma = 0.5; **(J)** i = 6°, Ma = 0.8.

SUPPLEMENTARY FIGURE S10
Radial pressure gradient and surface limiting streamlines on the suction surface, transverse pressure gradient and surface limiting streamlines on the endwall, and the distribution of total pressure loss coefficient across the trailing edge (h/b = 1, σ = 1.8, θ = 44°) **(A)** i = –1°, Ma = 0.5; **(B)** i = -1°, Ma = 0.8; **(C)** i = 0°, Ma = 0.5; **(D)** i = 0°, Ma = 0.8; **(E)** i = 2°, Ma = 0.5; **(F)** i = 2°, Ma = 0.8; **(G)** i = 4°, Ma = 0.5; **(H)** i = 4°, Ma = 0.8; **(I)** i = 5°, Ma = 0.5; **(J)** i = 5°, Ma = 0.8.

SUPPLEMENTARY FIGURE S11
Radial pressure gradient and surface limiting streamlines on the suction surface, transverse pressure gradient and surface limiting streamlines on the endwall, and the distribution of total pressure loss coefficient across the trailing edge (h/b = 1, σ = 1.8, θ = 46°) **(A)** i = –0.5°, Ma = 0.5; **(B)** i = –0.5°, Ma = 0.8; **(C)** i = 0°, Ma = 0.5; **(D)** i = 0°, Ma = 0.8; **(E)** i = 2°, Ma = 0.5; **(F)** i = 2°, Ma = 0.8; **(G)** i = 4°, Ma = 0.5; **(H)** i = 4°, Ma = 0.8; **(I)** i = 5°, Ma = 0.5; **(J)** i = 5°, Ma = 0.8.

SUPPLEMENTARY FIGURE S12
Radial pressure gradient and surface limiting streamlines on the suction surface, transverse pressure gradient and surface limiting streamlines on the endwall, and the distribution of total pressure loss coefficient across the trailing edge (h/b = 1, σ = 1.8, θ = 48°) **(A)** i = –0.5°, Ma = 0.5; **(B)** i = –0.5°, Ma = 0.8; **(C)** i = 0°, Ma = 0.5; **(D)** i = 0°, Ma = 0.8; **(E)** i = 2°, Ma = 0.5; **(F)** i = 2°, Ma = 0.8; **(G)** i = 4°, Ma = 0.5; **(H)** i = 4°, Ma = 0.8; **(I)** i = 4.5°, Ma = 0.5; **(J)** i = 4.5°, Ma = 0.8.

SUPPLEMENTARY FIGURE S13
Radial pressure gradient and surface limiting streamlines on the pressure surface, transverse pressure gradient and surface limiting streamlines on the endwall, and the distribution of total pressure loss coefficient across the trailing edge (h/b = 1, σ = 1.8, Ma = 0.8) **(A)** θ = 40°, i = –0.5°; **(B)** θ = 40°, i = 0°; **(C)** θ = 44°, i = –0.5°; **(D)** θ = 44°, i = 0°; **(E)** θ = 46°, i = –0.5°; **(F)** θ = 46°, i = 0°; **(G)** θ = 48°, i = –0.5°; **(H)** θ = 48°, i = 0°.

SUPPLEMENTARY FIGURE S14
Radial pressure gradient and surface limiting streamlines on the suction surface, transverse pressure gradient and surface limiting streamlines on the endwall, and the distribution of total pressure loss coefficient across the trailing edge (h/b = 1, σ = 1.8, **(A)** θ = 50°) i = 0°, Ma = 0.5; **(B)** i = 0°, Ma = 0.8; **(C)** i = 0.1°, Ma = 0.5; **(D)** i = 0.1°, Ma = 0.8; **(E)** i = 0.25°, Ma = 0.5; **(F)** i = 0.25°, Ma = 0.8; **(G)** i = 0.5°, Ma = 0.5; **(H)** i = 0.5°, Ma = 0.8; **(I)** i = 0.7°, Ma = 0.5; **(J)** i = 0.7°, Ma = 0.8.

SUPPLEMENTARY FIGURE S15
Radial pressure gradient and surface limiting streamlines on the pressure surface, transverse pressure gradient and surface limiting streamlines on the endwall, and the distribution of total pressure loss coefficient across the trailing edge (h/b = 1, σ = 1.8, θ = 50°) **(A)** i = 0°, Ma = 0.5; **(B)** i = 0°, Ma = 0.8; **(C)** i = 0.1°, Ma = 0.5; **(D)** i = 0.1°, Ma = 0.8; **(E)** i = 0.25°, Ma = 0.5; **(F)** i = 0.25°, Ma = 0.8; **(G)** i = 0.5°, Ma = 0.5; **(H)** i = 0.5°, Ma = 0.8; **(I)** i = 0.7°, Ma = 0.5; **(J)** i = 0.7°, Ma = 0.8.

SUPPLEMENTARY FIGURE S16
Influence of solidity and dihedral angle on incidence characteristics of total pressure loss coefficient and diffusion factor with different camber angels (h/b = 1, Ma = 0.8) **(A)** θ = 40°, α = 0°; **(B)** θ = 40°, α = 20°; **(C)** θ = 40°, α = 30°; **(D)** θ = 44°, α = 0°; **(E)** θ = 44°, α = 20°; **(F)** θ = 44°, α = 30°; **(G)** θ = 48°, α = 0°; **(H)** θ = 48°, α = 20°; **(I)** θ = 48°, α = 30°; **(J)** θ = 50°, α = 0°; **(K)** θ = 50°, α = 20°; **(L)** θ = 50°, α = 30°.

SUPPLEMENTARY FIGURE S17
Axial distribution of surface static pressure coefficient at 50% relative height position at different solidities (h/b = 1, Ma = 0.8, θ = 44°) **(A)** i = 1°; **(B)** i = 2°.

SUPPLEMENTARY FIGURE S18
Radial pressure gradient and surface limiting streamlines on the suction surface, transverse pressure gradient and surface limiting streamlines on the endwall, and the distribution of total pressure loss coefficient across the trailing edge (h/b = 1, θ = 44°, Ma = 0.8) **(A)** i = 1°, σ = 1.4; **(B)** i = 1°, σ = 1.8; **(C)** i = 1°, σ = 2.2; **(D)** i = 2°, σ = 1.4; **(E)** i = 2°, σ = 1.8; **(F)** i = 2°, σ = 2.2.

SUPPLEMENTARY FIGURE S19
Influence of dihedral angle on incidence characteristics of total pressure loss coefficient with different camber angels (h/b = 1, Ma = 0.8, **(A)** σ = 1.8) θ = 40°; **(B)** θ = 44°; **(C)** θ = 48°.

SUPPLEMENTARY FIGURE S20
Radial pressure gradient and surface limiting streamlines on the suction surface, transverse pressure gradient and surface limiting streamlines on the endwall, and the distribution of total pressure loss coefficient across the trailing edge (h/b = 1, θ = 40°, Ma = 0.8, σ = 1.8) **(A)** α = 0°,i = 0°; **(B)** α = 0°,i = 2°; **(C)** α = 0°,i = 4°; **(D)** α = 10°,i = 0°; **(E)** α = 10°,i = 2°; **(F)** α = 10°,i = 4°; **(G)** α = 20°,i = 0°; **(H)** α = 20°,i = 2°; **(I)** α = 20°,i = 4°; **(J)** α = 30°,i = 0°; **(K)** α = 30°,i = 2°; **(L)** α = 30°,i = 4°.

SUPPLEMENTARY FIGURE S21
Influence of dihedral angle on the spanwise distribution of total pressure loss coefficient across the trailing edge (h/b = 1, Ma = 0.8, θ = 44°, σ = 1.8) **(A)** i = 0°; **(B)** i = 2°; **(C)** i = 4°.

SUPPLEMENTARY FIGURE S22
Influence of dihedral angle on the axial distribution of surface static pressure coefficient at 95% relative height position (h/b = 1, Ma = 0.8, θ = 44°, σ = 1.8) **(A)** i = 0°; **(B)** i = 2°; **(C)** i = 4°.

SUPPLEMENTARY FIGURE S23
Radial pressure gradient and surface limiting streamlines on the suction surface, transverse pressure gradient and surface limiting streamlines on the endwall, and the distribution of total pressure loss coefficient across the trailing edge (h/b = 1, θ = 44°, Ma = 0.8, σ = 1.8) **(A)** α = -30°,i = 0°; **(B)** α = -30°,i = 2°; **(C)** α = -30°,i = 4°; **(D)** α = -10°,i = 0°; **(E)** α = -10°,i = 2°; **(F)** α = -10°,i = 4°; **(G)** α = 0°,i = 0°; **(H)** α = 0°,i = 2°; **(I)** α = 0°,i = 4°; **(J)** α = 30°,i = 0°; **(K)** α = 30°,i = 2°; **(L)** α = 30°,i = 4°.

SUPPLEMENTARY FIGURE S24
Vortex structures identified by the iso-surface with Q = 5,000 of straight blade and compound lean blade with the dihedral angle of 30° at the incidence angle of 0° (h/b = 1, Ma = 0.8, θ = 44°, σ = 1.8) **(A)** α = 0°; **(B)** α = 30°.

SUPPLEMENTARY FIGURE S25
Vortex structures identified by the iso-surface with Q = 5,000 of straight blade and compound lean blade with the dihedral angle of 30° at the incidence angle of 4° (h/b = 1, Ma = 0.8, θ = 44°, σ = 1.8) **(A)** α = 0°; **(B)** α = 30°.

SUPPLEMENTARY FIGURE S26
Radial pressure gradient and surface limiting streamlines on the suction surface, transverse pressure gradient and surface limiting streamlines on the endwall, and the distribution of total pressure loss coefficient across the trailing edge (h/b = 1, θ = 48°, Ma = 0.8, σ = 1.8) **(A)** α = 0°,i = 1°; **(B)** α = 0°,i = 2°; **(C)** α = 0°,i = 3°; **(D)** α = 10°,i = 1°; **(E)** α = 10°,i = 2°; **(F)** α = 10°,i = 3°;

(G) $\alpha = 20^{\circ}, i = 1^{\circ}$; **(H)** $\alpha = 20^{\circ}, i = 2^{\circ}$; **(I)** $\alpha = 20^{\circ}, i = 3^{\circ}$; **(J)** $\alpha = 30^{\circ}, i = 1^{\circ}$; **(K)** $\alpha = 30^{\circ}, i = 2^{\circ}$; **(L)** $\alpha = 30^{\circ}, i = 3^{\circ}$.

SUPPLEMENTARY FIGURE S27
Influence of dihedral angle on incidence characteristics of total pressure loss coefficient with a camber angel of 50° ($h/b = 1$, $Ma = 0.8$, $\sigma = 1.8$).

SUPPLEMENTARY FIGURE S28
Influence of dihedral angle on the spanwise distribution of total pressure loss coefficient across the trailing edge at the incidence angle of 0.5° ($h/b = 1$, $Ma = 0.8$, $\theta = 50^{\circ}$, $\sigma = 1.8$).

SUPPLEMENTARY FIGURE S29
Radial pressure gradient and surface limiting streamlines on the suction surface, transverse pressure gradient and surface limiting streamlines on the endwall, and the distribution of total pressure loss coefficient across the trailing edge ($h/b = 1$, $\sigma = 1.8$, $\theta = 50^{\circ}$) **(A)** $\alpha = 0^{\circ}, i = 0^{\circ}$; **(B)** $\alpha = 20^{\circ}, i = 0^{\circ}$; **(C)** $\alpha = 30^{\circ}, i = 0^{\circ}$; **(D)** $\alpha = 0^{\circ}, i = 0.1^{\circ}$; **(E)** $\alpha = 20^{\circ}, i = 0.1^{\circ}$; **(F)** $\alpha = 30^{\circ}, i = 0.1^{\circ}$; **(G)** $\alpha = 0^{\circ}, i = 0.25^{\circ}$; **(H)** $\alpha = 20^{\circ}, i = 0.25^{\circ}$; **(I)** $\alpha = 30^{\circ}, i = 0.25^{\circ}$; **(J)** $\alpha = 0^{\circ}, i = 0.5^{\circ}$; **(K)** $\alpha = 20^{\circ}, i = 0.5^{\circ}$; **(L)** $\alpha = 30^{\circ}, i = 0.5^{\circ}$; **(M)** $\alpha = 0^{\circ}, i = 0.7^{\circ}$; **(N)** $\alpha = 20^{\circ}, i = 0.7^{\circ}$; **(O)** $\alpha = 30^{\circ}, i = 0.7^{\circ}$.

SUPPLEMENTARY FIGURE S30
3-D streamlines and distribution of total pressure loss coefficient across the trailing edge of straight blade and compound lean blade with the dihedral angle of 30° at the incidence angle of 0.5°. ($h/b = 1$, $Ma = 0.8$, $\theta = 50^{\circ}$, $\sigma = 1.8$) **(A)** $\alpha = 0^{\circ}$; **(B)** $\alpha = 30^{\circ}$.

SUPPLEMENTARY FIGURE S31
Radial pressure gradient and surface limiting streamlines on the pressure surface, transverse pressure gradient and surface limiting streamlines on the endwall, and the distribution of total pressure loss coefficient across the trailing edge ($h/b = 1$, $\sigma = 1.8$, $\theta = 50^{\circ}$) **(A)** $\alpha = 0^{\circ}, i = 0^{\circ}$; **(B)** $\alpha = 20^{\circ}, i = 0^{\circ}$; **(C)** $\alpha = 30^{\circ}, i = 0^{\circ}$; **(D)** $\alpha = 0^{\circ}, i = 0.1^{\circ}$; **(E)** $\alpha = 20^{\circ}, i = 0.1^{\circ}$; **(F)** $\alpha = 30^{\circ}, i = 0.1^{\circ}$; **(G)** $\alpha = 0^{\circ}, i = 0.25^{\circ}$; **(H)** $\alpha = 20^{\circ}, i = 0.25^{\circ}$; **(I)** $\alpha = 30^{\circ}, i = 0.25^{\circ}$; **(J)** $\alpha = 0^{\circ}, i = 0.5^{\circ}$; **(K)** $\alpha = 20^{\circ}, i = 0.5^{\circ}$; **(L)** $\alpha = 30^{\circ}, i = 0.5^{\circ}$; **(M)** $\alpha = 0^{\circ}, i = 0.7^{\circ}$; **(N)** $\alpha = 20^{\circ}, i = 0.7^{\circ}$; **(O)** $\alpha = 30^{\circ}, i = 0.7^{\circ}$.

SUPPLEMENTARY FIGURE S32
Vortex structures identified by the iso-surface with $Q = 5{,}000$ of straight blade and compound lean blade with the dihedral angle of 30° at the incidence angle of 0.5° ($h/b = 1$, $Ma = 0.8$, $\theta = 50^{\circ}$, $\sigma = 1.8$) **(A)** $\alpha = 0^{\circ}$; **(B)** $\alpha = 30^{\circ}$.

References

Bruna, D., Cravero, C., and Turner, M. G. (2006). The Development of an Aerodynamic Performance Prediction Tool for Modern Axial Flow Compressor Profiles. *Proc. ASME Turbo Expo* 6, 113–122. doi:10.1115/GT2006-90187

Carter, A. D. S. (1950). The Low Speed Performance of Related Aerofoils in Cascades. *Aeronaut. Res. Counc.* Washington, DC: Tech. Report, NGTE.

Chakraborty, P., Balachandar, S., and Adrian, R. J. (2005). On the Relationships between Local Vortex Identification Schemes. *J. Fluid Mech.* 535, 189–214. doi:10.1017/S0022112005004726

Denton, J. D. (1993). The 1993 IGTI Scholar Lecture: Loss Mechanisms in Turbomachines. *J. Turbomach.* 115, 621–656. doi:10.1115/1.2929299

Dickens, T., and Day, I. (2011). The Design of Highly Loaded Axial Compressors. *J. Turbomach.* 133. doi:10.1115/1.4001226

Ding, J., Chen, S., Cai, L., Wang, S., Wang, Z., and Shen, J. (2018). The Synergistic Effect between Compound Lean and Aspiration on Aerodynamic Performance in Compressor Cascades. *Proc. Institution Mech. Eng. Part G J. Aerosp. Eng.* 232, 3034–3048. doi:10.1177/0954410017723362

Gümmer, V., Wenger, U., and Kau, H. P. (2001). Using Sweep and Dihedral to Control Three-Dimensional Flow in Transonic Stators of Axial Compressors. *J. Turbomach.* 123, 40–48. doi:10.1115/1.1330268

Howell, A. R. (1945). Fluid Dynamics of Axial Compressors. *Proc. Institution Mech. Eng.* 153, 441–452. doi:10.1243/pime_proc_1945_153_049_02

Hu, H., Yu, J., Song, Y., and Chen, F. (2021). The Application of Support Vector Regression and Mesh Deformation Technique in the Optimization of Transonic Compressor Design. *Aerosp. Sci. Technol.* 112, 106589. doi:10.1016/j.ast.2021.106589

Ju, Z., Teng, J., Zhu, M., Ma, Y., Qiang, X., Fan, L., et al. (2020). Flow Characteristics on a 4-Stage Low-Speed Research Compressor with a Cantilevered Stator. *Aerosp. Sci. Technol.* 105, 106033. doi:10.1016/j.ast.2020.106033

Koller, U., Monig, R., Kusters, B., and Schreiber, H. A. (2000). 1999 Turbomachinery Committee Best Paper Award: Development of Advanced Compressor Airfoils for Heavy-Duty Gas Turbines— Part I: Design and Optimization. *J. Turbomach.* 122, 397–405. doi:10.1115/1.1302296

Kusters, B., Schreiber, H. A., Koller, U., and Monig, R. (2000). 1999 Turbomachinery Committee Best Paper Award: Development of Advanced Compressor Airfoils for Heavy-Duty Gas Turbines— Part II: Experimental and Theoretical Analysis. *J. Turbomach.* 122, 406–414. doi:10.1115/1.1302321

Li, J., Hu, J., and Zhang, C. (2020). Investigation of Vortical Structures and Turbulence Characteristics in Corner Separation in an Axial Compressor Stator Using DDES. *Energies* 13, 2123. doi:10.3390/en13092123

Li, L., Song, Y., Chen, F., and Liu, H. (2016). Flow Control Investigations of Steady and Pulsed Jets in Bowed Compressor Cascades. *Proc. ASME Turbo Expo*, V02AT37A025. doi:10.1115/GT2016-56855

Li, L. T., Song, Y. P., Chen, F., and Liu, H. P. (2017). Effects of Endwall Jet on Flow Fields in Bowed Compressor Cascades at Different Inlet Boundary Layers. *Tuijin Jishu/Journal Propuls. Technol* 38 (6), 1278–1286. doi:10.13675/j.cnki.tjjs.2017.06.010

Lieblein, S., Schwenk, F., and Broderick, R. (1953). *Diffusion Factor for Estimating Losses and Limiting Blade Loadings in Axial-Flow-Compressor Blade Elements*. National Advisory Committee for Aeronautics Cleveland Oh Lewis Flight Propulsion Lab.

Lin, Z. R., Han, Y., and Yuan, X. (2014). Investigation and Application of Non-axisymmetric Endwall and Bowed Blade Joint Profiling. *J. Eng. Thermophys* 2014 (11), 5.

Ling, J., Du, X., Wang, S., and Wang, Z. (2014). Relationship between Optimum Curved Blade Generate Line and Cascade Parameters in Subsonic Axial Compressor. *Proc. ASME Turbo Expo*, V02BT39A015. doi:10.1115/GT2014-25799

Numeca International (2015). *IGG v10.1, User Manual*. Brussels: NUMECA International.

Qiang, X., Wang, S., Feng, G., and Wang, Z. (2008). Aerodynamic Design and Analysis of a Low-Reaction Axial Compressor Stage. *Chin. J. Aeronautics* 21, 1–7. doi:10.1016/S1000-9361(08)60001-1

Sans, J., Resmini, M., Brouckaert, J. F., and Hiernaux, S. (2014). Numerical Investigation of the Solidity Effect on Linear Compressor Cascades. *Proc. ASME Turbo Expo*, V02AT37A013. doi:10.1115/GT2014-25532

Shi, H., and Ji, L. (2021). Leading Edge Redesign of Dual-Peak Type Variable Inlet Guide Vane and its Effect on Aerodynamic Performance. *Proc. Institution Mech. Eng. Part G J. Aerosp. Eng.* 235, 1077–1090. doi:10.1177/0954410020966168

Song, B., Gui, X., Li, S. M., Douglas, J., and Ng, W. F. (2002). "Flow Periodicity Improvement in a High Speed Compressor Cascade with a Large Turning-Angle," in 38th AIAA/ASME/SAE/ASEE Joint Propulsion Conference and Exhibit. doi:10.2514/6.2002-3539

Song, B., and Ng, W. F. (2006). Performance and Flow Characteristics of an Optimized Supercritical Compressor Stator Cascade. *J. Turbomach.* 128, 435–443. doi:10.1115/1.2183316

Song, B., Ng, W., Sonoda, T., and Arima, T. (2008). Loss Mechanisms of High-Turning Supercritical Compressor Cascades. *J. Propuls. Power* 24, 416–423. doi:10.2514/1.30579

Song, Y., Chen, F., Yang, J., and Wang, Z. (2006). A Numerical Investigation of Boundary Layer Suction in Compound Lean Compressor Cascades. *J. Turbomach.* 128, 357–366. doi:10.1115/1.2162181

Sun, S., Chen, S., Liu, W., Gong, Y., and Wang, S. (2018). Effect of Axisymmetric Endwall Contouring on the High-Load Low-Reaction Transonic Compressor Rotor with a Substantial Meridian Contraction. *Aerosp. Sci. Technol.* 81, 78–87. doi:10.1016/j.ast.2018.08.001

Sun, S., Hao, J., Yang, J., Zhou, L., and Ji, L. (2022). Impacts of Tandem Configurations on the Aerodynamic Performance of an Axial Supersonic Through-Flow Fan Cascade. *J. Turbomach.* 144. doi:10.1115/1.4052689

Sun, S., Wang, S., Chen, S., Tao, C., Cai, L., and Chen, J. (2019). The Impact of Various Forward Sweep Angles on the Performance of an Ultra-high-load Low-Reaction Transonic Compressor Rotor. *Appl. Therm. Eng.* 150, 953–966. doi:10.1016/j.applthermaleng.2019.01.045

Sun, S., Wang, S., and Chen, S. (2020). The Influence of Diversified Forward Sweep Heights on Operating Range and Performance of an Ultra-high-load Low-Reaction Transonic Compressor Rotor. *Energy* 194, 116857. doi:10.1016/j.energy.2019.116857

Sun, S., Wang, S., Zhang, L., and Ji, L. (2021). Design and Performance Analysis of a Two-Stage Transonic Low-Reaction Counter-rotating Aspirated Fan/Compressor with Inlet Counter-swirl. *Aerosp. Sci. Technol.* 111, 106519. doi:10.1016/j.ast.2021.106519

Tang, Y., and Liu, Y. (2020). Aerodynamic Investigation of Datum and Slotted Blade Profiles under Different Mach Number Conditions. *Energies* 13, 1673. doi:10.3390/en13071673

Tang, Y., Liu, Y., Lu, L., Lu, H., and Wang, M. (2020). Passive Separation Control with Blade-End Slots in a Highly Loaded Compressor Cascade. *AIAA J.* 58, 85–97. doi:10.2514/1.J058488

Tao, C., Du, X., Ding, J., Luo, Y., and Wang, Z. (2021). Maximum Thickness Location Selection of High Subsonic Axial Compressor Airfoils and its Effect on Aerodynamic Performance. *Front. Energy Res.* 9. doi:10.3389/fenrg.2021.791542

Vuong, T. D., and Kim, K. Y. (2021). Stability Enhancement of a Single-Stage Transonic Axial Compressor Using Inclined Oblique Slots. *Energies* 14, 2346. doi:10.3390/en14092346

Wang, Z. Q. (1981). Aerodynamic Calculation of Turbine Stage with Long Blades and Discussion of its Results. *J. Eng. Thermophys*.

Weingold, H. D., Neubert, R. J., Behlke, R. F., and Potter, G. E. (1995). Reduction of Compressor Stator Endwall Losses through the Use of Bowed Stators. *Proc. ASME Turbo Expo*. doi:10.1115/95-GT-380

Xu, W., Du, X., Tao, C., Wang, S., and Wang, Z. (2019). Correlation of Solidity, Aspect Ratio and Compound Lean Blade in Compressor Cascade Design. *Appl. Therm. Eng.* 150, 175–192. doi:10.1016/j.applthermaleng.2018.12.167

Xu, W., Du, X., Wang, S., and Wang, Z. (2018). Correlation of Solidity and Curved Blade in Compressor Cascade Design. *Appl. Therm. Eng.* 131, 244–259. doi:10.1016/j.applthermaleng.2017.12.003

Zhang, L., Wang, S., and Zhu, W. (2019). Application of Endwall Contouring in a High-Subsonic Tandem Cascade with Endwall Boundary Layer Suction. *Aerosp. Sci. Technol.* 84, 245–256. doi:10.1016/j.ast.2018.08.041

Zhao, W., Zheng, Q., Jiang, B., and Lin, A. (2020). A Passive Control Method of Hub Corner Stall in a 1.5-Stage Axial Compressor under Low-Speed Conditions. *Energies* 13, 2691. doi:10.3390/en13112691

Zheng, T., Qiang, X., Teng, J., and Feng, J. (2021). Investigation of Leading Edge Tubercles with Different Wavelengths in an Annular Compressor Cascade. *Int. J. Turbo Jet. Engines* 38, 153–162. doi:10.1515/tjj-2017-0064

Zweifel, O. (1945). The Spacing of Turbo-Machine Blading, Especially with Large Angular Deflection. *Brown Boveri Rev.* 32, 436–444.

Nomenclature

Abbreviations

h/b aspect ratio
h blade height
b chord
R^2 coefficient of determination
kk curvature of camber
D diffusion factor
P* total pressure
T* total temperature
v velocity
c thickness
i incidence angle
Ma Mach number
e/b maximum thickness location
t Pitch
P static pressure
Cp_2 static pressure rise coefficient

Greek symbol

β_p blade angle
θ camber angle
ω the total pressure loss coefficient
ΔD errors of diffusion factor
$\delta\omega$ Total loss variation
δD improvement of diffusion factor
δCp_2 improvement of static pressure rise coefficient
$\delta\theta$ improvement of camber angle
Δv velocity-difference
σ solidity
Δi errors of incidence
ΔCp_2 errors of static pressure rise coefficient
$\Delta\omega$ errors of total pressure loss coefficient

Subscripts

o minimum incidence
Mod model
u tangential
1 inlet
2 outlet
max maximum
min minimum

frontiers | Frontiers in Energy Research

TYPE Original Research
PUBLISHED 21 September 2022
DOI 10.3389/fenrg.2022.989883

OPEN ACCESS

EDITED BY
Kaiqiang Zhang,
Imperial College London,
United Kingdom

REVIEWED BY
Xiaoxu Kan,
Shanghai Maritime University, China
Shaopeng Lu,
Shanghai Jiao Tong University, China
Hongxin Zhang,
Nanjing University of Aeronautics and Astronautics, China

*CORRESPONDENCE
Le Cai,
earcle@yeah.net

SPECIALTY SECTION
This article was submitted to Advanced Clean Fuel Technologies, a section of the journal Frontiers in Energy Research

RECEIVED 09 July 2022
ACCEPTED 05 September 2022
PUBLISHED 21 September 2022

CITATION
Liu B, Cai L, Xu H, Fu H and Wang S (2022), Numerical investigations on oscillating aspirations controlling separation flows in linear highly loaded compressor cascades.
Front. Energy Res. 10:989883.
doi: 10.3389/fenrg.2022.989883

Numerical investigations on oscillating aspirations controlling separation flows in linear highly loaded compressor cascades

Bao Liu, Le Cai*, Hao Xu, Haiyan Fu and Songtao Wang

School of Energy Science and Engineering, Harbin Institute of Technology, Harbin, China

The effect of boundary layer oscillating suction (BLOS) on the vortex structure of high-load linear compressor cascades is studied by a high-fidelity numerical calculation. The oscillation parameters (amplitude and frequency) and suction control parameters (suction position and mass flow) are continuously adjusted. It was found that higher aerodynamic efficiency could be obtained with suitable oscillation parameters and suction control parameters. This is achieved because BLOS not only absorbs the low-energy fluid in the boundary layer but also optimizes the vortex structure in the compressor passage.

KEYWORDS

compressor cascade, boundary layer, oscillating suction, separated flow control, vortex structure

1 Introduction

Viscous effects, non-constant flow properties, and inverse pressure gradients inside highly loaded compressors often cause complex separation flows and vortex structures. Suppressing the boundary layer separation is an important means to improve the performance of the compressor while reducing engine weight and increasing blade load. Basically, the average skin friction increasing in front can have an inhibitory effect on separation, which can be achieved through momentum transfer (Jahanmiri, 2010). In addition, more effective control can be obtained by introducing oscillatory momentum coupled with flow instabilities (Seifert et al., 1996). Momentum transfer is widely used for active separation control, such as synthetic jets (Guendogdu et al., 2008; Pawan et al., 2022; Sushanta and Shantanu, 2022), plasma drives (Zheng et al., 2014; Hamrin et al., 2018; Lee et al., 2020; Vytenis, 2020), boundary layer suction (Merchant, 2000; Song et al., 2005; Gümmer et al., 2008; Kerrebrock et al., 2008; Dorfner et al., 2011; Schlaps et al., 2014; Siemann and Seume, 2015; Zhang et al., 2016), and jet streams (Culley et al., 2003a).

Prior to the concept of the boundary layer, Plante proposed a method to achieve separation control by sucking out the low-energy fluid inside the boundary layer. Loughery et al. (1971) systematically studied the effect of boundary layer suction on the performance of compressor cascades, and the results proved that suction could significantly improve the efficiency of the compressor. Before 1998, Kerrebrock et al.

TABLE 1 Compressor cascade geometry and inlet aerodynamic parameters.

Blade geometry	
Chord	95.8 mm
Solidity	1.86
Aspect ratio	1.04
Stagger angle	6.5°
Blade inlet angle	56.3°
Blade exit angle	-8.7°
Inlet aerodynamic parameters	
Re_1	5.12×10^5
Ma_1	0.28

(1997) studied in detail the effect of suction in the fan, compressor rotor, and guide vane, and he finally designed a single-stage pressure ratio of 1.6 for the suction compressor. Culley et al. (2003b) conducted an experimental study on the boundary layer suction of the guide vane and showed that only 0.4% of the flow inside the passage needs to be suctioned to reduce the total pressure loss by 22%. Boundary layer suction control in a large bending angle compressor was experimentally investigated under transonic conditions by Vandeputte (2000), and the results showed that a suction flow rate of 1.6% can effectively reduce the separation of the suction surface of the blade passage, weaken wake strength, and reduce the total pressure loss by about 65%.

There is no human intervention in the original boundary layer suction (BLS), but in fact it is difficult to guarantee the absolute constancy of the suction. The non-constant nature of the flow field itself always causes unsteady states, which is more evident in the flow field of a compressor machine. On this basis, Cai Le (2015) proposed the concept of boundary layer oscillating suction. He introduced a non-constant excitation in the suction process to make the mass flow change periodically and realized the non-constant control of suction by controlling the parameters. Boundary layer oscillating suction specifically refers to the non-constant process in which the suction flow rate oscillates periodically according to a sine or cosine function relationship. This study concentrates on the separation characteristics of the linear compressor blade flow field. We perform a comparative analysis for with and without aspiration. Different control effects of the steady and oscillatory suction on the separation region will be shown to get a reference for the optimal excitation parameters. The numerical study was set at an incidence angle of 11° and an incoming Mach number of 0.22.

\This study is organized as follows: section 2 gives the numerical method used in this study, including blade geometry, boundary layer suction structure, and oscillatory parameters. This is the basis of all research. It also verifies the accuracy of the numerical calculation based on experimental results; section 3 analyzes the role of suction position, suction flow rate, and oscillatory control parameters on separation flow control by presenting the numerical calculation results. Various vortex identification methods and loss assessment methods are mentioned in this section; section 4 details a comprehensive presentation and clarifies the conclusions of this study. It provides a new idea for the next vortex active control method.

2 Numerical methods

2.1 Geometric configuration

This study is based on the low-reaction compressor by Wang et al. (2007). The geometric and aerodynamic parameters of the blade are shown in Table 1, and the compressor cascade domain extracted from these parameters is given in Figure 1. The two-dimensional grid forms a three-dimensional grid by base-stacking along the blade height direction. The suction slots simulated by the slices extracted from the blade surface are placed at different axial chord lengths from the leading edge. The normal velocity condition of the boundary is specified at the suction outlet. For the non-constant suction control, the suction velocity u(t) can be simulated as a combination of periodic parameters with constant velocity, which is written as Eq. 1:

$$\boldsymbol{u(t) = U_0 \sin(2\pi f t + \varphi) + U_s} \tag{1}$$

where U_0 represents the oscillating amplitude, f is frequency, and φ is the phase. U_s is the velocity condition exerted on the steady aspiration, which was adjusted to ensure the time-averaged suction rate meets the requirement. The control parameters such as f and U_0 are adjusted to investigate their effects on separation control. The oscillation fluctuations are shown Figure 2.

The computational domain is discretized into approximately 1.15 million finite volumes in the form of HOH-type structural meshes. In order to have higher resolution near the solid walls, grid nodes are concentrated near the walls, leading and trailing edges, which ensures that the global y + value is less than 5.

Flow fields for an analysis in this research are solved by ANSYS CFX v17.2. The second-order backward Euler method is used for time discretization, and the central difference JST scheme with suitable artificial viscosity achieves convective flow calculation with second-order accuracy. Approximation of the turbulent viscosity is carried out using a modified two-equation model RNG k-Epsilon, which will be compared with other models afterward.

For the incompressible flow problem in this study, the computational domain inlet is given in the total temperature, total pressure, and velocity directions. The inlet total pressure

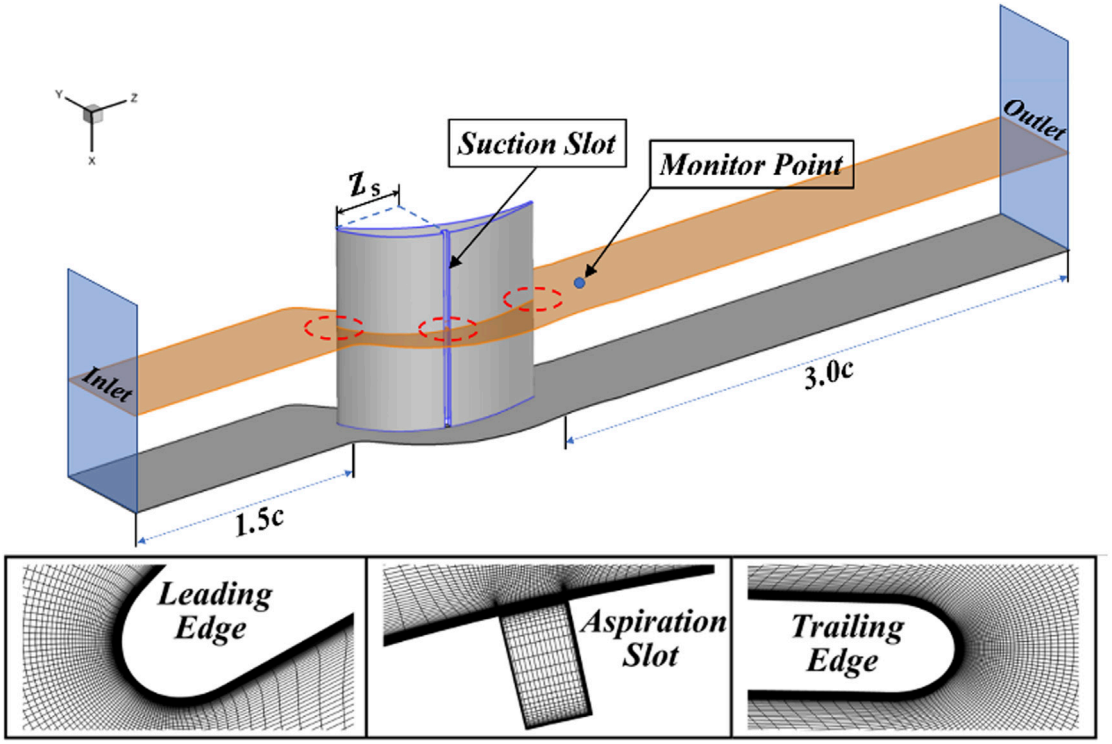

FIGURE 1
Schematic of blade geometry and computational domain.

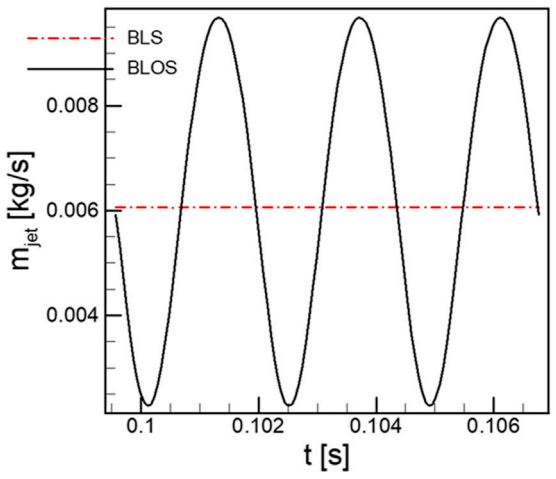

FIGURE 2
Periodic signal of the mass flow rate modeled by Eq. 1.

$P^* = P + \rho\vec{U}^2/2$, where the values of static pressure P and velocity $\vec{U}$ are calculated iteratively with the internal flow field; the subsonic flow outlet is given a pressure boundary condition to eliminate non-physical reflections; the blade and end wall surfaces are given a no-slip boundary condition $\vec{V} \cdot \vec{n} = 0$; and the pitch direction is given a periodic boundary condition $\phi_a = \phi_{a+\Delta\theta}$, where ϕ is the value of the variable and θ is the period. To maintain the free stream Mach number of 0.24 at various incidences, the value of the pressure outlet can be adjusted.

Unsteady calculations are achieved by adding virtual time steps. Based on the intense unsteadiness and three-dimensionality in the compressor passage flow, a uniform time step of 1.0 × 10–5 has been set in the computation. The CFL numbers led by this configuration are controlled within 5.0.

TABLE 2 Compressor cascade geometry and inlet aerodynamic parameters documented by Loughery et al. (1971).

Blade geometry	
Chord	120 mm
Solidity	1.28
Aspect ratio	1.3
Stagger angle	15.3°
Blade inlet angle	40°
Blade exit angle	100°

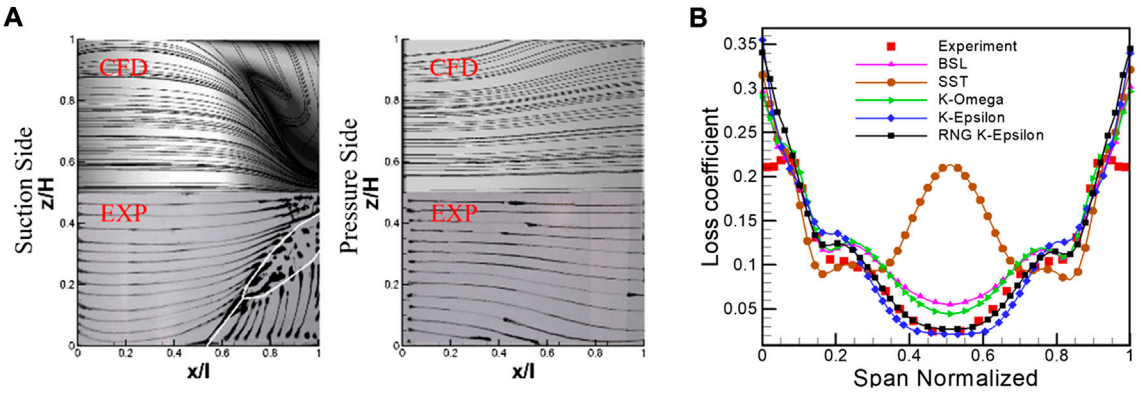

FIGURE 3
Validation of the 3-D simulation model. **(A)** Limiting stream lines of CFD and experimental results; **(B)** the spanwise distribution of total pressure loss coefficient at outlet.

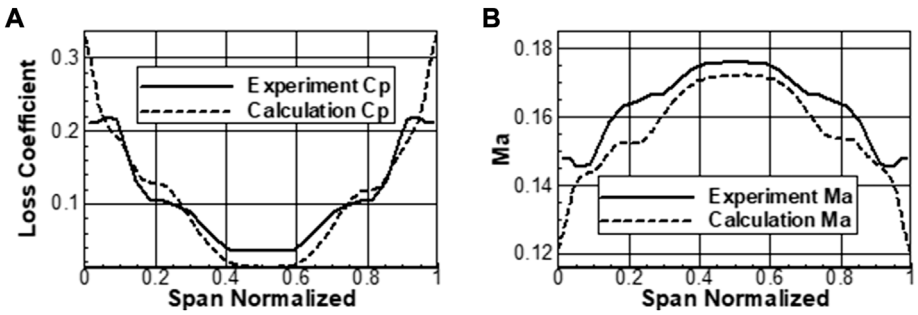

FIGURE 4
Total pressure loss coefficient and Mach number comparison. **(A)** Total pressure loss coefficient; **(B)** Mach Number.

All the unsteady calculations use the results of steady calculations as the initial condition.

2.2 Numerical validation

This section is the validation of numerical calculation. We use the data provided by Soria and Cantwell (1993) as criteria to validate the numerical calculation configuration. The experimental parameters are shown in Table 2. During the numerical calculation of the high-load compressor, large-scale separated flow is bound to exist, and in order to be able to accurately describe the three-dimensional flow structure, the numerical parameter configurations in this study are set strictly based on the results of the numerical calculation calibration. These include the number of meshes, wall y + values, and the time and spatial discrete schemes.

The choice of turbulence is first examined. As shown in Figure 3B, the spanwise distribution of the pitch-averaged total pressure loss coefficient (defined by Eq. 2) calculated with the RNG k-Epsilon model matches better with the experimental data than other models. The comparison of the total pressure loss coefficient and the outlet Mach number is shown in Figure 4A, B, respectively, which can prove the accuracy of the numerical calculation results. In the spatial dimension Figure 3A, the separation topology, such as the onset and extent of the corner separation region, captured by ink flow visualization in the experiment, is remarkably predicted by the numerical results. Therefore, the present numerical configuration is reliable for revealing the flow characteristics in a high-load cascade.

$$\omega_2 = \frac{p_1^* - p_2^*}{p_1^* - p_1} \tag{2}$$

.

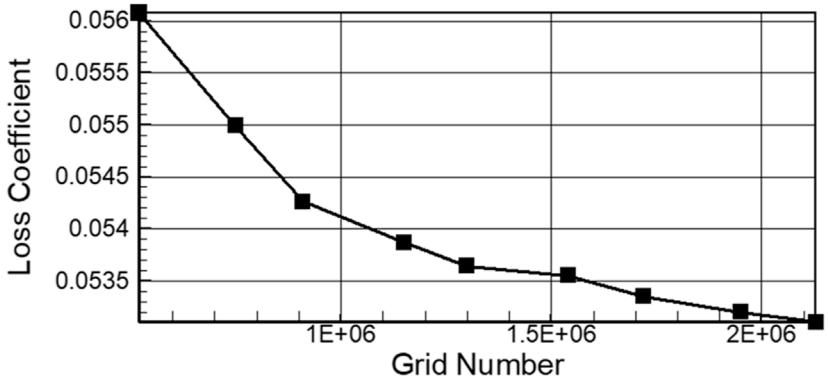

FIGURE 5
Grid independent validation of 3-D simulation.

The grid independence is investigated to ensure reasonability of the numerical configuration used in the current study. Figure 5 presents the variation of the total pressure loss coefficient with respect to the total grid numbers. The results show that further refinements (grid number larger than 1.15 million) of grids leads to less than 0.5% difference of loss coefficients, which indicates the consistency of the current simulations with respect to the variation of grid resolution.

3 Results and discussion

A detailed numerical analysis of the oscillation parameters and suction control parameters is presented in this section. Changes of the oscillating aspiration on the structure of the vortex are also investigated in depth. For a more accurate representation of the flow field structure, the Q-criterion, absolute value of the vorticity Ω, dissipation function Ω, and the total pressure loss coefficient ω are introduced.

Vorticity Ω expresses the rotational velocity of the fluid, which can be calculated using the following Eq. 3:

$$\boldsymbol{\Omega} = \nabla \times \boldsymbol{V}, \tag{3}$$

where Q-criterion is used to identify vortex structures. Q is the second matrix invariant of the velocity gradient, which can be calculated using the following Eq. 4:

$$\boldsymbol{Q} = \frac{1}{2}\left(\| \boldsymbol{\Omega} \|^2 - \| \boldsymbol{S} \|^2\right) \tag{4}$$

.

It can be seen that Q is a function which contains the angular velocity tensor Ω and the strain rate tensor S, and operator $\|\|$ represents the Euclide norm. The magnitude of Q represents the relationship between rotation and deformation in the flow passage. Based on the experience gained during this study, Q insists on giving preference to methods based on vorticity or streamlines in vortex identification.

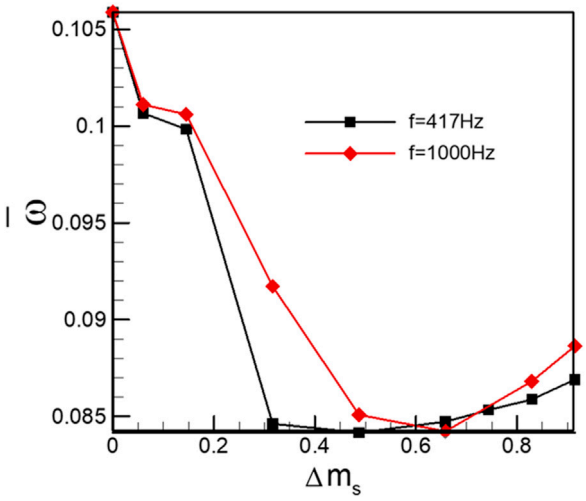

FIGURE 6
Distribution of total pressure loss according to the oscillation amplitude in the control of BLOS (0.39 $\bar{Z}$, m_s = 1.77%, α = 25°, i = 0°).

The entropy production of turbomachinery can be divided into two parts: dissipative entropy production and heat transfer entropy production. The dissipation function Φ can be obtained through entropy transport Eq. 5. It can be used to describe the sources of loss inside the passage.

$$T\frac{\boldsymbol{Ds}}{\boldsymbol{dt}} = \frac{\boldsymbol{Dq}}{\boldsymbol{dt}} + \frac{\boldsymbol{\Phi}}{\boldsymbol{\rho}} \tag{5}$$

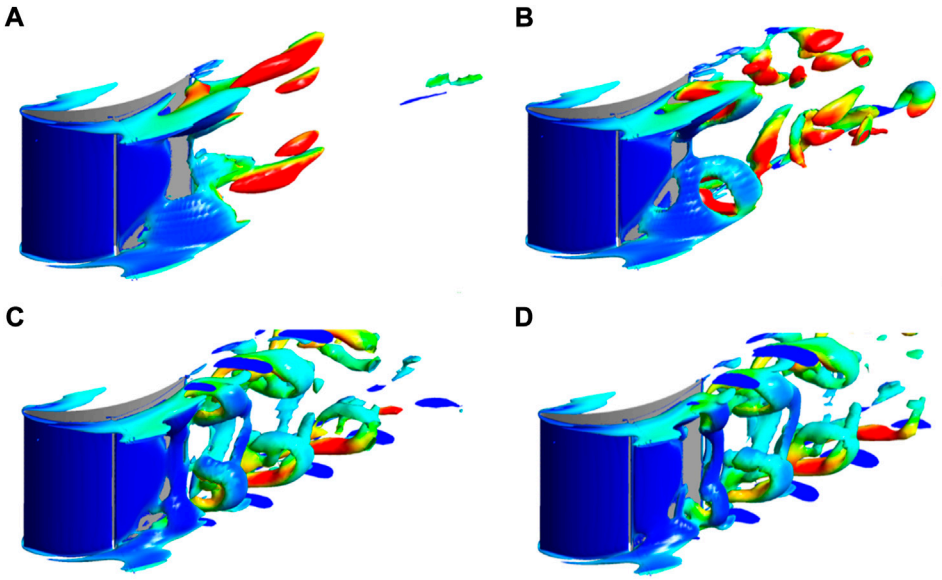

FIGURE 7
Instantaneous vortex structures of the cascade in the control with different oscillation amplitudes (Q = **2** × **10^6**, 0.39 $\bar{Z}$, m_s = 1.77%, f = 1,000 Hz, α = 25°, i = 0°). **(A)** Δm_s = 0.00%, BLS; **(B)** Δm_s = 5.98%, BLOS; **(C)** Δm_s = 48.71%, BLOS; and **(D)** Δm_s = 82.91%, BLOS.

3.1 Influences of excitation parameters on control effects

3.1.1 The effect of excitation amplitudes

Figure 6 shows the variation of the total pressure loss coefficient with excitation amplitude. Both situations with f = 417 Hz and f = 1,000 Hz are considered here. The total pressure loss reaches 0.106 when Δm_s = 0.0, the BLS case. It can be seen that only when the excitation amplitude exceeds the threshold value of 0.2 does it have a significant positive effect on cascade performance. Optimal control is achieved in the following ranges from Δm_s = 0.316 to Δm_s = 0.7, with the maximum loss reduction approaching 8.42% for the case of f = 417 Hz. The change in frequencies, from 417 to 1,000 Hz, also affects the control effect, which can be concluded from the narrowed optimal region. It should be noticed that, beyond the optimal amplitudes, the control effects tend to deteriorate in both cases. Because of the inevitable introduction of additional viscous dissipation into the flow field, led by mass flow oscillation in the BLOS case, excessive increase in excitation amplitudes gives rise to more viscous loss and hence weakens the overall control effects.

The enhanced performance is indicative of promoted flow fields, which could be detected from flow topologies visualized by iso-surfaces of Q-value in Figure 7. In the BLS case Figure 7A, the separation vortices bearing the appearances of layer structures on the suction surface stably resides in the corner regions near the end walls. As the excitation amplitude approaches 5.98%, the layer-shaped separation vortices are forced to break down near the trailing edge, which can be attributed to the introduced unsteady effects by periodical oscillation in aspirating flow rates. Furthermore, the increased amplitudes, between 48.71 and 82.91%, tend to intensify the unsteady actuation in the separation vortices. The substantial change in the vortex

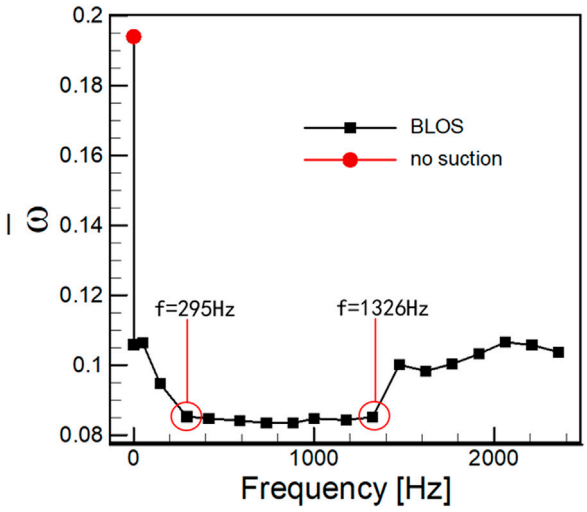

FIGURE 8
Distribution of total pressure loss according to the oscillation frequency in the control of BLOS (0.39 $\bar{Z}$, ms = 1.77%, Δm_s = 48.71%, α = 25°, i = 0°).

TABLE 3 Spectrum graph of total pressure with different excitation frequencies.

f_{excit}	$f_{monitor}$ (Hz)				
	10% H	30% H	50% H	70% H	90% H
147	147	147	147	147	147
417	417	417	417	417	417
736	736	736	736	736	736
884	884	884	884	884	884
1,178	1,178	1,178	1,178	1,178	1,178
1,326	1,326	1,326	1,326	1,326	1,326
1,767	1767	1767	1767	1767	1767
1,915	1915	1915	1915	1915	1915
2,062	2062	2062	2062	2062	2062
2,209	2,209	2,209	2,209	2,209	2,209
2,357	2,357	2,357	2,357	2,357	2,357

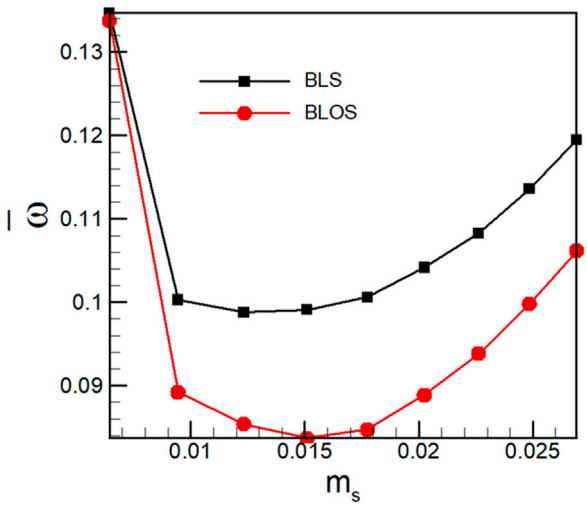

FIGURE 9
Distribution of time-averaged total pressure loss by the time-averaged suction mass flow in the control of BLOS and BLS.

structure due to BLOS is manifested in the splitting of the steady laminar separated vortex into a series of vortex tubes. These vortex tubes are simultaneously swept up by the lateral secondary flow near the end wall, forming a donut-like structure, and then periodically shed into the wake, which inevitably causes significant periodic oscillations in the flow field, thereby restoring the instability that the fluid inherently possesses.

It is the spatiotemporal alteration in vortical structures that distinguishes the control effects in the BLS and BLOS cases. More detailed discussions about the transformed separation topology and related performance variation will be presented subsequently.

3.1.2 The effect of excitation frequencies

The effect of another key control parameter, i.e., frequency on the control effect was investigated with an excitation amplitude of 48.71%. The variation of temporal-averaged total pressure loss coefficient is plotted in Figure 8. The uncontrolled case is used as a reference and is represented as a red circular solid dot in the aforementioned figure. The BLS and BLOS methods greatly improve the cascade performance by effectively mitigating large-scale separation in the uncontrolled flow field. The benefits of stabilized suction have been extensively documented in previous studies. The introduction of oscillations in the suction stream can further reduce losses within a certain optimal bandwidth. As labelled by red circular rings in Figure 8, the most effective controls are achieved in the range of f = 295 Hz through f = 1,326 Hz, with the maximum relative loss reduction approaching 20.5% of that in the BLS case. Beyond this range, the BLOS method no longer shows great advantages over the BLS method. This relative wide effective excitation bandwidth, discovered currently, indicates a large tolerance for choosing excitation frequencies in practical applications.

The temporal features of controlled flow fields with various excitation frequencies are revealed in Table 3. The five monitor points are placed at the streamwise location shown in Figure 1 and evenly distributed from 10 to 90% span. The time histories of total pressure captured by these monitor points are processed *via* fast Fourier transformation to extract the characteristic frequencies. As shown in the aforementioned table, the main frequencies captured in the flow field are in line with the excitation frequencies, which indicates that the unsteady properties in BLOS controlled flow fields are fully restrained by the oscillating aspiration flow rate. Furthermore, it could be argued that active flow control methods always have the tendency to impose some of their inherent physical properties on the flow field by means of mass, momentum, or energy exchange.

3.2 The response of effects to varied suction arrangement

An initial understanding about the process of boundary layer oscillation aspiration controlling a separation flow, especially the introduction of unsteady effect into the flow, is established in the previous section. The advantages possessed by BLOS over BLS in the control effects have also been proven to some extent. In this part, we perform further comparative investigations between BLS and BLOS on their susceptibility to varying operating conditions containing various suction flow rate, incidences, and suction locations.

3.2.1 The response to the mass flow rate of aspirations

The fundamental physical mechanism behind the boundary layer suction technique is to remove the low-energy fluid within

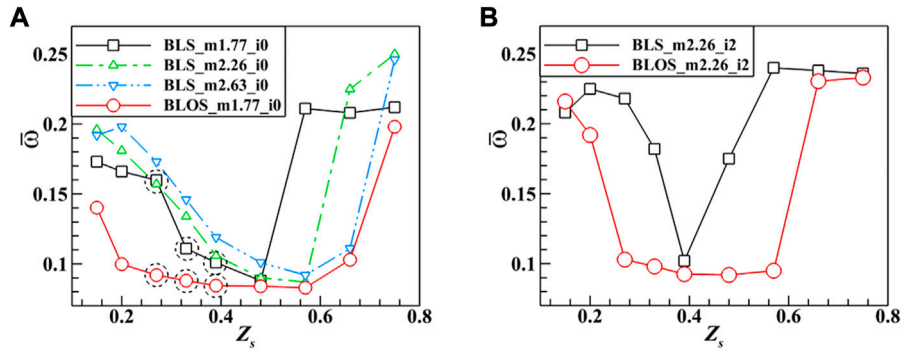

FIGURE 10
Distribution of time averaged total pressure loss according to the suction location in the control of BLOS and BLS. **(A)** m_s = 1.77%, i = 0° and **(B)** m_s = 2.26%, i = 2°.

the boundary layers. Achieving the most effective control at the lowest cost, mostly the aspirating flow rate, is always pursued, which can lead to the least impact on the main flow in cascades. In Figure 9, the performance variations with increasing aspirating flow rates for both BLS and BLOS cases are presented. In both cases, the suction control fails until the flow rate exceeds 1%. Afterward, both the control methods improve the performance of the cascade, with the BLOS method showing an advantage, with the largest relative loss reduction being 15.77% of that in the BLS case. This indicates that oscillatory suction is more effective than steady suction in controlling the separation flow at the same flow rate, or, from another point of view, the BLOS method can achieve the same control as the BLS case with a low suction flow rate.

3.2.2 The response to aspiration locations

To illustrate the influences of aspiration locations on the control processes, the performance variations for both BLS and BLOS cases with some selected parameters are shown in Figure 10. It can be observed that the effects led by the BLS method bear great sensitivity to the locations from Figure 10A. The enhancements only occur in a narrow location range of Z_s = 0.33 through Z_s = 0.48 when the aspiration flow rate is equal to 1.77%. In addition, even in this narrow range, the control effects vary obviously with different values of Z_s. Further increasing the suction flow rate to 2.26% results in slight extension in the effective range. As the incidence is increased to 2 in Figure 10B, the effective control could only be realized at Z_s = 0.39 for the BLS cases. This indicates that the sensitivity of BLS control to locations is intensified at off-design conditions. The similar conclusion to that widely documented in previous research studies could be drawn that it is the dramatic sensitivity to geometric suction configurations that significantly prohibits the boundary layer aspiration technology from practical applications in engineering.

On contrast, the BLOS method gives rise to suppression on the sensitivity of control effects to suction locations, which can be verified by the extended location range of Z_s = 0.2 through Z_s = 0.66 presented in Figure 10A. Meanwhile, the loss reductions in this region are close in value, indicating robustness in the control effects owned by the BLOS method. In addition, it is worth noting that a wider effective range can be achieved at a lower suction flow rate *via* the BLOS method (m = 1.77%) than that *via* the BLS method (m = 2.26%). Also, at off-design conditions, the less exaggerated sensitivity of the control effect, reflected by a wider effective range from Z_s = 0.39 to Z_s = 0.57 in Figure 10B, repeatedly demonstrates the advantages of the BLOS method.

Another issue considered currently is to exclude the possibility that the aforementioned advantages of the BLOS method are resulted from the instantaneous increase in the suction flow rate during a half-oscillation period. Thus, in Figure 10A, we additionally present a BLS result with a suction flow rate equal to 2.63%, which is the peak value of the sinusoidally varied suction flow rate in BLOS. The result turns out that this BLS configuration still not only fails to effectively improve the performance to the same extent as the BLOS case, but even worsens the performance globally. The resultant conclusion could be drawn that the introduction of unsteady effects by the oscillating suction flow rate is the main cause of the superiority possessed by the BLOS method to the BLS one.

The different spatiotemporal alterations of separation structures for the BLS and BLOS cases are examined subsequently. The flow fields of cases, as labelled by dashed circles, with Z_s = 0.27, 0.33, and 0.39 in Figure 10A, are selected to perform detailed analysis. The limiting streamlines on solid surfaces for selected cases are presented in Figure 11. In the case with suction location being 0.27 axial chord length, the BLS method fails to effectively suppress large-scale separation on the suction

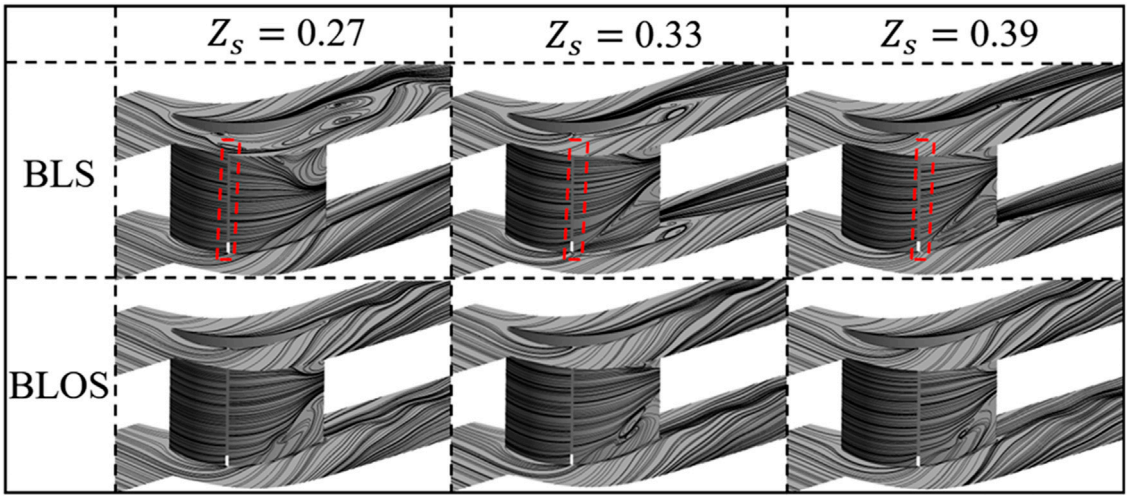

FIGURE 11
Instantaneous limiting streamlines by different suction locations in the control of BLOS and BLS.

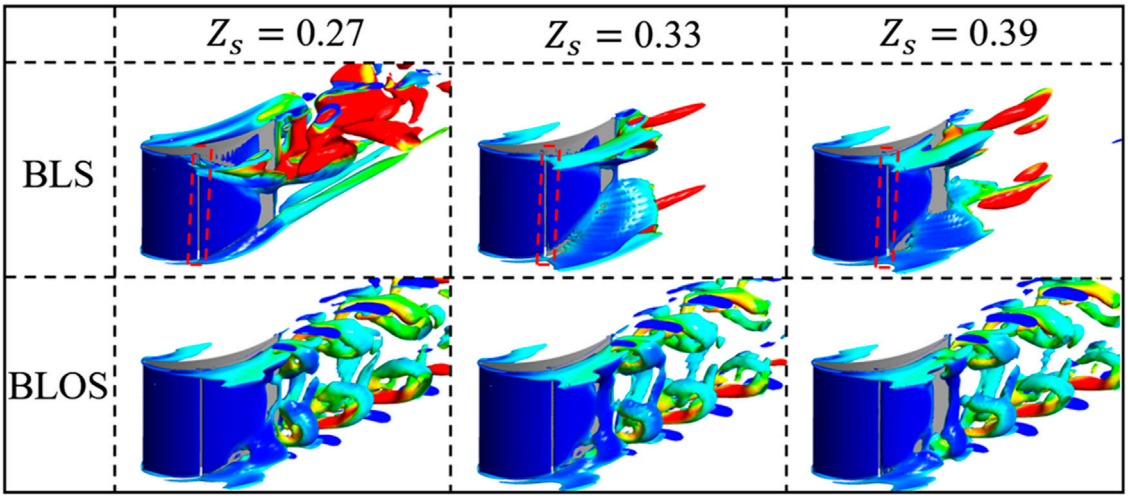

FIGURE 12
Instantaneous vortex structures by different suction locations in the control of BLOS and BLS.

surface. As a result, the cascade stall occurs throughout the entire span, giving rise to enormous losses. As the suction location moves downstream to 0.33 axial chord length, the BLS method starts to take effect by alleviating the cascade stall to the corner stall, which can be observed from the streamlines on both the suction surface and end walls. The flow topology in the BLS case becomes less severe when Z_s = 0.39, which bears resemblance to the corner separation topology. On the other hand, BLOS, in all the situations considered here, successfully prevents the cascade from stalling by reorganizing the vortical structures and hence maintaining the high performance in the critical load cascade. It should be pointed out that even though streamline topologies presented in both BLS and BLOS cases at Z_s = 0.39 are similar, the vortical structures literally differ from each other, which will be discussed in the following section.

The instantaneous vortical structures visualized in terms of Q iso-surfaces for selected cases are presented in Figure 12 in order to describe the entirely different vortical evolutions in the steadily and unsteadily controlled flow fields. The difference between the

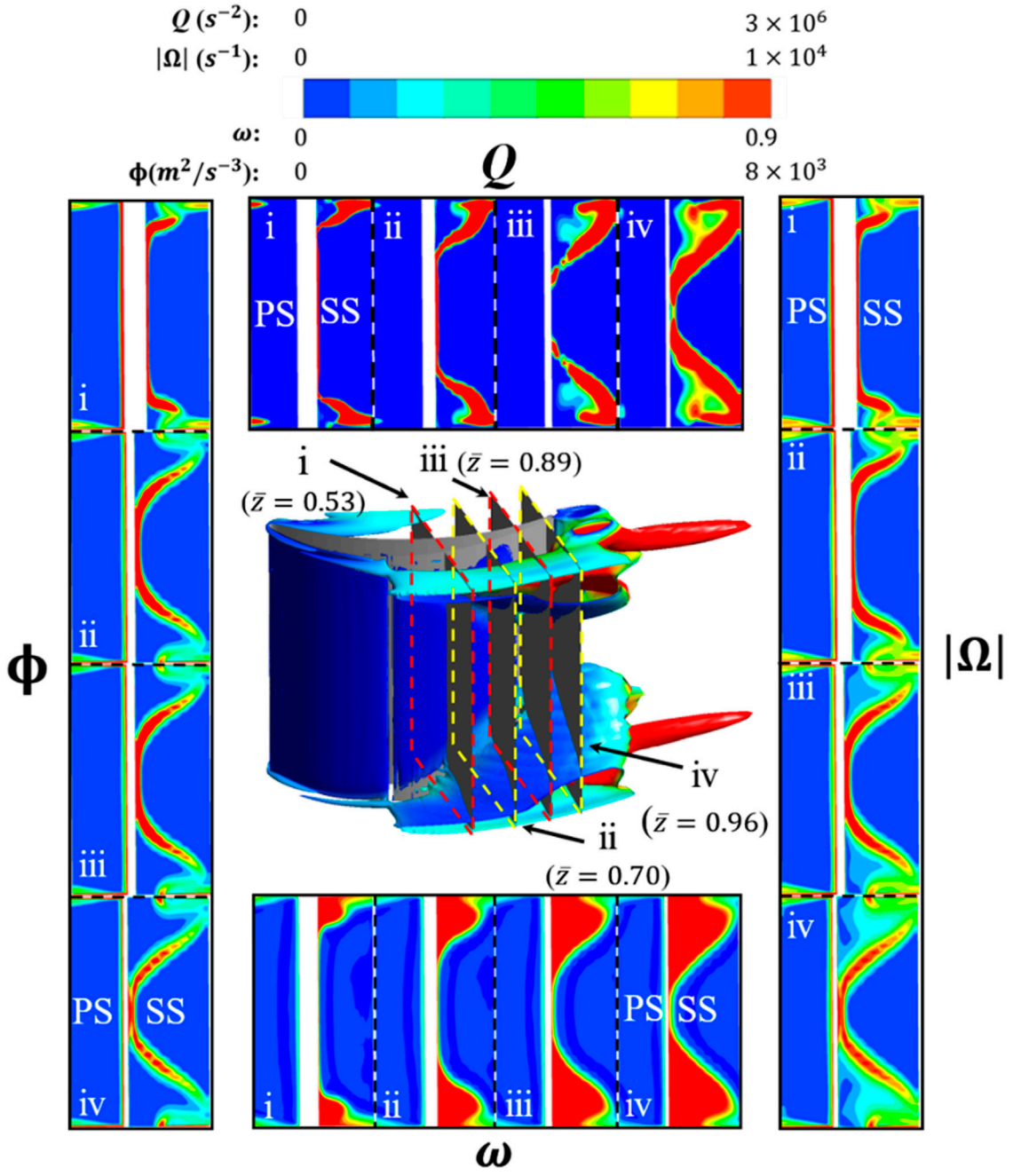

FIGURE 13
Instantaneous vortex structure and loss of stream-wise observing section in the control of BLS.

BLS and BLOS controlled flow fields manifests itself not in the structural transformations of the quasi-columnar vortices such as horse-shoe vortices and passage vortices but exclusively in the development of separation vortices on suction surfaces. In situations where the BLS method is adopted, the separation vortices on the suction surface show a relatively stable layer-shaped structure. The spatial extents of these structures shrink gradually as the control effects become strengthened from Z_s = 0.27 to Z_s = 0.39 and stably distributed in the corner regions. The reason for this transformation is that the BLS method removes the low-energy fluids within the boundary layer and improves its capacity of resisting inverse pressure gradients. In this way, the boundary layer is re-allocated and induces new separation vortices which are consequently stabilized under the influence

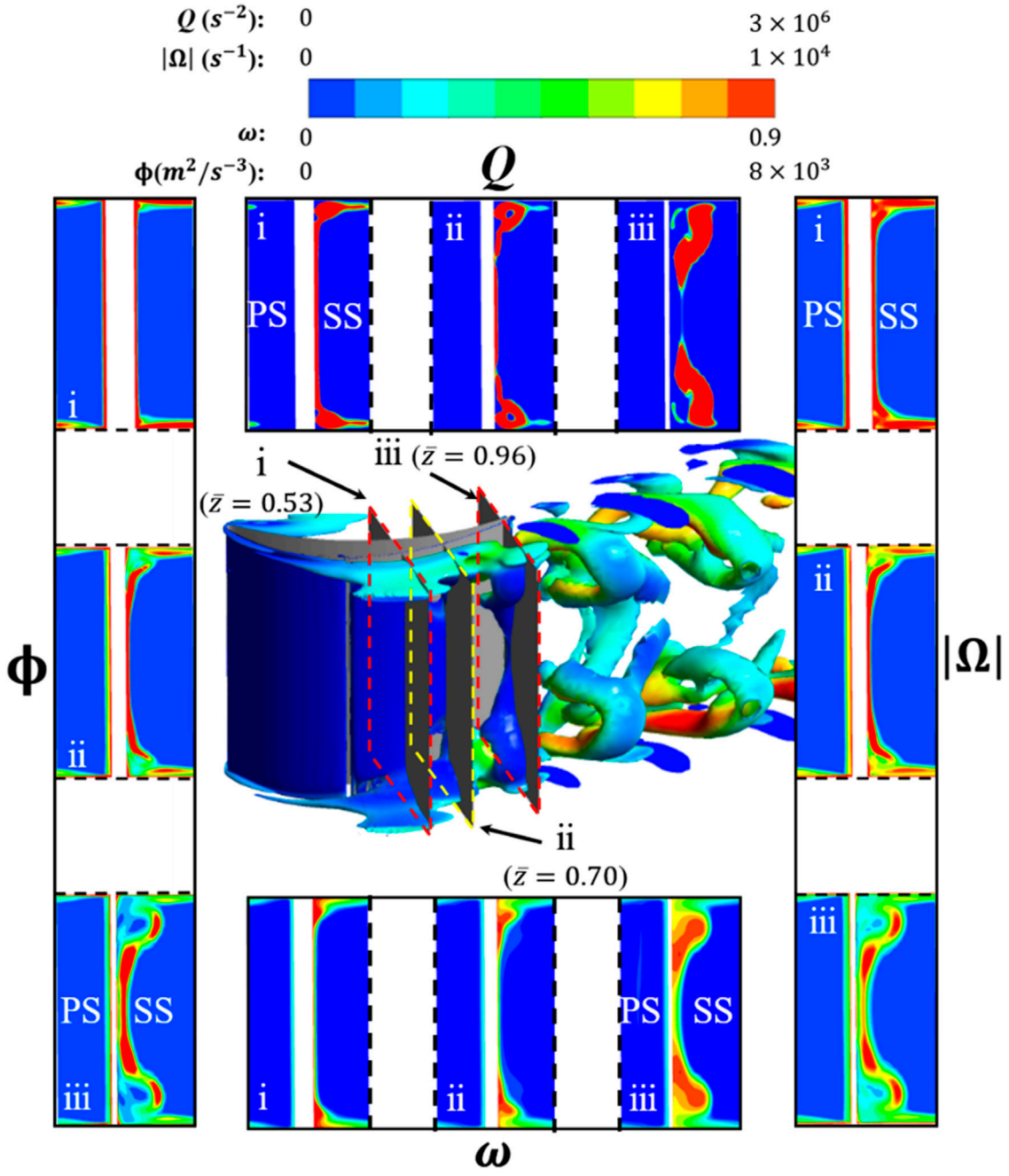

FIGURE 14
Instantaneous vortex structure and loss of stream-wise observing section in the control of BLOS.

of the 'steady properties' possessed by the BLS method. The BLOS controlled fields under consideration here consistently exhibit a series of discretized ring-like vortices convecting downstream in the corner regions. Thus, it could be deduced that this vortical-ring street structure can benefit the tolerance of cascades against the varied operating conditions more than the conventional corner separation topologies in diffusion cascades.

3.3 Spatiotemporal alterations in separation flows

The differences in performance improvement between BLS and BLOS are direct reflections of vortical alterations in flow fields which have been briefly described in the previous section. The relation between transformed separation topologies and

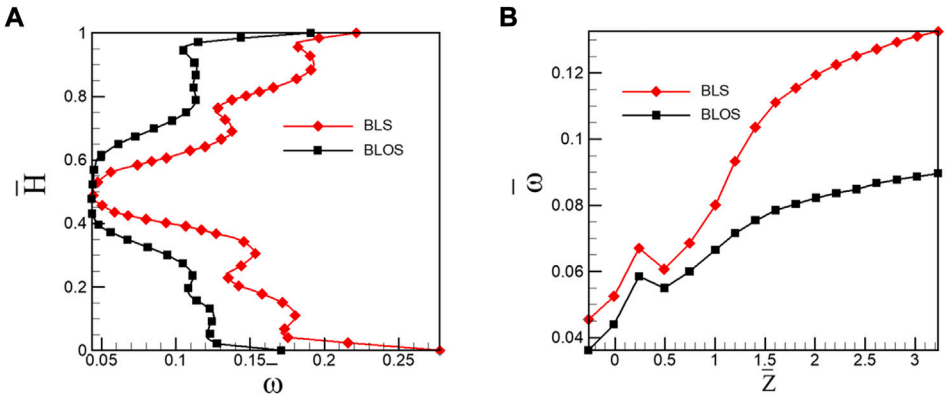

FIGURE 15
Span-wise distribution of pitch-averaged total pressure loss. **(A)** Stream-wise increase of overall mass-averaged total pressure loss and **(B)** in the outlet of cascade in the control with BLS and BLOS with the suction location of 0.33 $\bar{Z}$.

performance enhancement is emphasized in this section in order to advance our knowledge about the main cause of the different control effects.

The results with Z_s = 0.33, ms = 1.77% are under consideration. For the BLOS case, the frequency and amplitude are 1,000 Hz and 48.71%, respectively. The vortical evolution and the accompanying loss distributions are analyzed according to contours plotted on the streamwise slices as shown in Figures 13 and 14.

In the BLS controlled flow field, the layer-shaped separation vortices consistently possess high vorticity from the onset to the later evolutionary stage according to both Figure 13(Q) and ($|\Omega|$). This gives rise to significant local losses due to the strong shear stress (see Figure 13(ϕ)) in the regions where they reside. A large amount of low-energy fluids is meanwhile confined in the regions enclosed by the separation vortices and solid walls. Also, these fluids lead to extremely high total pressure loss regions in the corners as shown in Figure 13(ω). Thus, it could be concluded that in the BLS controlled flow field, the separation vortex consistently possesses high vortical strength, and the flow loss caused by it is the main source of the overall cascade loss.

For the BLOS case shown in Figure 14, vortical alterations induce different distributions of aerodynamic quantities. From the vortical evolution (slice 1 to 3) shown in Figure 14(Q), it can be observed that the separation vortices are effectively discretized and roll up forming ring-shaped structures because of periodic excitation. In addition, the separation vortices are weakened in vorticity (see Figure 14($|\Omega|$)) and cause less local viscous dissipation as shown in Figure 14(ϕ). The vortical transformation also shrinks the high-loss zones shown in Figure 14(ω) indicating less low-energy fluids bounded within the separation vortices and meanwhile enhanced the cascade throughflow.

The aforementioned changes bring about significant reduction in pitch-averaged loss at the cascade outlet in the entire span as shown in Figure 15A. In streamwise direction, the distribution of averaged total pressure loss presented in Figure 15B reveals that the loss reduction takes place not only in the flow passage but also in the wake. Compared with the BLS case, the BLOS case causes a loss reduction of 17.5% at the trailing edge and 34.6% two axial chord lengths downstream the trailing edge. This denotes that the BLOS-induced vortex ring streets generate less viscous dissipation as convecting in the wake.

Both the aspiration control methods are based on the effective removal of low-energy fluids. Moreover, the advantages possessed by the BLOS method in improving the cascade performance are achieved mainly through changing the layer-shaped separation vortices to the discretized donut-shaped vortex streets shedding into the wake. The benefits brought by the vortical transformation include (1) attenuated vorticity of separation vortices producing less local viscous dissipation; (2) narrowed blockage area trapping less low-energy fluids in the vicinity of corner regions; and (3) more energetic blockage fluids contributing to the mixing loss reduction in the wake.

4 Conclusion remarks

Simulations of the flow of a three-dimensional linear high-load compressor cascade controlled by the BLS and BLOS methods were carried out. The effect of oscillation parameters on the control effect was parametrically investigated. In addition, a comparative analysis of the sensitivity of the BLS and BLOS methods to different operating conditions was carried out. This work was performed to understand the basic aerodynamics of unsteady suction for controlled flow separation.

4.1 Control parameters

Oscillation amplitude and frequency are two crucial control parameters. The amplitude represents the energetic level of the unsteady excitation. Only when it exceeds a certain threshold can the BLOS method take effect, and in this study, the threshold value equals 0.31 approximately. However, due to the additional viscous dissipation introduced, excessive amplitudes weaken the control effect. A relative wide optimal frequency bandwidth within which the BLOS method surpasses the BLS method is detected in the current study. Also, in these situations, the characteristic frequency of the flow field is locked up to the excitation frequency.

4.2 Susceptibility to varying conditions

The BLOS method shows advantage over the BLS method on the control cost and the susceptibility to varying working conditions. With a fixed effective suction flow rate, the BLOS method can result in higher loss reduction. The variation in suction locations affects the BLOS controlled cascades less significantly than that with the BLS method. The operating range in terms of incidences is highly extended due to introduction of oscillation into the aspiration.

4.3 Flow structures

Oscillatory aspiration takes over the advantages of steady aspiration and further introduces structural reorganization in the flow field. The spatial transformation is mainly reflected in the discrete laminar separation vortex into a donut-shaped vortex street shedding to the wake flow. The vortical alteration leads to lower vorticity of separation vortices and hence decreases the viscous shear stress. The cascade blockage is also alleviated, indicating less low-energy fluids bounded in the corners. Furthermore, the donut-shaped vortex street contributes to the reduction in mixing loss in the wake.

Data availability statement

The original contributions presented in the study are included in the article/Supplementary Material; further inquiries can be directed to the corresponding author.

Author contributions

BL completed most of the numerical simulation work and processed and analyzed the numerical results; LC proposed the method of boundary layer oscillating suction; HX jointly completed the analysis of the numerical simulation results; HF jointly completed part of the analysis of the results and drew part of the charts; and SW gave theoretical guidance to numerical simulation and result analysis.

Conflict of interest

The authors declare that the research was conducted in the absence of any commercial or financial relationships that could be construed as a potential conflict of interest.

Publisher's note

References

Culley, D. E., Bright, M. M., and Prahst, P. S. (2003). "Active flow separation control of a stator vane using surface injection in a multistage compressor experiment," in Proceedings ASME Turbo Expo 2003, collocated with the 2003 International Joint Power Generation Conference, Atlanta, Georgia, USA, February 4, 2009 (American Society of Mechanical Engineers), 1039–1050. doi:10.1115/GT2003-38863

Culley, D. E., Bright, M. M., and Prahst, P. S. (2003). *Active flow separation control of a stator vane using surface injection in a multistage compressor experiment*. Washington, DC: ASME Paper.

Dorfner, C., Hergt, A., and Nicke, E. (2011). Advanced nonaxisymmetric endwall contouring for axial compressors by generating an aerodynamic separator—Part i: Principal cascade design and compressor application. *ASME J. Turbomach.* 133, 021026. doi:10.1115/1.4001223

Guendogdu, Y., Vorreiter, A., and Seume, J. R. (2008). "Design of a low solidity flow-controlled stator with coanda surface in a high speed compressor," in Proceeding ASME Turbo Expo 2008: Power for Land Sea, and Air, Berlin Germany, August 3 2009 (American Society of Mechanical Engineers), 629–639. doi:10.1115/GT2008-5118011

Gümmer, V., Goller, M., and Swoboda, M. (2008). Numerical investigation of end wall boundary layer removal on highly loaded axial compressor blade rows. *J. Turbomach.* 130 (1), 011015. doi:10.1115/1.2749297

Hamrin, M., Gunell, H., Lindkvist, J., Lindqvist, P.-A., Ergun, R. E., and Giles, B. L. (2018). Bow shock generator current systems: MMS observations of possible current closure. *JGR. Space Phys.* 123 (1), 242–258. doi:10.1002/2017JA024826

Jahanmiri, M. (2010). *Active flow control: A review*. Sweden: Chalmers University of Technology.

Kerrebrock, J. L., Epstein, A. H., Merchant, A. A., Guenette, G. R., Parker, D., Onnee, J. F., et al. (2008). Design and test of an aspirated counter-rotating fan. *J. Turbomach.* 130 (2), 021004. doi:10.1115/1.2776951

Kerrebrock, J. L., Reijnen, D. P., Ziminsky, W. S., and Smilg, L. M. (1997). "Aspirated compressors," in Proceedings ASME 1997 International Gas Turbine

and Aeroengine Congress and Exhibition, Orlando Florida USA, December 24, 2014 (American Society of Mechanical Engineers.). doi:10.1115/97-GT-525

Le, C. (2015). *Investigation on separation structure and its steady & unsteady control in low reaction high load compressor cascade*. China: Harbin Institute of Technology.

Lee, M. U., Ji, J.-Y., and Yun, G. S. (2020). Cold-hot coupled waves in a flowing magnetized plasma. *Nucl. Fusion* 60, 126036. doi:10.1088/1741-4326/abb61a

Loughery, R. J., Horn, R. A., and Tramm, P. C. (1971). *Single stage experimental evaluation of boundary layer blowing and bleed techniques for high lift stator blades*. Washington, D.C.: NASA CR-54573.

Merchant, A. A. (2000). "Aerodynamic design and analysis of a high pressure ratio aspirated compressor stage," in Proceeding ASME Turbo Expo 2000: Power for Land, Sea, and Air, Munich, Germany, August 4, 2014 (American Society of Mechanical Engineers.), 10. doi:10.1115/2000-GT-0619

Pawan, S., Santosh, K. S., and Harekrishna, Y. (2022). Experimental investigation of flow and thermal characteristics of synthetic jet issuing from sharp-edged orifices. *Exp. Heat. Transf.* 9, 1–25. doi:10.1080/08916152.2022.2105449

Schlaps, R. C., Shahpar, S., and Gümmer, V. (2014). "Automatic three-dimensional optimisation of a modern tandem compressor Vane," in Proceedings of ASME TURBO, 2014, Düsseldorf Germany (ASME). doi:10.13140/2.1.2633.6007

Seifert, A., Darabi, A., and Wyganski, I. (1996). Delay of airfoil stall by periodic excitation. *J. Aircr.* 33 (4), 691–698. doi:10.2514/3.47003

Siemann, J., and Seume, J. R. (2015). "Design of an aspirated compressor stator by means of doe," in Proceeding ASME Turbo Expo 2015: Turbine Technical Conference and Exposition, Montreal Quebec Canada, August 12, 2015 (American Society of Mechanical Engineers.), 13. doi:10.1115/GT2015-42474

Song, Y. P., Chen, F., Yang, J., and Wang, Z. Q. (2005). *A numerical investigation of boundary layer suction in compound lean compressor cascades. Turbine technical conference and exposition*. USA. New York: ASME.

Soria, J., and Cantwell, B. J. (1993). Identification and classification of topological structures in free shear flows. *Eddy Struct. Identif. Free Turbul. Shear Flows* 21, 379–390. doi:10.1007/978-94-011-2098-2_31

Sushanta, D., and Shantanu (2022). Effects of the synthetic jet on the flow field and heat transfer over a surface-mounted square rib. *Exp. Therm. Fluid Sci.* 139, 110708. doi:10.1016/j.expthermflusci.2022.110708

Vandeputte, T. W. (2000). Effects of flow control on the aerodynamics of a tandem inlet guide vane, Master's thesis. Blacksburg, Virginia: Virginia Polytechnic Institute and State University.

Vytenis, M. (2020). Magnetosphere: From plasma observations to reconnection theory. *J. Geophys. Res. Space Phys.* 125 (9), JA027865. doi:10.1029/2020JA027865

Wang, S., Qiang, X., and Feng, G. (2007). "Highly-loaded low-reaction boundary layer suction axial flow compressor," in Proceeding ASME Turbo Expo 2007: Power for Land, Sea, and Air, Montreal, Canada, March 10, 2009 (ASME), 405–412. doi:10.1115/GT2007-28191

Zhang, L., Du, X., and Liu, X. (2016). "3D unsteady simulation of a low speed low-reaction aspirated compressor," in Proceeding ASME Turbo Expo 2016: Turbomachinery Technical Conference and Exposition, Seoul South Korea, September 20, 2016 (American Society of Mechanical Engineers.). doi:10.1115/GT2016-56888

Zheng, J. G., Zhao, Z. J., Li, J., Cui, Y. D., and Khoo, B. C. (2014). Numerical simulation of nanosecond pulsed dielectric barrier discharge actuator in a quiescent flow. *Phys. Fluids* 26 (3), 036102. doi:10.1063/1.4867708

Nomenclature

A Correlation matrix

C Chord length

C_p Pressure coefficient

E_p Projection errors

f Frequency of oscillation

H Characteristic length of the separation zone

i Incidence

N_m Total number of POD modesTotal number of POD modes

N_s Total number of snapshotsTotal number of snapshots

α_k Temporal coefficient of the *k*th modeTemporal coefficient of the *k*th mode

Ma Mach number

N_m Total number of POD modesTotal number of POD modes

N_s Total number of snapshotsTotal number of snapshots

p Static pressure

p_1 Mass-averaged static pressure at the inlet

p_1^* Mass-averaged total pressure at the inlet

p_2^* Mass-averaged total pressure at the outlet

Pr Pressure ratio

Q Q-criterion

Re Reynolds number

S Strain tensor

St Strouhal number

t Time

U Streamwies velocity

U_{out} Time-averaged velocity at the outlet

U_s Time-averaged velocity at suction slot exit

U_0 Oscillation amplitude

u Velocity

u′ Fluctuating velocity

$\bar{\mathbf{u}}$ Time-averaged velocity

α_k Temporal coefficient of the *k*th modeTemporal coefficient of the *k*th mode

φ Phase of the excitation

λ_k *k*th eigenvalue

ω Total pressure loss coefficient

Abbreviations

AOA Angle of attack

AVDR Axial velocity density ratio

BLS Boundary layer suction

BLOS Boundary layer oscillation suction

CFD Computational flow dynamics

SST Shear stress transport

DES Detached eddy simulation

LES Large eddy simulation

TE Trailing edge

frontiers | Frontiers in Energy Research

TYPE Original Research
PUBLISHED 06 January 2023
DOI 10.3389/fenrg.2022.966713

OPEN ACCESS

EDITED BY
Lei Luo,
Harbin Institute of Technology, China

REVIEWED BY
Jinlong Liu,
Zhejiang University, China
Jian Li,
Shanghai Jiao Tong University, China

*CORRESPONDENCE
Zhitao Wang,
wangzhitao@hrbeu.edu.cn

SPECIALTY SECTION
This article was submitted to Advanced Clean Fuel Technologies, a section of the journal Frontiers in Energy Research

RECEIVED 11 June 2022
ACCEPTED 03 August 2022
PUBLISHED 06 January 2023

CITATION
Ming L, Wang Z, Zhang J, Zheng P and Zhang K (2023), Numerical study on the evolution law and correction method of turbine characteristics of the gas turbine under alternative fuel conditions. *Front. Energy Res.* 10:966713. doi: 10.3389/fenrg.2022.966713

Numerical study on the evolution law and correction method of turbine characteristics of the gas turbine under alternative fuel conditions

Liang Ming[1], Zhitao Wang[1]*, Jingkai Zhang[1], Peiying Zheng[2] and Ke Zhang[2]

[1]College of Power and Energy Engineering, Harbin Engineering University, Harbin, China, [2]AVIC Shenyang Engine Design Institute, Shenyang, China

Reducing carbon emissions is an urgent need in the field of marine power. Gas turbines are of great importance in the marine industry. The use of clean or industrial-associated fuels can increase the fuel adaptability of designed, manufactured, or in-service gas turbines to realize the goal of expanding fuel sources, reducing fuel waste, lowering energy demand, and remitting environmental pressure. By changing from fossil fuel to alternative energy, the change in the physical properties of the combustion products will lead to changes in the working medium of the turbines, which result in a profound effect on the performance. In this study, based on the actual law of working medium property change, the evolution mechanism of turbine characteristics is lucubrated in depth, focusing on the key parameters of the influence of working medium properties on turbine characteristics under alternative fuel conditions, and a correction method is proposed to predict the evolution law of the turbine characteristics as working medium varies.

KEYWORDS

turbine characteristics, evolution law, correction method, alternative fuels, gas turbine

Background

In recent years, carbon peaks and neutrality have been among the most important issues in the energy sector. To reduce carbon emissions, a wide application of clean and industrial-associated fuels are the necessary pathway for marine power. It can meet the future economic and social needs for various types of energy, further improve the comprehensive utilization efficiency of energy, realize the cascade utilization of energy, and play an increasingly important role in social and economic development and energy security (Siemens, 2021).

In the existing research, the field of marine gas turbines rarely involves a large change in the physical properties of turbines. There are a few studies on the mechanism of the influence of the properties of the working mass on the turbine characteristics of the

marine gas turbines. However, in the field of fuel-rich working medium turbines and some closed Breton cycle areas, there are some cases of turbine or circulating working medium changes, so there is a certain research basis.

In the previous studies, the fluid model directly determines the calculation of its thermal properties and influences the performance simulation of the turbine. Gas can be divided into two categories: ideal gas and real gas. For the former, C_p, γ, etc. are just single-valued functions of temperature, and the equation of state is $P = \rho RT$. Such assumptions can be made of both elemental and mixtures without chemical reactions. In particular, C_p and γ are constant values as a calorimetric perfect gas. For the latter, C_p, γ, etc. of the real gas are not only a function of temperature, but also a function of pressure. Such assumptions can be made of mixtures of elemental and chemical reactions. There are many such gas equations of state; the most famous ones are the van der Waals, the Redlich–Kwong, the Peng–Robinson, and the Virtual equations. Typically, when studying at a fuel-rich working medium turbine, the gas is assumed as a calorimetric perfect gas. However, with the increase in the number of turbine stages, the temperature and pressure in front of the turbine are gradually increased, the total temperature drop and the total pressure ratio are gradually increased, and C_p and γ will change with temperature and sometimes will be affected by pressure. Different gases have different C_p and γ. In summary, the calorimetric perfect gas assumption is not fully applicable to all applications, and its errors on the overall and aerodynamic performance of the turbine cannot be ignored sometimes. According to the published literature, scholars have made relevant explorations to study the effects of C_p and γ on turbine performance. These explorations can be roughly divided into three means to describe C_p and γ: constants, single-valued functions of temperature, or functions of temperature and pressure.

Calorimetry perfect gas is a gas, in which C_p and γ are constants; it is a special class of perfect gas. This type of model is simple with a fast numerical calculation speed. However, the scope of application is narrow, which is only suitable for turbines with small temperature drops or compressors with small temperature rises (Roberts and Sjolander, 2002; Canepa and Satta, 2012). Thermal perfect gas is also an idealized gas that does not consider the cohesion between molecules and the volume of the molecule. It only considers the thermal motion of the molecules, so C_p and γ are only the single-value functions of temperature. This model has a moderate speed at calculation, and the results are closer to the actual situation than the calorimetry perfect gas (Jackson et al., 2000; Yao and Amos, 2004; Northall, 2005; Rubechini et al., 2006; Sethi et al., 2008). The real gas model is characterized by thermal parameters such as C_p and γ as functions of temperature and pressure. Specific heat is a complete gas. This model fully considers the influence of pressure. There are many kinds of state equations and a wide range of applications, but the calculation speed is slow, and the requirements for computing resources are high (Cravero and Satta, 2000; Boncinelli et al., 2004; Colonna et al., 2008; Harinck et al., 2010; Gallar et al., 2012; Mirko et al., 2012; Zhang et al., 2014).

When the components change, the thermal properties of the gas mixture, such as constant pressure specific heat and insulation index, change, which will affect the enthalpy of the gas, Mach number, pressure, and other important parameters, and finally change the aerodynamic characteristics of the turbine. Existing studies have shown that the use of the calorimetry perfect gas model, thermal perfect gas model, and real gas model can be applied to different application backgrounds to obtain corresponding research conclusions. The models have advantages and disadvantages in different application backgrounds. The existing research focused on selecting the mathematical model of the same working medium during simulation rather than correcting different working mediums described by the same mathematical model. However, conclusions are instructive, which show that C_p and γ are the core influencing factors.

Analysis of influencing factors of turbine characteristics in gas turbine

The similitude theory is a good perspective to have a clear view of the core influencing factors of the evolution of turbine characteristics.

Differential equation analysis is one of the methods to obtain the similitude criteria. It requires that the basic system of differential equations of the phenomenon and all the single-value conditions be written first. Then, all similar criteria can be found in two ways. One is the so-called differential equation similar transfer method, and the other is the integral analogy method, which is the latter method used in the study.

By using a system of fundamental differential equations describing turbine flow and all single-value conditions for dimensionless processing, all similitude criteria for this phenomenon can be derived. The basic system of equations for viscous fluid mechanics is a system of second-order nonlinear partial differential equations. The continuous equation, the equation of motion, and the energy equation are used as the original description equations for dimensionlessness, and at the same time, similitude criteria are derived. First, a set of characteristic quantities is selected, and the characteristic quantities are simplified according to the basic assumptions. The basic physical quantities are selected as length, velocity, pressure, density, and time, divided by the corresponding variables in the boundary conditions. The resulting dimensionless variables are redefined, and the dimensionless equations and dimensionless boundary conditions are obtained. At the

TABLE 1 The Results of the Mesh Independence Study.

Number of grids	Flow rate (kg/s)	Expansion ratio	Efficiency (%)
102656	1.466	1.05	28.49
196354	4.466	1.13	56.46
356251	6.465	1.16	76.26
564798	8.226	1.18	81.34
681564	8.235	1.2	82.62
846243	8.235	1.2	82.62
1086654	8.236	1.2	82.62
1506599	8.236	1.2	82.62
2341665	8.236	1.2	82.62
2981665	8.236	1.2	82.62

same time, a series of dimensionless combinations are obtained, and the terms in the equation are compared by orders of magnitude, simplifying the similitude criteria as a basis for similarity in model experiments (Liang et al., 2008; Ming et al., 2019a; Ming et al., 2019b).

The basic differential equations are

$$\begin{cases} \dfrac{\partial \rho}{\partial t} + \nabla \cdot \rho v = 0 \\ \rho \dfrac{\partial \rho}{\partial t} + \rho v \cdot \nabla v = -\nabla p - [\nabla \cdot \tau] \\ \rho C_p \dfrac{\partial T}{\partial t} + \rho C_p v \cdot \nabla T = -(\nabla \cdot q) - \left(\dfrac{\partial \ln \rho}{\partial \ln T}\right)_p \dfrac{Dp}{Dt} - [\tau : \nabla v] \end{cases},$$

which are the mass conservation, momentum conservation, and energy conservation equations.

In the equations, τ can be represented by Newton's law of viscosity as follows:

$$\tau = -\mu(\nabla v + (\nabla v)^+) + \left(\frac{2}{3}\mu - \kappa\right)(\nabla \cdot v)\delta,$$

To nondimensionalize with the following proportions:

$$\bar{t} = \frac{v_0 t}{L_0}\ \bar{x} = \frac{x}{L_0}\ \bar{y} = \frac{y}{L_0}\ \bar{z} = \frac{z}{L_0}\ \bar{p} = \frac{p}{p_0}\ \bar{v} = \frac{v}{v_0}\ \bar{T} = \frac{T - T_0}{T_1 - T_0}$$
$$\bar{\rho} = \frac{\rho}{p_0},$$

conservation equations can be nondimensionalized as

$$\begin{cases} \dfrac{\partial \bar{\rho}}{\partial \bar{t}} + \bar{\nabla} \cdot \bar{\rho}\bar{v} = 0 \\ \dfrac{\partial \bar{v}}{\partial \bar{t}} + \bar{v} \cdot \bar{\nabla}\bar{v} = -\dfrac{P_0}{\rho_0 v_0^2}\dfrac{1}{\bar{\rho}}\bar{\nabla}\bar{p} + \dfrac{\mu}{\rho_0 v_0 L_0}\dfrac{1}{\bar{\rho}}\left[\bar{\nabla} \cdot (\bar{\nabla}\bar{v}) + \dfrac{1}{3}\bar{\nabla}(\bar{\nabla} \cdot \bar{v})\right] \\ \dfrac{\partial \bar{T}}{\partial \bar{t}} + \bar{v} \cdot \bar{\nabla}\bar{T} = \dfrac{\lambda}{\rho_0 v_0 L_0 C_p}\dfrac{1}{\bar{\rho}}\bar{\nabla}^2\bar{T} + \dfrac{v_0^2}{C_p \Delta T}\bar{v} \cdot \bar{\nabla}\bar{p} + \dfrac{\mu v_0}{\rho_0 L_0 C_p \Delta T}\dfrac{1}{\bar{\rho}}\bar{\phi}_v \end{cases}.$$

They can also be written as

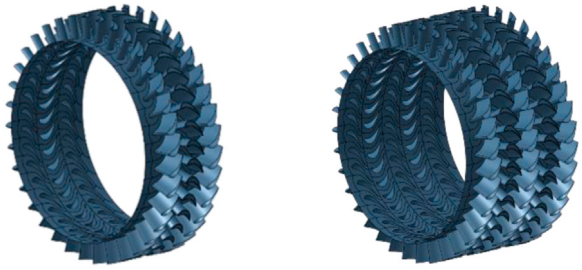

FIGURE 1
Geometry of turbines.

$$\begin{cases} \dfrac{\partial \bar{\rho}}{\partial \bar{t}} + \bar{\nabla} \cdot \bar{\rho}\bar{v} = 0 \\ \dfrac{\partial \bar{v}}{\partial \bar{t}} + \bar{v} \cdot \bar{\nabla}\bar{v} = -\boldsymbol{Eu}\dfrac{1}{\bar{\rho}}\bar{\nabla}\bar{p} + \dfrac{1}{\boldsymbol{Re}}\dfrac{1}{\bar{\rho}}\left[\bar{\nabla} \cdot (\bar{\nabla}\bar{v}) + \dfrac{1}{3}\bar{\nabla}(\bar{\nabla} \cdot \bar{v})\right] \\ \dfrac{\partial \bar{T}}{\partial \bar{t}} + \bar{v} \cdot \bar{\nabla}\bar{T} = \dfrac{1}{\boldsymbol{Re} \cdot \boldsymbol{Pr}}\dfrac{1}{\bar{\rho}}\bar{\nabla}^2\bar{T} + \boldsymbol{Ec}\bar{v} \cdot \bar{\nabla}\bar{p} + \dfrac{\boldsymbol{Br}}{\boldsymbol{Re} \cdot \boldsymbol{Pr}}\dfrac{1}{\bar{\rho}}\bar{\phi}_v \end{cases}.$$

When all the coefficients in the equation are equal, the same solution should be obtained under the same fixed solution conditions.

$\boldsymbol{Sr} = \frac{L_0}{v_0 t_0}$ characterizes the amorphism of the fluid.
$\boldsymbol{Re} = \frac{\rho_0 v_0 L_0}{\mu}$ characterizes the ratio of inertial force to viscous shear force.
$\boldsymbol{Eu} = \frac{P_0}{\rho_0 v_0^2}$ characterizes the ratio of pressure to inertial force.
$\boldsymbol{Pr} = \frac{C_p \mu}{\lambda}$ characterizes the effects of fluid properties.
$\boldsymbol{Ec} = \frac{v_0^2}{C_p \Delta T}$ characterizes the effects of fluid compressibility and heat dissipation.
$\boldsymbol{Br} = \frac{\mu v_0 l^2}{\lambda \Delta T l_0}$ characterizes the ratio of dissipatively transferred heat to heat released by heat conduction.

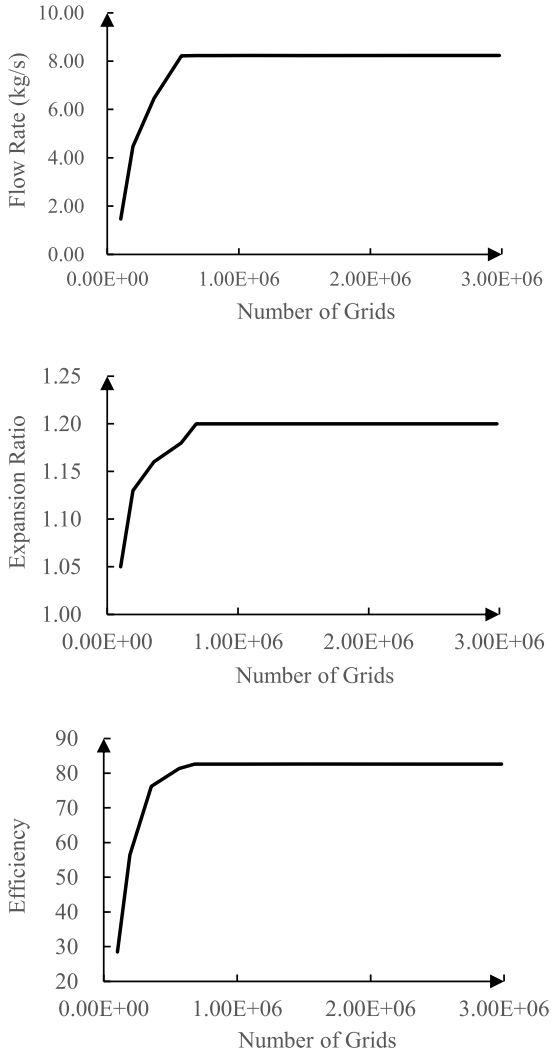

FIGURE 2
The mesh independence study in the design condition.

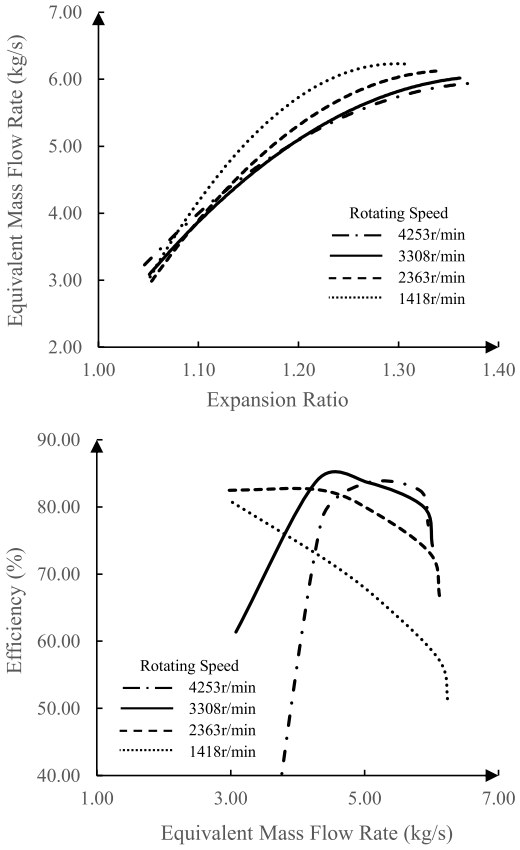

FIGURE 3
Characteristic curves of the turbine.

In the mass conservation equation and momentum conservation equation, ***Sr***, ***Re***, and ***Eu*** are the basis. It must be ensured that the Strouhal, Reynolds, and Euler numbers are equal to ensure that the basic turbine condition point corresponds, and the study in subsequent research can find the corresponding meaning in the original working condition.

In the actual operation process, especially when the physical properties of the working medium change, theoretically, it is impossible to completely make all the similar criterion dimensionless numbers equal at the same time. The difference in the coefficients of the control equation caused by the physical properties of the working medium is mainly reflected in ***Pr***, ***Ec***, and ***Br***. The Brinkman, Prandtl, and Eckert numbers mainly characterize changes in the physical properties of the working medium.

The Brinkman number characterizes the ratio of the heat transferred by dissipation to the heat released by heat conduction. Because the working medium rapidly passes through the turbine runner during turbine operation, the Brinkman number has a limited impact on the entire energy equation. However, the assumption is based on the adiabatic process, and the difference between the adiabatic process and the isothermal process is the isochoric process, which means that γ defines whether consumable items can be ignored.

The Prandtl number is, in most cases, a physical quantity that is only related to the state of the fluid. Because Prandtl contains two important migratory properties, viscosity and thermal conductivity, and constant pressure-specific heat, and as a dimensionless quantity, it reflects the interrelationship between energy transport and momentum transport processes. Therefore, it has been widely used in thermal calculations. The Eckert number represents the relationship between the flow kinetic energy and the enthalpy difference of the boundary layer. It is used to characterize the compressibility and heat dissipation capacity of the working medium. The changes in the Prandtl and Eckert

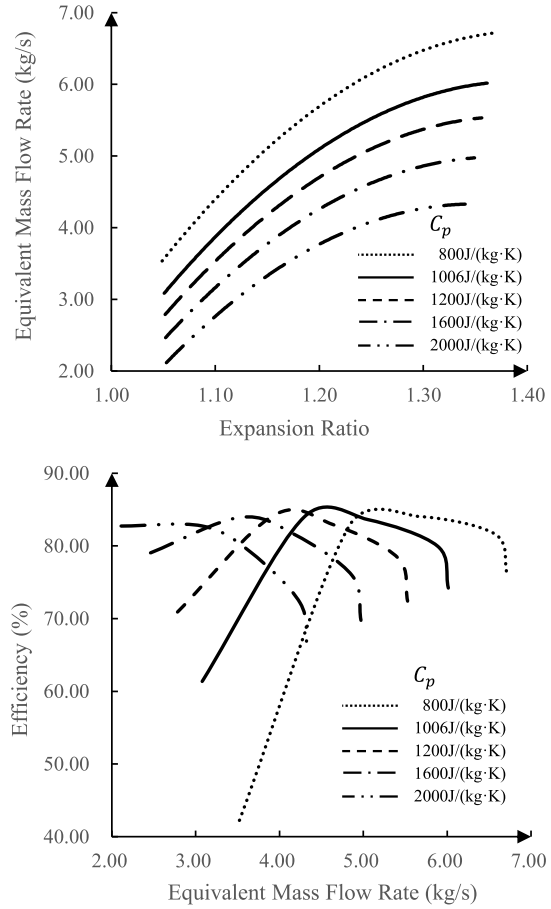

FIGURE 4
Aerodynamic properties evolve withC_p.

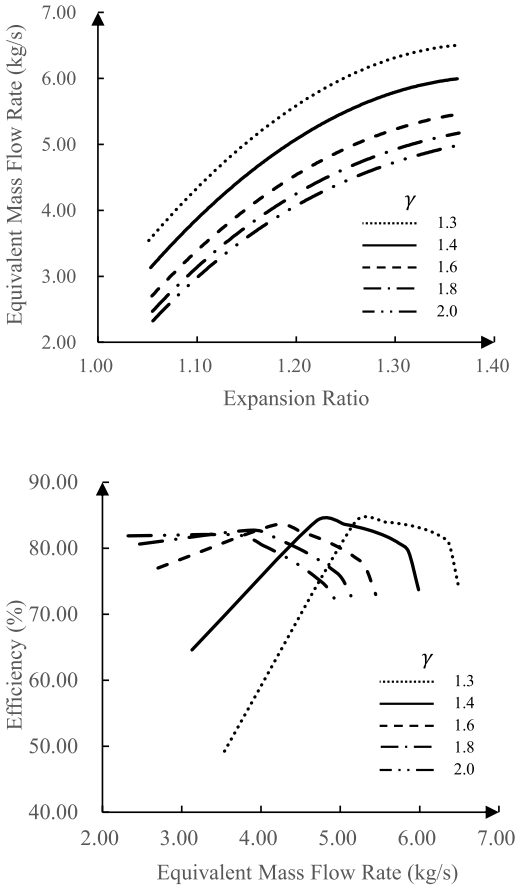

FIGURE 5
Aerodynamic properties evolve withγ.

numbers are usually ignored when studying the aerodynamic properties of the same working medium in the turbine.

Therefore, $\boldsymbol{C_p}$, $\boldsymbol{\gamma}$, $\boldsymbol{\mu}$, and $\boldsymbol{\lambda}$ are the influencing factors when the working medium changes, and among them $\boldsymbol{C_p}$ and $\boldsymbol{\gamma}$ are the core influencing factors.

In the simulation study of the overall performance of the gas turbine, the physical properties of the combustion products are calculated with the assumption that air and gas are treated according to the gas mixture of variable specific heat when the temperature does not exceed 1,600°C. The assumption is widely and fully verified in many industrial productions. In the assumption, C_p and γ can be calculated from specific enthalpy, specific entropy, and temperature.

In this article, the study of the turbine performance evolution is conducted from the perspective of the overall performance simulation of the gas turbine. The CFD numerical calculation method is used to obtain the evolutionary law of turbine characteristics, and the correction methods were proposed to estimate the evolutionary trend of turbine characteristics.

CFD calculation model of turbine

In this article, a 1.5-stage subsonic axial multi-stage turbine in the FINE/TURBO program calculation examples is selected, which is a publicly available study verified by Gallus and Walraevens in 1995 and 1998 by experimental and numerical calculations, respectively. The low-scale chordal ratio blades and constant tip and hub end wall profiles in this study enhance the strong secondary flow, so as a sufficiently representative multistage axial flow turbine is included as a study by the FINE/TURBO program. The model is a flow channel of equal inner and outer diameters, including one stage of guide blades, one stage of rotating blades, and one stage of static blades, of which the guide and static stages contain 36 blades per circumference and the rotating stage contains 41 blades, all of which are equal in width and unscrewed.

This study demonstrates the Ability of Fine/TURBO to simulate the flow of a multi-unit axial turbine in a steady-state subsonic range using experimentally validated calculations using the Spalart–Allmaras turbulence model. The

TABLE 2 Value of $A_{\eta ij}$.

i \ j	0	1	2	3	4
1	1.05670E+00	3.69779E-05	−3.14442E-07	2.96237E-10	−7.54444E-14
2	−3.85477E-02	1.29104E-04	−1.51799E-07	7.84341E-11	−1.71440E-14
3	1.30115E-05	−3.51326E-07	7.52886E-10	−5.44579E-13	1.29772E-16
4	1.28149E-02	−6.60114E-05	1.03564E-07	−6.53945E-11	1.49981E-14
5	−2.60196E-09	5.90317E-11	−1.25082E-13	9.02132E-17	−2.15224E-20
6	−1.39666E-05	1.24409E-07	−2.30467E-10	1.56180E-13	−3.60826E-17
7	−9.71779E-04	5.05784E-06	−7.81446E-09	4.81702E-12	−1.08584E-15
8	1.92934E-14	4.93649E-16	−1.04962E-18	6.87043E-22	−1.49511E-25
9	−4.62134E-07	2.34651E-09	−4.18994E-12	3.07573E-15	−7.70850E-19
10	2.73442E-09	−2.25879E-11	4.15139E-14	−2.82347E-17	6.56253E-21

TABLE 3 Value of A_{Gij}.

i \ j	0	1	2	3	4
1	1.37725E+00	−4.79699E-03	1.05227E-05	−8.09089E-09	1.98847E-12
2	−1.83080E+00	8.14116E-03	−1.21955E-05	7.52613E-09	−1.63958E-12
3	4.03823E-03	−1.03343E-05	9.42800E-09	−3.64725E-12	5.17334E-16
4	5.46105E-01	−2.07571E-03	2.81780E-06	−1.62935E-09	3.40938E-13
5	−9.55168E-07	2.62401E-09	−2.65915E-12	1.19315E-15	−2.03262E-19
6	−4.65340E-04	8.28750E-07	−2.85626E-10	−1.50466E-13	7.21252E-17
7	−4.17674E-02	1.48121E-04	−1.91659E-07	1.07418E-10	−2.21043E-14
8	7.22697E-11	−2.07200E-13	2.22734E-16	−1.07698E-19	1.99242E-23
9	1.40007E-05	4.39533E-10	−4.49252E-11	4.03860E-14	−9.85548E-18
10	4.85563E-08	−1.10155E-10	8.12156E-14	−1.98112E-17	2.30438E-22

TABLE 4 Value of $A_{\eta ij}$.

i j	0	1	2	3	4
1	−1.57694E+03	4.98798E+00	−5.75734E-03	2.86555E-06	−5.18231E-10
2	5.58363E+02	−1.76339E+00	2.03412E-03	−1.01205E-06	1.82949E-10
3	5.91380E-01	−1.87537E-03	2.16900E-06	v1.08059E-09	1.95547E-13
4	−6.04107E+01	1.90532E-01	−2.19580E-04	1.09180E-07	−1.97208E-11
5	−6.67032E-05	2.12382E-07	−2.46267E-10	1.22838E-13	−2.22459E-17
6	−1.46638E-01	4.64294E-04	−5.36437E-07	2.67098E-10	−4.83126E-14
7	1.73768E+00	−5.45806E-03	6.27000E-06	−3.10945E-09	5.59863E-13
8	2.23547E-09	−7.16506E-12	8.34649E-15	−4.17498E-18	7.57869E-22
9	9.07009E-03	−2.86970E-05	3.31474E-08	−1.65078E-11	2.98712E-15
10	8.27713E-06	−2.62689E-08	3.03859E-11	−1.51301E-14	2.73555E-18

turbine stage uses an HOH topology discrete, with each cell automatically generated using IGG/AutoGrid5 for a total of approximately 1.1 million grid points. The working medium is treated as an ideal gas of air. Along the inlet boundary, the pitch average experimental absolute total pressure, total temperature, and flow angle are applied. Along the outlet boundary, static pressure is applied to a radius, and its radial distribution is calculated using radial equilibrium conditions.

TABLE 5 Value of $B_{\pi ij}$.

i \ j	0	1	2	3	4
1	0.00000E+00	0.00000E+00	0.00000E+00	0.00000E+00	0.00000E+00
2	2.59794E+01	−5.99115E+01	5.07976E+01	−1.87421E+01	2.54103E+00
3	−3.79264E-02	8.97482E-02	−7.60396E-02	2.80369E-02	−3.79989E-03
4	−2.13571E+00	4.90106E+00	−4.12647E+00	1.50935E+00	−2.02926E-01
5	1.99126E-05	−4.67714E-05	3.97398E-05	−1.47034E-05	1.99934E-06
6	−1.02890E-02	2.38241E-02	−2.03135E-02	7.54548E-03	−1.02952E-03
7	9.78481E-02	−2.24013E-01	1.88052E-01	−6.85561E-02	9.19042E-03
8	−3.02038E-09	7.06880E-09	−6.01404E-09	2.22875E-09	−3.03520E-10
9	2.01619E-04	−4.65240E-04	3.94377E-04	−1.45340E-04	1.96666E-05
10	1.48116E-06	−3.43179E-06	2.92908E-06	−1.08946E-06	1.48850E-07

TABLE 6 Value of B_{Gij}.

i \ j	0	1	2	3	4
1	0.00000E+00	0.00000E+00	0.00000E+00	0.00000E+00	0.00000E+00
2	1.59912E+02	−3.68095E+02	3.10560E+02	−1.13700E+02	1.52846E+01
3	−5.19815E-01	1.19899E+00	−1.01279E+00	3.71595E-01	−5.00685E-02
4	−1.84320E+01	4.25590E+01	−3.59806E+01	1.31875E+01	−1.77405E+00
5	1.95877E-04	−4.51185E-04	3.80702E-04	−1.39541E-04	1.87846E-05
6	−1.31877E-02	2.98140E-02	−2.47200E-02	8.90196E-03	−1.17856E-03
7	8.33607E-01	−1.93249E+00	1.63920E+00	−6.02391E-01	8.12176E-02
8	−2.25970E-08	5.20325E-08	−4.38935E-08	1.60852E-08	−2.16492E-09
9	2.96490E-04	−6.45362E-04	5.11526E-04	−1.74914E-04	2.19678E-05
10	8.47158E-07	−1.92764E-06	1.60999E-06	−5.84349E-07	7.79389E-08

TABLE 7 Value of $B_{\eta ij}$.

i \ j	0	1	2	3	4
1	0.00000E+00	0.00000E+00	0.00000E+00	0.00000E+00	0.00000E+00
2	3.23356E+03	−7.41200E+03	6.25516E+03	−2.29992E+03	3.10833E+02
3	−6.27292E+00	1.43804E+01	−1.21357E+01	4.46213E+00	−6.03067E-01
4	−5.52556E+02	1.26691E+03	−1.06942E+03	3.93288E+02	−5.31622E+01
5	2.16373E-03	−4.95910E-03	4.18411E-03	−1.53813E-03	2.07845E-04
6	−4.41834E-02	1.00105E-01	−8.35291E-02	3.03846E-02	−4.06655E-03
7	3.36190E+01	−7.70867E+01	6.50741E+01	−2.39327E+01	3.23524E+00
8	−2.59557E-07	5.94799E-07	−5.01784E-07	1.84442E-07	−2.49209E-08
9	−1.02946E-02	2.36251E-02	−1.99629E-02	7.34971E-03	−9.94617E-04
10	2.71816E-05	−6.21587E-05	5.23429E-05	−1.92084E-05	2.59172E-06

Because the guide stage of the geometric model has the same shape and parameters as the static stage, the rotating and static stages are repeated once after the original geometric model to obtain a 2.5-stage turbine. The 2.5-stage turbine contains one guide stage, two rotating stages, and two static stages. The geometric parameters of each level are consistent with the original information, and the relevant settings are also the same as in the original study. The 1.5-stage turbine is calculated to obtain the correction method and the 2.5-stage turbine is calculated to verify the applicability. The geometry of turbines is shown in Figure 1.

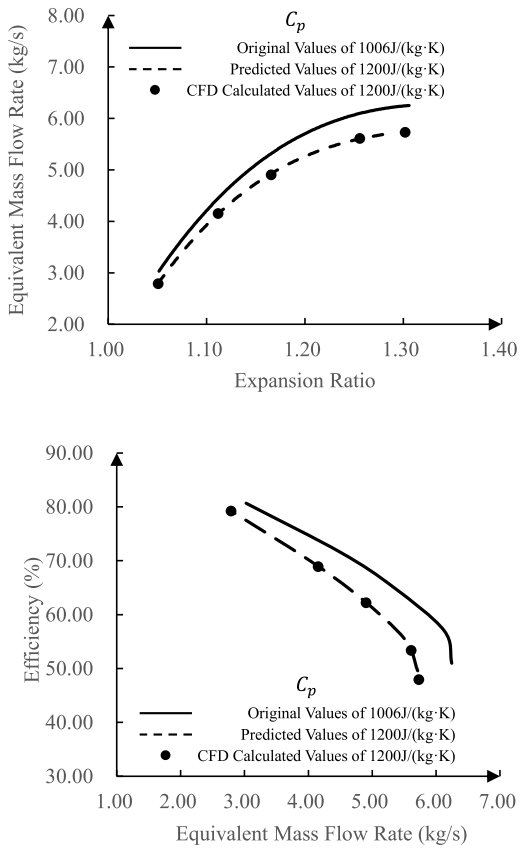

FIGURE 6
Comparison between prediction and CFD calculations as C_p evolves in the 1.5-stage turbine.

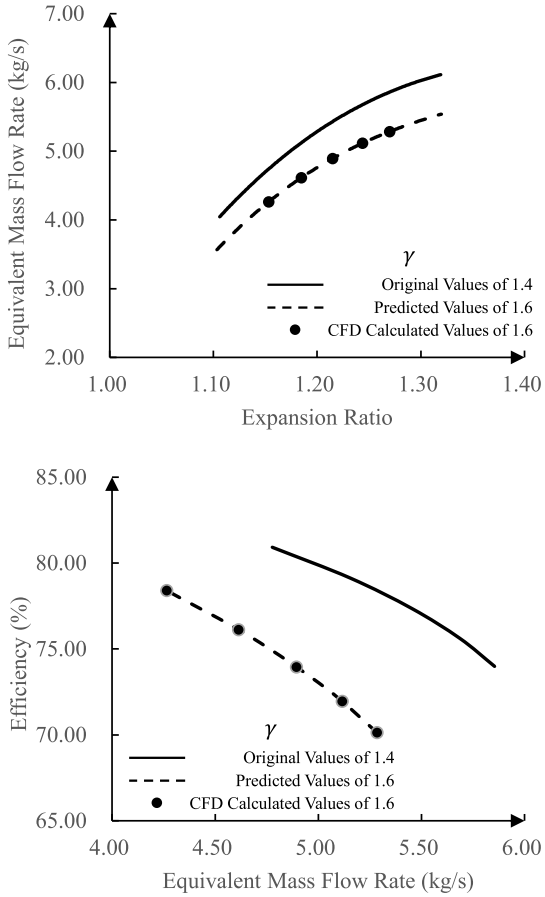

FIGURE 7
Comparison between prediction and CFD calculations as γ evolves in the 1.5-stage turbine.

The mesh independence study of the 1.5-stage turbine in the design condition is carried out with a number of grids from about 100,000 to over 2,000,000.

The results are shown in Table 1 and Figure 2.

The number of grids of the 1.5-stage turbine is chosen as 1,500,000 for the following study, and the number of grids of the 2.5-stage turbine is redistricted with the same mesh density as the 1.5-stage turbine.

Firstly, the aerodynamic performance of the turbine is calculated using the default settings in the example to calculate the aerodynamic performance of the turbine based on the designed rotating speed of 3,500 r/min, the average inlet total pressure of 169,500 Pa, and the average outlet static pressure of 112,500 Pa. The design point speed is 3,500 r/min (equivalent to 3,308.15 r/min), the mass flow rate is 8.205 kg/s (equivalent to 5.052 kg/s), the expansion ratio is 1.198, and the efficiency is 83.63%. The working medium is air with C_p as 1,006 J/(kgK) and γ as 1.4. The characteristic curves of the turbine are shown in Figure 3.

On the basis, change C_p and γ of the working medium, respectively. Under the condition of different working medium C_p values or γ values, calculate the complete aerodynamic performance of the turbine, considering that CO_2 and H_2O are not only representative components of the combustion product but also in the value of C_p and γ, the range of C_p is selected as 800–2,000 J/(kgK), and the range of γ is selected as 1.3–2.0, which can basically cover the value of C_p and γ in the physical parameters of various mixture working mediums after the combustion of different components of fuel.

At the rotating speed of 3,308.15 r/min, the evolution of aerodynamic properties of the turbine is shown in Figure 4 when C_p changes from 800 to 2,000 J/(kgK).

At the rotating speed of 3,308.15 r/min, the evolution of aerodynamic properties of the turbine is shown in Figure 5 when γ changes from 1.3 to 2.0.

In Figure 4 and Figure 5, the equivalent mass flow rate drops at the same expansion ratio, and the efficiency shifts with a lower equivalent mass flow rate as C_p or γ of the working medium

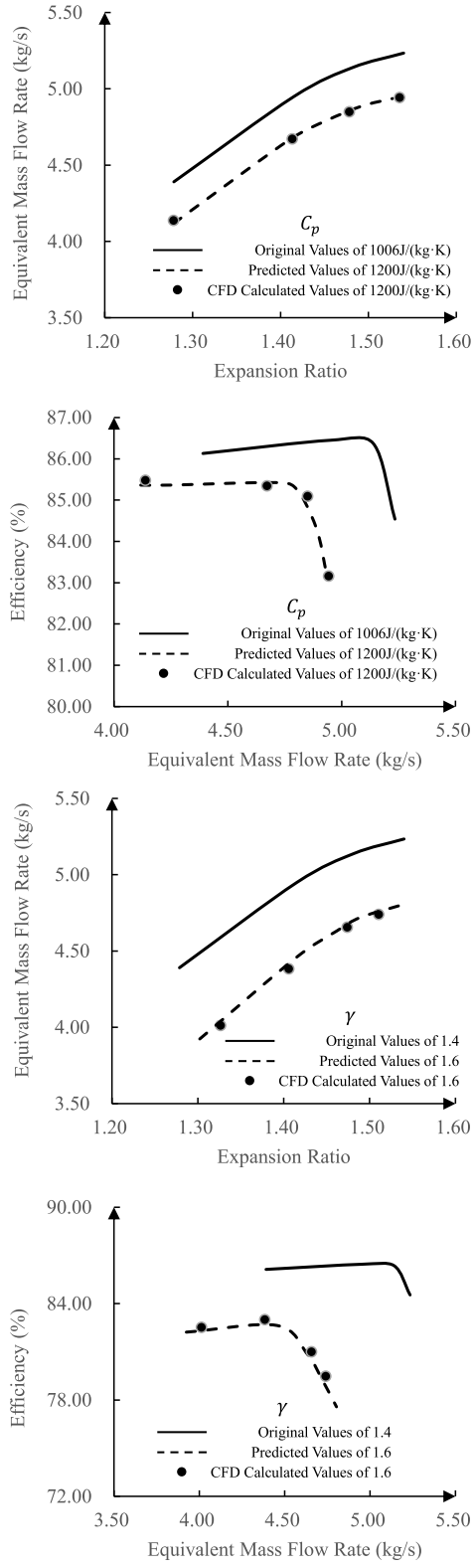

FIGURE 8
Comparison between prediction and CFD calculations as C_p and γ evolve in the 2.5-stage turbine.

increases. It illustrates that the increase in C_p or γ leads to a decrease in equivalent mass flow rate.

Correction method of turbine characteristics

In the previous section, C_p or γ is treated as a variable associated with the evolution of characteristics of the 1.5-stage turbine at the design speed. The original characteristic lines can be corrected to the target characteristic lines by following certain rules. Meanwhile, the correction method is obtained.

First, the original characteristic line should be densified by the beta line method. The design points of the pending turbine may be different from the original characteristic line, so the seek points are scaled and the pending points are mapped to the original property map.

Then, by using the polynomial fitting, the relationship between the pressure ratio, flow rate, and efficiency value of the same beta point is predicted as a result of the eigenvalue.

The pending flow rate point is known after scaling, the correspondence is obtained by interpolating the beta value to the flow rate point, and the multinomial coefficients are obtained by the beta value and the other known quantity. The pressure ratio, flow rate, and efficiency of the operating point can be calculated as a result of the eigenvalue change. The correction formulas are obtained by multivariate polynomial analysis, allowing the property to be corrected by giving a certain operating and design point.

In this case, the correction method of turbine characteristics is solved with fine-grained scaling as follows:

$$\begin{cases} \pi^* = \pi \cdot \sum_{j=0}^{4} \left(A_{\pi 1,j} + A_{\pi 2,j}G + A_{\pi 3,j}n + A_{\pi 4,j}G^2 + A_{\pi 5,j}n^2 + A_{\pi 6,j}Gn + A_{\pi 7,j}G^3 + A_{\pi 8,j}n^3 + A_{\pi 2,j}G^2n + A_{\pi 2,j}Gn^2\right)C_p^j \\ G^* = G \cdot \sum_{j=0}^{4} \left(A_{G1,j} + A_{G2,j}G + A_{G3,j}n + A_{G4,j}G^2 + A_{G5,j}n^2 + A_{G6,j}Gn + A_{G7,j}G^3 + A_{G8,j}n^3 + A_{G2,j}G^2n + A_{G2,j}Gn^2\right)C_p^j \\ \eta^* = \eta \cdot \sum_{j=0}^{4} \left(A_{\eta 1,j} + A_{\eta 2,j}G + A_{\eta 3,j}n + A_{\eta 4,j}G^2 + A_{\eta 5,j}n^2 + A_{\eta 6,j}Gn + A_{\eta 7,j}G^3 + A_{\eta 8,j}n^3 + A_{\eta 2,j}G^2n + A_{\eta 2,j}Gn^2\right)C_p^j \end{cases}$$

$$\begin{cases} \pi^* = \pi \cdot \sum_{j=0}^{4} \left(B_{\pi 1,j} + B_{\pi 2,j}G + B_{\pi 3,j}n + B_{\pi 4,j}G^2 + B_{\pi 5,j}n^2 + B_{\pi 6,j}Gn + B_{\pi 7,j}G^3 + B_{\pi 8,j}n^3 + B_{\pi 2,j}G^2n + B_{\pi 2,j}Gn^2\right)\gamma^j \\ G^* = G \cdot \sum_{j=0}^{4} \left(B_{G1,j} + B_{G2,j}G + B_{G3,j}n + B_{G4,j}G^2 + B_{G5,j}n^2 + B_{G6,j}Gn + B_{G7,j}G^3 + B_{G8,j}n^3 + B_{G2,j}G^2n + B_{G2,j}Gn^2\right)\gamma^j, \\ \eta^* = \eta \cdot \sum_{j=0}^{4} \left(B_{\eta 1,j} + B_{\eta 2,j}G + B_{\eta 3,j}n + B_{\eta 4,j}G^2 + B_{\eta 5,j}n^2 + B_{\eta 6,j}Gn + B_{\eta 7,j}G^3 + B_{\eta 8,j}n^3 + B_{\eta 2,j}G^2n + B_{\eta 2,j}Gn^2\right)\gamma^j \end{cases}$$

where π stands for the expansion ratio; G stands for the equivalent mass flow rate; η stands for efficiency; n stands for the rotating speed; $B_{\pi i,j}$, $B_{Gi,j}$, and $B_{\eta i,j}$ stand for correction factors.

Superscript $*$ stands for the predicted value. π, G, η, and n without superscript stand for original values.

Correction factors are shown in Tables 2–7.

By putting the correction formula into the other speeds of the 1.5-stage turbine, turbine characteristics adopting different working mediums with different C_p can be predicted by the correction method, and the deviations are overall below 1%

within equivalent rotating speed from 1,418 to 4,253 r/min. The demonstration at a rotating speed of 1,418 r/min is shown in Figure 6.

Putting the correction formula into the other speeds of the 1.5-stage turbine, turbine characteristics adopting different working mediums with different γ can be predicted by the correction method. The deviations are all below 0.5% within equivalent rotating speed from 1,418 to 4,253 r/min. The demonstration at a rotating speed of 2,363 r/min is shown in Figure 7.

In order to verify the universality of the correction method, the correction formula is put into the design working point and non-design working conditions of the 2.5-stage turbine. The comparison at a rotating speed of 3,308 r/min is shown Figure 8.

Conclusion

In this article, from the perspective of the application of the low-carbon clean fuel or industrial-associated fuel, the gas turbine performance is significantly affected because the thermal physical properties of the working medium vary.

In this article, a theoretical study on the mechanism of influencing turbine characteristics is conducted when the turbine working medium changes, and conclusions are obtained as C_p and γ are the key influencing factors of turbine characteristics in the problem of working medium changing. The CFD calculation method is used to quantitatively obtain the evolution law of turbine characteristics under C_p and γ variation conditions using multi-stage turbine examples.

A turbine characteristic correction method based on fine scaling is proposed aiming at the working medium changing problem of the turbine. After scaling is carried out using the design points, the coefficients of polynomial fitting are solved with the scaled equivalent flow rate. By giving certain operating and design points, the characteristics are corrected and the turbine characteristic line correction method suitable for this working medium property change problem is obtained. This correction method has been validated to apply to repetitive multi-stage turbines based on the same set structure. The applicability of the correction method using the same correction coefficient for turbines with different geometries has yet to be verified. The fine scaling method proposed in this article can realize the method of polynomial fitting for the working mass changing problem and obtain the corresponding correction method.

Data availability statement

The raw data supporting the conclusions of this article will be made available by the authors without undue reservation.

Author contributions

LM: methodology; ZW: conceptualization; JZ: data curation; PZ: supervision; KZ: resources.

Funding

National Science and Technology Major Project (J2019-I-0007-0007).

Conflict of interest

The authors declare that the research was conducted in the absence of any commercial or financial relationships that could be construed as a potential conflict of interest.

Publisher's note

All claims expressed in this article are solely those of the authors and do not necessarily represent those of their affiliated organizations or those of the publisher, the editors, and the reviewers. Any product that may be evaluated in this article, or claim that may be made by its manufacturer, is not guaranteed or endorsed by the publisher.

References

Boncinelli, P., Rubechini, F., Amone, A., Cecconi, M., and Cortese, C. (2004). *Real gas effects in turbomachinery flows: A computational fluid dynamics model for fast computations[C].* ASME Paper GT2003-38101.

Canepa, R., and Satta, A. (2012). *Influence of working fluid composition on the performance of turbomachinery in semi-closed gas turbine cycles[C].* ASME Paper GT2012-69453.

Colonna, P., Harinck, J., Rebay, S., and Guardone, A. (2008). Real-gas effects in organic rankine cycle turbine nozzles. *J. Propuls. Power* 24 (2), 282–294. doi:10.2514/1.29718

Cravero, C., and Satta, A. (2000). *A CFD model for real gas flows[C].* ASME PaperGT2000-518.

Gallar, L., Volpe, V., Salussolia, M., Pachidis, V., and Jackson, A. (2012). Thermodynamic gas model effect on gas turbine performance simulations. *J. Propuls. Power* 28 (4), 719–727. doi:10.2514/1.b34359

Harinck, J., Colonna, P., Guardone, A., and Rebay, S. (2010). Influence of thermodynamic models in two-dimensional flow simulations of turboexpanders [J]. *ASME J. Turbomach.* 132 (1), 011001.1–011001.17.

Jackson, J. B., Neto, A. C., Whellens, M. W., and Audus, H. (2000). *Gas turbine performance using carbon dioxide as working fluid in closed cycle operation[C].* ASME Papar GT2000-153.

Liang, M., Zhang, Y., Wang, J., and Yang, X. (2008). "Researches of similitude laws obtained by differential equations for axial-flow helium compressors," in The

Proceedings of the International Conference on Nuclear Engineering(ICONE), 2015–1977.

Ming, L., Yang, X. Y., Zhang, Y. J., and Wang, J. (2019). Experimental study on performance of helium high pressure compressors of HTR-10GT. *Ann. Nucl. Energy* 125, 318–327. doi:10.1016/j.anucene.2018.11.007

Ming, L., Yang, X. Y., Zhang, Y. J., and Wang, J. (2019). Experimental study on performance of helium low pressure compressor of HTR-10GT. *Prog. Nucl. Energy* 111 (111), 156–164. doi:10.1016/j.pnucene.2018.11.008

Mirko, Z. S., Linke, P., Athanasios, I. P., and Aleksandar, S. G. (2012). On the role of working fluid properties in organic rankine cycle performance[J]. *Appl. Therm. Eng.* 36, 406–413.

Northall, J. D. (2005). *The influence of variable gas properties on turbomachinery computational fluid dynamics[C]*. ASME Paper GT2005-68478.

Roberts, S. K., and Sjolander, S. A. (2002). *Semi-closed cycle 02/ C02 combustion gas turbines: Influence of fluid properties on the aerodynamic performance of the turbomachinery[C]*. ASME Paper GT2002-30410.

Rubechini, F., Marconcini, M., Amone, A., Maritano, M., and Cecchi, S. (2006). *The impact of gas modelling in the numerical analysis of a multistage gasturbine[C]*. ASME Paper GT2006-90129.

Sethi, V., Diara, F., Atabak, S., Jackson, A., Bala, A., and Pilidis, P. (2008). *Advanced modelling of fluid thermodynamic properties for gas turbine performance simulation[C]*. ASME Paper GT2008-51126.

Siemens (2021). *Power generation packages for oil and gas applications[Z]*, 165–176.

Yao, Y., and Amos, I. (2004). *Numerical study of axial turbine flow with variable gas property[C]*. ASME Paper GT2004-53748.

Zhang, L., Zhuge, W., Peng, J., and Zhang, Y. (2014). *The influence of real gas thermodynamics on ICE-ORC turbine flow fields[C]*. ASME Paper GT2014-26470.

10.3389/fenrg.2022.966713

Nomenclature

γ Adiabatic index

Br Brinkman number

ρ Density

Ec Eckert number

Eu Euler number

C_p Heat capacity ratio under constant pressure

q Heat transfer energy

τ Internal friction force

Pr Prandtl number

p Pressure

Re Reynolds number

Sr Strouhal number

T Temperature

t Time

v Velocity

frontiers | Frontiers in Energy Research

TYPE Original Research
PUBLISHED 09 January 2023
DOI 10.3389/fenrg.2022.933591

OPEN ACCESS

EDITED BY
Lei Luo,
Harbin Institute of Technology, China

REVIEWED BY
Xiongbo Duan,
Hunan University, China
Haifeng Liu,
Tianjin University, China
Lei Shi,
Shanghai Jiao Tong University, China

*CORRESPONDENCE
Long Liu,
liulong@hrbeu.edu.cn

SPECIALTY SECTION
This article was submitted to Advanced Clean Fuel Technologies, a section of the journal Frontiers in Energy Research

RECEIVED 01 May 2022
ACCEPTED 07 September 2022
PUBLISHED 09 January 2023

CITATION
Naruemon I, Liu L, Mei Q, Wu Y, Ma X and Nishida K (2023), Investigating the effects of split injection with different injection patterns on diesel spray mixing.
Front. Energy Res. 10:933591.
doi: 10.3389/fenrg.2022.933591

Investigating the effects of split injection with different injection patterns on diesel spray mixing

Intarat Naruemon[1,2], Long Liu[2]*, Qihao Mei[2], Yue Wu[2], Xiuzhen Ma[2] and Keiya Nishida[3]

[1]College of Power and Energy Engineering, Harbin Engineering University, Harbin, China, [2]Mechanical Engineering Program, Faculty of Engineering, Thaksin University, Phatthalung, Thailand, [3]Department of Mechanical System Engineering, University of Hiroshima, Higashi-Hiroshima, Japan

In recent studies, it has been established that improvements in the injection rate results in improved mixing, combustion efficiency, and reduced pollutant emissions. Varying injection rates have been observed to find out the optimization injection rate. In this study, split injection with different injection rates was used as the flexible injection to investigate the diesel spray mixing efficiency. Large eddy simulation (LES) was used to investigate the complex diesel mixing processes of unsteady turbulence. The split injection was combined with different fuel injection rates to approximate the ramping-down rate shape. The simulation results of flexible injection rates showed the formation of a highly unstable aerosol vapor structure with the turbulence structure that produces the vortex in the spray area. The powerful injection rates provide a very strong spray turbulence structure and vortex formation. The backflow and vortex are evident when the dwell time of injection is setup. The flexible injection rates have a huge influence on the mixing efficiency of the fuel spray. Basic mixing efficiency predictions revealed that the dwell time of the split injection and inverse injection pressure affect the turbulence structure. Another prediction is that the initial pressure of the injection rate has a significant impact on evaporation and mixing efficiency, even using the same fuel quantity and same condition. The double-rectangular split injection has a slight effect on the spray radial extension, and the spray area grows rapidly while the equivalence ratio is low. The double-drop split injection with a high pressure difference has a great influence on the spray radial extension and spray length. Additionally, the higher injection pressure results in lower equivalence ratios and more efficient mixing.

KEYWORDS

spray mixing, large eddy simulation, split injection, different injection rates, ultrahigh injection pressure

1 Introduction

At present, there are significant challenges in increasing the mixing efficiency and reducing emissions of diesel engines, for which optimizing the spray formation behavior is essential. Past research has included strategies for improving the efficiency and reducing the emissions of diesel engines, but ultimately the varying injection rates of fuel injection play an important role in improving the new diesel engine. Liu et al. (2015) found that although soot emissions decreased with higher injection times, the combustion efficiency decreased.

Currently, a large amount of research is being focused on improving the injection and injection pattern simultaneously in search of better efficiency of fuel sprays for further effect on mixing and combustion efficiency. Such as Shuai et al. (2009) who suggested from simulation results that the rectangular shape and boot rate geometry can reduce UHC CO and soot emissions. Tay et al. (2017) have supported that the boot injection rate can reduce soot particle size and avoid exchange of NOx and CO, while Knox et al. (2015) have shown that ramp-down injection significantly reduces the equivalence ratio on the axis of the fuel spray. The research by Edzuan Bin Abdullah et al. (2018) and Akiyama et al. (2019) present an inversed-delta injection rate. It shows reduced catch-up, resulting in decreased formation of a rich mixture at the spray tip and enhancing air entrainment in spray (Edzuan Bin Abdullah et al., 2019), supporting fuel–air mixing, thereby enabling good mixing. Liu et al. (2022) developed a spray model to satisfy the diesel spray penetration calculation with different injection rate shapes. The review reveals that there is a fair amount of research into the study of different injection rate patterns on the combustion and emission processes of diesel engines. These research are in line with our previous study (Naruemon et al., 2020) that found the injection rate pattern had the highest initial injection, and it gradually decreases with ultrahigh injection pressure showing the best spray mixing efficiency, which is of the same shape as that of the boot, ramp-down, and inversed-delta injection rates. This shows that the injection rate pattern has a significant influence on the spray efficiency, especially the injection rate with a high initial injection and the unsteady injection rate, but most of the research is still on the general continuous injection rate. And research on the influence of injection rate determination on the dynamic behavior of fuel particles in the spray mixing process are relatively less, with most of it being limited to the typical injection pressure and single-injection rate. Therefore, the study of the flexible injection rate and behavior of the fuel spray process to gain a deeper understanding is much needed.

Using the split injection can represent varying injection rates. Past research has developed a split injection strategy by optimizing the injection time and fuel mass. Research by Cung et al. (2015) and Moiz et al. (2016) presented that those split injections can show a strong interaction between the previously injected combustion jet and the impending cold spray, giving this reaction a strong influence on the ignition process and emissions for the split injection. In addition, Skeen et al. (2015) found that the first injection combustion causes higher temperature gas entrainment, increases pressure and local temperature, creating good conditions for the earlier start of the second injection (Bolla et al., 2017). Although past research have shown that a split injection strategy had been developed, it still uses a general injection rate. Therefore, using split injection can offer a new injection shape that decreases the fuel injection mass post injection, which can represent the high initial injection of varying injection rates. Zheng et al. (2015) found that adopting the pilot injection close to the main injection can effectively reduce the peak of the premixed heat release rate and the maximum pressure rise rate. The pilot main moment had a more pronounced effect on smoke than the pilot injection rate, and smoke emissions decreased as the main pilot period increased. Longer main post-injection interval results in lower heat release rates and longer combustion times, while the post-injection rate had little effect on the post-injection start-up of ignition. Smoke emissions increase first and then decrease with time after retardation post injection.

In addition, our previous study (Naruemon et al., 2020) had found that the injection rate with ultrahigh injection pressure showed greater influence on diesel mixing behavior. In recent years, ultrahigh injection pressure has been widely discussed, such as in the study by Yu (2019) in the atomization of fuel spray using experimental methods under ultrahigh injection pressure in the range of 200–350 MPa. The results showed that the increased fuel injection pressure had an impact on the evolution of aerosols and the penetration of the spray tip was faster and the induced shock waves appeared more clear. Jia et al. (2017) studied an experiment with an injection pressure of 300 MPa and showed that when the injection pressure was higher, a smaller shock wave angle was observed and the Sauter mean diameter (SMD) of the spray was smaller. Yu et al. (2019) who studied diesel injection with an injection pressure of 350 MPa confirmed that under ultrahigh injection pressure conditions, the SMD of all droplets was significantly smaller. In addition, Yu et al. (2017) conducted both experimental and simulated studies of the spray characteristics at an injection pressure of 240 MPa. The results showed that an increase in the vortex at the lower part of the spray was effective in improving atomization. The aforementioned research found that for diesel engines, ultrahigh injection pressure results in a higher spray mixing efficiency. However, there is still a lack of research on ultrahigh injection pressure of intermittent and nonconstant injection rates, hence this study is challenging research of various injection rate patterns with ultrahigh injection pressures. Although the challenge of determining the ultrahigh injection rate is a big problem, the newly developed fuel injection technology has been capable of controlling the injection pressure precisely and generating very high injection pressures. The study by Wang et al. (2019) showed that with ultrahigh

voltage test settings, initial testing of the high-pressure system can produce a maximum pressure of approximately 870 MPa.

The current technology can precisely control the injection volume and injection pattern. Hence, controlling a wide range of injection patterns is possible here. Although the fuel injection rate shaping strategy is highly efficient, using a high injection pressure rate and dividing very short injection intervals also presents challenges in itself. According to the author's knowledge, it can be said that there has not yet been a detailed analytical study of the varying injection rates with ultrahigh injection pressure and short injection duration in terms of the effect on fuel particle dissociation and mixing efficiency, especially the split injection with different injection patterns.

The existing research on the development and improvement of diesel engine performance is often studied in the performance of the entire system of combustion in diesel engines. There have been few studies looking at controlled combustion chamber areas. Diesel spray behavior is the key to mixing and combustion efficiencies, and the diesel spray mixing behavior is very complex and difficult to investigate. Thus, studying such behavior remains challenging. In addition, although there are many studies of technologies for improving and developing diesel engines from past research, the study of diesel spray through a detailed study of the spray behavior, such as breakup, evaporation, turbulence, and mixing, remains limited and has not been studied. The injection rate shape did not determine which shape was the best injection rate shape. Therefore, it is attractive to study the spray behavior to find the most effective new injection rate shaping strategies.

In order to fill in the gaps in the past research, the authors foresee that varying injection rates are influential and significantly effective for mixing and combustion control, but there remains a challenge in shaping complex injection rate patterns. The split injection strategy also plays an important role, no less. Past research that was aimed at the astonishing ability of the injection rate, with a high initial injection rate, offers great difference and excellent performance. In addition, the ultrahigh injection pressure has a great influence on the diesel mixing behavior. Here, split injections are used to represent a variable injection rate. In addition, split injection strategies are created with different injection rates to present a flexible injection pattern that is attractively representative of the varying injection rate studies, and all study conditions of newly flexible injection patterns were using ultrahigh injection pressure. This study applies the concept of using split injection with different injection patterns to improve the spray mixing and combustion efficiency of the diesel engine. However, the spraying and mixing behavior remain a challenge for researchers, and there is a great need to study them in detail.

This article studies the spray formation behavior to understand the spray history with an emphasis on the effect of injection pattern and dwell time on the turbulence structure. In order to consider these phenomena, it is necessary to have a study technique that can study the patterns of multiphase aerosol turbulence that occurs during spraying. We propose a multiphase spray investigation using numerical simulation of the LES model. By this method, it is possible to display the results of different states during the process (liquid and vapor). Matheis and Hickel (2018) showed that the LES model can create a multicomponent model of high-pressure fuel injection, and the study of the vortex flow evolution and fuel cavitation of Piscaglia et al. (2021) showed that the LES model simulations can show the formation of an unsteady vapor structure that agrees with the experimental data. Therefore, in this study, the model created can not only predict the spray area and aerosol dispersion but also be a suitable model and predict the collision effect of aerosols. The created LES model was validated with the baseline information from ECN (Anonymnous, 2021). Finally, the numerical results have been compared quantitatively and qualitatively. The findings of this study are expected to provide useful insights for the injection rate setting of future trials aimed at improving the diesel fuel mixing efficiency.

2 Methodology and numerical methods

The study used numerical simulations to study the behavior of spray and diesel mixing. This study's approach involved using the LES model in conjunction with the KH-RT model under basic conditions ECN Spray A. The SGS was built using the dynamic structure model. The generated model was used to analyze the spray turbulence structure in the spray behavior to analyze the influence of different flexible injection patterns.

2.1 Spray modeling

The spray of diesel engines is characterized by a short liquid core and rapid atomization. Hence, from the point of view of the modeling of calculation, the fuel (n-dodecane) is injected in a cylindrical volume geometry with the initial droplet size distribution to determine the drips those separate from the upstream wall, then allowing an upstream hot ambient entrainment.

The present study uses the KH-RT model for droplet secondary breakup. The KH-RT model is a hybrid method consisting of the KH wave model and RT, the instability of normal acceleration to the droplet surface. The KH mechanism considers droplets to be liquid jets that have been stripped after being injected into the gas environment, while the RT mechanism is driven by changes in density in the normal direction of the liquid–gas interface. The KH model based on the disruptive growth rate Ω_{KH} and the wavelength $\wedge_{KH}$ that corresponds to the fastest Ω_{KH} has a characteristic breakup time τ_{KH}, which can be defined as follows:

TABLE 1 Modeling and constant values of the numerical parameter.

Numerical setup	
Modeling Tool	Converge
Spray models	
Drop evaporation model	Frossling model
Collision model	NTC collision
Collision outcome	O'Rourke collision outcomes
Drop drag model	Dynamic drop drag
Breakup	KH-RT model
Turbulence model	LES, dynamic structure
Grid control	
Base grid size	4,000 μm
Finest grid size	125 μm
KH-RT model constants	
B_0	0.61
B_1	5
C_τ	0.1
C_{RT}	0.1
C_{bl}	1.0

TABLE 2 Operating conditions are based on Spray A from the ECN website.

Spray A specification	
Injection conditions	
Fuel	n-dodecane (n-$C_{12}H_{26}$)
Nominal nozzle diameter	84 μm
Injection pressure	50, 100, and 150 MPa
Ambient conditions	
Ambient temperature	440, 900 K
Ambient density	22.8 kg/m^3

$$\tau_{KH} = \frac{3.276B_1 r}{\Lambda_{KH}\Omega_{KH}}, \quad (1)$$

where r represents the radius of the initial droplets. The stable diameter is calculated as $d_c = 2B_0\Lambda_{KH}$. The KH model constants B_1 and B_0 control the breakup time and wavelength, respectively, and the options of the aforementioned parameters will be modified later. The injected droplet's size under the conditions of ECN Spray A is generally within a few micrometers. Therefore, for the corresponding KH wavelength of the wave droplet, the surface is separated from the much larger grid. When considering the RT model by assuming that there is linear disturbance growth, the growth rate of Ω_{RT} and $\wedge_{RT}$ of the wavelength can be determined. The RT breakup time is given by the multiplicative inverse of the growth rate:

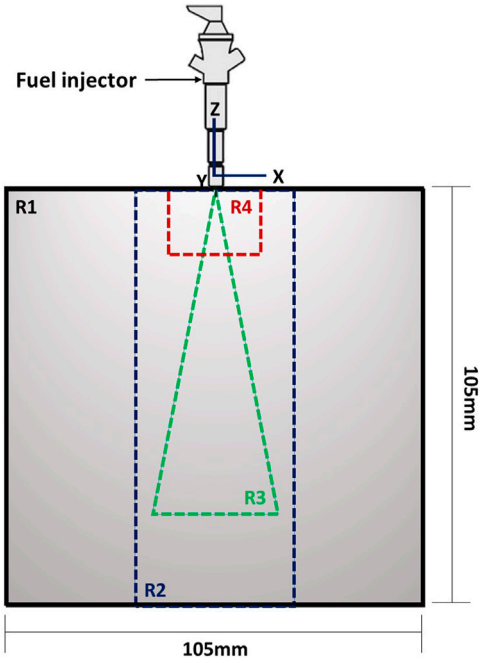

FIGURE 1
Geometry characteristics of the combustion chamber and computational domain of the studied LES.

$$\tau_{RT} = C_\tau \frac{1}{\Omega_{RT}}, \quad (2)$$

where C is the correction factor to delay the breakup under certain conditions.

2.2 Spray turbulence interactions

The effects of turbulence distribution on spray droplets are significant in engine spray simulation, such as the penetration of liquid and vapor, which are important spray parameters. This study presents in detail the characteristics of the spray flow fields to study the influence of the injection pattern on spray behavior and vortex formation produced from overlapping flow motions. Backflow movement occurs in cases of suspension of injection pressure and injection pressure changes interfere with the surrounding gas pressure. The distribution of fuel and the evolution of vortex with counterflow and radial expansion were investigated. The calculation of turbulent distribution uses velocity fluctuations in each direction of coordinates obtained from the Gaussian probability function, as detailed in Xin et al. (1998). The turbulent distribution of spray droplets is incorporated through a stochastic calculation of drag force fluctuations in droplets. In the context of the LES method used for dispersion caused only by sub-grid turbulence scales when the dispersion caused by the large eddies is captured by the drag force calculated by considering the

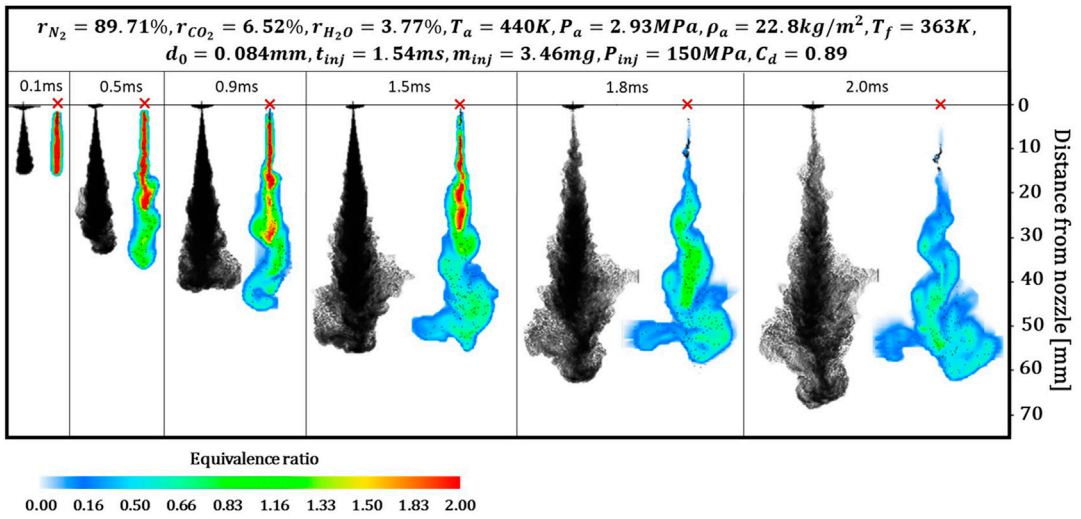

FIGURE 2
Spray shapes and equivalence ratio histories at 440 K ambient temperature.

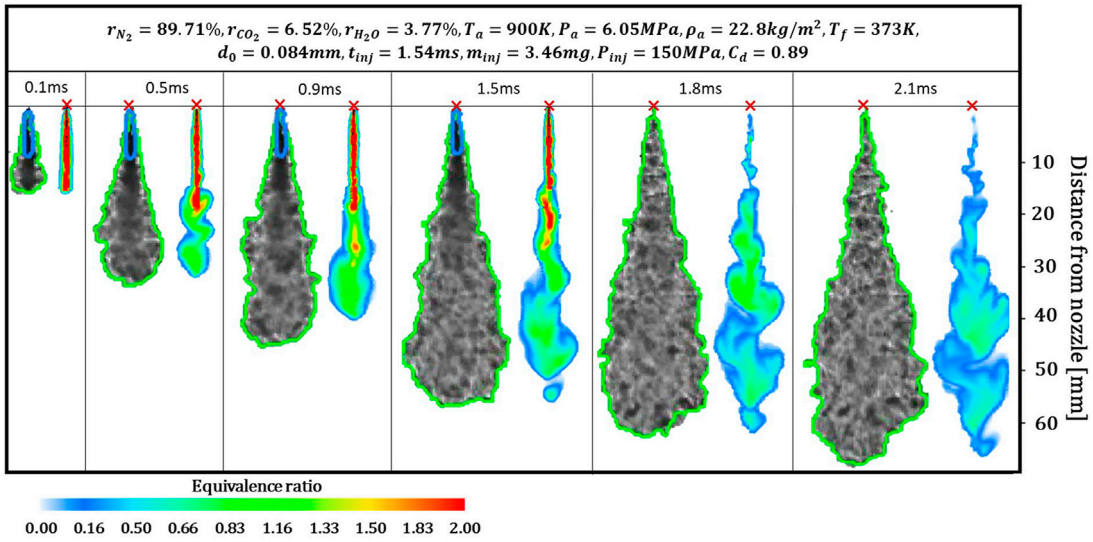

FIGURE 3
Spray shapes and equivalence ratio histories at 900 K ambient temperature (injection pressure, 150 MPa).

calculated fluctuations in the velocity that corresponds to the large structure.

3 Computational setup

In this work, the "CONVERGE" CFD software version 2.4 was used to simulate the spraying and atomization of a constant volume combustion chamber as shown in Figure 1. Based on the independent analysis of the mesh, it has been found that the grid size setting should be less than or equal to 125 μm because determining the size of the grid must consider the surrounding context, which is necessary to consider the size of the nozzle diameter. The use of fine grid sizes in the spray appearance area is required as are the rough grids in the noncritical areas (areas without spray presence) to reduce the cost of computation.

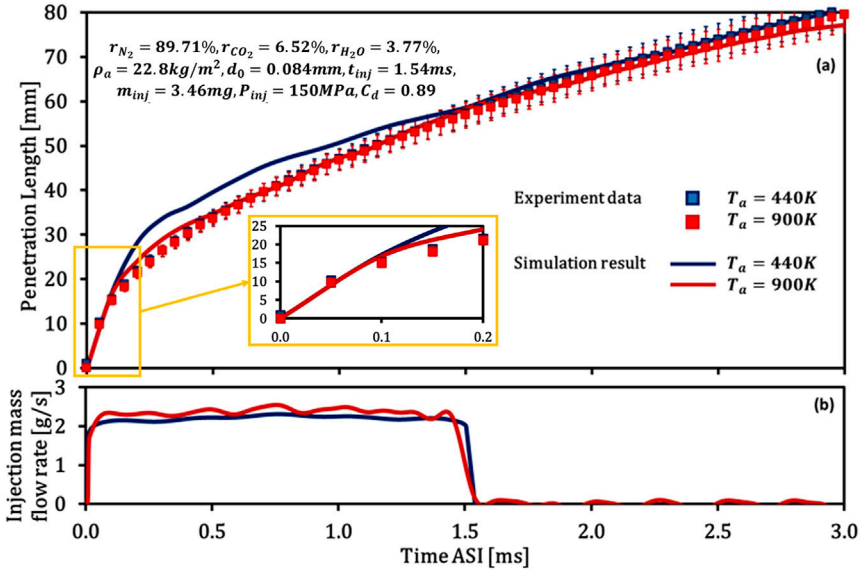

FIGURE 4
Spray penetration under different ambient temperatures. **(A)** Spray penetration and **(B)** injection mass flow rate.

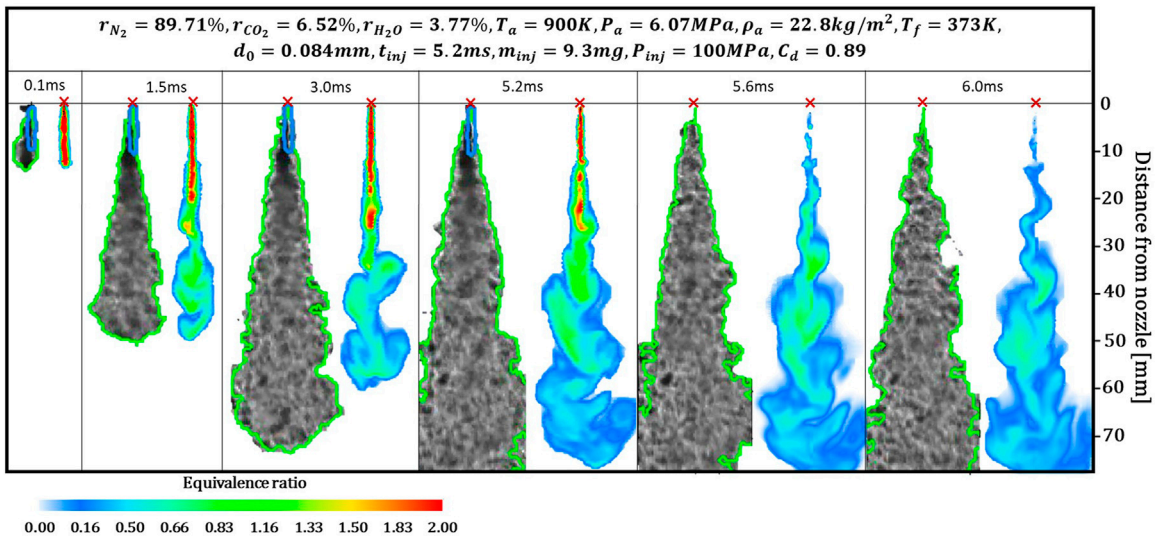

FIGURE 5
Spray shapes and equivalence ratio histories of case injection pressure: 100 MPa.

In this study, the mesh is independent. The simulation results concluded that different grid sizes have a minimal impact on spray penetration when the mesh size of the model created is independent. The finest cell size (125 μm) covers a 15-mm gap between the nozzle and downstream to ensure sufficient resolution in the position where the mixing density takes place, and the rest of the vapor penetration region is set up with a cell size of 250 μm. The computational domain of the studied LES is separated into a mesh with different levels of cell sizes. The adjustment layer is specified with R1, R2, R3, and R4 as shown in Figure 1, which corresponds to the cell sizes 4,000, 2,000, 250, and 125 μm, respectively. The separate domains correspond to the volume of the experimental combustion vessel at the Sandia National Laboratories, which consists of approximately 1.9 million hexahedral cells. The time step in all cases is set to 10 ns.

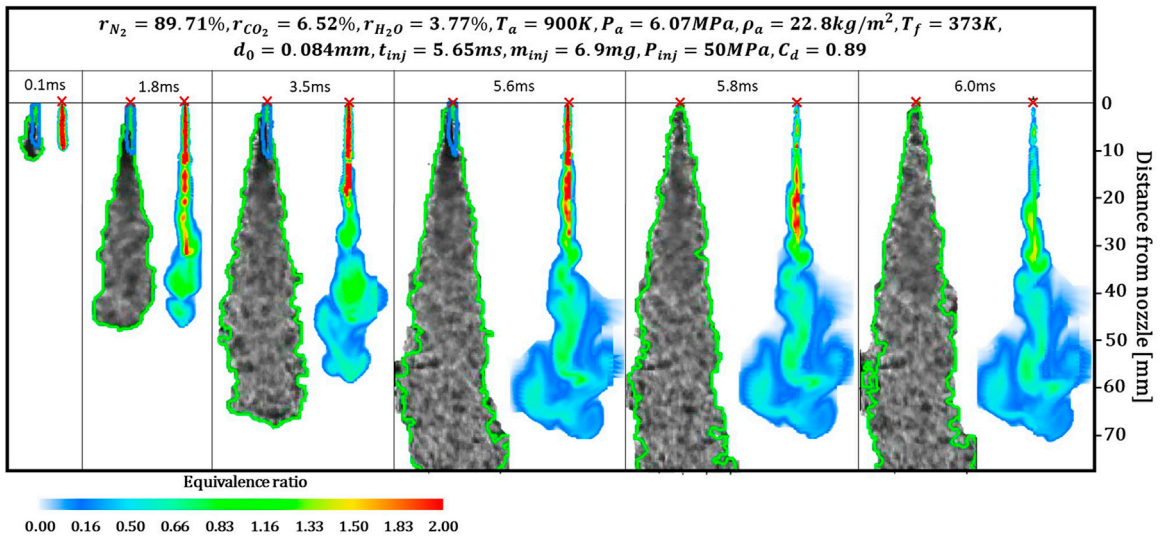

FIGURE 6
Spray shapes and equivalence ratio histories of case injection pressure: 50 MPa.

The spray characterization study was performed using the KH-RT breakup model in conjunction with LES. The modeling and constant values of the numerical parameters used in the fuel injection simulations model are shown in Table 1. The selected values shown in Table 1 are relevant to the initial knowledge of the spatial data on the primary breakup and droplet formation.

The current work analyzed different injection rates, while the relationship between the spray cone angle and injection pressure was discussed in our previous work (Naruemon et al., 2020). However, this study used a constant fuel injection quantity and injection duration time for all case studies, therefore the same input data of spray cone angle was used (21°).

4 Results and discussion

4.1 Model validation

To clarify the performance of the model, the generated model was examined under basic ECN Spray A experimental conditions as shown in Table 2. At first, the different ambient temperatures were considered to study the spray formation behavior when the reaction rate varies due to different temperatures, and next, the different injection pressures were considered to study the spray penetration behavior when the velocity rate varies due to different pressures.

Current calculations are performed by liquid n-dodecane, injected from a nozzle hole into the combustion vessel with the ambient gas composition: N_2, 89.71%; CO_2, 6.52%; and H_2O, 3.77% under thermodynamic conditions.

Figures 2, 3 show the spray behavior of the simulation result as compared with the experimental data of 440 and 900 K ambient temperatures, respectively. The results in Figure 3 reveal that the simulation result of the spray shape was narrower than the experimental results, but turbulence waves and expanding spray appears to be a real phenomenon. The dispersion density in Figures 2, 3 tend to match the experimental results. It can be stated that the created model is efficient in providing a spray formation behavior capable of displaying an interesting turbulence structure, as well as in presenting the swirling and spray flow.

In addition, Figure 4 shows the higher deviation of spray penetration length at an ambient temperature of 440 K than at an ambient temperature of 900 K when compared to the experimental data, while the experimental data remains almost the same in both cases. However, in reality, in cases with the same injection pressure but different ambient pressures, the lower ambient pressure should result in longer spray penetration, which is consistent with the simulation result in this study. The initial injection demonstrated that both cases correctly captured the initial ramp for spray penetration. These findings indicate that the generated model performed well in spray simulation under a variety of ambient temperature conditions.

To ensure that the generated model was effective enough, this study validates the model with three different injection pressure conditions as shown in Table 2. The comparison results of the spray behavior and the equivalence ratio histories of injection pressure 150, 100, and 50 MPa conditions are shown in Figures 3, 5, 6, respectively. The results of the comparison show that the spray shape and turbulence characteristics matched those of the

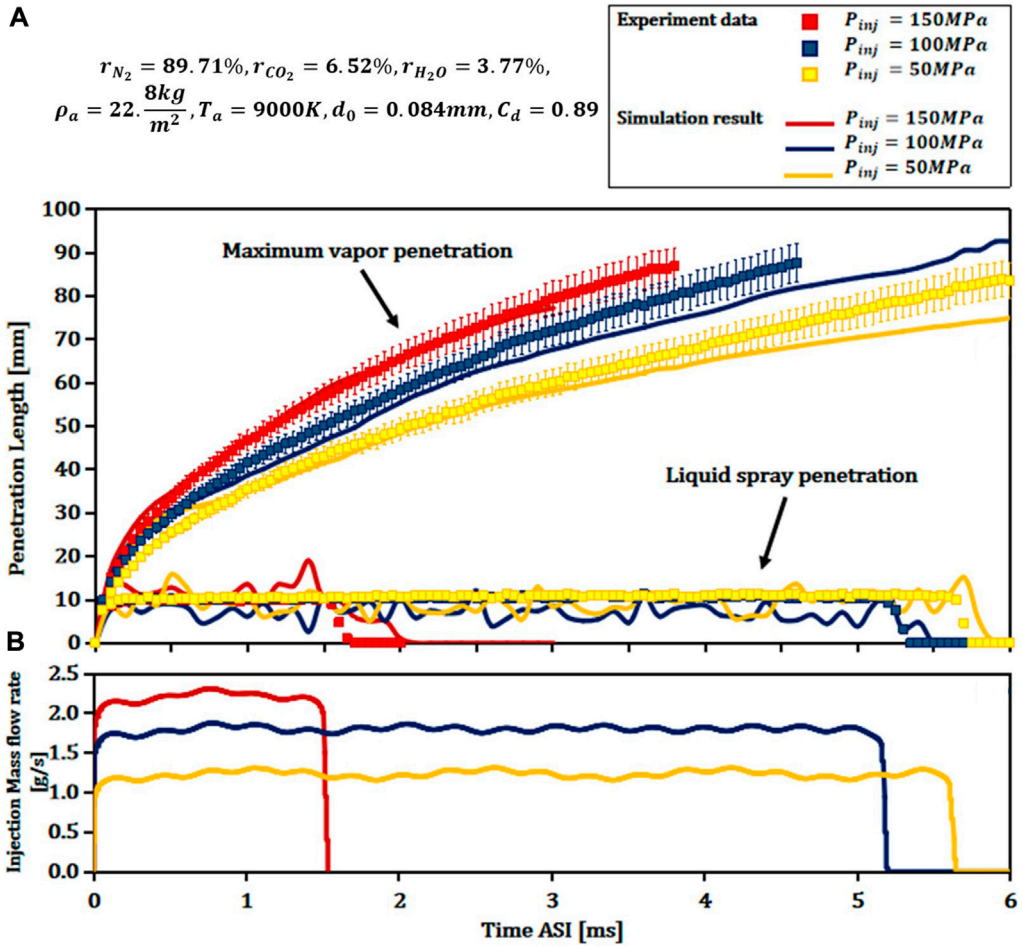

FIGURE 7
Spray penetration of different injection pressures. **(A)** Spray penetration and **(B)** injection mass flow rate.

experimental data. Although the spray width and spray penetration length do not match 100%, the simulation results can show clear transient turbulence of the spray structure since the nozzle exit includes the backflow and vortex formations.

Figure 5 shows that the simulation results of the vapor penetration are shorter than the experiment data, starting from injection time 3.0 ms, while Figure 6 shows that vapor penetration results are shorter than 3.5 ms. However, the overall simulation results of the different injection pressures show good agreement with the experimental data; in particular, the results of the injection pressure 150 MPa condition (Figure 3).

In addition, Figure 7 compares the spray penetration length under various injection pressure conditions. It can be seen that the spray penetration length at injection pressure 150 MPa shows good simulation results, while the injection pressure 100 and 50 MPa are in good agreement with the experimental data at the start of injection. These results can be explained by the spray transient turbulent formation using different cell size layers. Such a design produces poor simulation results for longer injection duration cases while producing excellent simulation results for the short injection duration cases. This is because the spray usually disperses near the nozzle exit shortly after injection begins. When spray expands due to turbulence structural waves and move downstream, it implies that these phenomena must take time and adjust the grid size level. For longer injection durations, such phenomena might result in simulation performance errors. The discrepancy result was a model error after the end of the injection approximately twice the injection duration of the case of injection pressure 150 MPa. Therefore, the model created was effective enough to predict spray behavior both during the injection process and after the end of the injection at no more than the estimated 3.0-ms injection duration time.

It has been observed that the LES could obtain a temporary spray structure in relation to the fractional distribution of the

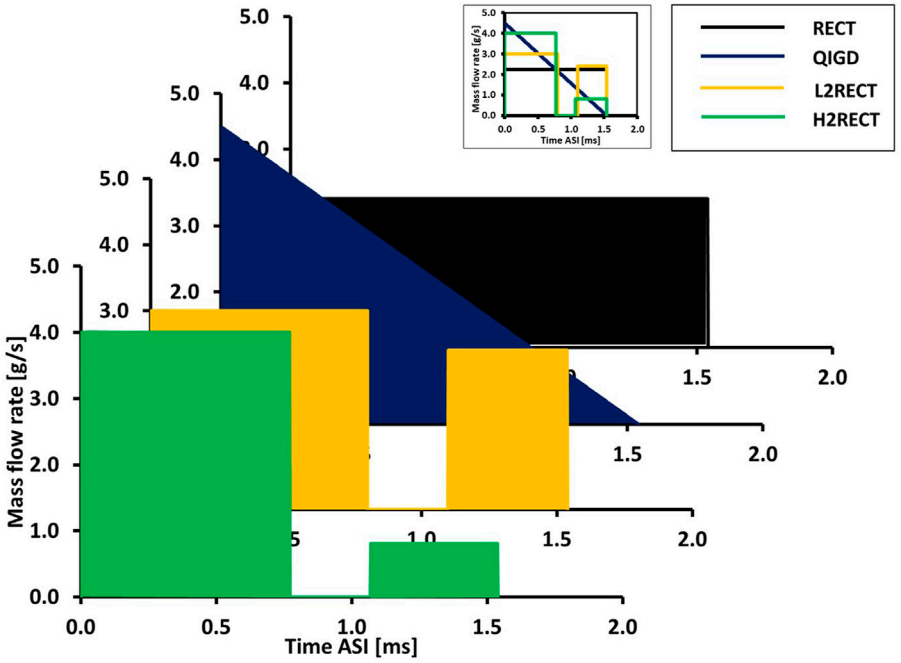

FIGURE 8
Varying injection patterns.

mixture, temperature, and pressure. The simulation results of the LES model showed the momentum exchange behavior between the hot gas in the combustion chamber and the spray injected more clearly than the simulation result of the RANS model from our previous study (Naruemon et al., 2020). More importantly, the LES can capture multiple spray change points, and the LES can depict turbulence waves of the shear force at the interface between the fuel spray and the surrounding air. The next section presents the characteristics and behavior of the flow and mixing patterns of fuel sprays with different injection patterns.

4.2 Effect of injection rate

This study examines the effect of the injection rate on spray behavior. Before going any further, it is worth clarifying that since there is no oxygen concentration in all study cases. This study analysis only considers fuel mixing with gas flow, and the intensity shown is the fuel density. This section examines the study condition operation under the same conditions with the experimental conditions of the ambient temperature of 900 K and injection pressure 150 MPa.

Figure 8 shows five different injection patterns, where RECT represents the typical fuel injection pattern, QIGD represents the peak injection rate at initial injection duration as in our previous study (Naruemon et al., 2020). The 2QIQD represents the same injection rate as that of the QIQD but is divided into two injections (t^{1st}0.77 ms/t^{dwell}0.30 ms/t^{2nd}0.77 ms) to represent the split injections, while the L2RECT represents the 2QIQD represents the two rectangular injection rates (t^{1st}0.80 ms/t^{dwell}0.30 ms/t^{2nd}0.44 ms) to study the different injection patterns, and the two rectangular injection rates of the H2RECT are the same as those of the L2RECT (t^{1st}0.77 ms/t^{dwell}0.30 ms/t^{2nd}0.47 ms) but have larger differences between the first and second injection rates to study the effect of the initial pressure. The L2RECT and H2RECT injection rates shape the injection rates to study the influence of the initial injection rate. The injection rates of the L2RECT and H2RECT were clearly different from the first injection rate, where the L2RECT injection rate has a lower first injection rate than that of the H2RECT injection rate. The injection duration of RECT, QIGD, L2RECT, and H2RECT are the same (1.54 ms), while the injection duration of the 2QIQD was set at 1.84 ms. In this study, the RECT, QIGD, L2RECT, and H2RECT injection rates used the same injection duration and the same injection quantity in all cases, with just differences in the setting of the injection rates. This is because the timing and amount of fuel injection are often the important factors in engine control. The main purpose of this research is to study the influence of different fuel injection rates. Therefore, setting the same fuel injection timing and amount in all cases is an effective control variable for studying the influence of the fuel injection rate. In addition, different injection patterns were employed at different peak injection pressures. Peak injection pressures were set at 150,

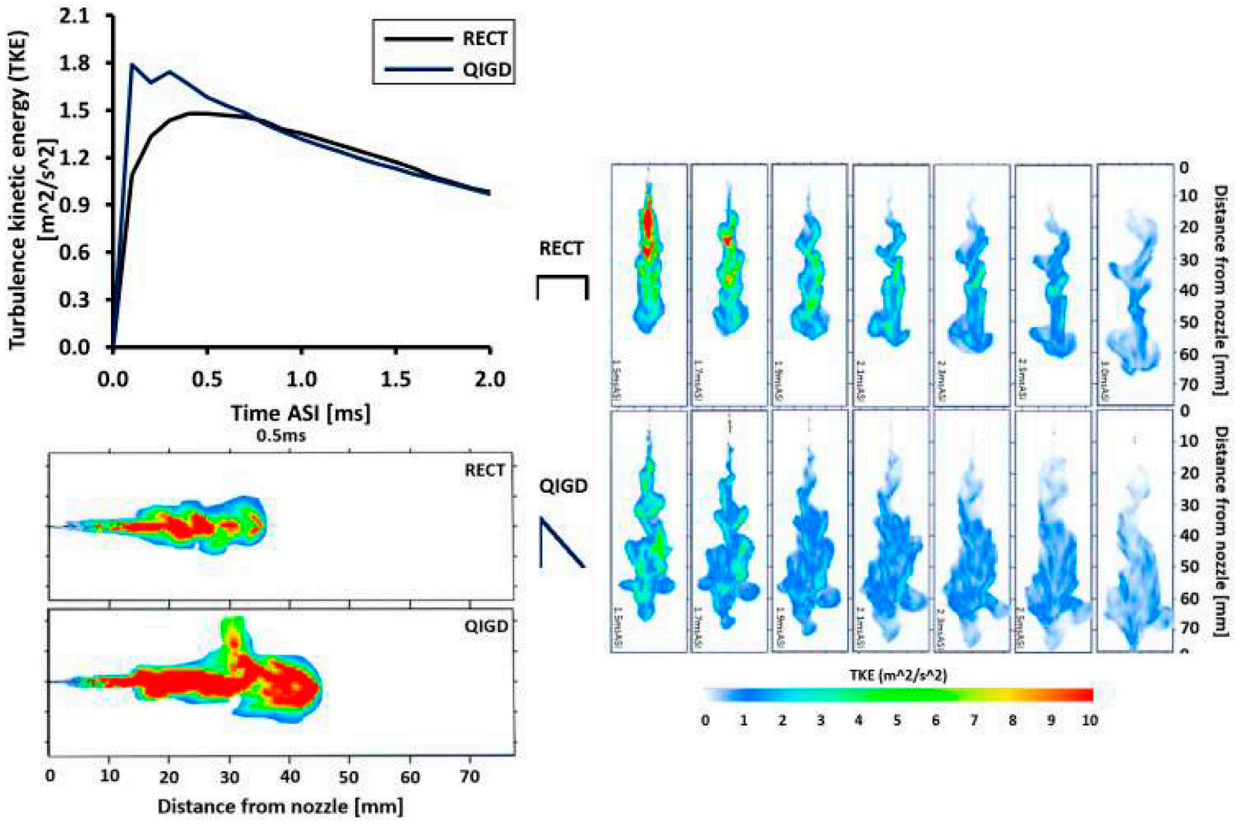

FIGURE 9
TKE values and TKE distribution for RECT and QIGD.

600, 600, 266, and 470 MPa for the RECT, QIGD, 2QIQD, L2RECT, and H2RECT, respectively. However, although the maximum injection pressure of 600 MPa exceeds current technology, the review shows that creating ultrahigh pressure fuel injection is practical. We also calibrated and validated the spray model using experimental data with different injection pressures. We concluded that the generated model could predict spray behavior when injection rates and injection pressures change. Hence, five injection patterns were used to study the influence of flexible injection on spray behavior and the spray mixing process.

4.2.1 Influence of initial injection rate

Although past research have shown interest in different injection rates in groups of the boot, ramp-down, or even inversed-delta injection patterns those represent high initial injection rates, most of the past research had been focused on the general injection rate with normal injection pressure. In this study, interest has been shown in studying the short injection rate with ultrahigh injection pressure to find out outstanding advantages of the new flexible injection rate. This section presents the results of a comparative study of the RECT and QIGD in understanding the influence of the initial injection rate.

The TKE of RECT and QIGD are compared in Figure 9. It can be seen that the TKE of QIGD is higher at the start and gradually decreases until it is equal to the TKE of RECT, while the TKE distribution behavior of the QIGD is significantly larger. This is because the ultrahigh injection pressure of the QIGD causes a lot of turbulence in the spray field.

In addition, Figure 10 shows that the fluid penetration distances are similar in both cases, although there was a very high change in injection pressure at the start, while the vapor behavior of the QIGD expands wider and longer with higher injection pressure. The QIGD with ultrahigh initial injection pressure also represents the equivalence ratio behavior that quickly dilutes and distributes, as shown by the direction of dispersion by the influence of velocity on the velocity arrow vector. This means that the gas mass flow rate can be increased as the injection pressure increases.

Figure 11 shows that the QIGD has a bigger spray area and spray angle than that of the RECT. The spray area at the section near the nozzle exit shows a small spray angle. This is because increasing the injection pressure increases the radial speed from

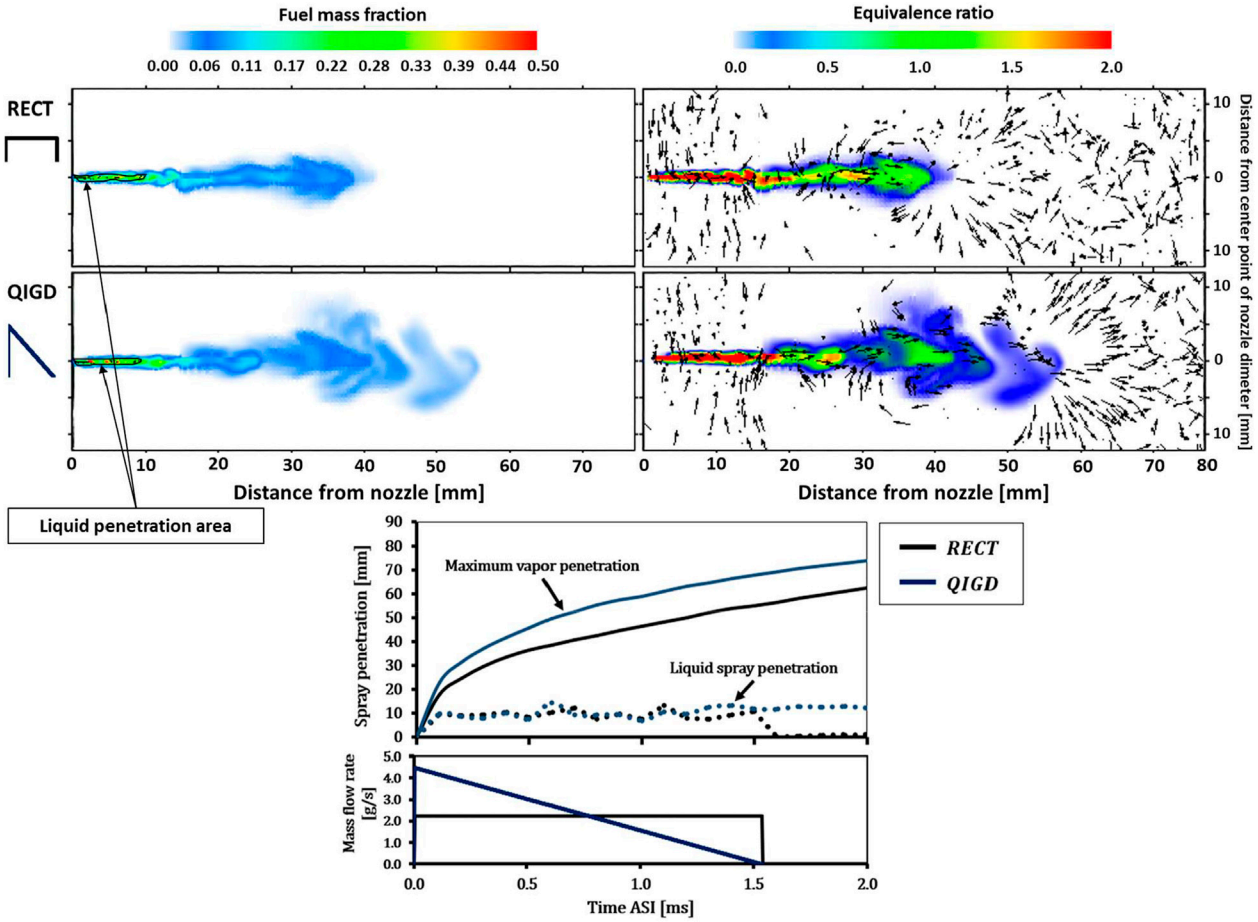

FIGURE 10
Comparisons of distribution of liquid, fuel mass fraction, and equivalence ratio at 0.9 ms ASOI, and spray penetration of RECT and QIGD.

the ambient gas retention, the spray area quickly moves to the center and the spray tip, which causes a larger expansion of the spray tip. This section shows that the ultrahigh initial injection pressure influences the terms of spray spread and turbulence.

4.2.2 Influence of split injections

The varying injection rates are an important effective strategy for controlling mixing and combustion efficiency, but there are still limitations in the formulation of various injection rates. Therefore, the split injection strategy has emerged as the leading option that can serve this purpose. The split injection strategy can offer increase–decrease injections to create varying injection rate patterns. In this section, the QIGD and 2QIQD were examined for the effect of split injection.

The simulation result in Figure 12 shows that the spray penetration of QIGD and 2QIGD has different shapes due to the effect of the split injections. Figure 12 shows that after the dwell time (1.3 ms), the spray behavior of the 2QIGD injection rate case shows a velocity vector with a reverse direction of spray flow. This is because the fuel pressure is weakened during the dwell time of injection, causing the surrounding gas pressure to beat the injection pressure, demonstrating the potential for eddy current formation, causing the air entrainment and formation of a spray mixing, which causes the faster dilution equivalence ratio. It can be said that this behavior will complete the mixing process faster.

In addition, Figure 13 shows that the liquid phase is only available in a small area near the nozzle for both shapes, a phenomenon attributed to an increase in the injection pressure. Meanwhile the 2QIGD shows higher TKE values due to the dwell time. Clearly, with double injection, the temperature absorbing is increased due to the local temperature absorption that the second spray is affected by the previous injection, where the second injection penetrates through the preexisting environment, greatly reducing the resistance of the second injection, causing the faster increase of the axial velocity for the second spray.

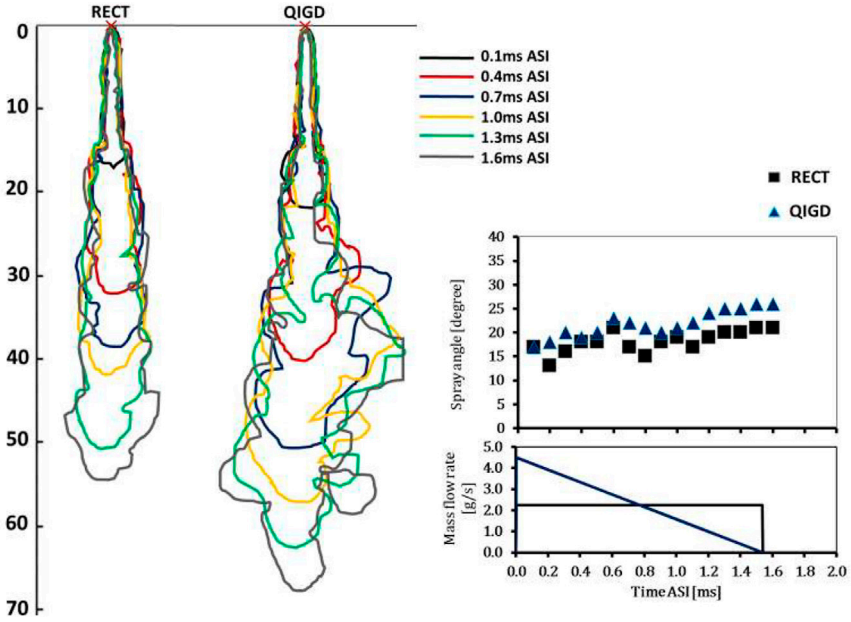

FIGURE 11
Comparisons of spray area boundaries and spray angle of RECT and QIGD.

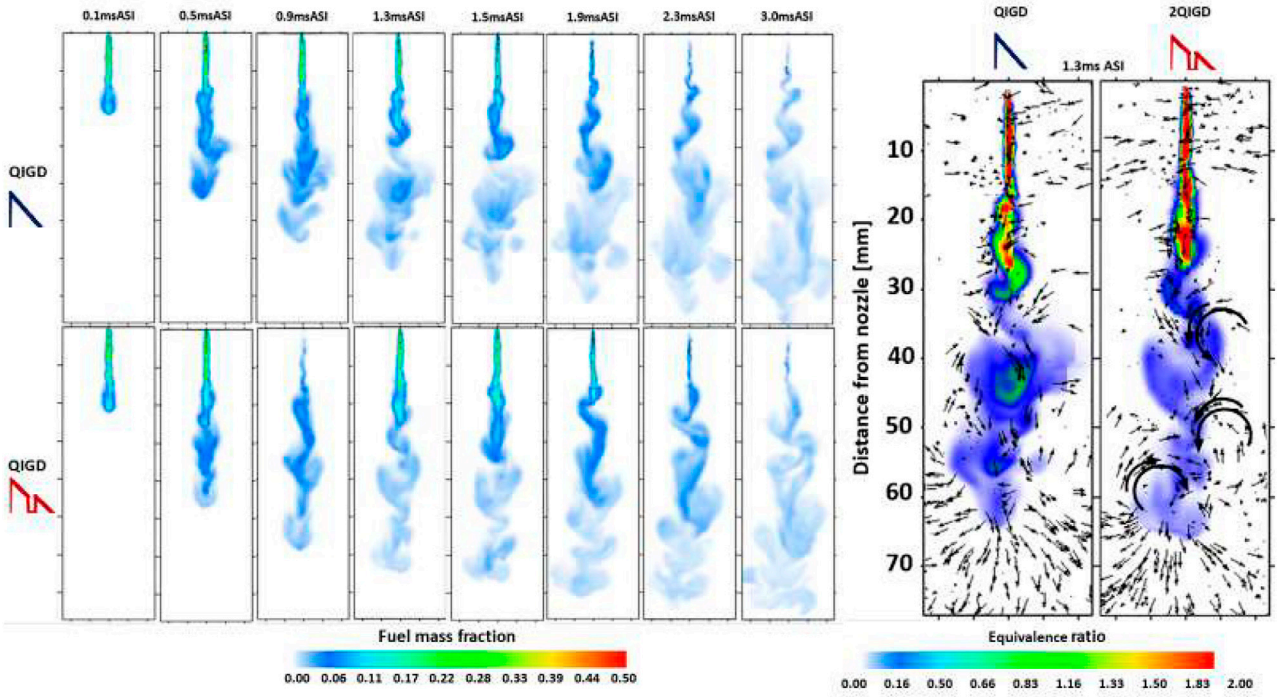

FIGURE 12
Fuel mass fraction history, equivalence ratio history, and velocity vector of QIGD and 2QIGD.

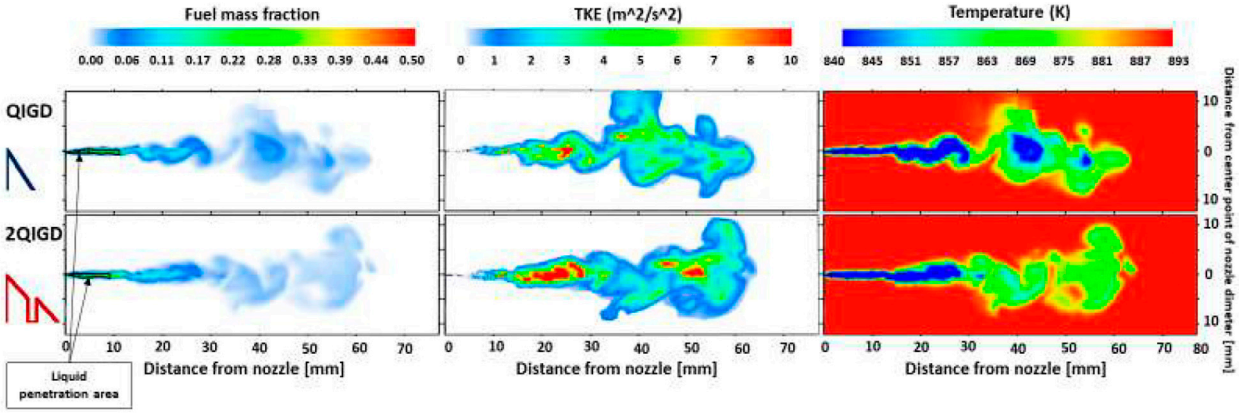

FIGURE 13
Comparisons of distribution of liquid, fuel mass fraction, TKE, and temperature history of QIGD and 2QIGD at 1.3 ms.

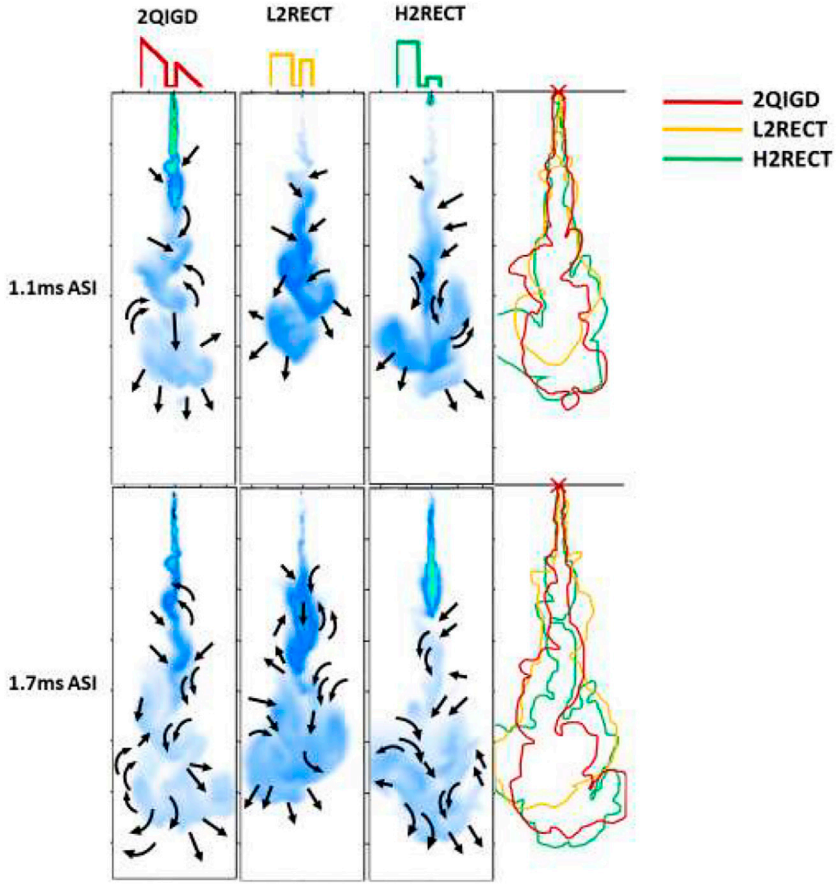

FIGURE 14
Velocity vector direction of vortex and spray area boundary.

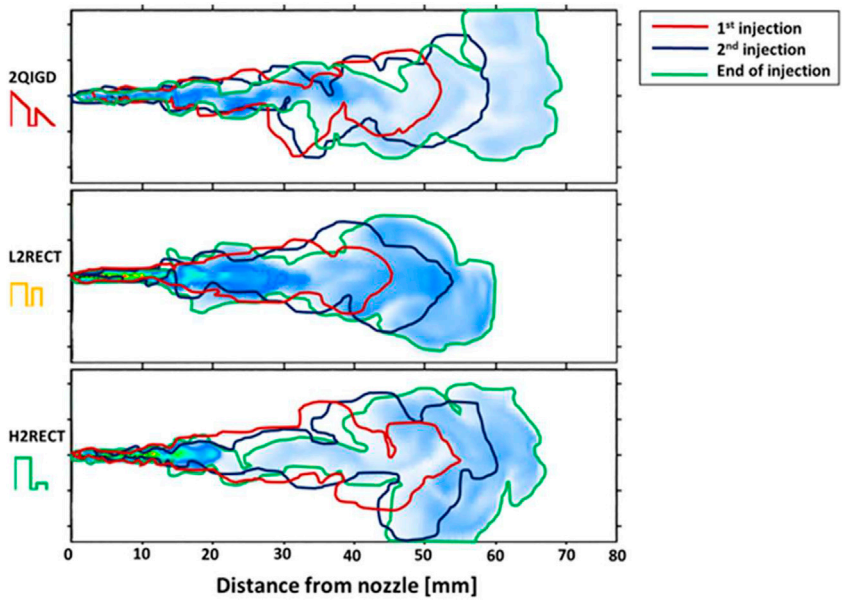

FIGURE 15
Spray area boundary for different spraying ranges. The first injection boundary is shown at the end of the first injection. The second injection boundary is shown at the beginning of the second injection. The end of the injection boundary is shown at the end of the injection point, which is different in each case.

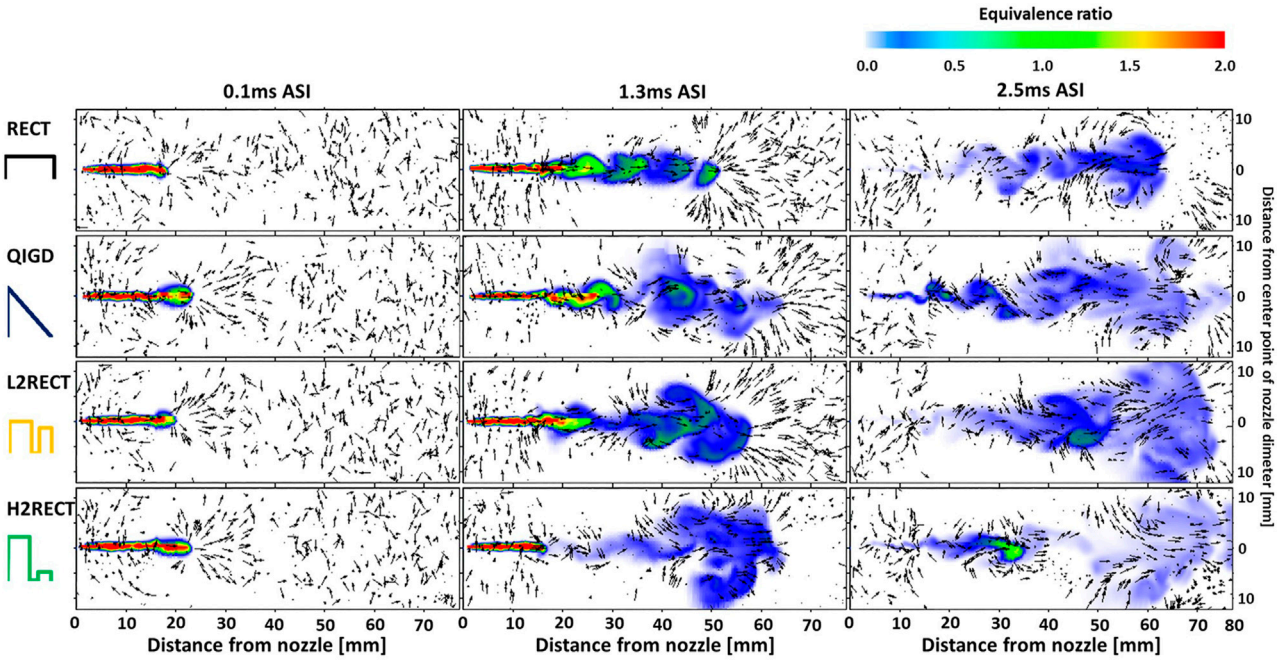

FIGURE 16
History of equivalence ratio and spray velocity vector direction at various injection rates.

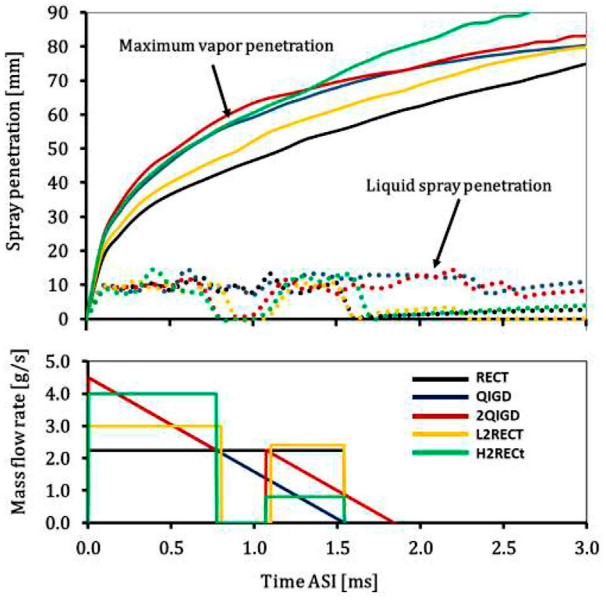

FIGURE 17
Simulated spray penetration of different injection patterns.

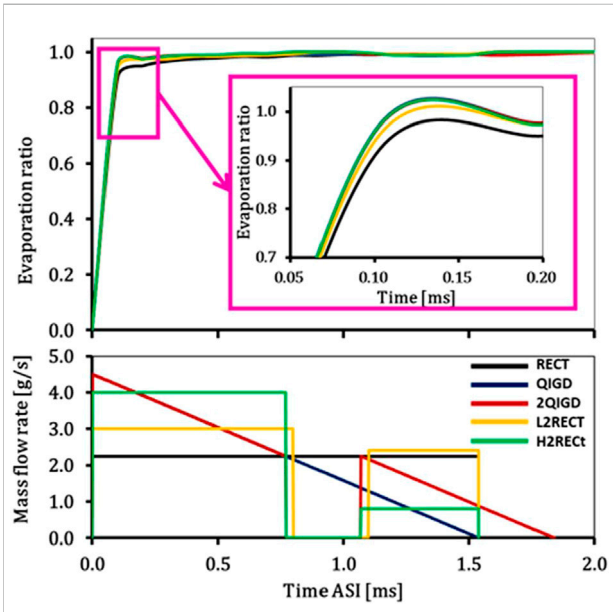

FIGURE 18
Evaporation ratio of different injection patterns.

Therefore, the split injections with ultrahigh injection pressure strategy become one of the strategies for improving the fuel injection system, which will discuss the influence of split injection with different injection patterns in the next section.

4.2.3 Influence of different flexible injection patterns

In addition to raising awareness that the injection pattern plays an important role in the proposed spray behavior. Flexible injection rates are represented by the split injections with different injection patterns. Due to the complexity of this injection pattern, the complexity of the resulting process cannot be avoided. Therefore, the study of spray behavior and complex mixing processes were analyzed in this section. In this section, the 2QIGD, L2RECT, and H2RECT representing the split injection with different injection patterns were examined and compared with the influence of different flexible injection patterns.

The vortex formation behavior is shown with the direction of the velocity vector in Figure 14. It has been found that sustained higher injection pressure at the starting point of the H2RECT increases vortex formation and spray area. This phenomenon has been shown to produce a wider dispersed spray shape. These reveal that the spray penetration length and the spray diffusion width depend on the spray injection mass flow rate. In addition, Figure 14 shows that the highest initial injection pressure of the 2QIGD yields a long spray tip penetration, while the H2RECT with a slightly lower initial injection pressure but sustained high initial injection pressure shows longer spray tip penetration. Also, the H2RECT has superior efficiency in the spray diffusion behavior, showing the largest spray area boundary as compared to the other cases. It can be seen that the initial injection pressure shows a great influence on the spray penetration behavior. The effect of multiple injections shows an increase in turbulence at the first injection when the second injection was joined.

In addition, different flexible injection patterns of split injections exhibit different spray shapes as shown in Figure 15. The simulation results in Figure 15 show the clear expansion of the radial spray area, especially for the H2RECT with a continuous very high first injection and low second injection, and this is due to the phenomenon of pressure inversion. When considering the boundary area at the end of the injection point, the L2RECT shows the narrowest radial spray expansion and the shortest spray tip penetration. This is because the injection pressure settings of the first and second injections are not largely different; this behavior is due to the weakness of pressure inversion, while the other two injection patterns show a high-pressure reversal from a large pressure difference. However, the simulation result shows that the spray penetration length depends on the peak injection, in which the QIGD is the longest, the H2RECT is second, then the L2RECT. Overall, Figure 15 shows that the continuous high injection pressure has a small effect on the radial spray expansion, but the high inverse injection pressure and the peak injection show a significant effect on both radial extension and spray penetration length.

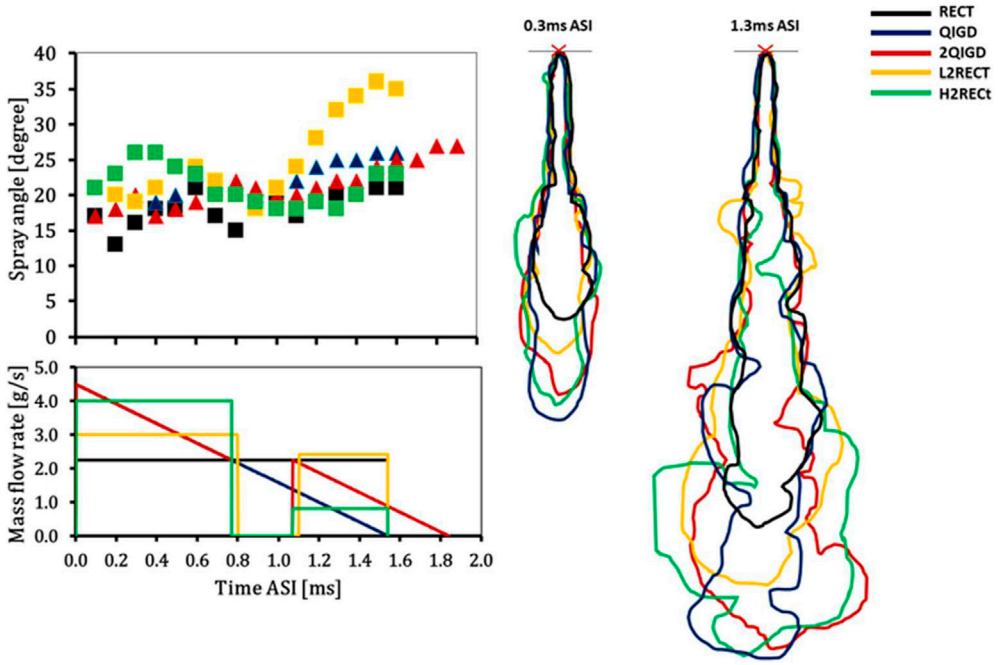

FIGURE 19
Comparison of spray angle of different injection patterns.

4.3 Effective injection pattern

As the past findings show, the effective injection rate is the injection rate with ultrahigh injection pressure, high initial injection rate, and split injection, which include a combination of such strategies.

Finally, this section discusses the overall influence of all the different injection patterns in order to present the most effective injection patterns on the mixing efficiency of diesel spray. Figure 16 shows that the axial movement of the spray is directly proportional to the initial injection pressure. It can be seen that the injection pattern with a low initial injection rate shows a shorter spray penetration, and the dwell time increases the vortex interval as shown by the direction of the velocity vector. In addition, the higher peak injection has shown a faster dilute equivalence ratio.

Figure 16 shows that the H2RECT injection rate has the rapid dilution equivalence ratio at the spray tip, which has a positive effect on reducing liquid fuel collisions with combustion chamber walls. This result shows that an injection rate of continued high initial injection with sufficiently high injection pressure causes the droplets to spread throughout the fuel spray area and results in a lower equivalence ratio, thereby inhibiting the formation of soot precursors causing good mixing and combustion efficiency.

Figure 17 shows the spray penetration history results of spray penetration for understanding well the spray breakup process. The H2RECT injection rate shows the longest vapor penetration length in the final stage, while the RECT injection rate shows the shortest. This is because vapor penetration increases with injection acceleration rate and continues to increase with the injection rate before EOI. It can be seen that as the injection rate breaks down during the dwell time, the liquid spray penetration length drops to almost zero. However, it is clear that in the QIGD and 2QIGD injection rate cases with high peak injection rates, the injection pressure decreases steadily and decreases at the second injection, showing that the liquid spray penetration length was still visible after the EOI. This behavior can be explained by the influence of injection pressure that results in the particle's shear force. A decreased shear force of the particles is not enough to change the liquid state to vapor state. The remaining liquid after the EOI is significant and may affect pollution due to the possibility of unburned residual fuel.

To understand the relationship between the fuel injection rate and fuel droplet breakup efficiency, Figure 18 presents the simulation results of the evaporation ratio under different injection patterns. It shows clear rapid evaporation in the QIGD, 2QIGD, and H2RECT injection rate cases than in the other injection patterns. However, the L2RECT injection rate case shows the same evaporation ratio as the aforementioned cases just after 0.15 ms ASI, while the RECT injection rate case shows the lowest evaporation ratio; this is because of the lower peak injection pressure. The QIGD, 2QIGD, L2RECT, and H2RECT injection rate cases have different peak injection

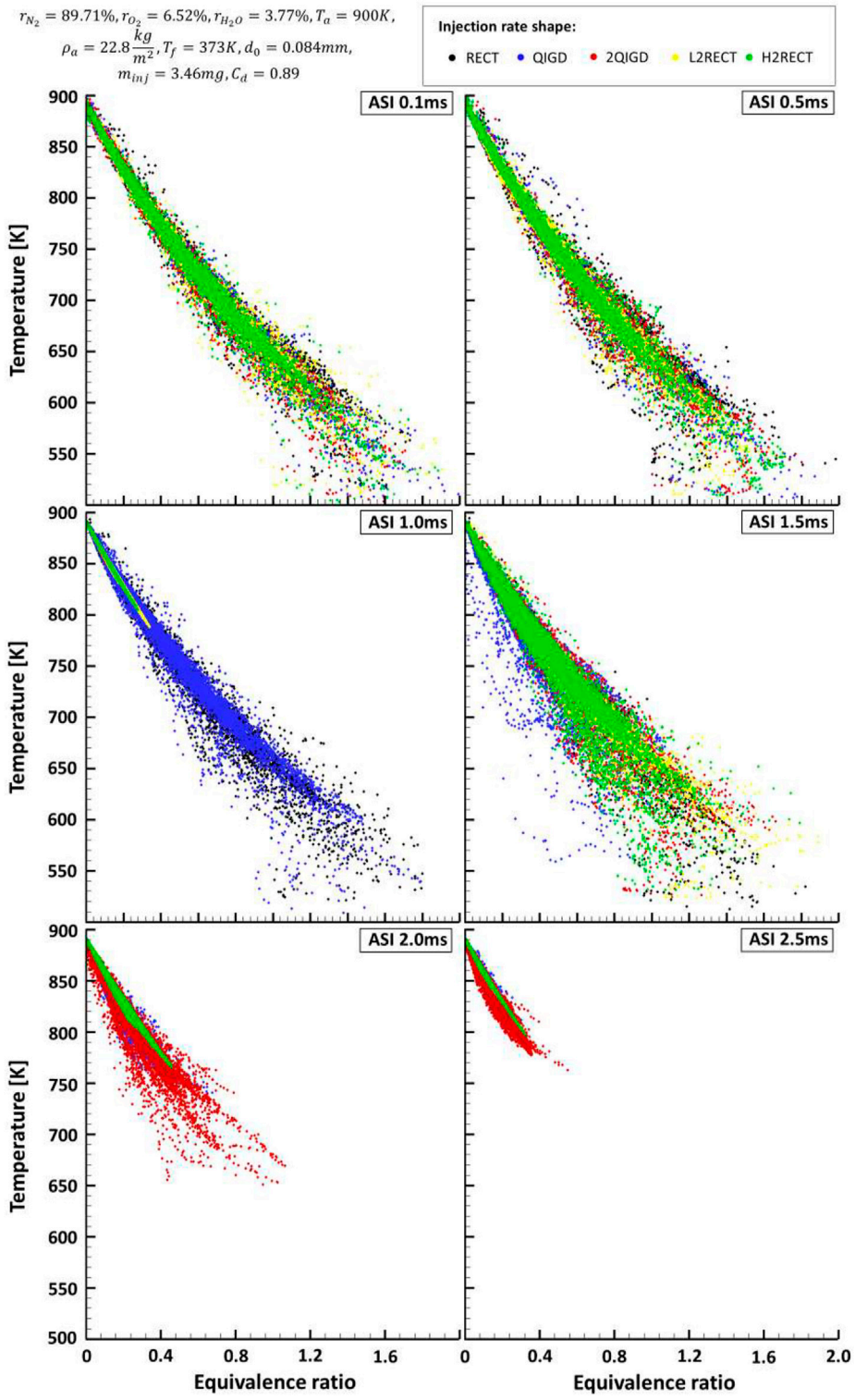

FIGURE 20
Spray temporal evolution in the resolution of equivalence ratio and temperature for different injection patterns.

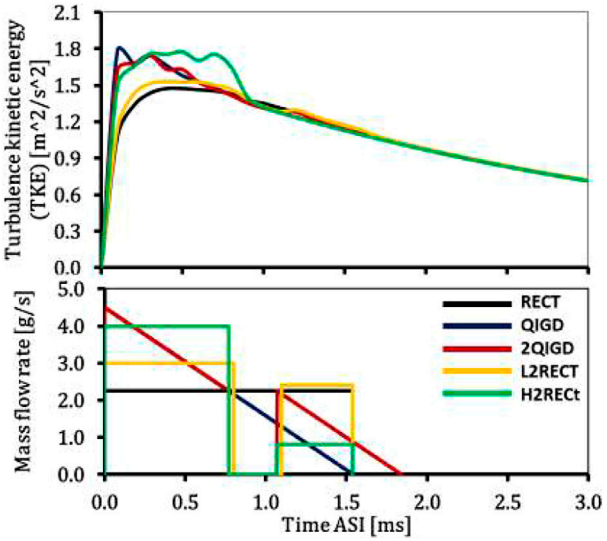

FIGURE 21
TKE of different injection patterns.

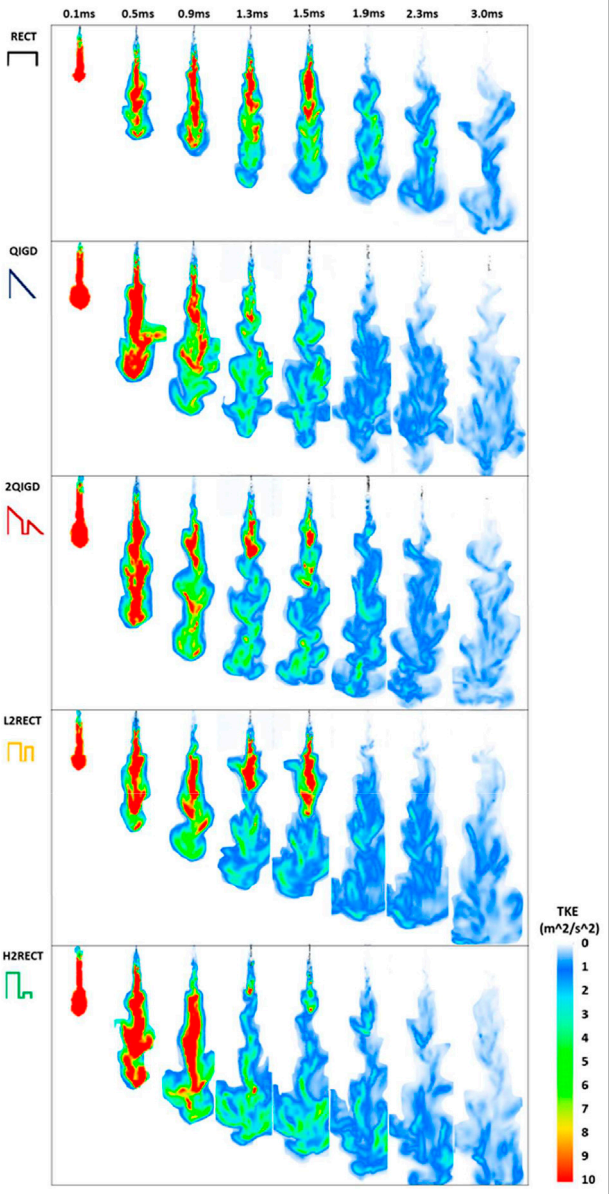

FIGURE 22
TKE distribution for different injection patterns.

pressures; the high enough peak injection pressure effect is of a good evaporation ratio. This is consistent with the results of the discussion of predicting the value of the equivalence ratio.

The detailed information of the spray field region and spray angle is significant for a complete understanding of spray mixing. Figure 19 shows different spray angles, and it can be observed that the spray angle depends on the injection rate in each period. The H2RECT injection rate has the largest spray angle in the first injection period, and this is because evaporation is faster than in other cases which causes high spray distribution. Meanwhile the L2RECT injection rate shows the largest spray angle in the second injection phase. However, the QIGD injection rate shows a bigger spray angle than the second injection phase of the 2QIGD injection rate case. This is because the QIGD injection rate case has a continuous injection, while in the cases of 2QIGD and H2RECT injection rates, the fuel is injected in the second injection, resulting in a new high in-cylinder pressure and renewed spray expansion. This demonstrates that the injection rate and dwell time have a significant effect on spray distribution. The effect of dwell time on the spray angle is an interesting observation. The larger the spray angle, the higher the gas entrainment.

Figure 20 shows the temperature history in equivalence ratio, and the scatter points represent the equivalence ratio effect on the temperature history. Figure 20 shows the weak scatter of the equivalence ratio at high temperature and longer injection time, especially for the QIGD and 2QIGD cases, showing stronger scatter than for the RECT, L2RECT, and H2RECT cases. They show strong scatter at low temperatures for all considered cases, and this is due to the lower temperatures presenting incomplete mixing processes, when the temperature increases result in increasing the mixing efficiency. This phenomenal observation from changing the injection rate because the RECT, L2RECT, and H2RECT cases have a high injection rate from the beginning results in a high temperature and causes strong mixing. Until after the EOI, all study cases show a low value of equivalence ratio with high temperature, which shows the weakest scatter due to almost complete mixing. However, the results in the case of QIDG and 2QIDG still show some scatter of the equivalence ratio at this part because of the low injection rate before the EOI,

assuming that these cases might give incomplete mixing. In this section, results show that higher injection causes higher temperature and higher mixing efficiency, as well as causing reduced ignition delay and resulting in faster combustion.

The intensity of the turbulent movement in the spray process was investigated in the TKE as shown in Figure 21 to explain the phenomenon of the equivalence ratio. The result shows that the TKE is highest at the peak injection rate for all cases. During the first injection, the H2RECT injection rate case shows a stronger TKE that lasts longer than for the other cases, and additional TKE distribution histories is considered in Figure 22. The turbulent process produces a small vortex that circulates the mixture, thus having a different mixing. Figure 22 shows that changes in injection rates have a significant effect on turbulence behavior. Higher injection rates increase the fuel mass flux and the turbulence wave results in increased mixing efficiency.

5 Conclusion

In this study, the generated model using the LES model under basic conditions of ECN Spray A that investigated the effects of various injection patterns by split injection with different injection patterns on the spray characteristics can be concluded as follows:

1) Split injection has a great effect on spray boundary occurrence and the emergence of the spray vortex movement. The spray angle of the L2RECT injection rate shape increases by approximately 76% in the second injection when compared with the RECT injection rate shape (typical shape). The dwell time poses a significant effect on spray expansion, which results in higher gas entrainment because the fuel pressure is weakened during the dwell time, causing a faster dilution equivalence ratio, quickly completing the mixing process.
2) A maintained high injection rate shows low equivalence ratio and reveals rapid growth of the spray area due to the development of turbulence structure from the velocity effect, resulting in better mixing. The injection rate with a sufficiently high injection pressure causes the droplets to spread throughout the fuel spray area and results in a lower equivalence ratio, resulting in good mixing and combustion efficiency and inhibiting the formation of soot precursors. The H2RECT injection rate shape shows the highest amount of heat released, which can give a better mixing process and complete combustion.
3) The continuous high injection pressure and the different high injection pressures of the double injection show a significant effect on both the radial extension and spray tip length. The H2RECT injection rate shape shows that the vapor penetration increased by approximately 26.7% from the RECT injection rate shape (typical shape) and increased about 20% more than that from the L2RECT injection rate shape. Due to the influence of the injection pressure and a maintained high injection rate, the resulting particle's shear forces the droplets to spread throughout the fuel spray area causing a low equivalence ratio, resulting in better mixing and combustion efficiency and inhibiting the formation of soot precursors.
4) The injection rate and dwell time have a great effect on spray distribution. The spray turbulence behavior is an indicator of airflow in the spray, while the spray angle is an indicator of the movement of the mixture. The formation of turbulence structure that results in the formation of the vortex at the spray head creates a lean equivalence ratio which creates a good mixing behavior, causing as a result a larger spray angle that results in higher gas entrainment.
5) The split injection and initial injection rates play a key role in evaporation, turbulence kinetics, and reaction processes. The H2RECT injection rate shape is the most effective in diesel spray mixing because the ultrahigh injection pressure of split injection with a high first injection and small second injection is effective to create a ready-mix from the first injection, resulting in quick complete mixing.

Finally, the results from the simulation show that the structure of the spray mixing is significantly affected by the flexible injection patterns. The split injection with different injection patterns have shown remarkable efficacy in this study, where the split injection and initial injection rates play a key role in evaporation, turbulence kinetics, and reaction processes.

Data availability statement

The original contributions presented in the study are included in the article/Supplementary Material; further inquiries can be directed to the corresponding author.

Author contributions

Conceptualization: LL. Methodology: IN. Software: IN. Validation: IN, QM, and YW. Formal analysis: LL, XM, and KN. Data curation: IN. Writing—original draft preparation: IN. Writing—review and editing: LL. Project administration: XM.

Funding

This work was supported by the Natural Science Foundation for Distinguished Young Scholars of Heilongjiang Province (Grant No. JQ2020E005), and the

International Exchange Program of Harbin Engineering University for Innovation-oriented Talents Cultivation. The experimental data are referenced from the Engine Combustion Network website that is maintained and operated by the Engine Combustion Department of Sandia National Laboratories.

Conflict of interest

The authors declare that the research was conducted in the absence of any commercial or financial relationships that could be construed as a potential conflict of interest.

Publisher's note

Supplementary material

The Supplementary Material for this article can be found online at: https://www.frontiersin.org/articles/10.3389/fenrg.2022.933591/full#supplementary-material

References

Akiyama, S., Toyama, Y., Saruwatari, S., Shimada, T., Noguchi, Y., and Aizawa, T. (2019). TAIZAC -TAndem Injectors zapping activation- towards thermal efficiency improvement of diesel engine. *Soc. Automot. Eng. Jpn.* 50 (2), 279–284. doi:10.11351/jsaeronbun.50.279

Anonymnous, Author. Home page: Engine combustion network (ECN): Experimental diagnostics and experimental data: Available at: https://ecn.sandia.gov/diesel-spray-combustion/. (Accessed 16.01.2021).

Bolla, M., Chishty, M. A., Hawkes, E. R., and Kook, S. (2017). Modeling combustion under engine combustion network Spray A conditions with multiple injections using the transported probability density function method. *Int. J. Engine Res.* 18 (1-2), 6–14. doi:10.1177/1468087416689174

Cung, K., Moiz, A., Johnson, J., Lee, S.-Y., Kweon, C.-B., and Montanaro, A. (2015). Spray–combustion interaction mechanism of multiple-injection under diesel engine conditions. *Proc. Combust. Inst.* 35 (3), 3061–3068. doi:10.1016/j.proci.2014.07.054

Edzuan Bin Abdullah, M. F., Shinobu, A., Tomoki, K., and Aizawa, T. (2019). Effects of inversed-delta injection rate shaping on diesel spray flame liquid length, lift-off length and soot onset. *Fuel* 258, 116170. doi:10.1016/j.fuel.2019.116170

Edzuan Bin Abdullah, M. F., Toyama, Y., Takahara, K., SaruwatariAkiyama, S,S., Akiyama, S., Shimada, T., et al. (2018). Optical diagnostics of inversed-delta rate shaping diesel spray flame toward reduction of late combustion. SAE Technical Paper 2018-01-1793. doi:10.4271/2018-01-1793

Jia, T.-M., Yu, Y.-S., and Li, G.-X. (2017). Experimental investigation of effects of super high injection pressure on diesel spray and induced shock waves characteristics. *Exp. Therm. Fluid Sci.* 85, 399–408. doi:10.1016/j.expthermflusci.2017.03.026

Knox, B. W., Genzale, C. L., Pickett, L. M., Garcia-Oliver, J. M., and Vera-Tudela, W. (2015). Combustion recession after end of injection in diesel sprays. *SAE Int. J. Engines* 8 (2), 679–695. doi:10.4271/2015-01-0797

Liu, H., Ma, S., Zhang, Z., Zheng, Z., and Yao, M. (2015). Study of the control strategies on soot reduction under early-injection conditions on a diesel engine. *Fuel* 139, 472–481. doi:10.1016/j.fuel.2014.09.011

Liu, L, Mei, Q, and Jia, W (2022). A flexible diesel spray model for advanced injection strategy. *Fuel* 314, 122784. doi:10.1016/j.fuel.2021.122784

Matheis, J., and Hickel, S. (2018). Multi-component vapor-liquid equilibrium model for LES of high-pressure fuel injection and application to ECN Spray A. *Int. J. Multiph. Flow* 99, 294–311. doi:10.1016/j.ijmultiphaseflow.2017.11.001

Moiz, A. A., Ameen, M. M., Lee, S.-Y., and Som, S. (2016). Study of soot production for double injections of n-dodecane in CI engine-like conditions. *Combust. Flame* 173, 123–131. doi:10.1016/j.combustflame.2016.08.005

Naruemon, I., Liu, L., Liu, D., Ma, X., and Nishida, K. (2020). An analysis on the effects of the fuel injection rate shape of the diesel spray mixing process using a numerical simulation. *Appl. Sci.* 10 (14), 4983. doi:10.3390/app10144983

Piscaglia, F., Giussani, F., Hèlie, J., Lamarque, N., and Aithal, S. M. (2021). Vortex flow and cavitation in liquid injection: A comparison between high-fidelity CFD simulations and experimental visualizations on transparent nozzle replicas. *Int. J. Multiph. Flow* 138, 103605. doi:10.1016/j.ijmultiphaseflow.2021.103605

Shuai, S., Abani, N., Yoshikawa, T., Reitz, R. D., and Park, S. W. (2009). Evaluation of the effects of injection timing and rate-shape on diesel low temperature combustion using advanced CFD modeling. *Fuel* 88 (7), 1235–1244. doi:10.1016/j.fuel.2009.01.012

Skeen, S., Manin, J., and Pickett, L. M. (2015). Visualization of ignition processes in high-pressure sprays with multiple injections of n-dodecane. *SAE Int. J. Engines* 8 (2), 696–715. doi:10.4271/2015-01-0799

Tay, K. L., Yang, W., Zhao, F., Yu, W., and Mohan, B. (2017). A numerical study on the effects of boot injection rate-shapes on the combustion and emissions of a kerosene-diesel fueled direct injection compression ignition engine. *Fuel* 203, 430–444. doi:10.1016/j.fuel.2017.04.142

Wang, L., Lowrie, J., Ngaile, G., and Fang, T. (2019). High injection pressure diesel sprays from a piezoelectric fuel injector. *Appl. Therm. Eng.* 152, 807–824. doi:10.1016/j.applthermaleng.2019.02.095

Xin, J., Ricart, L., and Reitz, R. D. (1998). Computer modeling of diesel spray atomization and combustion. *Combust. Sci. Technol.* 137 (1-6), 171–194. doi:10.1080/00102209808952050

Yu, S., Yin, B., Jia, H., and Yu, J. (2017). Numerical research on micro diesel spray characteristics under ultra-high injection pressure by Large Eddy Simulation (LES). *Int. J. Heat Fluid Flow* 64, 129–136. doi:10.1016/j.ijheatfluidflow.2017.03.003

Yu, Y. (2019). Experimental study on effects of ethanol-diesel fuel blended on spray characteristics under ultra-high injection pressure up to 350 MPa. *Energy* 186, 115768. doi:10.1016/j.energy.2019.07.098

Yu, Y., Lin, W., Li, L., and Zhang, Z. (2019). Effects of hydrogen addition on the combustion characteristics of diesel fuel jets under ultra-high injection pressures. *Int. J. Hydrogen Energy* 45 (17), 10592–10601. doi:10.1016/j.ijhydene.2019.08.242

Zheng, Z., Yue, L., Liu, H., Zhu, Y., Zhong, X., and Yao, M. (2015). Effect of two-stage injection on combustion and emissions under high EGR rate on a diesel engine by fueling blends of diesel/gasoline, diesel/n-butanol, diesel/gasoline/n-butanol and pure diesel. *Energy Convers. Manag.* 90, 1–11. doi:10.1016/j.enconman.2014.11.011

Nomenclature

ECN engine combustion network
CFD computational fluid dynamics
EOI end of injection
ASI after start of injection
SMD Sauter mean diameter
TKE turbulence kinetic energy
RANS Reynolds-averaged Navier–Stokes
LES large eddy simulations
SGS sub-grid scale
NTC no time counter model
KH Kelvin–Helmholtz instability model
RT Rayleigh–Taylor instability model
NO_x nitrogen oxides
CO carbon monoxide
CO_2 carbon dioxide
$C_{12}H_{26}$ n-dodecane
T_a ambient temperature [K]
P_a ambient pressure [MPa]
ρ_a ambient density [kg/m^2]
T_f fuel temperature [K]
t_{inj} injection time [ms]
m_{inj} injection mass [mg]
P_{inj} injection pressure [MPa]
d_o orifice diameter
$\boldsymbol{C_d}$ steady flow discharge coefficient
Ω maximum growth rate of varicose waves
Λ wavelength
N_2 nitrogen
H_2O water
O_2 oxygen
r_{N_2} nitrogen ratio [%]
r_{H_2O} water ratio [%]
r_{O_2} oxygen ratio [%]
r_{CO_2} carbon dioxide [%]
$\boldsymbol{B_0}$ KH model breakup size constant
$\boldsymbol{B_1}$ KH model breakup time constant
C_τ RT model breakup time constant
C_{RT} RT model size constant
K_{RT} RT model weave number
r droplet radius
τ breakup time
L_b breakup length
C_{bl} breakup length constant
ρ_l fuel density
ρ_g ambient gas density

Frontiers in
Energy Research

Advances and innovation in sustainable, reliable and affordable energy

Explores sustainable and environmental developments in energy. It focuses on technological advances supporting Sustainable Development Goal 7: access to affordable, reliable, sustainable and modern energy for all.

Discover the latest Research Topics

See more →

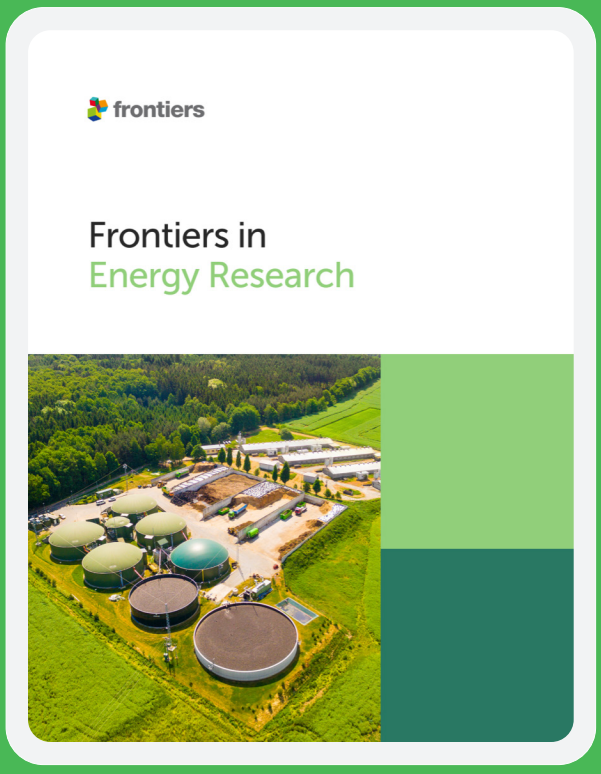

Frontiers

Avenue du Tribunal-Fédéral 34
1005 Lausanne, Switzerland
frontiersin.org

Contact us

+41 (0)21 510 17 00
frontiersin.org/about/contact